Alaska Department of Transportation & Public Facilities

Alaska University Transportation Center

Strain Limits for Concrete Filled Steel Tubes in AASHTO Seismic Provisions

Prepared By:

Nicole King Brown

Dr. Mervyn Kowalsky

Dr. James Nau

North Carolina State University , Raleigh NC

August 2013

Prepared By:

Alaska University Transportation Center
Duckering Building Room 245
P.O. Box 755900
Fairbanks, AK 99775-5900

Alaska Department of Transportation
Research, Development, and Technology Transfer
2301 Peger Road
Fairbanks, AK 99709-5399

INE/AUTC 13.13

FHWA-AK-RD-13-05

REPORT DOCUMENTATION PAGE

Form approved OMB No.

1. AGENCY USE ONLY (LEAVE BLANK)	2. REPORT DATE	3. REPORT TYPE AND DATES COVERED
FHWA-AK-RD-13-05	August 2013	FINAL REPORT (7/2011 – 5/2013)

4. TITLE AND SUBTITLE

Strain Limits for Concrete Filled Steel Tubes in AASHTO Seismic Provisions

5. FUNDING NUMBERS

DTRT06-G-0011
AUTC #510001
T2-11-03

6. AUTHOR(S)
Nicole King Brown
Dr. Mervyn Kowalsky
Dr. James Nau
North Carolina State University, Raleigh NC

7. PERFORMING ORGANIZATION NAME(S) AND ADDRESS(ES)
Alaska University Transportation Center
Institute of Northern Engineering
College of Engineers and Mines
PO Box 755900
Fairbanks, AK 99775-5900

8. PERFORMING ORGANIZATION REPORT NUMBER

INE/AUTC 13.03

9. SPONSORING/MONITORING AGENCY NAME(S) AND ADDRESS(ES)
Research and Innovative Technology Administration (RITA), U.S. Dept. of Transportation (USDOT)
1200 New Jersey Ave, SE, Washington, DC 20590
Alaska Department of Transportation: Research, Development, and Technology Transfer
2301 Peger Road, Fairbanks, AK 99709-5399
Fairbanks North Star Borough ,
P.O. Box 71267, Fairbanks, AK 99707-1267

10. SPONSORING/MONITORING AGENCY REPORT NUMBER

FHWA-AK-RD-13-05

11. SUPPLEMENTARY NOTES

12a. DISTRIBUTION / AVAILABILITY STATEMENT

No restrictions.

12b. DISTRIBUTION CODE

13. ABSTRACT (Maximum 200 words)

Reinforced concrete filled steel tubes (RCFSTs) are commonly used as bridge pipe piles in high seismic regions. The pipe piles in high seismic regions. The pipe-piles consist of reinforced concrete encased in a steel tube. The steel tube is used as a permanent casing which eases construction. The concrete is confined by the steel tube, increasing the compressive strength, and the concrete core prevents the steel tube from buckling inward. This research program presents experimental test performed on twelve large scare RCFSTs. The pipe-piles were subjected to reversed cyclic four-point bending with a constant moment region centered in the pile. The tests focused on two variables: (1) diameter to thickness ration and (2) internal reinforcement ratio. The large scale specimens consisted of outer diameters of 20-24 inches and diameter-to-thickness rations between 33 and 192. The thin walled piles were tested with varying internal reinforcement ratios ranging from 0.78% to 2.43%. The effect of D/t ratio and internal reinforcement ratio on the initiation of buckling and rupture, ductility, damping, and strain compatibility were determined. Analyses were performed to compare the curvature distribution and plastic hinge length of RCFSTs and convention reinforced concrete columns. A finite element model was created to capture the monotonic response of the specimens.

14. KEYWORDS :
Reinforced concrete pipe (Rbmdxnpcr), Strain measurement (Gmck), Earthquake resistant design (Esdc)

15. NUMBER OF PAGES
340

16. PRICE CODE
N/A

17. SECURITY CLASSIFICATION OF REPORT	18. SECURITY CLASSIFICATION OF THIS PAGE	19. SECURITY CLASSIFICATION OF ABSTRACT	20. LIMITATION OF ABSTRACT
Unclassified	Unclassified	Unclassified	N/A

Notice

This document is disseminated under the sponsorship of the U.S. Department of Transportation in the interest of information exchange. The U.S. Government assumes no liability for the use of the information contained in this document.

The U.S. Government does not endorse products or manufacturers. Trademarks or manufacturers' names appear in this report only because they are considered essential to the objective of the document.

Quality Assurance Statement

The Federal Highway Administration (FHWA) provides high-quality information to serve Government, industry, and the public in a manner that promotes public understanding. Standards and policies are used to ensure and maximize the quality, objectivity, utility, and integrity of its information. FHWA periodically reviews quality issues and adjusts its programs and processes to ensure continuous quality improvement.

Author's Disclaimer

Opinions and conclusions expressed or implied in the report are those of the author. They are not necessarily those of the Alaska DOT&PF or funding agencies.

SI* (MODERN METRIC) CONVERSION FACTORS

APPROXIMATE CONVERSIONS TO SI UNITS

Symbol	When You Know	Multiply By	To Find	Symbol
		LENGTH		
in	inches	25.4	millimeters	mm
ft	feet	0.305	meters	m
yd	yards	0.914	meters	m
mi	miles	1.61	kilometers	km
		AREA		
in^2	square inches	645.2	square millimeters	mm^2
ft^2	square feet	0.093	square meters	m^2
yd^2	square yard	0.836	square meters	m^2
ac	acres	0.405	hectares	ha
mi^2	square miles	2.59	square kilometers	km^2
		VOLUME		
fl oz	fluid ounces	29.57	milliliters	mL
gal	gallons	3.785	liters	L
ft^3	cubic feet	0.028	cubic meters	m^3
yd^3	cubic yards	0.765	cubic meters	m^3
		NOTE: volumes greater than 1000 L shall be shown in m^3		
		MASS		
oz	ounces	28.35	grams	g
lb	pounds	0.454	kilograms	kg
T	short tons (2000 lb)	0.907	megagrams (or "metric ton")	Mg (or "t")
		TEMPERATURE (exact degrees)		
^oF	Fahrenheit	5 (F-32)/9 or (F-32)/1.8	Celsius	^oC
		ILLUMINATION		
fc	foot-candles	10.76	lux	lx
fl	foot-Lamberts	3.426	$candela/m^2$	cd/m^2
		FORCE and PRESSURE or STRESS		
lbf	poundforce	4.45	newtons	N
lbf/in^2	poundforce per square inch	6.89	kilopascals	kPa

APPROXIMATE CONVERSIONS FROM SI UNITS

Symbol	When You Know	Multiply By	To Find	Symbol
		LENGTH		
mm	millimeters	0.039	inches	in
m	meters	3.28	feet	ft
m	meters	1.09	yards	yd
km	kilometers	0.621	miles	mi
		AREA		
mm^2	square millimeters	0.0016	square inches	in^2
m^2	square meters	10.764	square feet	ft^2
m^2	square meters	1.195	square yards	yd^2
ha	hectares	2.47	acres	ac
km^2	square kilometers	0.386	square miles	mi^2
		VOLUME		
mL	milliliters	0.034	fluid ounces	fl oz
L	liters	0.264	gallons	gal
m^3	cubic meters	35.314	cubic feet	ft^3
m^3	cubic meters	1.307	cubic yards	yd^3
		MASS		
g	grams	0.035	ounces	oz
kg	kilograms	2.202	pounds	lb
Mg (or "t")	megagrams (or "metric ton")	1.103	short tons (2000 lb)	T
		TEMPERATURE (exact degrees)		
^oC	Celsius	1.8C+32	Fahrenheit	^oF
		ILLUMINATION		
lx	lux	0.0929	foot-candles	fc
cd/m^2	$candela/m^2$	0.2919	foot-Lamberts	fl
		FORCE and PRESSURE or STRESS		
N	newtons	0.225	poundforce	lbf
kPa	kilopascals	0.145	poundforce per square inch	lbf/in^2

*SI is the symbol for the International System of Units. Appropriate rounding should be made to comply with Section 4 of ASTM E380.
(Revised March 2003)

List of Figures

List of Tables

Acknowledgements

The authors wish to acknowledge Alaska DOT&PF and Alaska University Transportation Center (AUTC) who supported this research through a series of grants. Special acknowledgement goes to Elmer Marx of Alaska DOT&PF who was closely involved in this research as the primary technical contact. Lastly, the assistance of the entire staff of the Constructed Facilities Laboratory is greatly appreciated.

Abstract

Reinforced concrete filled steel tubes (RCFSTs) are commonly used as bridge pipe piles in high seismic regions. The pipe-piles consist of reinforced concrete encased in a steel tube. The steel tube is used as a permanent casing which eases construction. The concrete is confined by the steel tube, increasing the compressive strength, and the concrete core prevents the steel tube from buckling inward.

This research program presents experimental tests performed on twelve large scale RCFSTs. The pipe-piles were subjected to reversed cyclic four-point bending with a constant moment region centered in the pile. The tests focused on two variables: (1) diameter-to-thickness ratio and (2) internal reinforcement ratio. The large scale specimens consisted of outer diameters of 20 to 24 inches and diameter-to-thickness ratios between 33 and 192. The thin walled piles were tested with varying internal reinforcement ratios ranging from 0.78% to 2.43%. The effect of D/t ratio and internal reinforcement ratio on the initiation of buckling and rupture, ductility, damping, and strain compatibility were determined.

Analyses were performed to compare the curvature distribution and plastic hinge length of RCFSTs and convention reinforced concrete columns. A finite element model was created to capture the monotonic response of the specimens.

Summary of Findings

Twelve large-scale reinforced concrete filled steel tubes (RCFSTs) were experimentally tested to determine the effect of diameter – to – thickness ratio and internal reinforcement ratio on the behavior of the pipe pile. D/t ratios of 33 to 192 were tested and internal reinforcement ratios of 0.78%, 1.67% and 2.43% were evaluated in the thinner pipes (D/t from 160 to 192). A six foot constant moment region was created with two point loads in the center of the specimens. All specimens were subjected to reversed cyclic loading to failure.

Typical behavior of the pipe piles consisted of outward buckling of the steel tube in the constant moment region. The buckles increased in size as the deformation of the pile increased until rupture of the pipe. Results showed that the diameter-to-thickness ratio of the section influenced the initiation of local buckling of the steel pipes. The thinner pipes buckled at lower levels of displacement and deformation than the thicker pipes. The thinnest pipe, with a D/t ratio of 192 buckled right after first yield while the thickest pipe, with a D/t ratio of 33 did not buckle until ductility four. Although the thinner pipes buckled earlier, all of the tests ruptured at approximately the same ultimate strain and curvature. Thus, the rupture, and hence ultimate capacity, of the pipe was independent of D/t ratio.

The D/t ratio also affected the shape of the hysteretic response and thus the energy dissipation and damping of the system. The thinner pipes had extensive local buckling in the constant moment region and had "pinched" hysteresis. The thicker pipes had less local buckling throughout the constant moment region and as a consequence less "pinching" in the hysteresis. As a result, the thicker pipes had higher energy dissipation and higher levels of damping.

The internal reinforcement ratio had no effect on the overall behavior of the piles. The specimens buckled and ruptured at the same level of deformation and the hysteretic loops resulted in the same amount of energy dissipation.

Strains prior to buckling were compatible along the cross section, but were non-linear after the steel tube suffered local buckling, as expected. However due to the cyclic loading, the stresses in the section remained linear. Thus, predicting section capacities assuming strains were compatible and plane sections remained plane resulted in accurate predictions, even after the onset of local buckling.

Analyses were performed to compare the plastic hinge length due to the curvature distribution for conventional and reinforced concrete filled steel tubes. The curvature distributions were similar for the two types of cross sections resulting in approximately the same plastic hinge lengths. Lastly, a finite element model was created to capture the monotonic response of the RCFSTs, however more work needs to be done in order to capture the cyclic response and damage initiation.

CHAPTER 1 - INTRODUCTION

2.1. Background

Concrete filled steel tubes are used in a variety of structures including bridge columns, high rise buildings, and power plants. They are often used in structures where large moments and displacements must be resisted, such as in high seismic regions. They have many advantages over conventional reinforced concrete and hollow steel tubes.

The composite system combines the high tensile strength and ductility of steel with the compressive strength and stiffness of concrete. The steel tube is located at the perimeter of the section, where it is most effective in resisting moments and increases the moment of inertia of the system. The concrete core is confined by the steel which increases its compressive strength and ductility. The expansion of the concrete delays the buckling of the steel by not allowing it to buckle inward. The system also has high displacement capacity and energy dissipation which is favorable for seismic design. The composite construction has economic and construction benefits. The steel tube serves as formwork for the column which allows the structure to be constructed more easily and quickly, reducing labor costs.

Concrete filled steel tubes (CFSTs) have been constructed for over 50 years and have become increasingly more common in a variety of structures as the behavior of this system is becoming better understood. Their primary use has been in axial applications, but as understanding of their flexural behavior and other advantages increases, they are being used more commonly in high seismic areas. CFSTs are currently used all over the world in a variety of structures. Over 200 arch bridges in China have been constructed with concrete filled tubes, such as the Hanjiang Bridge in Wuhan City (Chen & Wang, 2009). They have also been utilized in bridges throughout Alaska.

There has been substantially less research conducted on (and fewer field applications of) concrete filled tubes with internal reinforcement, referred to as reinforced concrete filled steel tubes (RCFSTs). The study of RCFTSs is important for several reasons. First, there is little research available focused on pipes with relatively thin walls (i.e. relatively large D/t ratios) where the internal reinforcement could have more of an impact on behavior since it represents a larger proportion of the total steel area. Also, internal reinforcement in relatively thin-walled pipes is necessary in case of corrosion of the steel wall.

Although RCFST columns are less common than CFSTs, an example of their use in the O'Malley Bridge in Alaska is shown in Figure 1-1. In this example, the pipe pile serves as a column above ground and as the foundation below grade. This research focused on these pipe-pile systems with internal reinforcement. They can be constructed either as drilled shafts (for thinner pile sections), or as driven piles (for thick walled sections). In each case, the pipes are filled with reinforced concrete. Under the effect of seismic forces, these piles develop two potential plastic hinges (locations of damage). The first will most likely occur at the top of the column, at the pile-cap interface. At this location, there is a gap between the

steel tube and the cap and thus the internal reinforcement provides the necessary flexural strength in this location. The second plastic hinge forms below ground, where the steel tube also contributes to the flexural strength of the system. The behavior of the plastic hinge at the top of the column is well-understood and can be designed for; the plastic hinge located underground is less understood and is the focus of this research.

Figure 1-1: O'Malley Bridge (Courtesy of Elmer Marx)

2.2. Research Objective

Available research has shown that Concrete Filled Steel Tubes (CFSTs) and Reinforced Concrete Filled Steel Tubes (RCFSTs) have satisfactory performance but many questions remain about their behavior. These questions include: (1) the impact of internal reinforcing steel on the behavior of the pile-column, (2) the accuracy of analysis methods in predicting moment-curvature and force-displacement responses, (3) the impact of the ratio of tube diameter to tube thickness ratio (D/t ratio) on strain limits associated with serviceability, repairable and ultimate response, and (4) the plastic hinge length for the below-ground plastic hinge developed in the pile-column.

2.3. Scope

The research program was initiated with a thorough literature review to determine the current state of knowledge of CFSTs and RCFSTs. The experimental portion of the research consisted of twelve large-scale tests, tested in reversed cyclic four-point bending, with a constant moment region in the center of each specimen. The tested piles differed in D/t ratio and internal reinforcement ratio. Test results were examined to determine the strains

associated with various limit states, the moment-curvature response, and the ductility. A finite element model was created to capture the monotonic response of the specimen although more work needs to be performed on the model to capture the response of the specimens under cyclic loading. Lastly, the experimental results were used to guide the development of design recommendations.

2.4. Layout of Document

This document will begin with an overview of past research performed on concrete filled steel tubes, with and without internal reinforcement (Chapter 2). Observations and photographs of all twelve experimental tests will be shown in Chapter 3. Chapter 4 will contain data analysis from the experimental tests, and the results will be explained and compared on the basis of D/t ratio and internal reinforcement ratio. After the results of the experimental portion of the research program, the plastic hinge length compared to a conventional reinforced concrete column will be explored in Chapter 5. The progress of the finite element model under monotonic and cyclic load histories will be explained in Chapter 6. Chapter 7 will conclude the thesis with a summary of the results, design recommendations and recommendations for future research.

CHAPTER 2 - LITERATURE REVIEW

Literature on the subject of "Concrete Filled Steel Tubes" is vast and dates back to the 1950s, as noted by Park (1983) and Knowles (1969). Although there has been substantial research on rectangular concrete filled steel tubes, it is not relevant to this research and will not be included. The focus of past research can be divided into five areas: (1) Axial loading, (2) Level of confinement, (3) Strain compatibility, (4) D/t ratio, and (5) Internal reinforcement ratio.

2.1. Axial Loading

The primary use of Concrete Filled Steel Tubes has been as compression members and thus, the majority of research surrounding these specimens applied axial load to the specimen. The literature covered varied axial load and its effect on specimen behavior is included in this section. The literature wherein axial load is held constant and other parameters are varied will be discussed later.

Fam et al. (2004) tested five short column CFSTs, 457 mm long, 152 mm in diameter and 3.12 mm thick resulting in a diameter-to-thickness ratio of 49. The specimens had two loading configurations: one column was loaded across its entire cross section, and the remainder of the tests loaded only the concrete core. The column loaded across the composite section had a lower yielding load but the loading method had less than 3% difference on the axial capacity of the column. The study also consisted of five beam-column tests, with the same variation in axial load application and a cyclic lateral load applied at mid-span. In both loading scenarios, an increase in compressive axial load increased the lateral capacity of the system. When the composite section was loaded, an increase in axial load decreased the yield moment of the section, and when the concrete core was loaded there was no significant change in the yield moment. (Fam, Quie, & Rizkalla, 2004).

Elremaily et al (2002) performed two-third scaled experiments on CFSTs with a constant axial load and lateral seismic loads. The project consisted of ten tests with many variables; however the CFSTs in all performed in a ductile manner with high energy dissipation, which is favorable for seismic design. Considering only the impact of axial load, the columns with higher axial compressive load resulted in higher ultimate moment capacity, as agrees with the experiments of Fam, et al (2004). (Elremaily & Azizinamini, 2002).

2.2. Level of Confinement

The steel tube in a CFST provides confinement to the concrete core. Researchers accept that the confinement effect of a steel tube is higher than that of a conventional reinforced concrete system. Many projects have attempted to quantify the additional increase in confinement in the system. In typical reinforced concrete sections, Mander's model is the most common method of calculating the confined concrete strength and assumes that the transverse steel

yields at the ultimate moment. The confined strength using Mander's model is shown in Equation 2-1 (Priestley, Calvi, & Kowalsky, 2007).

$$\mathbf{f_{cc} = f_{c0}(-1.254 + 2.254\sqrt{1 + \frac{7.94f_l}{f_{c0}}} - \frac{2f_l}{f_{c0}})} \qquad \textbf{Equation 2-1}$$

Elremaily et al. (2000) determined that assuming the transverse steel yields was not appropriate for CFSTs due to the biaxial state of stress in the tube. Although they performed six experimental tests, the lateral strains were not able to be measured in the experimental setup. To calculate the confinement effect, they assumed that the pipes did not yield in the transverse direction and used the Von Mises criterion for steel to calculate the corresponding longitudinal stresses for a chosen transverse stress. Using a range of lateral stresses less than yield, they used Mander's model to calculate the confined stress-strain curve of the concrete. After their analysis, they recommended that a hoop stress of 0.1Fy is appropriate for CFSTs. (Elremaily & Azizinamini, 2002).

Chitawadagi et al (2009) predicted the confinement of the concrete core using the confinement factor and flexural strength index proposed by Han-Lin in 2004. Han-Lin summarized a variety of past experimental tests to quantify a value for confinement of the concrete core. The expression for the confinement factor (ξ) is shown in Equation 2-2. The confinement factor was then used to calculate the flexural strength index, which was used to calculate the flexural strength of the section as shown below in Equation 2-3. The additional steel provided by a CFST increased the confinement factor, which also increased the strength and ductility of a system, as would be expected. (Chitawadagi & Narasimhan, 2009).

$$\xi = (A_s f_{sy})/(A_c f_{ck}) \qquad \textbf{Equation 2-2}$$

$$\gamma_m = 1.1 + 0.48\ln(0.1 + \xi) \qquad \textbf{Equation 2-3}$$

$$M_u = \gamma_m W_{scm} f_{scy} \qquad \text{Equation 2-4}$$

Rupp et al (2012) summarized five axial load test results on CFSTs tested between 1987 to 2000. The first model created by Zhong and Miao in 1987, divided the response into three sections. The first portion is linear and occurs before the steel tube yields, after yield of the tube they performed ultrasonic tests to prove that the concrete crushes inside of the tube and the concrete strength almost plateaus. The model created by Cai in 1987 was also divided into three parts. However, Cai stated that before the concrete cracks, the steel tube has no restraining effect on the concrete. As the compressive longitudinal strains increase, the transverse strains also start to increase. The concrete core will begin to expand outward, applying a lateral stress against the tube and thus, the tube begins to confine and strengthen the concrete. From this point until yielding, the stress-strain curve is relatively linear. After the steel tube yields, the stiffness decreases but the concrete continues to increase in strength. The increase in strength after yield depends upon the thickness of the tube; the thicker the tube, the higher the increase in strength. (Rupp, 2012).

In 2001, Susantha et al. created an empirical model based on multiple tests. In 2008, Hatzigeorgiou built on the tests by Susantha et al. (2001) with additional experimental tests and analytical results, and created a stress-strain response that was also divided into three distinct sections. The first was linear until the steel yields; in the second, the stress increases parabolically until the peak compressive stress; in the third, the stress decreases until crushing. The peak compressive stress was calculated by summing the compressive stress of the unconfined concrete and a factor dependent on the transverse stress reached in the tube. In 2000, O'Shea and Bridge adjusted the constants in the Mander model equation for the compressive strength to match test results. The resulting equation is shown in Equation 2-5 and the definitions of the variables are expressed in Equation 2-6 through Equation 2-8. (Rupp, 2012).

$$f_{cc} = f_{c0}\left(-1.228 + 2.172\sqrt{1 + \frac{7.46f_l}{f_{c0}}} - \frac{2p}{f_{c0}}\right) \quad \textbf{Equation 2-5}$$

$$\mathbf{p = p_{yield}\left(0.7 - \sqrt{\frac{f_c}{f_y}}\right)\left(\frac{10}{3}\right)} \quad \textbf{Equation 2-6}$$

$$\mathbf{p_{yield} = \frac{2f_y t}{D}} \quad \textbf{Equation 2-7}$$

$$\mathbf{\varepsilon_{cc} = \varepsilon_c\left(1 + (8 + 0.05f_c)\left(\frac{p}{f_c}\right)\right)} \quad \textbf{Equation 2-8}$$

The interesting facet from this model that is not shown in the other models is the impact of the concrete strength on the lateral stress in the tube and on the ultimate confining strain. Rupp evaluated the effectiveness of these models with experimental tests. The model created by Zhong and Miao (1987) was most accurate, however, it only predicted the ultimate strength (not the overall response). The models created by Susantha (2001) and O'Shea (2000) were not as accurate as the model created by Zhong and Miao (1987) but they did predict the stress-strain curve of the confined core. The model created by Hatzigeorgiou (2008) was found to only be accurate for a small range of columns and was not recommended to be used to predict the confinement in a CFST. (Rupp, 2012).

A series of tests was performed by Fam et al. (2004) tested 5 short columns in axial compression, and an additional 5 columns were subjected to axial compression and reversed cyclic lateral load. The five axial compression tests examined the effect of the tube-core bond and the loading conditions (pipe and core, or core only). All specimens had a D/t ratio of 49. The authors concluded that the loads were higher in the case of columns where only the core was loaded. This was attributed to the higher level of confining stress. When both the pipe and core were loaded, the pipe compressed and expanded, thus reducing the confining stress, as opposed to the case where only the core is loaded, which mobilized higher levels of radial stress in the pipe. As was the case for the work of Elremaily et al. (2002), Fam et al. also applied the Von Mises yield surface to characterize the longitudinal strain in the steel for

bonded specimens, and specimens subjected to core and pipe loading. (Fam, Quie, & Rizkalla, 2004).

Park et al. (1987) studied the multi-axial stress state of concrete filled steel tubes. He created a lateral interaction model based on thirty-three tests performed by Tomii et al. Tomii et al. tested specimens with D/t ratios ranging from 19 to 75. The researchers did not specify how the strains on the specimens were measured, however, they were able to measure longitudinal and lateral strains on the outer surface of the steel tube. They loaded the specimens axially in compression; and in tension. In these tests, the lateral strains were about 75% of the longitudinal strains, reaching values of about 3%. The thin-walled pipes resulted in higher lateral strains than the thick-walled pipes. From these test results, Park created two lateral interaction models: one for the specimens in tension axial loading and one for the specimens in axial compression loading. Park recognized a multi-axial stress state exists in the system due to the lateral confining strains and lateral strains induced by the longitudinal strains and Poisson's ratio and included this in the lateral interaction models. (Park, 1983).

When the specimens were loaded in tension, the steel tube attempts to contract laterally more than the concrete due to a higher Poisson's ratio in the steel. As the tension strains create cracks in the concrete core, the strain gradient over the length of the specimen changes. The longitudinal strains and stresses are higher in the steel tube at the location of the concrete cracks. Park's lateral interaction model accounts for the change in longitudinal strains and assumes the strains are compatible across multiple sections. He acknowledges two limitations of this model. The first is this model was created based on results from small-scale tests, and there was minimal shrinkage of the concrete core. In a larger specimen, the shrinkage in the concrete would be larger and may result in a gap between the steel tube and the concrete. The second limitation that Park noted was that the model was created only for axial tension loading and cannot be applied to sections with lateral loading. (Park, 1983).

Park created a similar model for concrete filled tubes under axial compression. Under low loads, before yield, a small gap will develop between the tube and the core because the Poisson's ratio of the steel tube is initially larger than that of the concrete core. As the load increases, the Poisson's ratio of the concrete increases more quickly than that of the steel, closing the gap between the material. Once the gap is closed, the concrete core will begin to push laterally against the steel tube. (Park, 1983).

As mentioned earlier, the level of confinement provided by a steel tube is much higher than the level provided in a typical reinforced concrete section. Mander's model overestimates the confined concrete stress when the core is confined by a steel tube. In compression loading, the confining effect of the steel tube is delayed since a small gap forms between the two materials under low loads. Mander's model does not take this phenomena into account which leads to an underestimation of the strain at maximum stress. The strain at maximum stress differs based on the diameter-thickness ratio of the tube. A smaller gap forms in the thinner piles and the confining effect begins earlier leading to a lower strain at maximum stress than a thicker pile where the confining effect is delayed longer. However, as expected,

thicker piles confine the concrete core more and increase the compressive strength more than do thinner piles. (Park, 1983).

Park created the lateral interaction models based on test results by Tommii et al. and checked the results by performing tests of his own with a diameter to thickness ratio of 25.6. He performed tests under three different loading conditions: monotonic compression, monotonic tension, and cyclic tension and compression. Park compared the compression interaction model created with uniaxial compression tests with a diameter to thickness ratio of 25.6. He observed that the lateral strains reached about 80% of the longitudinal strains at ultimate strength, however he did note that before yield the lateral strains were 30%-60% of the corresponding longitudinal strains. These lateral strains are higher than that seen in empty tubes due to the expansion and confinement of the concrete core. When the specimens were placed in tension, the lateral strains were 10%-30% of the longitudinal strains. He found that the lateral interaction model he created for both compression and tension worked well when the longitudinal strains are below 8%, after this point the longitudinal stresses were over-estimated and the lateral stresses were under-estimated. This was attributed to assuming a constant longitudinal stress at a high strain in the lateral interaction model. (Park, 1983).

2.3. **Strain Compatibility**

Strain compatibility between the concrete core and the steel tube implies perfect bond between the steel and the concrete. Current analysis methods for predicting moment-curvature responses and force-displacement responses are based on the assumption that strains are compatible throughout the section. One of the problems addressed by the current research is whether strain compatibility exists in concrete filled steel tubes (with and without internal reinforcement), and whether current analysis methods accurately predict the response of the member. Many researchers have assumed strain compatibility in calculating flexural strengths, and have found that their predictions match well with the experimental results. However, measuring strains inside the concrete core are difficult and there have been few tests which measure strains both inside the core and on the surface of the steel tube to prove this assumption.

In 2004, Bruneau and Marson compared a database of tests to the provisions in various codes calculating flexural strength; they found the codes were generally conservative. They developed a model with closed form solutions for moment strength, based on traditional principles of equilibrium and compatibility. While they did not present detailed data comparing their model to past tests, they did indicate that their model resulted in an average ratio of experimental to predicted strength of 1.38, with a standard deviation of 0.8. Their model is the basis for the current hand calculation methods in the AASHTO Guide Specifications for LRFD Seismic Bridge Design. (Marson & Bruneau, 2004).

In addition to the closed form solutions to calculate flexural strength, Section 7.6 of the AASHTO seismic guide specifications for concrete filled steel pipes allows the use of strain compatibility and equilibrium which applies to all sections, assuming bond between the steel

tube and concrete core. This section is only applicable for pipes without internal reinforcement.

Aly et al. (2010) utilized a section analysis approach employing the usual assumptions of equilibrium and compatibility and obtained good agreement with their test data. They utilized a stress-strain curve for confined concrete whose origin is not immediately obvious; however, it does include the effect of confinement on the strain capacity of the concrete. (Thayalan, Aly, & Patnaikuni, 2009).

Gonzalez et al. (2008, 2009) tested 18 large-scale concrete filled pipe piles with internal reinforcement under four point reversed cyclic loading. Of the 18 tests, 10 were 24" in diameter and 39' long, while the remaining 8 specimens were 12" in diameter and 20' long. The primary purpose of these tests was to study the impact of the spiral welding manufacturing process on strength and ductility. As a consequence, all 18 tests had the same D/t ratio of 48. Envelope predictions of the hysteretic response were conducted using moment curvature analysis with the usual assumptions of strain compatibility and equilibrium. Accuracy of the predicted response can be seen in Figure 2-1. (Gonzalez Roman, Kowalsky, Nau, & Hassan, 2008).

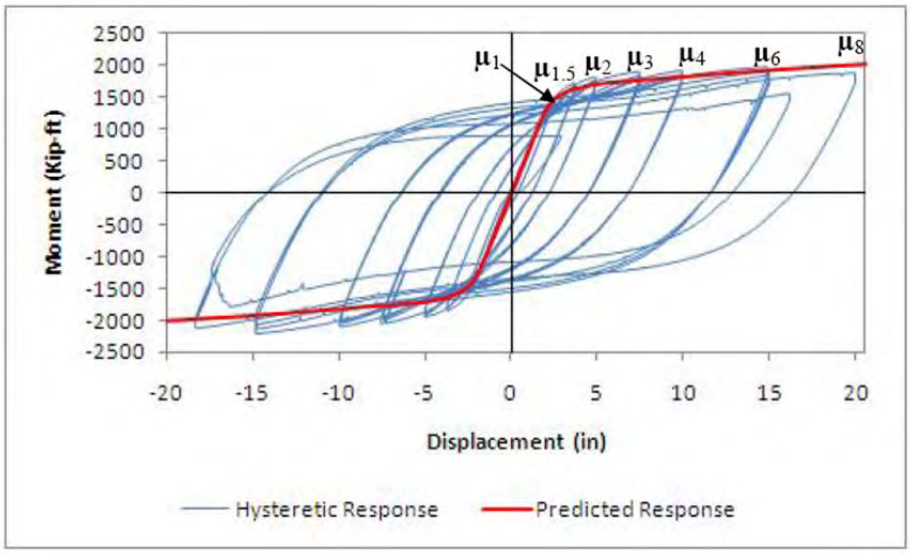

Figure 2-1: Typical force-displacement response and envelope prediction for concrete filled pipe pile with internal reinforcement (Gonzalez, 2008).

The bond between the steel tube and concrete core creates strain compatibility. There have been many studies on the bond between the shell and core, the majority of which have been tested under axial loading with different conditions on the interior of the steel tube.

In 1968, Furlong conducted a series of tests on concrete filled steel tubes under different bonding and loading conditions. The interior of the steel tubes were either greased or non-greased and the specimens were either subjected to pure axial or pure bending loads. As expected, the curves for the greased (unbonded) and non-greased (bonded) were very close for the axial load tests since both of the specimens are expected to have the same longitudinal strains. The two curves were also very similar for the flexural tests, which the researchers found surprising. Based on these results, they concluded that bond provided little or no strength contribution to the system, and the strength came from the physical pressure between the steel tube and the concrete core. (Furlong, 1968).

Virdi and Dowling performed "push-out" tests in 1975. They concluded that the bond strength was a function of interlock caused by surface roughness and variation of the circular cross section. They appear to be the first researchers to propose a bond strength, which they reported to be 145 psi. (Virdi & Dowling, 1975).

Twelve concrete filled steel beams were tested by Lu and Kennedy (1992) under monotonic four point bending. It is important to note that these were rectangular sections approximately 150 mm in width but the results are valuable to this research. The instrumentation used was able to measure the slip between the steel and concrete. No appreciable slip occurred and the slip remained relatively small until the maximum moment was reached, when slip of 0.5 mm to 1 mm occurred. They observed "slip" in the constant moment region and attributed this to the relative movement between the steel and the concrete when the steel buckled and the concrete crushed. Foil type electrical resistance strain gages measured the strains on the steel tube and strains in the concrete core were measured between Demec points fastened to the concrete in the compression zone. The strains on the steel tube and inside the concrete core agreed with one another and the researchers concluded that the section behaves as a composite section and the strains were compatible across the different materials. (Lu & Kennedy, 1992).

In 1999, Kilpatrick and Rangan tested CFSTs under three different bond conditions: maximum bond, partial bond and minimum bond. The maximum bond condition was created by inserting screws through the thickness of the steel tube and into the concrete core, acting as shear studs; the specimen was then treated in an acid bath, and alkaline bath to improve the chemical bond between the steel and concrete. The partial bond condition was created by removing the grease on the interior of the steel tube. The interior of the steel tube was greased to create a minimum bond between the two materials. The test results showed that the bond conditions had almost no effect on the axial load capacity of the specimens and a small effect (less than 8%) on the flexural capacity of the section. These tests were small-scale (102 mm in diameter) and the researchers cautioned that in larger sections the shrinkage of the concrete could lead to a gap between the core and the shell and this could lead to a reduction in composite action, however this gap would likely be closed by concrete expansion. (Kilpatrick & Rangan, 1997).

In 2006, Nezamian et al. studied the bond between the steel and concrete by performing pull-out tests, push-out tests and cyclic tests on fifteen reinforced concrete-filled steel tubes with different concrete plug lengths. In the first phase of their work, pull-out tests were done on each configuration, and then axial cyclic tests were conducted on identical test units at 25 to 40% of the ultimate pull-out strength. The second phase of work consisted of the same procedure except with push-out tests. The axial cyclic tests were then concluded with a pull-out test to failure. In the pull-out tests, the loads were applied by pulling on the internal rebar. For the push-out portion, only the concrete was pushed with a steel plate. They measured the bond strength and the maximum slip of each test. The cyclic tests resulted in lower bond strengths than the push out and pull out bond strengths. The static pull-out bond strength was 4.27 MPa, the static push out bond strength was 2.37 MPa and the cyclic bond strengths were 2.77MPa and 1.70MPa. These values are significantly higher than values reported by past research; the researchers attributed this to the presence of internal reinforcement and the use of a smaller concrete plug. The slips measured in the cyclic portion of the tests were quite low (less than 1 mm), however the slip did increase as the bond strength decreased with more cycles. (Nezamian, R., & P., 2006).

Elchalakani et al (2001) conducted extensive tests on small-scale concrete-filled steel tubes. The researchers observed no visible slip and their model, which measured strains both inside the core and on the tube, indicated no slip. Their predictions assuming no slip agreed with the experimental flexural response of the specimens. (Elchalakani, Zhao, & Grzebieta, 2001)

Roeder investigated the bond stress and level of composite action of CFSTs in bending. The researchers performed 20 large-scale experimental tests investigating the effect of the diameter, thickness and shrinkage on the bond stress between the steel tube and the concrete core. The slip between the two materials at the ultimate load was approximately 0.25 mm, which is about 0.1% of the outer diameter. The researchers also found that larger diameters and larger D/t ratios decreased the compatibility between the shell and the core. In a following project, Roeder et al. greased the interior of some of the steel tube casing and found that even when greasing the interior of the shell, the bearing provided by bending was enough to ensure composite action. (Roeder, Cameron, & Brown, 1999).

Park (1987) performed moment curvature analyses to create theoretical monotonic envelopes and compared these to experimentally obtained cyclic responses. In these calculations multiple assumptions were made: (1) plane sections remain plane, (2) strains are linear across the section, (3) perfect bond exists between casing, longitudinal reinforcement and concrete, (4) local buckling of the steel casing was assumed not to alter the stress-strain characteristics of this material. The researchers developed a lateral interaction model which was used to model the confined stress-strain curve of the concrete core. In general, the envelope of the experimental responses was in good agreement with the theoretical response. Lateral force deflection predictions were also created and had good agreement with the experimental responses. However, it will be noted that the specimens Park tested had steel end plates welded to both sides of the specimens which could have forced strain compatibility within the section. (Park, 1983).

2.4. **D/t Ratio**

It has been well established that slenderness parameters influence the capacity to develop full moment strength in hollow steel tube sections. In the case of these hollow steel tube sections, the current AASHTO Guide Specifications for LRFD Seismic Bridge Design require a hollow pipe maximum D/t of 0.09E/Fy for essentially elastic elements, and 0.044E/Fy for ductile elements. For typical values of E and Fy (29,000 ksi and 50 ksi, respectively) this implies D/t limits of 52 (elastic) and 26 (ductile). While these limits may be suitable for hollow sections, they are likely overly-conservative for concrete-filled sections (Boyd, Cofer, & McLean, 1995).

Boyd investigated the flexural behavior of five CFSTs subjected to a constant axial load and reversed cyclic load. All the specimens were 8 inches in diameter and had D/t ratios of 73 and 107. The researchers found the steel shell increased the energy dissipation when compared to conventional reinforced concrete columns. They also found a thicker shell resulted in a higher flexural strength and energy dissipation than those with a thinner shell. However, the piles with higher D/t ratios resulted in a higher deformation capacity. This is not what was expected and the researchers attributed the higher deformation capacity to the steel pipe having a higher ductility than the thicker pipe. (Boyd, Cofer, & McLean, 1995).

Bruneau and Marson (2004) tested four CFST bridge columns with diameters ranging from 324 mm to 406 mm and diameter – to – thickness ratios of 31, 42, 51, and 64. Unlike the tests performed by Boyd, the thicker pipes had a higher deformation capacity than those of the thinner pipes. In specimens with D/t ratios of 34, 42, and 64 buckling occurred at drifts of 2% and 3%. The thicker pipe (D/t = 34) buckled at 3% drift, one cycle later than the tests with D/t ratio of 42 and 64, which showed signs of buckling at 2%. The test with a D/t of 51 showed signs of buckling at 0.75% drift, the researchers noted that this was unexpected but offered no insight into the inconsistency when compared to the other tests. The tests with D/t ratios of 42 and 64 ruptured at a drift of 7%, the test with a D/t ratio ruptured at a drift of 6% and the testing equipment stopped working during the test with a D/t ratio of 34 and the test was not completed. As a summary, the thicker pipes buckled later but all the tests ruptured at approximately the same drift much higher than the buckling drifts. (Marson & Bruneau, 2004).

Chitawadagi et al. (2009) tested nine piles ranging in D/t ratio from 22 to 51 and three concrete strengths. The small-scale specimens, with diameters ranging from 44mm to 64mm, were tested under flexure to examine the flexural strength and deformation capacity. The researchers defined the Strength Increased Factor (SIF) as: SIF= (MCFT – M-Hollow)/Mcore. There was a nonlinear variation between SIF and the D/t ratio, and the lower D/t ratios had a higher SIF. The ultimate curvatures varied over the range of tests but there seemed to be no correlation between the D/t ratios. (Chitawadagi & Narasimhan, 2009).

Elchalakani et al. (2001) conducted multiple research projects to examine the effect of the diameter – to – thickness ratio on the performance of CFSTs. The first in the series of

project tested specimens 1500mm in length with D/t ratios ranging from 12 to 110 in pure bending. The specimens with D/t ratios ranging from 12 to 32 had approximately the same maximum rotation. With D/t ratios larger than 32 the maximum rotation capacity decreased rapidly with decreasing wall thickness, at a D/t of 110 the rotation capacity was about 15-20% of the rotation capacities of the thicker walled pipes. The concrete prevented buckling in tests with a D/t ratio less than 40 and small ripples appeared over the length of the specimens with D/t ratios from 70 to 110. They concluded that the thinnest pipe they tested (D/t ratio of 110) was sufficient to develop the plastic moment capacity of the section. (Elchalakani, Zhao, & Grzebieta, 2001).

The second of relevant research projects performed by Elchalakani et al. (2004) consisted of small-scale cyclic bending tests on different CFTs with D/t ratios ranging from 20 to 162. The specimens began to form plasticity in the early cycles, the ripples continued to grow with cycling until the tube fractured accompanied with concrete crushing. The CFSTs in this project reached an average ductility of 9.6 before rupture. (Elchalakani, Zhao, & Grzebieta, 2004).

Elchalakani et al. (2008) continued to research CFSTs in 2008 with 10 tests ranging in D/t ratio from 32 to 120. The specimens were subjected to variable amplitude Incrementally Increased Cyclic Loading. The moment strength of the specimens were under predicted by the AISC-LRFD and the Architectural Institute of Japan codes, however, the Eurocode prediction was more accurate. The ultimate rotational capacities of the specimens had a linear relationship with respect to the D/t ratio. The thicker pipes had a larger ultimate rotational capacity than the thinner steel tubes. (Elchalakani & Zhao, Concrete-filled cold-formed circular steel tubes subjected to variable amplitude cyclic pure bending, 2008).

Elremaily et al. (2002) conducted six tests on CFSTs with diameter to thickness ratios of 34 and 51, all with a 12.75 inch diameter. The specimens were subjected to a constant axial load and lateral cyclic loading at mid span to mimic the effect of a floor slab in an earthquake. Many of their tests reached the limit of the testing equipment prior to failure of the specimens which made it hard to compare the tests. Buckles began to appear at the location of the cyclic loading after yield and the buckle increased until a ring was formed around the circumference of the pile, however, no decrease in strength was observed. Most of the specimens maintained their lateral load capacity until a ductility of 10; this ductility is based on the first yield displacement, not the equivalent first yield displacement. Since the testing equipment reached its limits prior to the end of the test, the researchers could not compare the ultimate behavior based on the D/t ratio. The one comparison available is based on moment strength; the specimen with a thicker wall had greater moment strength, as expected. (Elremaily & Azizinamini, 2002).

Han et al. (2006) performed relatively small-scale tests on thirty-six composite beams in 2006, with diameters ranging from 100mm to 200mm and lengths ranging from 800mm to 1800mm. Not all of the tests are relevant to the current research since they tested many rectangular beams, and one of the main goals of the project was to determine the effect of

concrete mix and aspect ratio on the performance of the specimens in flexure. However, the researchers did test circular sections of three different D/t ratios ranging from 47 to 105. Selected ultimate strains and curvatures from these tests were reported. The ultimate strains (before fracture of the steel tube) with D/t ratios of 46.7 and 60 are 0.03 and 0.028 respectively. These values are fairly close to one another but there were not enough D/t ratios tested to determine a relationship between the ultimate state and the thickness of the steel shell. The ultimate curvature of the specimens with a D/t of 47 was approximately 0.05 1/m (0.013 1/in). All the specimens performed in a ductile manner and exhibited outward buckling of the steel pipe early in the test; the steel pipe ruptured at the location of the buckles later in the test. (Han, Lu, Yao, & Liao, 2006).

Park (1983) tested reinforced concrete filled steel tubes with a wide range of diameter to thickness ratios (34 to 214) and studied their performance under lateral cyclic loading and seismic performance. The specimens were 3.6 meters (142 inches) in length and the outer diameters ranged from 270 mm (10.63 in) to 450 mm (17.7 in). The piles were tested under a two cycle set until rupture of the steel pipe or until the limitations of the equipment was met. A point load was applied at mid-span of the pile through a concrete block which wrapped around the pipe. The mode of failure of the piles was similar for all D/t ratios, the steel pipe buckled outward near the loading point. The buckles increased in size until rupture of the steel pipe or maximum capacity of the equipment. The thickest pile (D/t = 34) buckled at ductility four and the remainder of the piles buckled at a ductility of two. The height of the buckles was relatively larger in the thinner pipes (with a higher D/t ratio) than in the thicker pipes. However, the affected area or "length" of the buckles was longer in the thicker pipes than the thinner pipes. (Park, 1983).

The theoretical flexural strengths of the sections were calculated using equivalent reinforced concrete section-assuming strain compatibility, a stress block for the concrete in compression, an ultimate concrete strain of 0.003, and an assumed concrete strength and steel yield stress. These assumptions led to an underestimation of the actual flexural strengths of these sections with a wide range of error. The error in the flexural strengths ranged from 5% to 30%. This error is largely due to the assumption that the section was a reinforced concrete section, Mander's model was used to predict the concrete strength, and that the actual strengths of the steel and the concrete were not used in the calculations. (Park, 1983).

All of the tests exhibited good energy dissipation, which is favorable for seismic design. The hysteretic loops were "pinched" due to the concrete cracking and the closing of these cracks in the reverse loading direction. The "pinching" was worse in the specimens with thin walls than for those with thick walls. This difference indicated that the thin-walled piles, with a lower percentage of steel, created a response more similar to reinforced concrete than thicker walled piles. (Park, 1983).

Electrical resistance strain gages were placed on the surface of the steel tube and on the internal reinforcing cage in a rectangular rosette which allowed the researchers to obtain the lateral strains, longitudinal strains and section curvatures. A maximum longitudinal strain of

about 2.5% was seen in all tests, regardless of D/t ratio. Park defined the confining strains as the measured lateral strains (εh) plus Poisson's ratio multiplied by the longitudinal strains (0.3 εl): εconf = εh + 0.3 εl. The confining strains varied depending on the thickness of the steel tube. The thickest walled specimen (D/t = 34) reached confining strains of almost 5% and the thinnest walled specimen (D/t = 214) reached confining strains of approximately 1% - 1.5%. This result was due to the thicker steel providing higher confinement to the reinforced concrete core. The curvatures were calculated from the strain gages placed around the circumference of the steel tube. The curvature ductility was thus calculated from the measured curvatures, in all the sections the curvature ductility increased at a faster rate after buckling of the steel tube than before buckling. (Park, 1983).

The curvature distribution along the span shows the curvatures at the mid-span were much higher than those throughout the rest of the span. This created a relatively short plastic hinge length. Due to the similar shape of the response curve in relation to conventional reinforced concrete sections, the same plastic hinge equation was used and gave a good approximation of the force- deflection response. (Park, 1983).

2.5. Internal Reinforcement Ratio

Park (1983) was the only research project found with concrete filled steel tubes with internal reinforcement and lateral loading. Although Park tested a wide variety of D/t ratios, all of the specimens had a 1% internal reinforcement ratio. The steel casing prevented the concrete from spalling and thus prevented the internal reinforcing bars from buckling. The researchers determined the specimens were suitable for seismic design because of the high level of ductility reached and the energy dissipated by the system. Moment strengths were predicted assuming the strains were compatible across the steel tube, internal reinforcement and the concrete core and had good agreement with the experimental results. (Park, 1983).

No past research projects have been found which vary the internal reinforcement ratio of the pipe of a RCFST. Chang et al (2012) modeled concrete filled steel tubular columns under lateral cyclic loading with finite element analysis. The internal steel, shown in Figure 2-2, is a steel section encased in concrete rather than internal reinforcing bars.

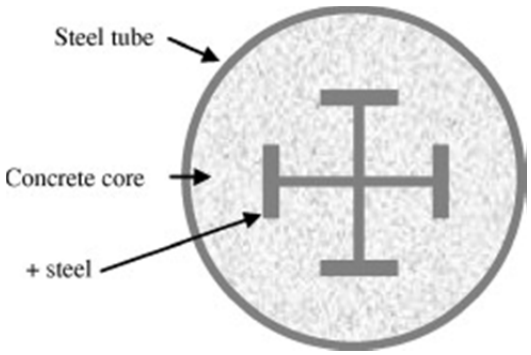

Figure 2-2 Concrete filled steel tubular column cross section (Chang et al, 2012)

A parametric study was conducted to determine the effect of the ratio of section steel (0 to 20 percent) on the force-displacement envelope curves for the columns and the maximum lateral displacement sustained by the columns. The yield force and maximum lateral displacements were increased by approximately fifty percent from the section with no internal steel to that with twenty percent internal steel. This amount of steel is far larger than would be found in a RCFST. The internal reinforcement ratios in these specimens typically range from 0% to 2.5%. Between 0% and 2.5% steel for the circular filled steel tubular columns, the yield force was increased by approximately 10 percent and the maximum lateral displacement was increased to approximately 7%. (Chang, Wei, & Yun, Analysis of steel-reinforced concrete-filled steel tubular (SRCFST) columns under cyclic loading, 2012). The internal reinforcement has a different configuration and is not directly applicable to RCFSTs but the results demonstrated that the amount of internal steel affected the overall performance of the concrete filled steel tubular columns and it is important to investigate the effect of the internal reinforcement in RCFSTs.

CHAPTER 3 EXPERIMENTAL PROGRAM

3.1. Overview

For the research described in this report, twelve large-scale tests were performed on RCFSTs under reversed cyclic four-point bending. The first phase of testing consisted of five tests and focused on the impact of D/t ratio while keeping the internal reinforcement ratio constant. The second phase of testing consisted of the remaining seven specimens. The first two tests in the second phase expanded the range of D/t ratios with the same internal reinforcement ratio as Phase One. The remaining five tests consisted of varying internal reinforcement ratios for thin walled pipes. The cross sectional properties of these specimens are discussed in this chapter along with the test setup, instrumentation, material properties and experimental observations.

3.2. Test Setup

The experimental portion of this research project was conducted at the Constructed Facilities Laboratory (CFL) in Raleigh, North Carolina. In this facility, the concrete filled pipe piles were tested on a large-scale. For these tests, two MTS hydraulic actuators applied the load to the pile. The actuators were hung from steel frames and the specimens were supported by a steel support at either end of the pile. The steel frames and the steel supports were bolted to the lab strong floor. Three-dimensional renderings of the test set up are shown in Figure 3-1 and Figure 3-2.

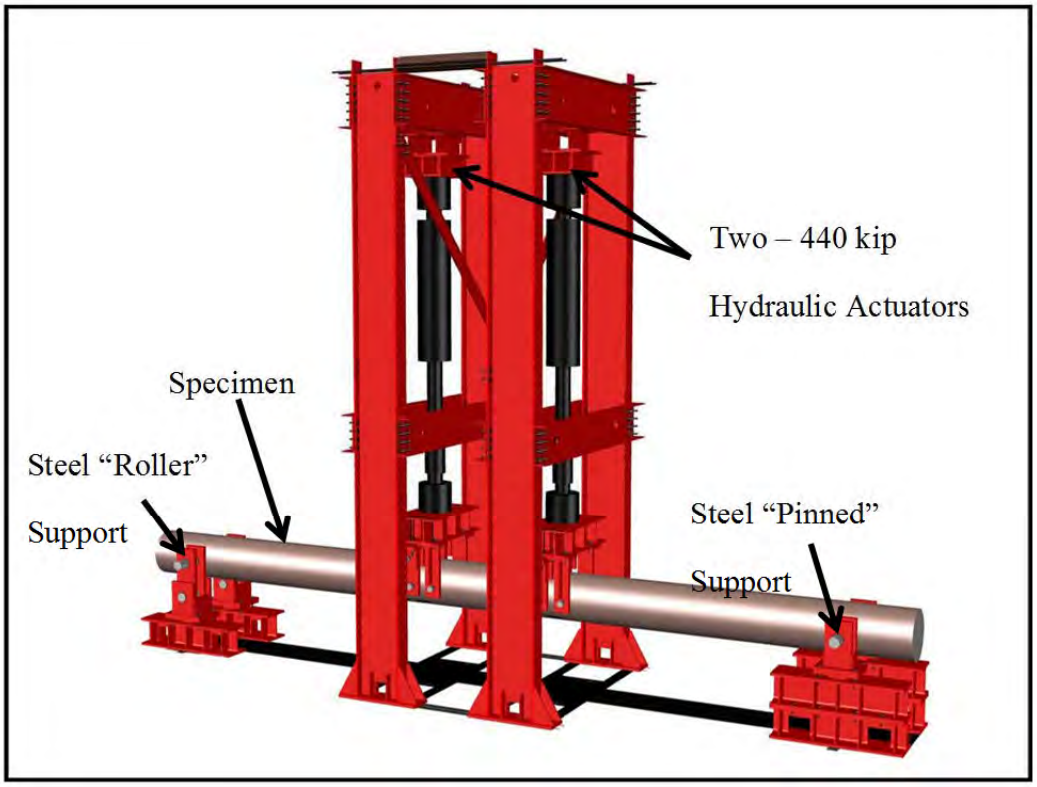

Figure 3-1: Three – dimensional rendering of test setup.

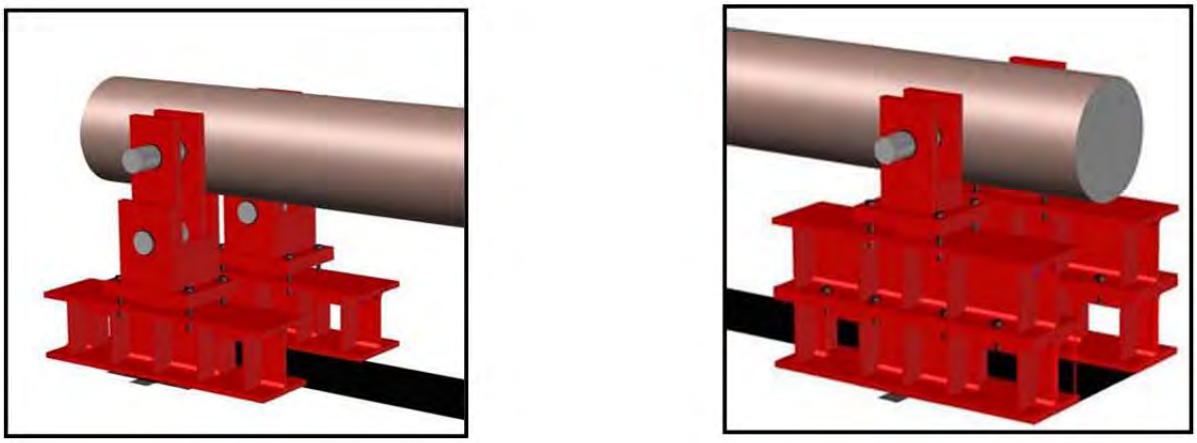

Figure 3-2: Three – dimensional rendering of specimen supports: "Roller" support is shown on left, "Pinned" support is shown on right.

As seen in Figure 3-2, the specimen supports are composed of various steel shapes which raise the centerline of the specimen to four feet above the floor, allowing for adequate displacement capacity of the pile. The "pinned" support does not allow any rotation of the pile. The "roller" support has a mechanism created by connecting two steel pieces with a small steel pin allowing rotation of the pile. The details of each support are shown in Figure 3-3.

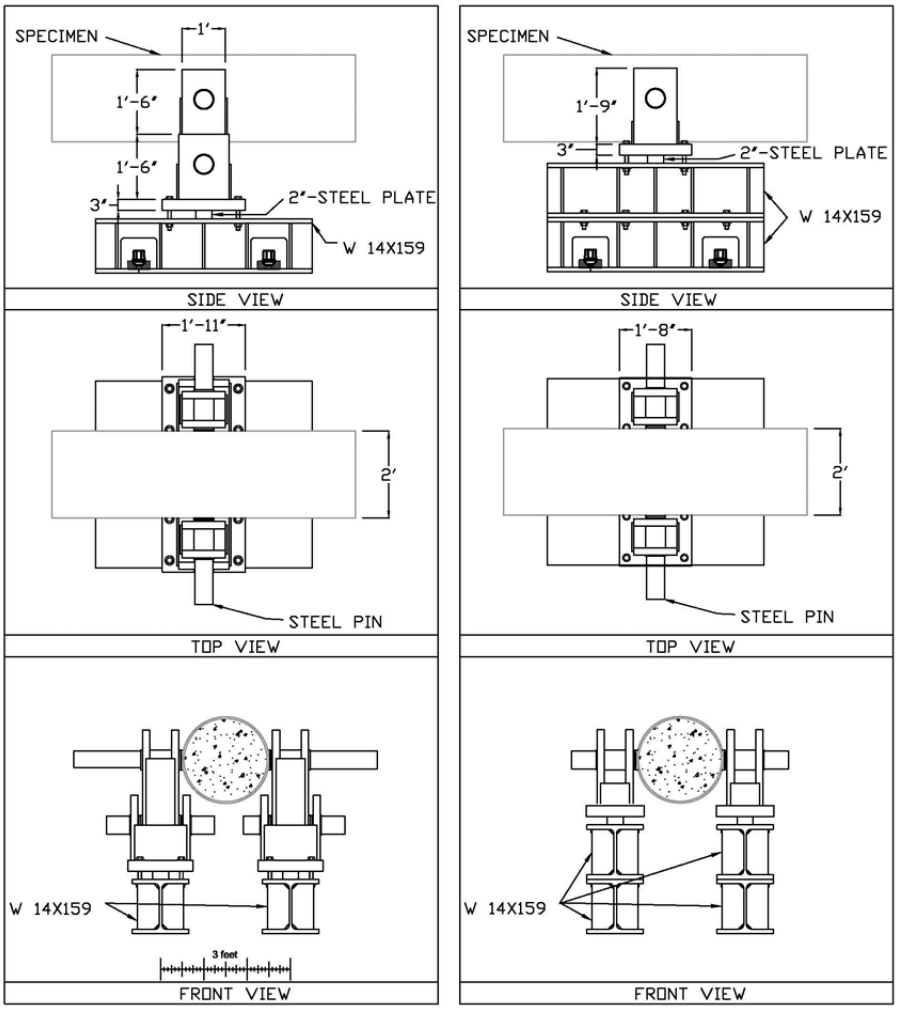

Figure 3-3: Specimen support details: "Roller" support is on left, "Pinned" support is on right.

Two steel frames were constructed over the specimen at each loading point; they were spaced six feet apart centered about the mid-span of the pile as shown in Figure 3-4. The hydraulic actuators were connected to the frames via steel "shoes". The "shoes" lined up with the bolt connection in the frame and the bottom of the "shoes" lined up with the bolt pattern of the hydraulic actuators. The steel frame and steel shoe details are shown in Figure 3-5. As the

specimens were loaded and the pile developed a slope, the actuator heads rotated with the pile. This created an angle in the actuator head and induced a small horizontal load. When the actuators were pulling the specimen (away from the floor) the actuator heads were tilted toward the mid-span of the pile. This horizontal load pushed the tops of the steel frames away from each other. To counteract this action, threaded rods were placed between the two frames to take the tension force induced when the actuator heads rotated. When the actuators pushed the pile down (toward the floor) the loads directions were reversed. A 6x6 block of wood was placed between the frames at a neutral position and supported the compressive force between the frames.

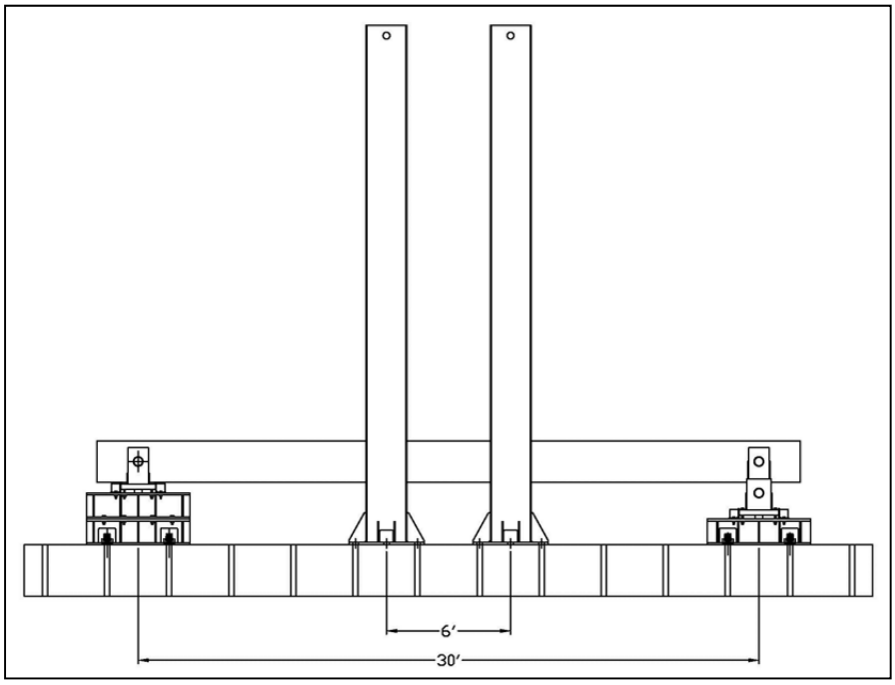

Figure 3-4: Overall Test Setup

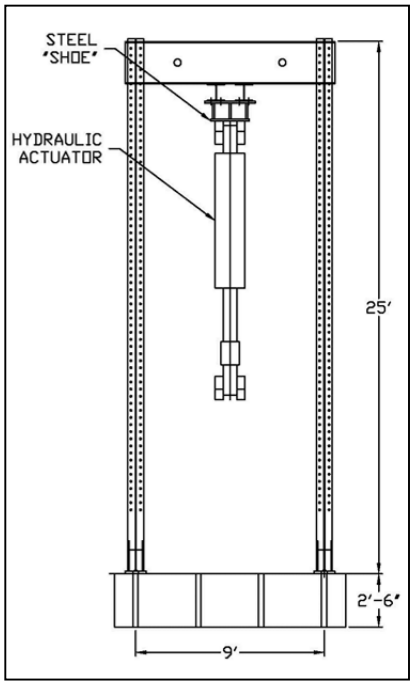

Figure 3-5: Steel Frame Detail

3.3. **Instrumentation**

Multiple instrumentation systems were utilized. The instrumentation was concentrated in the constant moment region, where the damage would be located. One load cell was connected to each hydraulic actuator to measure the load magnitude at a frequency of 1 Hz throughout the test. The loads were calibrated and zeroed prior to each test. In addition to the load cells: strain gages, string pots, and a non-contact three-dimensional position measurement system, were used to measure displacements and strains throughout the test.

3.3.1. Strain Gages

The data acquisition system used to collect data allowed a maximum of twenty strain gages for each test. The data from each strain gage was recorded at a frequency of 1 Hz. The majority of the strain gages were placed in the constant moment region; however four strain gages were placed outside the constant moment region. The experimental program was conducted in two phases: the first phase was focused on analyzing the effect of D/t ratio and the second phase expanded the range of D/t ratios tested and focused on the effect of internal reinforcement in the piles. The placement of strain gages was different in the two phases of testing.

3.3.1.1. Phase One

In Phase One, four strain gages were placed outside the constant moment region, and sixteen were placed in the constant moment region. The gages outside the maximum moment region were located six feet from the loading points on both sides with gages located on the extreme tension and compression fibers (the top and bottom of the steel pipe). The sixteen gages placed in the maximum moment region were divided into two circumferences, each having eight gages. Each circumference of gages was offset one foot from the mid-span of the constant moment region. The eight gages were comprised of four measuring longitudinal strains and four measuring lateral strains. The gages were placed at the extreme fiber locations and at the center of the pile. The location of the strain gages in the Phase One tests is shown in Figure 3-6.

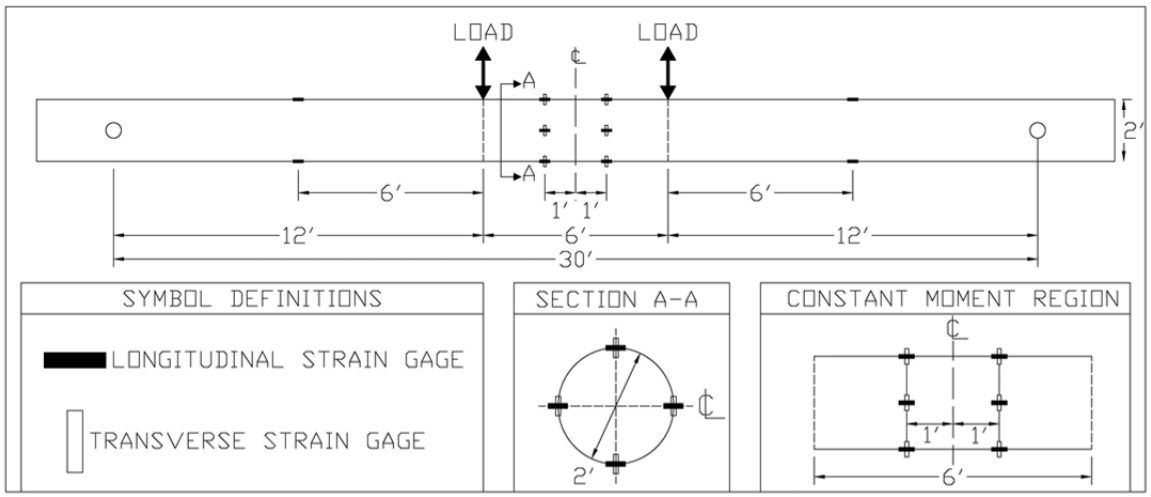

Figure 3-6: Strain Gage Locations in Phase One

3.3.1.2. Phase Two

The maximum longitudinal strains reached in the first phase were larger than the gages were able to record. During Phase Two, more strain gages were placed in the transverse direction than in the longitudinal direction. Also, the transverse strains in the center of the section were small during phase one, since they were close to the neutral axis. To measure more substantial strains during Phase Two, the transverse strain gages were concentrated more toward the extreme fibers. The revised strain gage locations used during phase two are shown in Figure 3-7 and Figure 3-8 for the 24 inch and 20 inch outer diameter pipes, respectively.

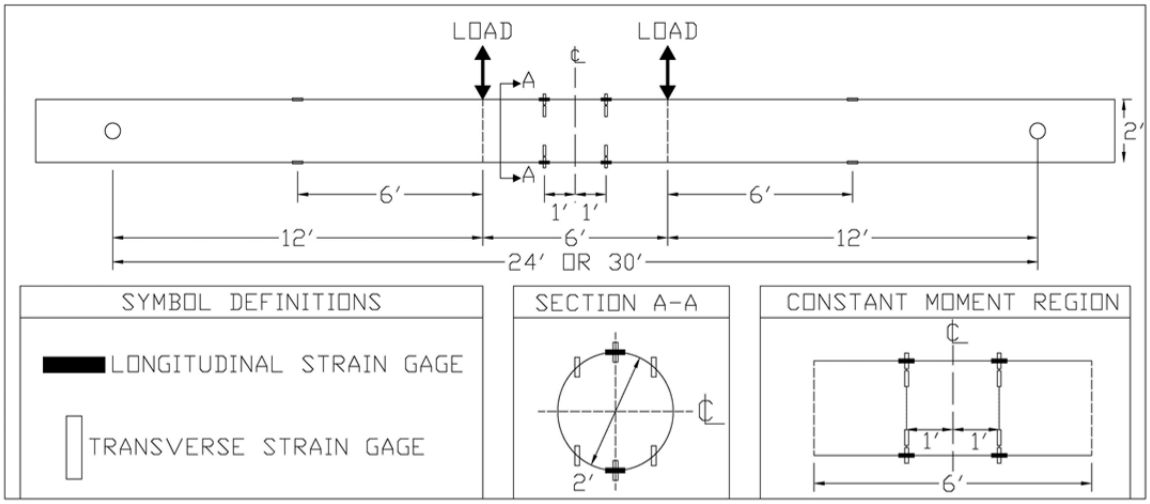

Figure 3-7: Strain Gage Locations in Phase Two (24 inch pipe)

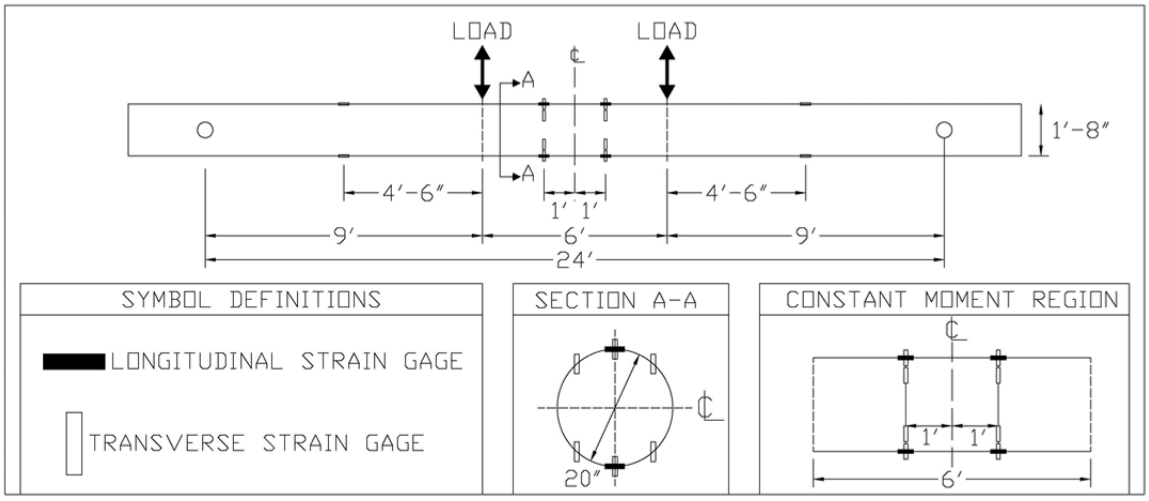

Figure 3-8: Strain Gage Locations in Phase Two (20 inch pipe)

3.3.2. String Pots

String pots were placed in the constant moment region and attached to the pinned support. Two string pots were attached to the pinned support to monitor any slip in the support. Three string pots were placed in the constant moment region: one under each loading point and one at mid-span. These string pots were attached to the underside of the steel pipe. The location of these string pots were the same in Phase One and Phase Two and can be seen in Figure 3-9.

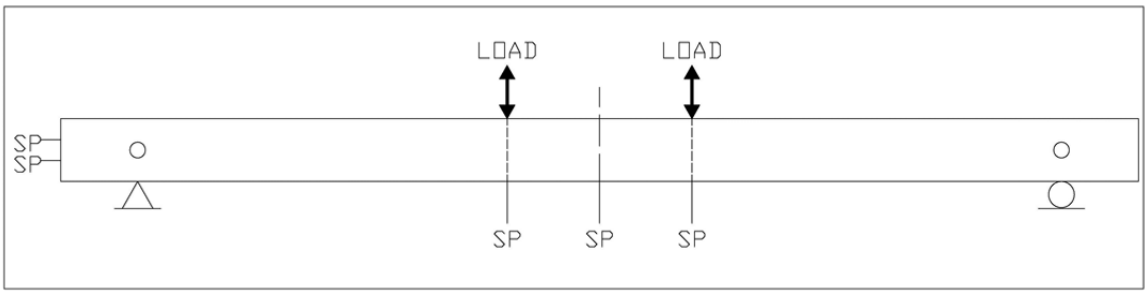

Figure 3-9: String Pot Locations

3.3.3. Optotrak Certus HD

The Optotrak Certus HD system is a non-contact three-dimensional position measurement system. The system is capable of monitoring up to five-hundred targets at an accuracy of 0.05mm. In previous tests, the Optotrak has proven to be very effective in monitoring large deformations in structural elements during testing. Traditional electrical resistance strain gauges are effective in measuring smaller strains, but they tend to be unreliable beyond 1% to 2% strain. Other traditional instruments, such as linear potentiometers, are able to measure large deformation, yet the gage length can be large, and connection of the devices to a test specimen can impact the behavior of the specimen. The advantage of the Optotrack system is that it is a noncontact device that measures position via the use of targets and a camera system. The position data collected from the targets can then be used to calculate strain, curvature, rotation, and displacement.

3.3.3.1. Phase One

To obtain thorough data throughout the length of the constant moment region and around the circumference of the pile, a rectangular grid was created with the LED targets. In the first test, LED targets were placed on both sides of the pile (around the entire circumference). A camera was placed on each side of the pile to capture the targets movements, the placement of the targets are shown in Figure 3-10. However, one of the cameras was placed too close to the pile and could not record all of the targets at maximum displacements. Due to the space limitations of the lab, the camera could not be moved far enough from the specimen to capture the full range of motion. In theory, both sides of the pile have identical deformations. The data from the first test was analyzed and the measurements on each side of the pile were very similar.

The second camera was moved for the remainder of the tests in Phase One, in order to record measurements for the full range of motion and to avoid redundant information. In the remainder of the tests in Phase One, targets were placed under one of the loading points to try and capture the bucking mechanism of the steel pipe. The LED target locations for the remainder of the tests in Phase One (tests 2- 5) are shown in Figure 3-11.

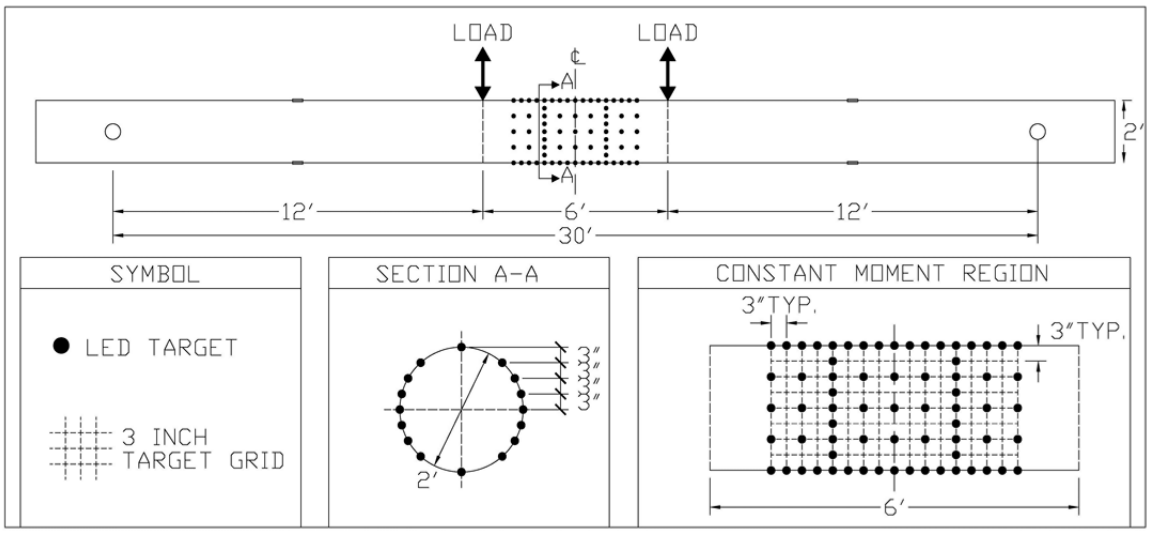

Figure 3-10: LED target locations in test one

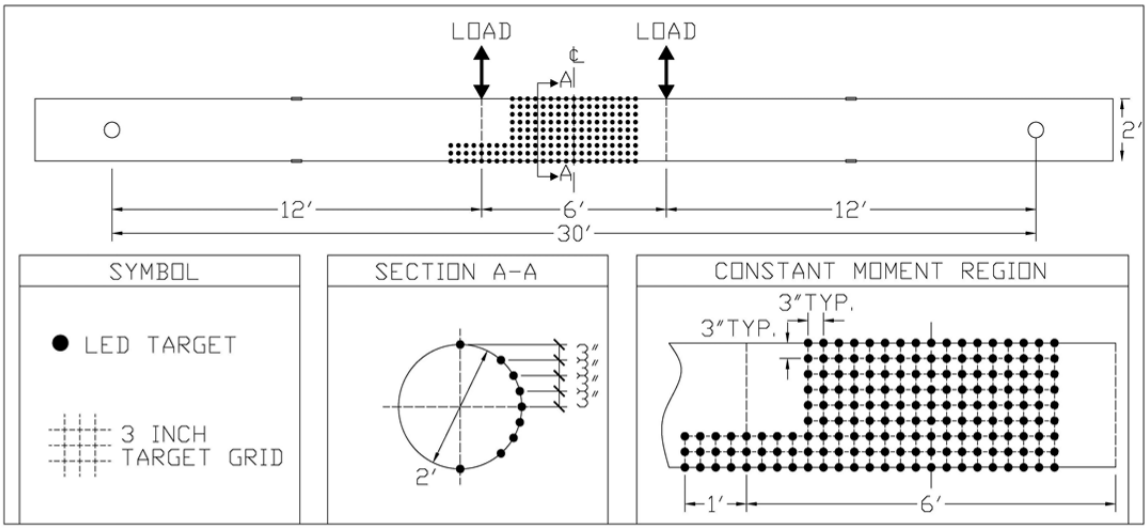

Figure 3-11: LED target locations in tests two through five

3.3.3.2. Phase Two

In Phase One, the LED targets at the extreme fibers had to be placed on small metal angle brackets so they would be visible to the Optotrak cameras. In Phase One, the buckling of the

steel tube caused the angle brackets to rotate and led to inaccurate measurements of the deformations. The angle brackets also did not allow for accurate calculations of lateral strains since they were not placed directly on the surface of the steel pipe. To reduce the number of angle brackets in Phase Two, an Optotrak camera was hung above the pile, pointing down toward the top surface of the pile. This allowed more targets to be placed in the extreme fiber region and eliminated the need for angle brackets on the top surface of the specimen. The layouts of the LED targets in Phase Two are shown in Figure 3-12 and Figure 3-13 for the 24 inch and 20 inch outer diameter pipes, respectively.

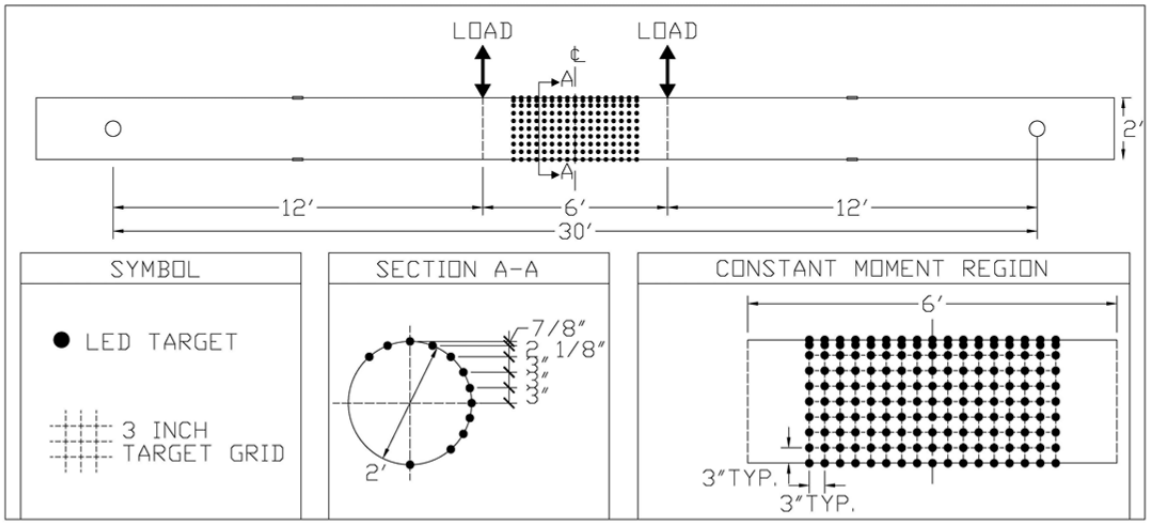

Figure 3-12: LED target locations in Phase Two (24 inch pipes)

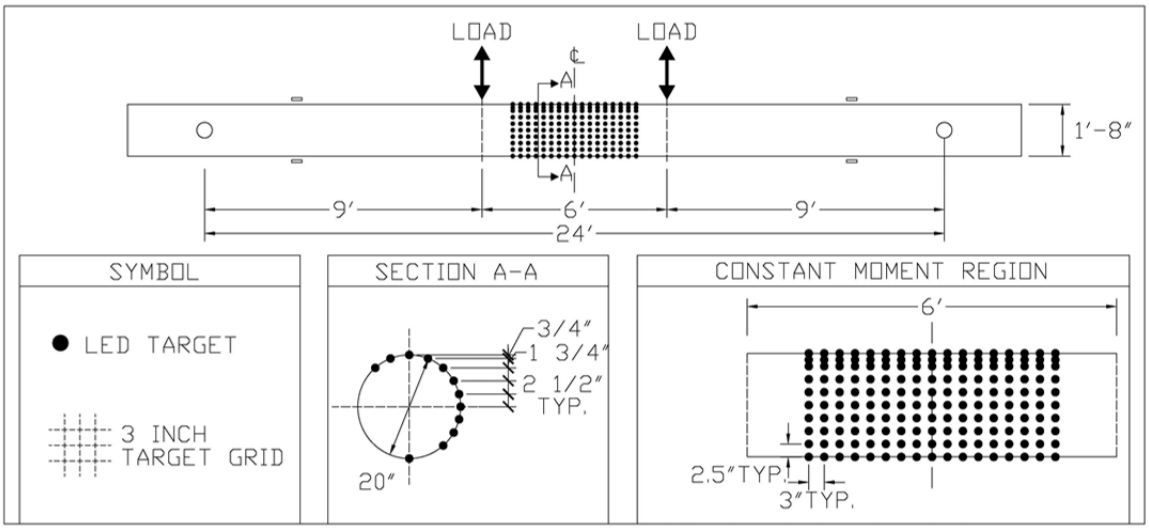

Figure 3-13: LED target locations in Phase Two (20 inch pipes)

3.4. Specimen Design

The specimen design in this research project was dependent on three main factors: the required grade of the steel, the scope of the project, and the limitations imposed by the layout of the laboratory. The actual thicknesses of the steel tubes were chosen from available sizes from a variety of manufacturers. All of the wall thicknesses were not available in seam welded pipes, so thus, the pipes were a mixture of seam welded and spirally welded pipes. The different types of welds did not have an effect on the tests, as proven by Gonzalez (2010).

3.4.1. Required Material Properties

Due to the high seismic demands in Alaska, the Alaska Department of Transportation has high standards for structural steel. The steel tubes were required to meet one of the following standards: ASTM A500, ASTM A709, API2B, API5l or ASTM A139. The internal reinforcement had to be ASTM A706. Details of the requirements and the actual material properties for each pipe are discussed later.

3.4.2. Limitations

All of the experimental tests were conducted in the Constructed Facilities Laboratory at North Carolina State University. The lab contains a strong floor which allows the test set up to be attached to the floor through holes which extend through the 30 inch depth of the floor. As seen in Figure 3-14, these holes are aligned in a square grid measuring 3 feet on each side,

and all of the supports and testing frames must be bolted through these holes. This restricted the overall span and constant moment length of the pipe piles to multiples of three feet.

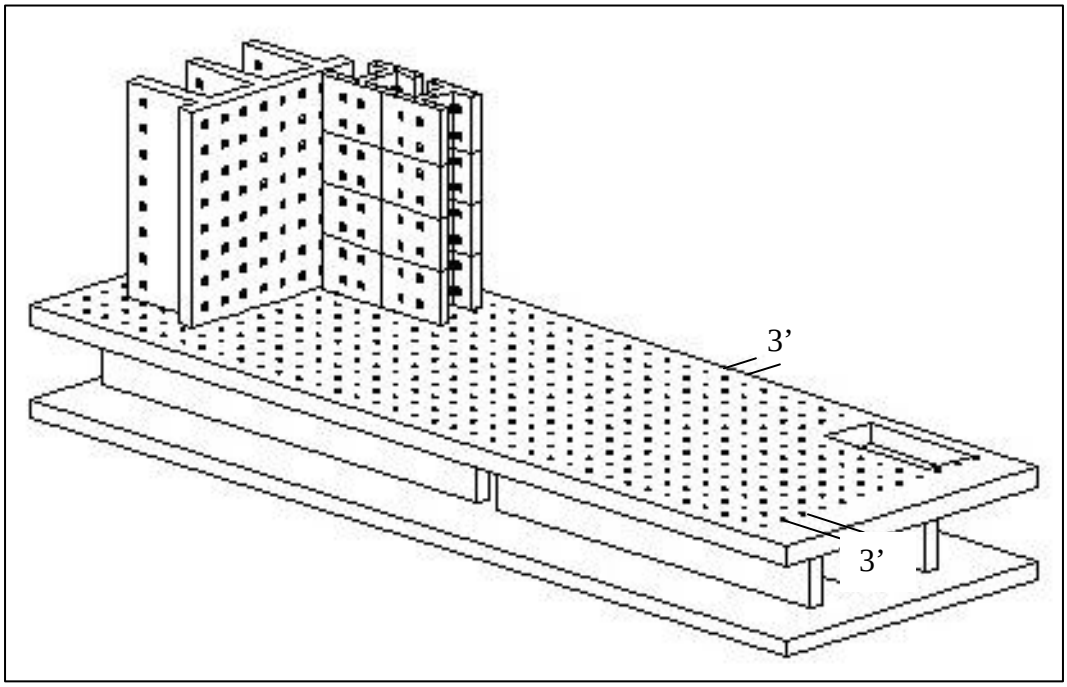

Figure 3-14: Constructed Facilities Laboratory Strong Floor

The second limitation was the force limit of the hydraulic actuators. The nominal moment of the designed pipe pile with an additional safety factor had to be lower than the maximum capacity of the actuators.

3.4.3. Scope

The first goal of the project was to determine the effect of diameter-to-thickness ratio on limit states. In order to achieve this, many D/t ratios needed to be tested. Past research has been performed on tests from D/t ratio from 24 to 214, as noted in the literature review. However, many of these tests were small-scale tests, and large-scale tests were needed to verify the findings. Past tests at North Carolina State University had been performed on twenty-four inch diameter piles with a 0.5 inch wall thickness, resulting in a D/t ratio of 48, and an internal reinforcement ratio of 1.67%. As stated previously, the purpose of those prior tests was to determine the effect of weld type on the performance of concrete filled steel tubes.

3.4.4. Phase One

In order to make use the data collected from Gonzalez (2010) and due to the limitations of the test setup, twenty-four inch outer diameter pipes were chosen for the first phase of tests. Since there has been significantly less research on the higher range of D/t ratios, the first phase was focused on testing a range of diameter-to-thickness ratios larger than 48. The thinnest pile available at an outer diameter of 24 inches had a thickness of 0.125 inch. This pile resulted in an upper limit of 192 for the tests. Instead of repeating a test performed by Gonzalez (2010) on pipe piles with D/t = 48 and an internal reinforcement ratio of 1.67%, the first test of this project used the same pipes as were used in the past project but with no internal reinforcement. The remainder of the test details for Phase One is shown in Table 3-1.

Table 3-1: Phase One Specimen Design

Test No	Diameter (in)	Nominal Thickness (in)	D/t Ratio	Longitudinal Rebar			Transverse Rebar (Spiral)	
				Number	Size	Ratio (ρ)	Size	Spacing (in)
1	24	0.5	48	0	N/A	0.00%	N/A	N/A
2	24	0.125	192	12	US #7	1.60%	#3	12
3	24	0.1875	128	12	US #7	1.60%	#3	12
4	24	0.375	64	12	US #7	1.60%	#3	12
5	24	0.281	85	12	US #7	1.60%	#3	12

3.4.5. Phase Two

The results from Phase One demonstrated that the diameter to thickness ratio had an effect on the initiation of buckling. In order to complete this relationship, two more piles with different D/t ratios were tested (Tests 6 and 7).

The first test in this Phase (Test 6) was performed on a low D/t ratio; the optimal D/t ratio for this test was 24 however a pile with a twenty-four inch outer diameter and a one inch thickness would have require a force larger than that available in the actuators to reach the nominal moment of the section. To achieve the lowest D/t ratio possible, the outer diameter was reduced to twenty inches and the thickest wall available at this diameter was 0.6 inches resulting in a D/t ratio of 33.

The purpose of the second test in this Phase (Test 7) was to fill in the gap between D/t ratios of 133 and 192. A D/t ratio of 160 was chosen with an outer diameter of 20 inches and a thickness of 0.125 inches.

The first goal of the project, to determine the effect of D/t ratio, had been thoroughly investigated in the first seven tests of the research project. The second goal of the project was to determine the effect of internal reinforcement on the limit states of concrete filled steel tubes. The researchers believed changing the internal reinforcement ratio on thin-walled pipes would have a larger effect on the performance of the pipe piles than in a thick-walled pile since the overall steel ratio in the pile is affected more in the thin-walled piles. The steel ratio in the first seven tests was 1.67%. The normal range of internal reinforcement used in reinforced concrete filled steel tubes in the field range from 0.7 % to 2.5%. Of the previously tested piles, the three highest D/t ratios were tested with different internal reinforcement ratios. The dimensions and internal reinforcement ratios for all the tests in Phase Two are listed in Table 3-2.

Table 3-2: Phase Two Specimen Designs

Test No	Diameter (in)	Nominal Thickness (in)	D/t Ratio	Longitudinal Rebar			Transverse Rebar (Spiral)	
				Number	Size	Ratio (ρ)	Size	Spacing (in)
6	20	0.625	32	12	US #6	1.69%	#3	12
7	20	0.125	160	12	US #6	1.69%	#3	12
8	20	0.125	160	8	US #5	0.78%	#3	3
9	24	0.125	192	8	US #6	0.78%	#3	3
10	24	0.125	192	14	US #8	2.43%	#3	3
11	24	0.1875	128	8	US #6	0.78%	#3	3
12	24	0.1875	128	14	US #8	2.43%	#3	3

3.5. **Pre-Test Calculations**

3.5.1. Definitions and Processes

Prior to testing, calculations were performed to predict the overall response. A moment-curvature analysis was conducted to predict each section's first yield moment, first yield curvature, and nominal moment. All of the actual material properties obtained from material testing were used in the moment curvature analysis. The first yield moment was used to calculate the first yield force as seen in Equation 3-1. This was necessary for the cycles prior to yield.

The pipe piles were tested horizontally in the lab; the self-weight of the piles was significant. To avoid uneven responses in the push and pull directions due to the self-weight, the weight was taken into account by determining the force required in each actuator to set the moments equal to zero before any loading occurred. This essentially "zeroed" the system and all measurements were taken after the self-weight was accounted for, as shown in Equation 3-2 to Equation 3-5.

Before yield, the loading of the pile was force-based and separated into four increments: quarter yield force, half yield force, three-quarter yield force, and yield force. After yield, the loading of the pile was displacement based, using the equivalent yield displacement as the basis for the increments. The calculation of the equivalent yield displacement is shown in demonstrated in Equation 3-6; the nominal moment and first yield moment used in the calculations were obtained from the moment curvature analysis. The full displacement history over a course of a typical test is shown in Figure 3-15. The nominal moment was calculated when the concrete reached a strain of 0.004. The yield moment was calculated when the outer steel reached its yield strain, determined from the tensile tests. It is important to note, at first yield the internal reinforcement had not reached yield. The nominal moment and first yield moment are shown on a typical moment curvature response in Figure 3-16. The moment at which the internal reinforcing bar yields is also shown. In conventional reinforced concrete, the yield moment is defined when the rebar yields. Although it yields at a higher curvature and displacement the ratio of nominal moment to yield moment at that point is smaller, resulting in about the same equivalent yield displacement.

$$F_y = (M_y)/(L_{arm}) \quad \textbf{Equation 3-1}$$

$$F_{zero} = (M_{reaction} - M_{self})/(L_{arm}) \quad \textbf{Equation 3-2}$$

$$M_{reaction} = (R_{reaction})(L_{arm}) \quad \textbf{Equation 3-3}$$

$$R_{reaction} = (w_{self})(L_{span}/2) \quad \textbf{Equation 3-4}$$

$$M_{self} = (w_{self})\left[\frac{L_{arm}^2}{2} - \frac{(L_{span}/2 - L_{arm})^2}{2}\right] \quad \textbf{Equation 3-5}$$

$$\Delta_y = \Delta_y'(M_n/M_y) \quad \textbf{Equation 3-6}$$

F_y: First Yield Force

M_y: First Yield Moment

M_n: Nominal Moment

L_{arm}: Distance from support to load

$M_{reaction}$: Moment at the loading point due to the support reaction

$R_{reaction}$: Support reaction

L_{span}: Span length of the pile

w_{self}: Self weight of the concrete filled steel tube

Δ_y: Equivalent first yield displacement

Δ_y': Experimental first yield displacement

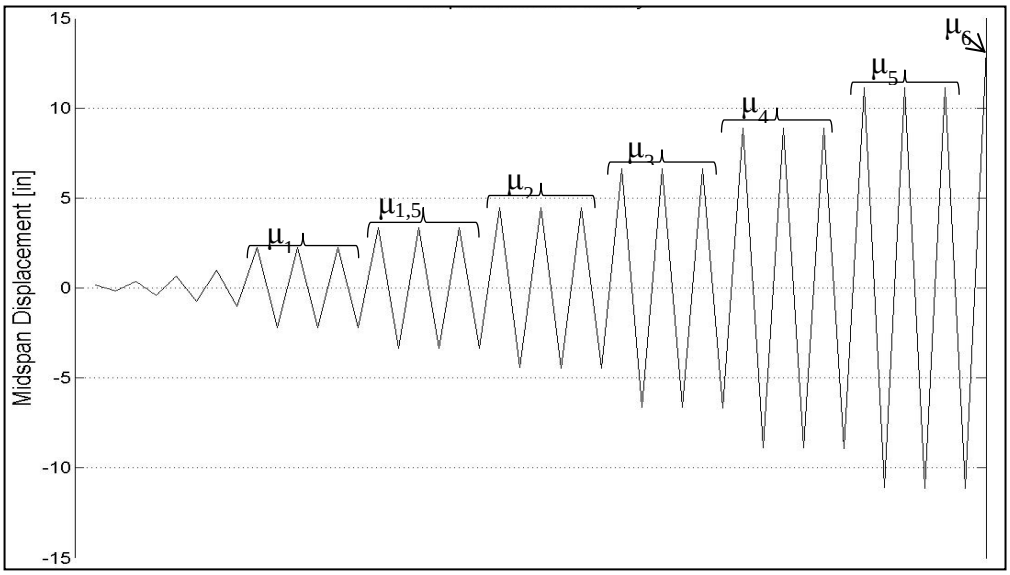

Figure 3-15: Typical Displacement History

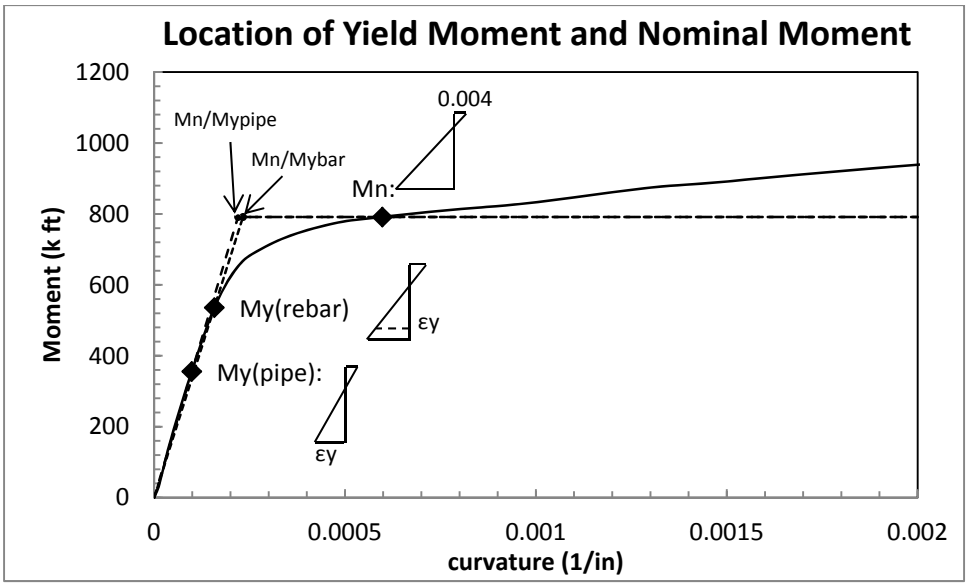

Figure 3-16: Nominal and Yield Moment from Moment-Curvature Analysis

3.5.2. Calculations for tests

The results of the pre-test calculations following the method described above for each of the twelve experimental tests are shown in Table 3-3.

Table 3-3: Pre-Test Calculation Results

Test No.	Values used in Calculations						Calculation Results					
	Pile Dimensions and Weight			From M-Φ Analysis		Δ_y' (in)	F_y (k)	R_{react} (k)	M_{react} (k-ft)	M_{self} (k-ft)	F_{zero} (k)	Δ_y (in)
	L_{span} (ft)	L_{arm} (ft)	w_{self} (k/ft)	M_y (k-ft)	M_n (k-ft)							
1	30	12	0.558	1347.2	2020.0	2.34	112.3	8.4	100.4	37.7	5.2	3.5
2	30	12	0.493	296.7	813.0	1.20	24.7	7.4	88.74	33.3	4.6	3.3
3	30	12	0.503	346.6	1031.9	1.02	28.9	7.5	90.54	34.0	4.7	3.0
4	30	12	0.537	937.1	1679.9	1.58	78.1	8.1	96.66	36.2	5.0	2.8
5	30	12	0.521	1058.1	1527.0	2.28	88.2	7.8	93.78	35.2	4.9	3.3
6	24	9	0.414	995.5	1408.2	1.84	110.6	5.0	44.71	14.9	3.3	2.6
7	24	9	0.347	212.7	445.8	0.90	23.6	4.2	37.47	12.5	2.8	1.9
8	24	9	0.347	171.3	356.9	0.80	19.0	4.2	37.47	12.5	2.8	1.7
9	30	12	0.494	294.7	560.0	1.49	24.6	7.4	88.92	33.3	4.6	2.8
10	30	12	0.494	391.4	842.2	1.10	32.6	7.4	88.92	33.3	4.6	2.4
11	30	12	0.503	396.5	662.1	1.20	33.0	7.5	90.54	34.0	4.7	2.0
12	30	12	0.503	425.7	937.6	1.00	35.5	7.5	90.54	34.0	4.7	2.2

3.6. **Material Properties**

Prior to testing each pile, steel pipe tension tests, rebar tension tests and concrete cylinders were performed to determine material properties. The steel pipe tension tests are shown in Figure 3-17 and Figure 3-18. All of the materials from all the pipes met the requirements, noted in 3.4.1 Required Material Properties. The chemical compositions of the pipes as reported by the manufacturers are shown in Table 3-4. Tension tests were also performed on all internal reinforcing bar sizes, the stress-strain curves obtained from these tests are shown in Figure 3-19 and the yield and ultimate stresses are tabulated in Table 3-6. The average compressive concrete strengths obtained within twenty-four hours of testing for each specimen are shown in Table 3-7.

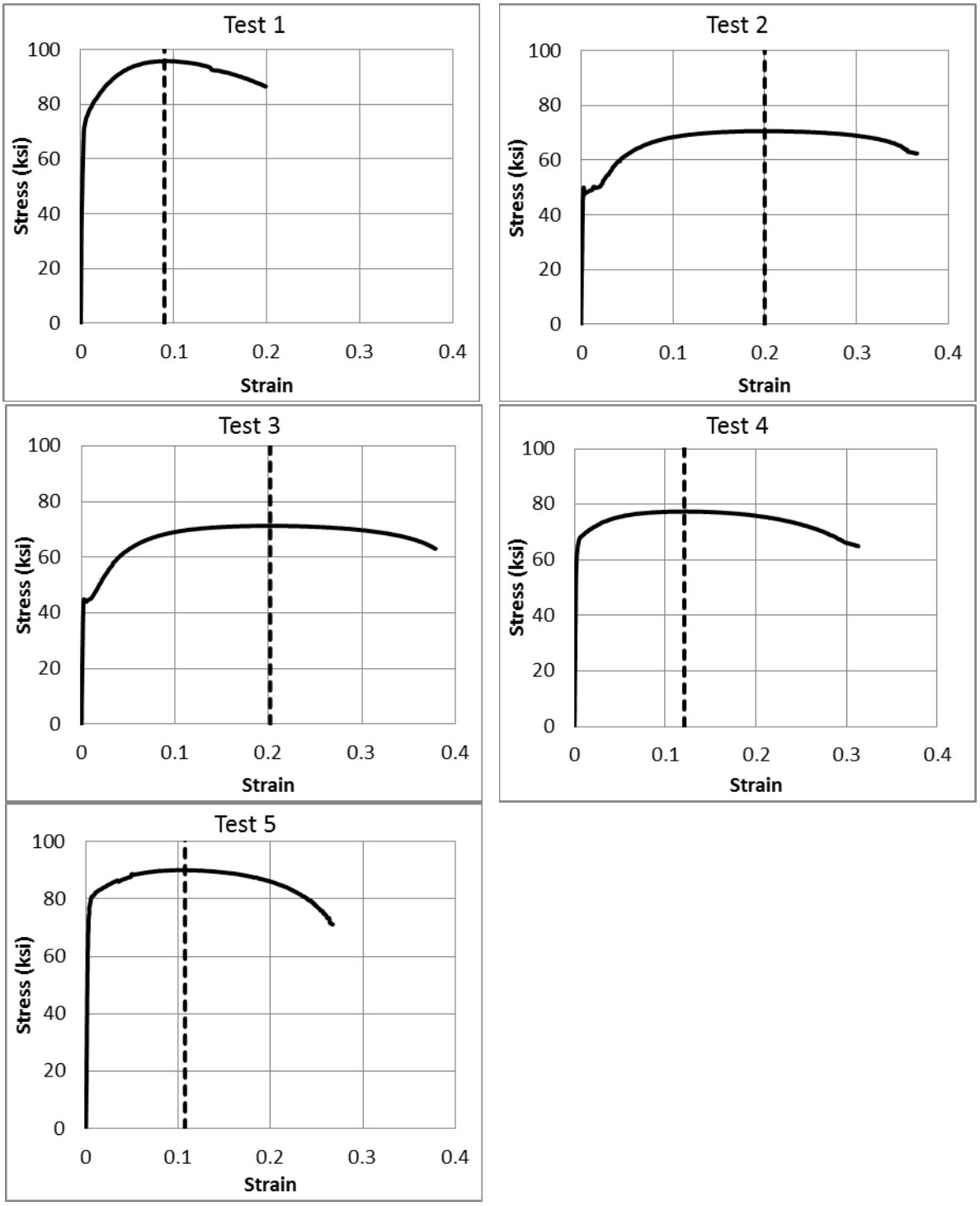

Figure 3-17 : Phase One Steel Pipe Tension Tests

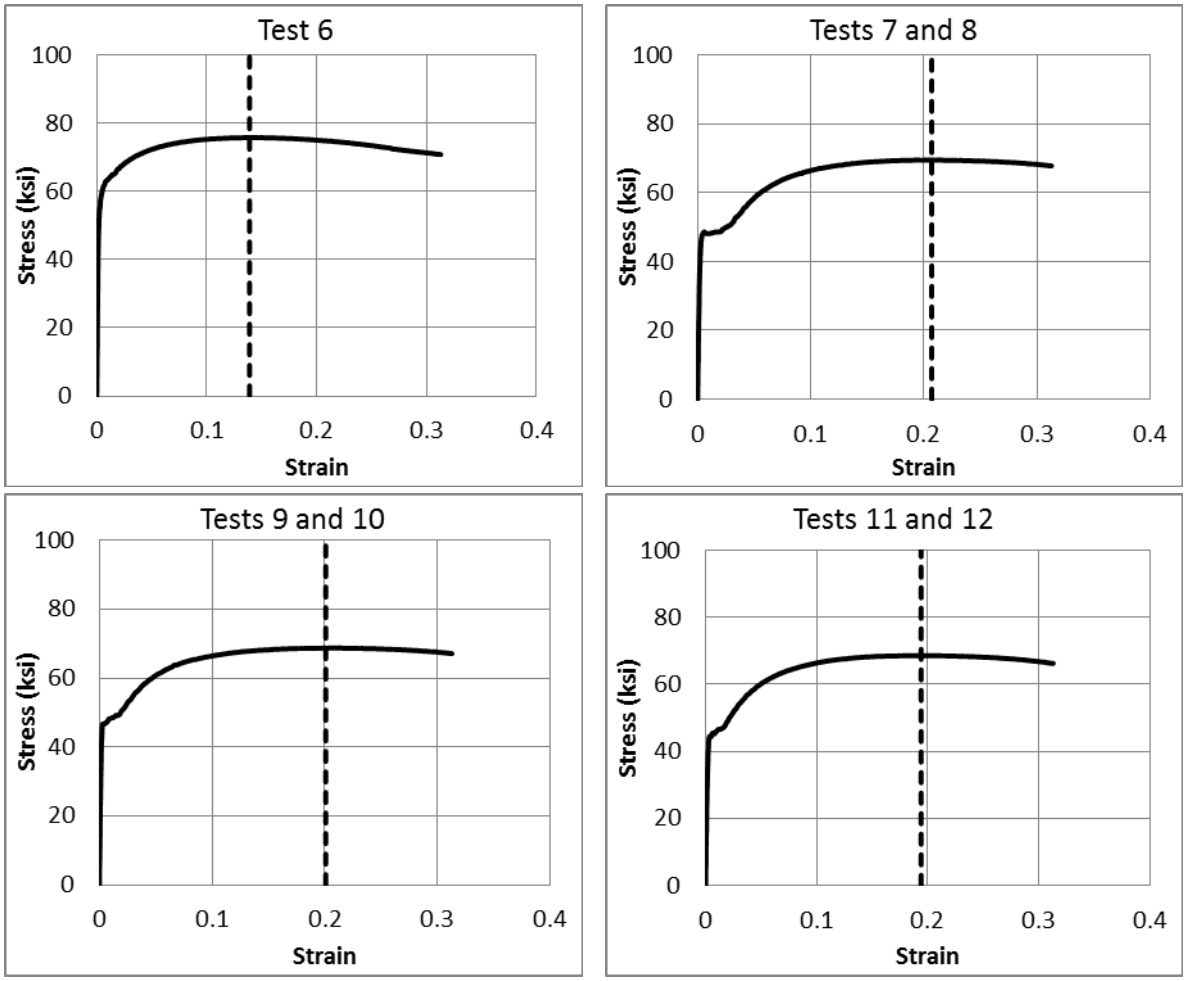

Figure 3-18: Phase Two Steel Pipe Tension Tests

Table 3-4: Chemical Composition of Steel Pipes

Required Chemical Composition				
	Carbon, max, %	Manganese, max, %	Phosphorus, max, %	Sulfur, max, %
API5LX42	0.28	1.4	0.03	0.03
Actual Chemical Composition for tests meeting this requirement				
	Carbon, max, %	Manganese, max, %	Phosphorus, max, %	Sulfur, max, %
Test 4 (t = 0.375")	0.057	0.547	0.013	0
Test 6 (t = 0.675")	0.057	0.547	0.013	0
Required Chemical Composition				
	Carbon, max, %	Manganese, max, %	Phosphorus, max, %	Sulfur, max, %
API5LX60	0.26	1.4	0.03	0.03
Actual Chemical Composition for tests meeting this requirement				
	Carbon, max, %	Manganese, max, %	Phosphorus, max, %	Sulfur, max, %
Test 5 (t = 0.281")	0.05	1.27	0.013	0.003
Required Chemical Composition				
	Carbon, max, %	Manganese, max, %	Phosphorus, max, %	Sulfur, max, %
ASTM A139, Grade D,E	0.3	1.3	0.035	0.035
Actual Chemical Composition for tests meeting this requirement				
	Carbon, max, %	Manganese, max, %	Phosphorus, max, %	Sulfur, max, %
Test 3 (t = 0.178")	0.22	0.75	0.01	0.005
Test 2 (t = 0.128")	0.2	0.77	0.008	0.004
Required Chemical Composition				
	Carbon, max, %	Manganese, max, %	Phosphorus, max, %	Sulfur, max, %
ASTM A139, Grade B	0.3	1.3	0.035	0.035
Actual Chemical Composition for tests meeting this requirement				
	Carbon, max, %	Manganese, max, %	Phosphorus, max, %	Sulfur, max, %
Tests 7 & 8 (t = 0.178")	0.22	0.72	0.008	0.006
Tests 9 & 10 (t = 0.128")	0.2	0.78	0.014	0.003
Tests 11 & 12 (t = 0.180")	0.22	0.72	0.008	0.006

Table 3-5 Tensile Properties of Steel Pipes

Required Tensile Properties		
	Yield Strength (ksi)	Tensile Strength (ksi)
API5LX42	42.1 - 71.8	60.2 - 110.2
Actual Tensile Properties for tests meeting this requirement		
	Yield Strength (ksi)	Tensile Strength (ksi)
Test 4 (t = 0.375")	65.23	77.43
Test 6 (t = 0.675")	58.46	75.75
Required Tensile Properties		
	Yield Strength (ksi)	Tensile Strength (ksi)
API5LX60	60.2 - 81.9	75.4 - 110.2
Actual Tensile Properties for tests meeting this requirement		
	Yield Strength (ksi)	Tensile Strength (ksi)
Test 5 (t = 0.281")	79.05	90.1
Required Tensile Properties		
	Yield Strength (ksi)	Tensile Strength (ksi)
ASTM A139, Grade D,E	46+	60+
Actual Tensile Properties for tests meeting this requirement		
	Yield Strength (ksi)	Tensile Strength (ksi)
Test 3 (t = 0.178")	44.54	71.3
Test 2 (t = 0.128")	48.23	70.63
Required Tensile Properties		
	Yield Strength (ksi)	Tensile Strength (ksi)
ASTM A139, Grade B	35+	60+
Actual Tensile Properties for tests meeting this requirement		
	Yield Strength (ksi)	Tensile Strength (ksi)
Tests 7 & 8 (t = 0.178")	47.51	69.46
Tests 9 & 10 (t = 0.128")	47.61	68.76
Tests 11 & 12 (t = 0.180")	44.27	68.64

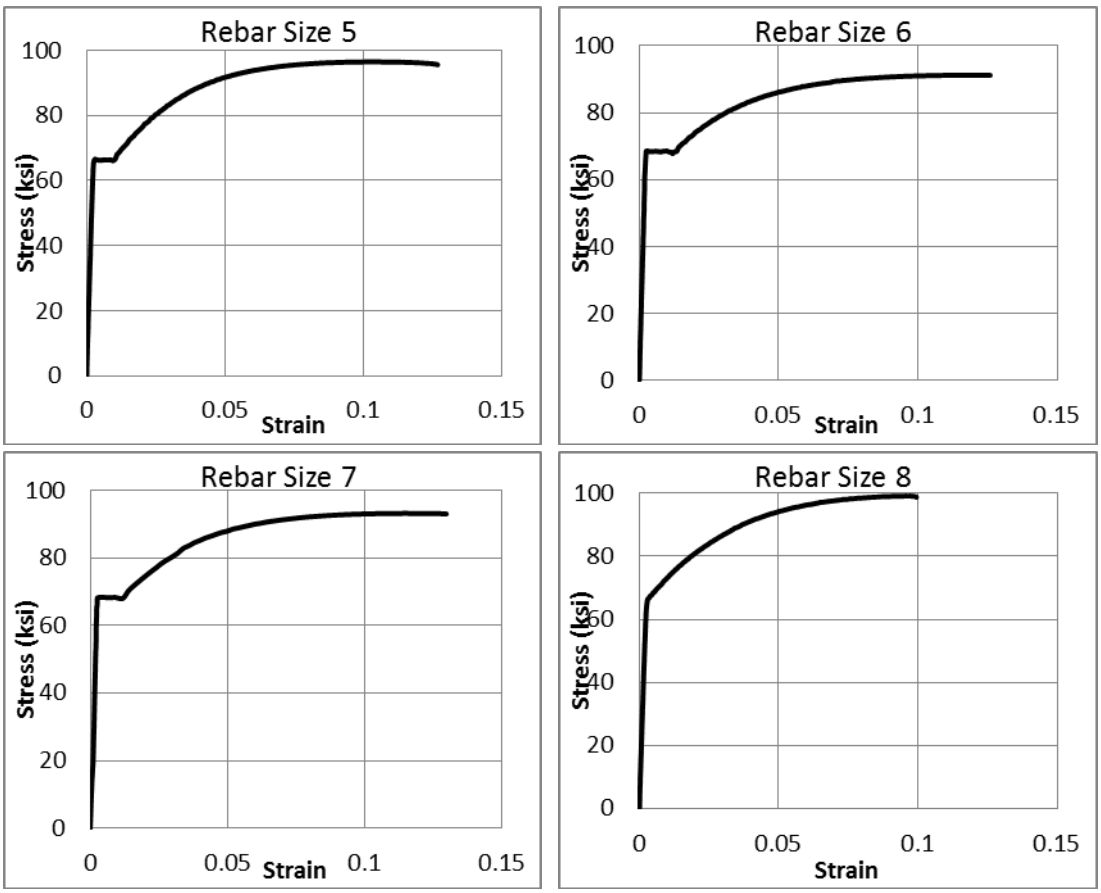

Figure 3-19: Internal Reinforcing Bars Tension Tests

Table 3-6 Tensile Properties of Internal Reinforcing Bars

Required Tensile Properties		
	Yield Strength (ksi)	Tensile Strength (ksi)
ASTM A706 Gr 60	60 -78	80+
Actual Tensile Properties for tests meeting this requirement		
	Yield Strength (ksi)	Tensile Strength (ksi)
Size 5	66.4	96.3
Size 6	68.3	91.2
Size 7	68.3	93.3
Size 8	66.4	99.1

Table 3-7: Average Concrete Compressive Strengths

Test No.	4	5	6	7	8	9	10	11	12
Avg. Concrete Strength (ksi)	6.47	5.22	5.76	4.88	5.62	5.83	5.49	5.39	5.52
Standard Deviation (ksi)	0.22	0.04	0.10	0.09	0.12	0.08	0.25	0.20	0.14

3.7. Experimental Observations

A total of twelve experimental tests were performed for this research project. Observations and photographs recorded during each test are summarized below, analysis of the data and comparison of the results will be discussed later.

3.7.1. Test One

Test 1 consisted of a concrete filled steel tube without internal reinforcement; the tube was spirally welded with an outer diameter equal to 24 inches and a thickness equal to 0.5 inches resulting in a diameter-thickness ratio of 48.

The pile showed no signs of buckling until the first cycle of ductility four. In the first push of ductility four at a mid-span displacement of 13.67 inches, small buckles, less than 0.5 inch in height, appeared at the loading points. In the remainder of the constant moment region other small ridges began to form on the top of the pile (Figure 3-20). During the pull cycle small ridges also began to form only under the loading points and were significantly smaller than the buckles on the top of the pile. No significant changes occurred during the second cycle of ductility four. The buckles visibly increased during the third push and pull of the third cycle. Eight total buckles were observed on the top of the pile during the push cycle, the largest were about ½ inch tall and were located at the north loading point, two slightly smaller buckles were located under the south actuator and four small ridges were located in between those. During the third pull cycle, two buckles under the south actuator increased to almost half an inch, five others were evenly spaced throughout the constant moment region however these buckles were smaller than those on the top of the pile during the push cycle.

Figure 3-20: First signs of buckling at ductility 4 push 1, 13.67 inch displacement.

The first cycle of the fifth ductility level, a displacement of 17.07 inches, the damage became more apparent, the profile of this cycle can be seen in Figure 3-21. During the push cycle the existing buckles increased but no other buckles formed. The two buckles under the north loading point increased in height to approximately 0.75 inches, as seen in Figure 3-22, while the other six buckles increased to approximately 0.5 inches height. The majority of the buckling was perpendicular to the loading however one of the minor buckles near the south actuator ran along the direction of the spiral. During the second push cycle the buckles under each loading point almost doubled in size (Figure 3-23). The first pull cycle also increased the height of the existing buckles. The largest with a height slightly greater than 0.75 inches was located under the north loading point while the others were spaced 8 to 12 inches apart along the constant moment region. All the buckles on the bottom of the pile were perpendicular to the loading.

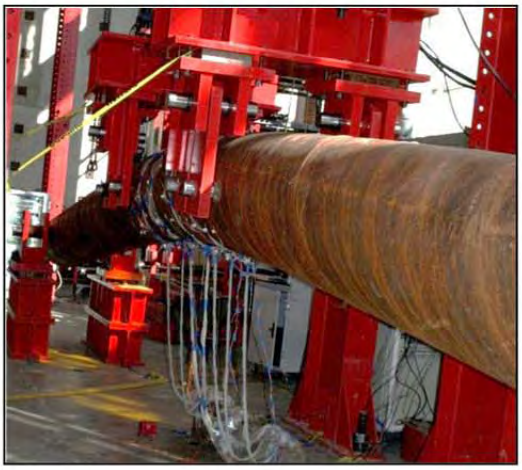

Figure 3-21: Pipe pile profile at ductility 5 and a displacement of 17.07 inches

Figure 3-22: Buckling under north loading point at ductility 5 push 1, at a displacement of 17.07 inches

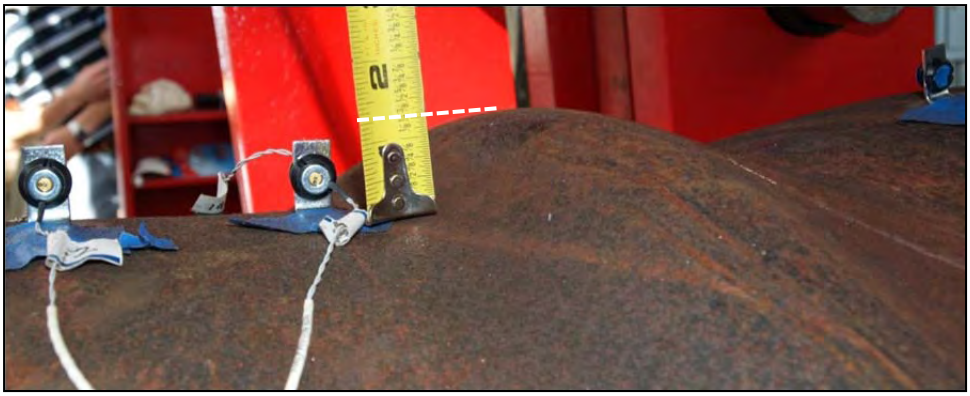

Figure 3-23: Buckling under north loading at ductility 5 push 2, at a displacement of 17.07 inches

The pile ruptured on the top of the pipe during the second pull cycle under the north loading point. In accordance with previous tests conducted on spirally welded pipes at the Constructed Facilities Lab, the weld did not affect the location of rupture because although the rupture was located near the spiral weld it was not on the weld or in the direction of the weld. The rupture was about six inches long with a 3/8" width and the concrete under the rupture was crushed however the concrete under the portion of the pipe that was not buckled, the concrete was still intact. The rupture can be seen in Figure 3-24. During the third push cycle no rupture occurred and no significant change was observed in the bottom of the pile however the rupture on the top grew to about 9 inches in length and 1.5 inches wide as seen in Figure 3-25.

Figure 3-24: First rupture at the second pull of ductility 5 and a displacement of 17.07 inches

Figure 3-25: Rupture at the third push of ductility 5, a displacement of 17.07 inches

The third pull cycle was not completed because the rupture increased to span over the top 180 degrees of the pile. The two actuators were running under equal pressure with one actuator controlling the displacement and translating the pressure to the other actuator. After the rupture, the stiffness of the pile was significantly different under each actuator therefore the area on the pile with the rupture displaced at an increased rate compared to the non-ruptured side causing the rupture to spread quickly and stopping the test (Figure 3-26).

Figure 3-26: Rupture after the test completion

In summary, Test 1 conducted at the Constructed Facilities Lab began on Monday January 30, 2012 and concluded on Tuesday January 31, 2012. The pile was a concrete filled steel tube; the tube was spirally welded with an outer diameter equal to 24 inches and a thickness equal to 0.5 inches resulting in a diameter-thickness ratio of 48. Buckling of the specimen began on the first cycle of ductility four and the size of the buckles continued to increase until pipe rupture occurred on the second pull of ductility cycle 5.

3.7.2. Test Two

Test 2 consisted of a concrete filled steel tube with 12#7 ASTM A706 internal reinforcing bars creating an internal reinforcement ratio of 1.6%; the tube was spirally welded with an outer diameter equal to 24 inches and a thickness equal to 0.125 inches resulting in a diameter-thickness ratio of 192.

The underside of the pile had visible signs of buckling in the third pull of ductility 1.5, at a displacement of 3.06 inches, as seen in Figure 3-27. Small buckling also appeared on the top of the pile during the first push cycle of ductility two with the most apparent buckles located under each actuator where the moment gradient increases and a couple smaller buckles in between. During the remainder of ductility two, four evenly spaced buckles formed on both the top and bottom of the pile. They appeared to be spaced evenly apart (16 to 20 inch spacing) and were all relatively the same size as seen in Figure 3-28 and Figure 3-29. This symmetric behavior continued into ductility 3, with the buckles increasing in height to 0.5 inches to 0.75 inches in height. They continued to be the same size on the top and bottom of the pile during the push and pull cycles respectively. However during the opposing cycles there was no residual buckling, the buckles on the top returned to a smooth surface during the pull cycles and the buckles on the bottom returned to a smooth surface during the push cycles.

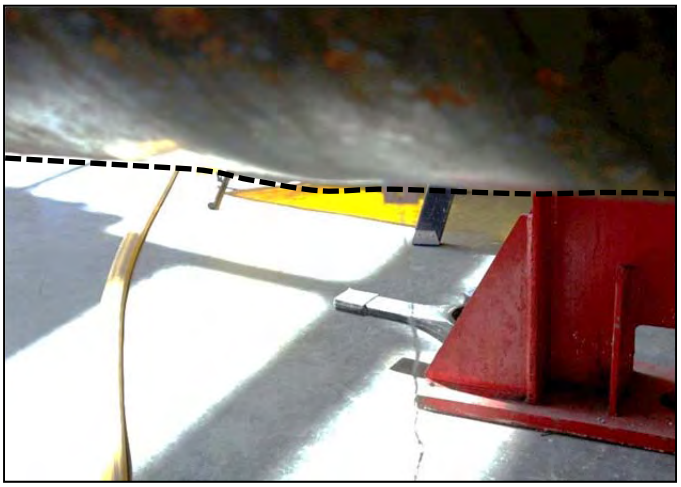

Figure 3-27: Ductility 1.5 – first signs of buckling

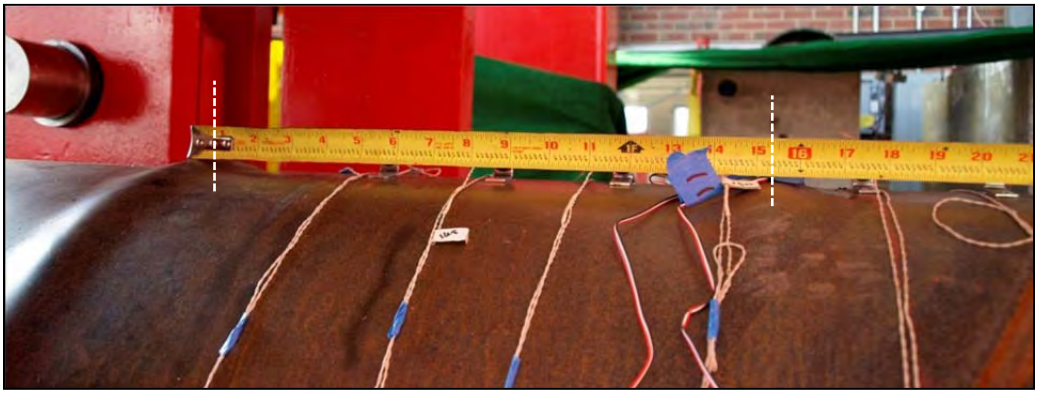

Figure 3-28: Ductility 3 Push 1, buckles spaced 16-20 inches

Figure 3-29: Ductility 3 Pull 1, buckles spaced 16-20 inches

The pile sustained the damage throughout ductility four (a displacement of 8.15 inches), the buckles did not visibly increase in height and no more buckles appeared. During ductility five (a displacement of 10.5 inches) the buckles slightly increased in size and became narrow and the pile continued to behave symmetrically in the push and pull cycles. Residual buckling was observed in the opposite cycles, the buckles were not returning to a smooth surface when they were in tension. The crushing of the concrete under the buckles was heard during the first cycle of ductility six, at a displacement of 12.25 inches. During the second push of ductility six rupture occurred under the north actuator. The rupture was about 15 inches long and occurred along the buckle. The concrete at the rupture location was powder, see Figure 3-30. During the next pull cycle the pile continued to behave symmetrically as the top of the pile ruptured under the North actuator on the peak of the buckle, Figure 3-31. During the third push cycle of ductility six the cracks in the steel grew in both length and

width. When the cracks extended to the side of the pile that had not buckled, the concrete underneath the crack was still solid as seen in Figure 3-32. This leads to the possibility that the concrete only crushes where the buckles form due to the lack of confinement but the concrete remains solid in the rest of the pile.

Overall, the damage of the pile was symmetric and although the pile buckled in an early ductility cycle of 1.5 it sustained its damage until rupture at ductility six. The progression of the damage from ductility 2 until ductility 6 can be seen in Figure 3-33. The buckles grow significantly between ductility 2 and 3 but after ductility 3 there is no significant change in the size of the buckles until rupture.

Figure 3-30: Rupture during the second push of ductility six, at a displacement of 12.5 inches

Figure 3-31: Rupture during the second pull of ductility six, at a displacement of 12.5 inches

Figure 3-32: Concrete is still intact after rupture occurred where buckling had not

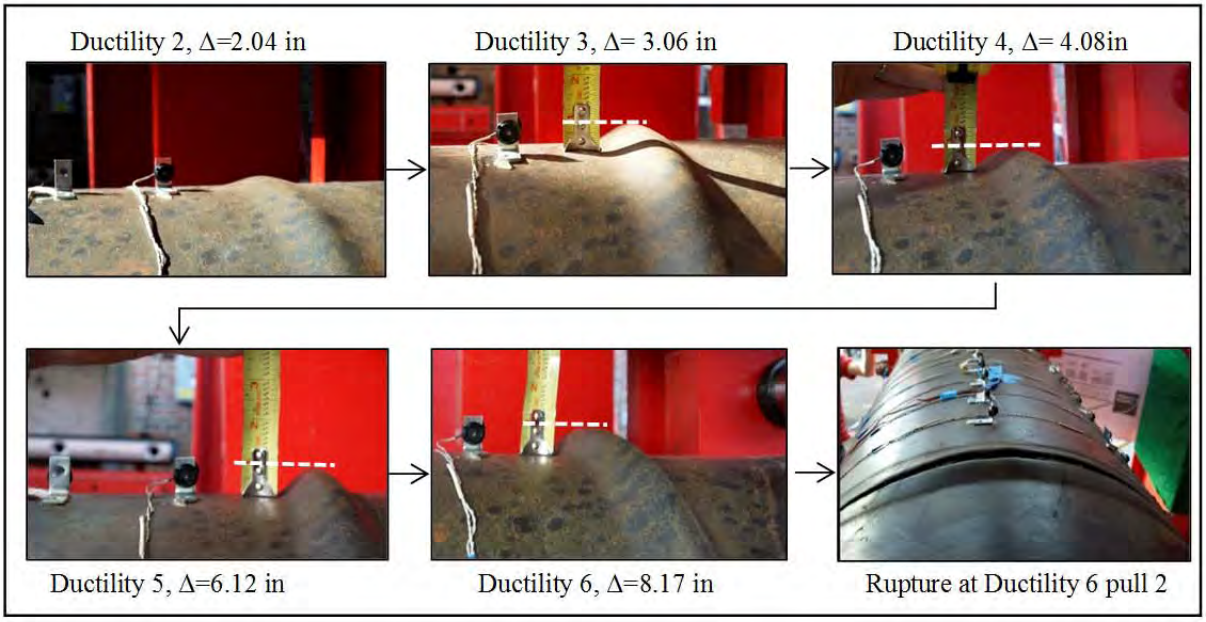

Figure 3-33: Progression of buckling

The force-displacement hysteresis of this test, after the dead weight of the pile had been accounted for, is shown in Figure 3-34. The force-displacement envelopes for the first, second, and third cycles are shown in Figure 3-35. The pile had an average ultimate force of about 62 kips and did not lose strength until the pile ruptured in the second cycle of ductility six.

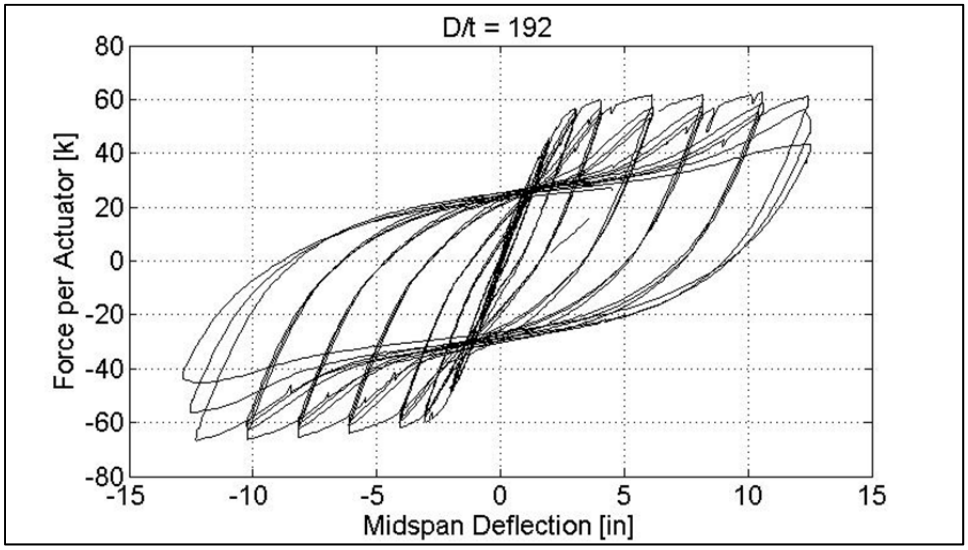

Figure 3-34: Force – Displacement Hysteresis

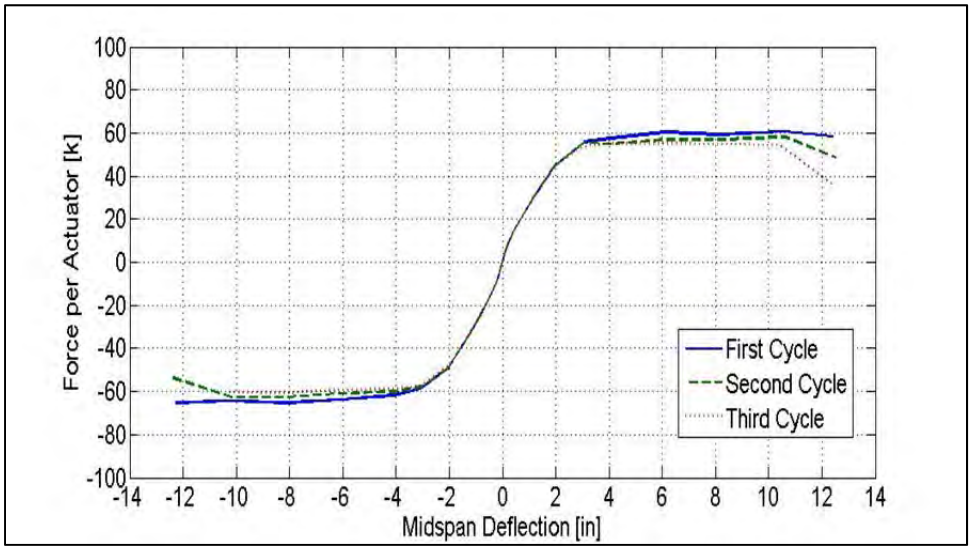

Figure 3-35: Force – Displacement Envelopes

Test 2 was conducted at the Constructed Facilities Lab on Wednesday February 15, 2012. The pile was a concrete filled steel tube; the tube was spirally welded with an outer diameter equal to 24 inches and a thickness equal to 0.125 inches resulting in a diameter-thickness ratio of 192. Visible buckling of the specimen began in the third cycle of ductility 1.5, however the pile sustained the damage without strength degradation until rupture in the second cycle of ductility 6.

3.7.3. Test Three

Test 3 consisted of a concrete filled steel tube with 12#7 ASTM A706 internal reinforcing bars creating an internal reinforcement ratio of 1.6%; the tube was spirally welded with an outer diameter equal to 24 inches and a thickness equal to 0.1875 inches resulting in a diameter-thickness ratio of 128.

The top side of the pile had signs of buckling in the first push of ductility two, at a displacement of 4.5 inches. Signs of buckling also appeared on the bottom of the pile during the first pull cycle of ductility two with the most apparent buckles located under each actuator where the moment gradient increases. The two buckles (one located under each actuator) on the top of the pile became more apparent during the first cycle of ductility three, at a displacement of 6.8 inches, as seen in Figure 3-36. In the reverse pull cycle, two smaller buckles appeared under the pile between the existing buckles, as seen in Figure 3-37. Similarly, two smaller buckles formed on the top of the pile during the second push cycle in addition to the two existing under the actuator. Throughout the remainder of ductility three, the four buckles on either side of the pile all increased to a height of about 0.5 inches. There was no residual buckling during ductility three, when the loading direction was reversed the buckles on the side in tension side became smooth again.

Figure 3-36: Visible signs of buckling under the actuator at ductility 3, displacement = 6.8 inches

Figure 3-37: Four buckles located in the constant moment region at ductility 3, displacement = 6.8 inches

During ductility four at a displacement of 8.4 inches, no additional buckles formed and the existing buckles increased to a height of about 0.75 inches. The buckles were spaced approximately 18 to 20 inches along the constant moment region on either side of the pile as shown in Figure 3-38. Residual buckling started to occur during this cycle, meaning as the loading direction was reversed the buckles being placed into tension did not return to a smooth state but sustained small ripples where the buckling occurred in the previous cycle. The buckles continued to increase in size to a height of approximately one inch during ductility five.

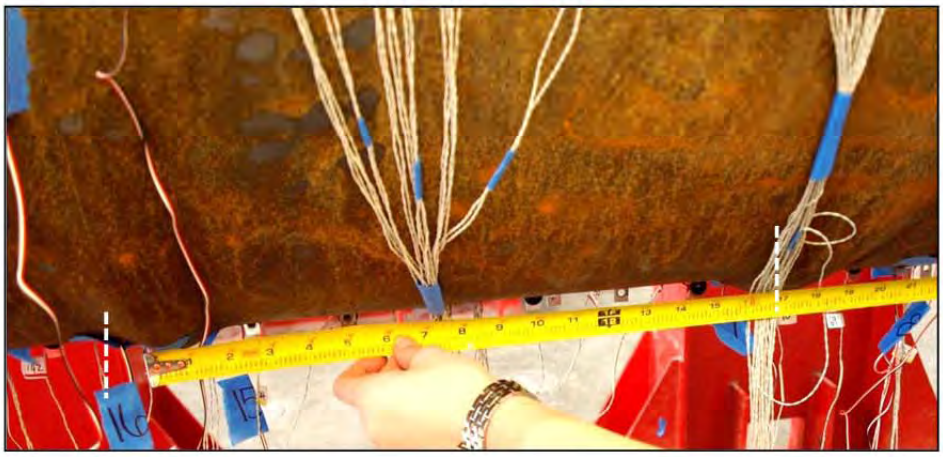

Figure 3-38: Buckles spaced 18-20" at ductility 4, displacement = 8.4 inches

The pile sustained the damage though the first two cycles of ductility six; the buckles' size did not increase. Rupture occurred on the underside of the pile under the north actuator when placed into tension during the third push of ductility six at a displacement of 12 inches, Figure 3-39. The rupture occurred along the crease of the previous buckle and the concrete inside the pile was crushed due to the lack of confinement. During the next reversal (third pull) the pile did not rupture on the top of the pile when placed into tension however signs of necking did appear along the buckled regions under both actuators, Figure 3-40.

Figure 3-39: Rupture at ductility six, push three, displacement = 12 inches

Figure 3-40: Necking of the pile, ductility six pull three, displacement = 12.8 inches

Overall, the damage of the pile was symmetric and although the pile buckled in an early cycle of ductility two it sustained its damage until rupture at ductility six. The progression of the damage from ductility three until ductility six can be seen in Figure 3-41. The buckles continued to increase in size between ductility three and five but there was no significant change in ductility six.

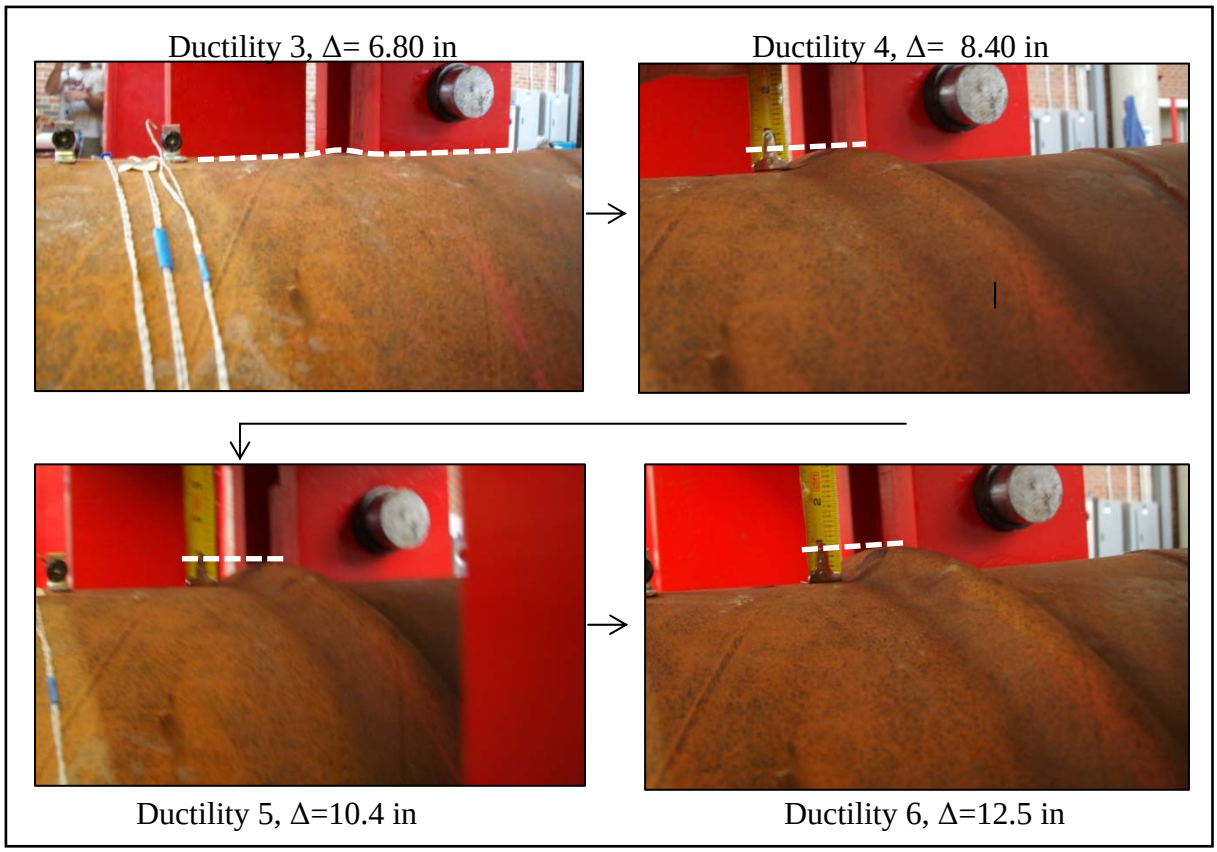

Figure 3-41: Progression of buckling

The force-displacement hysteresis of this test, after the dead weight of the pile had been accounted for, is shown in Figure 3-42. The force-displacement envelopes for the first, second, and third cycles are shown in Figure 3-43. The pile had an average ultimate force of about 75 kips and did not lose strength until the pile ruptured in the third cycle of ductility six.

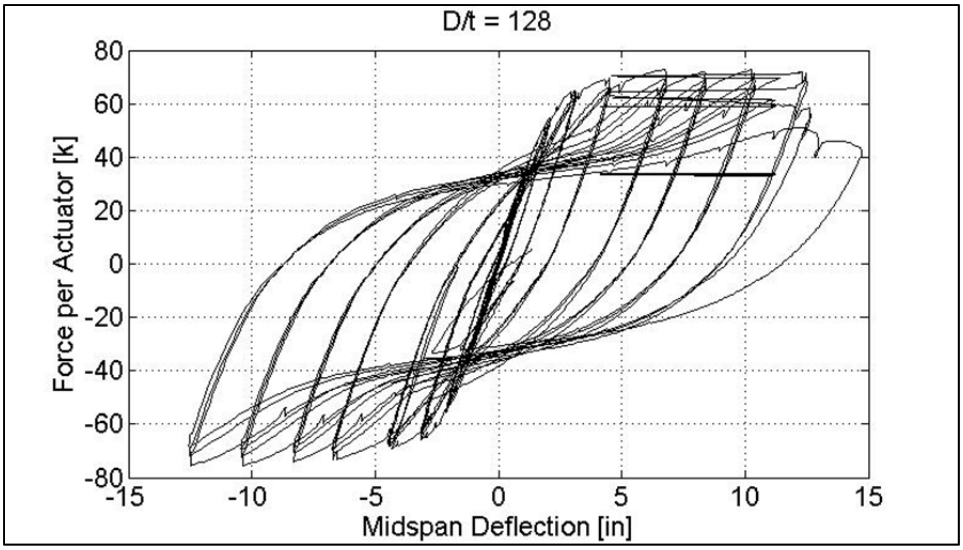

Figure 3-42: Force-Displacement Hysteresis

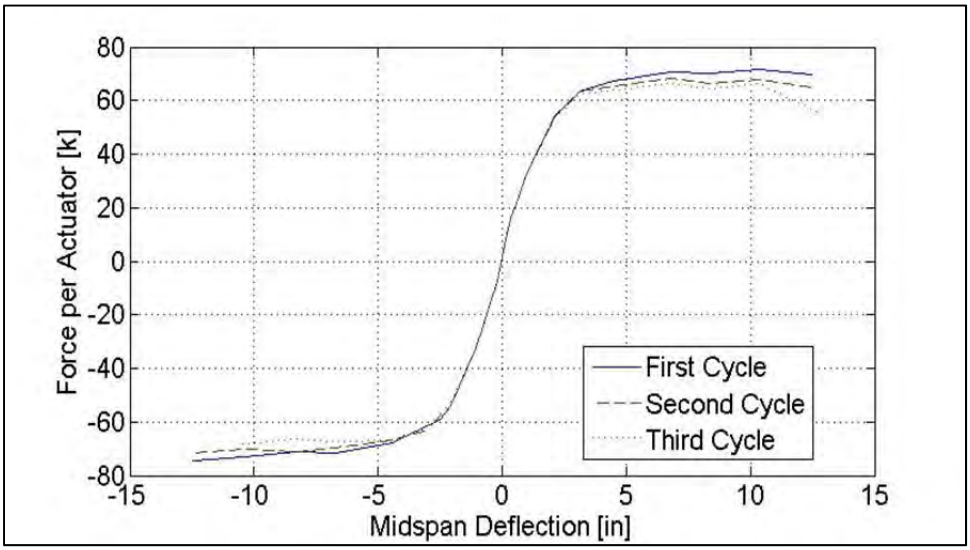

Figure 3-43: Force-Displacement Envelopes

Test 3 conducted at the Constructed Facilities Lab was conducted on Wednesday February 29, 2012. The pile was a concrete filled steel tube; the tube was spirally welded with an outer diameter equal to 24 inches and a thickness equal to 0.1875 inches, resulting in a diameter-thickness ratio of 128. Buckling of the specimen began in the first cycle of ductility

two, however the pile sustained the damage without strength degradation until rupture in the third cycle of ductility six.

3.7.4. Test Four

Test 4 consisted of a concrete filled steel tube with 12#7 ASTM A706 internal reinforcing bars creating an internal reinforcement ratio of 1.6%, the tube had an outer diameter equal to 24 inches and a thickness equal to 0.375 inches resulting in a diameter-thickness ratio of 64.

The pile showed signs of buckling at ductility three, at a displacement of 9 inches. Buckling initiated in the first pull of ductility three on the underside of the pile (Figure 3-44), the compressive region, and when the cycle was reversed (the second push) and the top of the pile developed compression stress and small signs of buckling were observed. During the initiation of buckling, buckles only began to form under each loading point. As the pile continued to be pushed and pulled nine inches in each direction during ductility three, smaller ripples began forming in between the two previous formed buckles, both on the underside of the pile during the pull cycles and the top of the pile during the push cycles (Figure 3-45).

Figure 3-44: Buckling initiated under pile during the first pull of ductility three

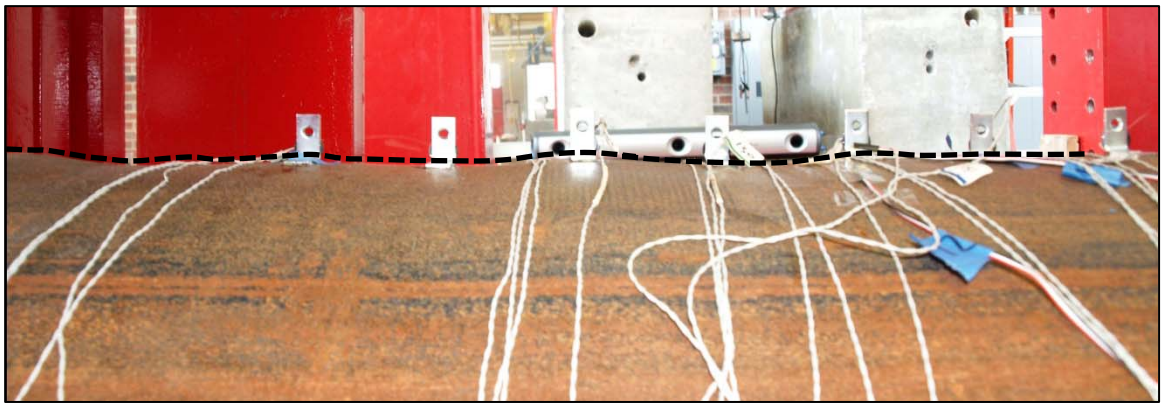

Figure 3-45: Ripples forming on top of the pile during the third push of ductility three

When the displacements increased to twelve inches in each direction, in ductility four, the buckles under each loading point increased in size. During the second push and pull set the small ripples in between the loading points were concentrated into two buckles spaced about 20 inches apart- resulting in a total of four buckles on either side of the pile (Figure 3-46). The buckles continued to grow in size throughout the loading in ductility four. At the end of ductility four the buckles were all approximately 1 – 1.25 inches in height; the largest buckles occurred at the change in moment gradient under each loading point (Figure 3-47 and Figure 3-48).

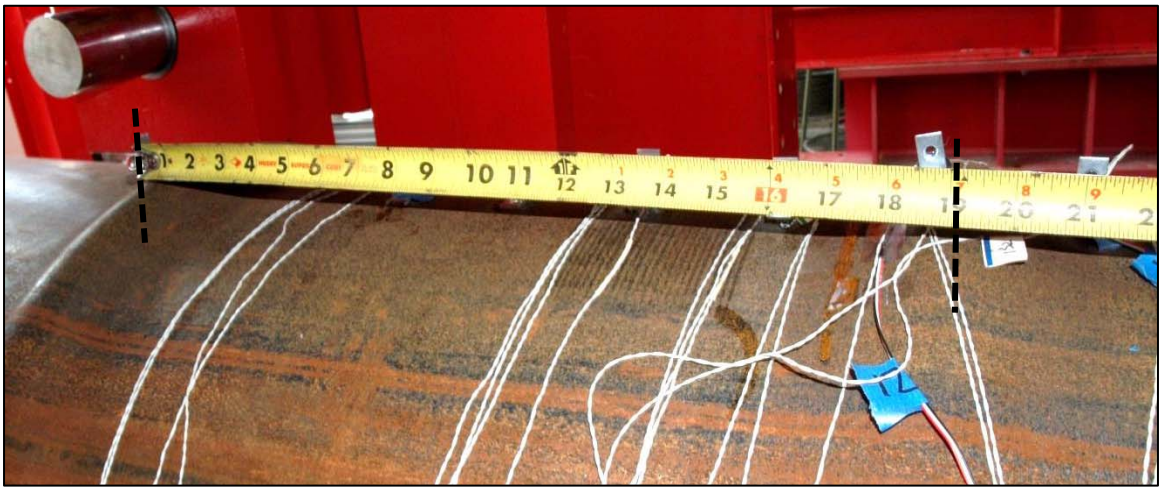

Figure 3-46: Buckles spaced at approximately 20 inches, during ductility four (Δ=12 inches)

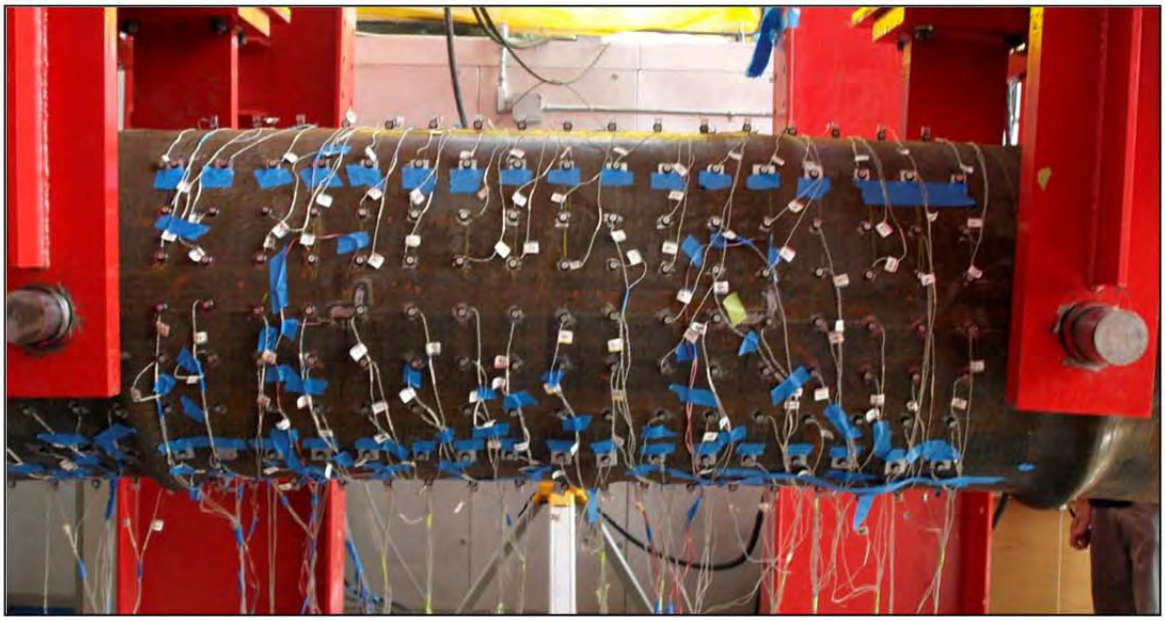

Figure 3-47: Constant moment region, ductility four (Δ=12 inches)

Figure 3-48: Buckle under the loading point during ductility four (Δ=12 inches)

After ductility four ended, the buckles which were not located under the loading points showed no significant changes throughout the remainder of the test, the damage became concentrated in the two buckles under each loading point. These buckles continued to increase in size as the pile underwent displacements of 15 inches in either direction in ductility five (Figure 3-49), reaching a maximum height of approximately two inches. During the second pull of ductility five, one of the longitudinal reinforcing bars ruptured

resulting in a 15 kip strength loss of the pile. As the pile reached 15 inches of displacement in the second push and pull cycles, tension cracks appeared on the side of the pile undergoing tensile stress, the underside of the pile during the push cycle and the top of the pile during the pull cycle (Figure 3-50). These cracks formed along the edges of the buckles. During the third pull cycle, the pile ruptured at one of the loading points along the edge of the buckle where the tension cracks had previously formed (Figure 3-51). The progression of the pile buckling leading up to rupture can be seen in Figure 3-52.

Figure 3-49: Pile profile at ductility five (Δ = 15 inches)

Figure 3-50: Tension cracks under the pile during the third push of ductility 5 (Δ=15in)

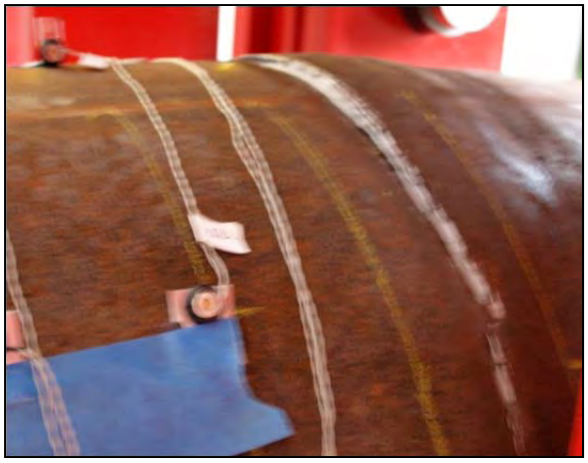

Figure 3-51: Pile Rupture, ductility five (Δ = 15 inches)

Figure 3-52: Progression of buckling

The force-displacement hysteresis of this test, after the dead weight of the pile had been accounted for, is shown in Figure 3-53. The force-displacement envelopes for the first, second, and third cycles are shown in Figure 3-54. The pile had an average ultimate force of about 150 kips and lost 15 kips of strength after the longitudinal reinforcing bar ruptured on the second pull of ductility five.

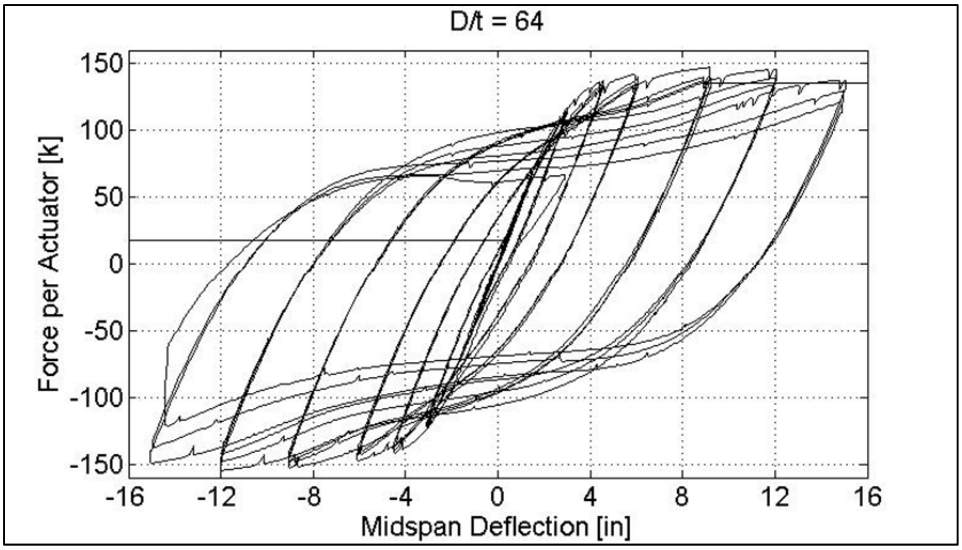

Figure 3-53: Force-Displacement Hysteresis

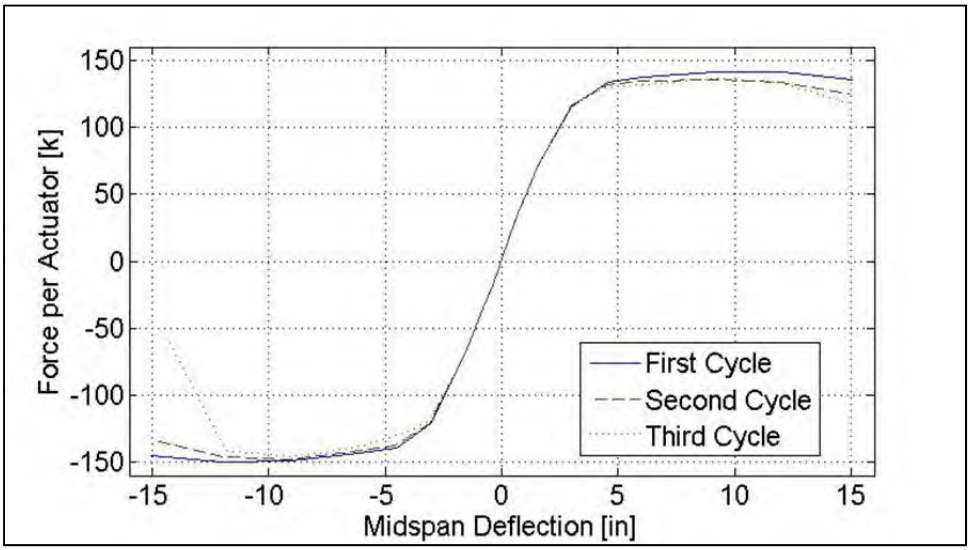

Figure 3-54: Force-Displacement Envelopes

Test 4 was conducted at the Constructed Facilities Lab on Friday March 14, 2012. The pile was a concrete filled steel tube; the tube had an outer diameter equal to 24 inches and a thickness equal to 0.375 inches, resulting in a diameter-thickness ratio of 64. Buckling of the specimen began in the first cycle of ductility three. The pile sustained the damage without strength degradation until rebar rupture in the second cycle of ductility five and rupture of the steel pipe followed in the third cycle of ductility five.

3.7.5. Test Five

Test 5 consisted of a concrete filled steel tube with 12#7 ASTM A706 internal reinforcing bars creating an internal reinforcement ratio of 1.6%; the pile had an outer diameter equal to 24 inches and a thickness equal to 0.28 inches resulting in a diameter-thickness ratio of 85.

The pile showed signs of buckling at ductility three, a displacement of 9.8 inches. Buckling initiated in the first pull of ductility three on the underside of the pile (Figure 3-55), the compressive region, and when the cycle was reversed (the second push) the top of the pile developed compression stress and small signs of buckling were observed. As buckling initiated, the pile developed multiple small buckles along the length of the constant moment region. In the first pull of ductility three, six small buckles formed on the underside of the pile. The two most significant buckles were located under the loading points and the other four were small ridges evenly spaced in the constant moment region. When buckling of the top of the pile began, in the reverse push direction, a total of eight buckles formed on the top of the pile. However, similar to the other side of the pile in the pull direction, the two buckles located under each loading point were significantly larger than the remainder of the buckles throughout the constant moment region.

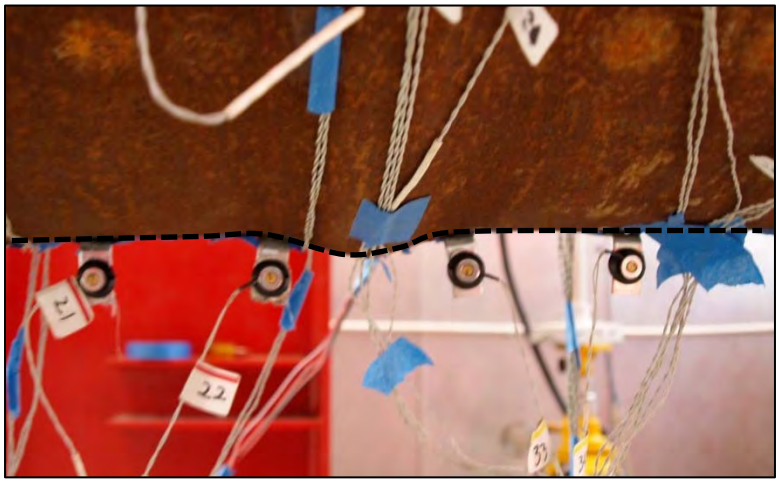

Figure 3-55: Initiation of buckling at ductility three, Δ = 9.8 inches

As the pile continued to undergo displacements of 9.8 inches in each direction, the “ripples” of buckles in the constant moment region concentrated themselves to a few buckles on either side of the pile. By the third pull of ductility three, the six buckles which had previously formed on the bottom of the pile condensed to four buckles. The two largest were still located under the loading points and had a height of approximately 0.75 inches (Figure 3-56), the smaller two buckles were about 0.25 inches in height (Figure 3-57) and spaced 16-20

inches apart (Figure 3-58). After the third push of ductility three, the eight buckles which previously formed on the top of the pile had reduced to three buckles, the two largest located under the loading points, and the last was approximately six inches off center from the center of the constant moment region (Figure 3-59). Unlike the behavior on the bottom of the pile in the push directions, the buckles located at the loading points were not significantly larger than the one located in the center of the constant moment region.

Figure 3-56: Buckle under loading point, ductility 3, Δ = 9.8 inches

Figure 3-57: Buckle in constant moment region, ductility 3, Δ = 9.8 inches

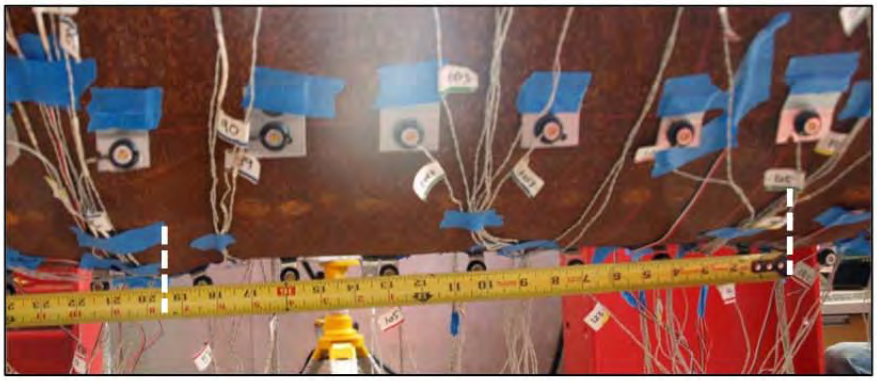

Figure 3-58: Spacing of buckles at ductility 3-pull 2, Δ = 9.8 inches

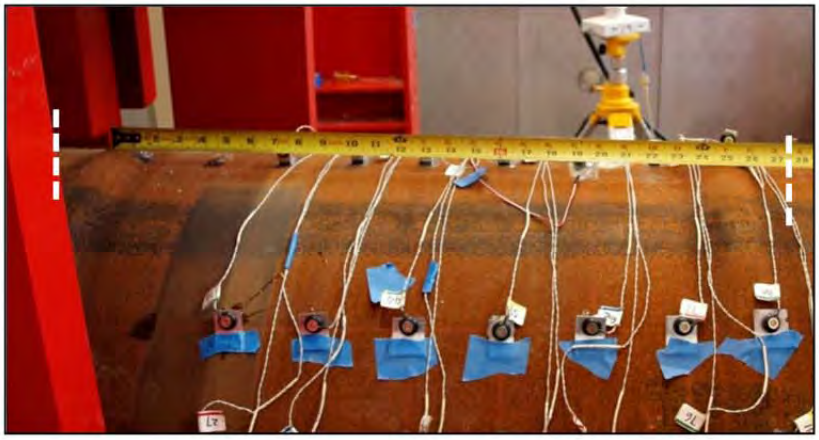

Figure 3-59: Spacing of buckles at ductility 3, Δ = 9.8 inches

In ductility four, the pile displacements increased to 13.1 inches in both directions of loading. During these push and pull cycles the buckles continued to increase in size until they reached a height of about one inch (Figure 3-60). Throughout the test, the buckles under the loading points, at the change of moment gradient, remained larger than those spaced throughout the constant moment region. In the push direction, three total buckles formed on the top of the pile (Figure 3-61) and in the pull direction four total buckles formed on the underside of the pile. During the third pull of ductility four, the test was temporarily stopped at a displacement of 11.3 inches to observe the tension cracks which had appeared on the top of the pile at the creases of the two largest buckles (under the loading points) as seen in Figure 3-62. The test continued to be pulled until the pile ruptured under the north loading point at a center displacement of 13 inches in the last pull of ductility four (Figure 3-63). The loading was reversed once again and while being pushed, the underside of the pile ruptured on the

same diameter that the top of the pile had previously ruptured (Figure 3-64). The progression of buckling leading to rupture is shown in Figure 3-65.

Figure 3-60: Size of buckle at ductility 4, Δ = 13.1 inches

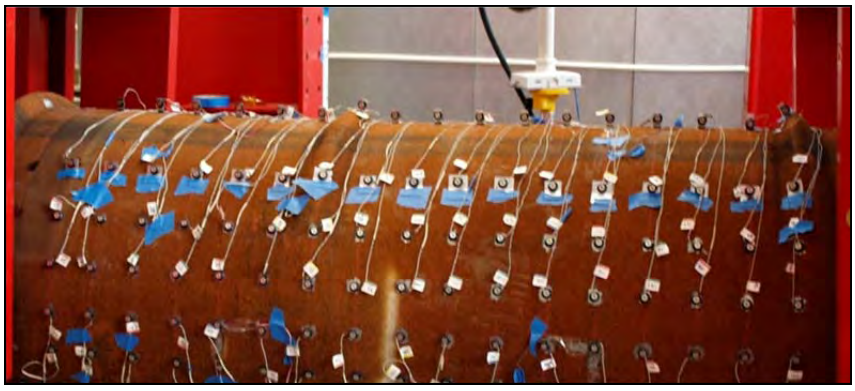

Figure 3-61: Damage concentrated into 3 buckles at ductility 4, Δ = 13.1 in

Figure 3-62: Tension cracking during the third pull, at 11 inches displacement, approaching the 13 inch displacement at ductility 4

Figure 3-63: Rupture on top of the pile, ductility 4 pull 3, Δ = 13 inches

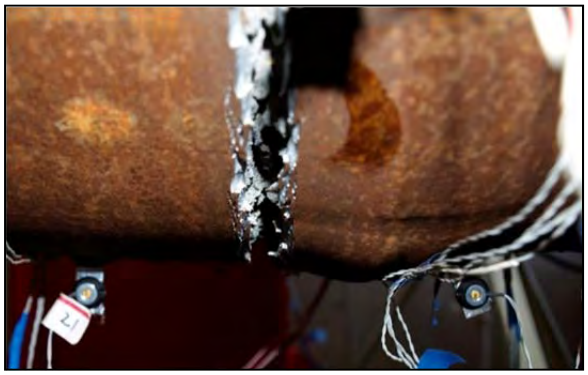

Figure 3-64: Rupture on the bottom of the pile

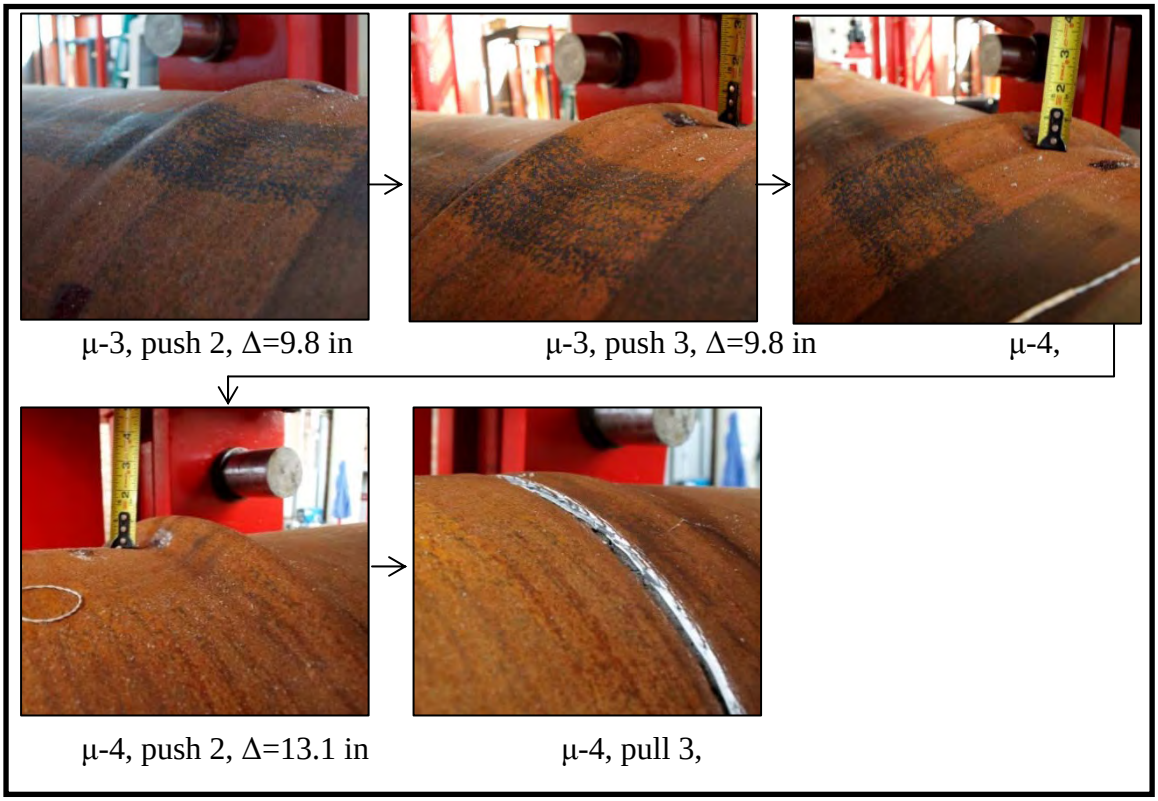

Figure 3-65: Progression of buckling

The force-displacement hysteresis of this test, after the dead weight of the pile had been accounted for, is shown in Figure 3-66. The force-displacement envelopes for the first, second, and third cycles are shown in Figure 3-67. The pile had an average ultimate force of about 135 kips and had little strength degradation between ductility levels before the pile ruptured.

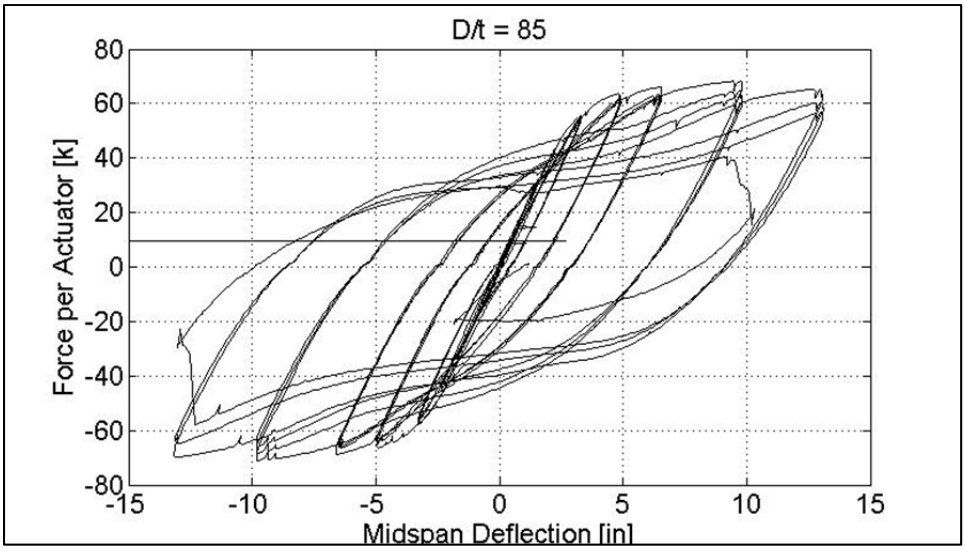

Figure 3-66: Force-Displacement Hysteresis

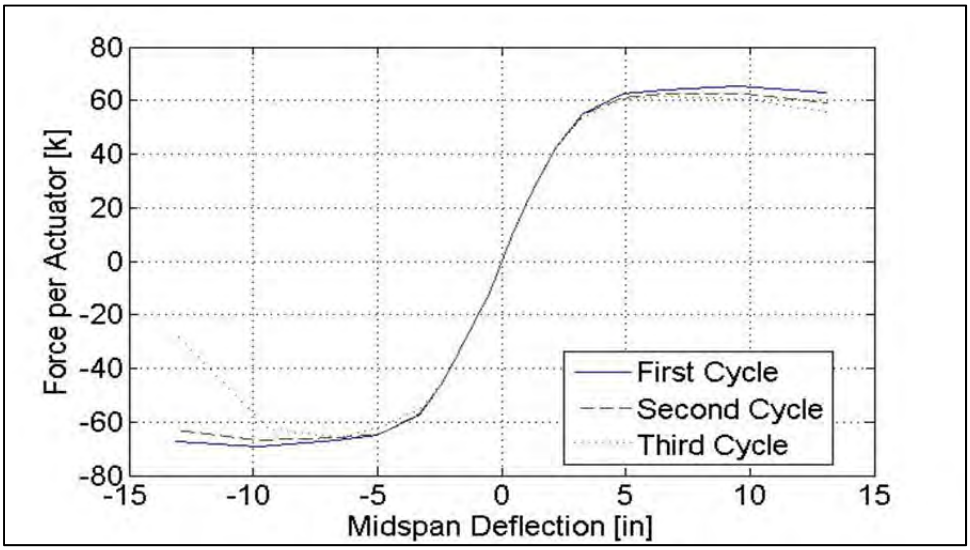

Figure 3-67: Force-Displacement Envelopes

Test 5 was conducted at the Constructed Facilities Lab on Friday March 30, 2012. The pile was a concrete filled steel tube; the tube had an outer diameter equal to 24 inches and a thickness equal to 0.28 inches, resulting in a diameter-thickness ratio of 85. Buckling of the specimen began in the first cycle of ductility three. The pile sustained the damage without strength degradation until pile rupture in the third pull of ductility four.

3.7.6. Test Six

Test 6 consisted of a concrete filled steel tube with 12#6 ASTM A706 internal reinforcing bars creating an internal reinforcement ratio of 1.6%; the pipe had an outer diameter equal to 20 inches and a thickness equal to 0.606 inches resulting in a diameter-thickness ratio of 33.

The pile showed visible signs of buckling at ductility five, a displacement of 13 inches. Buckling initiated in the first push of ductility five on the top of the pile (Figure 3-68), the compressive region, and when the cycle was reversed (the second push) and the underside of the pile developed compression stress and small signs of buckling were observed. During the initiation of buckling, buckles only began to form under each loading point. As the pile continued to be pushed and pulled thirteen inches in each direction during ductility five, no more visible buckles occurred between the loading points however the buckles located under each loading point increased in size. Figure 3-69 shows a buckle on the underside of the pile during the third pull of ductility five.

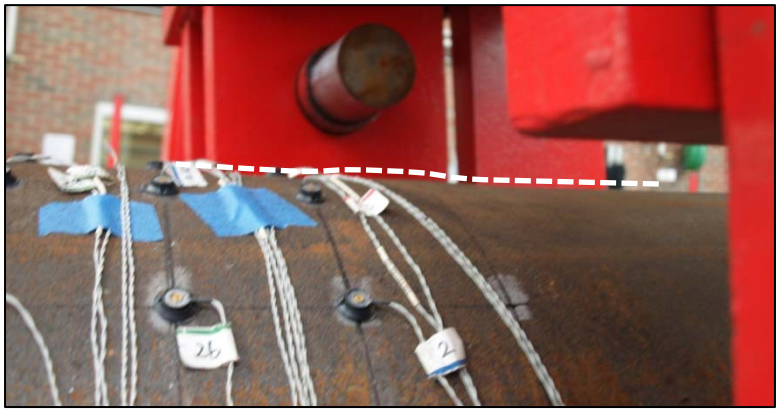

Figure 3-68: Buckling initiated under pile during the first push of ductility five

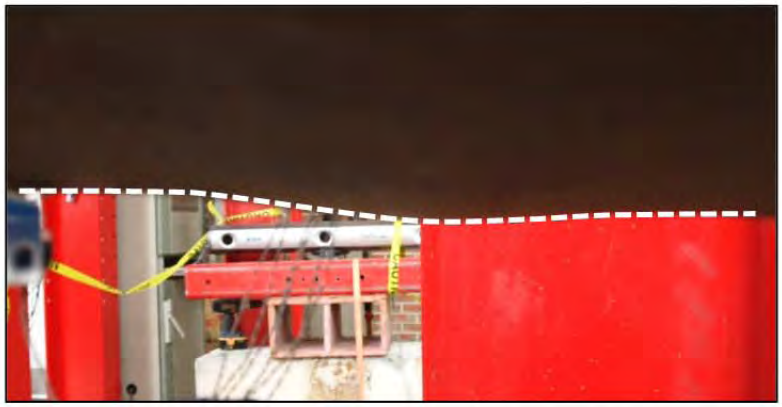

Figure 3-69: Buckle on the underside during ductility five, Δ = 13 inches

The displacement in each direction increased to 15.6 inches during ductility 6, a profile of the pile during this displacement is seen in Figure 3-70. During the first cycle of ductility six the buckles under the loading points increased in size and the steel pipe began to form small ripples throughout the constant moment region. The most significant new buckle was located on the top of the pile directly next to the existing buckle under the North loading point on the outer edge of the constant moment region (Figure 3-71). As the three cycle set continued into the second and third cycles, more "ripples" began to form in the constant moment region (Figure 3-72), and the buckles under the loading points continued to increase in size. Throughout the three cycle set the most significant buckles were still located under each loading point. During the third cycle the buckles under each loading point were about 1.5 inches in height (Figure 3-73).

Figure 3-70: Pile profile with a mid-span displacement of 15.6 inches (ductility six)

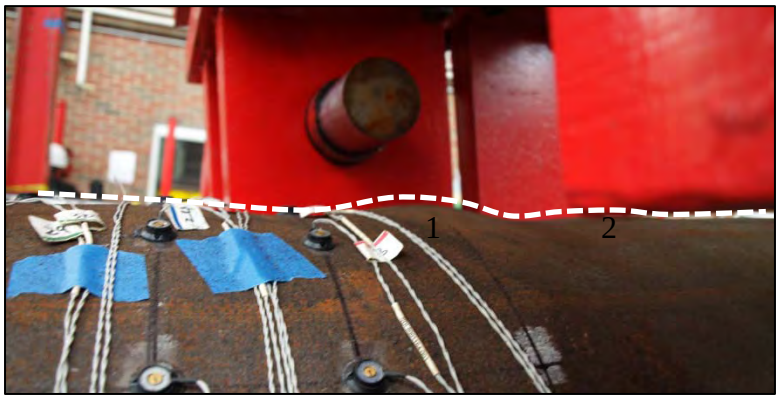

Figure 3-71: Formation of buckles under north loading point-first push ductility six, Δ=15.6 in

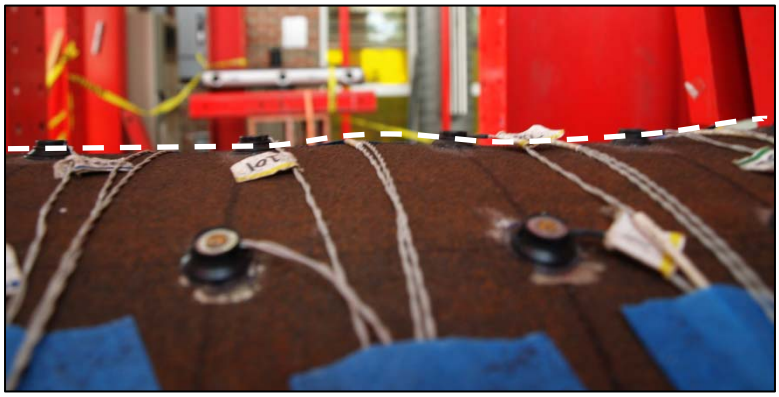

Figure 3-72: "Ripples" in the constant moment region, second push ductility six, Δ = 15.6 in

.

Figure 3-73: Buckle under North loading point during the third pull of ductility six, Δ = 15.6 in

The next ductility level, ductility seven pushed the pile to a mid-span displacement of 18.2 inches; the profile of this level of deformation is seen in Figure 3-74. The first push of ductility seven caused the buckles under each loading point to increase in size. However the steel pipe had more damage under the north loading point, demonstrated by the size of the buckle which was about 2 inches in height, 25% larger than that under the south loading point (Figure 3-75). In the reverse cycle, the first pull of ductility seven the top of the pile could not deform to level of tension strain due to the large levels of compressive strains encountered during the first push and the steel pipe fractured during the first pull. The fracture occurred next to the sleeve under the north loading point and extended from the sleeve up the pile (Figure 3-76). As the pile continued to deform, the crack increased in length and width and the concrete inside the pile was crushed as expected (Figure 3-77). The pile was not able to reach the full displacement of 18.2 inches in the pull direction due to the fracture of the steel pile. The progression of buckling which began in ductility five to rupture in ductility seven can be seen in Figure 3-78.

Figure 3-74: Pile profile with a mid-span displacement of 18.2 inches (ductility seven).

Figure 3-75: Buckle under North loading point during ductility seven, Δ = 18.2 in

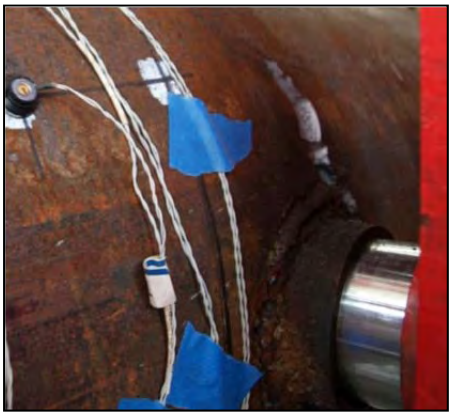

Figure 3-76: Initial rupture of the steel pipe during the first pull of ductility seven

Figure 3-77: Rupture of the steel pipe during the first pull of ductility seven

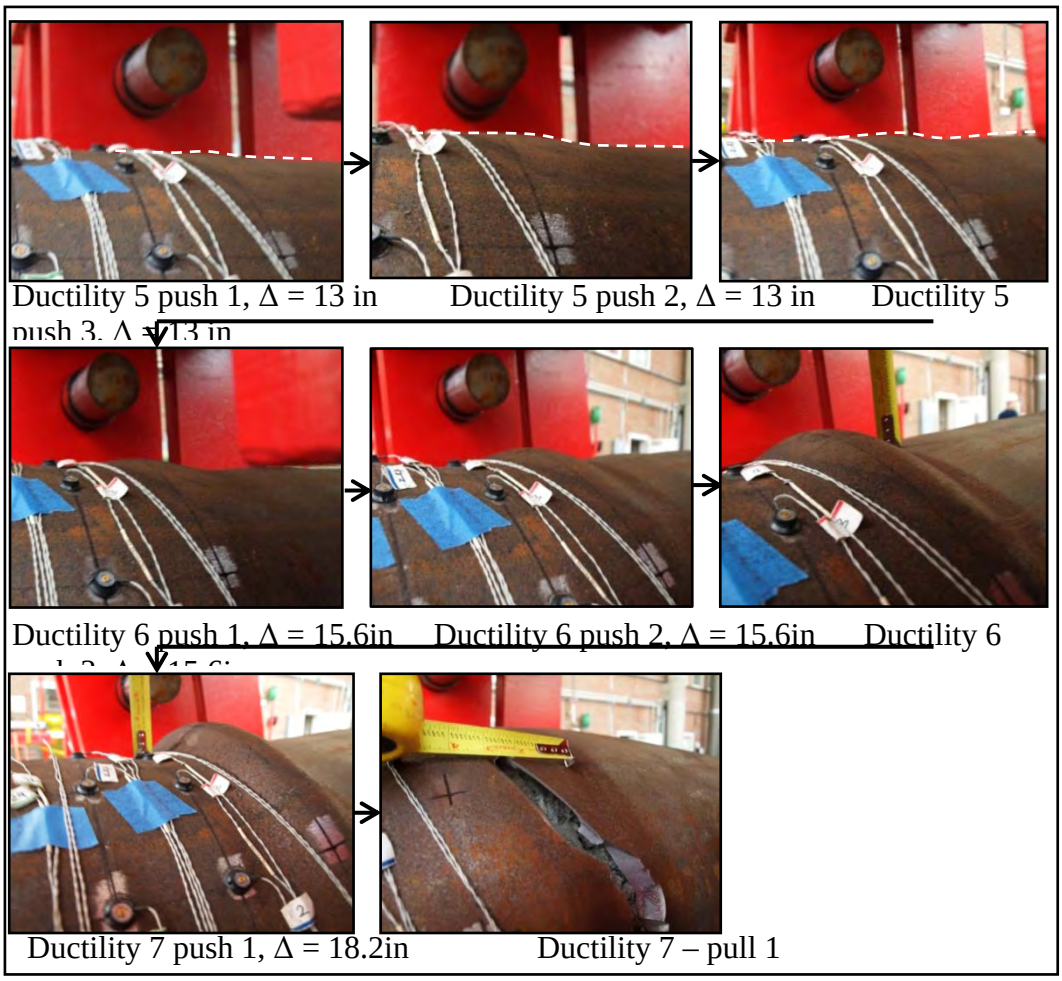

Figure 3-78: Progression of buckling

The force-displacement hysteresis of this test, after the dead weight of the pile had been accounted for, is shown in Figure 3-79. The force-displacement envelopes for the first, second, and third cycles are shown in Figure 3-80. The pile had an average ultimate force of about 164 kips.

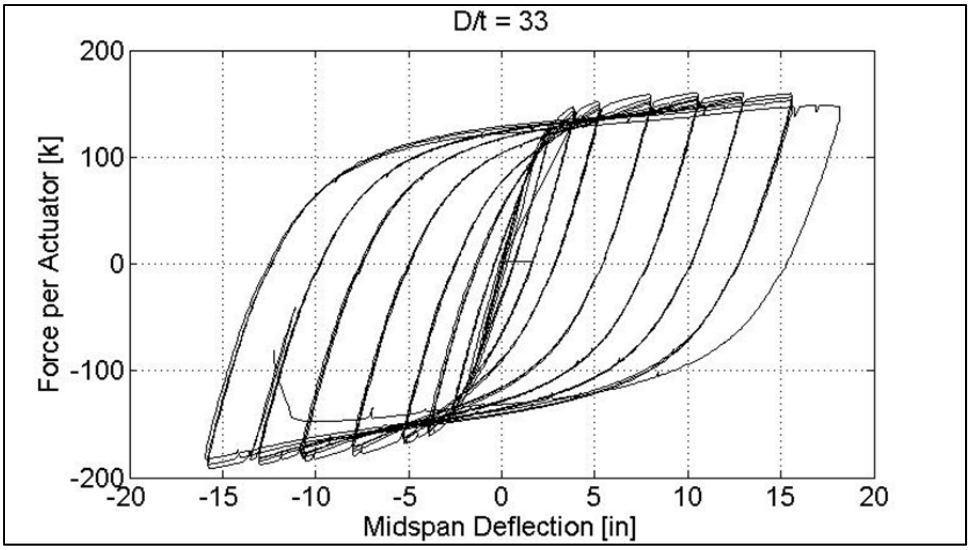

Figure 3-79: Force-Displacement Hysteresis

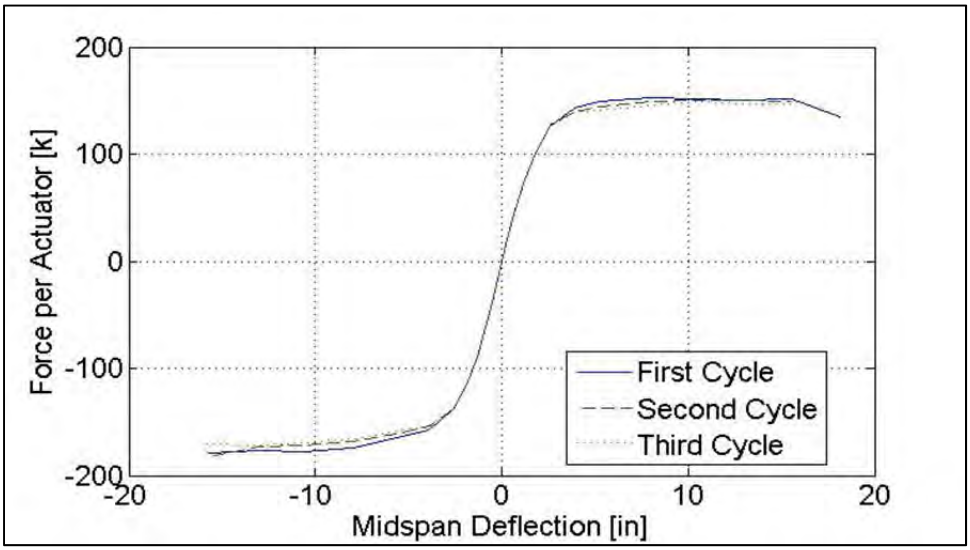

Figure 3-80: Force-Displacement Envelopes

Test 6 was conducted at the Constructed Facilities Lab. The test began on Tuesday, August 14th and concluded on Wednesday, August 15th 2012. The pile was a concrete filled steel tube; the tube had an outer diameter equal to 20 inches and a thickness equal to 0.606 inches, resulting in a diameter-thickness ratio of 33. Visible buckling of the specimen began in the first cycle of ductility five at a displacement of 13 inches in both directions. The pile sustained the damage without strength degradation until rupture in the first cycle of ductility seven.

3.7.7. Test Seven

Test 7 consisted of a concrete filled steel tube with 12#6 ASTM A706 internal reinforcing bars, creating an internal reinforcement ratio of 1.6%; the pipe had an outer diameter equal to 20 inches and a thickness equal to 0.125 inches resulting in a diameter-thickness ratio of 160.

Pile buckling was first visible early in the test, at ductility one and a half at a mid-span displacement of 1.8 inches. Buckling initiated in the first pull of ductility one and a half on the underside of the pile which was in compression. Buckles formed under each loading point where the moment gradient changed and one buckle was observed in the center of the constant moment region (Figure 3-81). When the cycle was reversed the pile began to buckle on the top of the pile which was in compression, buckles were only visible under the loading points. At the conclusion of the ductility level, two buckles had formed on the top of the pile one under each loading point as seen in Figure 3-82 and three had formed on the underside of the pile (one under each loading point and one in the center). The buckles formed during the pull cycles, on the underside of the pile, were larger than those during the push cycles, on the top of the pile.

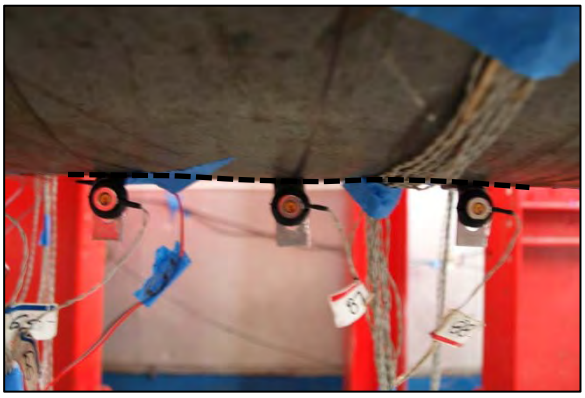

Figure 3-81: Initiation of buckling, Ductility 1.5 first pull, Δ=1.8 inches

Figure 3-82: Pile buckling, Ductility 1.5 third push, Δ=1.8 inches

The damage in the pile began to increase during the next ductility level (ductility two) when the specimen was pushed and pulled 3.8 inches in each direction (Figure 3-83). During the push cycles, a total of nine ripples had formed on the top surface of the pile. The buckles located underneath each loading points were slightly larger than the seven which were located in the constant moment region between them. Examples of the "ripples" are shown in Figure 3-84Figure 3-85. The behavior of the underside of the pile during the pull cycles was slightly different, instead of forming many small ripples only 5 buckles formed but they were significantly larger than those on the top of the pile during the push cycles. Three of the four buckles were located either directly under the loading points or directly next to them (Figure 3-86), however the largest buckle was located in the constant moment region about twelve inches away from the centerline of the pile (Figure 3-87).

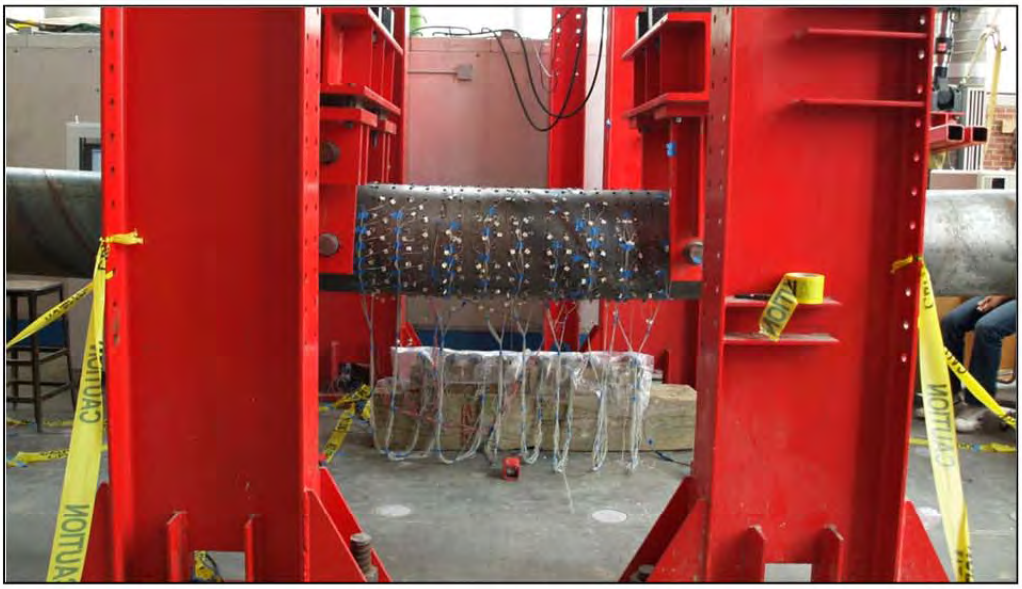

Figure 3-83: Specimen profile, Ductility 2, Δ=3.8in

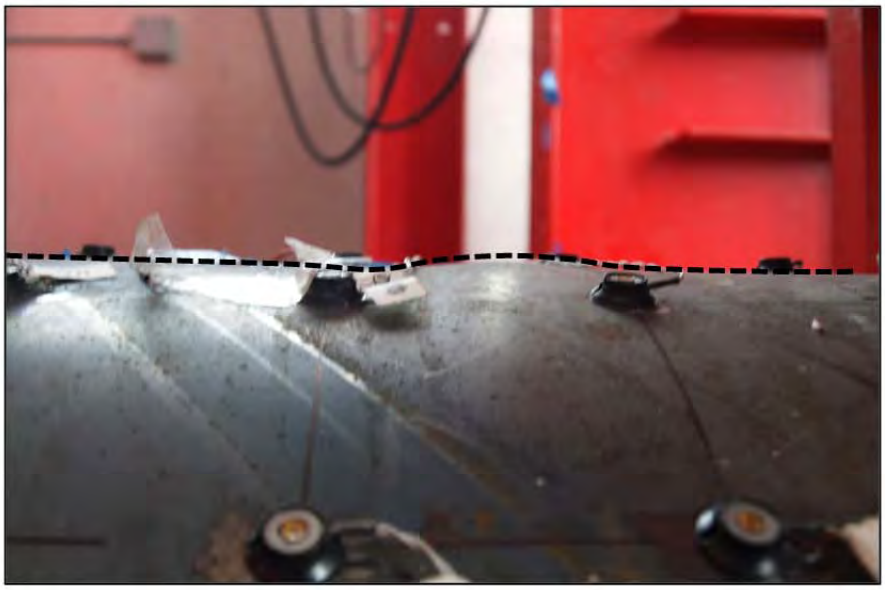

Figure 3-84: "Ripple" in the constant moment region, Ductility 2, Δ=3.8in

.

Figure 3-85: "Ripple" under loading point, Ductility 2, Δ=3.8in

Figure 3-86: "Ripples" under loading point, Ductility 2, Δ=3.8in

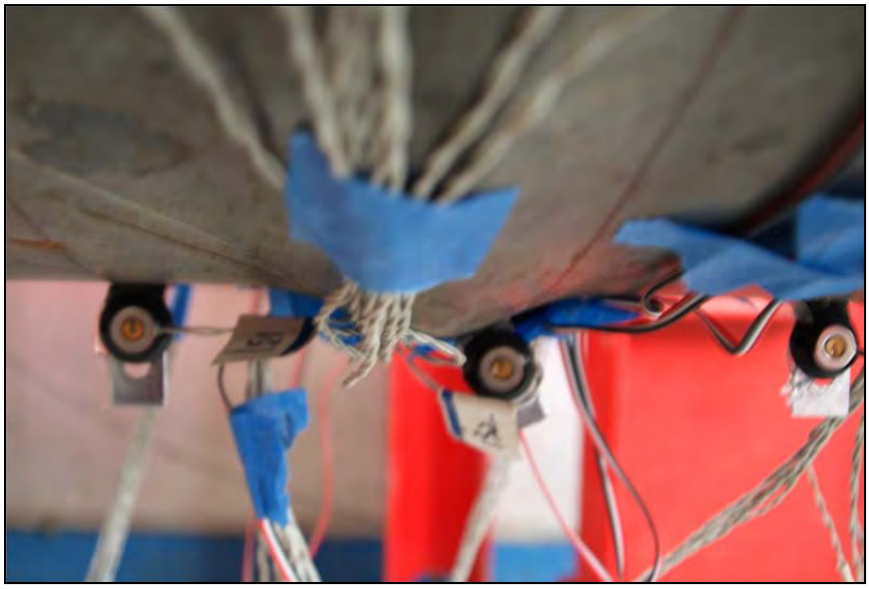

Figure 3-87: Buckle in the constant moment region, Ductility 2, Δ=3.8in

The third ductility three-cycle set increased the mid-span displacement to 5.6 inches in each direction (Figure 3-88). The increase in displacement increased the damage in the pile. The buckles on the top of the pile condensed from 9 "ripples" to four main buckles during the push cycles. The four buckles consisted of one buckle located under each loading point and two located in the constant moment region, each about 12 inches from the centerline of the pile (Figure 3-89). The buckles were evenly spaced with approximately 17 – 20 inches in between them. The four buckles on the underside of the pile present at the conclusion of the last three cycle set continued to increase in height and become narrow as seen in Figure 3-90. At the conclusion of the ductility level, the buckles on both sides of the pile were about ½ inch in height, and spaced 17 – 20 inches apart, as seen in Figure 3-91 and Figure 3-92 creating symmetric behavior which evenly distributed the damage.

Figure 3-88: Pile profile, Ductility 3, Δ = 5.6 in

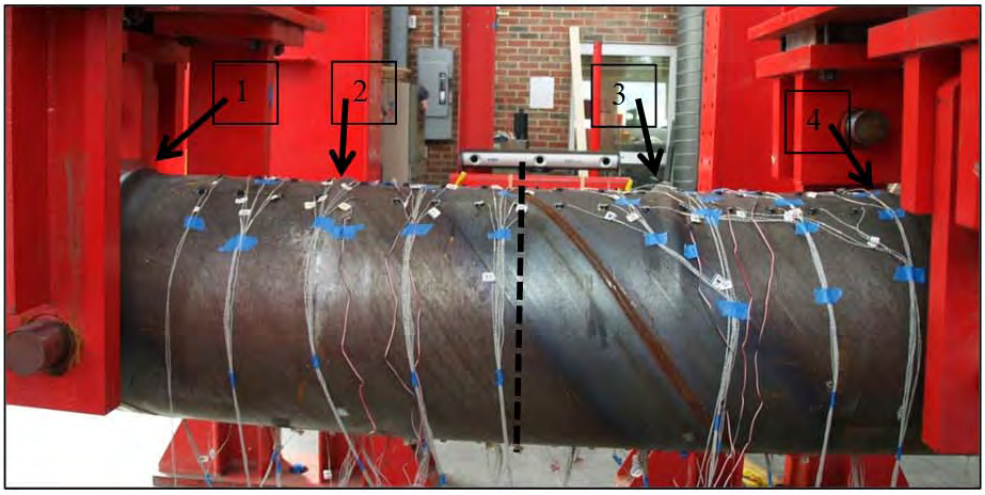

Figure 3-89: Buckles in constant moment region, Ductility 3, Δ = 5.6 in

Figure 3-90: Buckle on underside of pile, Ductility 3, Δ = 5.6 in

Figure 3-91: Buckles with a height of ½ inch, , Ductility 3, Δ = 5.6 in

Figure 3-92: Buckles spaced evenly (17-20" apart), Ductility 3, Δ = 5.6 in

The mid-span displacement of the piles was increased to 7.5 inches and 9.4 inches in ductility cycles four and five, respectively (Figure 3-93Figure 3-94). During these cycles, no more buckles formed and the existing four buckles continued to increase in height and became more narrow. They increased to right above 0.5 inches in height during ductility four as seen in Figure 3-95, and grew 50% more in ductility five to 0.75 inches (Figure 3-96). Over the course of these cycles the behavior of the pile remained symmetric and uniform during the push and pull cycles and symmetric about the centerline of the pile.

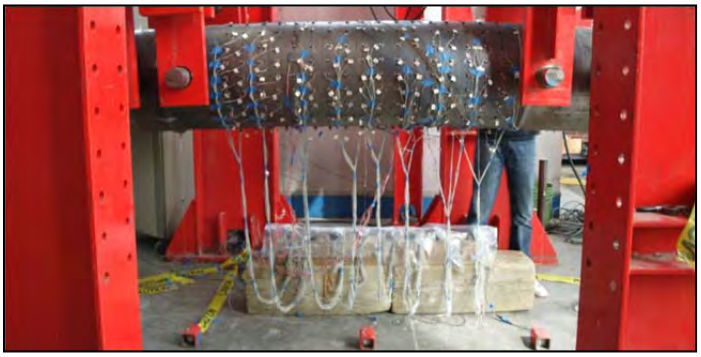

Figure 3-93: Pile profile, Ductility 4, Δ = 7.5 in

Figure 3-94: Pile profile, Ductility 5, Δ = 9.4 in

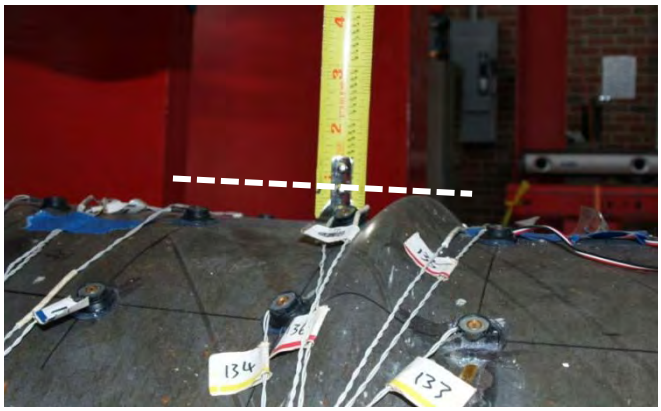

Figure 3-95: Buckle on top of pile, Ductility 4, Δ = 7.5 in

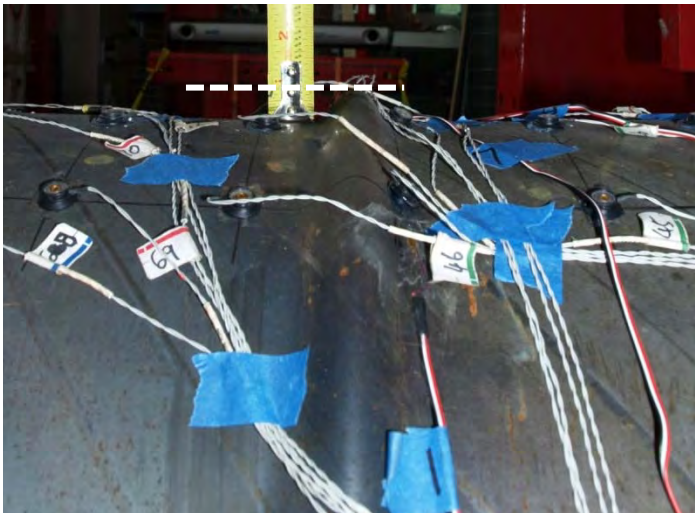

Figure 3-96: Buckle on top of pile, Ductility 5, Δ = 9.4 in

The pipe ruptured on the first push of ductility six, at a mid-span displacement of 8.98 inches. This was less than the mid-span displacement demand of ductility 6, 11.4 inches. It also ruptured at a lower displacement than the previous ductility cycle (ductility 5, Δ=9.4in). The rupture occurred on the underside of the pile when the steel pipe could not reach the tensile strain demands required due to the high compressive strains previously on the pipe in the last cycle. Figure 3-97 shows the rupture which occurred on the crease of the buckle inside the constant moment region, approximately 12 inches offset from the centerline of the pile, not under either of the loading points. The pile continued to be pushed to the ductility demand of 11.4 inches. The crack in the steel pipe opened as the displacement increased as seen in Figure 3-98. This showed that all of the concrete inside the pipe was not crushed, the only section that crushed was located under the buckle where the concrete had lost bond with

the steel and no longer had confinement. The process of buckling over the course of the test leading up to rupture is shown in Figure 3-99.

Figure 3-97: Rupture on underside of pile, Δ = 8.98 in

Figure 3-98: Rupture on underside of pile, Ductility 6, Δ = 11.4 in

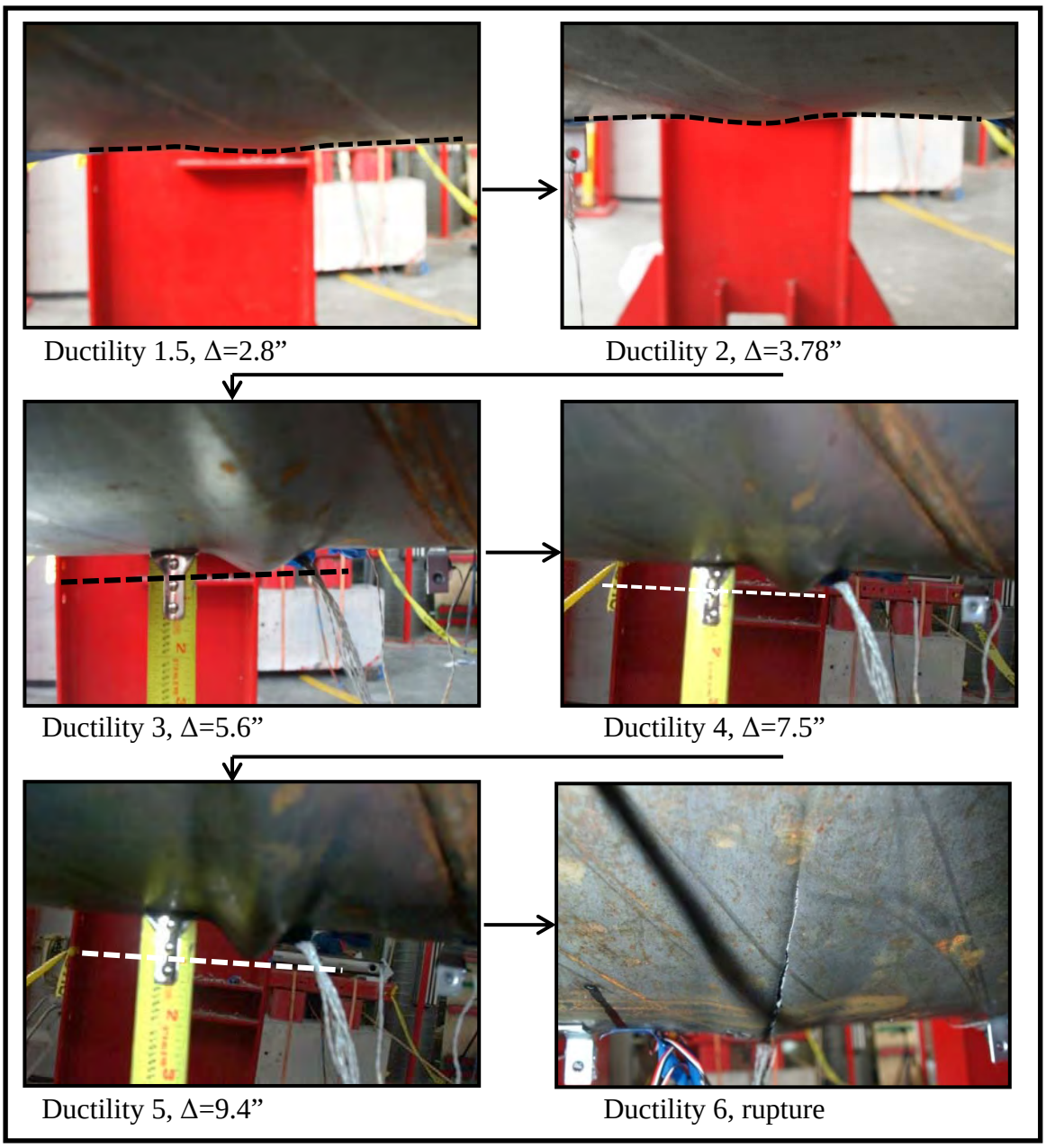

Figure 3-99: Progression of buckling

The force-displacement hysteresis of this test, after the dead weight of the pile had been accounted for, is shown in Figure 23. The force-displacement envelopes for the first, second, and third cycle are shown in Figures 24-27. The pile had an average ultimate force of about 51 kips. After rupture in the first push of ductility six, the pile lost about 12 kips of strength.

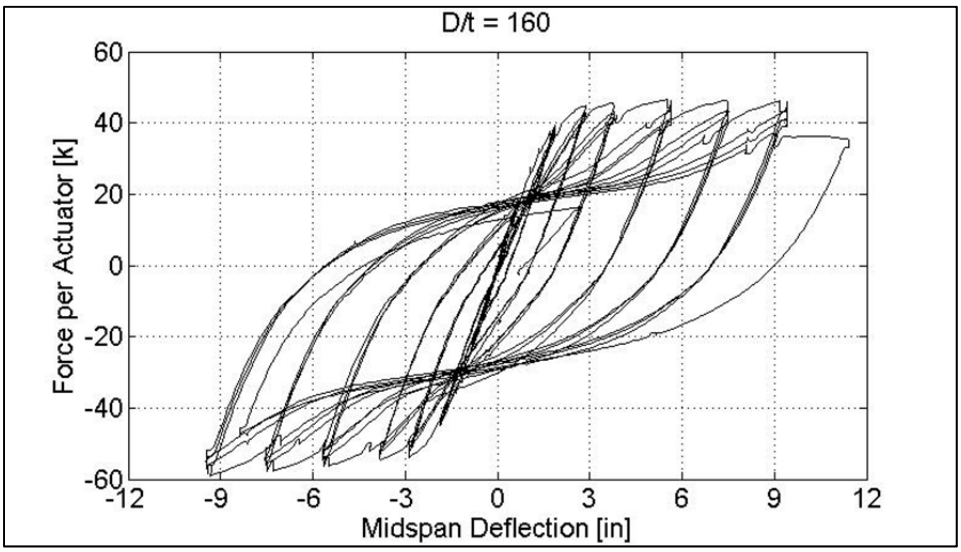

Figure 3-100: Force-Displacement Hysteresis

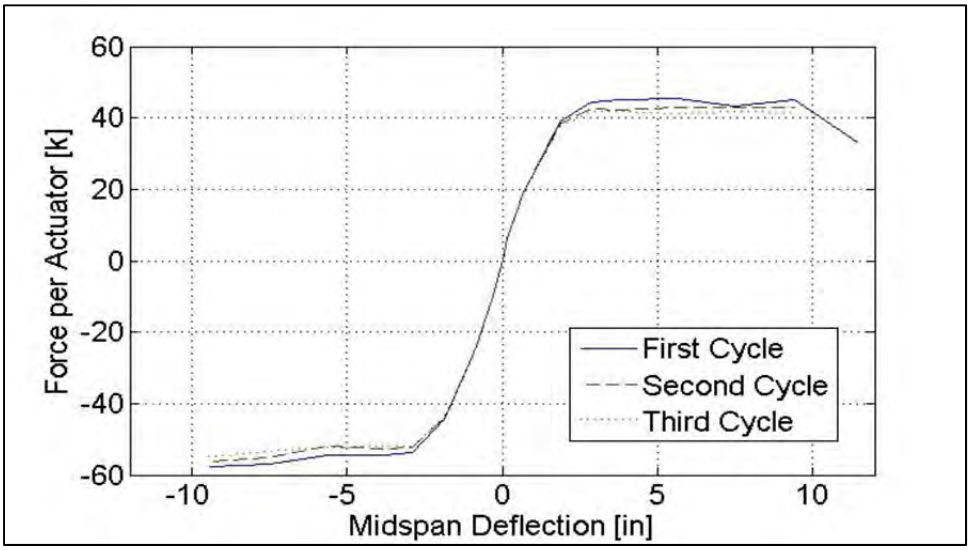

Figure 3-101: Force-Displacement Envelopes

Test 7 was conducted at the Constructed Facilities Lab on Tuesday, August 28th. The pile was a concrete filled steel tube; the tube had an outer diameter equal to 20 inches and a thickness equal to 0.132 inches, resulting in a diameter-thickness ratio of 160. Visible buckling of the specimen began in the first pull of ductility one and a half at a displacement

of 2.8 inches in both directions. The pile sustained the damage without strength degradation until rupture in the first cycle of ductility six.

3.7.8. Test Eight

Test 8 consisted of a concrete filled steel tube with 8#5 ASTM A706 internal reinforcing bars creating an internal reinforcement ratio of 0.78%; the pipe had an outer diameter equal to 20 inches and a thickness equal to 0.125 inches resulting in a diameter-thickness ratio of 160.

Visible buckling of the test specimen began in the second push of ductility one, at a mid-span displacement of 1.67 inches. At this point, one small ripple had formed under each loading point, an example of one of these "ripples" is shown in Figure 3-102. The buckling of the specimen was also detected by the change in temperature of the pipe at the location of buckling, due to energy dissipation. Buckling also appeared on the underside of the pile during the second pull cycle in ductility one. The buckles became more visible as the ductility level continued; a buckle from the third pull is shown in Figure 3-103.

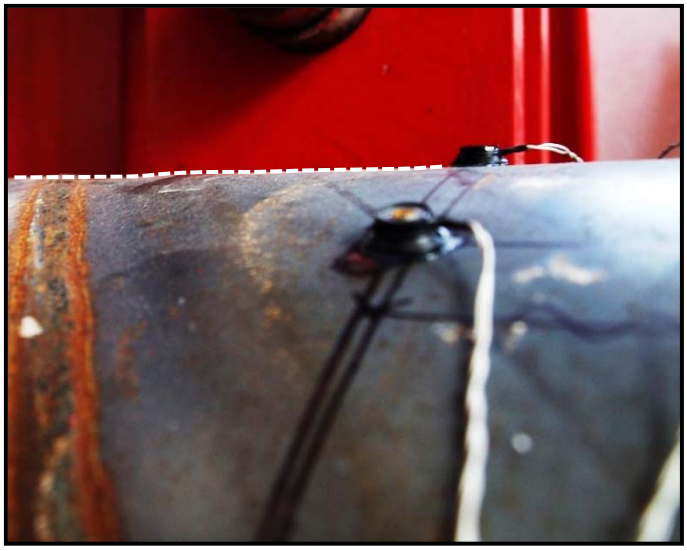

Figure 3-102: Initiation of buckling, Ductility 1- 2nd push, Δ = 1.67 in

Figure 3-103: Initiation of buckling, Ductility 1-3rd pull, Δ = 1.67 in

The next ductility cycle increased the mid-span displacement to one and a half the equivalent yield displacement, increasing the deflection to 2.5 inches. Over the course of the three cycle set, five small buckles formed on each side of the pile. A sketch of the buckle locations are shown in Figure 3-104. As seen in the figure, the buckles were evenly distributed about the centerline of the pile. The pile also exhibited symmetric behavior in the push and pull cycles, forming buckles at the same rate and approximately same locations on both sides of the pile. A photograph of the most significant buckle in the third pull of the cycle can be seen in Figure 3-105.

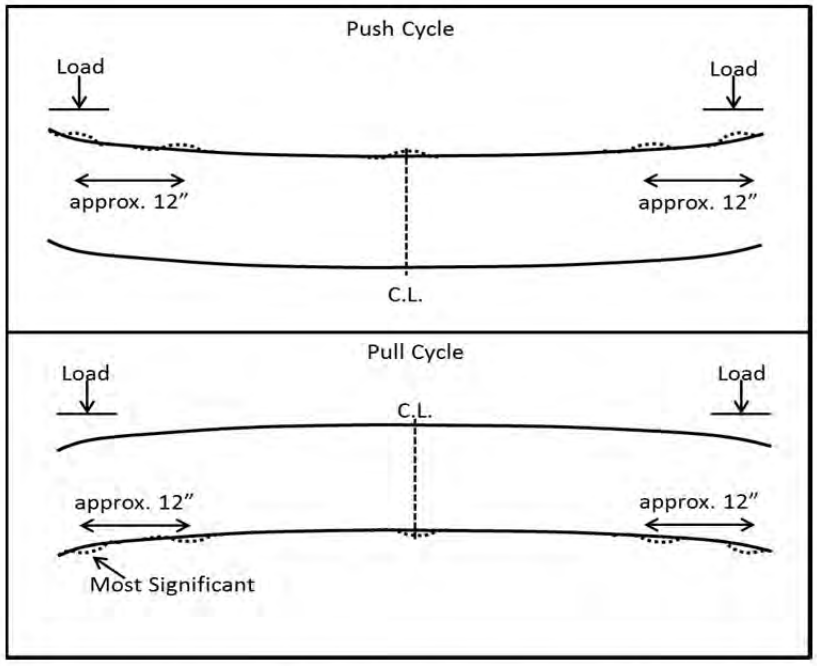

Figure 3-104: Outline of Specimen Profile, Ductility 1.5, Δ = 2.5 in

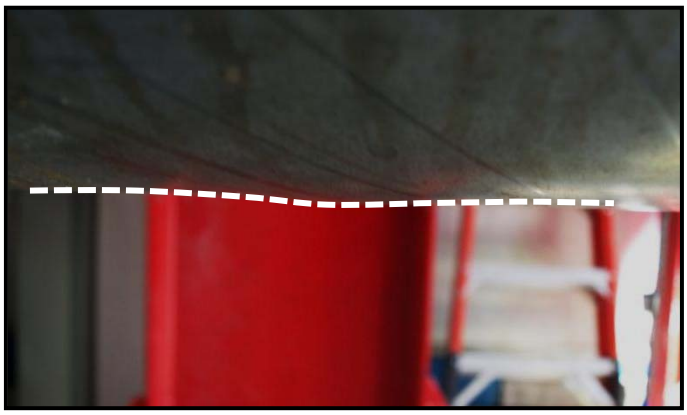

Figure 3-105: Outline of Specimen Profile, Ductility 1.5-pull 3, Δ = 2.5 in

The damage increased as the mid-span displacement increased to 3.4 inches during ductility two. The five existing buckles slightly increased in size during the first push and pull cycles (Figure 3-106). The second and third cycles created more small ripples on both sides of the pile: eight on the top of the pile and six on the underside of the pile. Although some of the buckles previously existed all appear to be the same size and spread evenly throughout the constant moment region. The location of these buckles within the constant moment region is shown in Figure 3-107.

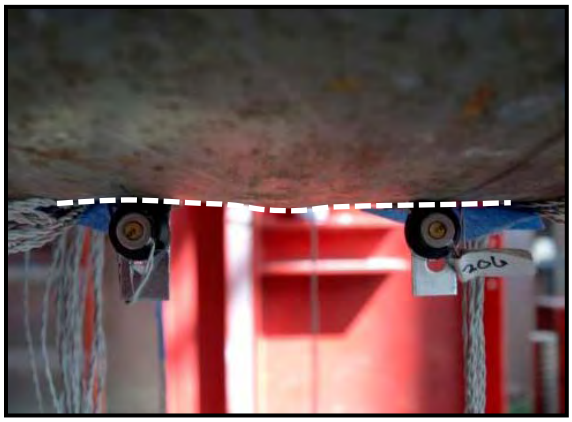

Figure 3-106: Pile buckle, Ductility 2-1st pull, Δ=3.3in

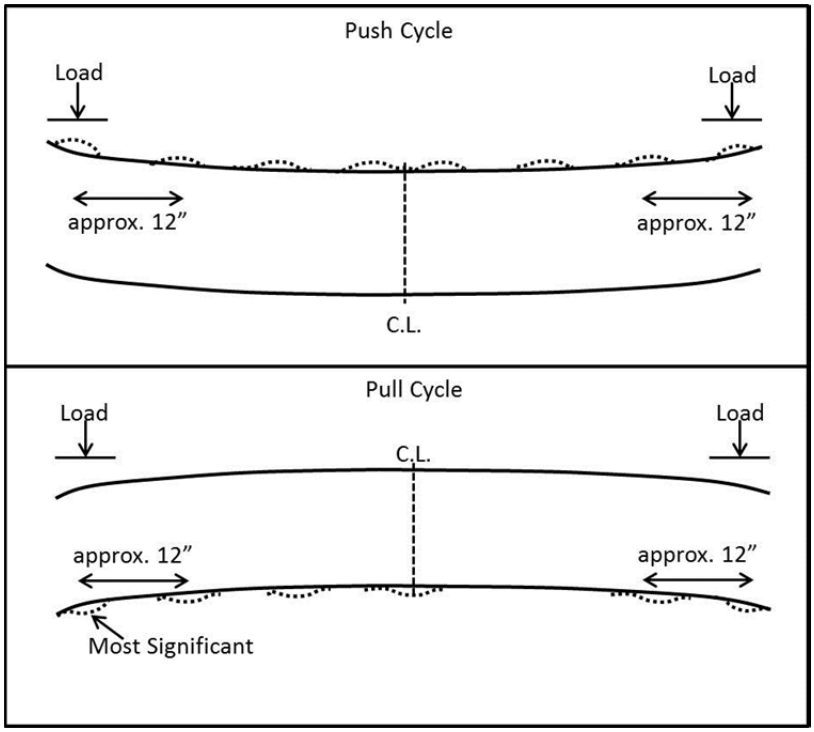

Figure 3-107: Outline of Specimen Profile, Ductility 2, Δ=3.3in

During the third ductility cycle, at a mid-span deflection of 5.0 inches, the damage started to concentrate to a few buckles. The first push cycle increased the buckle near the center of the pile and under one of the loading points. The second and third push cycles continued to increase the size of these buckles as well as the buckle under the other loading point to approximately ½" in height. The profile of the constant moment region at the conclusion of the third push cycle is shown in Figure 3-108 and an example of one of the buckles is shown in Figure 3-109. The underside of the pile demonstrated the same symmetric behavior during the pull cycles. Three buckles increased in size, one under both loading points and one in the center of the pile, these buckles were larger than those on the top of the pile. All three buckles can be seen in Figure 3-110 and a close-up of one of the buckles is shown in Figure 3-111. At the conclusion of the ductility level, three significant buckles increased in size to about 1/2" on the top of the pile during the push cycles, during the pull cycles three buckles increased in size to 5/8" on the underside of the pile.

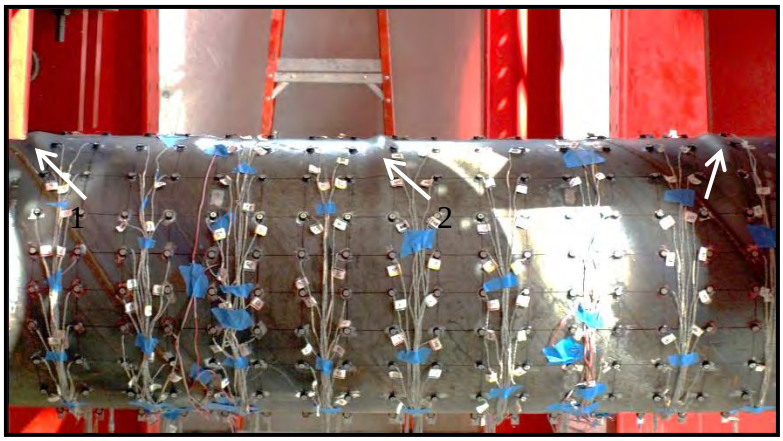

Figure 3-108: Profile of the constant moment region, Ductility 3-2nd push, Δ=5.0in

Figure 3-109: Buckle located in center of pile, Ductility 3-3rd push, Δ=5.0in

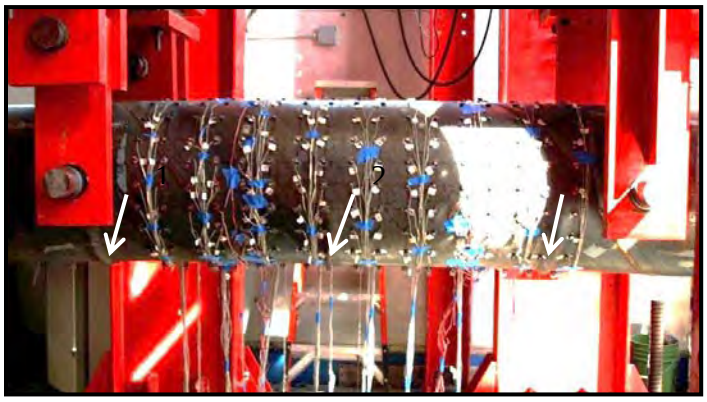

Figure 3-110: Profile of the constant moment region, Ductility 3-3rd pull, Δ=5.0in

Figure 3-111: Buckle located under loading point, Ductility 3-3rd pull, Δ=5.0in

The fourth ductility cycle pushed and pulled the pile to a deflection of 6.67 inches in both directions (Figure 3-112). During these cycles the three buckles on the top and underside of the pile increased in height to about 3/4" and became more narrow (Figure 3-113 Figure 3-114). As the buckles increased in height they also began to spread around the circumference of the pile. As this happened, the concrete was heard crushing as the steel buckled away from the concrete and the concrete lost its confinement. After the third push of the cycle, tension cracks were observed on the sides of the buckles.

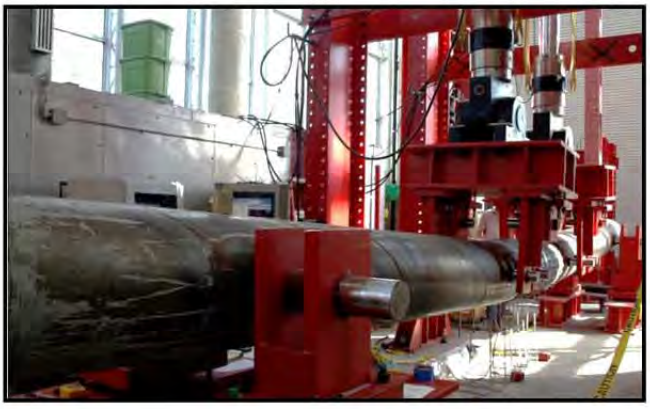

Figure 3-112: Pile profile, Ductility 4-1st push, Δ=6.67in.

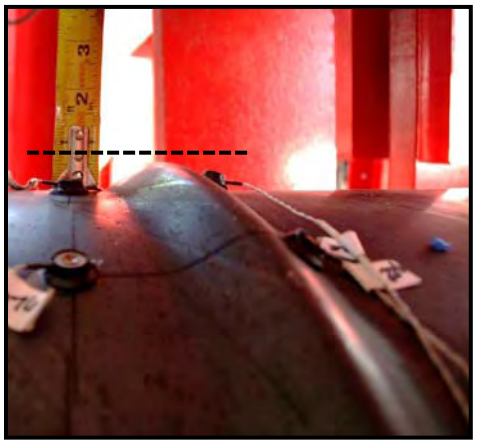

Figure 3-113: Buckle near loading point, Ductility 4-3rd push, Δ=6.67in

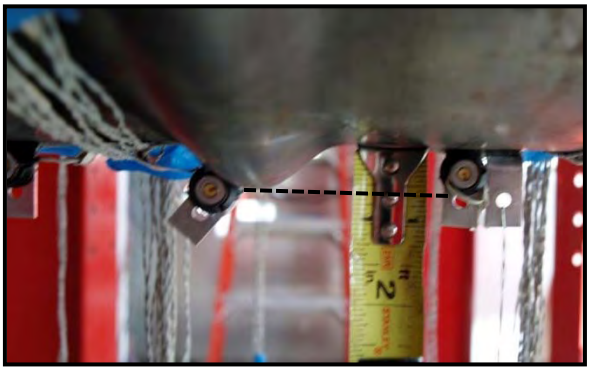

Figure 3-114: Buckle in center of pile, Ductility 4-3rd pull, Δ=6.67in

During the fifth ductility cycle, the mid-span displacement was increased to 8.33 inches (Figure 3-115). The damage in the pile was observed by the increase in size of the buckles on both sides of the pile. The three on each side of the pile increased in height to approximately 7/8" (Figure 3-116) and tension cracks began to appear on the creases of the buckles, indicating the high tensile strains demanded by the deflection were difficult for the steel pipe to sustain. The concrete continued to crush as the buckles spread around the circumference of the pile and tension cracks began to form on the creases of the buckles.

Figure 3-115: Pile Profile, Ductility 5-3rd pull, Δ=8.33in

Figure 3-116: Buckle locate, Ductility 5-3rd pull, Δ=8.33in

Ductility five proved to be the maximum deflection the pile could resist, the steel pipe ruptured at a deflection of 8.4 inches, while being pushed to displacement demand of ductility six, 9.67 inches. The rupture occurred on the underside of the pile on a buckle near the loading point; it is shown in Figure 3-117. At this displacement, a crack had also formed under the other loading point; however it had not ruptured as shown in Figure 3-118. The pile continued to be pushed to the full ductility six deflection, and the crack opened causing the pile ruptured in a second location (Figure 3-119). This additional deflection also caused the previous rupture crack to open more as seen in Figure 3-120. As expected, the pipe ruptured near the loading points where the moment gradient changes. A progression of buckling leading to the first rupture is displayed in Figure 3-121.

Figure 3-117: Steel pipe rupture, Δ=8.40in

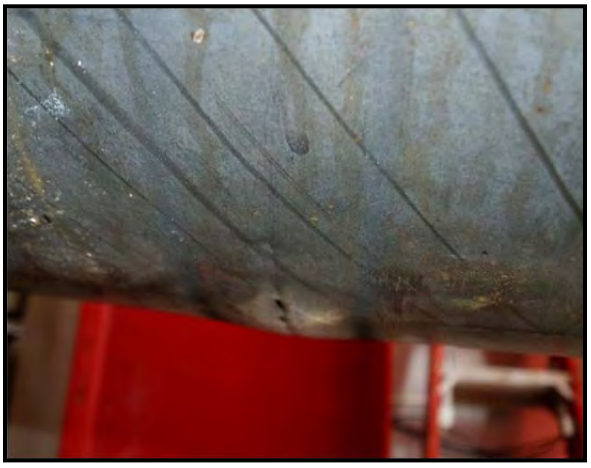

Figure 3-118: Steel pipe tensile crack, Δ=8.40in

Figure 3-119: Second steel pipe rupture, Ductility 6, Δ=9.67in

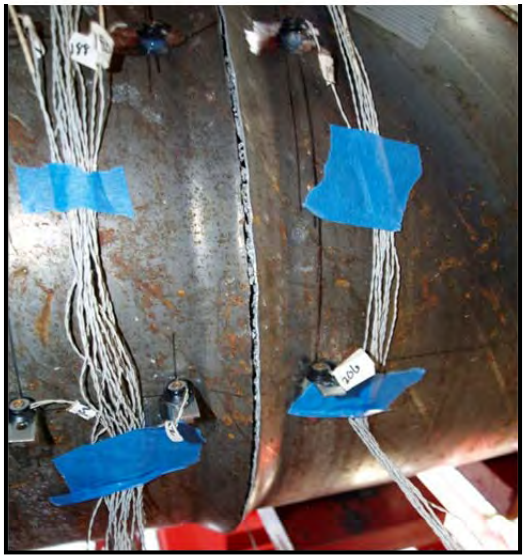

Figure 3-120: First pipe rupture, Ductility 6, Δ=9.67in

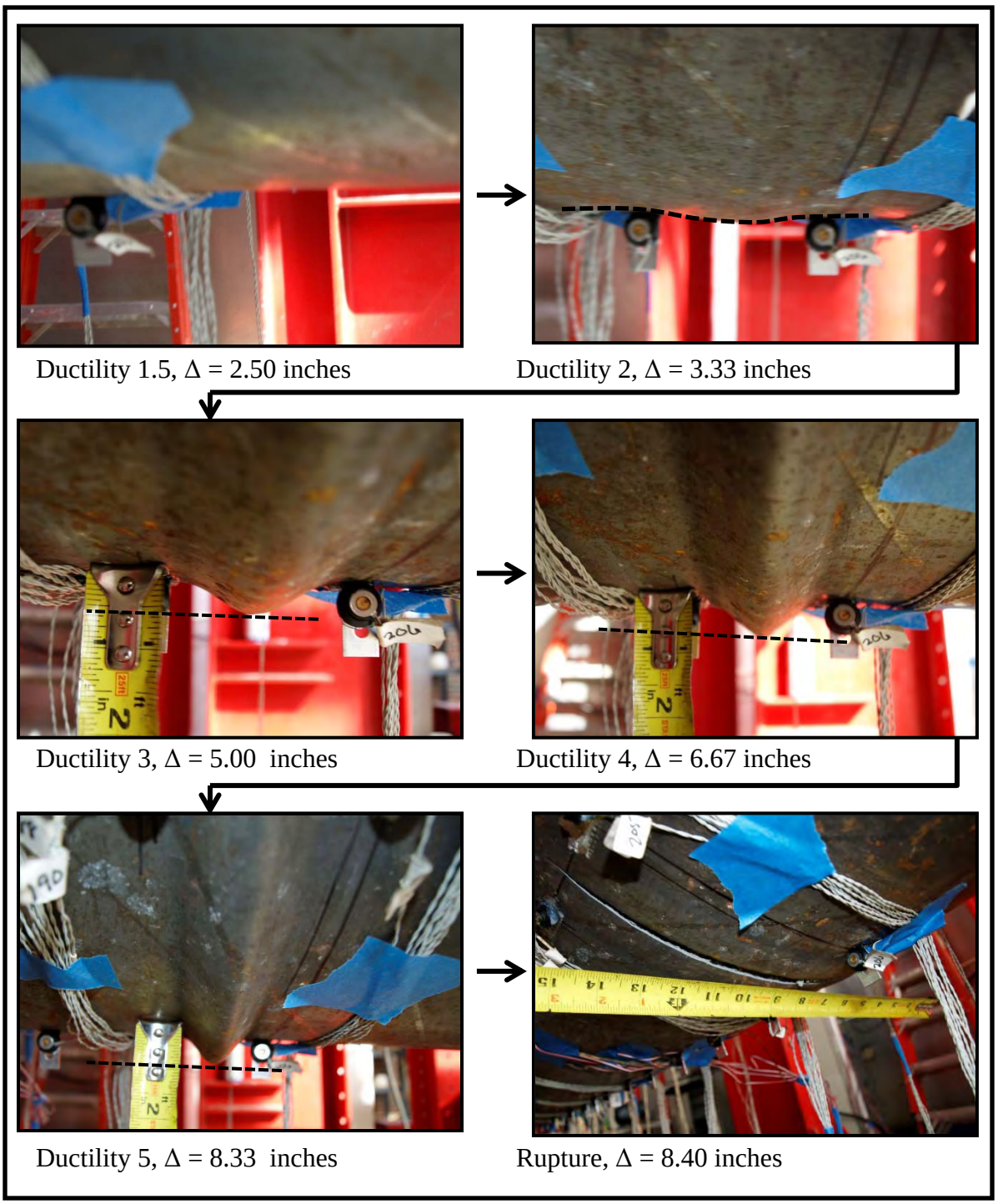

Figure 3-121: Progression of buckling

The force-displacement hysteresis of this test, after the dead weight of the pile had been accounted for, is shown in Figure 3-122. The force-displacement envelopes for the first, second, and third cycles are shown in Figure 3-123. The pile had an average ultimate force of about 40 kips, and as seen in the hysteresis the pile behaved in a ductile manner and had no strength loss until after rupture.

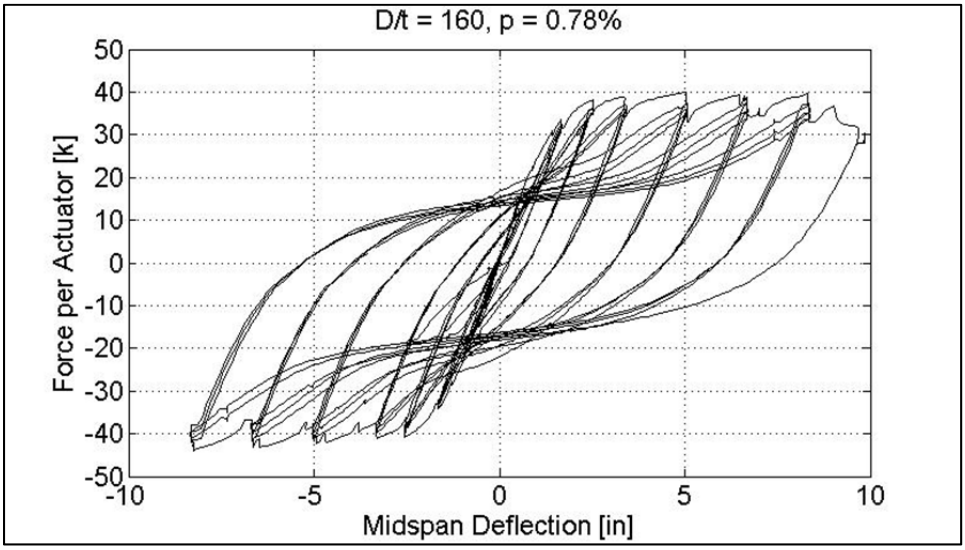

Figure 3-122: Force-Displacement Hysteresis

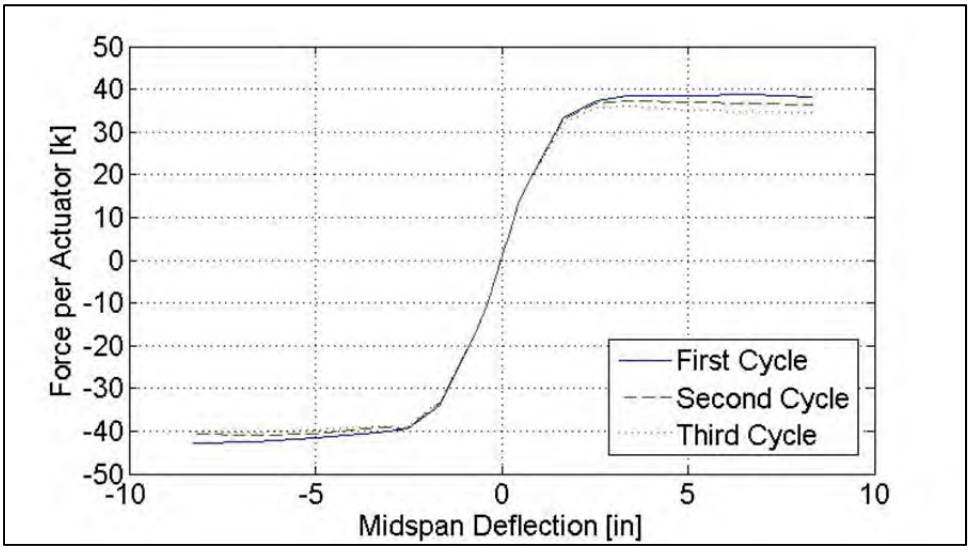

Figure 3-123: Force-Displacement Envelopes

Test 8 was conducted at the Constructed Facilities Lab on Thursday, September 20th. The pile was a concrete filled steel tube; the tube had an outer diameter equal to 20 inches and a thickness equal to 0.125 inches, resulting in a diameter-thickness ratio of 160 Visible buckling of the specimen began in the first pull of ductility one at a displacement of 1.7 inches in both directions. The pile sustained the damage without strength degradation until rupture in the first cycle of ductility six.

3.7.9. Test Nine

Test 9 consisted of a concrete filled steel tube with 8#6 ASTM A706 internal reinforcing bars creating an internal reinforcement ratio of 0.78%; the pipe had an outer diameter equal to 24 inches and a thickness equal to 0.125 inches resulting in a diameter-thickness ratio of 192.

Visible buckling of the test specimen began in the first pull of ductility one, at a mid-span displacement of 2.8 inches. At this point, one small ripple had formed under each loading point, an example of one of these "ripples" is shown in Figure 3-124. Buckling also appeared on the top of the pile during the second push in ductility one, as seen in Figure 3-125. These buckles remained visibly the same throughout the conclusion of the first ductility cycle.

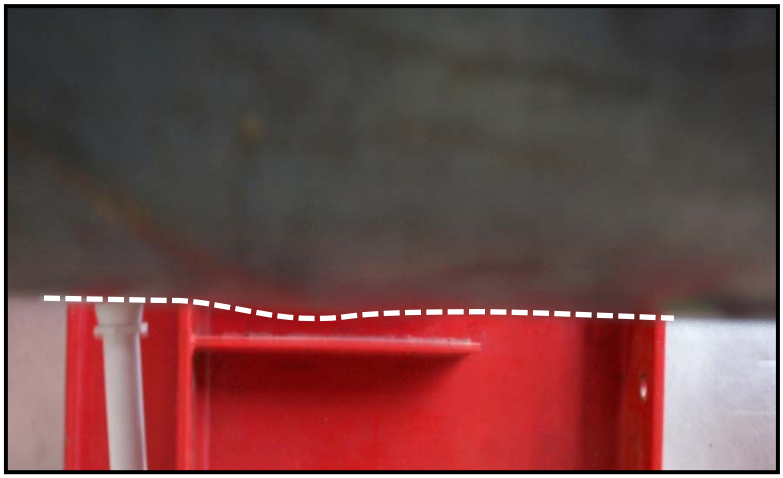

Figure 3-124: Initiation of buckling, Ductility 1- 1st pull, Δ = 2.80 in

Figure 3-125: Initiation of buckling, Ductility 1-2nd push, Δ = 2.80 in

The mid-span displacement was increased to 4.2 inches, one and a half times the equivalent yield during the next ductility cycle. The increased displacement resulted in more damage shown by the growth of the existing ripples and formation of new buckles. The first push did not result in significant change in the buckling behavior since the top of the pile had not been subjected to higher tensile strains at that point. During the first push the underside of the pile was subjected to higher tensile strains which resulted in more buckling during the second pull of ductility one and a half. The buckles under both loading points increased in size and one small buckle formed about 9 inches south of the centerline (Figure 3-126). The increase in damage was also evident in the second push of ductility 1.5. The buckles under the loading points increased in size and two new buckles formed in the constant moment region. The new buckle formed 12 inches north of the centerline is shown in Figure 3-127. The pile sustained the damage and the buckled behavior was consistent throughout the remainder of the ductility cycle.

Figure 3-126: Formation of buckle 9 in. south of centerline; ductility 1.5 pull 1, Δ=4.2 in

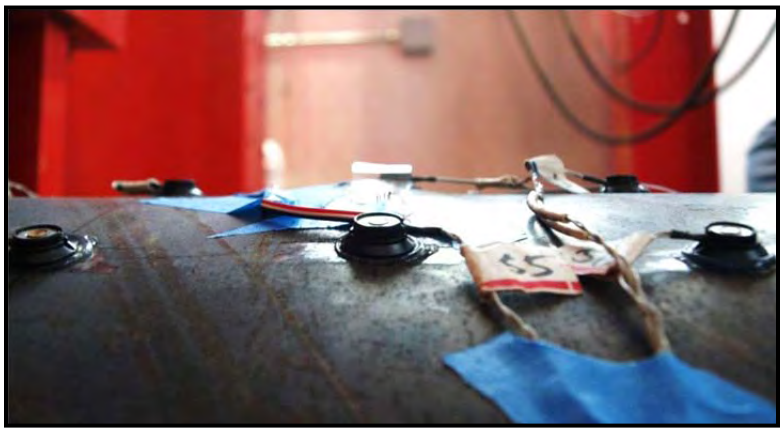

Figure 3-127: Formation of buckle 12 in. north of centerline; ductility 1.5 push 2, Δ=4.2 in

After the conclusion of ductility one and a half, the mid-span displacement was increased to 5.7 inches in each direction to meet the demands of ductility two. During this cycle, the existing buckles continued to increase in size and no new buckles were formed. At the conclusion of the cycle the buckles located under the loading points were 1/2" to 5/8" in height (Figure 3-128) and the buckles located in the constant moment region were 1/4" to 3/8" in height. The majority of the buckles formed perpendicular to the pile however one of the buckles on the top of the pile formed parallel to the spiral weld near it. This buckle is shown in Figure 3-129. Each side of the pile exhibited symmetric behavior with four total buckles on each side centered about the centerline of the pile. The pile profiles showing the location and heights of these buckles is shown in Figure 3-130.

Figure 3-128: Buckle located under one of the loading points, ductility 2, Δ=5.7 in

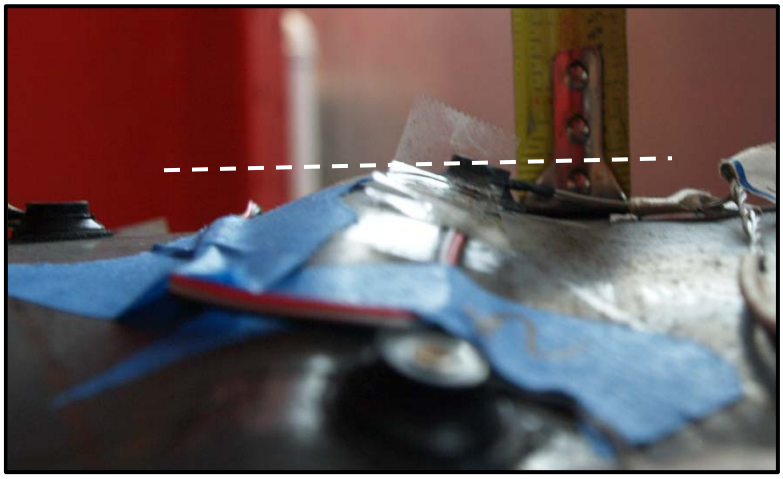

Figure 3-129: Buckle located between loading points, ductility 2, Δ=5.7 in

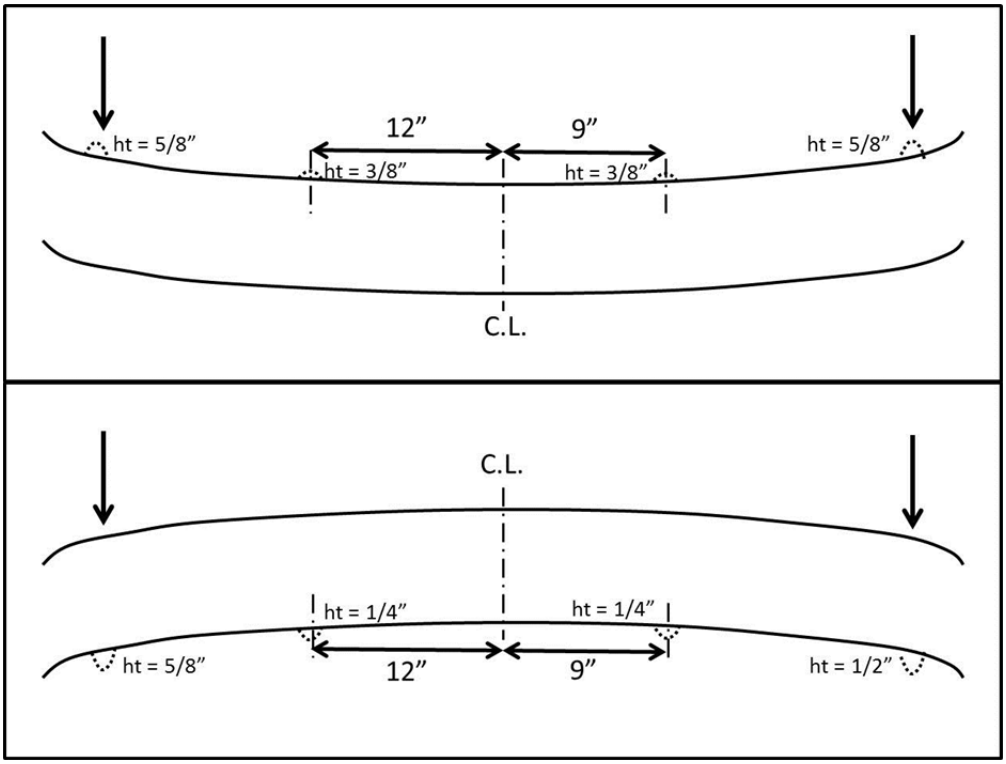

Figure 3-130: Pile profile outline, ductility 2, Δ=5.7 in

The damage continued to increase as the displacement increased in ductility cycles three. Ductility three demanded a mid-span displacement of 8.4 inches, the profile is shown in Figure 3-131. At the conclusion of ductility three, the buckles had grown in size and become narrow. The buckles under the actuators were about 3/4” in height on both the top and underside of the pile (Figure 3-132). The buckles in the center of the constant moment region were smaller on the underside of the pile (3/8”-1/2”) than those on the top of the pile which were about 5/8” in height as seen in Figure 3-133 Figure 3-134 respectively. Figure 3-134 also displays the buckle that formed parallel to the weld instead of perpendicular to the pile. The location and heights of the buckles are seen in Figure 3-135.

Figure 3-131; Displaced pile profile, ductility 3, Δ=8.4 inches

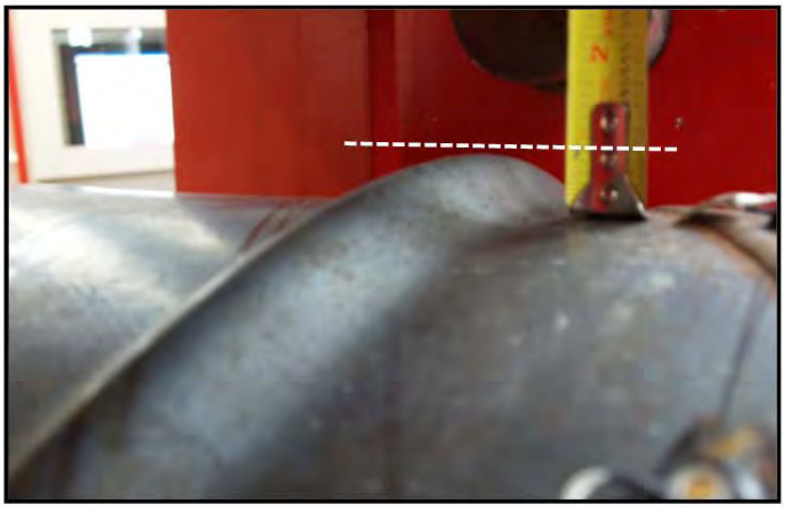

Figure 3-132: Buckle on top of pile under loading point, ductility 3, Δ = 8.4 in

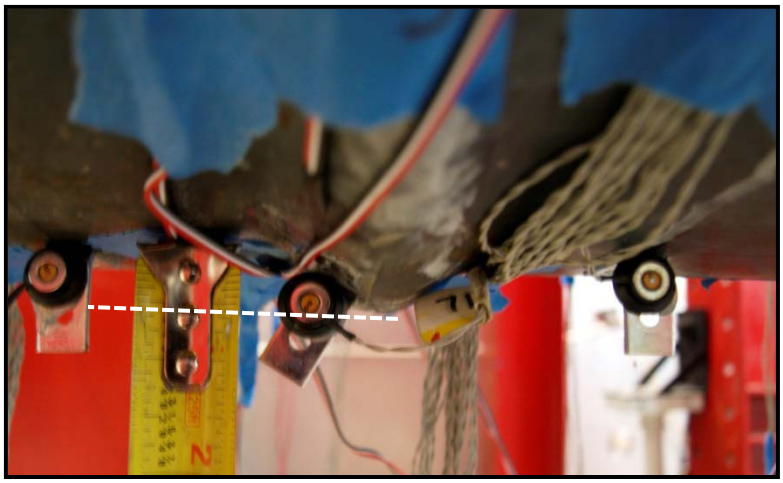

Figure 3-133: Buckle on underside of the pile in between loading points, ductility 3, Δ = 8.4 in

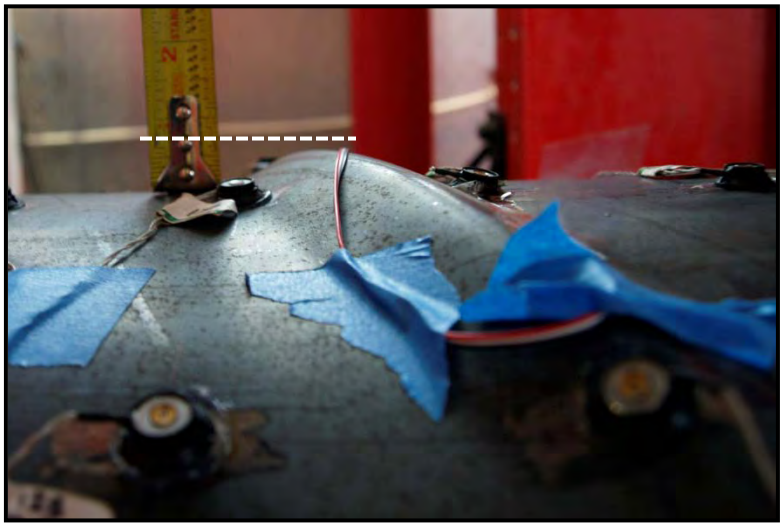

Figure 3-134: Buckle on top of pile in between loading points, ductility 3, Δ = 8.4 in

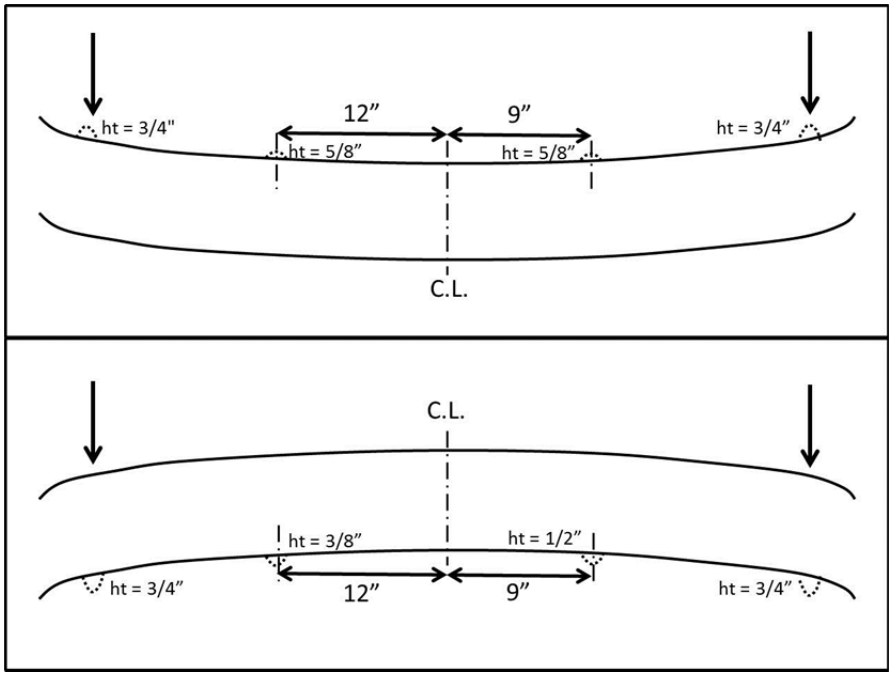

Figure 3-135: Pile profile outline, ductility 3, Δ=8.4 in

Ductility four demanded a displacement of 11.2 inches in each direction as seen in Figure 3-136. The buckles did not change in height during the first cycle of this ductility three cycle set however they did become more narrow. After the pile was pushed to 11.2 inches for the second time in ductility four, small tension cracks begin to appear on the underside of the pile under the loading points where the buckles formed when the underside of the pile is in compression (Figure 3-137). During this second push the buckles under the loading points on the top of the pile grew by approximately 50% to about 1 inch in height. The same damage continued in the second pull of ductility four. Tension cracks formed on the top of the pile under the loading points where buckles form when the top of the pile is in compression and the buckles under the loading points increased in height to about 1 inch (Figure 3-138).

Figure 3-136: Displaced pile profile, ductility 4, Δ=11.2 inches

Figure 3-137: Tension cracks observed on the underside of the pile, ductility 4, Δ=11.2 in

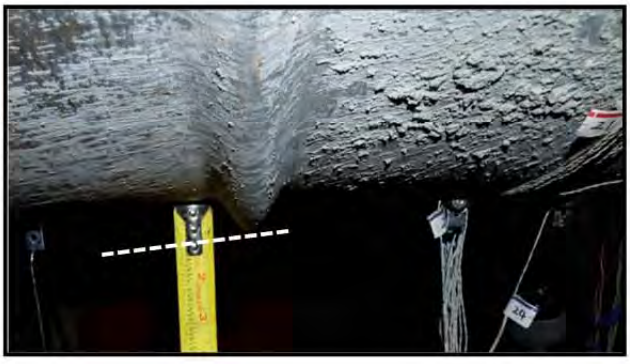

Figure 3-138: Buckle on the underside of the pile, ductility 4, Δ=11.2 in

The increase in damage proved to be the maximum damage the pile could sustain and the underside of the pile ruptured during the third push of ductility four at a displacement of 8.6 inches. As seen in Figure 3-139, the rupture occurred on the crease of the buckle under the north loading point. The crack in the pile grew in width and length as the pile was pushed to the full 11.2 inch displacement demand of ductility four (Figure 3-140). The increase in crack width shows the concrete is still intact under the portion of the pile that had not buckled. The pile lost approximately 15 kips of load after the rupture occurred in the push cycle. The pile lost no strength during the pull cycle since the crack closed as seen in Figure 3-141, which allowed it to sustain the steel's compressive strength. The full spectra of damage from initiation of buckling to rupture is shown in Figure 3-142.

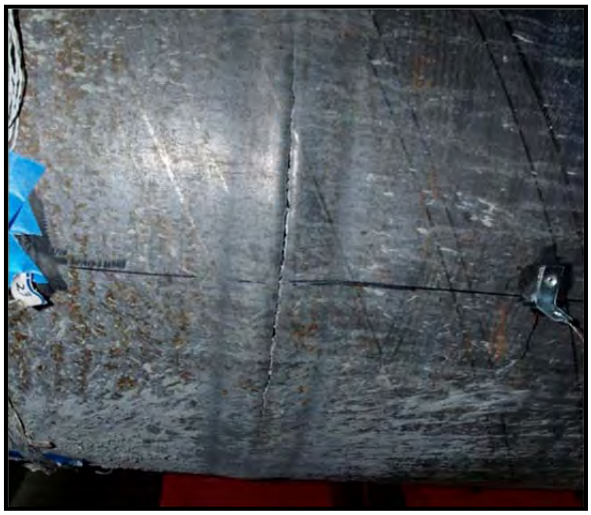

Figure 3-139: Rupture on the underside of the pile, during the first push of ductility 4

Figure 3-140: Rupture on the underside of the pile at full displacement of ductility 4, Δ=11.2 in

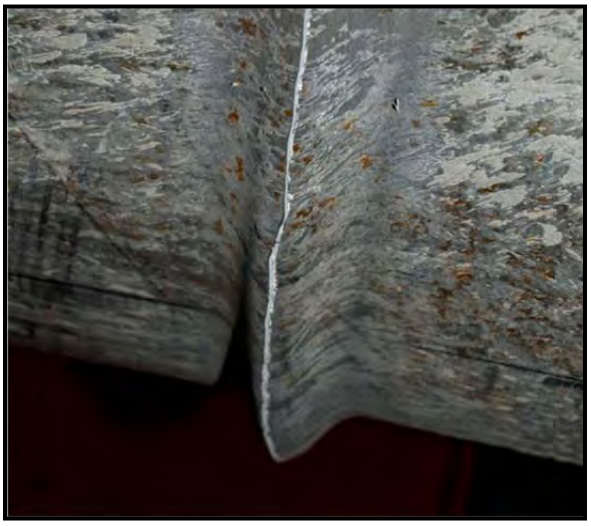

Figure 3-141: Steel pipe crack closing when in compression, ductility 4, Δ=11.2 in

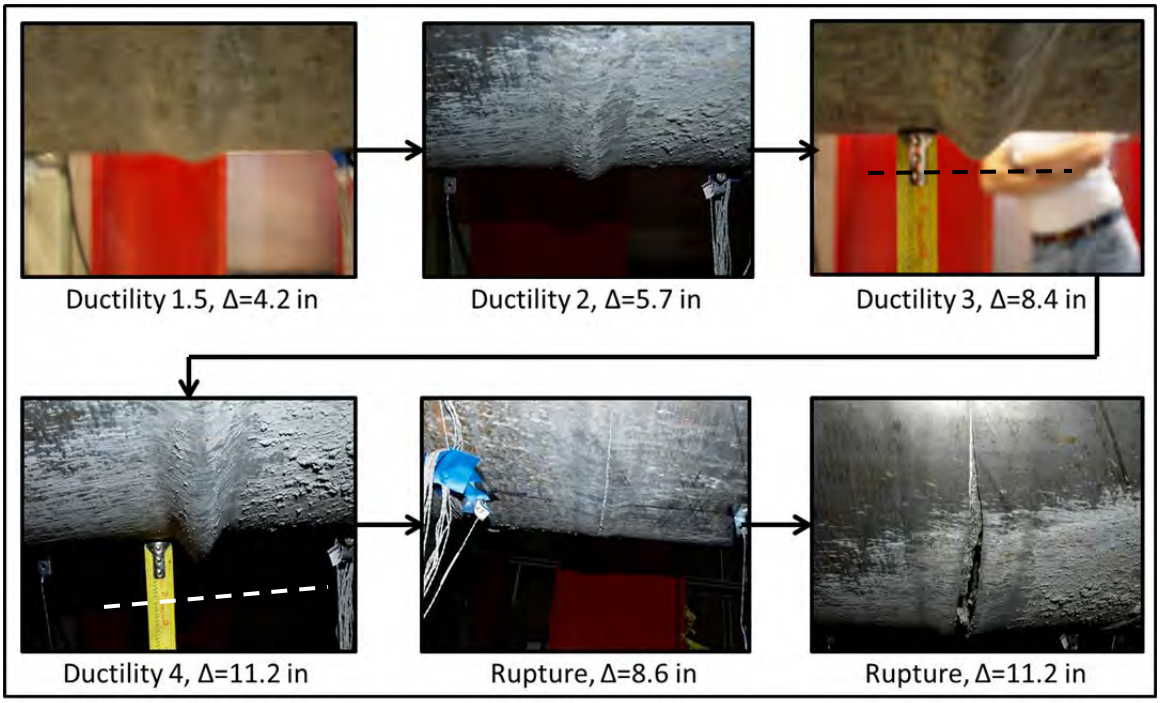

Figure 3-142: Progression of buckling throughout the test

The force-displacement hysteresis of this test, after the dead weight of the pile had been accounted for, is shown in Figure 23. The force-displacement envelopes for the first, second, and third cycle are shown in Figures 24 - 27. The pile had an average ultimate force of about 50 kips, and as seen in the hysteresis the pile behaved in a ductile manner and had no strength loss until rupture which resulted in a loss of approximately 15 kips.

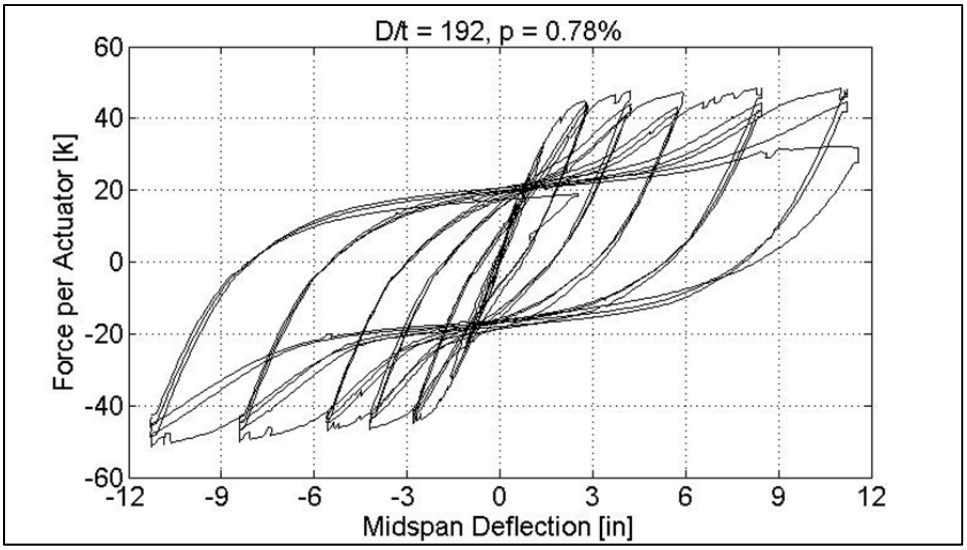

Figure 3-143: Force-Displacement Hysteresis

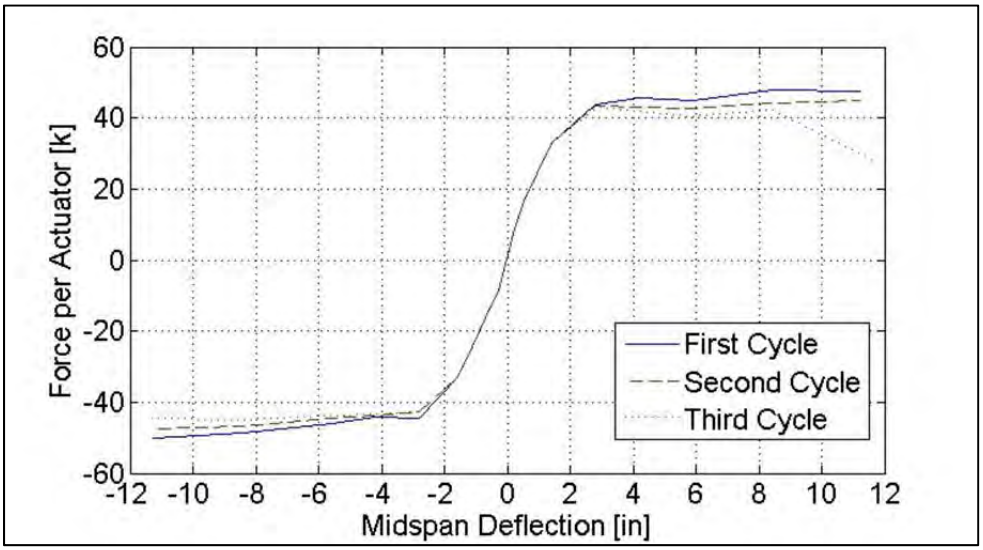

Figure 3-144: Force-Displacement Envelopes

Test 9 was conducted at the Constructed Facilities Lab on Monday, October 8th. The pile was a concrete filled steel tube; the tube had an outer diameter equal to 24 inches and a thickness equal to 0.125 inches, resulting in a diameter-thickness ratio of 192. Visible buckling of the specimen began in the first pull of ductility one at a displacement of 2.8

inches in both directions. The pile sustained the damage without strength degradation until rupture in the third cycle of ductility four.

3.7.10. Test Ten

Test 10 consisted of a concrete filled steel tube with 14#8 ASTM A706 internal reinforcing bars creating an internal reinforcement ratio of 2.43%; the pipe had an outer diameter equal to 24 inches and a thickness equal to 0.125 inches resulting in a diameter-thickness ratio of 192.

The underside of the steel tube began to buckle during the first pull of ductility one and a half, at a displacement of 3.5 inches. There were two buckles, one located under each loading point where the moment gradient began to change; one of the buckles is shown in Figure 3-145. During the first pull cycle, the top of the pile reached strains of about 0.5% and upon reversal of the load, the top of the pile was placed into compression and buckles formed under each loading point and two smaller buckles formed in the middle of the constant moment region. The buckle located under the South loading point is seen in Figure 3-146. In the remaining two cycles of this ductility level, a few small ripples formed in the constant moment region between the loading points: two formed on the underside of the pile during the pull cycles and three formed on the top of the pile during the push cycles, these are shown in Figure 3-147 and Figure 3-148 respectively.

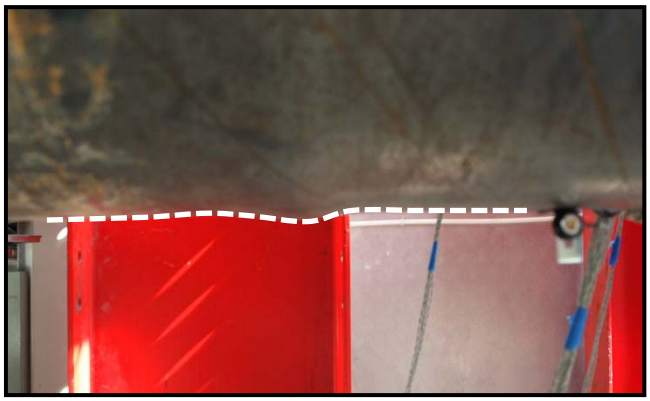

Figure 3-145: First buckling of the specimen, ductility 1.5, Δ = 3.5 inches

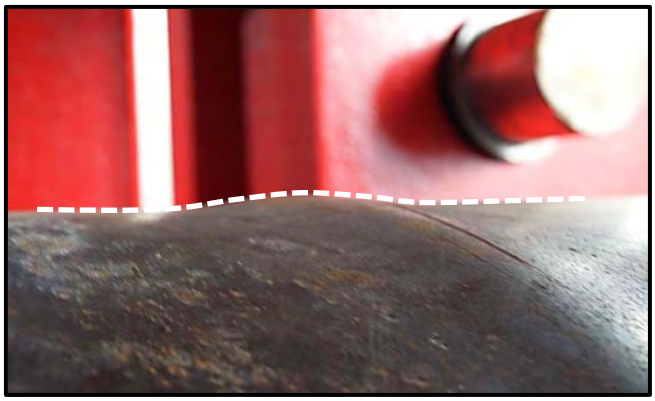

Figure 3-146: First buckling of the specimen, ductility 1.5, Δ = 3.5 inches

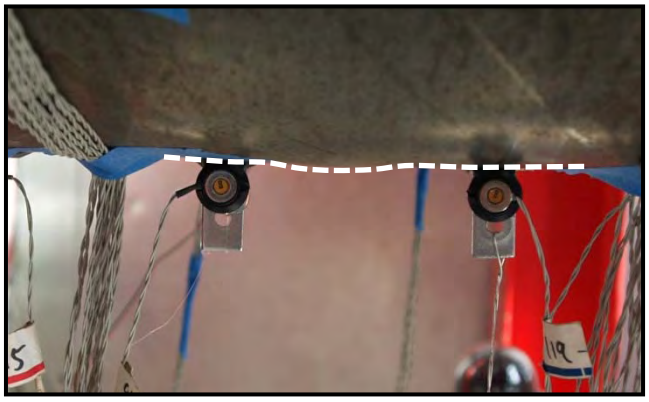

Figure 3-147: "Ripple" in the constant moment region, ductility 1.5, Δ = 3.5 inches

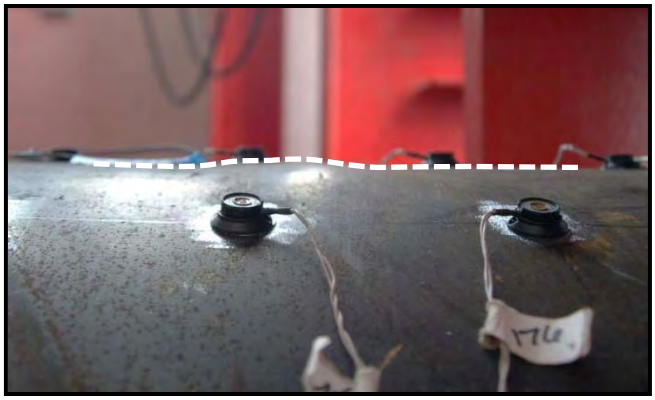

Figure 3-148: "Ripple" in the constant moment region, ductility 1.5, Δ = 3.5 inches

The displacement demand was increased to 4.6 inches in both directions for the second ductility cycle. The ripples on the top of the pile condensed to two larger buckles under each loading point and two smaller buckles in the constant moment region, one 3 inches North of the centerline and one 6 inches South of the centerline. The buckles on the underside of the pile also condensed to three buckles, one located under each loading point and one 12 inches south of the centerline of the pile. Unlike the top of the pile, the buckles on the underside of the pile were not symmetric about the centerline. An outline of the buckle distribution is shown in Figure 3-149. Over the course of the three cycle set, the buckles on both sides of the pile increased in size. At the conclusion of the ductility level, the buckles under the loading points were about 3/8" in height (Figure 3-150 and Figure 3-151).

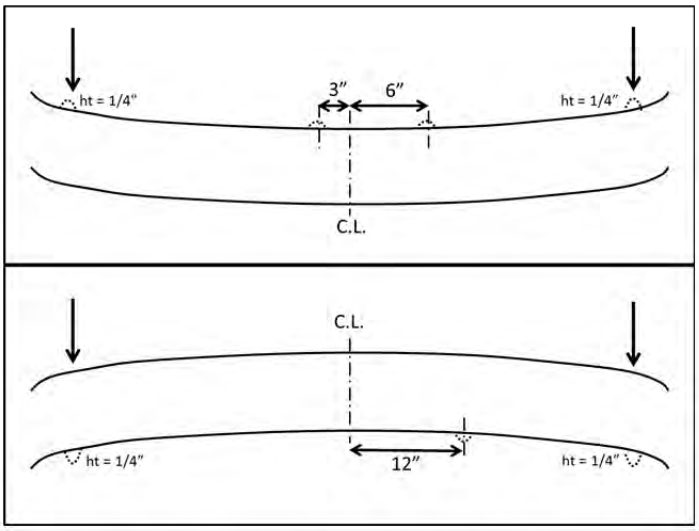

Figure 3-149: Outline of buckles at the conclusion of ductility 2, Δ = 4.6 inches

Figure 3-150: Buckle under loading point at ductility 2, Δ = 4.6 inches

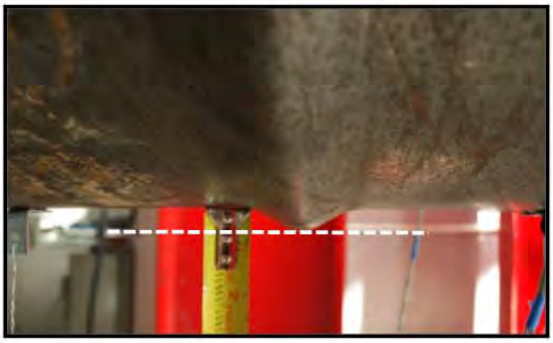

Figure 3-151: Buckle under loading point at ductility 2, Δ = 4.6 inches

The third ductility cycle demanded a mid-span displacement of 6.9 inches in both directions, the deformed profile of the pile under this displacement is shown in Figure 3-152. Over the course of the three cycle set, the buckles on either side of the pile increased in size and became narrow. On the top side of the pile, the buckles under the loading points increased in size quicker than those in the constant moment region. At the end of the ductility level, the buckles under the loading points had increased to 3/4" in height (Figure 3-153). The same behavior was not observed from the buckles in the constant moment region, one of the buckles grew in height to approximately 1/4" (Figure 3-154) while the other had no significant change from ductility two. The same unsymmetrical behavior was observed on the underside of the pile during the pull cycles. The buckles under the loading points both increased to about 3/4" in height and the buckle located in the constant moment region, 12 inches south of the centerline of the pile only increased to about 1/4" in height. By the end of the ductility cycle, the buckles (both on the top and underside of the pile) under the loading points had spread to half the circumference of the pile as seen in Figure 3-155. The buckling outline of the pile at the end of ductility three is shown in Figure 3-156.

Figure 3-152: Pile with a mid-span displacement of 6.9 inches, ductility 3

Figure 3-153: Buckle under loading point, ductility 3, Δ=6.9 inches

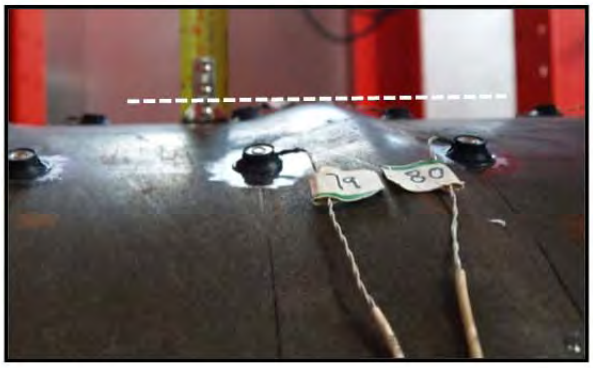

Figure 3-154: Buckle in constant moment region, ductility 3, Δ=6.9 inches

Figure 3-155: Buckle under the loading point, spreading half the circumference of the specimen, ductility 3, Δ=6.9 inches

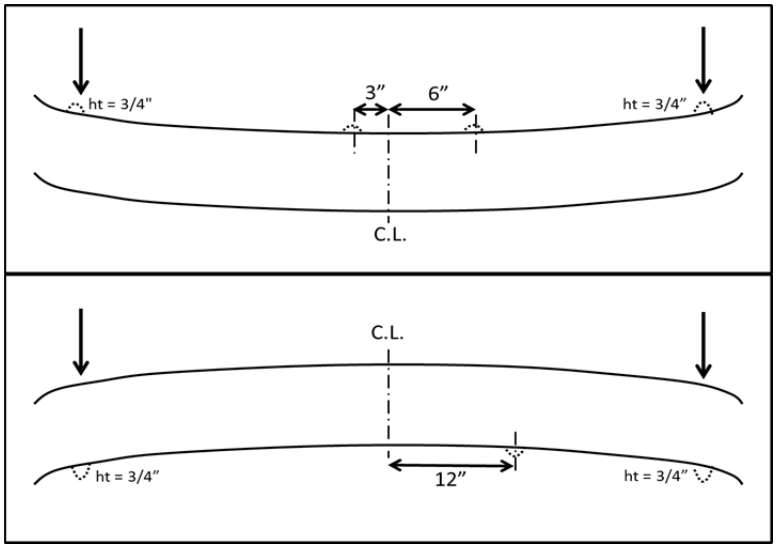

Figure 3-156: Outline of buckles at the conclusion of ductility 3, Δ=6.9 inches

The next three cycle set pushed and pulled the specimen to 9.2 inches in both directions, the displaced specimen is shown in Figure 3-157. The higher displacement increased the tensile strains on the pile which in turn led to larger buckles upon load reversal. Both the top and underside of the pile had similar responses to the increased displacement and strain demand. The buckles under the loading points became narrower than in the previous cycle and increased in height from 3/4" to 7/8" (Figure 3-158). The buckles in the constant moment region showed no change in size; all of the damage was concentrated in the buckles under the loading points.

Figure 3-157: Pile with a mid-span displacement of 9.2 inches, ductility 4

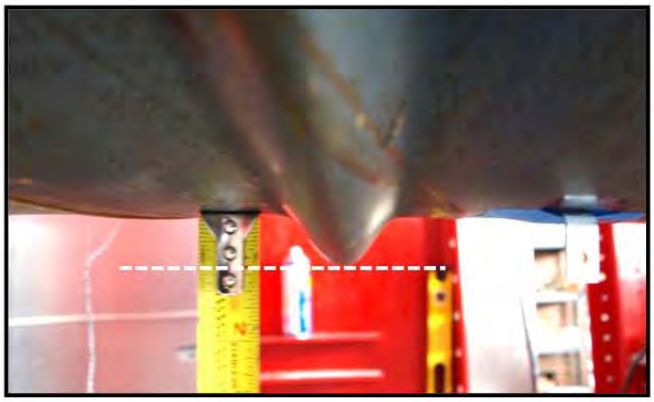

Figure 3-158: Buckle under loading point, ductility 4, Δ=9.2 inches

Ductility four proved to be the most displacement that the pile could undergo before rupture. The pile began to crack at one of the loading points on the underside of the pile at a displacement of 8.3 inches (Figure 3-159) on the path to the 11.5 inches, the ductility 5 displacement demand. The crack ruptured at a displacement of 9.05 inches, losing about 14 kips of load (Figure 3-160). At the displacement demand of 11.5 inches, the crack in the ruptured pile had opened significantly as shown in Figure 3-161. It is interesting to note that the concrete only crushed in the location of the buckle and is still intact where the buckle had not formed as seen in Figure 3-162. Upon reversal of the load, the pile ruptured at one of the loading points on the top side as seen in Figure 3-163, the rupture on the bottom of the pile

closed, regaining its compressive strength as shown in Figure 3-164. The progression of buckling leading to the initial rupture is shown in Figure 3-165.

Figure 3-159: Crack on the underside of pile leading to the first push of ductility 5, Δ=8.3 in

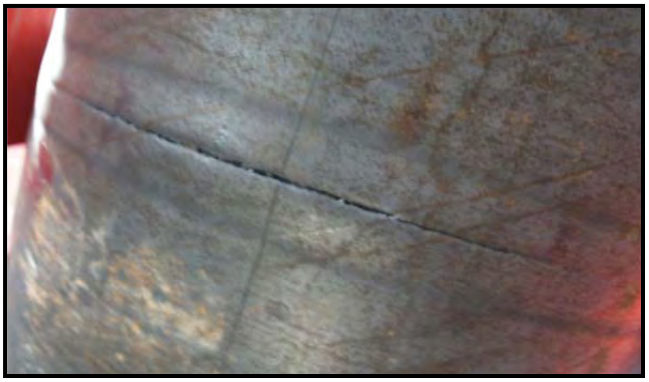

Figure 3-160: Crack opening on the pile leading to the first push of ductility 5, Δ=9.1 in

Figure 3-161: Crack opening on the pile at ductility 5, Δ=11.5 in

Figure 3-162: Concrete has not crushed under the buckle ductility 5, Δ=11.5 in

Figure 3-163: Rupture on top of the pile, first pull of ductility 5, Δ=11.5 in

Figure 3-164: Crack on underside of the pile closing, first pull of ductility 5, Δ=11.5 in

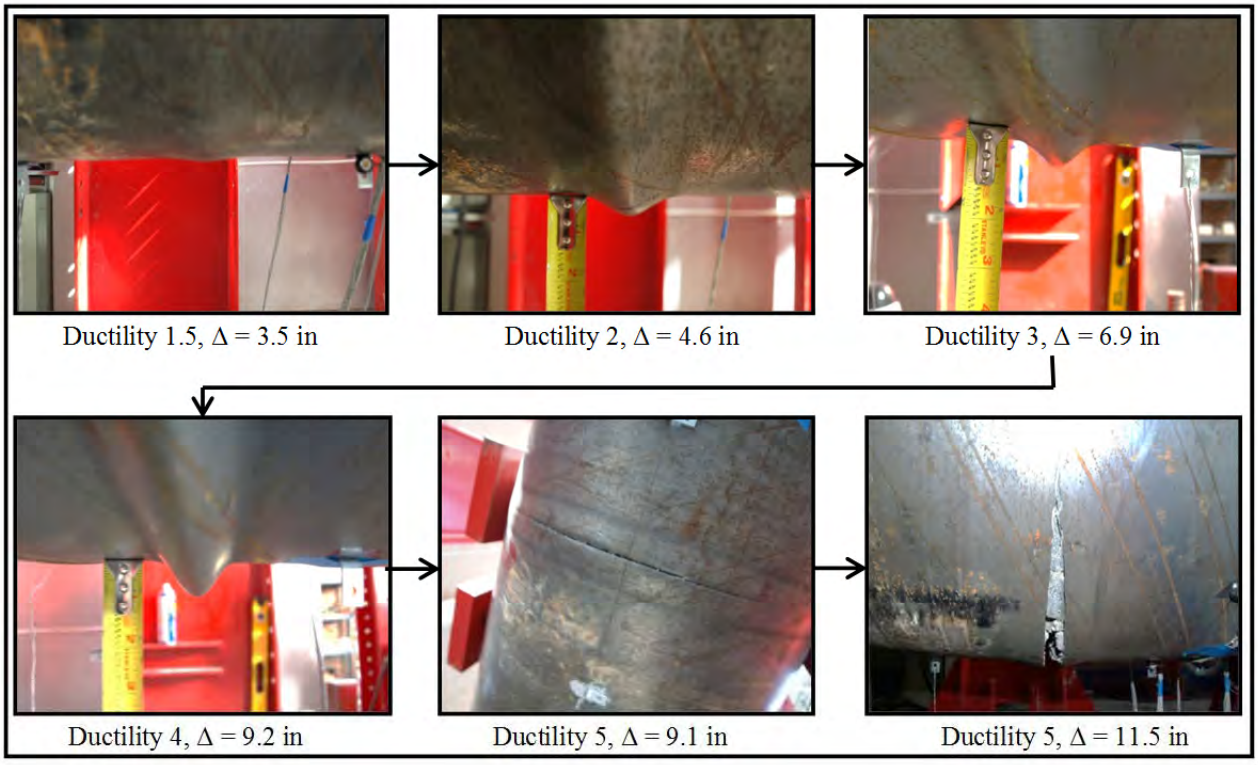

Figure 3-165: Progression of buckling

The force-displacement hysteresis of this test, after the dead weight of the pile had been accounted for, is shown in Figure 3-166. The force-displacement envelopes for the first, second, and third cycles are shown in Figure 3-167. The pile had an average ultimate force of about 70 kips, and as seen in the hysteresis the pile behaved in a ductile manner and had no strength loss until rupture which resulted in a loss of approximately 14 kips.

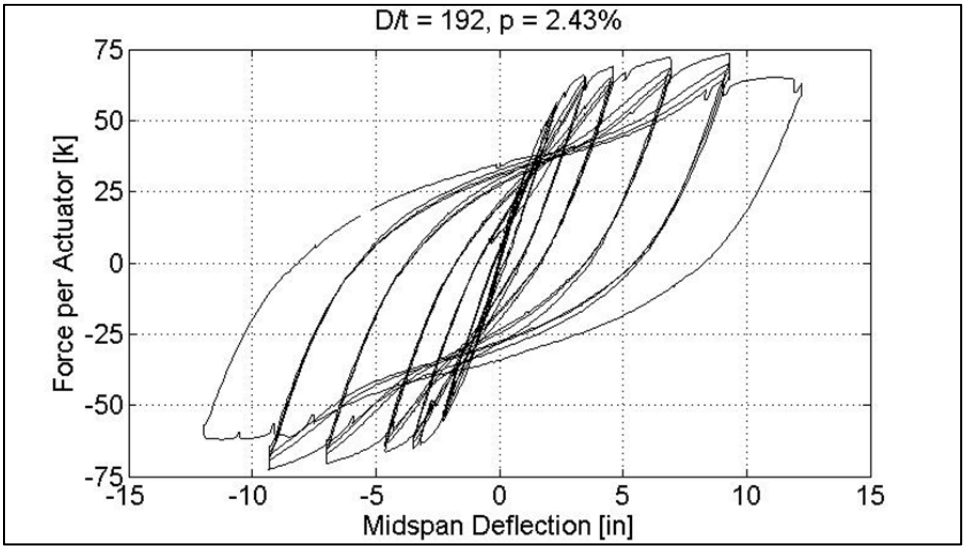

Figure 3-166: Force-Displacement Hysteresis

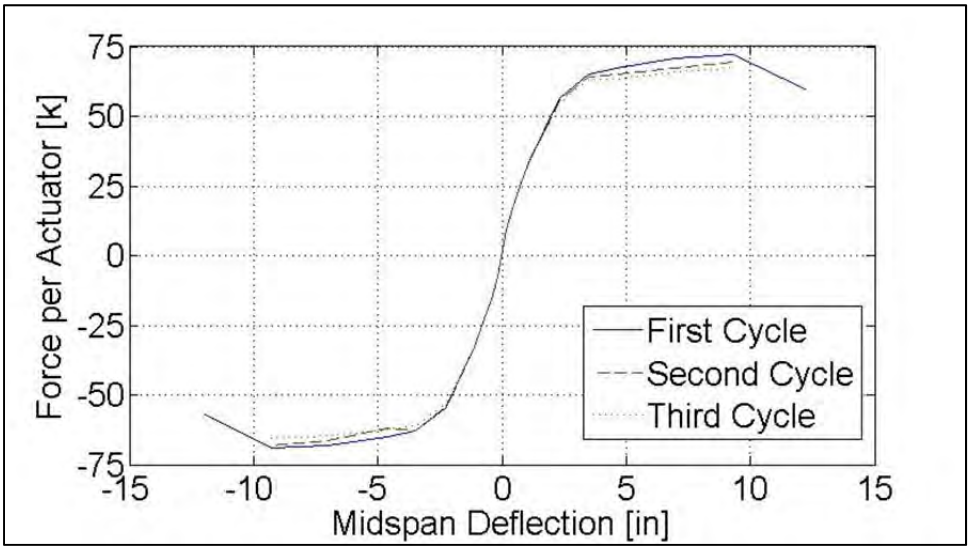

Figure 3-167: Force-Displacement Envelopes

Test 10 was conducted at the Constructed Facilities Lab on Thursday, October 18th. The pile was a concrete filled steel tube; the tube had an outer diameter equal to 24 inches and a thickness equal to 0.125 inches, resulting in a diameter-thickness ratio of 192. Visible buckling of the specimen began in the first push of ductility one and a half at a displacement of 3.47 inches in both directions. The pile sustained the damage without strength degradation until rupture in the first cycle of ductility five.

3.7.11. Test Eleven

Test 11 consisted of a concrete filled steel tube with 8#6 ASTM A706 internal reinforcing bars creating an internal reinforcement ratio of 0.78%; the pipe had an outer diameter equal to 24 inches and a thickness equal to 0.1875 inches resulting in a diameter-thickness ratio of 128.

The pile began to show visible signs of buckling during the second cycle of ductility two at a mid-span displacement of 4 inches. As expected, the buckles appeared under the loading points where the moment gradient changes; one of these small buckles is shown in Figure 3-168. The underside of the pile also showed signs of buckling under the loading points upon reversal in the pull direction (Figure 3-169).

Figure 3-168: Initiation of buckling, ductility 2, Δ = 4.0 inches

Figure 3-169: Initiation of buckling, ductility 2, Δ = 4.0 inches

The mid-span displacement demand was increased to 6 inches in either direction for ductility three; the specimen profile at this level of deformation is shown in Figure 3-170. As the displacement increased, the damage of the specimen increased as well. During the first cycle of this three cycle set, the steel tube began to ripple throughout the constant moment region as shown in Figure 3-171Figure 3-172. The repeated cyclic loading caused these "ripples" to condense into a few buckles and these buckles continued to increase in size throughout the ductility level. The location of the condensed buckles in the constant moment region at the conclusion of the ductility three is shown in Figure 3-173. The pile damage was similar in both the push and pull directions. As indicated in Figure 3-173, the buckles located under the loading points were the most severe, measuring a height of 1/4 – 1/2 of an inch. The two other buckles located in the center of the constant moment region were significantly smaller and were not large enough to measure. One of the buckles located under the loading points on the underside of the pile is shown in Figure 3-174, and one of the smaller buckles located in the center of the constant moment region is shown in Figure 3-175.

Figure 3-170: Pile profile, ductility 3, Δ = 6.0 inches

Figure 3-171: Ripples on steel pile, ductility 3 – 1st push, Δ = 6.0 inches

Figure 3-172: Ripples on steel pile, ductility 3 – 1st pull, Δ = 6.0 inches

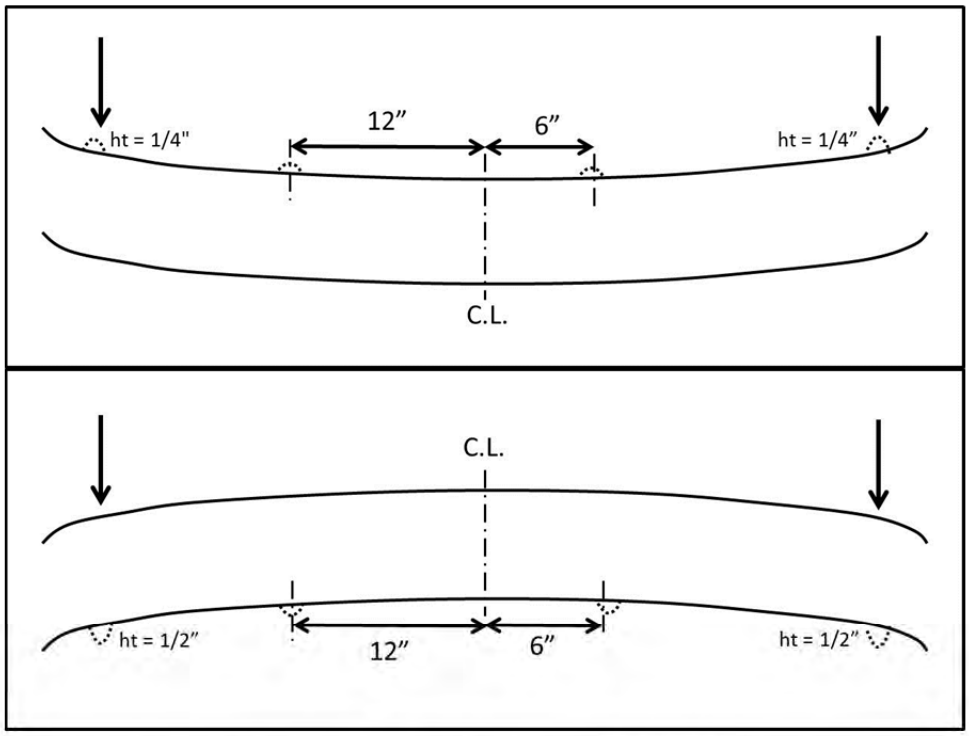

Figure 3-173: Pile profile outline, ductility 3, Δ = 6.0 inches

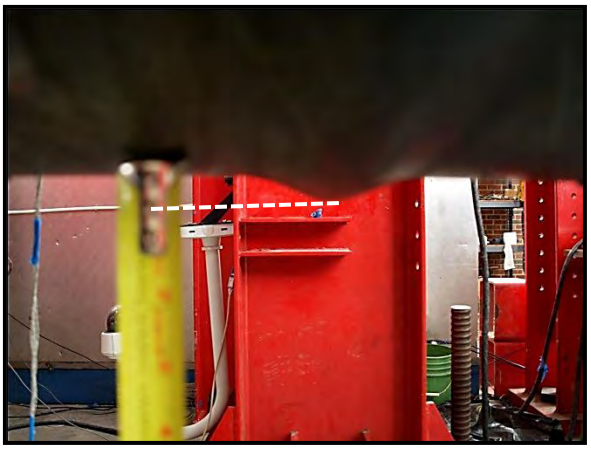

Figure 3-174: Buckle under loading point, ductility 3, Δ = 6.0 inches

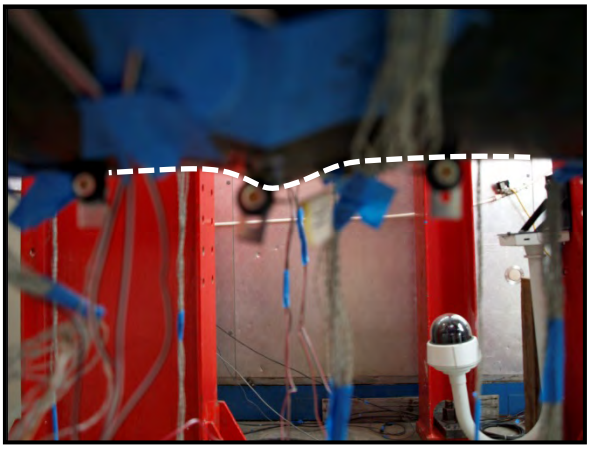

Figure 3-175: Buckle in constant moment region, ductility 3, Δ = 6.0 inches

The pile's damage continued to increase as the displacement was increased to 8 inches in either direction during ductility four (Figure 3-176). The most significant change in the buckle sizes, which correspond to the level of damage, occurred in the first pull and the second push of ductility four, the cycles directly after the pile had been subjected to higher plastic tensile strains which in turn made the buckles increase in size. The majority of the buckles were perpendicular the length of the specimen, however the buckle on the top of the pile under the South loading point formed along a weld on the pile and followed the diagonal direction of the weld as seen in Figure 3-177. This behavior did not affect the performance of the specimen. At the conclusion of the three cycle set with a mid-span deflection of 8 inches, the buckles under the loading points were approximately one inch in height and the two in the constant moment region were 1/4 – 3/8 of an inch in height. The outline of the

buckle locations at this point in the test are shown in Figure 3-178. Photographs of the buckles under the loading points and in the constant moment region on the top of the pile during the third push are shown in Figure 3-179 and Figure 3-180, respectively.

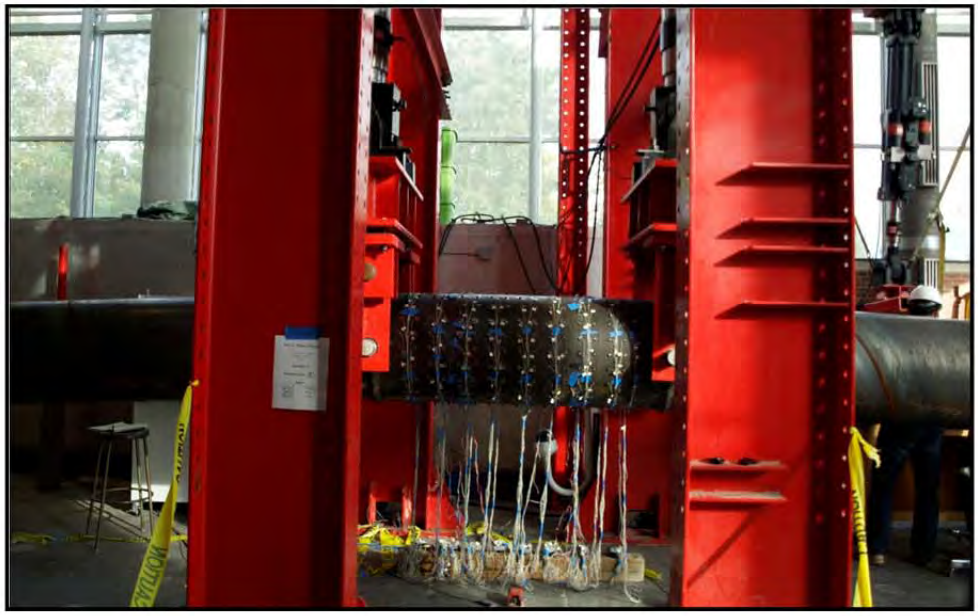

Figure 3-176: Specimen at maximum ductility displacement, ductility 4, Δ = 8.0 inches

Figure 3-177: Buckle following weld direction, ductility 4, Δ = 8.0 inches

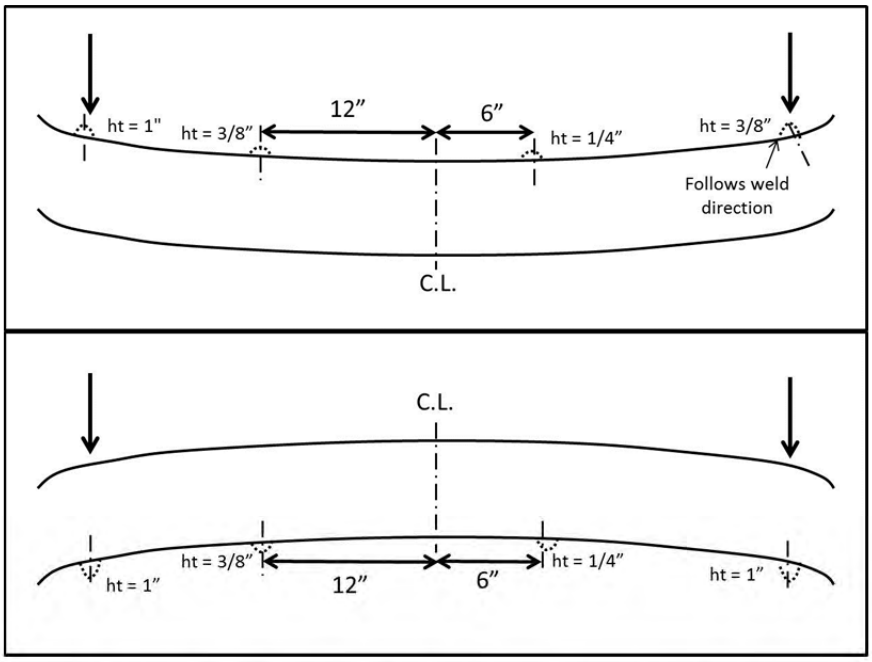

Figure 3-178: Pile profile outline, ductility 3, Δ = 8.0 inches

Figure 3-179: Buckle under loading point, ductility 4, Δ = 8.0 inches

Figure 3-180: Buckle in constant moment region, ductility 4, Δ = 8.0 inches

Ductility five was the last complete three cycle set the pile sustained without rupture of the steel pipe. The mid-span displacement during this three cycle set was 10 inches in both directions, as seen in Figure 3-181. Throughout the ductility level, the buckles increased in height and became narrow. The buckles under the loading points were approximately 1-1/4 inches in height (Figure 3-182), about three times the height of the buckles in the constant moment region which were only 3/8 to 1/2 of an inch in height (Figure 3-183). During the third pull, tension cracks were observed on the top of the pile under the North loading point as seen in Figure 3-184.

Figure 3-181: Specimen at maximum ductility displacement, ductility 5, Δ = 10.0 inches

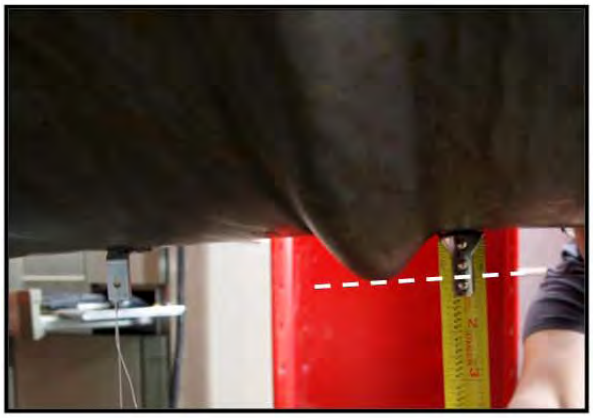

Figure 3-182: Buckle under loading point, ductility 5, Δ = 10.0 inches

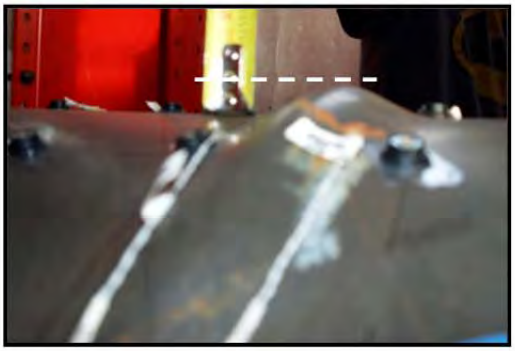

Figure 3-183: Buckle in constant moment region, ductility 5, Δ = 10.0 inches

Figure 3-184: Tension cracks on the top of the pile, ductility 5, Δ = 10.0 in

The mid-span displacement was increased to 12 inches during the first push of ductility six (Figure 3-185). The buckles grew in height and they became increasingly narrow. The increase in compression strain, and narrow buckle on the top of the pile led to rupture of the

steel pipe upon the reversal of load, during the first pull. The pile ruptured under the north loading point, where tension cracks were observed during the last pull of ductility five. The rupture is shown in Figure 3-186. As the mid-span displacement demand of the first pull displacement (12 inches) was reached the crack in the steel pile increased in width and circumference (Figure 3-187). The progression of the buckle leading to rupture throughout the course of the test is shown in Figure 3-188.

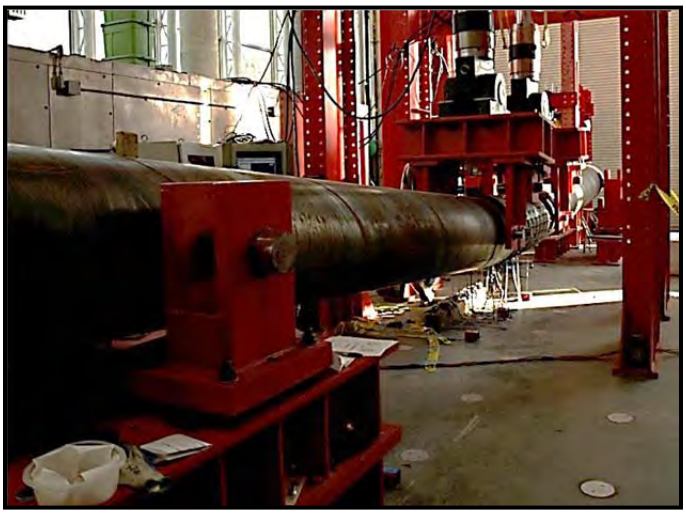

Figure 3-185: Specimen at maximum ductility displacement, ductility 6, Δ = 12.0 inches

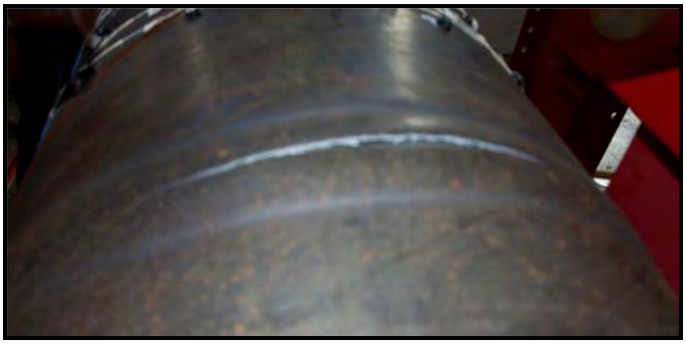

Figure 3-186: Rupture of the steel pile, en route ductility 6-1st pull

Figure 3-187: Rupture of the steel pile, ductility 6, Δ=12 inches

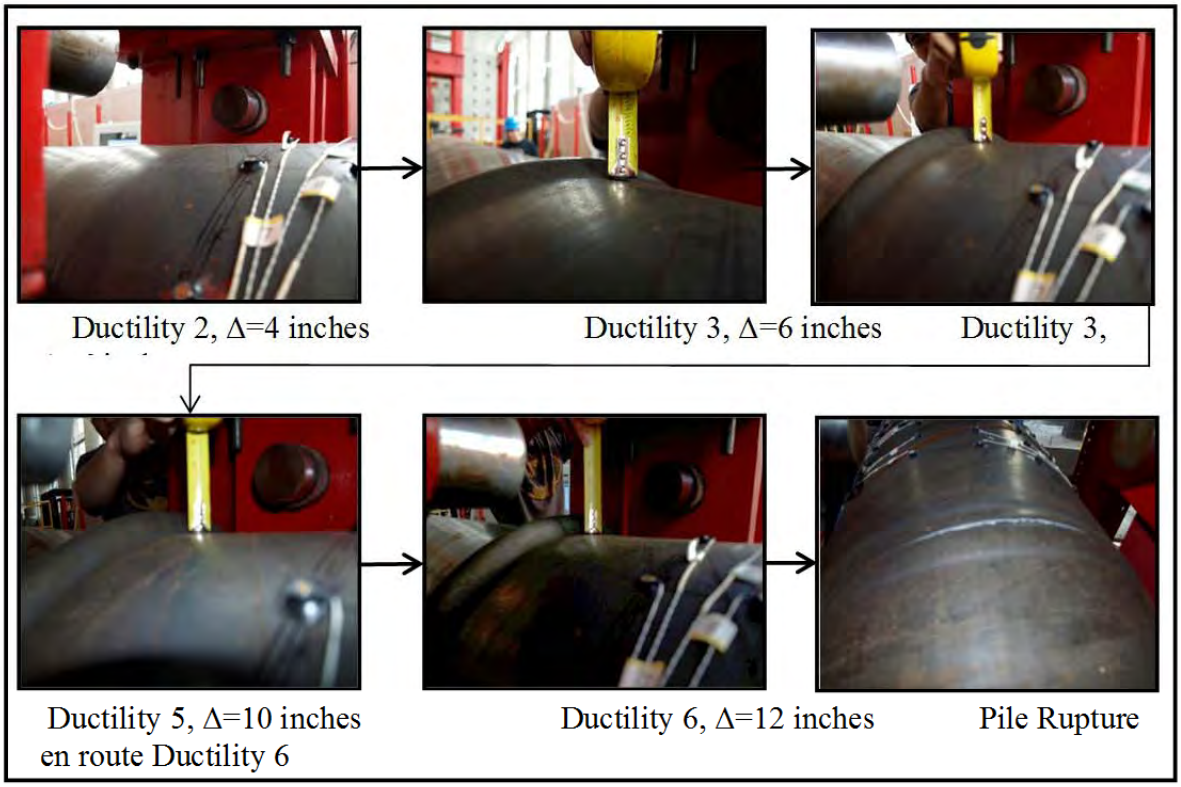

Figure 3-188: Progression of buckling throughout the test

The force-displacement hysteresis of this test, after the dead weight of the pile had been accounted for, is shown in Figure 3-189. The force-displacement envelopes for the first, second, and third cycles are shown in Figure 3-190. The pile had an average ultimate force

of about 58 kips, and as seen in the hysteresis the pile behaved in a ductile manner and had no strength loss until rupture with a loss of about 18 kips.

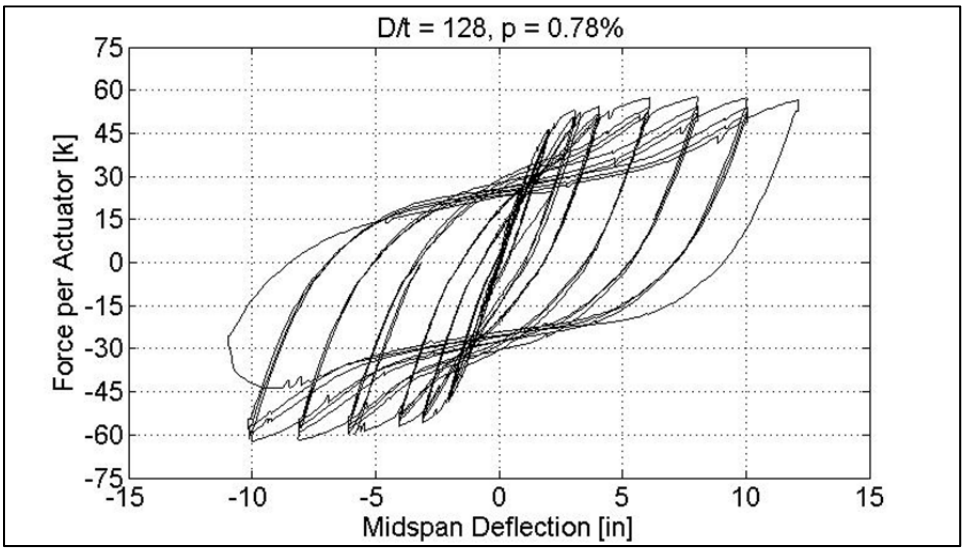

Figure 3-189: Force-Displacement Hysteresis

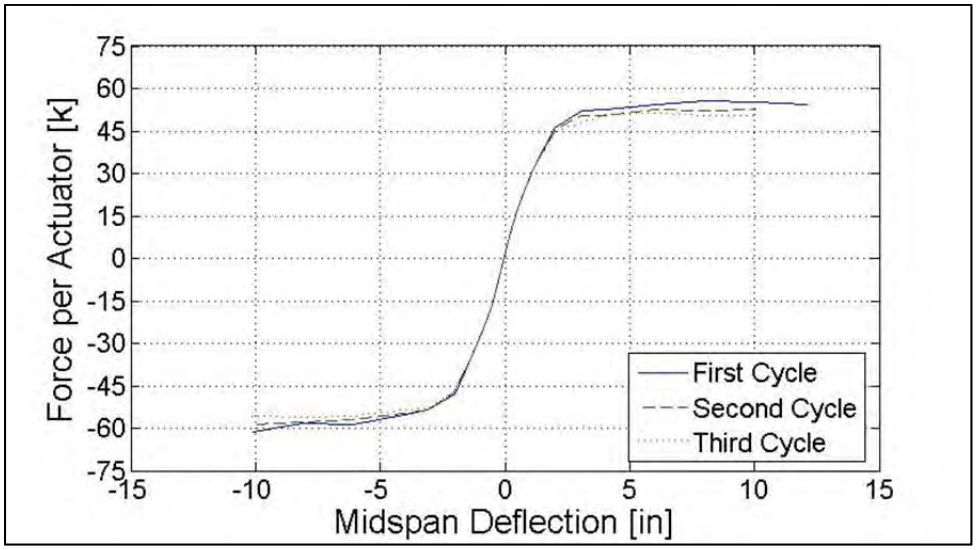

Figure 3-190: Force-Displacement Envelopes

Test 11 was conducted at the Constructed Facilities Lab on Wednesday, October 31st. The pile was a concrete filled steel tube; the tube had an outer diameter equal to 24 inches and a thickness equal to 0.180 inches, resulting in a diameter-thickness ratio of 133. Visible buckling of the specimen began in the second cycle of ductility two at a displacement of 4 inches in both directions. The pile sustained the damage without strength degradation until rupture in the first cycle of ductility six.

3.7.12. Test Twelve

Test 12 consisted of a concrete filled steel tube with 14#8 ASTM A706 internal reinforcing bars creating an internal reinforcement ratio of 2.43%; the pipe had an outer diameter equal to 24 inches and a thickness equal to 0.1875 inches resulting in a diameter-thickness ratio of 128.

The pile began to show visible signs of damage when the pile started to buckle at a mid-span displacement of 3.3 inches after the first pull of ductility one and a half. Only one buckle was observed at this point and it is shown in Figure 3-191. Upon the reversal of load when the pile was pushed to 3.3 inches for the second time the top of the pile also began to buckle under the south loading point (Figure 3-192). During the third and last cycle of this ductility level the pile behaved symmetrically with respect to the visible damage. There were four small “ripples” on the top and the underside of the pile when the respective side was in compression. The ripples at the conclusion of the ductility level were small as seen in Figure 3-193.

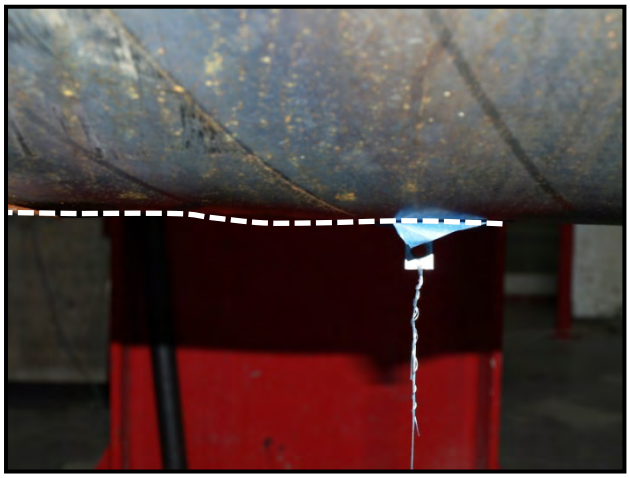

Figure 3-191: Initiation of buckling on underside of pile, ductility 1.5, Δ=3.3 in

Figure 3-192: Initiation of buckling on top of pile, ductility 1.5, Δ=3.3 in

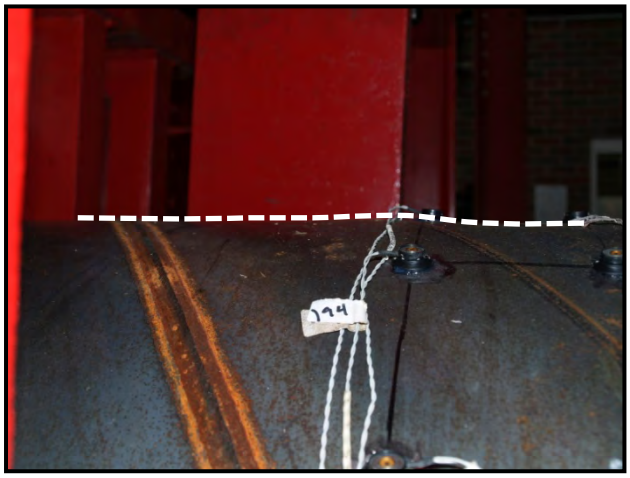

Figure 3-193: Typical buckle at the end of ductility 1.5, Δ=3.3 in

The damage in the pile increased as the mid-span displacement demand increased to 4.5 inches for ductility two. The buckles began to increase in size and number starting in the first pull of ductility two, after the underside of the pile had been introduced to new and higher tensile strains during the first push. The thin walled pipe began to form more ripples throughout the constant moment region, the most severe locations were located under the loading points were the moment gradient changes. One of the ripples located on the top of the pile during the second push cycle is shown in Figure 3-194. The more severe buckle located at the edge of the constant moment region near a loading point is shown in Figure 3-195. At the conclusion of the third push, six "ripples" had formed on the top of the pile, the locations of these ripples is shown in Figure 3-196. Similarly to the top of the pile, the

underside of the pile also formed a couple more buckles than in the previous ductility cycle, the five current buckles are also shown in Figure 3-196.

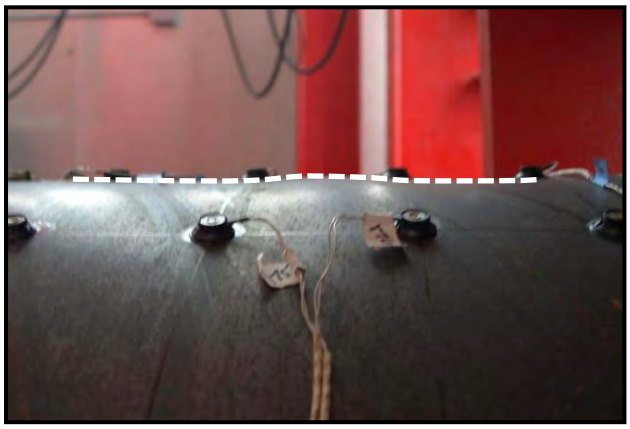

Figure 3-194: Ripple in the constant moment region, ductility 2, Δ=4.5 in

Figure 3-195: Ripple under the north loading point, ductility 2, Δ=4.5 in

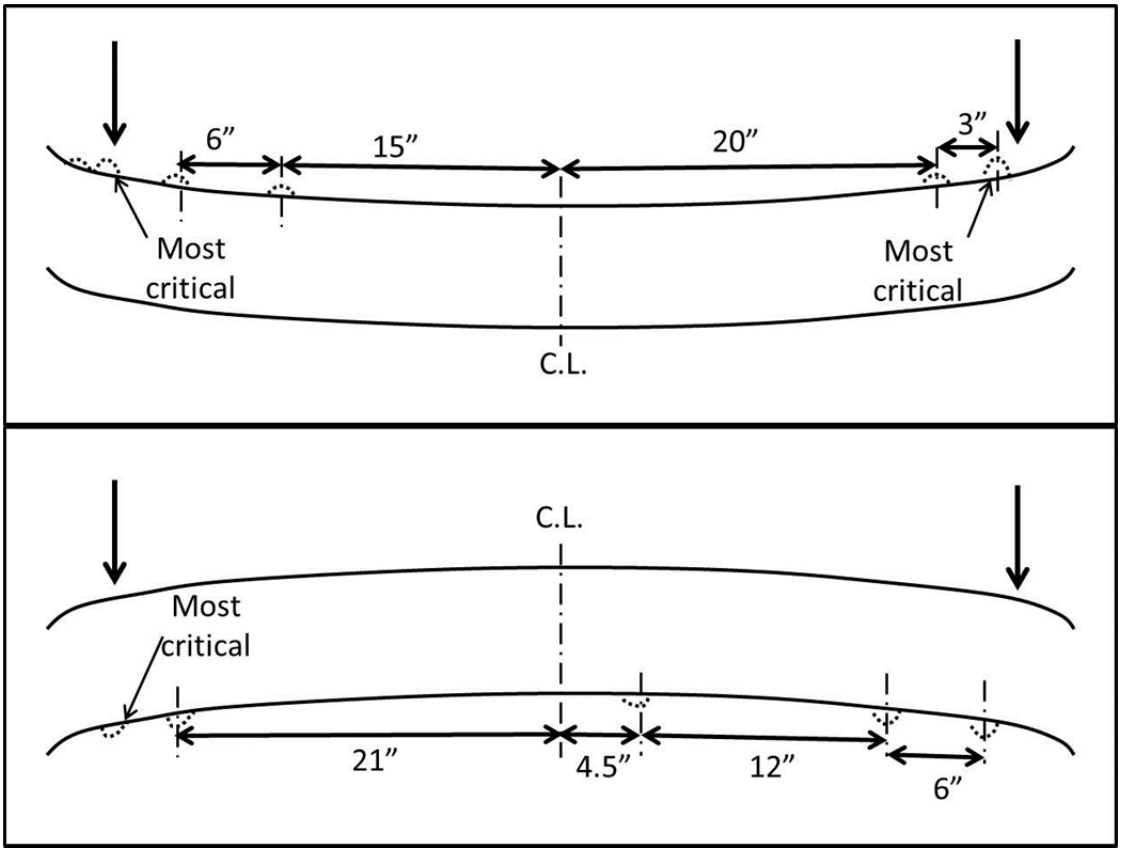

Figure 3-196: Location of buckles, ductility 2, Δ=4.5 in

The next three cycle set, ductility three, increased the mid-span displacement to 6.6 inches. The deformed specimen at this level of displacement is shown in Figure 3-197. As the specimen cycled through this displacement, the damage in the pile began to condense and only a few buckles continued to absorb the damage and therefore increase in height and circumference. On both the top and underside of the pile, the larger buckles became those under or near the loading points. The buckles did not condense until the first pull cycle, the existing ripples in the first push cycle are shown in Figure 3-198. Figure 3-199 and Figure 3-200 show the buckles in the constant moment region and near the loading point, respectively, on the top of the pile during the second push cycle, after the damage condensation began. The pile behaved symmetrically throughout the ductility cycle and at its conclusion the buckles under or near the loading points were approximately 1/2 – 5/8 of an inch in height and the smaller buckles in the constant moment region were about 1/8 of an inch in height. The location in the constant moment region and sizes of these buckles is demonstrated in Figure 3-201.

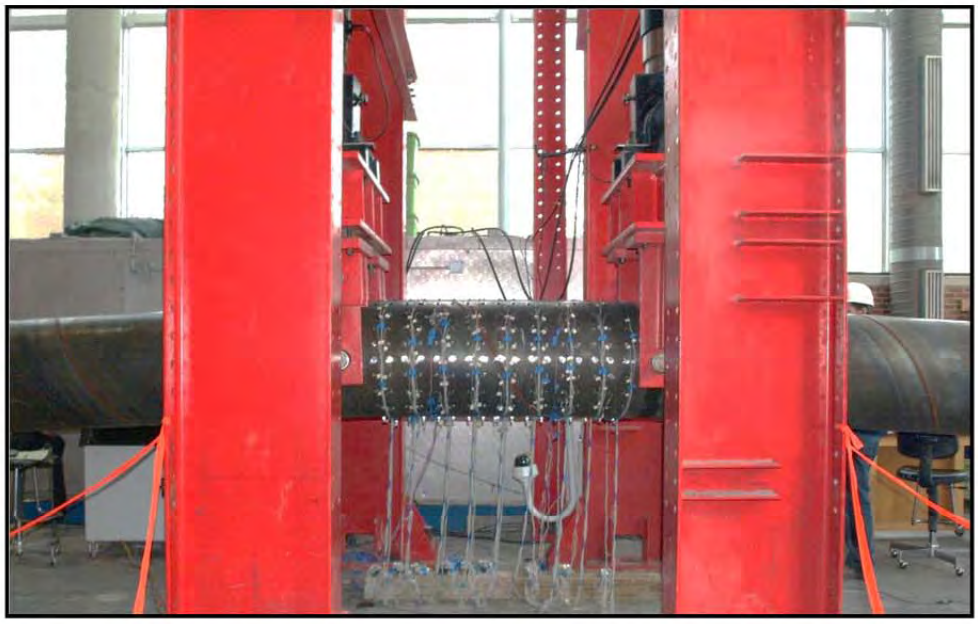

Figure 3-197: Deformed specimen, ductility 3, Δ=6.6 in

Figure 3-198: Ripples on top of pile, ductility 3-push 1, Δ=6.6 in

Figure 3-199: Buckle in constant moment region, ductility 3, Δ=6.6 in

Figure 3-200: Buckle near loading point, ductility 3, Δ=6.6 in

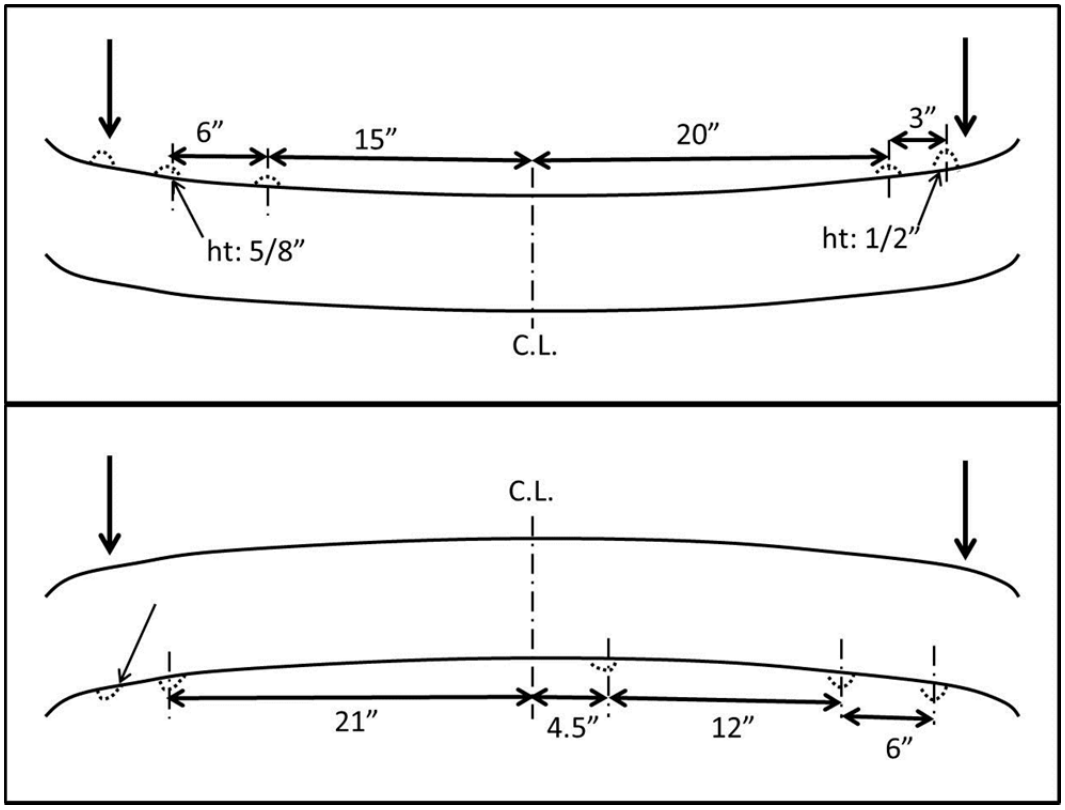

Figure 3-201: Location of buckles, ductility 3, Δ=6.6 in

Ductility four increased the mid-span displacement to 8.9 inches (Figure 3-202). In this three cycle set, the damage continued to increase. The buckles in the constant moment region did not change in height, however the buckles located near the loading points which were absorbing the damage grew significantly. After the three cycle set the buckles near the loading points were about 7/8 of an inch in height and had wrapped almost half way around the circumference of the pipe pile. The critical buckles on the top and underside of the pile are shown in Figure 3-203 and Figure 3-204, respectively. The buckle near the South loading point on the top of the pile was near one of the spiral welds and formed parallel to this weld instead of perpendicular to the pipe.

Figure 3-202: Deformed specimen, ductility 4, Δ=8.9 in

Figure 3-203: Buckle on the top of the pile, ductility 4, Δ=8.9 in

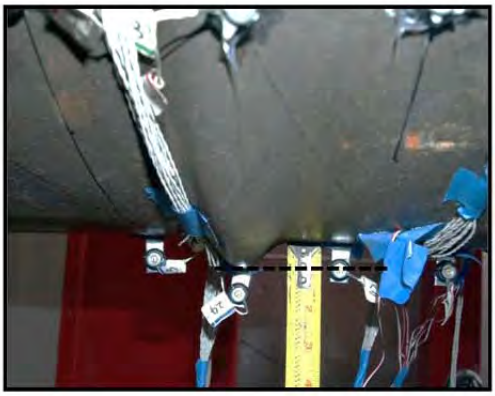

Figure 3-204: Buckle on the underside of the pile, ductility 4, Δ=8.9 in

Ductility five was the last complete three cycle set the pipe pile was able to undergo at a mid-span displacement of 11.1 inches as shown in Figure 3-205. The buckles under or near the loading points in this ductility cycle continued to increase, up to a height of approximately one inch (Figure 3-206). The buckles in the constant moment region showed no major change from previous cycles, one of these buckles is shown in Figure 3-207. The most significant change in damage over the course of ductility five was not the change in height of the buckle but the narrowness of the buckles. The buckle on top of the pile under the north loading point is a good example of how the buckles creased and bent almost 180 degrees (Figure 3-208).

Figure 3-205: Deformed specimen, ductility 5, Δ=11.1 in

Figure 3-206: Buckle on the top of the pile under loading point, ductility 5, Δ=11.1 in

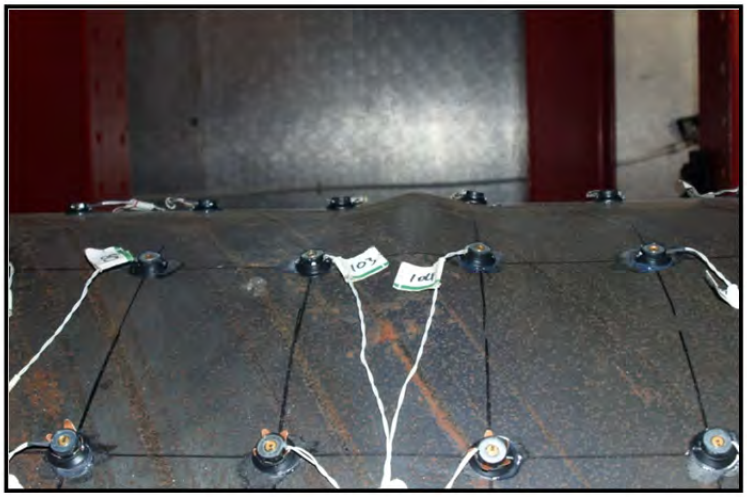

Figure 3-207: Buckle on the top of the pile in constant moment region, ductility 5, Δ=11.1 in

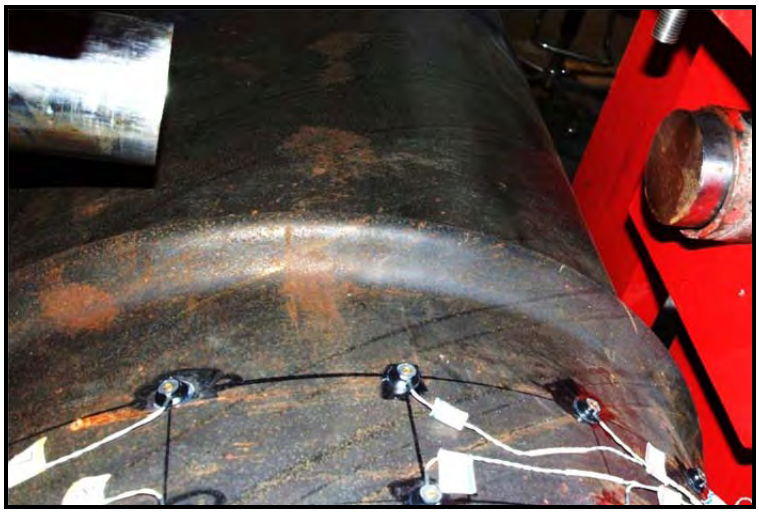

Figure 3-208: Narrow buckle on the top of the pile under loading point, ductility 5, Δ=11.1 in

The steel pipe ruptured on the underside of the pile, in tension, as the pile was moving toward the first cycle of ductility six. The rupture occurred at a mid-span displacement of 9.41 inches under the south loading point, shown in Figure 3-209. The pile continued to be pushed to the full displacement demand of 13.3 inches. As the displacement increased the rupture increased in width and length, the pile at the ruptured location after meeting the displacement demand of ductility six is shown in Figure 3-210. The pile lost about 13 kips of flexural strength in this cycle, which was about 15% of its maximum total strength. Upon reversal of the load the top of the pile ruptured under the north loading point at a mid-span displacement of 3.45 inches (Figure 3-211). During this pull cycle the rupture which occurred on the first push closed and regained its compressive strength as seen in Figure 3-212. The progression of buckling leading to the initial rupture over the course of the test is shown in Figure 3-213.

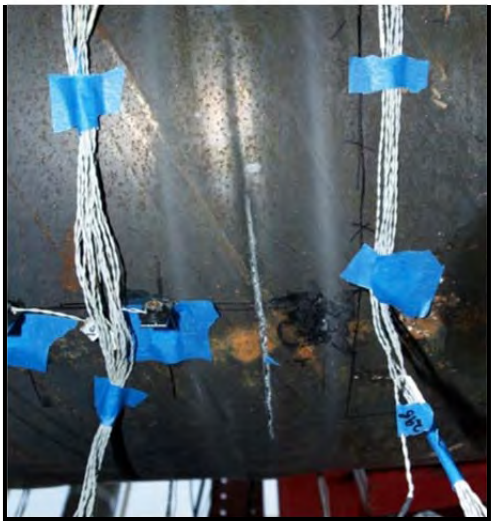

Figure 3-209: Initial rupture under south loading point, en route ductility 6, Δ=9.4 in

Figure 3-210: Rupture under south loading point, ductility 6, Δ=13.3 in

Figure 3-211: Second rupture under north loading point, en route ductility 6, Δ=3.45 in

Figure 3-212: First rupture closed under compressive stress, en route ductility 6, Δ=3.45 in

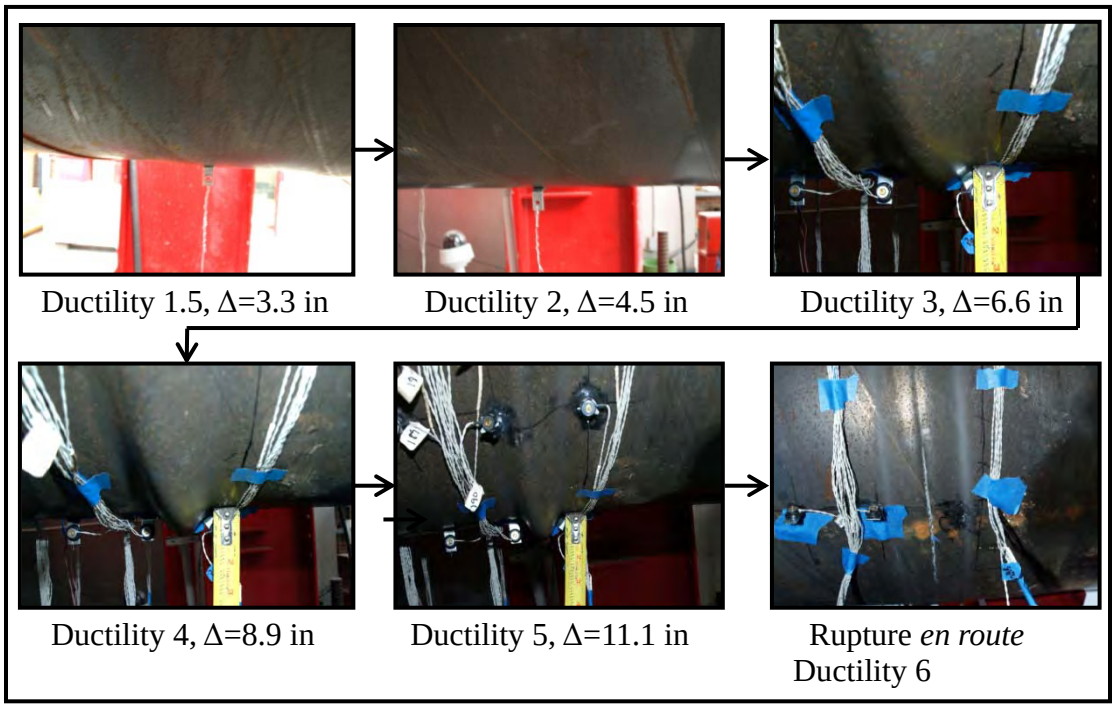

Figure 3-213: Progression of buckling leading to rupture

The force-displacement hysteresis of this test, after the dead weight of the pile had been accounted for, is shown in Figure 3-214. The force-displacement envelopes for the first, second, and third cycles are shown in Figure 3-215. The pile had an average ultimate force of about 82 kips, and as seen in the hysteresis the pile behaved in a ductile manner and had no strength loss until rupture with a loss of about 13 kips.

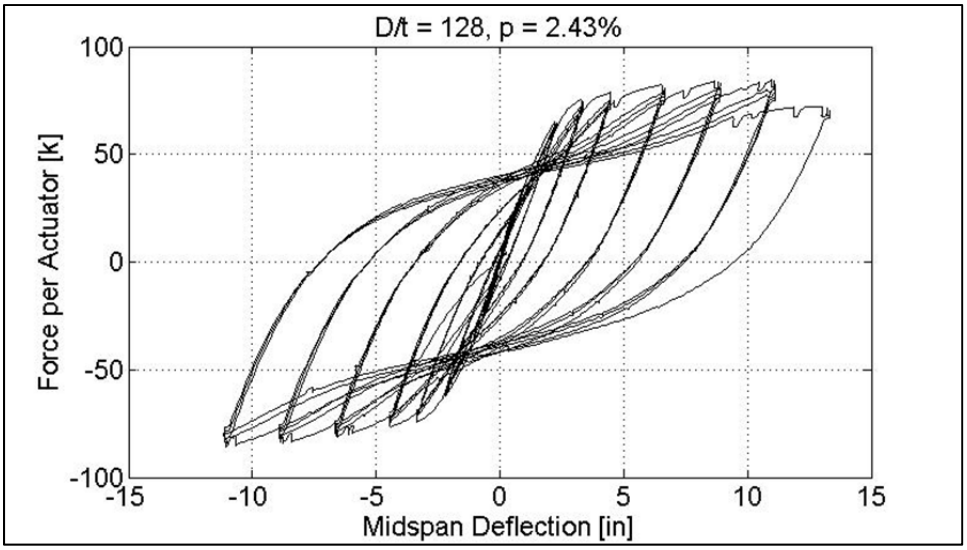

Figure 3-214: Force-Displacement Hysteresis

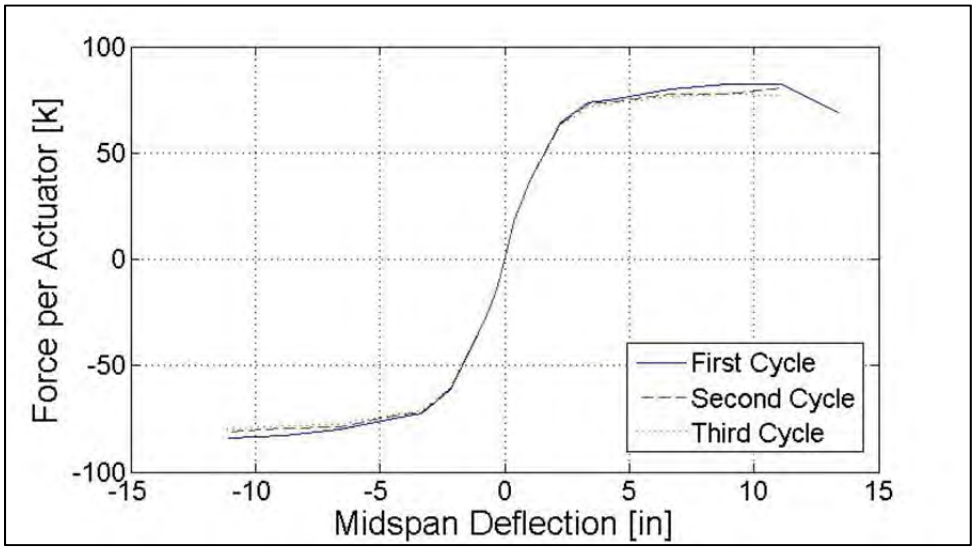

Figure 3-215: Force-Displacement Envelopes

Test 12 was conducted at the Constructed Facilities Lab on Monday, November 12th. The pile was a concrete filled steel tube; the tube had an outer diameter equal to 24 inches and a thickness equal to 0.180 inches, resulting in a diameter-thickness ratio of 133. Unlike the previous piles with this diameter to thickness ratio tested in this research project, the internal reinforcement ratio was 2.43% (previous tests had internal reinforcement ratios of 0.78% and

1.7%). Visible buckling of the specimen began in the first pull of ductility one and a half at a displacement of 3.4 inches in either direction. The pile sustained the damage without strength degradation until rupture in the first cycle of ductility six.

CHAPTER 4 EXPERIMENTAL RESULTS

4.1. Displacements, Strains and Curvatures

The strains on the steel tube were measured using the Optotrak Certus HD system and electrical resistance strain gages. The Optotrak system and LED placements allowed strains to be measured at various points along the constant moment region and at many locations around the circumference of the pile. Strain profiles were developed at different locations from this configuration.

4.1.1. Prior to Buckling

The strains measured on the surface of the steel tube prior to buckling resulted in a linear strain relationship. The strains and curvatures throughout the length of the constant moment region were approximately equal at each ductility level. The relationship between curvatures and strains is expressed in **Equation 4-1**. Figure 4-1 and Figure 4-2 display the maximum tensile strains and curvatures during the first pull cycles along the length of the constant moment region for Test 6 with a D/t ratio of 33. As seen in the figure, the values are constant in the regions not affected by buckling. To maximize the use of the collected data to obtain accurate and precise information, the strain profiles along the constant moment region were averaged to summarize the data at each loading point.

$$\varepsilon = \Phi z \qquad \text{Equation 4-1}$$

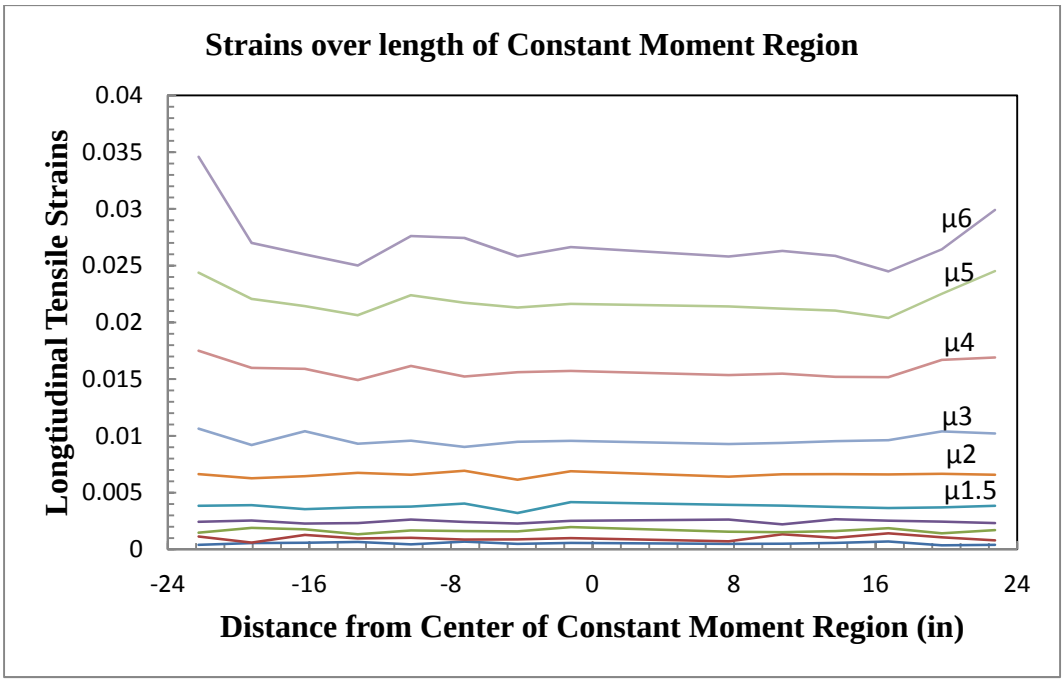

Figure 4-1 Strains along length of Constant Moment Region

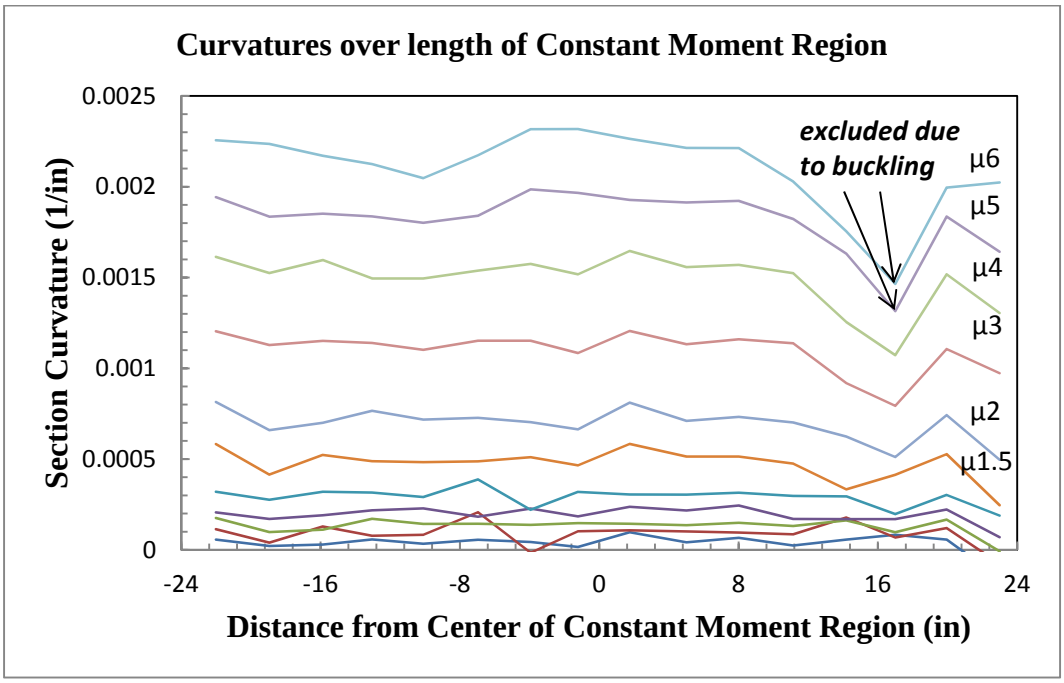

Figure 4-2 Curvatures along length of Constant Moment Region

Prior to buckling, the strain profiles were linear along the cross section of the concrete filled steel tube in the constant moment region. The initiation of buckling in each specimen was defined when the strain profiles became non-linear. This usually occurred before buckling was observed in the physical tests. Strain profiles prior to buckling for each test are shown below. From this point forward the results will be separated into two different groups: (1) varying diameter-to-thickness ratios and (2) varying internal reinforcement ratios. The first group of tests comparing D/t ratios includes Tests 2 through 7 as well as data from a past test performed at North Carolina State University, and will be labeled as 'Test 0' (Gonzalez). Figure 4-3 and Figure 4-6 show the strain profiles prior to buckling for the push and pull directions. The location of the selected profile and direct of loading are indicated with a diagram for each profile. The strain profiles include different ductility levels because the piles buckle at different levels of ductility, depending on the D/t ratio.

Figure 4-3. Strain profiles prior to buckling: varying D/t ratios: pull loading

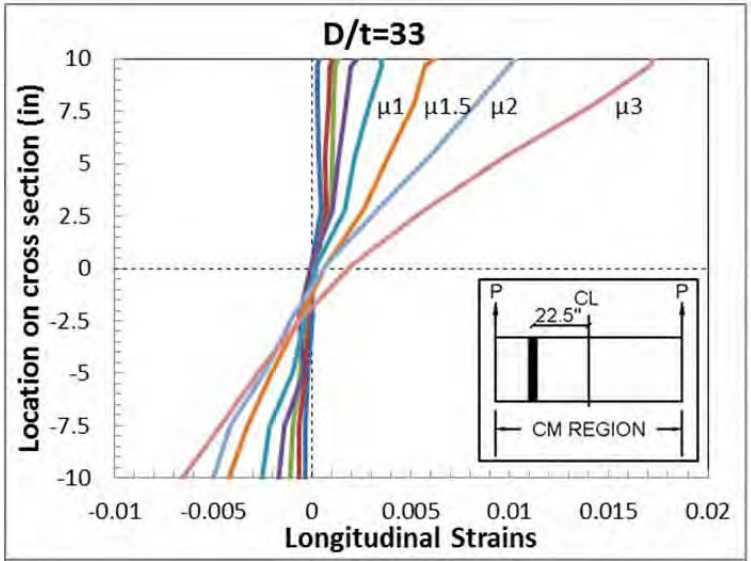
D/t=33
Location on cross section (in)
10
7.5
5
2.5
0
-2.5
-5
-7.5
-10
μ1
μ1.5
μ2
μ3
P
CL
P
22.5"
CM REGION
-0.01
-0.005
0
0.005
0.01
0.015
0.02
Longitudinal Strains

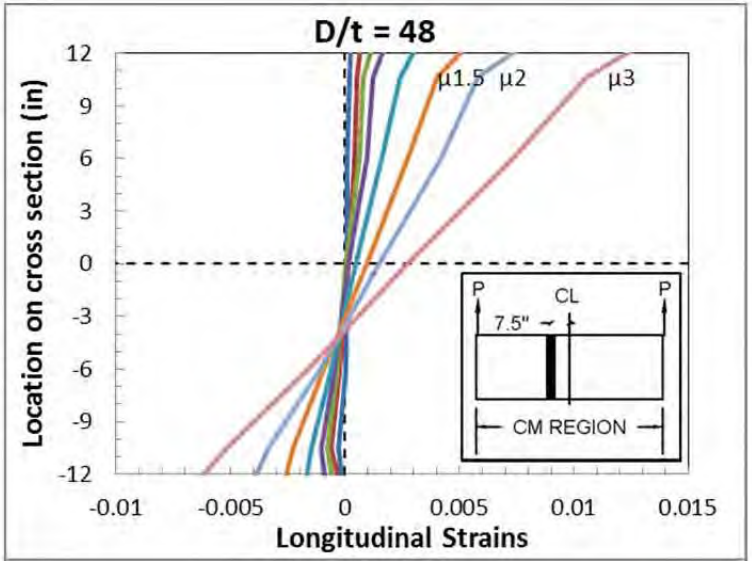
D/t = 48
Location on cross section (in)
12
9
6
3
0
-3
-6
-9
-12
μ1.5
μ2
μ3
P
CL
P
7.5"
CM REGION
-0.01
-0.005
0
0.005
0.01
0.015
Longitudinal Strains

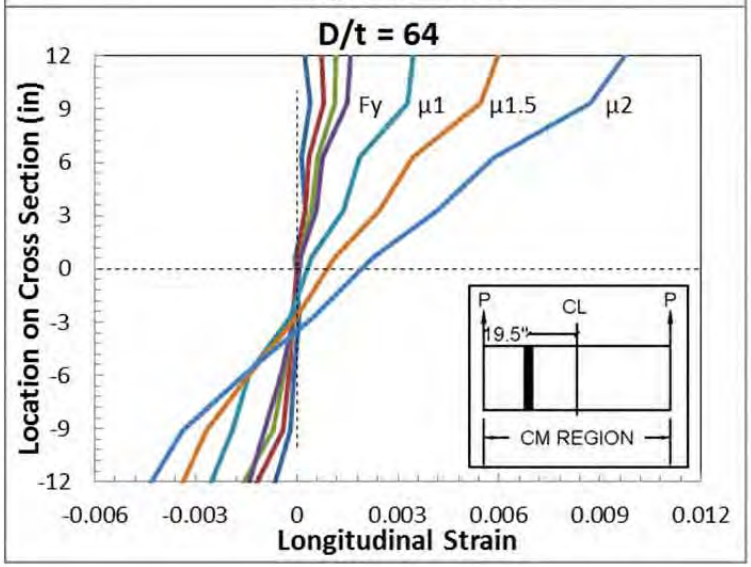
D/t = 64
Location on Cross Section (in)
12
9
6
3
0
-3
-6
-9
-12
Fy
μ1
μ1.5
μ2
P
CL
P
19.5"
CM REGION
-0.006
-0.003
0
0.003
0.006
0.009
0.012
Longitudinal Strain

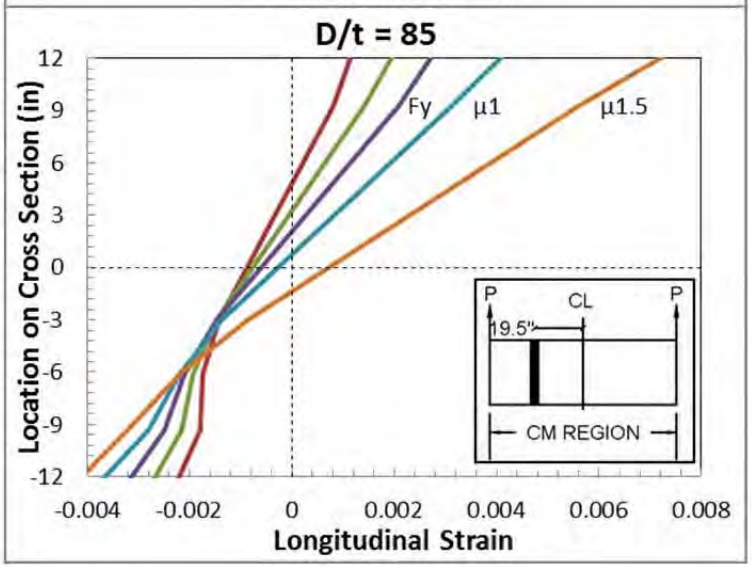
D/t = 85
Location on Cross Section (in)
12
9
6
3
0
-3
-6
-9
-12
Fy
μ1
μ1.5
P
CL
P
19.5"
CM REGION
-0.004
-0.002
0
0.002
0.004
0.006
0.008
Longitudinal Strain

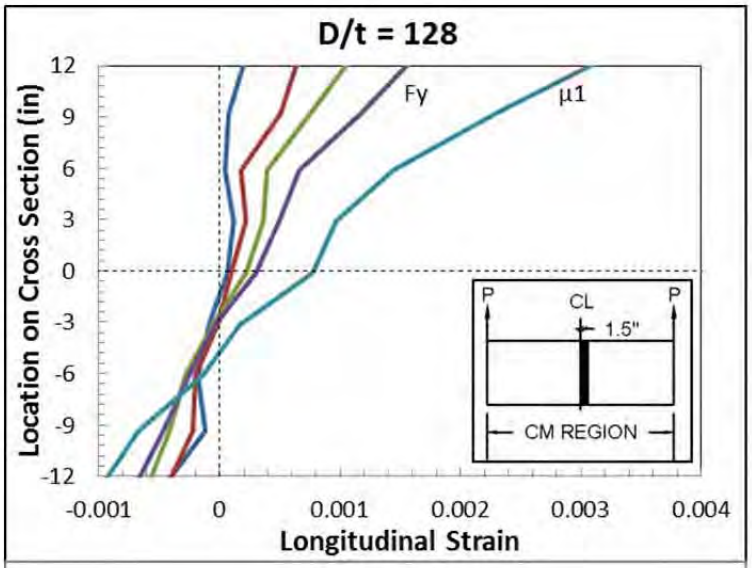
D/t = 128
Location on Cross Section (in)
12
9
6
3
0
-3
-6
-9
-12
Fy
μ1
P
CL
P
1.5"
CM REGION
-0.001
0
0.001
0.002
0.003
0.004
Longitudinal Strain

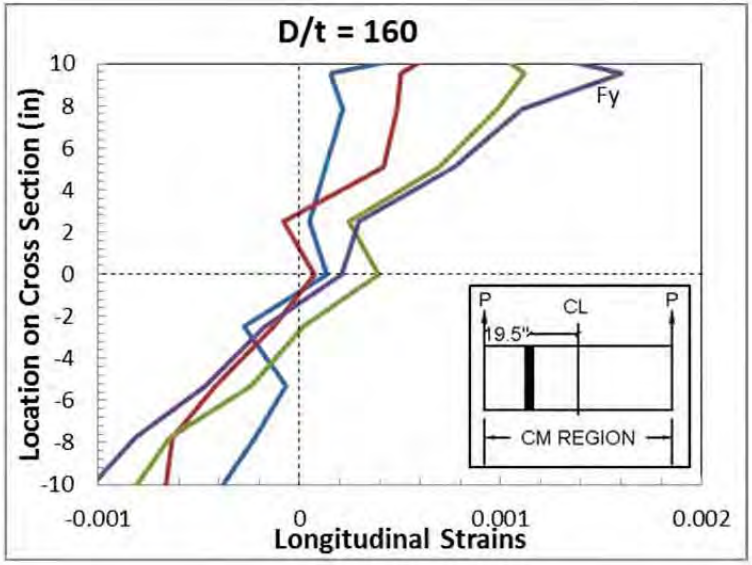
D/t = 160
Location on Cross Section (in)
10
8
6
4
2
0
-2
-4
-6
-8
-10
Fy
P
CL
P
19.5"
CM REGION
-0.001
0
0.001
0.002
Longitudinal Strains

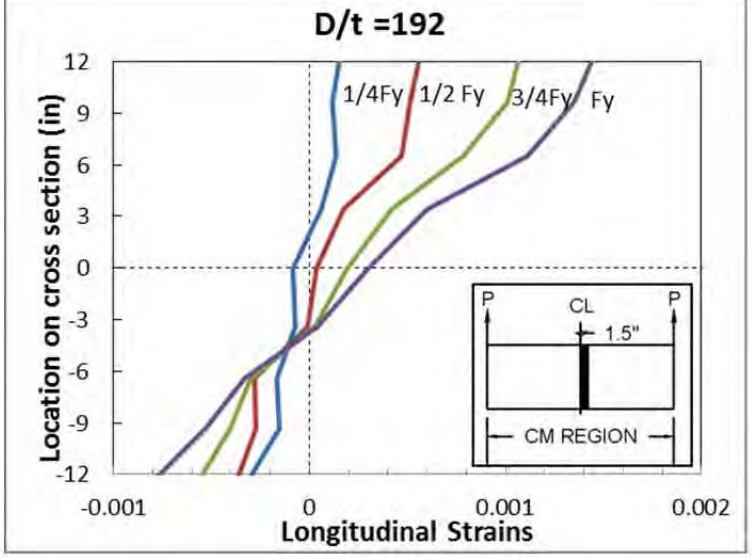
D/t =192
Location on cross section (in)
12
9
6
3
0
-3
-6
-9
-12
1/4Fy
1/2 Fy
3/4Fy
Fy
P
CL
P
1.5"
CM REGION
-0.001
0
0.001
0.002
Longitudinal Strains

Figure 4-4 Strain profiles prior to buckling: varying D/t ratios: push loading

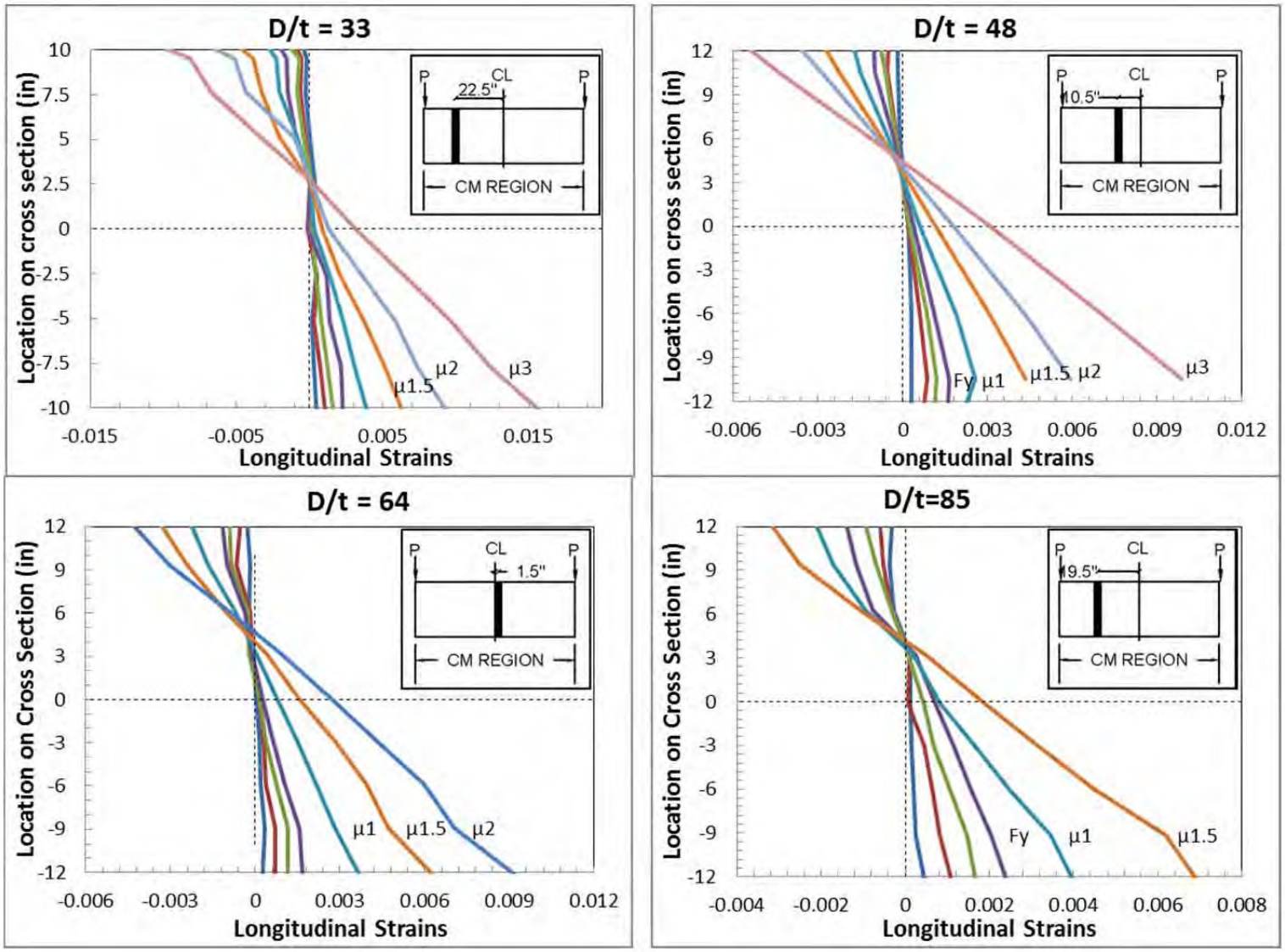
D/t = 33
Location on cross section (in)
Longitudinal Strains
P
CL
P
22.5"
CM REGION
μ1.5
μ2
μ3
D/t = 48
Location on cross section (in)
Longitudinal Strains
P
CL
P
10.5"
CM REGION
Fy
μ1
μ1.5
μ2
μ3
D/t = 64
Location on Cross Section (in)
Longitudinal Strains
P
CL
P
1.5"
CM REGION
μ1
μ1.5
μ2
D/t=85
Location on Cross Section (in)
Longitudinal Strains
P
CL
P
9.5"
CM REGION
Fy
μ1
μ1.5

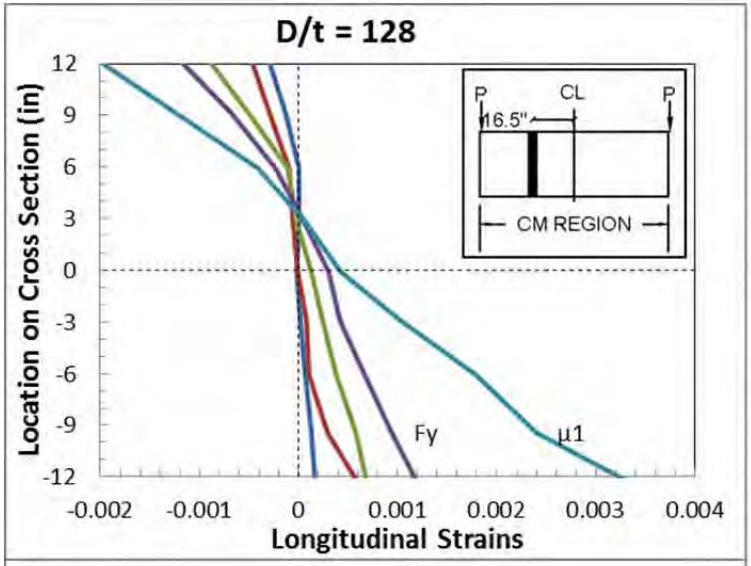
D/t = 128
Location on Cross Section (in)
12
9
6
3
0
-3
-6
-9
-12
-0.002
-0.001
0
0.001
0.002
0.003
0.004
Longitudinal Strains
P
CL
P
16.5"
CM REGION
Fy
μ1

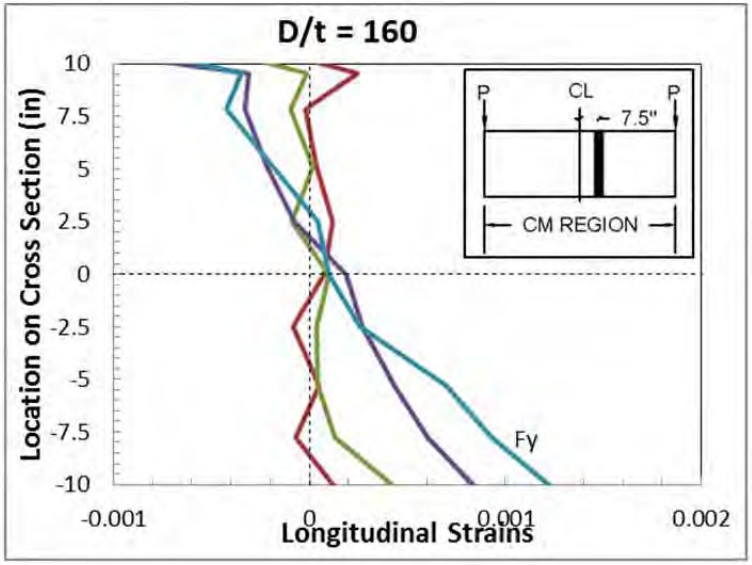
D/t = 160
Location on Cross Section (in)
10
7.5
5
2.5
0
-2.5
-5
-7.5
-10
-0.001
0
0.001
0.002
Longitudinal Strains
P
CL
P
7.5"
CM REGION
Fy

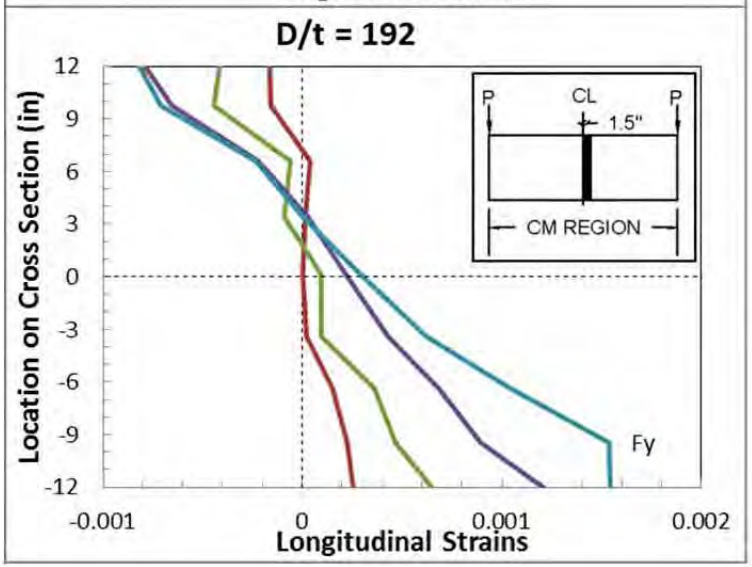
D/t = 192
Location on Cross Section (in)
12
9
6
3
0
-3
-6
-9
-12
-0.001
0
0.001
0.002
Longitudinal Strains
P
CL
P
1.5"
CM REGION
Fy

Figure 4-5. Strain profiles prior to buckling: varying internal reinforcement: pull loading

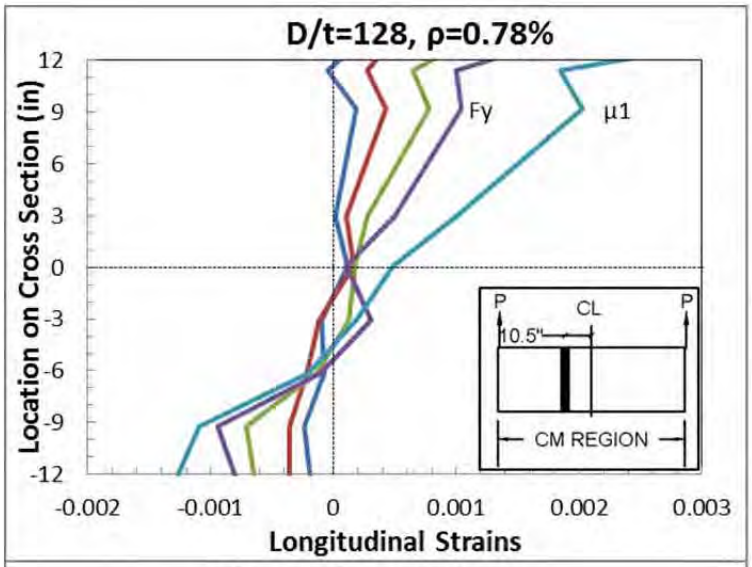
D/t=128, ρ=0.78%
Location on Cross Section (in)
12
9
6
3
0
-3
-6
-9
-12
-0.002
-0.001
0
0.001
0.002
0.003
Longitudinal Strains
Fy
μ1
P
CL
P
10.5"
CM REGION

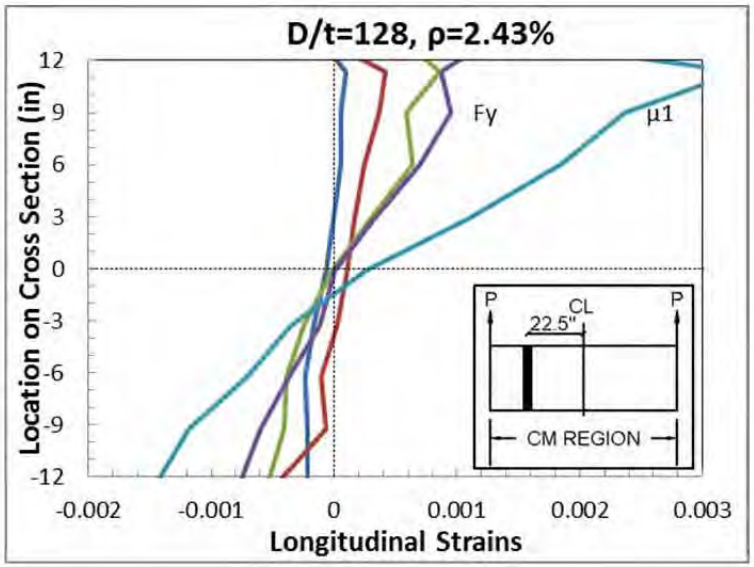
D/t=128, ρ=2.43%
Location on Cross Section (in)
12
9
6
3
0
-3
-6
-9
-12
-0.002
-0.001
0
0.001
0.002
0.003
Longitudinal Strains
Fy
μ1
P
CL
P
22.5"
CM REGION

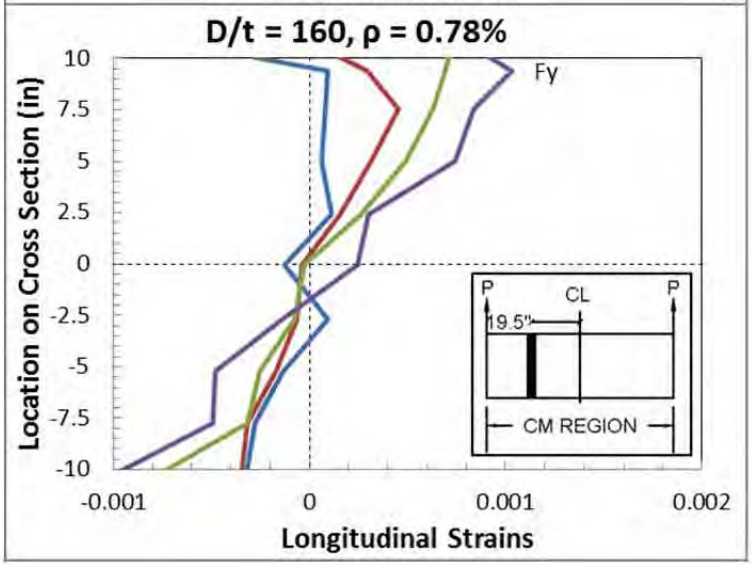
D/t = 160, ρ = 0.78%
Location on Cross Section (in)
10
7.5
5
2.5
0
-2.5
-5
-7.5
-10
-0.001
0
0.001
0.002
Longitudinal Strains
Fy
P
CL
P
19.5"
CM REGION

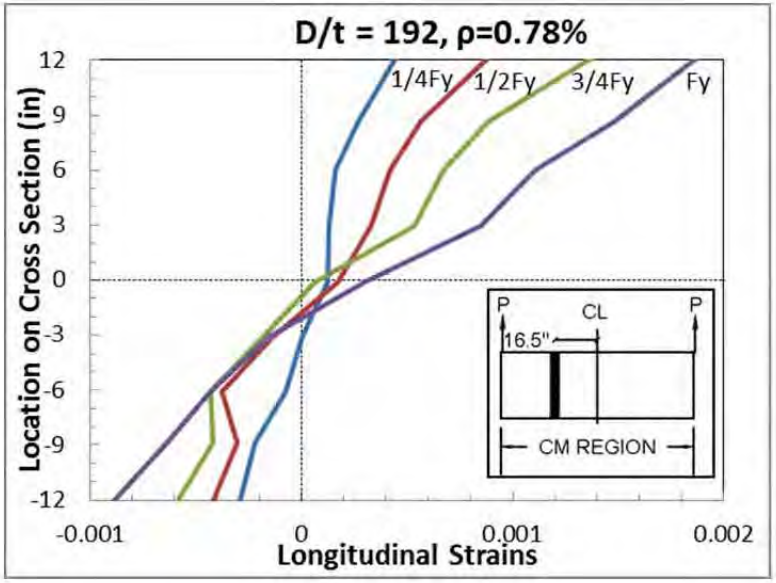
D/t = 192, ρ=0.78%
Location on Cross Section (in)
12
9
6
3
0
-3
-6
-9
-12
-0.001
0
0.001
0.002
Longitudinal Strains
1/4Fy
1/2Fy
3/4Fy
Fy
P
CL
P
16.5"
CM REGION

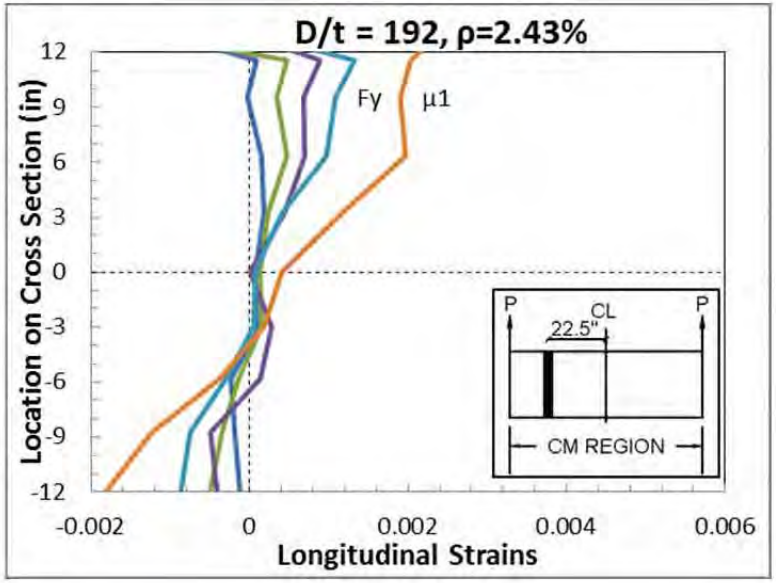
D/t = 192, ρ=2.43%
Location on Cross Section (in)
12
9
6
3
0
-3
-6
-9
-12
-0.002
0
0.002
0.004
0.006
Longitudinal Strains
Fy
μ1
P
CL
P
22.5"
CM REGION

Figure 4-6 Strain profiles prior to buckling: varying internal reinforcement: push loading

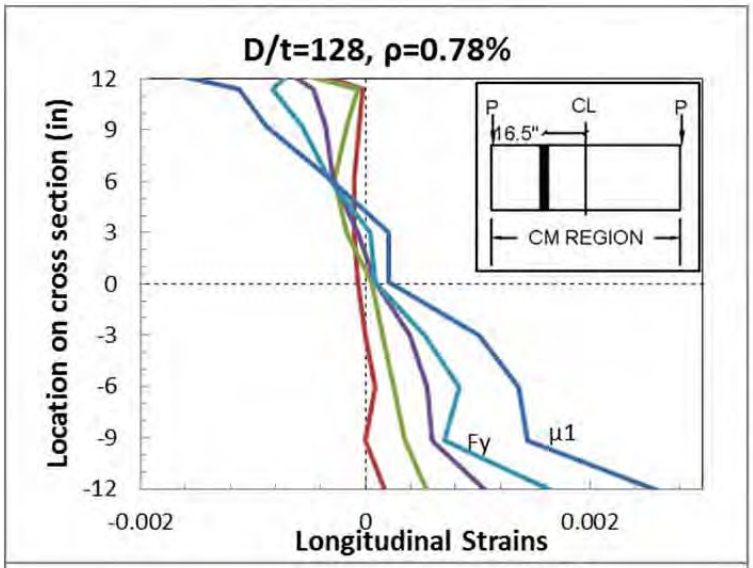
D/t=128, ρ=0.78%
Location on cross section (in)
12
9
6
3
0
-3
-6
-9
-12
-0.002
0
0.002
Longitudinal Strains
P
CL
P
16.5"
CM REGION
Fy
μ1

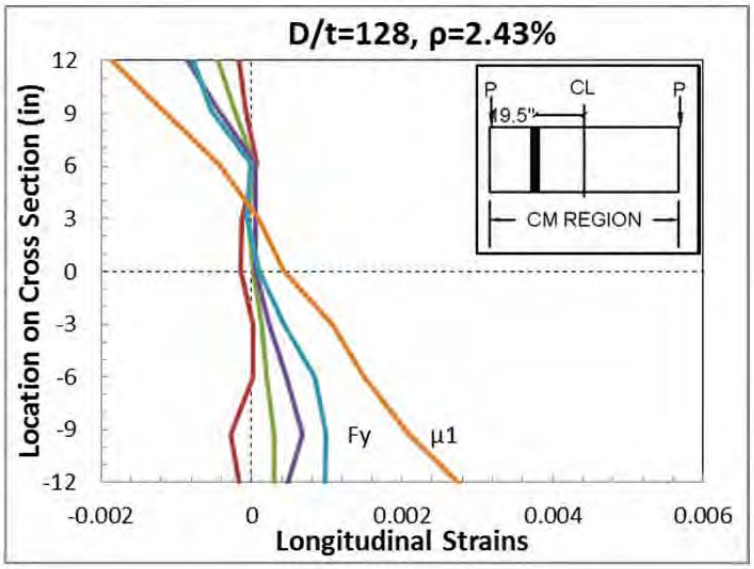
D/t=128, ρ=2.43%
Location on Cross Section (in)
12
9
6
3
0
-3
-6
-9
-12
-0.002
0
0.002
0.004
0.006
Longitudinal Strains
P
CL
P
19.5"
CM REGION
Fy
μ1

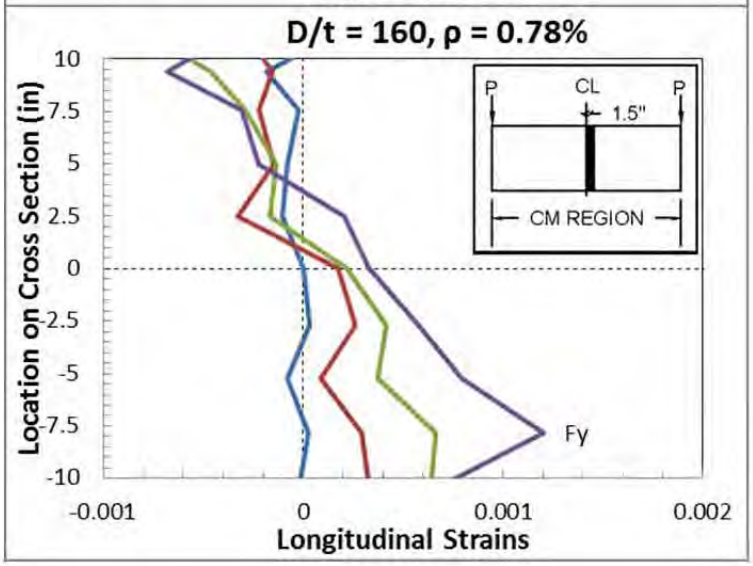
D/t = 160, ρ = 0.78%
Location on Cross Section (in)
10
7.5
5
2.5
0
-2.5
-5
-7.5
-10
-0.001
0
0.001
0.002
Longitudinal Strains
P
CL
P
1.5"
CM REGION
Fy

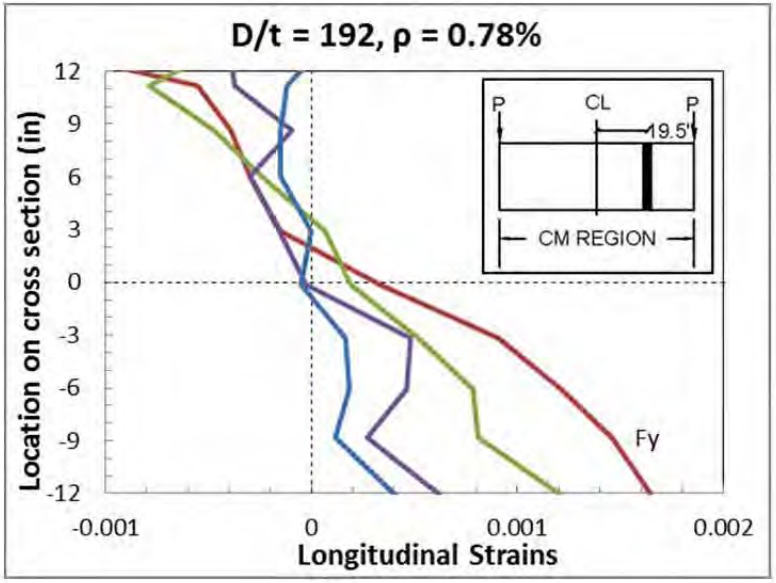
D/t = 192, ρ = 0.78%
Location on cross section (in)
12
9
6
3
0
-3
-6
-9
-12
-0.001
0
0.001
0.002
Longitudinal Strains
P
CL
P
19.5"
CM REGION
Fy

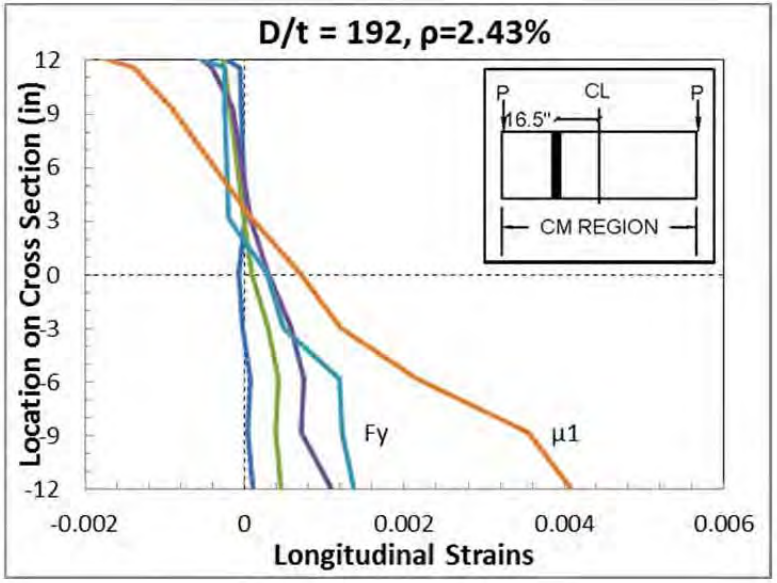
D/t = 192, ρ=2.43%
Location on Cross Section (in)
12
9
6
3
0
-3
-6
-9
-12
-0.002
0
0.002
0.004
0.006
Longitudinal Strains
P
CL
P
16.5"
CM REGION
Fy
μ1

4.1.2. After Buckling

In each test, the steel tube formed outward buckles in the constant moment region. Over the course of loading these buckles grew larger and the strain profiles became nonlinear. The LED targets at and directly next to the buckles could no longer be used to calculate strains due to their rotation and movement. The LED targets which were placed on metal brackets made this distortion worse, as shown for selected LEDs from Test 2 in Figure 4-7. The sections affected by the buckling behavior of the tube were excluded from the average of strains and curvatures across the constant moment region.

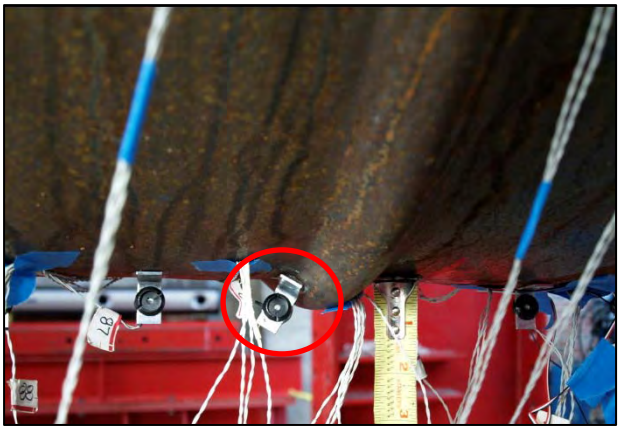

Figure 4-7. Rotation of Optotrak LED after buckling

The cyclic behavior of the steel pipe created tensile strain on the compressive region of the pipe in between the buckles. This was due to the high tensile strains on the pipe in the previous cycle. Although the overall strains are positive, the instantaneous strains from the previous cycle were negative. The spans of interest are highlighted in the photograph shown in Figure 4-8. This phenomena was more prevalent in the thinner-walled pipes, however the behavior occurred in pipes with D/t ratios ranging from 64 to 192. Strain profiles up to rupture of the "thin-walled" pipes are shown in Figure 4-9. As seen in the figure, the strains on the compressive side of the steel tube after buckling are positive, indicating tensile strains. The effect of this behavior with respect to strain compatibility will be discussed in Section 4.2. To calculate the effective curvatures of the section, the tensile strains were extrapolated through the compressive region and the curvature was calculated to be the slope of the strain profile as demonstrated in Figure 4-10.

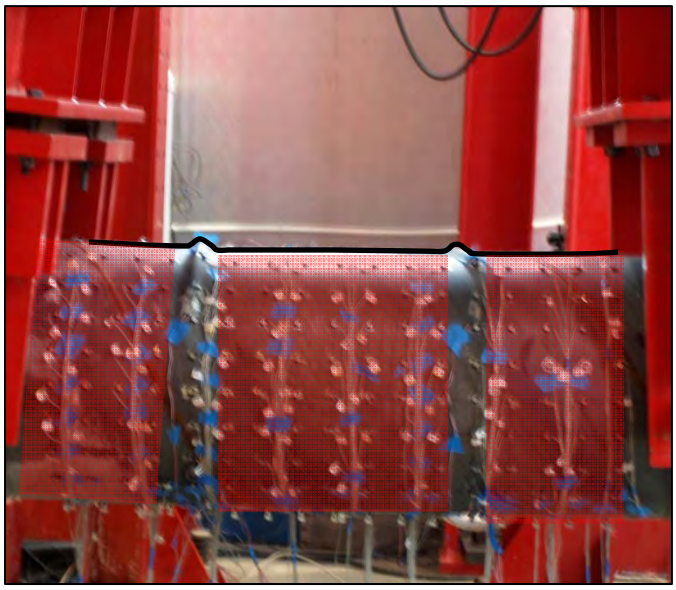

Figure 4-8 Spans between buckled region

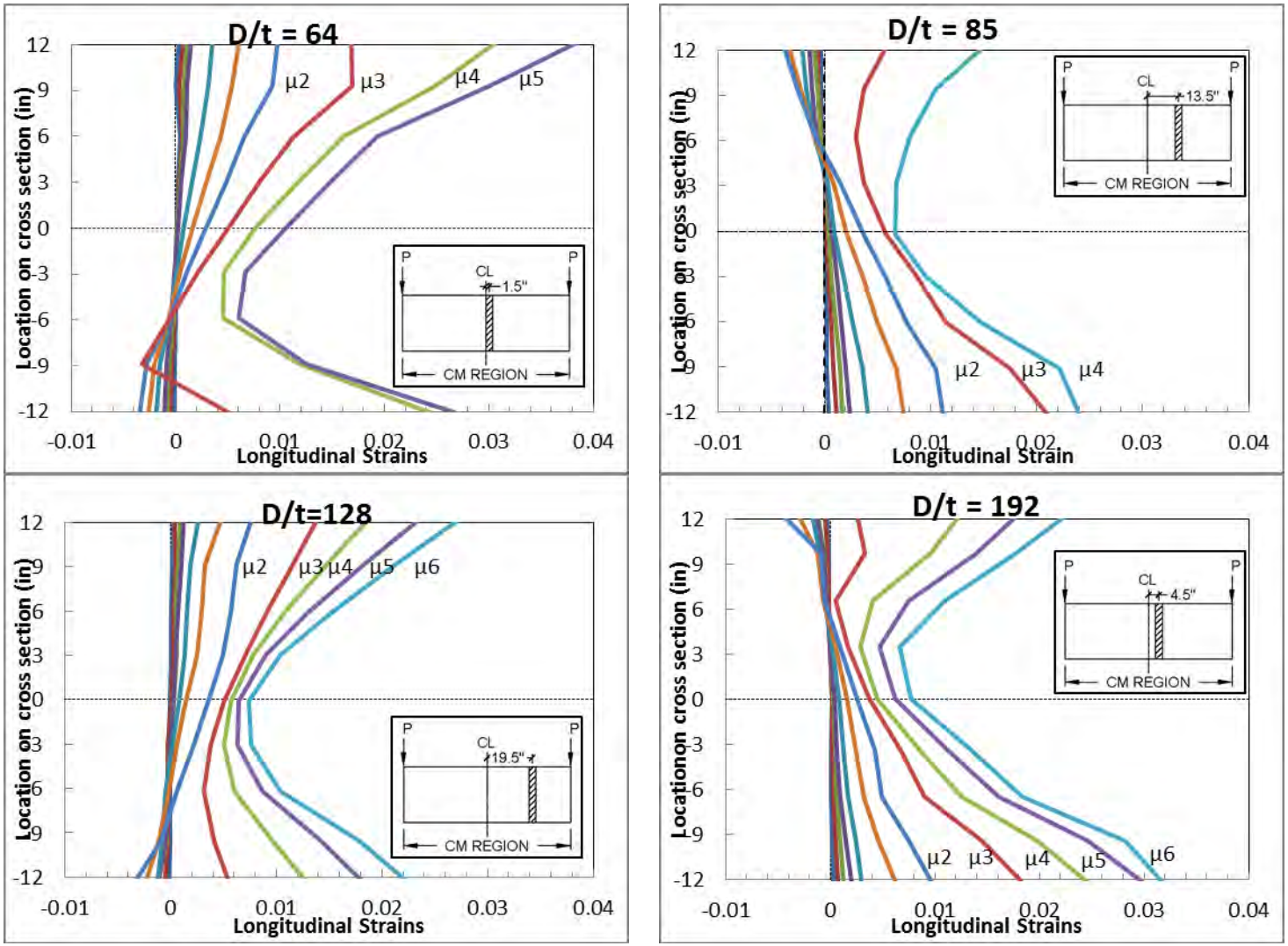

Figure 4-9 "Thin-walled" strain profiles until rupture.

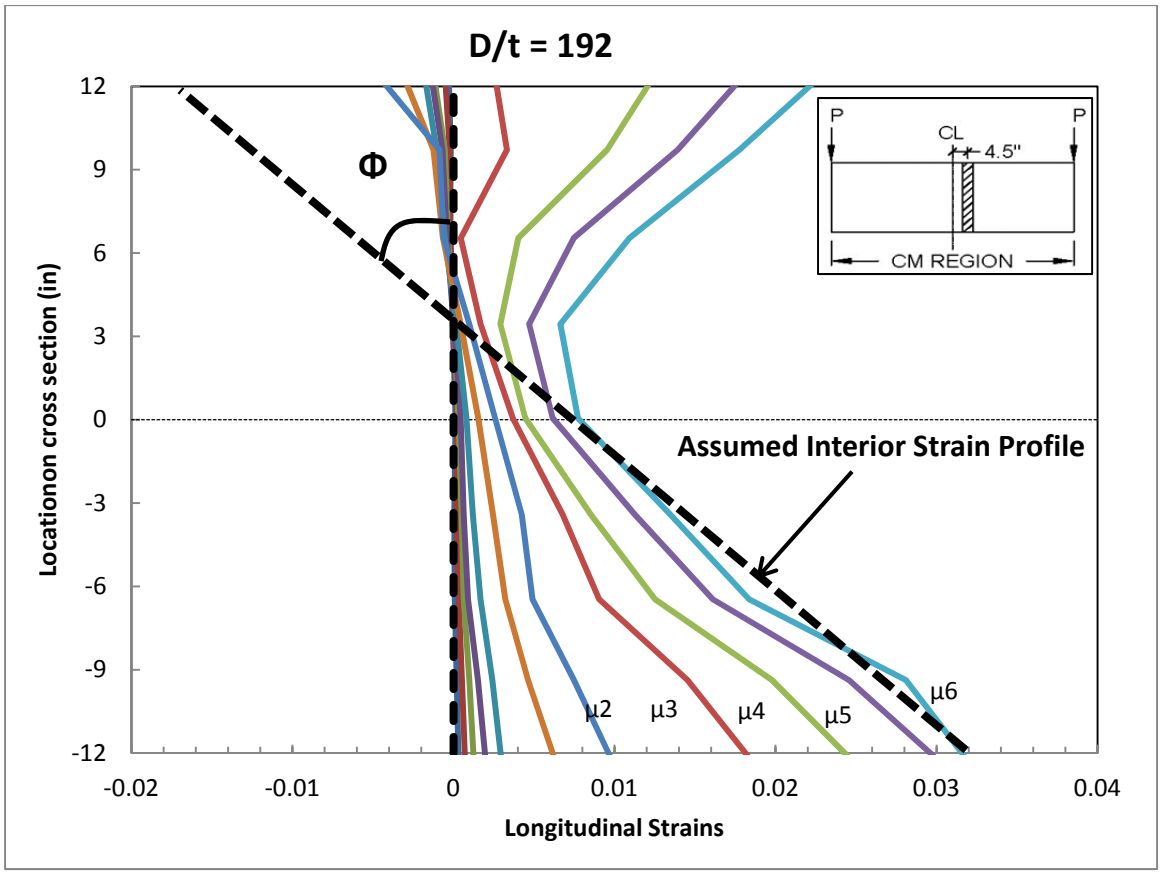

Figure 4-10 Extrapolating tensile strains to measure curvature.

As seen in Figure 4-9, all of the piles reached ultimate tensile strains of approximately 3% prior to rupture. The thick-walled piles reached the same ultimate strains and curvatures prior to rupture. Their profiles are shown in Figure 4 7. The buckles did not stretch the steel enough between the buckles to produce tensile strains on the compressive surface of the steel tube. Thus, their profiles remained linear throughout the test until rupture.

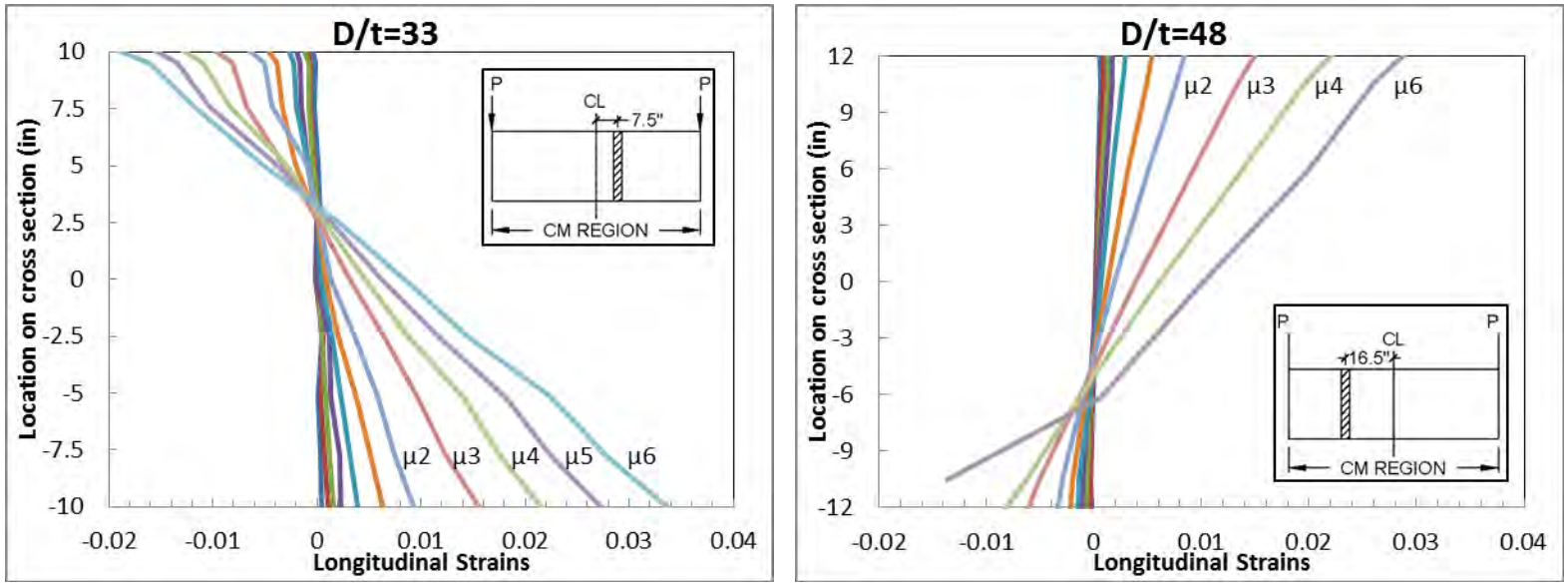

Figure 4-11 "Thick-walled" strain profiles until rupture

4.1.3. Comparison

4.1.3.1. Varying D/t Ratio

The diameter – to – thickness ratio had an effect on the buckling behavior of the concrete filled steel piles. The thinner piles (with higher D/t ratios) buckled at lower levels of ductility and strain than the thicker walled piles. Although the thin-walled piles buckled early they sustained the damage incurred by the buckling of the tube until the same level of ultimate ductility and strain as the thick – walled piles. The difference in onset of buckling between the thick and thin walled pipes can be explained by comparing the moments of inertia of a small section of the steel pipes. Figure 4-12 demonstrates the difference in moments of inertia between two small sections of the steel wall: the thickest and thinnest pile walls are compared. The thinner pile (on the left) has a much lower moment of inertia, making it easier for the section to bend and buckle.

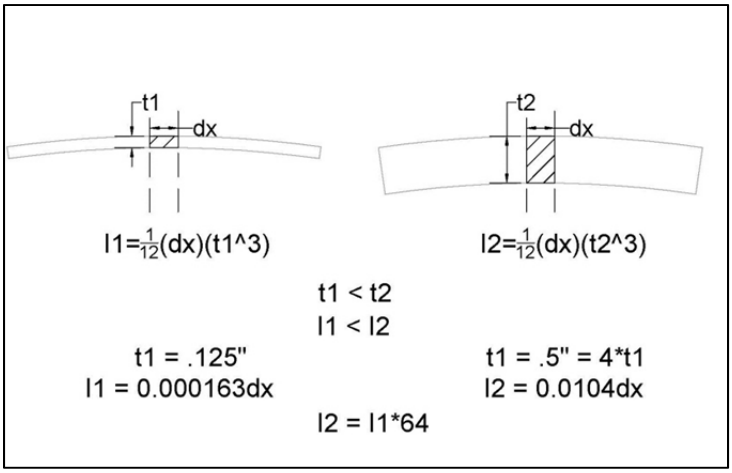

Figure 4-12 Comparison of moment of inertias

The inelastic Euler buckling load cannot be directly applied to calculate the buckling loads. The section of the steel tube that buckles is restrained in every direction, which is not accounted for in the inelastic buckling load calculation. However, the theory from the inelastic buckling load can be applied. The inelastic load calculation with an equivalent double modulus is shown in Equation 4-2, and the definition of the equivalent modulus is shown in Equation 4-3. The smaller moment of inertia will result in a much smaller buckling load.

$$P_r = \frac{\pi^2 \bar{E} I_x}{(KL)^2} \qquad \textbf{Equation 4-2}$$

$$\bar{E} = E I_1 + E_2 I_2 \qquad \textbf{Equation 4-3}$$

The experimental data support this theory: the sections with thinner steel tubes buckle earlier. The deformation capacities, strains, and curvatures prior to buckling are listed in Table 4-1. Figure 4-13 demonstrates the ratio of maximum displacement before rupture to the maximum displacement before buckling for the varying D/t ratios. As seen in the figure, the higher D/t ratios have a higher ratio of rupture to buckling displacement than the thicker piles, with the thinnest pile reaching six times the buckling displacement before rupture. The maximum tensile and compressive strains prior to buckling and rupture with respect to diameter-to-thickness ratios are shown in Figure 4-14 and Figure 4-15, respectively. A similar relationship between D/t ratio and curvature is shown in Figure 4-16. The figures show that the sections with higher D/t ratios buckle closer to yield, but sustain the damage until the steel pipe ruptures at approximately the same level of curvature (0.0015 1/in) and tensile strain (0.026) as the thicker-walled sections. The same trend was observed for displacement and curvature ductility prior to buckling and rupture. Prior to rupture, the piles sustained an average displacement ductility of 5.3 and an average curvature ductility of 7.6. There was more variation in the displacement ductility relationships due to the overall slip in the system, the material properties (strain and curvature) were not affected by the test setup and were more precise. The expressions for tensile strains, section curvature, displacement ductility and curvature ductility prior to buckling with respect to varying D/t ratios are shown in Equation 4-4 to Equation 4-7.

Table 4-1 Displacements, strains and curvatures prior to buckling and rupture

D/t Ratio	Buckling Cycle	Prior to Buckling				Prior to Rupture			
		Displ. (in)	Curv (1/in)	Strain (+)	Strain (-)	Displ. (in)	Curv (1/in)	Strain (+)	Strain (-)
33	μ 4 - pull 3	10.71	0.00155	0.0209	-0.01	18.18	0.00242	0.0337	-0.0147
48	μ3 -pull 3	6.80	0.00080	0.0134	-0.0057	17.10	0.00134	0.0247	-0.0074
64	μ 3 - pull 1	9.15	0.00107	0.0177	-0.0081	14.91	0.00136	0.0229	-0.0098
85	μ 2 -pull 3	6.51	0.00067	0.0108	-0.0053	13.08	0.00164	0.0257	-0.0137
128	μ 1.5 - pull 1	4.49	0.00028	0.0047	-0.0020	12.50	0.00163	0.0283	-0.0108
192	μ 1 - pull 1	1.95	0.00014	0.0024	-0.0011	12.29	0.00146	0.0281	-0.0070
160	μ 1-pull 1	1.85	0.00025	0.0031	-0.0018	9.47	0.00163	0.0238	-0.0088

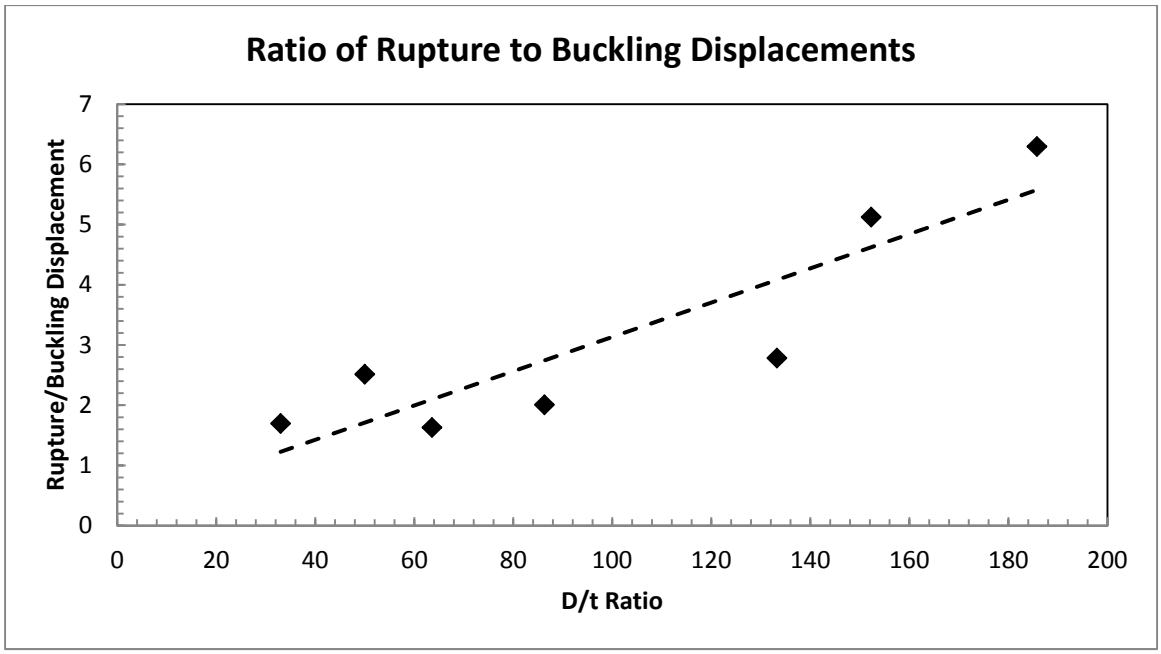

Figure 4-13 Ratio of Rupture Displacements to Buckling Displacements with respect to D/t ratio

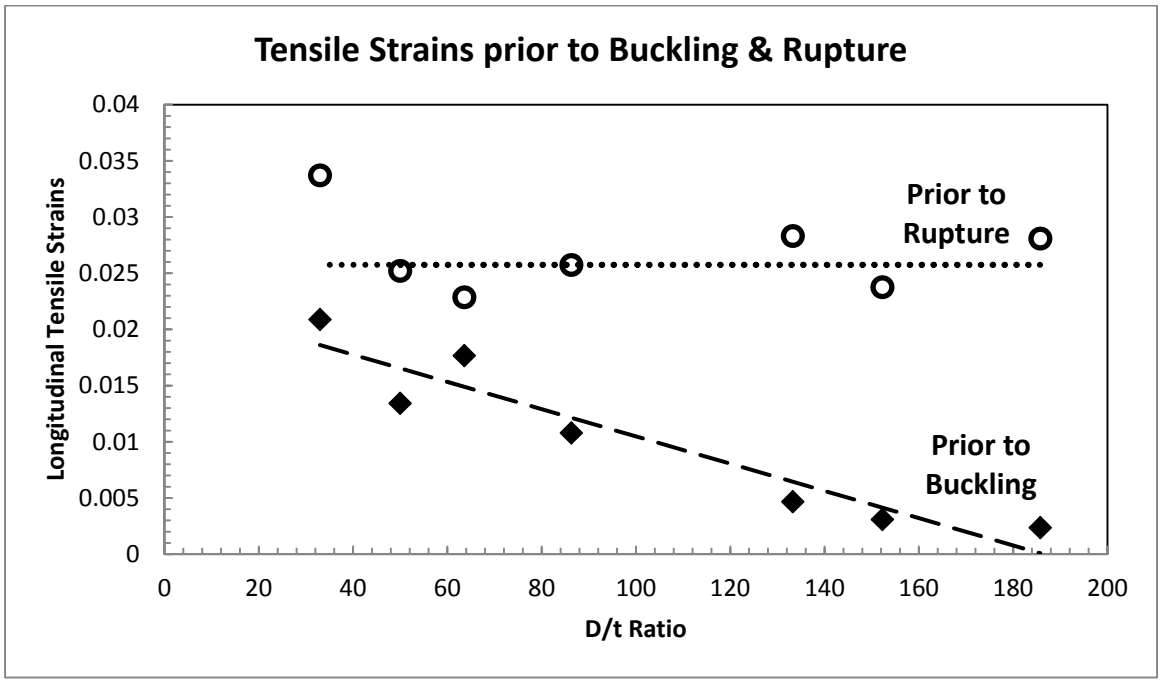

Figure 4-14 Tensile Strains prior to Buckling and Rupture with respect to D/t ratio

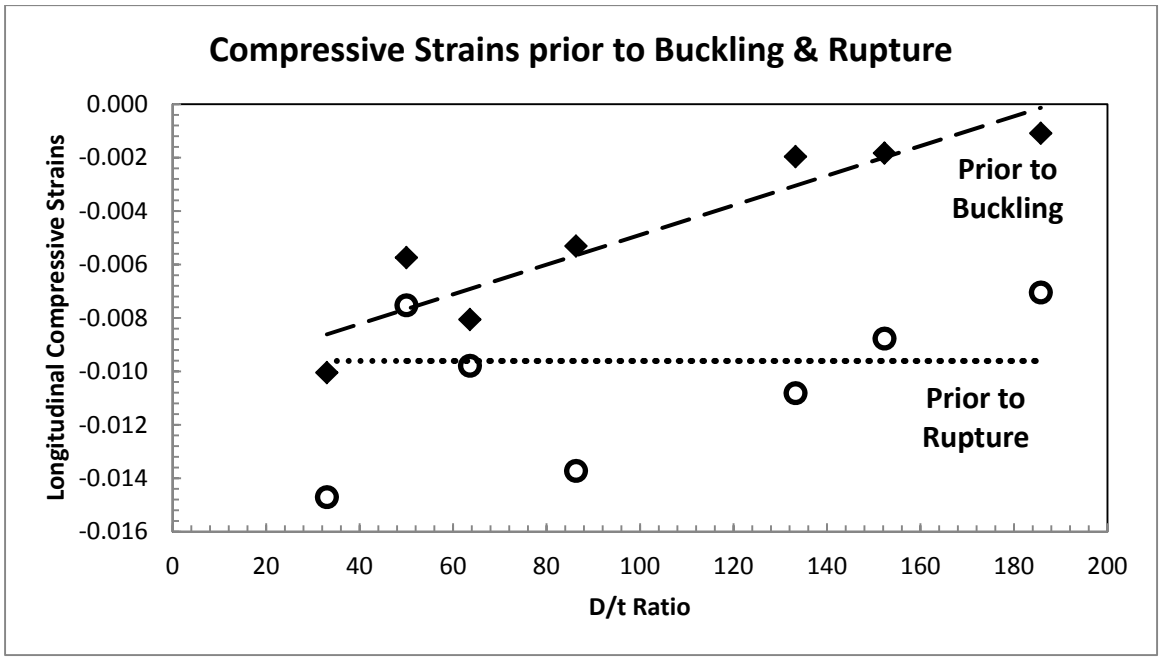

Figure 4-15 Compressive Strains prior to buckling and rupture with respect to D/t ratio

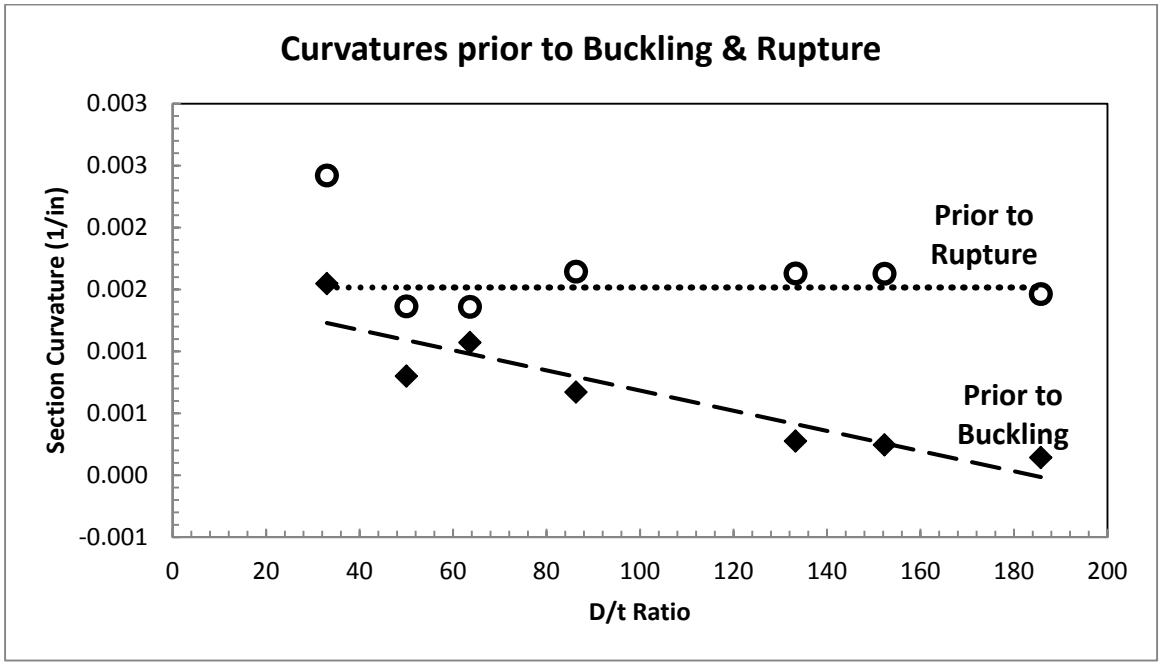

Figure 4-16 Curvatures prior to buckling and rupture with respect to D/t ratio

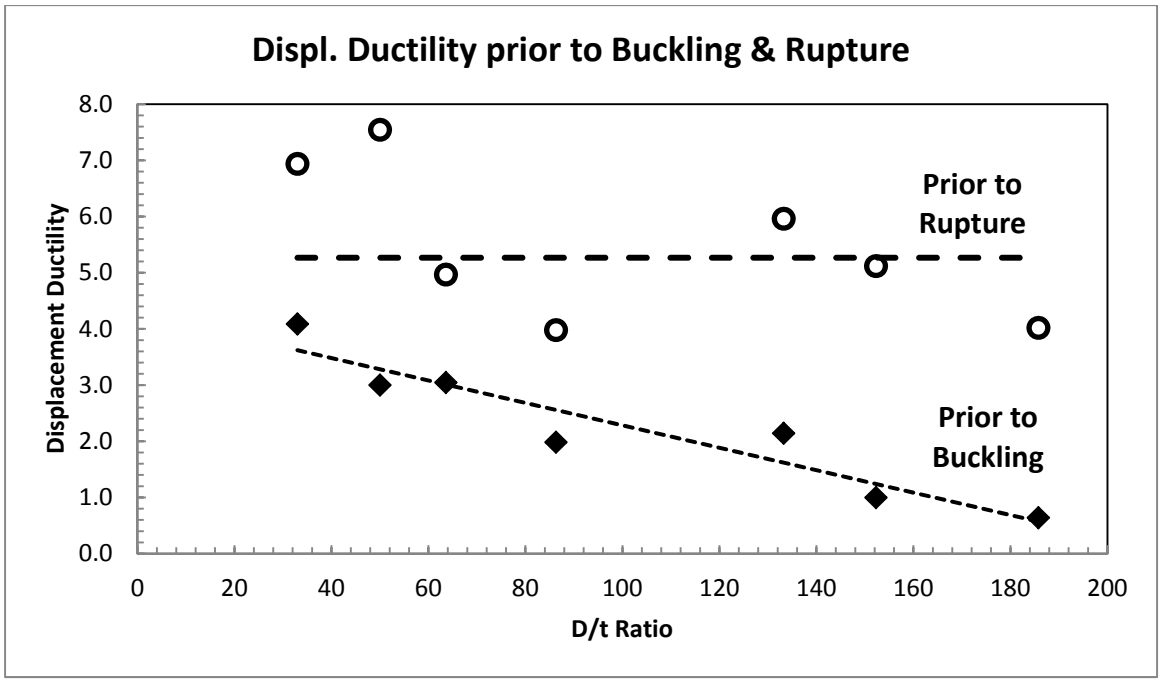

Figure 4-17 Displacement Ductility prior to buckling and rupture with respect to D/t ratio

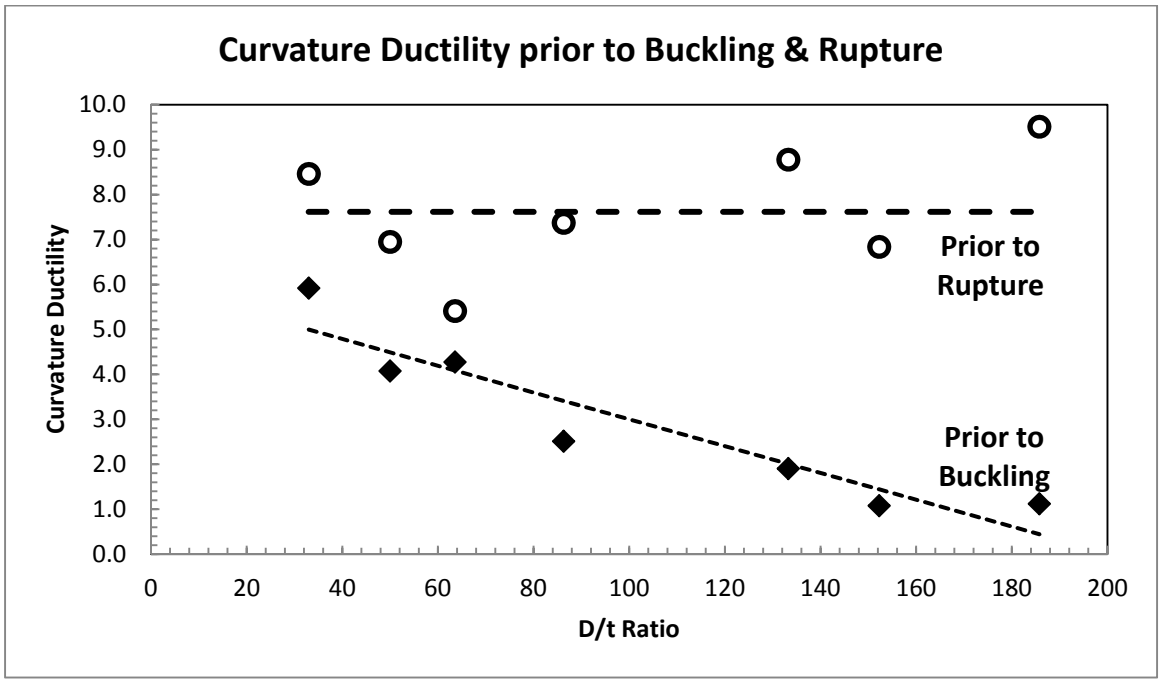

Figure 4-18 Curvature Ductility prior to buckling and rupture with respect to D/t ratio

$$\varepsilon_{buckling} = -0.00011(D/t) + 0.021 \quad \text{Equation 4-4}$$

$$\Phi_{buckling} = -0.0000064(D/t) + 0.00125 \quad \text{Equation 4-5}$$

$$\mu_{\Delta} = -0.02(D/t) + 4.28 \quad \text{Equation 4-6}$$

$$\mu_{\Phi} = -0.03(D/t) + 5.98 \quad \text{Equation 4-7}$$

4.1.3.2. Varying Internal Reinforcement

The internal reinforcement was the second factor considered in this experimental program to study the effect on the pile limit states. The three sections with the highest diameter-to-thickness ratios (128, 160, and 192) were tested with various internal reinforcement ratios to analyze the effect on the onset of buckling and rupture. The internal reinforcement did not have a noticeable effect on the onset of either limit state. In order to concentrate on the effect of internal reinforcement, the results are compared with a constant D/t ratio.

A D/t ratio of 128 was the thickest-walled pile tested with varying internal reinforcement ratios: 0.78%, 1.67%, and 2.43%. Table 4-2 displays the data from the two tests. Figure 4-19 and Figure 4-20 display the tensile strains and curvatures with respect to the internal reinforcement ratio.

Table 4-2 Displacements, curvatures and strains prior to buckling and rupture with varying internal reinforcement and D/t = 128

ρ (%)	Buckling Cycle	Prior to Buckling				Prior to Rupture			
		Displ. (in)	Curv (1/in)	Strain (+)	Strain (-)	Displ. (in)	Curv (1/in)	Strain (+)	Strain (-)
0.78%	μ1.5-pull 1	3.09	0.0004	0.0052	-0.0024	12.10	0.0016	0.0287	-0.0102
1.67%	μ1.5 -pull 1	4.49	0.0003	0.0047	-0.0020	12.50	0.0016	0.0283	-0.0108
2.43%	μ1.5-pull 1	3.34	0.0003	0.0047	-0.0026	-11.15	0.0016	0.0270	-0.0123

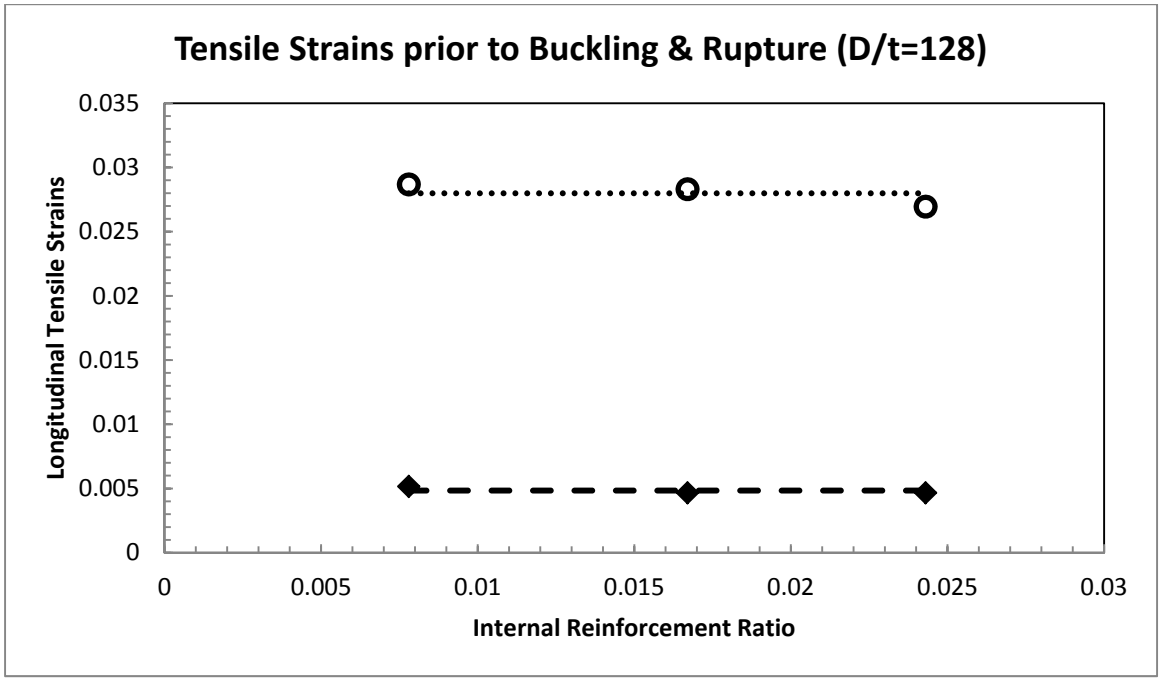

Figure 4-19 Tensile strains prior to buckling and rupture with varying internal reinforcement, D/t = 128

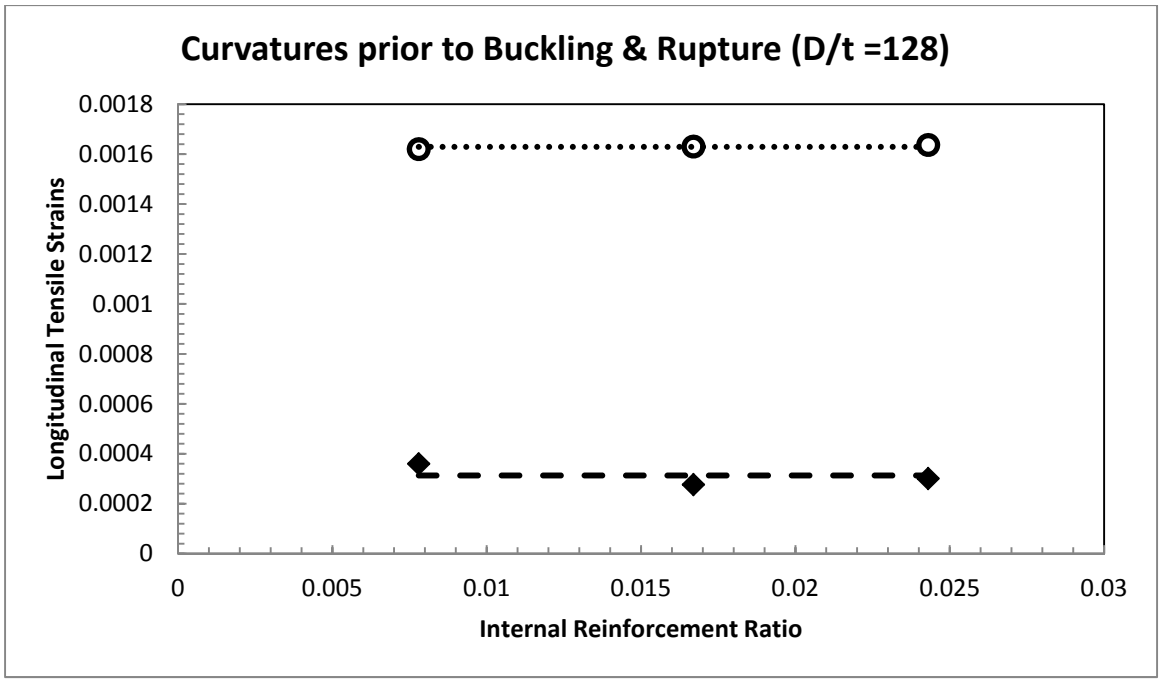

Figure 4-20 Curvatures prior to buckling and rupture with varying internal reinforcement, D/t = 128

A similar trend is seen in the tests with a D/t ratio of 160 varying internal reinforcement ratios: 0.78% and 1.67%. The piles buckle and rupture at the same cycles and approximately the same strains and curvatures. Table 4-3 displays the data from the two tests, Figure 4-21 and Figure 4-22 display the tensile strains and curvatures with respect to the internal reinforcement ratio.

Table 4-3 Displacements, curvatures and strains prior to buckling and rupture with varying internal reinforcement and D/t = 160

ρ (%)	Buckling Cycle	Prior to Buckling				Prior to Rupture			
		Displ. (in)	Curv (1/in)	Strain (+)	Strain (-)	Displ. (in)	Curv (1/in)	Strain (+)	Strain (-)
0.78%	μ1 - pull 1	1.66	0.0002	0.0027	-0.0014	8.33	0.0013	0.0214	-0.0055
1.67%	μ1-pull 1	1.85	0.0002	0.0031	-0.0018	9.47	0.0016	0.0238	-0.0088

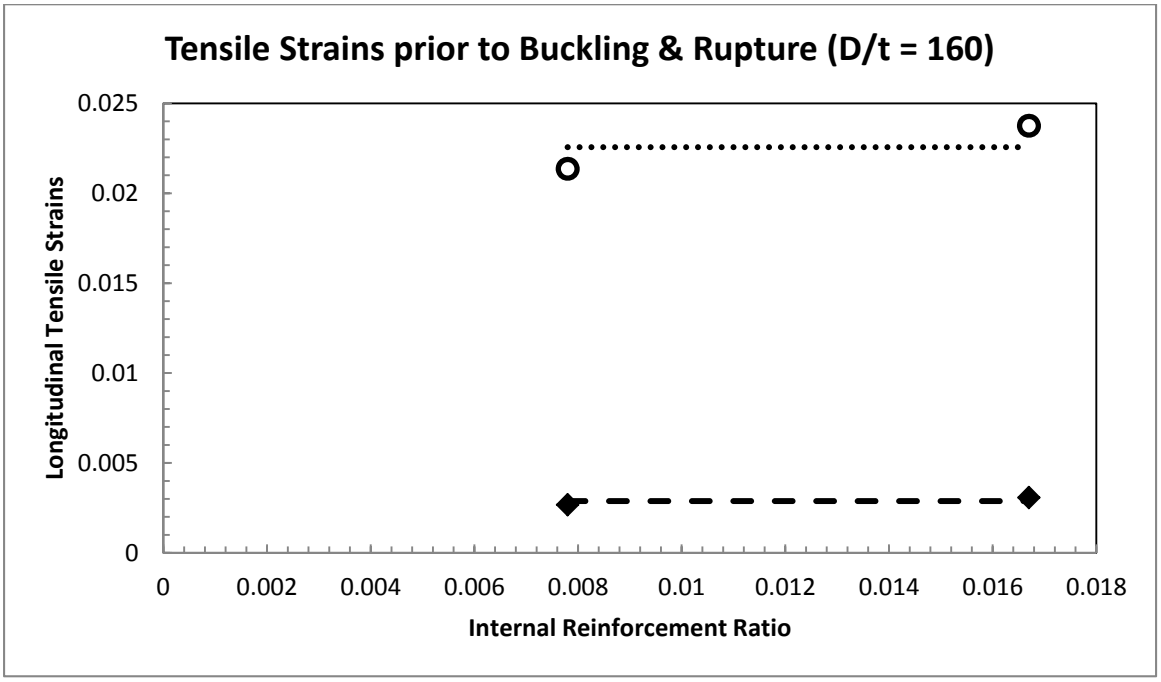

Figure 4-21 Tensile strains prior to buckling and rupture with varying internal reinforcement, D/t = 160

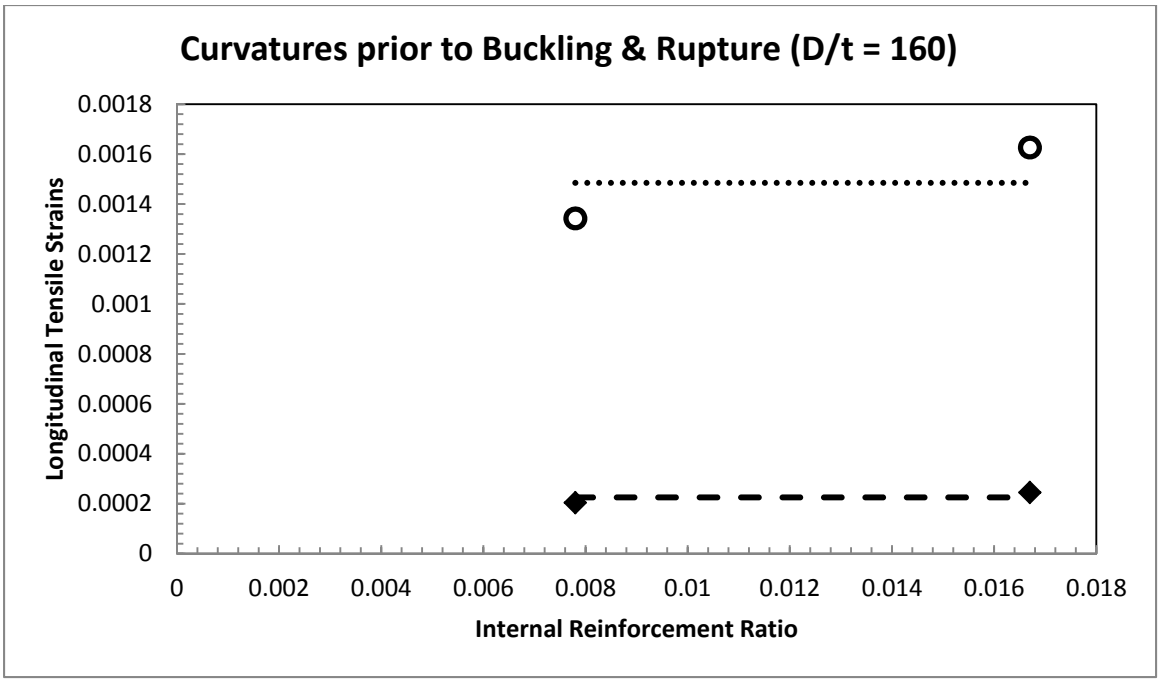

Figure 4-22 Curvatures prior to buckling and rupture with varying internal reinforcement, D/t = 160

As expected, the same trend is seen in the last set of tests with a D/t ratio of 192 varying internal reinforcement ratios: 0.78%, 1.67% and 2.43%. The results from this set are tests have more variation between the various internal reinforcement ratios concerning strains and curvatures. However, the variation sets no trend and the piles behaved the same overall. Table 4-4 displays the data from the two tests, Figure 4-23 and Figure 4-24 display the tensile strains and curvatures with respect to the internal reinforcement ratio.

Table 4-4 Displacements, curvatures and strains prior to buckling and rupture with varying internal reinforcement and D/t = 192

ρ (%)	Buckling Cycle	Prior to Buckling				Prior to Rupture			
		Displ. (in)	Curv (1/in)	Strain (+)	Strain (-)	Displ. (in)	Curv (1/in)	Strain (+)	Strain (-)
0.78%	μ1 - pull 1	2.80	0.00021	0.0037	-0.0014	11.58	0.00129	0.0250	-0.0059
1.67%	μ1 - Pull 1	1.95	0.00014	0.0024	-0.0011	12.29	0.00146	0.0281	-0.0070
2.43%	μ1.5 - pull 1	3.47	0.00025	0.0043	-0.0017	12.23	0.00110	0.0188	-0.0077

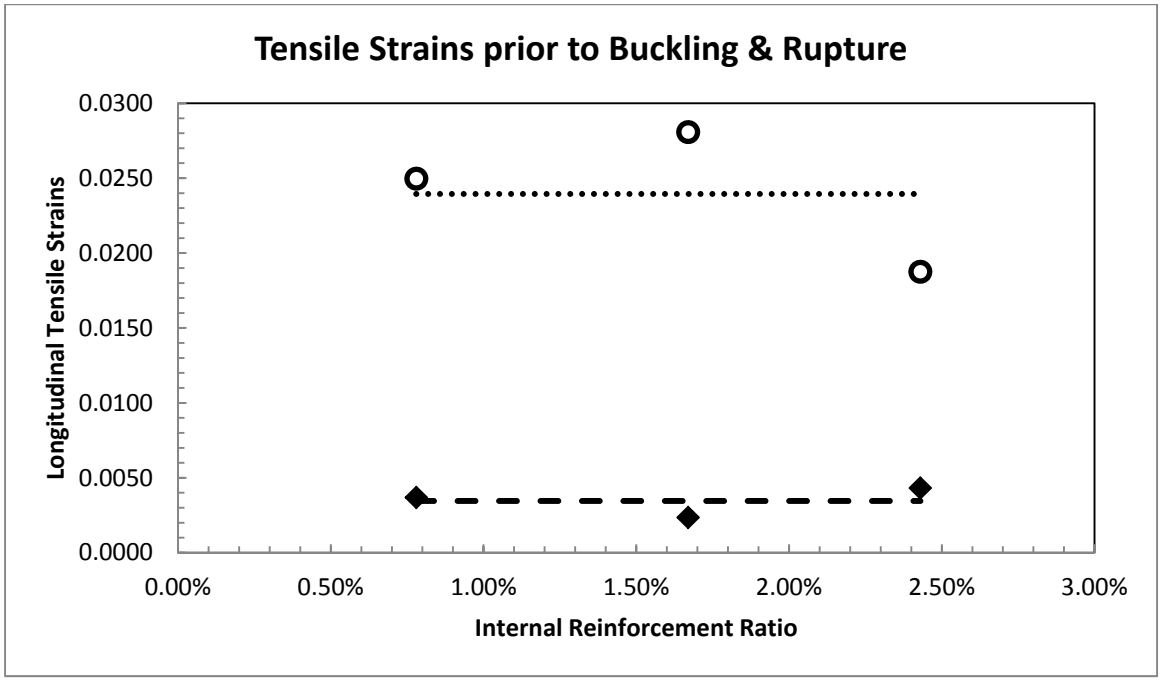

Figure 4-23 Tensile strains prior to buckling and rupture with varying internal reinforcement, D/t = 160

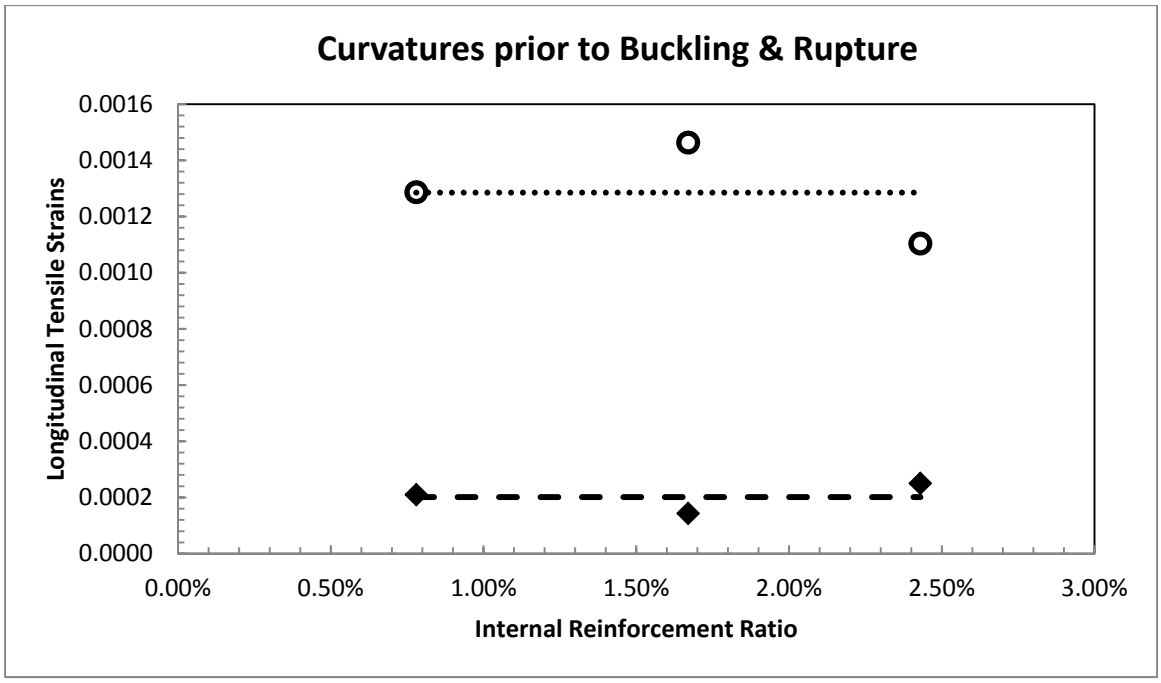

Figure 4-24 Curvatures prior to buckling and rupture with varying internal reinforcement, D/t = 192

4.1.4. Summary

In summary, the internal reinforcement had no effect on the onset of buckling and rupture in terms of ductility, strains, and curvatures. However, more tests may be necessary in the future to verify the findings. The diameter-to-thickness ratios of the piles have a profound effect on the onset of buckling. The thin-walled piles buckle early in the loading cycles at low levels of displacement, strains, and curvatures. Although they buckle early, all the piles sustained approximately the same level of damage reaching tensile strains of approximately 2.6% prior to rupture.

4.2. Strain Compatibility

4.2.1. Definition

Strain compatibility will exist between the concrete core and the steel tube if there is a perfect bond between the surfaces. Current analysis methods for predicting moment-curvature responses and force-displacement responses are based on the assumption that strains are compatible throughout the section, and plane sections remain plane.

The majority of past research measured slip between the steel tube and the concrete core, focused on specimens under high axial loads. The tests which measured the strains in the concrete core and on the surface of the steel tube under lateral loading conditions found that the strains were compatible (Lu and Kennedy). It is important to determine whether the steel tube was slipping, and if so, how this will change the methods used to predict the moment-curvature response of the system.

The tests performed in this research project concluded that there was no slip before buckling of the steel tube, but the steel tube slipped on the compression side of the pile after buckling initiated. The strain compatibility was evaluated for all tests by performing moment-curvature analyses on the piles assuming full compatibility and comparing the predictions with the experimental results (Section 4.2.3). In addition, during one of the tests, the slip was physically measured between the steel tube and the concrete (Section 4.2.2).

4.2.2. Slip

The slip between the steel tube and the concrete core was measured with LED targets in Test 10 of this experimental program. The targets were placed in the moment arm of the pile; the location of these sensors is shown in Figure 4-25 and Figure 4-26. The holes, drilled through the pile wall, were placed on the moment arm of the pile because holes in the constant moment region could have altered the strength of the section, the initiation of buckling and location of rupture for the test.

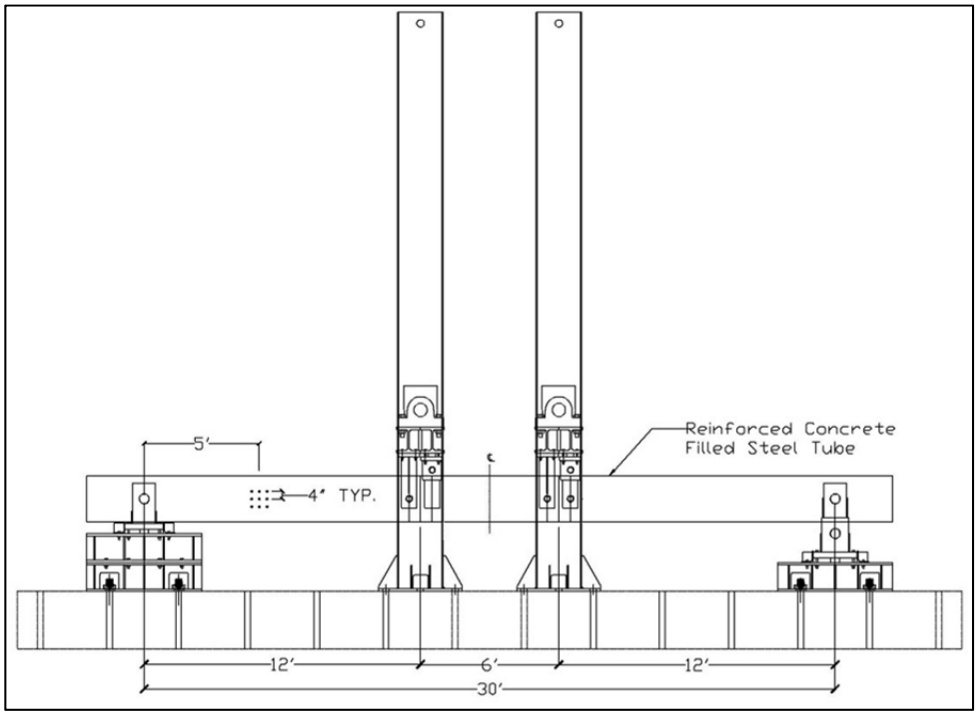

Figure 4-25 Location of the LED targets measuring slip between the steel tube and concrete

Figure 4-26 Photograph of the LED targets measuring the slip between the steel tube and concrete

No slip between the sensors was observed during the test, Figure 4-27 displays the LED targets at four different points during the test. As seen in the figure, there was no visible movement between the targets. However there may have been movement not visible to the human eye. If the strains were compatible then the strain profiles of the two materials should have been the same. Figure 4-28 and Figure 4-29 show the strain profiles of the concrete core and steel tube during ductility four, which was the largest three cycle set completed. As seen the strain profiles agree, confirming strain compatibility in the region.

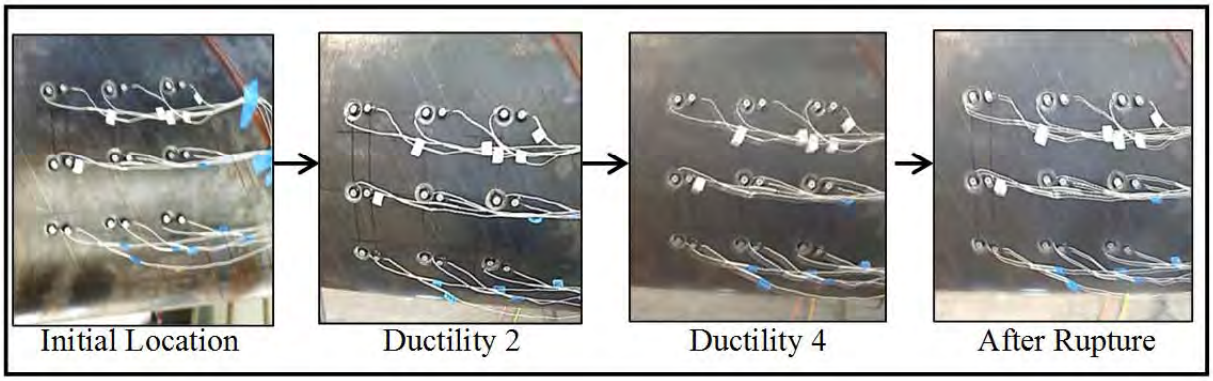

Figure 4-27 Photographs of LED targets measuring slip throughout the test

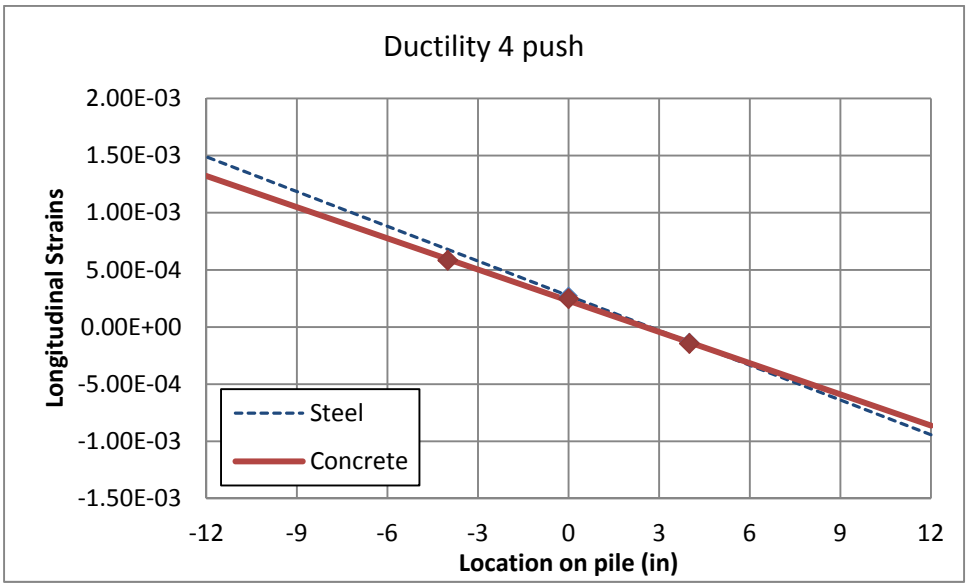

Figure 4-28 Strain profiles of the concrete core and steel tube during a push cycle of ductility four

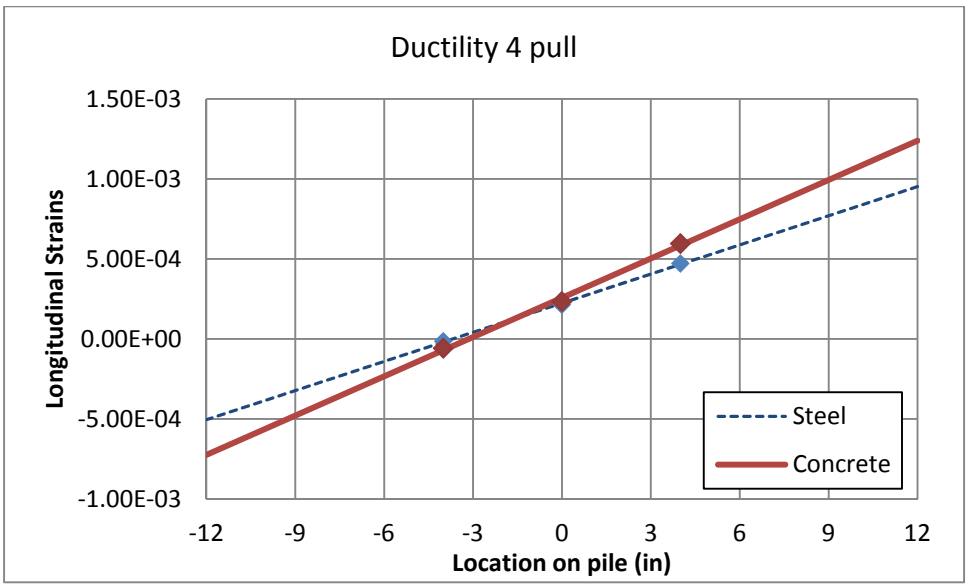

Figure 4-29 Strain profiles of the concrete core and steel tube during a pull cycle of ductility four

Determining that there was no slip in this region does not prove that there was strain compatibility in the entire section. This does conclude that there was no slip between the steel and the concrete prior to buckling and conventional prediction methods can accurately be used to predict the behavior of the reinforced concrete filled steel tubes at low levels of strain without damage.

4.2.3. Moment Curvature Analysis

If a composite section satisifes strain compatibility, the response of the section should be accurately predicted assuming strains are compatible and plane sections remain plane. To calculate the moment curvature response of the section, two methods of determining the stress in the steel tube were used. The first was more realistic and took into account the cyclic loading, accounting for strains not being compatible after buckling. The second assumed the strains were compatible and used a monotonic stress-strain curve for the steel tube.

4.2.3.1. Steel Material Models

Tension tests were performed on steel pipe coupons and reinforcing bar prior to specimen testing. The stress-strain curves obtained from the tension coupon tests were used as the actual material models for the moment-curvature analyses.

From the LED targets placed on the concrete core and steel tube in Test 10, it was evident that strain compatibility existed before buckling (Section 4.2.2). After buckling, the strain profiles became nonlinear (Section 4.1.2). At this point, the strain profiles of the steel tube and concrete were not compatible, because the concrete core was not affected by the buckling and did not develop the large tensile strains that were observed in the tube. The projected strain profiles of the tube and core are shown in Figure 4-30. The concrete core and internal reinforcing bars most likely follow the strain profile created by extrapolating the tension strains of the steel tube through the remainder of the section as shown in Figure 4-10.

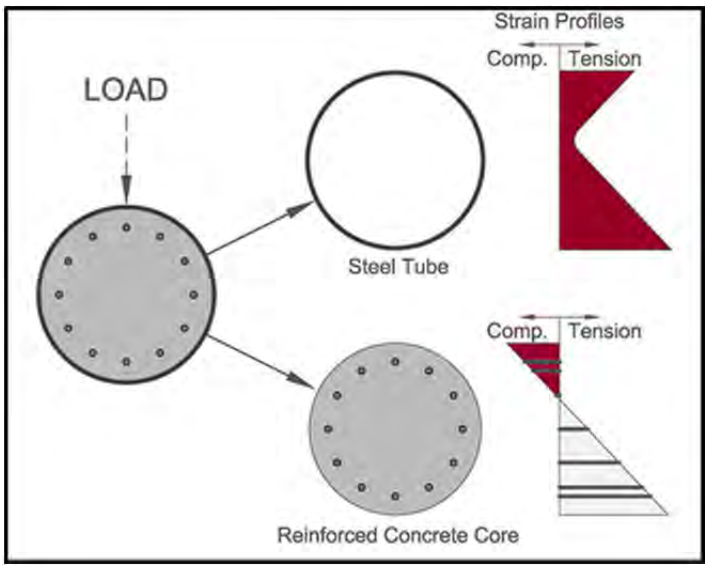

Figure 4-30 Strain Profiles of Concrete Core and Steel Tube after buckling

Although the steel tube exhibits tension strain on the "compression" side of the section after buckling, the cyclic loading and plastic response of the steel pipe could result in compressive stresses being developed in this region. Following a bilinear stress-strain model, shown in Figure 4-31, the steel tube could have tensile strain and compressive stress if the state of stress fell in the fourth quadrant. The yield strain (ε_y), yield stress (σ_y), maximum strain (ε_{max}), and maximum stress (σ_{max}) were obtained from the tensile coupon tests. The unloading paths follow the same slope of the loading paths.

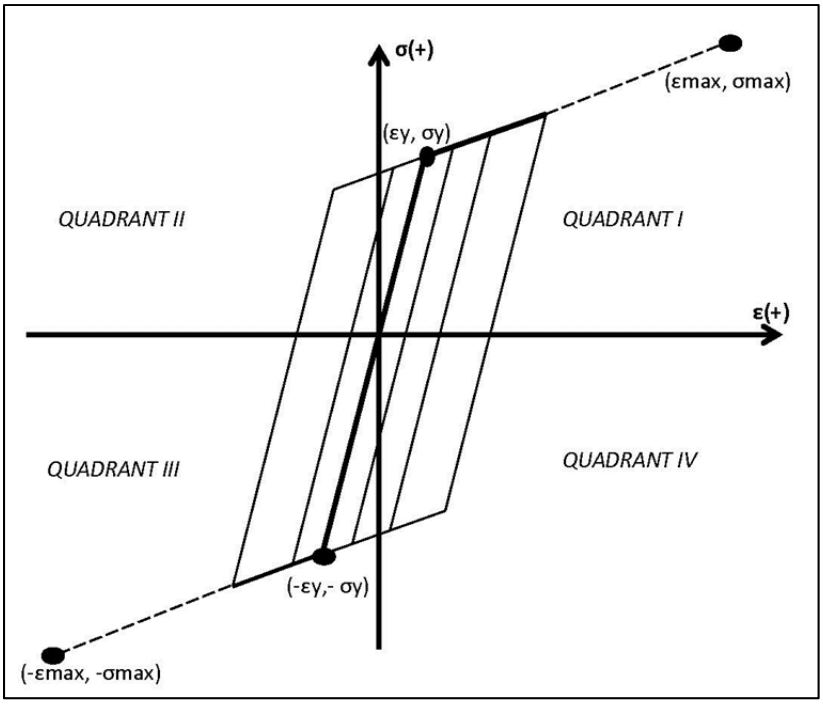

Figure 4-31 Bilinear Stress-strain Model

Strain hystereses were evaluated for nine locations around half of the circumference of the steel tube. The locations were determined by the placement of the Optotrack LED targets and are shown in Figure 4-32. The bilinear stress-strain model was applied to each strain hysteresis to determine the stresses in the tube throughout the test. Figure 4-33 shows a strain hysteresis located at location one (on the top of the pile) during Test 2, which had a D/t = 192. Compared to the remainder of the tests, this pile buckled earliest and exhibited a high level of tensile strains on the "compressive" side of the pile. The stress – strain curve, corresponding to the strain hysteresis in Figure 4-33, through the loading cycles is shown in Figure 4-34.

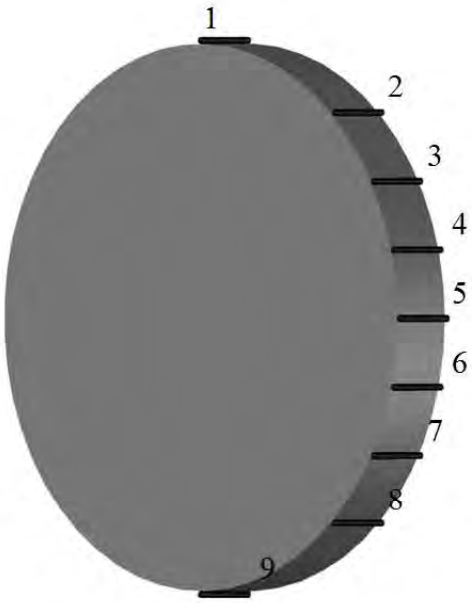

Figure 4-32 Locations of strain calculations around circumference of section

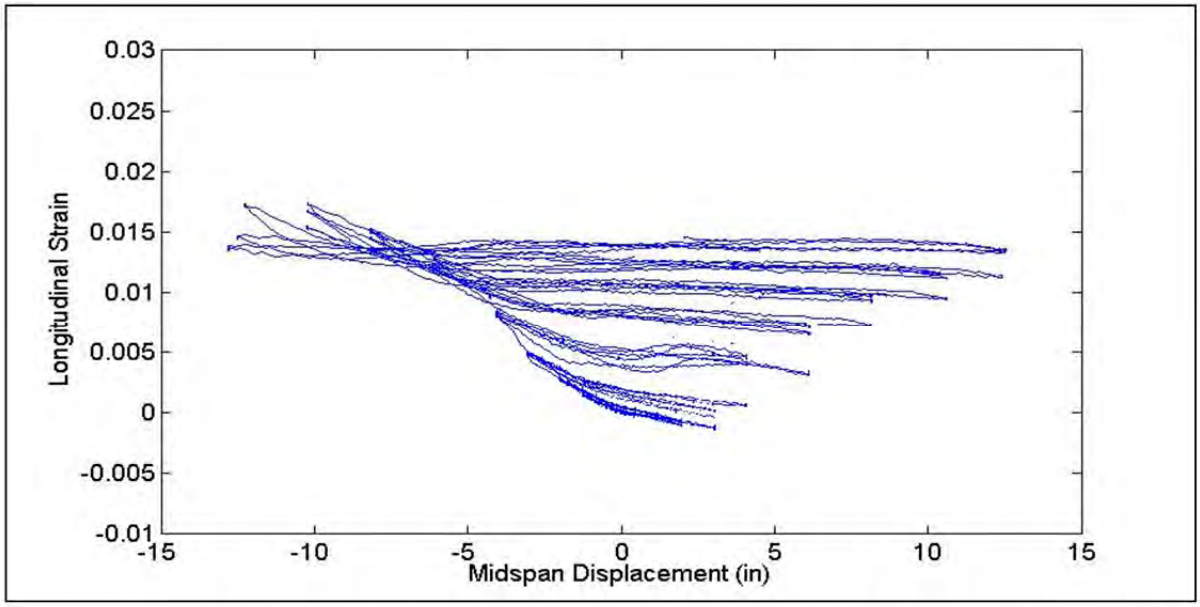

Figure 4-33 Longitudinal strain hysteresis at Location 1, Test 2, D/t =192

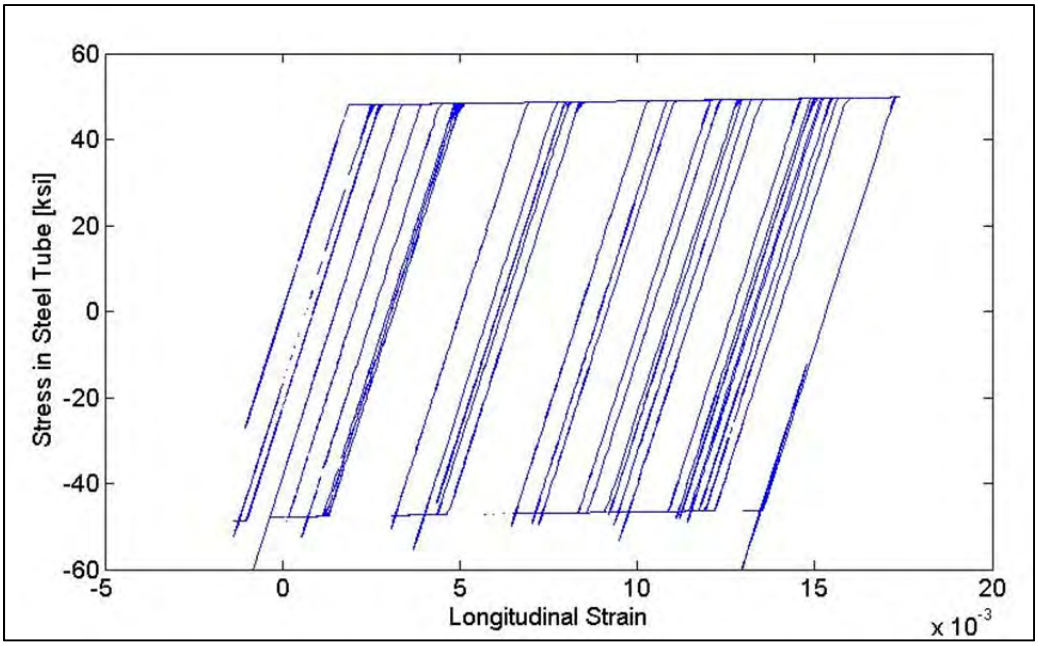

Figure 4-34 Stress-strain history over the loading history, Location 1, Test 2, D/t=192

The stress-strain history, developed from the bilinear stress-strain approximation, shows the steel pipe yielded in compression and tension throughout the plastic portion of the test. The stresses at the end of each loading cycle for Test 2 are summarized in Table 4-5. The stresses for the remaining eleven tests are tabulated in Appendix E, they show similar results: all developed the full compressive and tensile stresses of the steel tube at the extreme fibers. Since the pipes yielded in compression and, as they would be assuming a linear strain profile and monotonic stress-strain curve, using these assumptions is appropriate and will produce accurate results. The moment curvature results, using both monotonic and cyclic stress-strain curves are describedd in Section 4.2.3.3.

Table 4-5 Stresses in extreme fiber of steel tube (Test 2: D/t =192)

Cycle	1/4 Fy		1/2 Fy		3/4 Fy		Fy	
	push	pull	push	pull	push	pull	push	pull
Stress [ksi]	-2.82	4.85	-0.91	14.79	-8.23	39.03	-12.11	37.89
Cycle	Ductility 1		Ductility 1.5		Ductility 2		Ductility 3	
	push	pull	push	pull	push	pull	push	pull
Stress [ksi]	-23.46	48.10	-54.03	43.11	-47.70	48.72	-47.42	49.27
Cycle	Ductility 4		Ductility 5		Ductility 6			
	push	pull	push	pull	push	pull		
Stress [ksi]	-46.93	49.54	-46.69	49.80	-46.48	49.79		

4.2.3.2. Concrete Material Model

The reinforced concrete stress-strain curve was calculated using Mander's model. Mander's model was not developed to predict the confined stress with the high level of confinement that is found in a concrete filled steel tube.

The lateral strains were calculated in an attempt to back-calculate the confining strains in the steel tube. The steel tube was in a multi-axial stress state due to: (1) the expansion of the concrete core, and (2) contraction/expansion due to longitudinal strains and Poisson's ratio. If these were the only factors in calculating the lateral strains in the steel tube, the confining strains could be back calculated using Equation 4-8. The thickest pile (D/t = 33) had the least number of buckles, and confining strains were calculated. The confining strains during the push and pull cycles on the respective compressive side of the steel tube are shown in Table 4-6. The confining strains were high, approximately 45% of the corresponding tensile strains located in the section. The average confining strains, along the constant moment region (excluding regions affected by buckling), compared to the corresponding average longitudinal tensile strains are displayed in Figure 4-35.

$$\varepsilon_{confining} = \varepsilon_{lateral} + \upsilon\varepsilon_{longitudinal} \qquad \text{Equation 4-8}$$

Table 4-6 Confining Strains at various ductility levels

Confining Strains on Compressive Face of Section					
Yield	push	0.02%	Ductility 3	push	0.94%
	pull	0.04%		pull	0.55%
Ductility 1	push	0.01%	Ductility 4	push	1.21%
	pull	0.08%		pull	0.78%
Ductility 1.5	push	0.44%	Ductility 5	push	1.36%
	pull	0.17%		pull	1.00%
Ductility 2	push	0.72%	Ductility 6	push	1.45%
	pull	0.32%		pull	1.18%

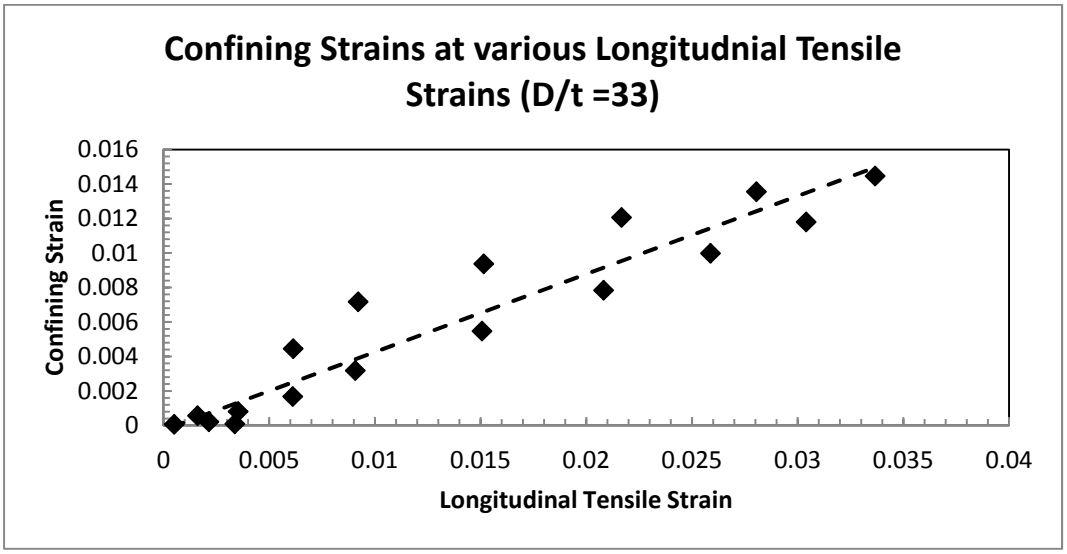

Figure 4-35 Confining Strains compared to the corresponding longitudinal tensile strains (D/t = 33)

The thinner-walled piles had buckles distributed throughout the constant moment region and this altered the lateral strains. The "confining" strains calculated for specimens with a high D/t ratio using Equation 4-8 gave unreasonable results. The calculations resulted in positive and negative "confining" strains. These results were unreasonable meaning there must have been another factor related to buckling of the pipe which affected the measured lateral strains, as demonstrated in Equation 4-9. The additional lateral strain effect due to buckling of the steel tube was likely a result of the high degree of non-linearity during buckling. Since buckling occurred proportionally earlier as the D/t increased, calculation of corresponding confining strains became problematic.

$$\varepsilon_{confining} = \varepsilon_{lateral} + \upsilon\varepsilon_{longitudinal} + \varepsilon_{buckling} \qquad \textbf{Equation 4-9}$$

The confining strains are necessary to determine the level of confinement in the concrete core, and the confined concrete strength. However, the confined stress of the concrete does not have a large effect on the flexural strength of reinforced concrete filled steel tubes.

To demonstrate the effect of concrete strength on the flexural strength of the section, the thickest-walled specimen (D/t =33) tested in this research project is used as an example. The input values for this test are shown in Table 4-7. Three different concrete stress-strain curves are used: all of them are a variation of Mander's model. The first curve uses the full confinement predicted by Mander's model (100% effective confinement), the second estimates 50% of the effective confinement predicted by Mander's model and the third estimates 10% of the effective confinemen. Figure 4-36 demonstrates the three levels of confinement and the unconfined concrete stress-strain curves.

Table 4-7 Input values for Mander's Model: Test 6

Input values for Mander's Model (Test 6)						
D =	20	in		thp =	0.6	in
fy_pipe=	58.5	ksi		f'c =	5.22	ksi
#bars =	12			dia bars=	0.75	in

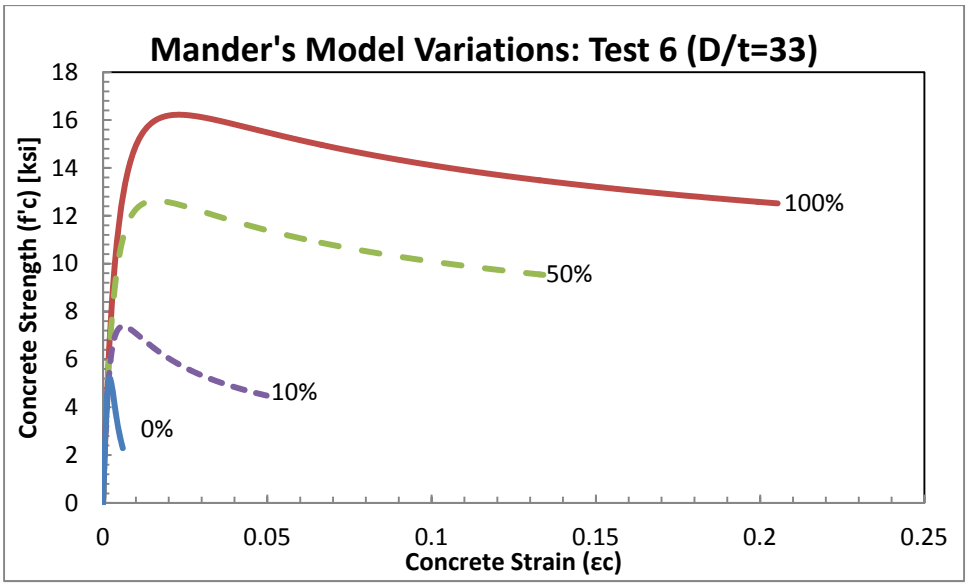

Figure 4-36 Various effective confinements using Mander's Model (D/t = 33)

As seen in the figure, the concrete strengths and ultimate strains vary depending on the effective confinement. As presented earlier in Figure 4-15, the ultimate compressive strain exhibited in the specimens reached approximately 1%. Figure 4-37 shows the same stress-strain curves as in Figure 4-36, except with a maximum strain of 0.01. All of the confined curves reach ultimate concrete strains higher than was achieved in the tests. The ultimate concrete strain does not control the failure of the concrete filled steel tubes, the rupture of the pile defined failure. At 1% strain, the confined concrete strengths vary from 7 ksi to 15 ksi. The effect of the change in strengths on the overall flexural strength needs to be considered.

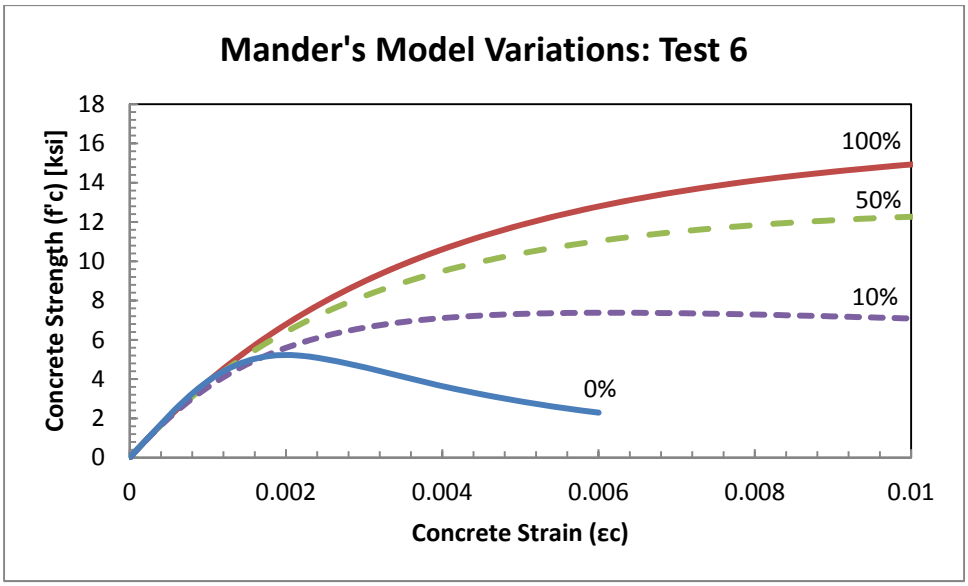

Figure 4-37 Various effective confinements using Mander's Model with max strain (D/t = 33)

Moment-curvature analyses were performed using all three of the above confined concrete stress-strain curves (10%, 50% and 100%). The results from the analyses are shown in Figure 4-38. The effective confinement does change the ultimate curvature reached by the section. However, the curvatures predicted by the analyses are larger than those achieved in experimental tests because concrete crushing does not control the failure of the specimen.

Figure 4-39 demonstrates the same stress-strain curves as the previous figure except the maximum curvature is limited to 0.0015 1/in: the average maximum curvature in the experimental tests. At this point, the moment capacities of the sections with different effective confinements, summarized in Table 4-8, are close to one another. The percent difference of the moment capacity between 10% and 100% effective confinement is 4.6%, the percent difference between 50% and 100% effective confinement is only 1.3%. The accuracy of these predictions for all of the tests will be discussed in Section 4.2.3.3.

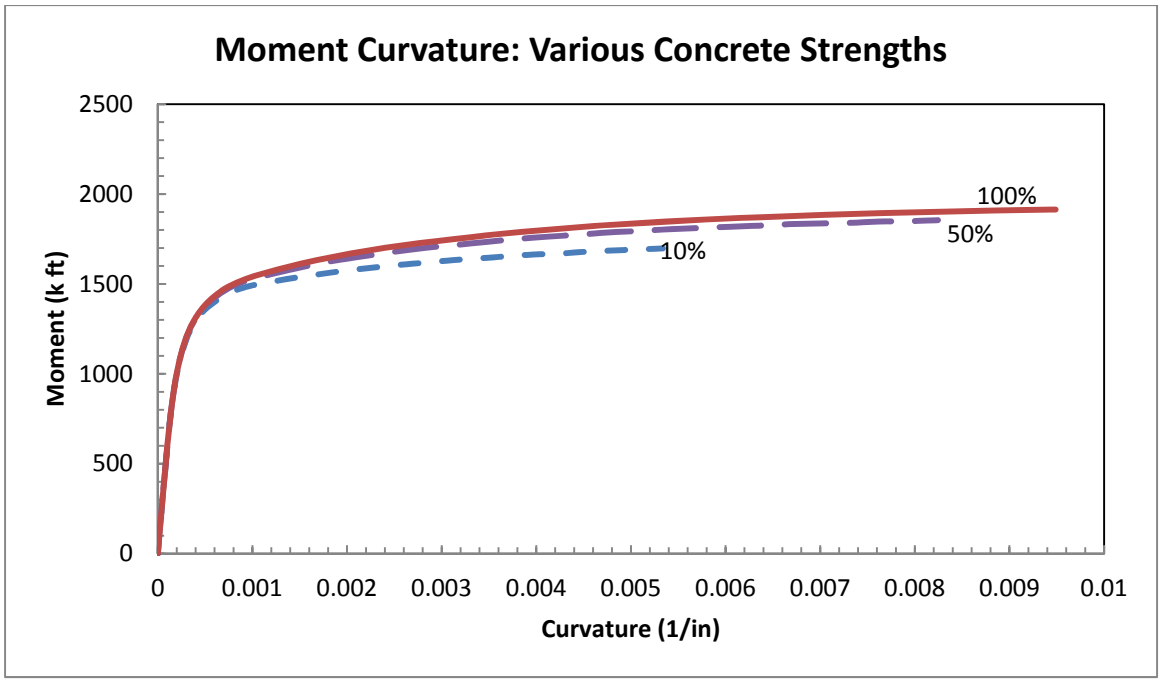

Figure 4-38 Moment Curvature Results for Various Confined Concrete Strengths (D/t =33)

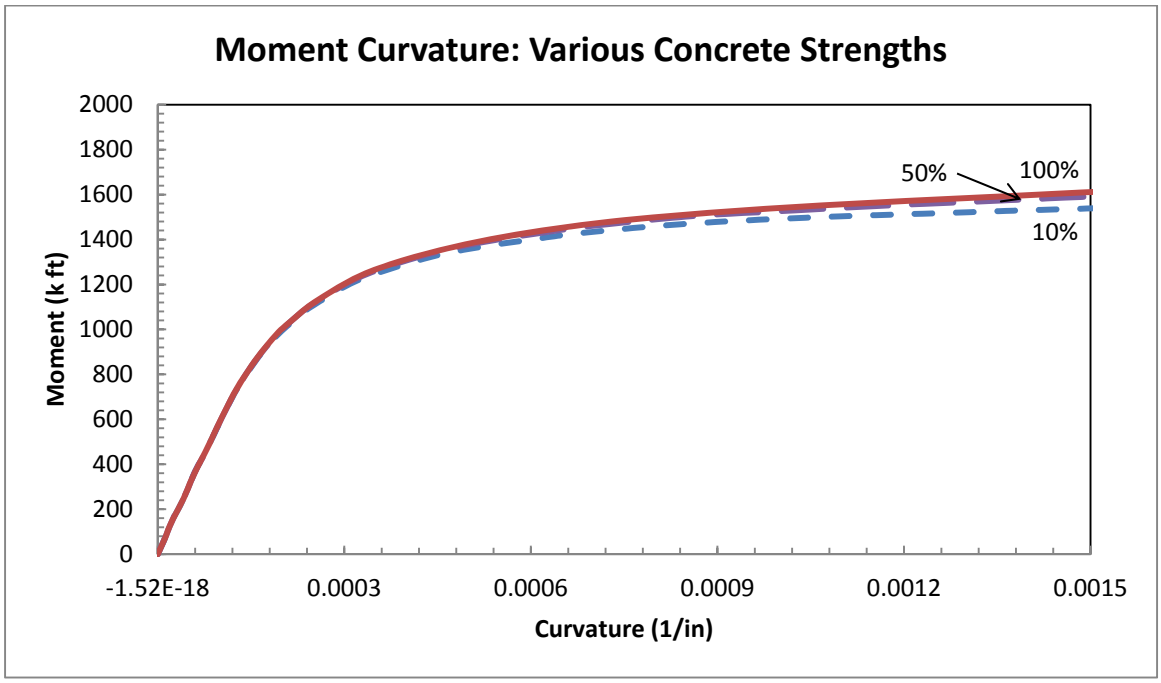

Figure 4-39 Moment Curvature Results for Various Confined Concrete Strengths with a maximum curvature (D/t =33)

Table 4-8 Moment Capacity at ultimate curvature (D/t = 33)

Effective Confinement	Moment Capacity at Φ=0.0015(1/in)
10%	1538.21 k-ft
50%	1591.05 k-ft
100%	1610.99 k-ft

Overall, the effective confinement has a small effect on the flexural strength of the pipe. The failure of the steel pipe controls the ultimate curvature, not the effectiveness of the confinement provided to the core. If the steel pipe was not allowed to buckle, then the confinement effectiveness of the steel pipe encasing the concrete core would need to be determined in order to determine the point of failure. In case of the steel tube buckling, an effective confinement factor from 50% to 100% is reasonable and will give accurate results; the accuracy of these results is discussed in Section 4.2.3.3.

4.2.3.3. Accuracy of Prediction

Two methods of applying the stress-strain curves of the steel tubes were used to calculate the moment curvature responses of the reinforced concrete filled steel tube. Both methods will be explained and discussed; results from the twelve experimental tests will be summarized and compared to the predictions.

4.2.3.4. Non-Linear Steel Tube Strain Profiles

The first prediction method applied the cyclic stress-strain curve, discussed in Section 4.2.3.1. The stresses in the steel tube were calculated at the end of each loading cycle around the circumference by applying the bi-linear stress-strain curve to the strain hysteresis. The areas, where each strain was calculated, were used to calculate the forces and moments contributed by the steel tube. The areas of each section are shaded in Figure 4-40. The areas are larger than they would be in a typical moment-curvature analysis because the locations of the data collected were limited.

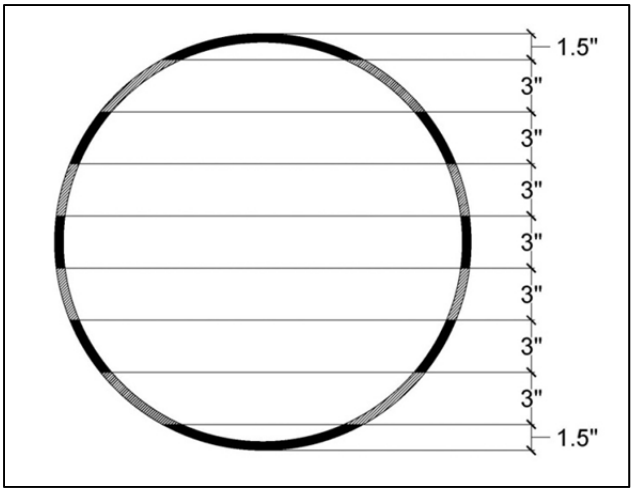

Figure 4-40 Sections of steel tube used in moment curvature prediction

The concrete core was split into 24 sections of equal thickness. Mander's full confined concrete strength and extrapolated linear strain profile (Figure 4-10) were used to calculate the compressive stress in each slice. The extrapolated strain profile and the stress-strain curve from the rebar tensile test were used to calculate the stresses in each bar. Forces were calculated for each material based on the stress and respective area, and the forces were summed about the extreme tensile face.

The results for the varying D/t ratios (Tests 2 through 7) are displayed in Figure 4-41, and the results for the varying internal reinforcement ratios (Tests 8 through 12) are displayed in Figure 4-42. As seen in the figures, the predicted moment capacities at each curvature agreed well with the experimental results. This method for calculating the moment capacities was accurate and supports the conclusion that the steel tube developed the full compressive stress on the "compressive" side of the section after buckling when it was exhibiting tensile strains.

Figure 4-41 Moment – Curvature comparison with Non-Linear Profile Predictions: Varying D/t ratios

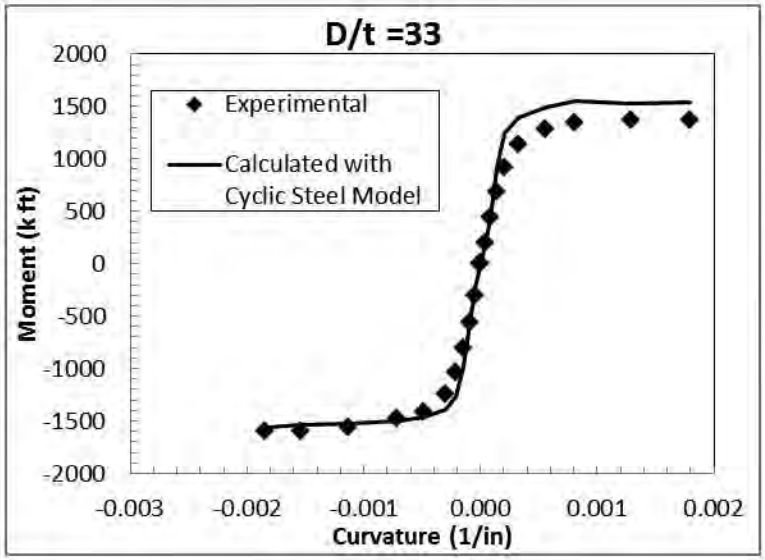
D/t =33
Experimental
Calculated with Cyclic Steel Model
Moment (k ft)
Curvature (1/in)
2000
1500
1000
500
0
-500
-1000
-1500
-2000
-0.003
-0.002
-0.001
0.000
0.001
0.002

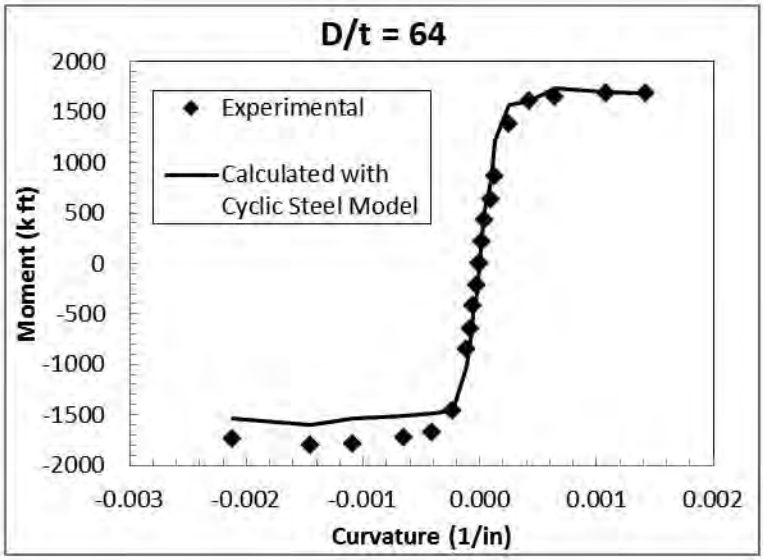
D/t = 64
Experimental
Calculated with Cyclic Steel Model
Moment (k ft)
Curvature (1/in)
2000
1500
1000
500
0
-500
-1000
-1500
-2000
-0.003
-0.002
-0.001
0.000
0.001
0.002

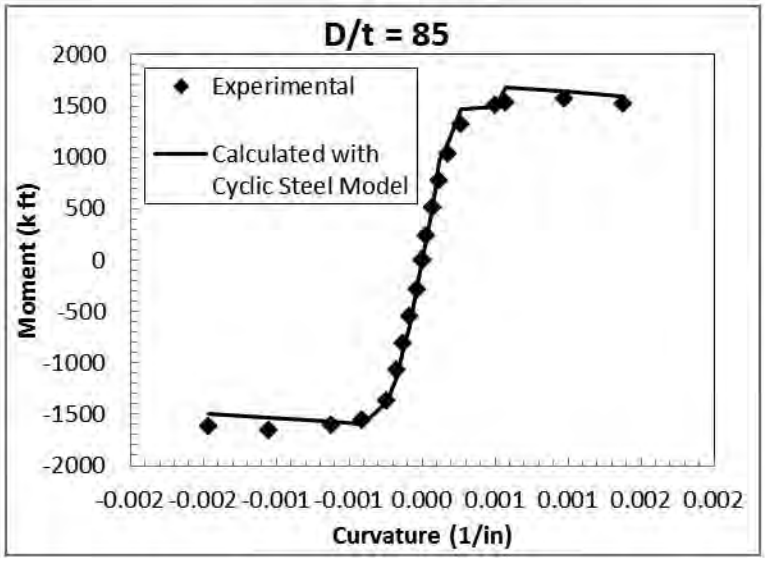
D/t = 85
Experimental
Calculated with Cyclic Steel Model
Moment (k ft)
Curvature (1/in)
2000
1500
1000
500
0
-500
-1000
-1500
-2000
-0.002 -0.002 -0.001 -0.001 0.000 0.001 0.001 0.002 0.002

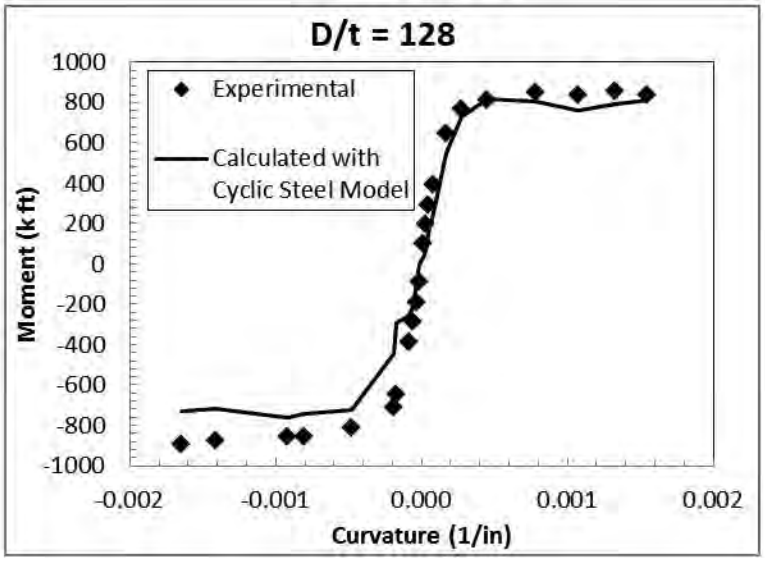
D/t = 128
Experimental
Calculated with Cyclic Steel Model
Moment (k ft)
Curvature (1/in)
1000
800
600
400
200
0
-200
-400
-600
-800
-1000
-0.002
-0.001
0.000
0.001
0.002

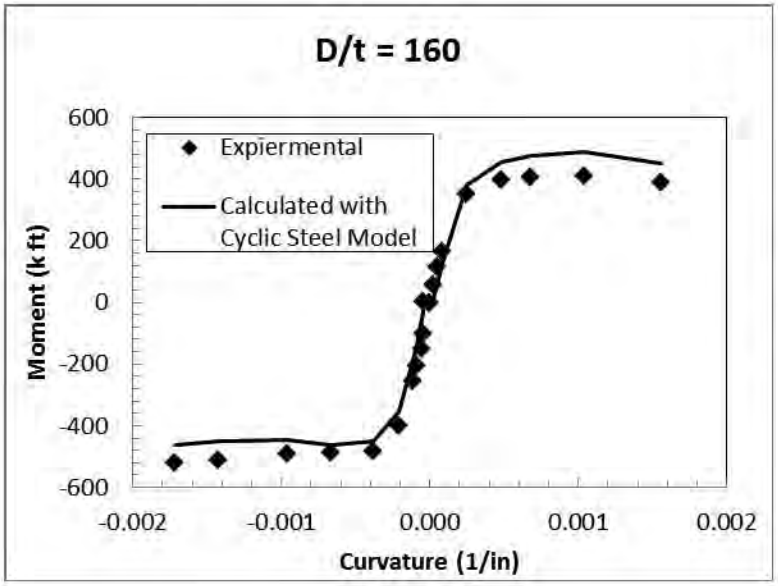
D/t = 160
Moment (k ft)
600
400
200
0
-200
-400
-600
-0.002
-0.001
0.000
0.001
0.002
Curvature (1/in)
Expiermental
Calculated with
Cyclic Steel Model

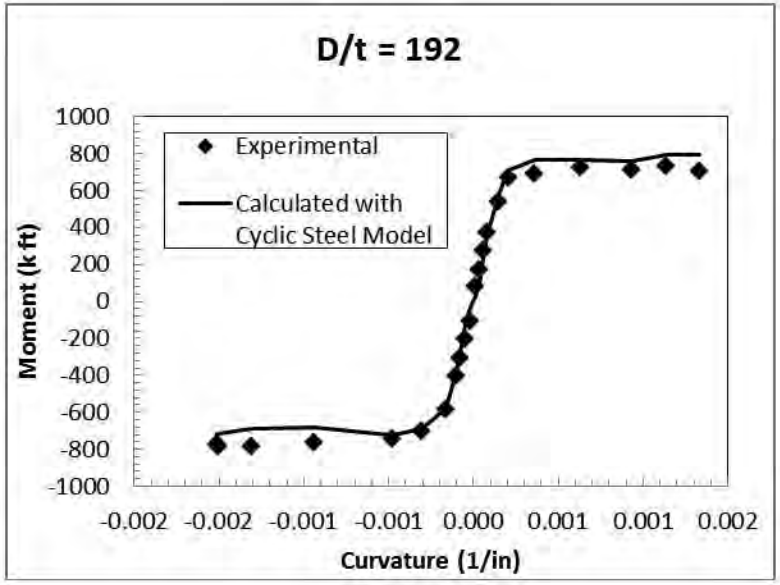
D/t = 192
Moment (k ft)
1000
800
600
400
200
0
-200
-400
-600
-800
-1000
-0.002 -0.002 -0.001 -0.001 0.000 0.001 0.001 0.002
Curvature (1/in)
Experimental
Calculated with
Cyclic Steel Model

Figure 4-42 Moment – Curvature comparison with Non-Linear Profile Predictions: Varying internal reinforcement ratios

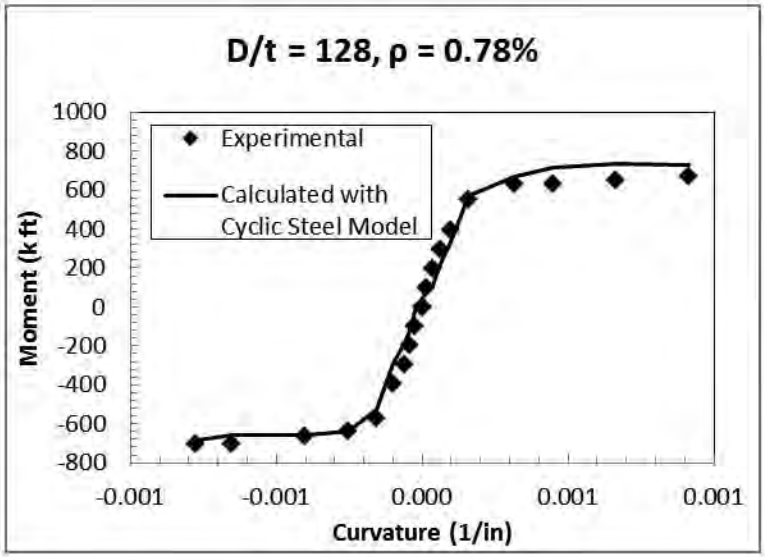
D/t = 128, ρ = 0.78%
Experimental
Calculated with Cyclic Steel Model
Moment (k ft)
Curvature (1/in)
1000
800
600
400
200
0
-200
-400
-600
-800
-0.001
-0.001
0.000
0.001
0.001

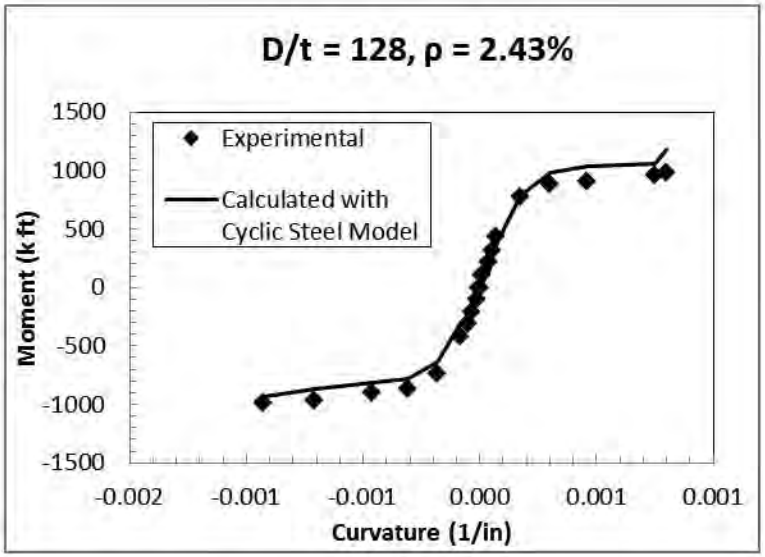
D/t = 128, ρ = 2.43%
Experimental
Calculated with Cyclic Steel Model
Moment (k ft)
Curvature (1/in)
1500
1000
500
0
-500
-1000
-1500
-0.002
-0.001
-0.001
0.000
0.001
0.001

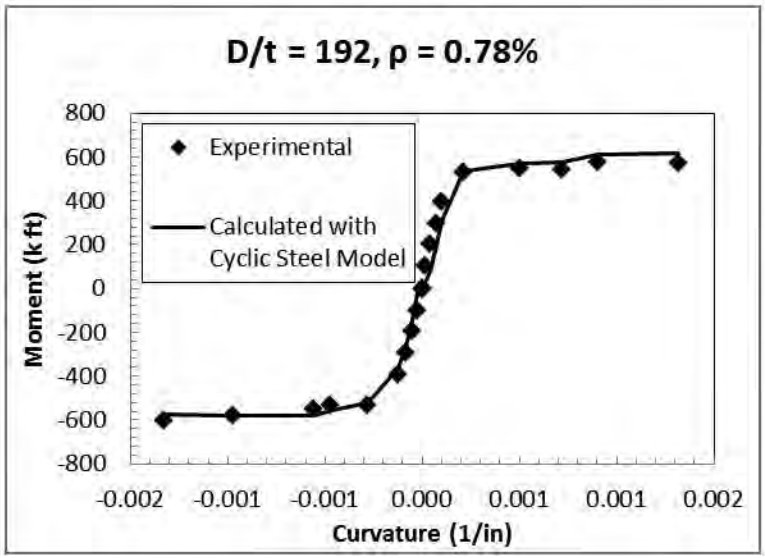
D/t = 192, ρ = 0.78%
Experimental
Calculated with Cyclic Steel Model
Moment (k ft)
Curvature (1/in)
800
600
400
200
0
-200
-400
-600
-800
-0.002
-0.001
-0.001
0.000
0.001
0.001
0.002

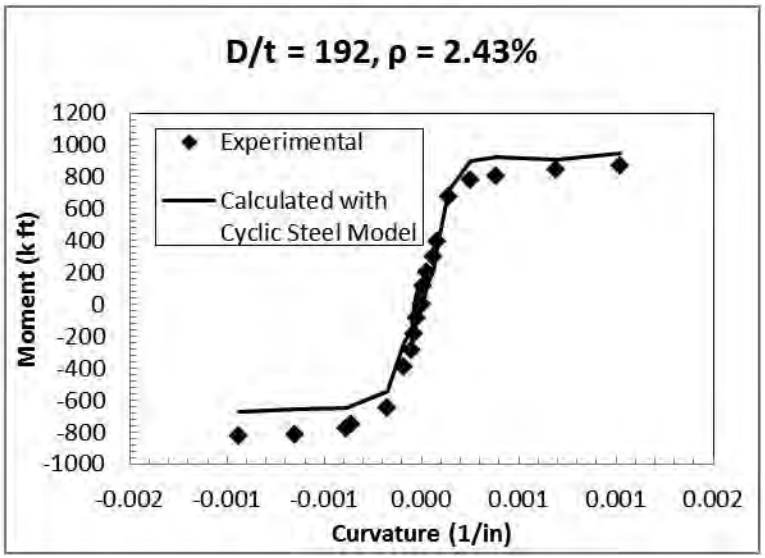
D/t = 192, ρ = 2.43%
Experimental
Calculated with Cyclic Steel Model
Moment (k ft)
Curvature (1/in)
1200
1000
800
600
400
200
0
-200
-400
-600
-800
-1000
-0.002
-0.001
-0.001
0.000
0.001
0.001
0.002

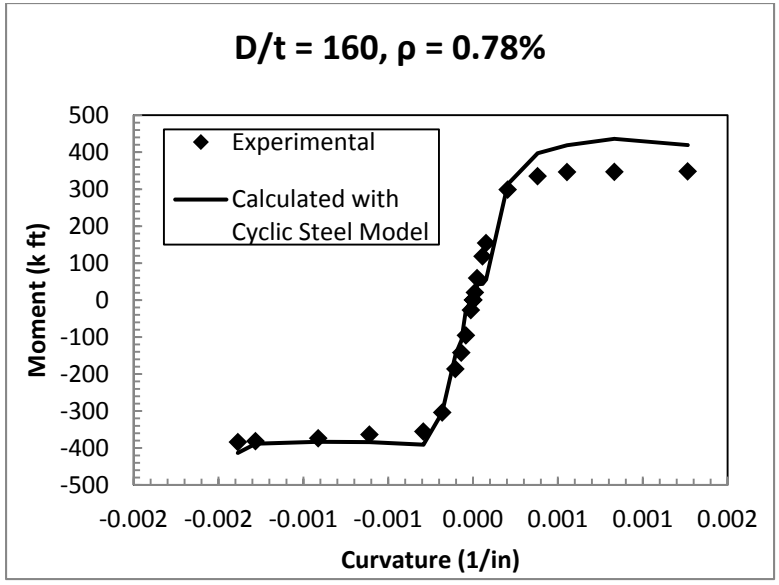
D/t = 160, ρ = 0.78%
Experimental
Calculated with Cyclic Steel Model
Moment (k ft)
500
400
300
200
100
0
-100
-200
-300
-400
-500
-0.002 -0.002 -0.001 -0.001 0.000 0.001 0.001 0.002
Curvature (1/in)

4.2.3.5. Linear Steel Tube Strain Profiles

Moment – curvature responses were calculated assuming a linear strain profile before and after buckling. The test data showed that the steel tube does not have a linear strain profile after buckling, but the stresses on the "compressive" side of the pipe were in compression even in the presence of tensile strains. This method accurately predicted the strength because the linear strain profile also assumed the "compressive" side of the pipe was in a compressive stress state.

The concrete models applied in these analyses assumed one-hundred percent of the effective confinement predicted by Mander's model. The internal reinforcement is also assumed to follow the same linear strain profile as the concrete core and the steel tube. The predictions matched well with the predicted results. The comparison of the experimental results and predicted flexural strengths for the tests with varying D/t ratios (Tests 2 through7) are shown in Figure 4-43. Figure 4-44 displays the comparison between the predicted responses and experimental responses for the sections with varying internal reinforcement ratios.

Figure 4-43 Moment – Curvature comparison with Linear Profile Predictions: Varying D/t ratios

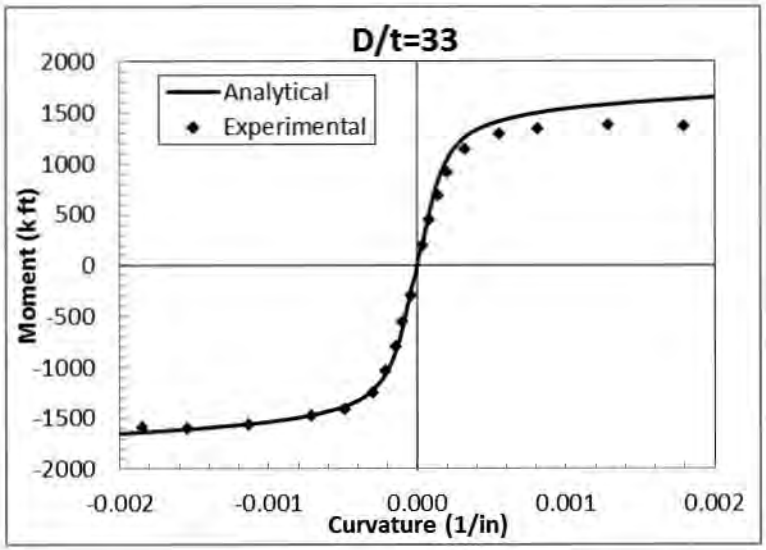
D/t=33
Analytical
Experimental
Moment (k ft)
2000
1500
1000
500
0
-500
-1000
-1500
-2000
-0.002
-0.001
0.000
0.001
0.002
Curvature (1/in)

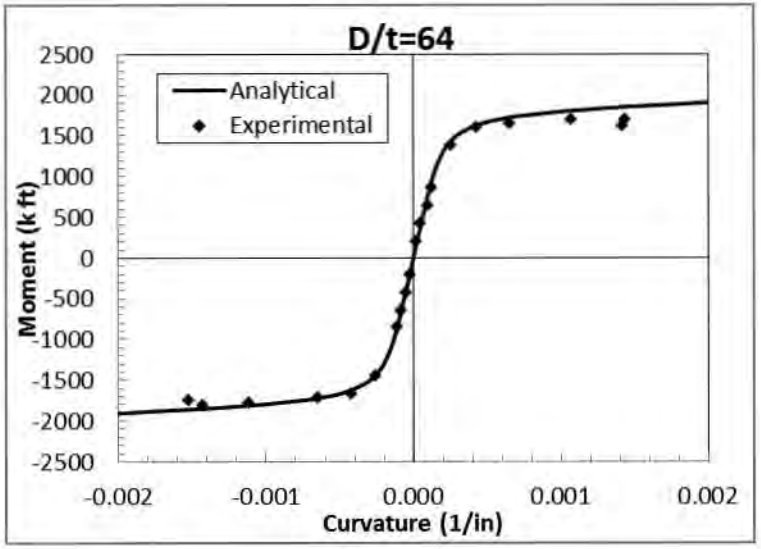
D/t=64
Analytical
Experimental
Moment (k ft)
2500
2000
1500
1000
500
0
-500
-1000
-1500
-2000
-2500
-0.002
-0.001
0.000
0.001
0.002
Curvature (1/in)

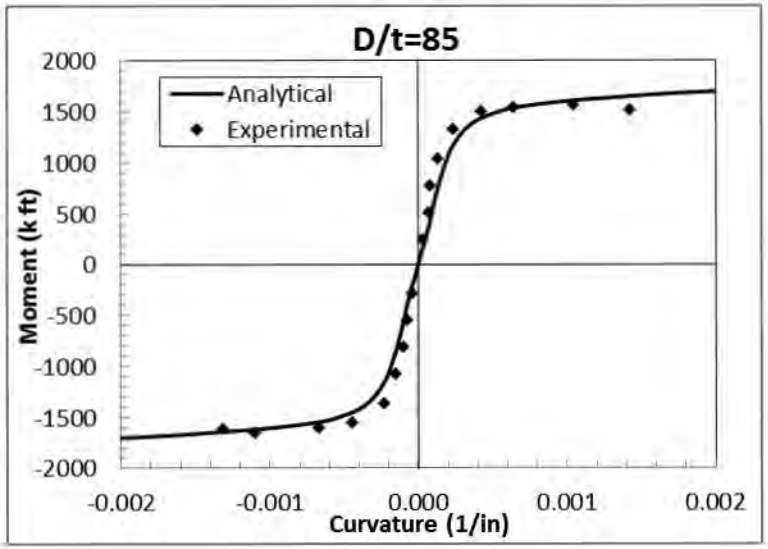
D/t=85
Analytical
Experimental
Moment (k ft)
2000
1500
1000
500
0
-500
-1000
-1500
-2000
-0.002
-0.001
0.000
0.001
0.002
Curvature (1/in)

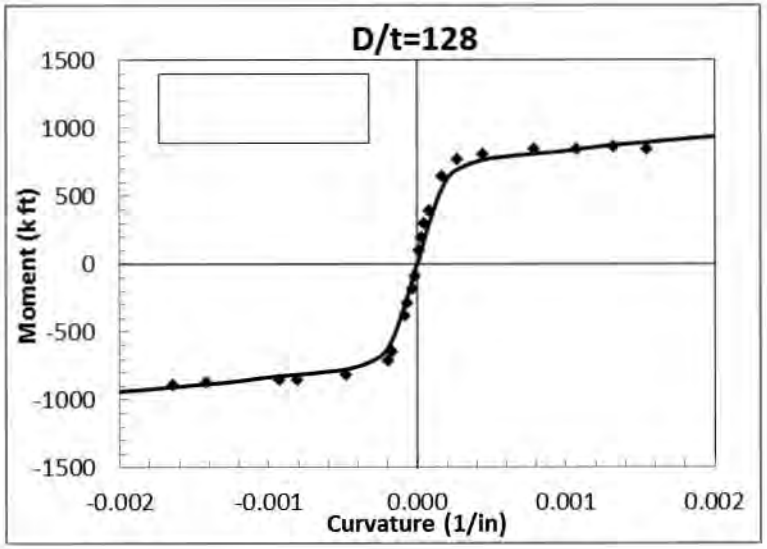
D/t=128
Moment (k ft)
1500
1000
500
0
-500
-1000
-1500
-0.002
-0.001
0.000
0.001
0.002
Curvature (1/in)

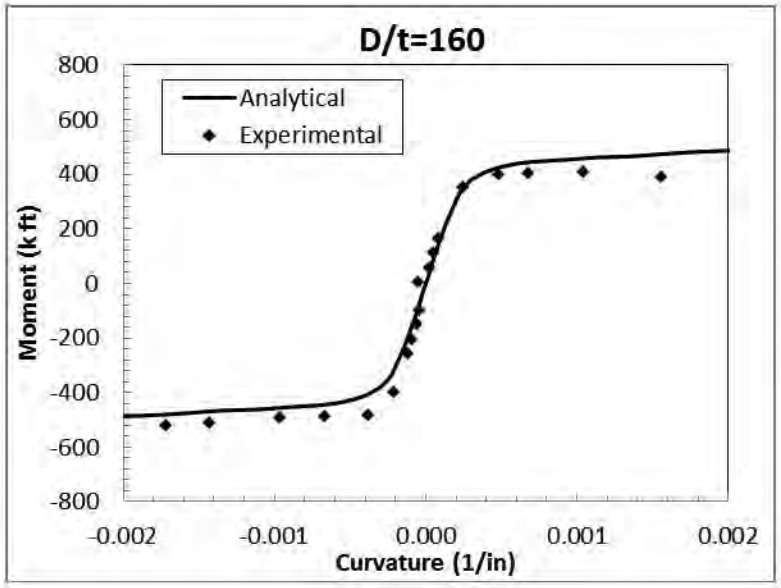
D/t=160
Analytical
Experimental
Moment (k ft)
Curvature (1/in)
800
600
400
200
0
-200
-400
-600
-800
-0.002
-0.001
0.000
0.001
0.002

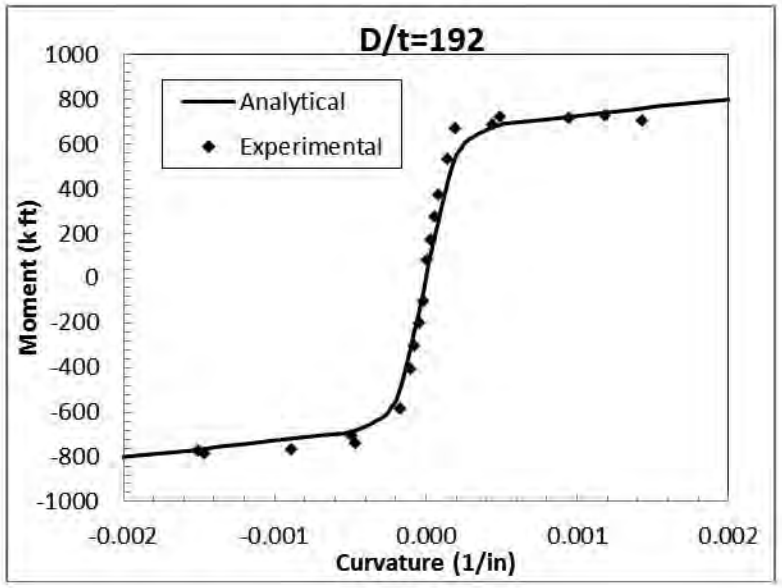
D/t=192
Analytical
Experimental
Moment (k ft)
Curvature (1/in)
1000
800
600
400
200
0
-200
-400
-600
-800
-1000
-0.002
-0.001
0.000
0.001
0.002

Figure 4-44 Moment – Curvature comparison with Linear Profile Predictions: Varying internal reinforcement ratios

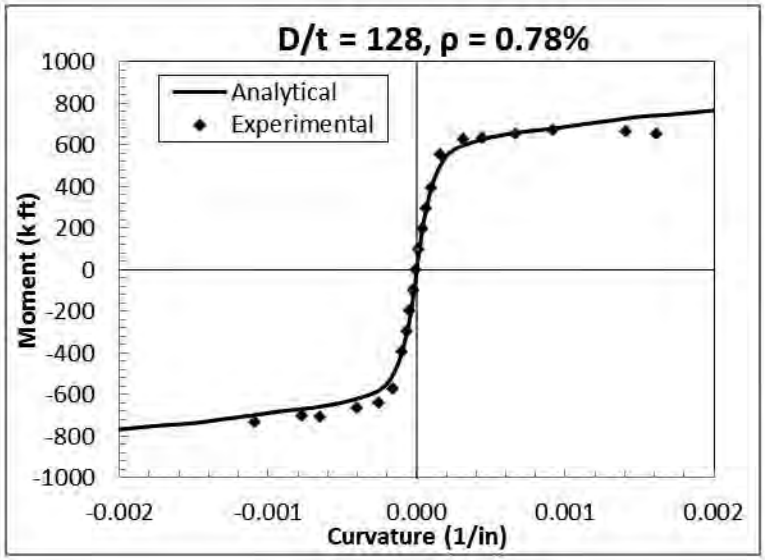
D/t = 128, ρ = 0.78%
Analytical
Experimental
Moment (k ft)
Curvature (1/in)
1000
800
600
400
200
0
-200
-400
-600
-800
-1000
-0.002
-0.001
0.000
0.001
0.002

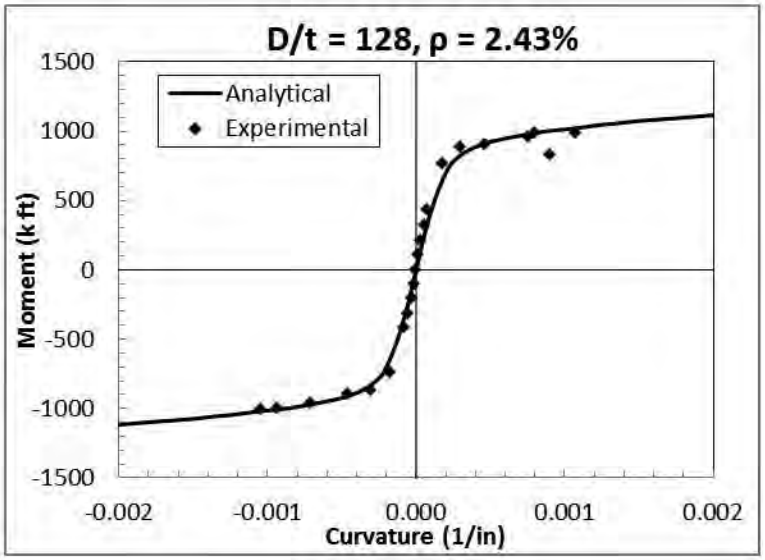
D/t = 128, ρ = 2.43%
Analytical
Experimental
Moment (k ft)
Curvature (1/in)
1500
1000
500
0
-500
-1000
-1500
-0.002
-0.001
0.000
0.001
0.002

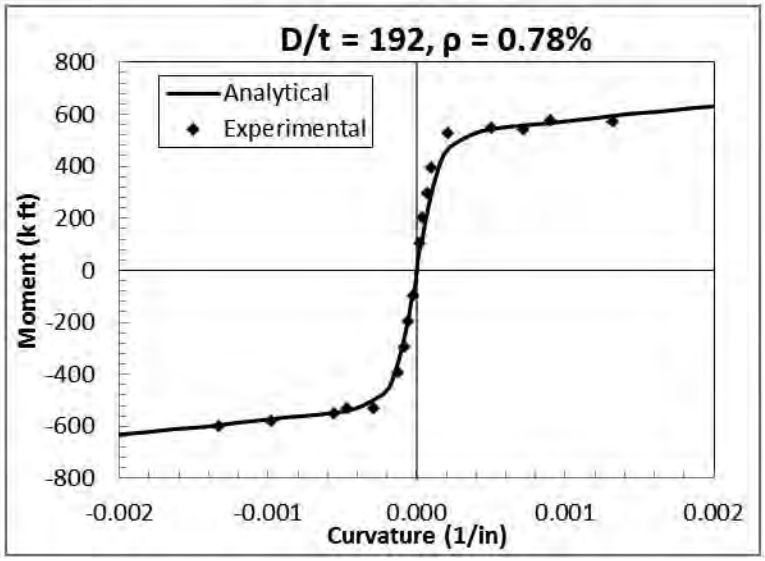
D/t = 192, ρ = 0.78%
Analytical
Experimental
Moment (k ft)
Curvature (1/in)
800
600
400
200
0
-200
-400
-600
-800
-0.002
-0.001
0.000
0.001
0.002

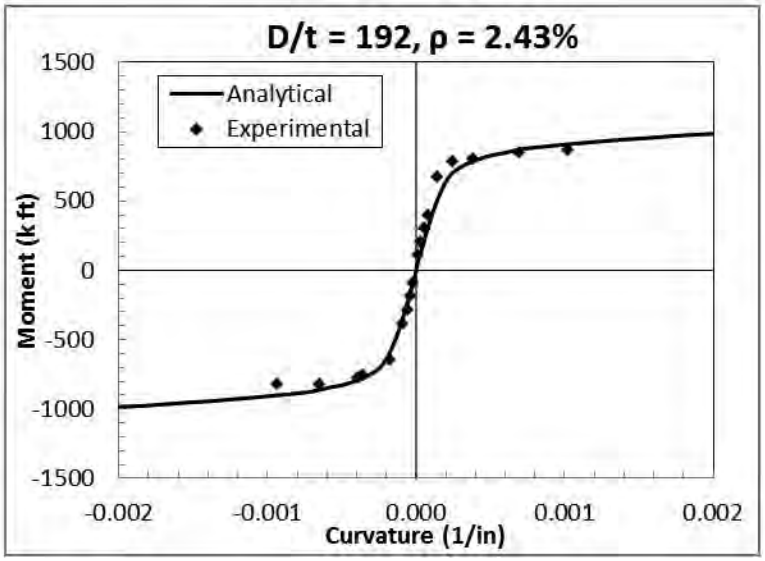
D/t = 192, ρ = 2.43%
Analytical
Experimental
Moment (k ft)
Curvature (1/in)
1500
1000
500
0
-500
-1000
-1500
-0.002
-0.001
0.000
0.001
0.002

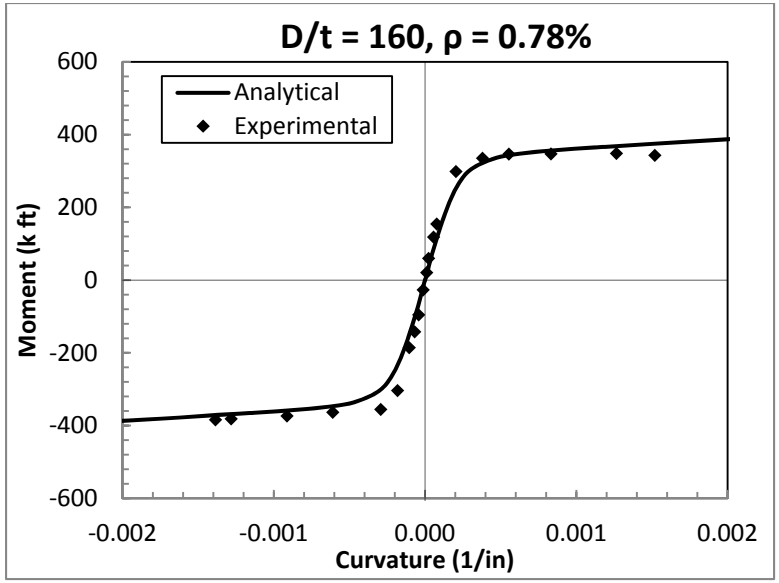
D/t = 160, ρ = 0.78%
Analytical
Experimental
Moment (k ft)
600
400
200
0
-200
-400
-600
-0.002
-0.001
0.000
0.001
0.002
Curvature (1/in)

4.2.4. Summary

There are multiple ways to model the different materials in a reinforced concrete filled steel tube. Conventional methods apply Mander's model to the concrete core and a monotonic stress-strain curve for the steel tube and internal reinforcing bars. Although the assumptions in these models are not strictly correct, they do yield an accurate moment capacity for a given curvature.

> The concrete core does not reach the predicted confined concrete strength, but the confined concrete strength has little effect on the moment capacity of the section.
>
> Data from the experimental tests show that the strain profiles of the steel tube are not linear. However, the steel tube reached the same compressive stresses that would be predicted assuming a linear strain profile, resulting in an accurate prediction of the moment capacity.

4.3. Verification of Curvatures

The section curvatures were the slope of the extrapolated strain profiles. To verify the accuracy of this assumption, the relationship between the curvature and a known variable must be calculated and compared with actual results. The mid-span displacements are known throughout the test and the curvatures can be used to calculate the mid-span displacements with the moment – area method.

The moment-area method was developed by Mohr (Caprani, 2007), and it is a tool for calculating the slopes and displacements of structures subjected to bending. From the Euler-Bernoulli Bending Theory, we know the change in rotation ($d\theta$) between two points on a beam (A and B) can be expressed as in Equation 4-10. This equation is be interpreted as the change in slope between A and B is equal to the area of the curvature diagram between A and B. This expression is extended to calculate displacements as shown in Equation 4-11. This expression is Mohr's second theorem which states: "For an originally straight beam, subject to bending moment, the vertical intercept between one terminal and the tangent to the curve of another terminal is the first moment of the curvature diagram about the terminal where the intercept is measured."

$$\int_A^B d\theta = \int_A^B \frac{M}{EI} dx \qquad \textbf{Equation 4-10}$$

$$\Delta_{BA} = \left[\int_A^B \frac{M}{EI} dx\right] \bar{x} \qquad \textbf{Equation 4-11}$$

The moment – area method was applied to the concrete filled steel tubes and the mid-span displacements were calculated. The strain profiles were only measured in the constant moment region, not over the length of the pile. The distance from the support where the pile became inelastic (d_{el}) was calculated using Equation 4-12. The forces were assumed to be perfectly linear from the support to the loading point, the yield force was known from moment-curvature analysis, and the location of this yield force on the beam at each cycle could was calculated (Figure 4-45).

$$\mathbf{d_{inel} = \frac{d_{arm}}{F_{max}} F_{yield}} \qquad \textbf{Equation 4-12}$$

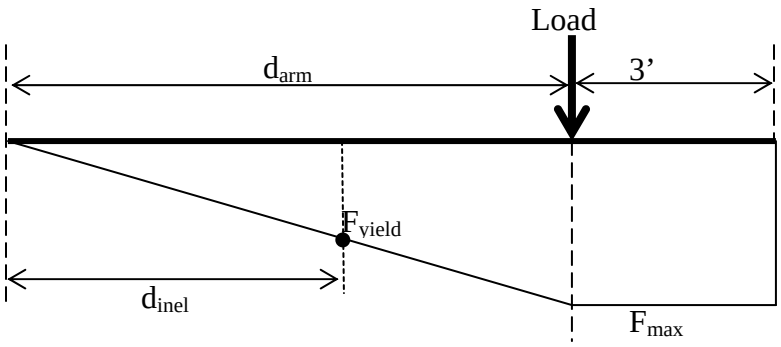

Figure 4-45 Assumed force distribution in pile

The change in curvature distribution in the inelastic region, before the constant moment region, was nonlinear. However, since the curvatures were not be measured in this region, a linear distribution was assumed to occur between the point where the pile becomes inelastic and the constant moment region. The full curvature profile after making this assumption is shown in Figure 4-46.

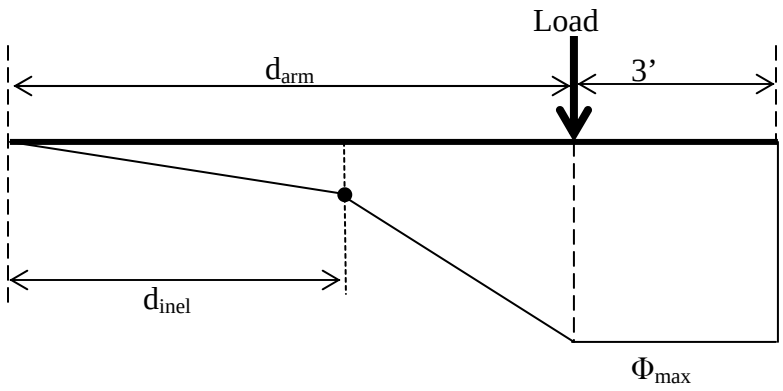

Figure 4-46 Assumed curvature distribution in pile

The moment – area method was applied at the end of each loading cycle and the mid-span displacement was calculated based on the curvature profile shown above. The results agreed with the experimental displacements, with average errors of about 20 percent. This error is due to the assumptions made in creating the curvature profile. The ratio of the calculated and experimental displacements for the thickest and thinnest pile (D/t = 33 and 192) are shown in and the values of these displacements at each ductility level are shown in Table 4-9. The force-displacement envelopes are shown in Figure 4-48. As seen in the figure, although the predictions of the displacements are not exact, the approximate method does agree with the experimental force-displacement envelope.

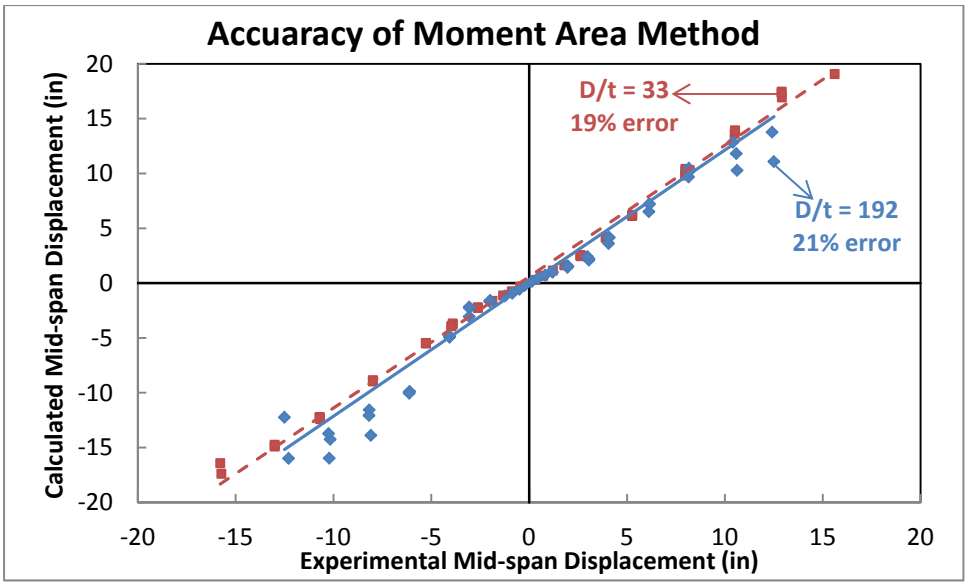

Figure 4-47 Ratio of displacements calculated with moment area method and experimental displacements

Table 4-9 Comparison of experimental displacements and calculated displacements from assumed curvature distribution

		D/t = 33		D/t = 192	
		Experimental Displ. (in)	Calculated Displ. (in)	Experimental Displ. (in)	Calculated Displ. (in)
1/4 Fy	push	0.32	0.29	0.14	0.16
	pull	-0.46	-0.33	-0.21	-0.18
1/2 Fy	push	0.73	0.67	0.42	0.40
	pull	-0.89	-0.74	-0.50	-0.56
3/4 Fy	push	1.21	1.14	0.82	0.73
	pull	-1.33	-1.13	-0.86	-0.93
Fy	push	1.80	1.63	1.20	1.00
	pull	-1.87	-1.63	-1.24	-1.17
Ductility 1	push 1	2.62	2.46	1.95	1.54
	pull 1	-2.61	-2.25	-2.01	-1.67
	push 2	2.63	2.54	1.96	1.44
	pull 2	-2.62	-2.22	-2.02	-1.67
	push 3	2.63	2.55	1.98	1.56
	pull 3	-2.62	-2.23	-1.99	-1.58
Ductility 1.5	push 1	3.91	4.16	3.06	2.09
	pull 1	-3.90	-3.68	-3.07	-3.06
	push 2	3.92	4.16	3.06	2.21
	pull 2	-3.90	-3.78	-3.05	-2.27
	push 3	3.94	4.15	2.98	2.41
	pull 3	-3.99	-3.93	-3.06	-2.18
Ductility 2	push 1	5.26	6.12	4.06	3.61
	pull 1	-5.27	-5.47	-4.07	-4.91
	push 2	5.27	6.21	4.08	4.15
	pull 2	-5.27	-5.47	-4.07	-4.93
	push 3	5.27	6.16	4.09	4.16
	pull 3	-5.28	-5.49	-4.07	-4.82
Ductility 3	push 1	7.97	9.82	6.12	6.51
	pull 1	-7.98	-8.96	-6.10	-9.89
	push 2	7.98	10.41	6.14	7.21
	pull 2	-7.98	-8.88	-6.14	-9.94
	push 3	7.98	10.22	6.15	7.22
	pull 3	-7.99	-8.87	-6.13	-10.04

Table 4-9 continued

		D/t = 33		D/t = 192	
		Experimental Displ. (in)	Calculated Displ. (in)	Experimental Displ. (in)	Calculated Displ. (in)
Ductility 4	push 1	10.50	13.63	8.14	9.68
	pull 1	-10.68	-12.41	-8.09	-13.88
	push 2	10.52	13.90	8.17	10.46
	pull 2	-10.70	-12.21	-8.17	-11.57
	push 3	10.53	13.91	8.17	10.15
	pull 3	-10.71	-12.23	-8.18	-12.07
Ductility 5	push 1	12.91	16.93	10.59	11.82
	pull 1	-13.01	-14.89	-10.21	-15.97
	push 2	12.90	17.46	10.62	10.28
	pull 2	-13.00	-14.88	-10.17	-14.24
	push 3	12.90	17.33	10.41	12.85
	pull 3	-13.00	-14.74	-10.25	-13.72
Ductility 6	push 1	15.55	20.48	12.42	13.78
	pull 1	-15.72	-17.38	-12.29	-15.98
	push 2	15.56	20.30	12.51	11.09
	pull 2	-15.78	-16.42	-12.50	-12.23
	push 3	15.61	19.07	N/A	N/A

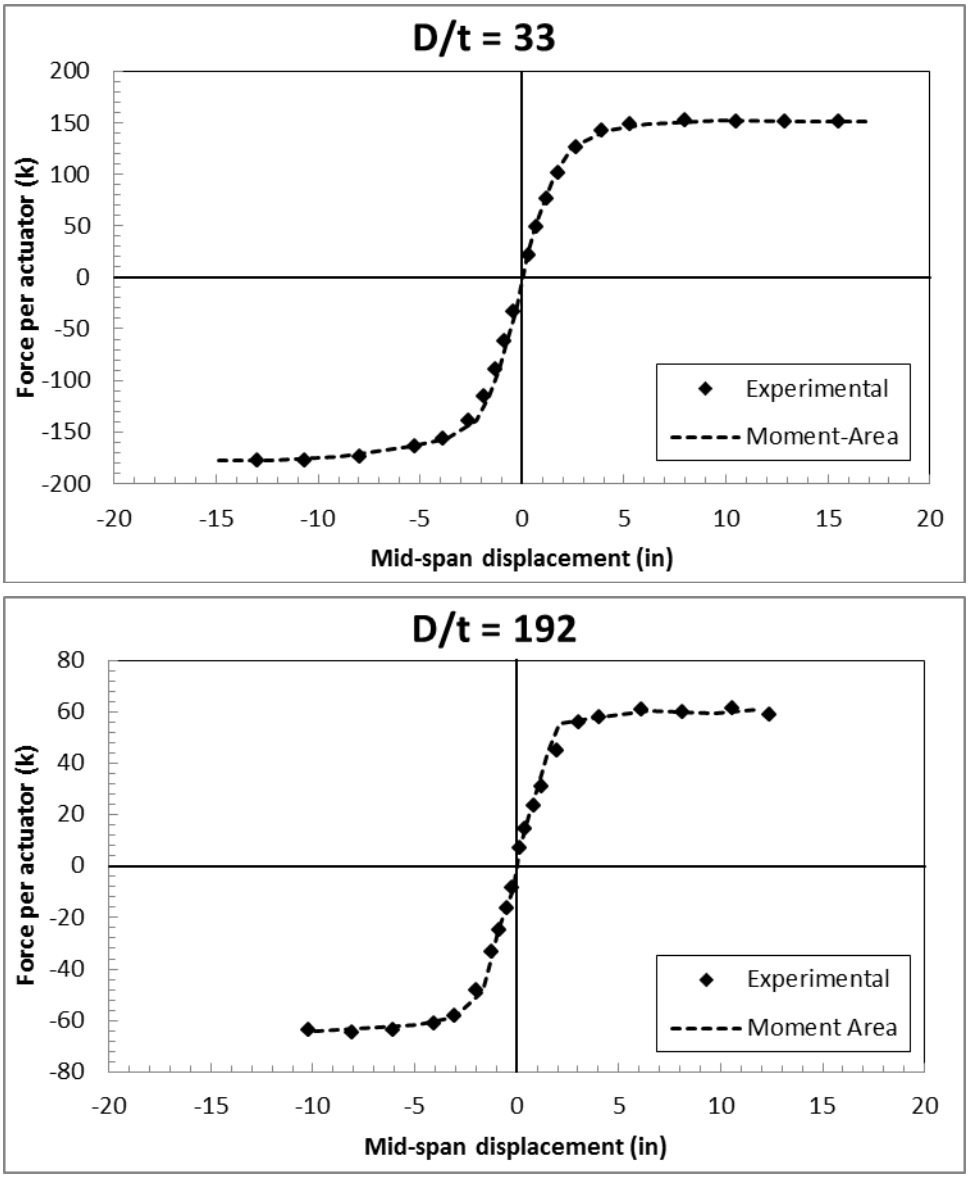

Figure 4-48 Moment curvature analysis comparison with moment area method approximation

The curvature distribution in the plastic region outside of the constant moment portion of the pile is not linear and follows more of a parabolic shape as shown in Figure 4-49. This approximation proved to be closer to reality than the linear approximation, resulting in an error of 7-9%. The comparison for the experimental and calculated results using this approximation for the thickest walled pipe (D/t = 33) and the thinnest walled pipe (D/t = 192) is shown in Figure 4-50.

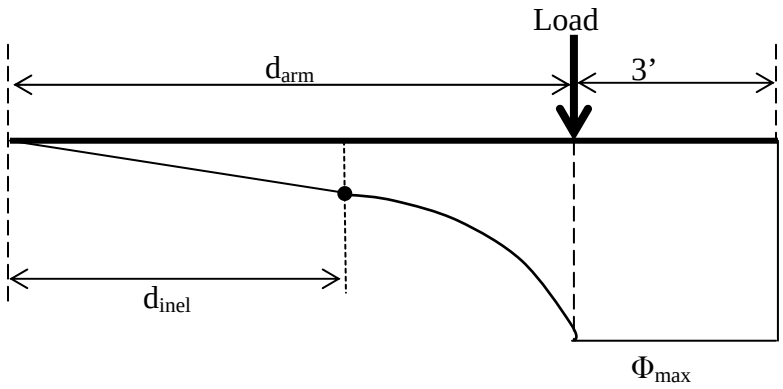

Figure 4-49 Parabolic Curvature Distribution in pile

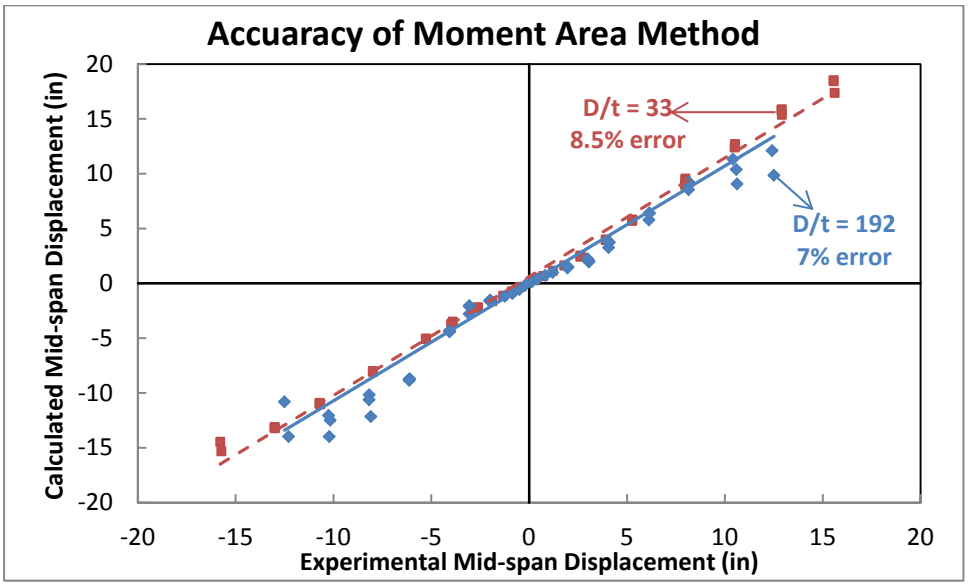

Figure 4-50 Accuracy of Moment Area Method-Parabolic Distribution

Although there was some error due to the assumptions made in calculating the displacements using the moment-area method, the calculated displacements are still close to those found in the experimental tests. This concludes that the method used to extrapolate the strain profiles and calculate the curvatures from the extrapolated strain profiles was accurate.

4.4. **Damping**

4.4.1. Definition

Equivalent viscous damping is an important variable in the Direct Displacement-Based Design (DDBD) method. In order to utilize the DDBD method for reinforced concrete filled steel tubes, expressions for the equivalent viscous damping need to be created. This research project focused on varying D/t ratios and internal reinforcement ratios and will be addressed with respect to damping. (Priestley, Calvi, & Kowalsky, 2007).

Jacobsen's approach is the most common procedure used to estimate the equivalent damping in a system. The equivalent damping is the combination of two factors: (1) hysteretic damping and (2) elastic damping. (Priestley, Calvi, & Kowalsky, 2007).

The displacement ductility was calculated based off the equivalent yield capacity. For RCFSTs, the nominal moment is about twice of the first yield moment, first yield moment and nominal moment are described in Section 3.5.1. This resulted in equivalent yield displacements about twice that of the first yield. Due to this large increase in displacement, plasticity had developed in the piles at ductility one. The plasticity resulted in higher levels of energy dissipation and damping than you would find in a reinforced concrete column which has a nominal moment to yield moment of approximately 1.3.

4.4.2. Hysteretic Damping

Jacobsen proposed an expression for equivalent viscous damping based on equating the energy absorbed by hysteretic steady-state cyclic response at a given displacement level to the equivalent viscous damping of the structure. His expression for the equivalent viscous damping coefficient, $\xi_{hsyt,}$ is shown in Equation 4-13. In the expression, A_h is the area of one complete force-displacement response, F_m is the maximum force achieved in this loop and Δ_m is the maximum displacement achieved in this loop. (Priestley, Calvi, & Kowalsky, 2007).

$$\boldsymbol{\xi_{hyst} = \frac{A_h}{2\pi} F_m \Delta_m} \qquad \textbf{Equation 4-13}$$

The complete force-displacement loops for the thinnest and thickest D/t ratio for each ductility level are shown in Figure 4-51. The left-hand side of the figure shows the force-displacement loops for a D/t of 192 and the right-hand side of the figure shows the loops for a D/t of 33. The loops for the thin-walled pile showed significant pinching due to cracking of the concrete and extensive buckling of the steel tube. The cracks in the concrete open during the unloading of a cycle and the slope of the force-displacement curve approaches zero; the slope increases as the cracks close and the section gains strength. As a result, the specimen with the high D/t ratio did not absorb as much energy as the thicker-walled pile. These two examples are the two extremes tested in this research program; the force-displacement loops

for the remaining tests can be seen in Appendix B. The moment-curvature hysteretic loops are shown in Appendix C.

Figure 4-51 Force – displacement loops for each ductility level: D/t 33 and 192

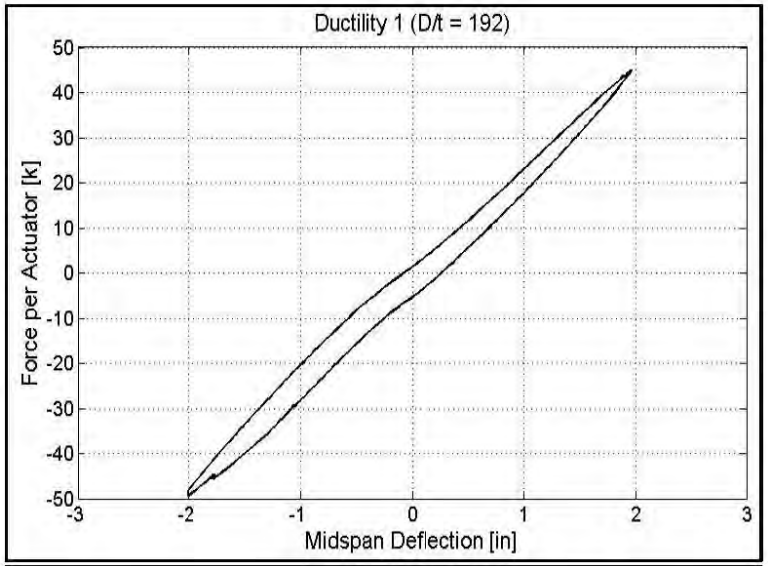
Ductility 1 (D/t = 192)
Force per Actuator [k]
Midspan Deflection [in]

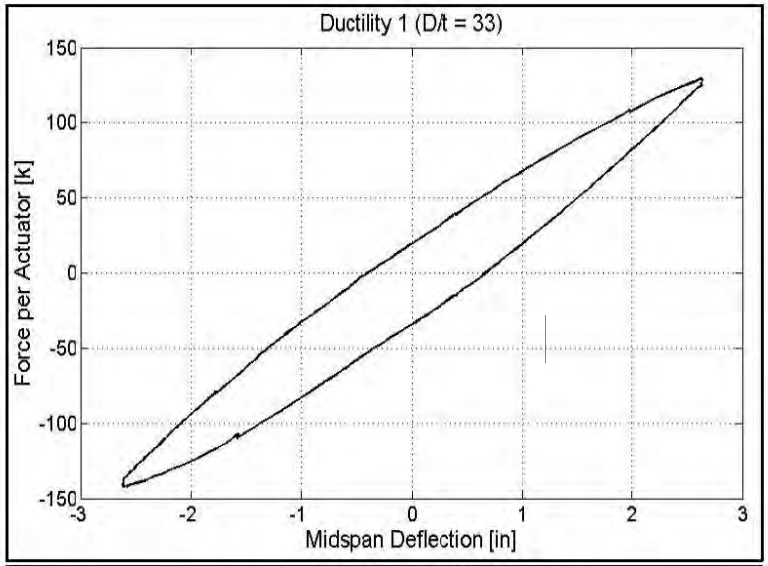
Ductility 1 (D/t = 33)
Force per Actuator [k]
Midspan Deflection [in]

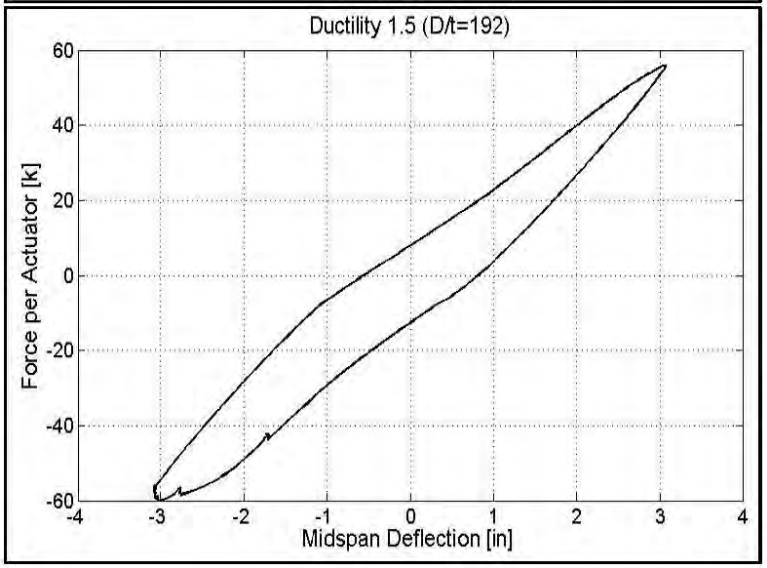
Ductility 1.5 (D/t=192)
Force per Actuator [k]
Midspan Deflection [in]

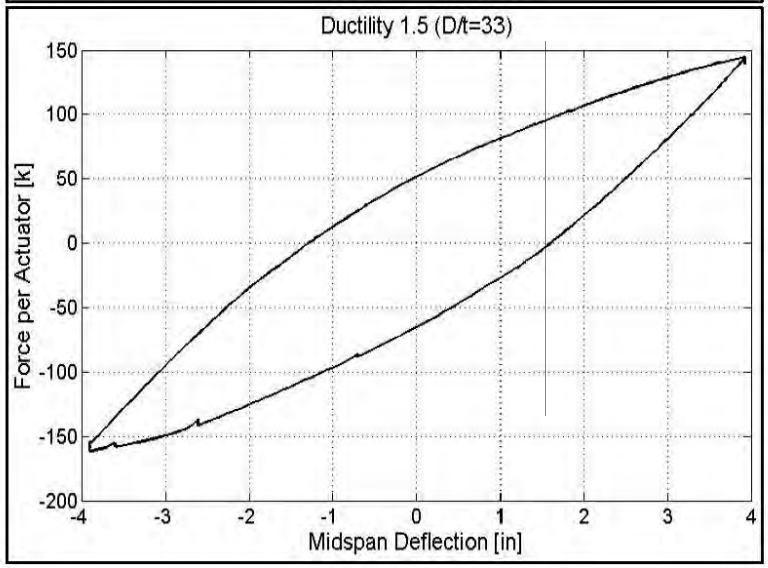
Ductility 1.5 (D/t=33)
Force per Actuator [k]
Midspan Deflection [in]

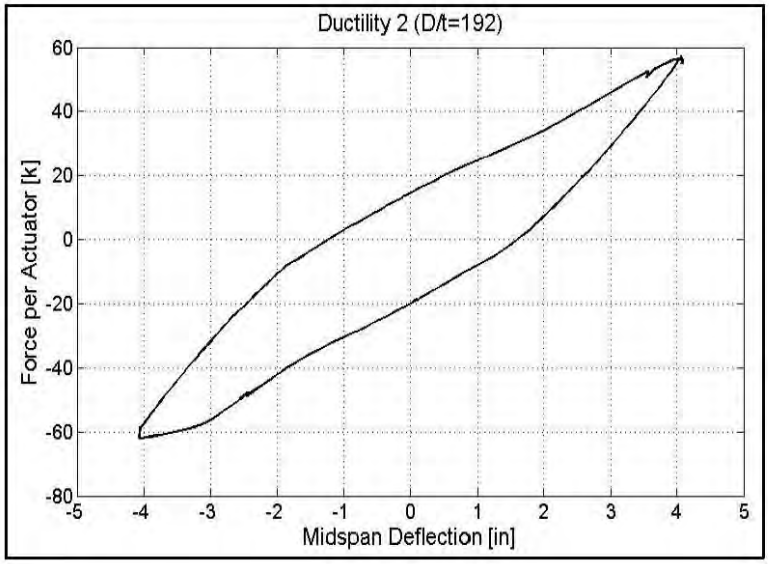
Ductility 2 (D/t=192)
Force per Actuator [k]
Midspan Deflection [in]

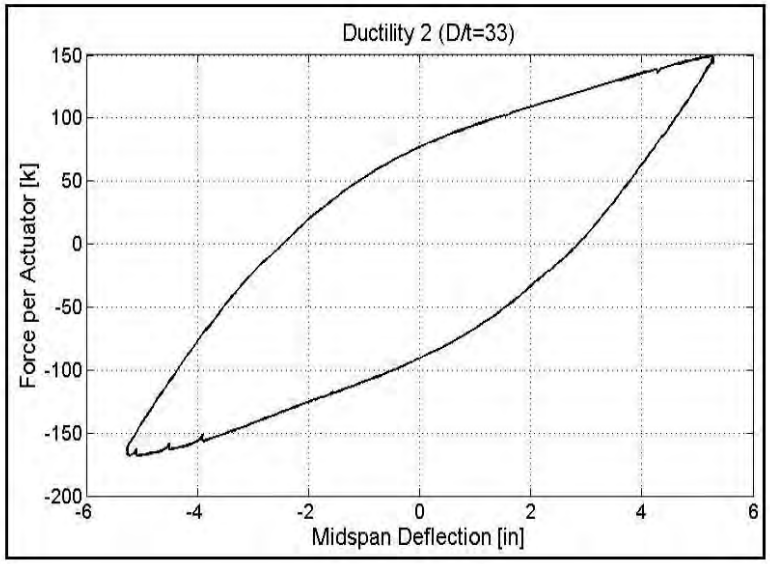
Ductility 2 (D/t=33)
Force per Actuator [k]
Midspan Deflection [in]


Ductility 3 (D/t=192)
Force per Actuator [k]
Midspan Deflection [in]

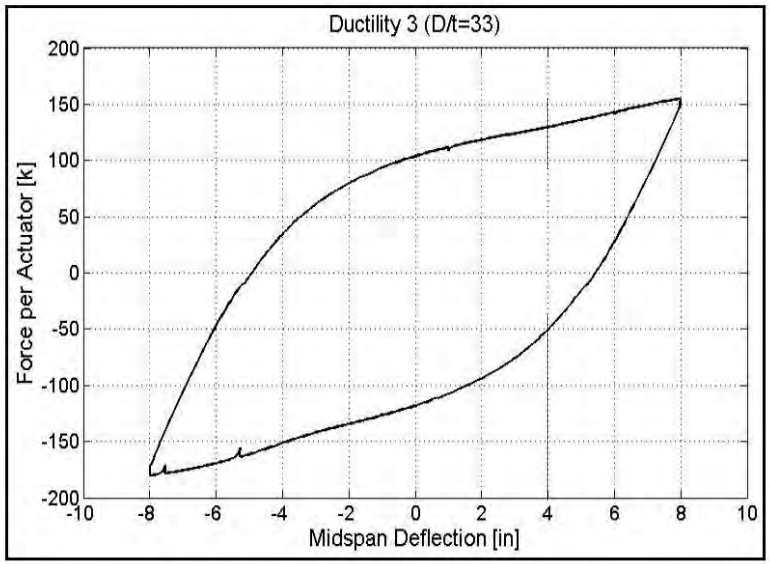
Ductility 3 (D/t=33)
Force per Actuator [k]
Midspan Deflection [in]

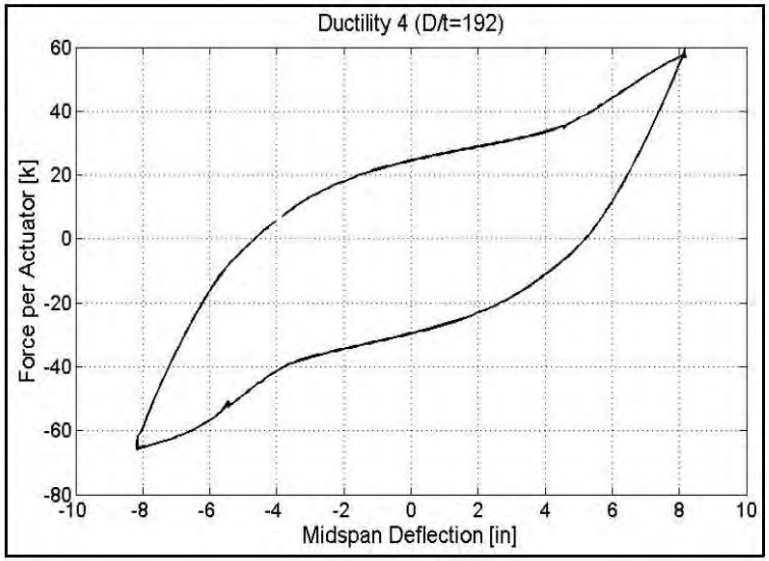
Ductility 4 (D/t=192)
Force per Actuator [k]
Midspan Deflection [in]

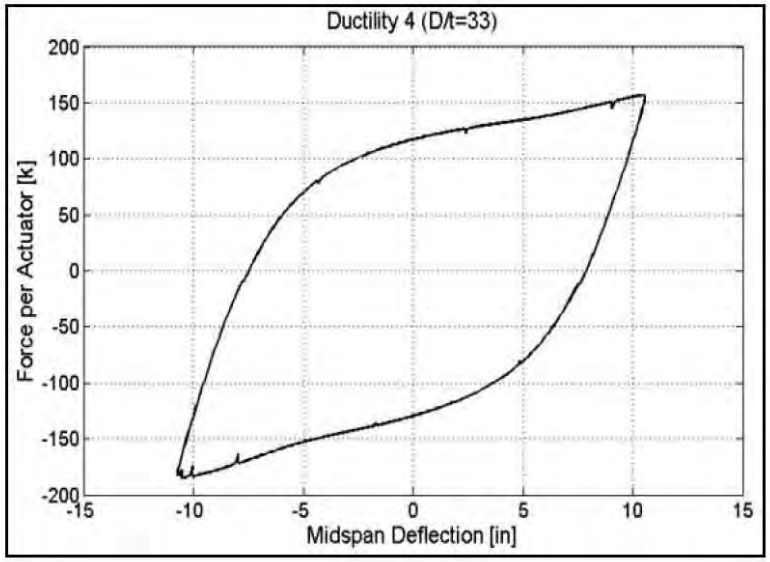
Ductility 4 (D/t=33)
Force per Actuator [k]
Midspan Deflection [in]

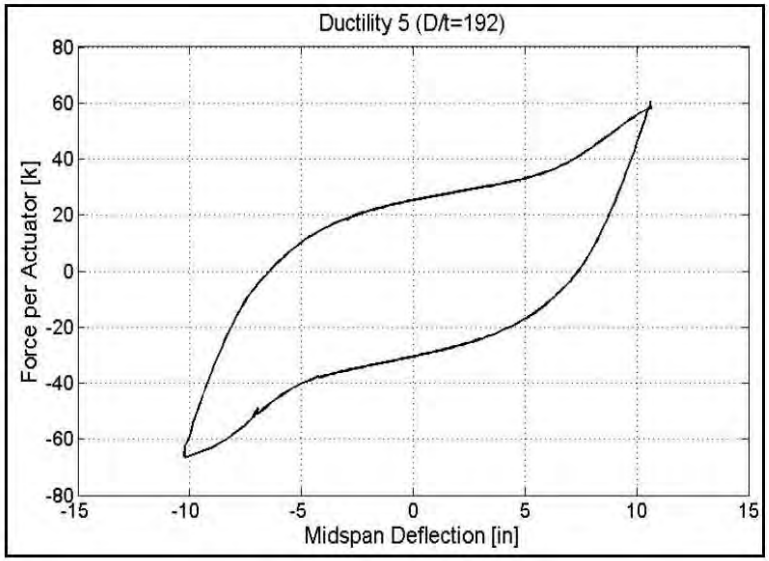
Ductility 5 (D/t=192)
Force per Actuator [k]
Midspan Deflection [in]

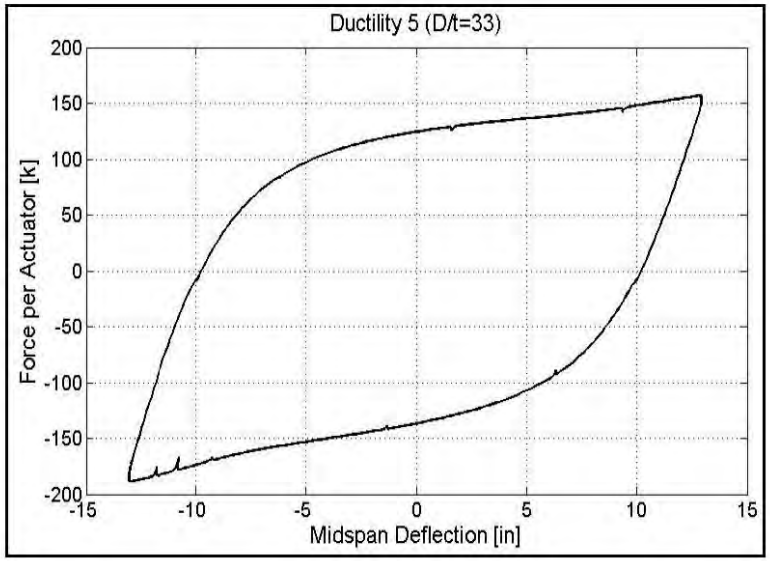
Ductility 5 (D/t=33)
Force per Actuator [k]
Midspan Deflection [in]

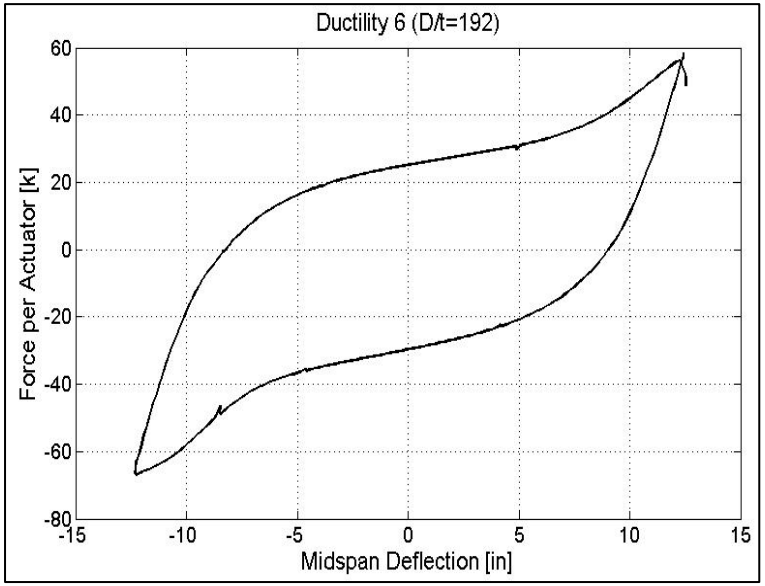
Ductility 6 (D/t=192)
Force per Actuator [k]
Midspan Deflection [in]
60
40
20
0
-20
-40
-60
-80
-15
-10
-5
0
5
10
15

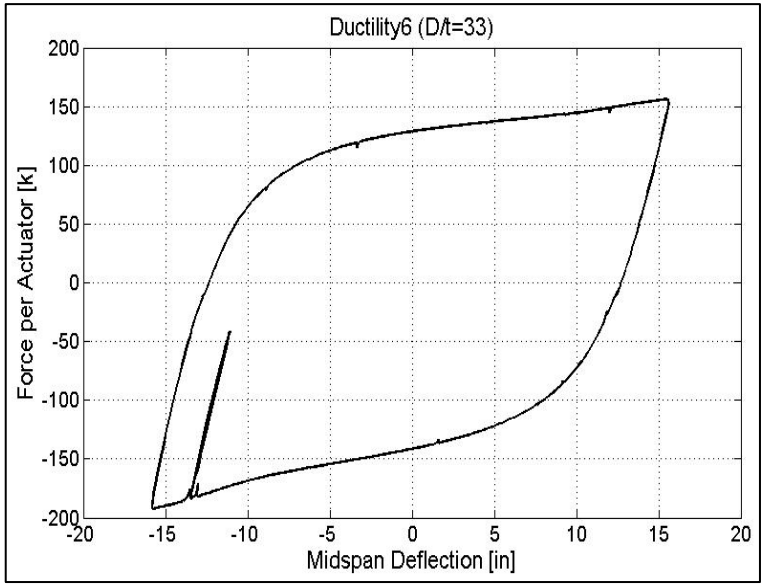
Ductility6 (D/t=33)
Force per Actuator [k]
Midspan Deflection [in]
200
150
100
50
0
-50
-100
-150
-200
-20
-15
-10
-5
0
5
10
15
20

The hysteretic damping coefficient with respect to the D/t ratio is shown in Figure 4-52. As was observed in the force-displacement loops, the D/t ratio affected the energy dissipation of the system and thus the hysteretic damping coefficient. The damping coefficients ranged from 14.8% for a D/t of 192 to 26.5% for a D/t of 33 at the sixth displacement ductility. The effect of the internal reinforcement ratio on the hysteretic damping of the concrete filled steel tubes was also calculated. Figure 4-55 plots the hysteretic damping coefficient with respect to the displacement capacity at different levels of internal reinforcement for D/t ratios of 128, 160, and 192 respectively. As seen in the figures, the damping coefficient curves are approximately the same for a given D/t ratio at all levels of internal reinforcement. This is because the cracking behaviors, and thus, the force-displacement loops, are approximately the same.

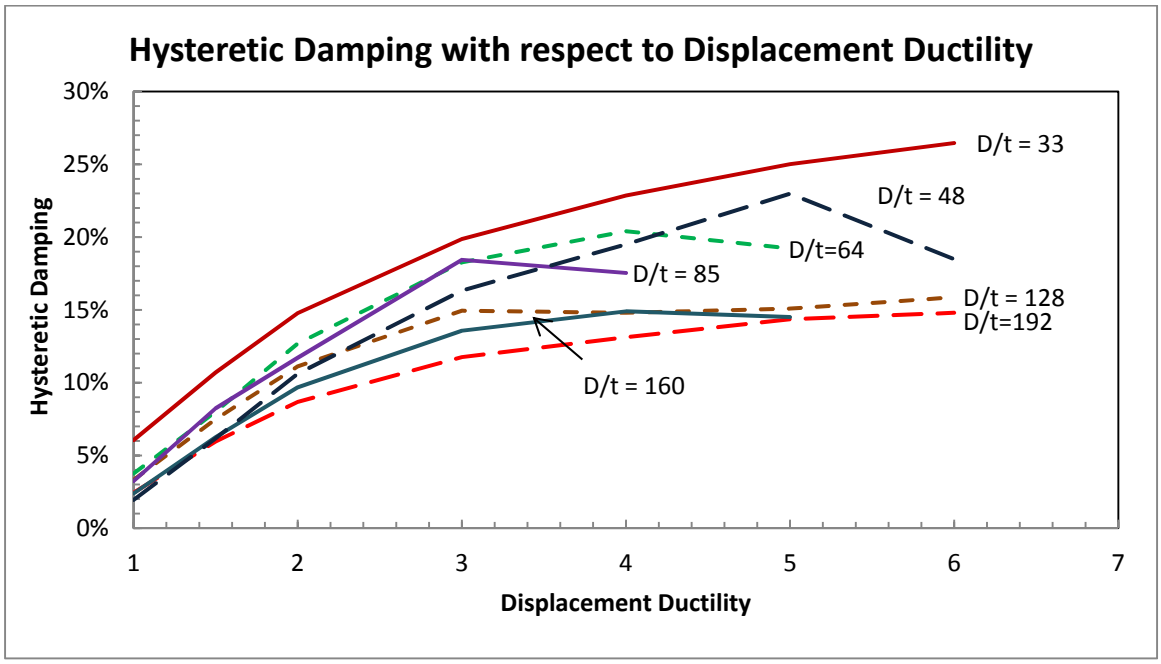

Figure 4-52 Jacobsen's Hysteretic Damping coefficient with respect to D/t ratio

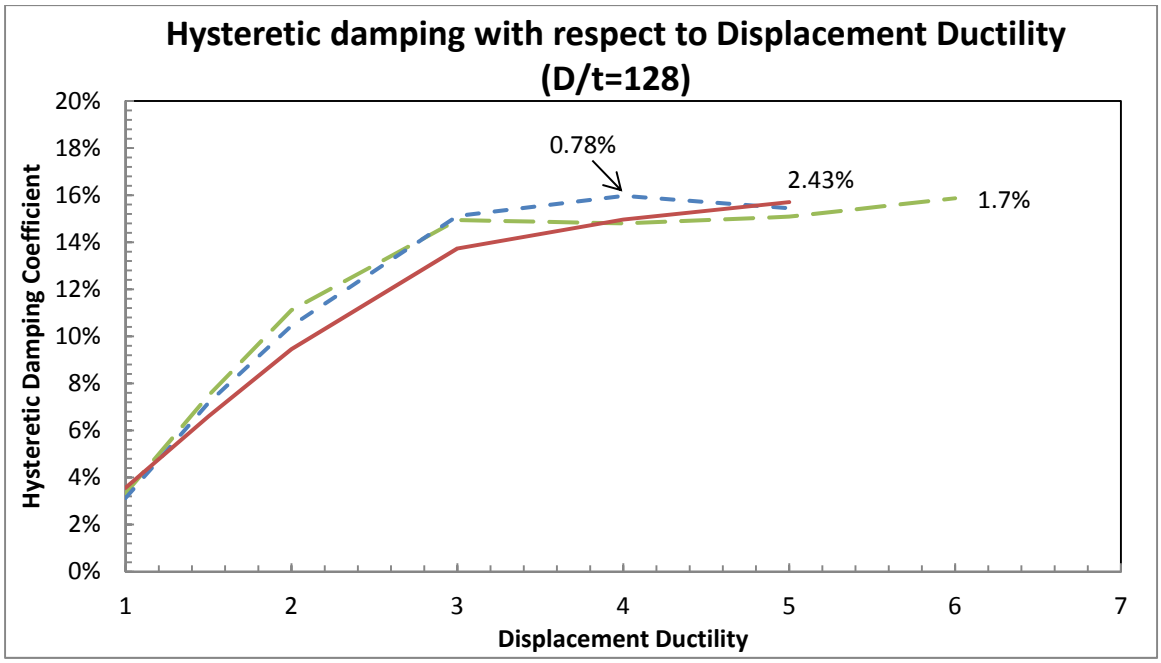

Figure 4-53 Hysteretic damping with respect to displacement ductility (D/t =128)

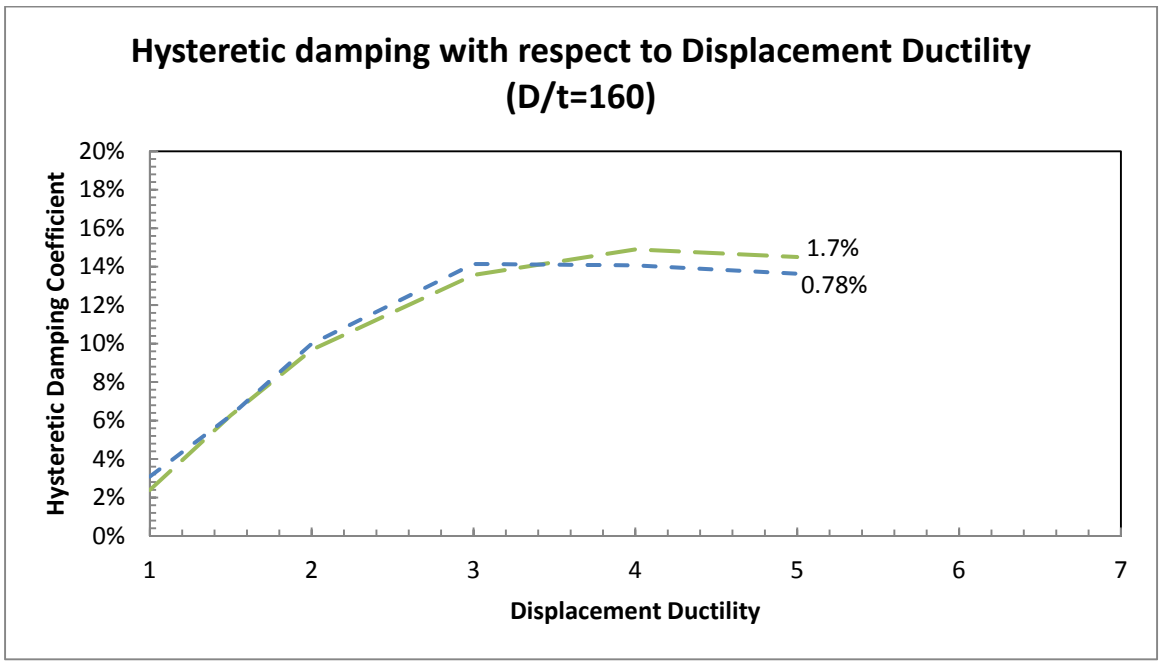

Figure 4-54 Hysteretic damping with respect to Displacement Ductility (D/t = 160)

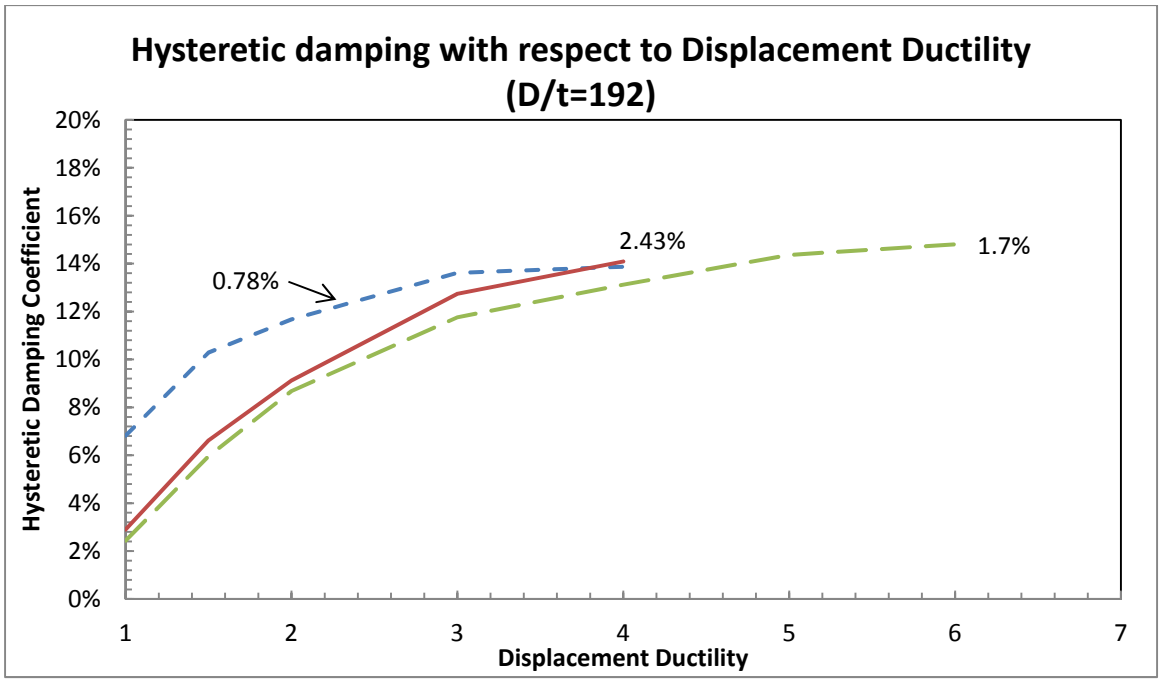

Figure 4-55 Hysteretic damping with respect to Displacement Ductility (D/t = 192)

Jacobsen's approach has good agreement with time history results for systems with low levels of energy dissipation in the hysteretic response. However, it did not have good agreement with systems that had a high level of energy dissipation. Correction factors were applied to Jacobsen's approach to accurately predict time history analyses for systems with low and high energy dissipation. The correction factor is a ratio of the hysteretic component of the equivalent viscous damping found from time-history analysis and Jacobsen's damping (area based equivalent viscous damping). The ratios depend on the value of Jacobsen's damping, the displacement ductility; the correction factors range from 0.2 to 1.2. The corrected hysteretic damping coefficients for varying D/t ratios are shown in Figure 4-56. The trend is the same as seen previously but the values have decreased due to the correction factors. Figure 4-57, Figure 4-58 and Figure 4-59 show the corrected hysteretic damping coefficients for varying internal reinforcement ratios at a given D/t.

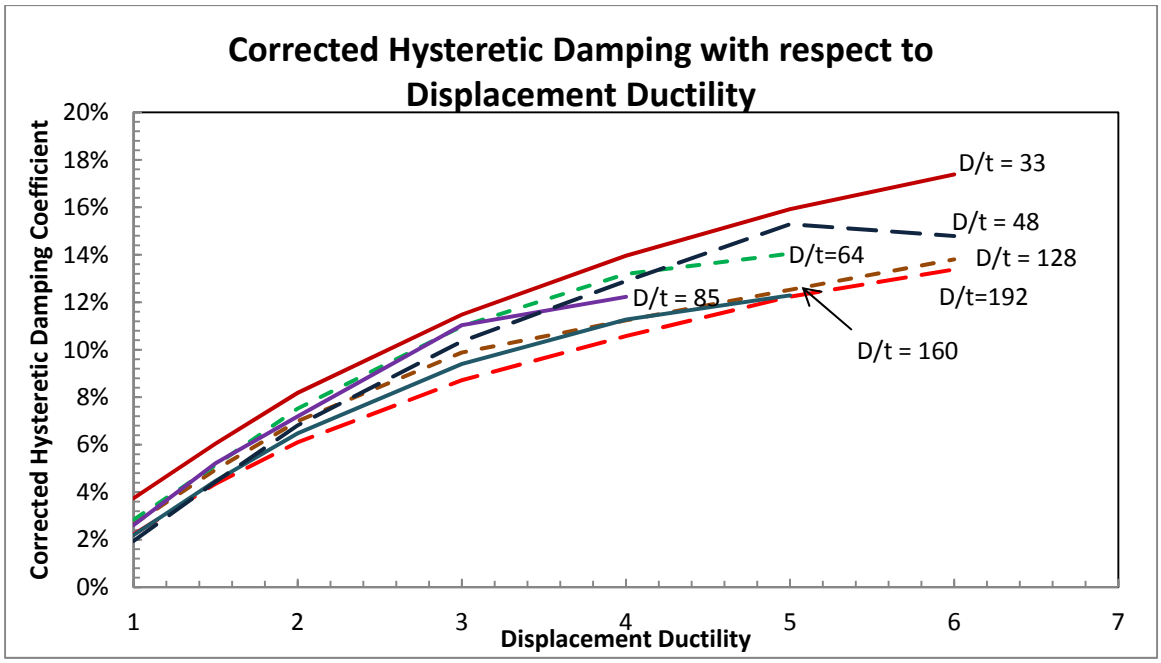

Figure 4-56 Corrected Hysteretic Damping with respect to Displacement Ductility

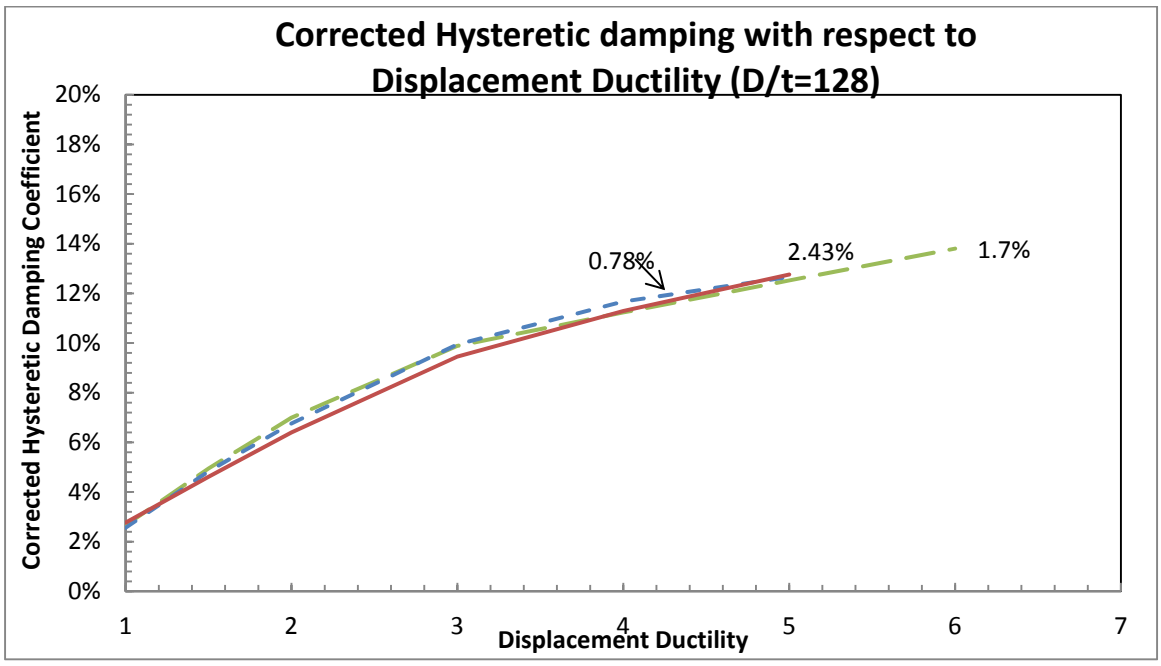

Figure 4-57 Corrected Hysteretic Damping with respect to Displacement Ductility (D/t=128)

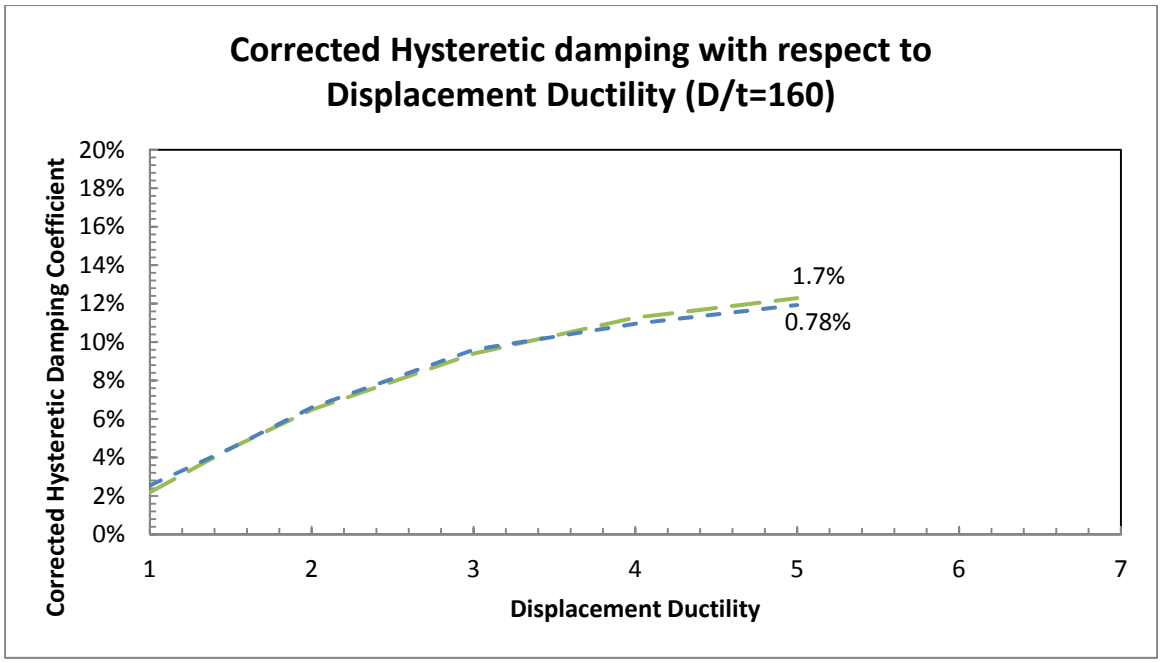

Figure 4-58 Corrected Hysteretic Damping with respect to Displacement Ductility (D/t=160)

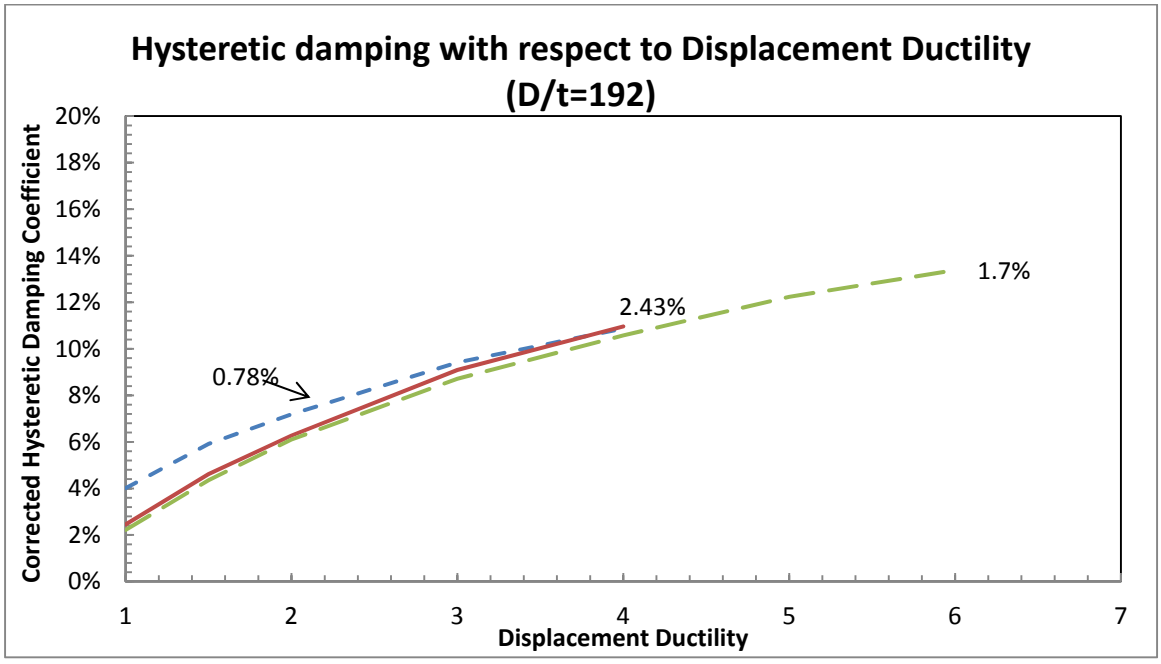

Figure 4-59 Corrected Hysteretic Damping with respect to Displacement Ductility (D/t=192)

The above figures demonstrate that the D/t ratios have an effect on the energy absorption and equivalent viscous damping of a concrete filled steel tube and the internal reinforcement ratio does not affect this aspect of its behavior. The equivalent viscous damping coefficients are expressed as a function of displacement ductility level and D/t ratio in Equation 4-14 and 15. This equation is graphed for various levels of D/t ratios in Figure 4-60. The comparison of this expression with the experimental test results is shown in Figure 4-61. This expression does cover a large range of D/t ratios but has only been verified for this range (D/t=33 to 192) and up to the sixth displacement ductility level.

$$\xi = (-0.0001(D/t) + 0.08)\ln(\mu) + 0.02 \qquad \textbf{Equation 4-14}$$

$$\xi = (-0.001(D/t) + 0.8) * (\mu - 1)/(\pi\mu + 9.1) + 0.02 \qquad \textbf{Equation 4-15}$$

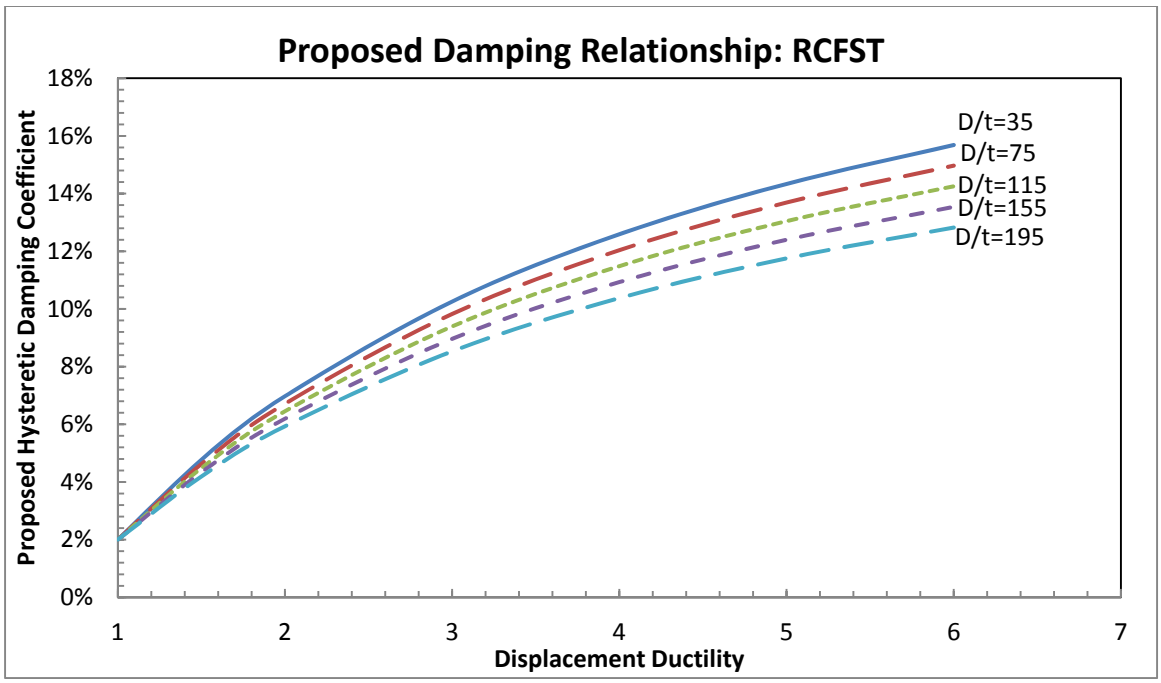

Figure 4-60 Proposed Damping Relationship for varying D/t ratios

Figure 4-61 Comparison of proposed damping relationship with experimental results

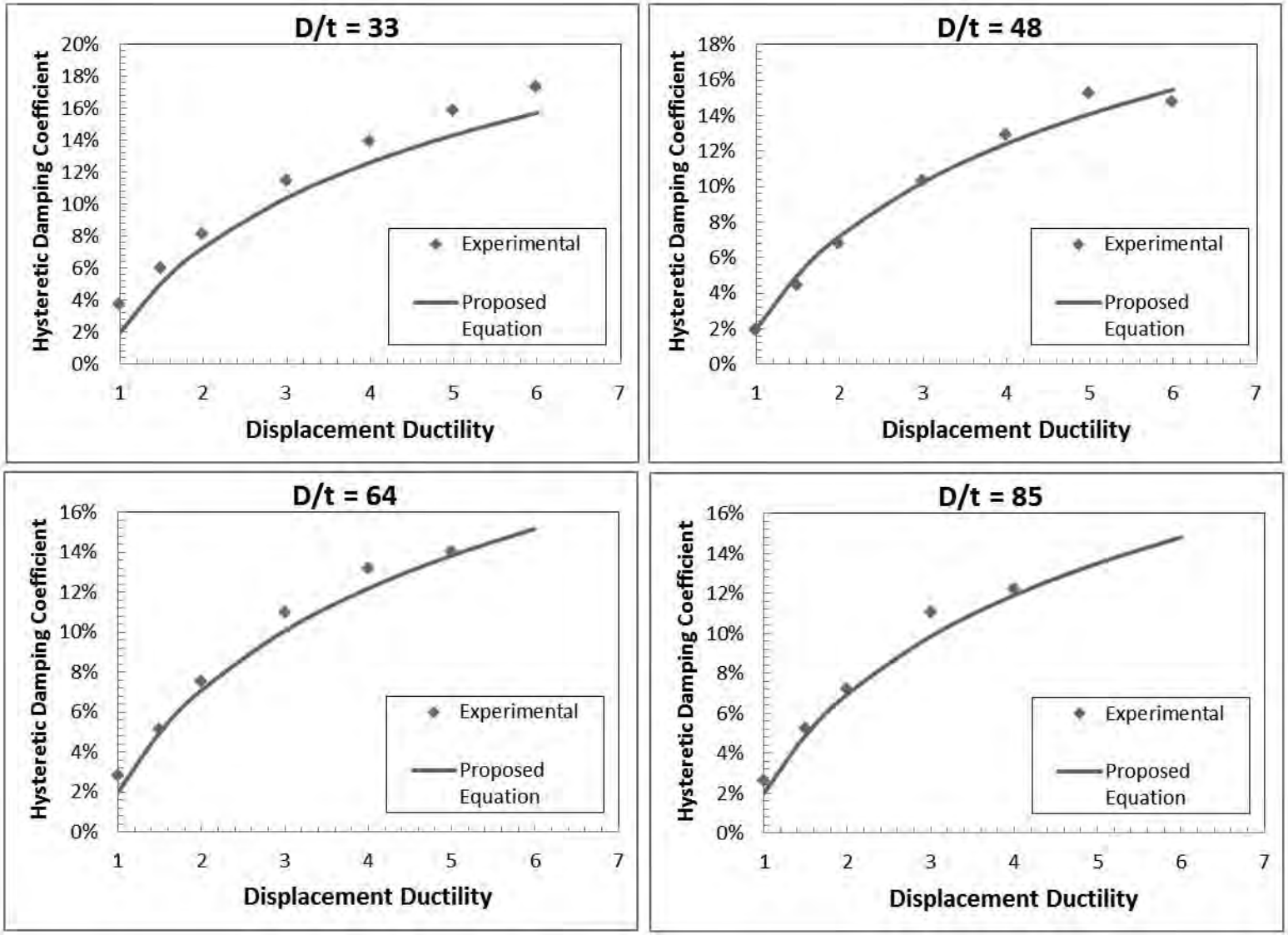
D/t = 33
Hysteretic Damping Coefficient
20%
18%
16%
14%
12%
10%
8%
6%
4%
2%
0%
1
2
3
4
5
6
7
Displacement Ductility
Experimental
Proposed Equation
D/t = 48
Hysteretic Damping Coefficient
18%
16%
14%
12%
10%
8%
6%
4%
2%
0%
1
2
3
4
5
6
7
Displacement Ductility
Experimental
Proposed Equation
D/t = 64
Hysteretic Damping Coefficient
16%
14%
12%
10%
8%
6%
4%
2%
0%
1
2
3
4
5
6
7
Displacement Ductility
Experimental
Proposed Equation
D/t = 85
Hysteretic Damping Coefficient
16%
14%
12%
10%
8%
6%
4%
2%
0%
1
2
3
4
5
6
7
Displacement Ductility
Experimental
Proposed Equation

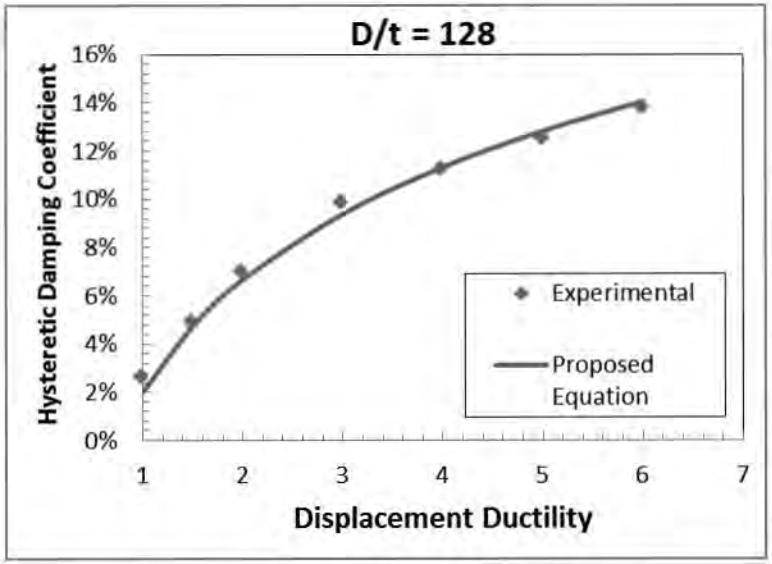
D/t = 128
Hysteretic Damping Coefficient
16%
14%
12%
10%
8%
6%
4%
2%
0%
1
2
3
4
5
6
7
Displacement Ductility
Experimental
Proposed Equation

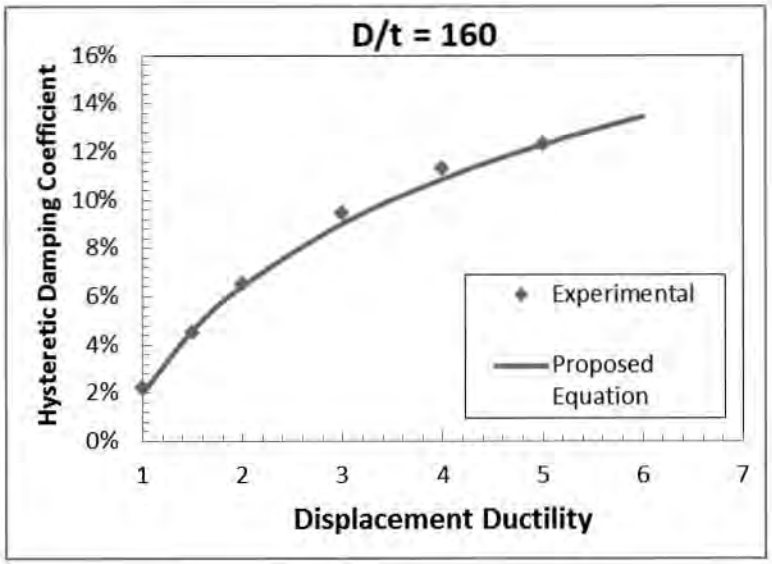
D/t = 160
Hysteretic Damping Coefficient
16%
14%
12%
10%
8%
6%
4%
2%
0%
1
2
3
4
5
6
7
Displacement Ductility
Experimental
Proposed Equation

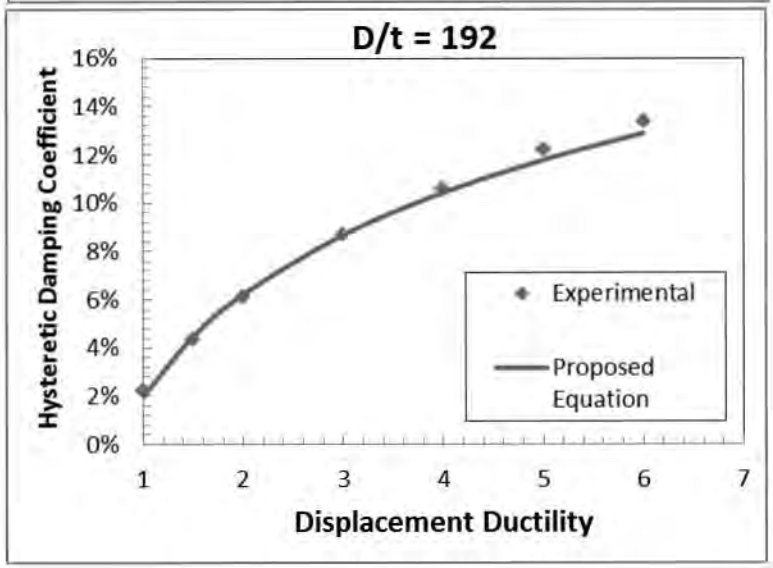
D/t = 192
Hysteretic Damping Coefficient
16%
14%
12%
10%
8%
6%
4%
2%
0%
1
2
3
4
5
6
7
Displacement Ductility
Experimental
Proposed Equation

4.4.3. Elastic Damping

As mentioned previously, damping is composed of two portions: hysteretic damping and elastic damping. Elastic damping is used in inelastic time-history analysis to represent damping not captured by the hysteretic model adopted for the analysis. The main factor that contributes to this is assuming that the hysteretic model has a perfectly linear response in the elastic range; however there is some amount of non-linearity in the elastic portion of a hysteresis. Grant et al compared results of elastic substitute-structure analyses with inelastic time history results to determine how to combine the elastic and viscous hysteretic damping. He concluded that simply summing them was not adequate, and created a factor to be applied to the elastic damping before adding it to the equivalent viscous damping. The expression created by Grant is shown in Equation 4-16. The correction factor (κ) is a function of displacement ductility (μ) and an elastic damping assumption (λ), shown in Equation 4-17.

$$\xi_{eq} = \kappa\xi_{el} + \xi_{hyst} \qquad \textbf{Equation 4-16}$$

$$\kappa = \mu^{\lambda} \qquad \textbf{Equation 4-17}$$

The variable, λ, depends on the hysteresis rule and elastic damping assumption. Figure 4 – 62 compares the "thin" takeda and "fat" takeda assumptions at the highest ductility level reached by each D/t ratio. As seen in the figure, the thin takeda model was a better assumption for the majority of the D/t ratios. The values of λ for the models are close to one another, as seen in Table 4-10. Since the "thin" takeda model was a better assumption overall, was used for calculating the total equivalent damping.

The expression for total equivalent damping created after taking the elastic damping into account is shown in Equation 4-18 and Equation 4-19. As seen in Figure 4-63, the initial damping at ductility one increases from 2% to 7% for all D/t ratios.

Current equations for other structural systems typically start at 5% damping, and to retain consistency with those other system, $\boldsymbol{\xi = (-0.00082(D/t) + 0.079)\ln(\mu) + 0.05}$ Equation 4-20 or $\boldsymbol{\xi = (-0.00072(D/t) + 0.78) * (\mu - 1)/(\pi\mu + 8.9) + 0.05}$ Equation 4-21 may be used. Note that this equation will underestimate the damping in the low ductility range, when compared to experimental results.

Figure 4-62 Comparison of hysteretic loops with thin and fat takeda models

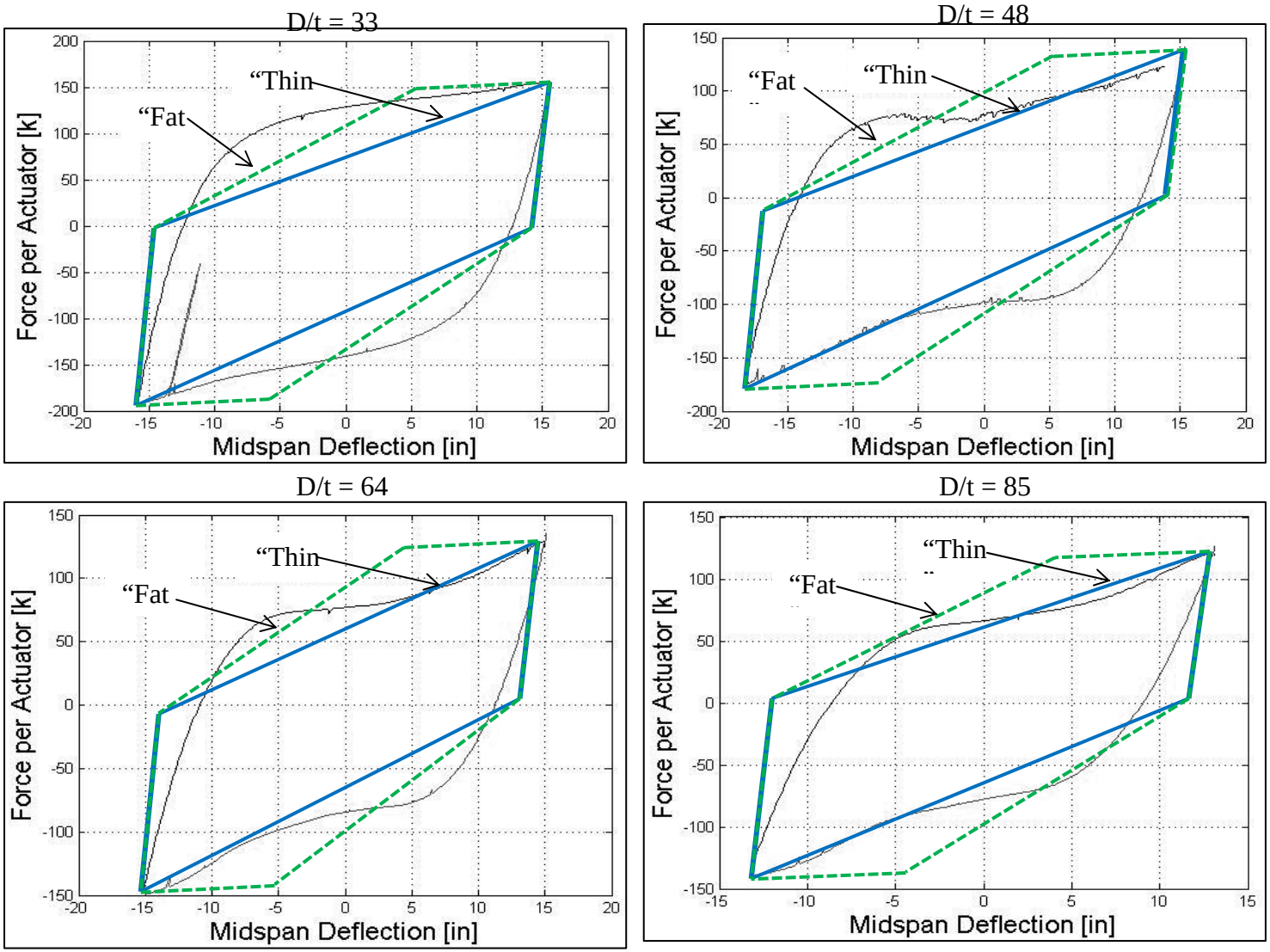
D/t = 33
"Thin
"Fat
Force per Actuator [k]
Midspan Deflection [in]
D/t = 48
"Fat
"Thin
Force per Actuator [k]
Midspan Deflection [in]
D/t = 64
"Thin
"Fat
Force per Actuator [k]
Midspan Deflection [in]
D/t = 85
"Thin
"Fat
Force per Actuator [k]
Midspan Deflection [in]

D/t = 128

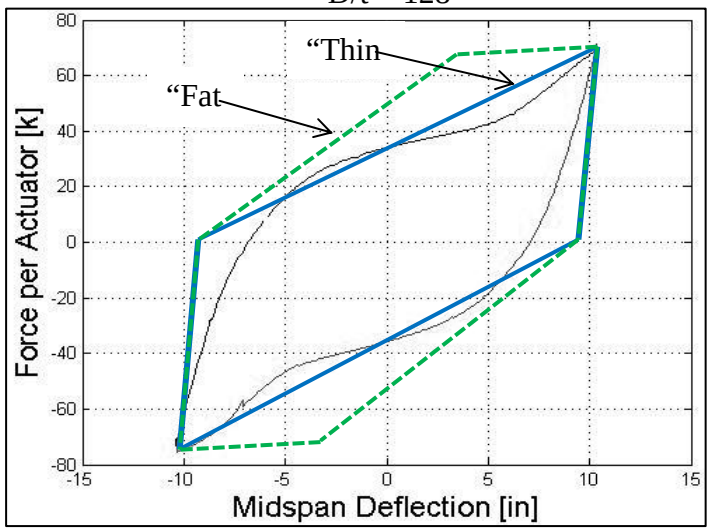

D/t = 160

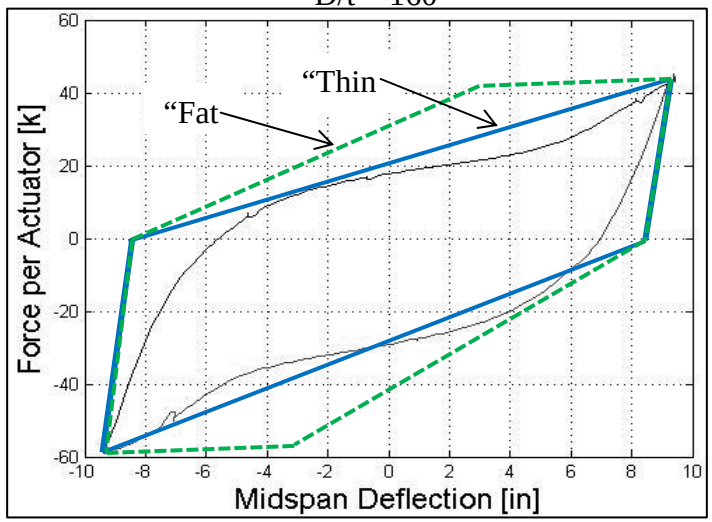

D/t = 192

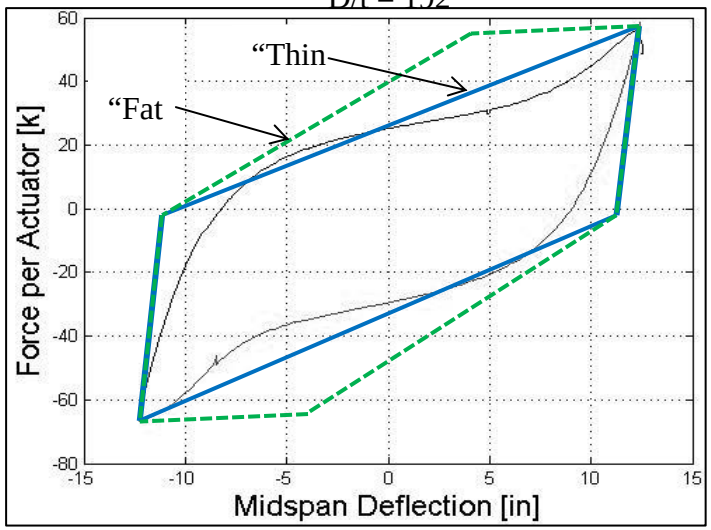

Table 4-10 Values of λ for Thin and Fat Takeda

	Initial Stiffness	Tangent Stiffness
Takeda Thin (TT)	0.340	-0.378
Takeda Fat (TF)	0.312	-0.313

$$\xi = (-0.00012(D/t) + 0.072)\ln(\mu) + 0.07 \quad \textbf{Equation 4-18}$$

$$\xi = (-0.001(D/t) + 0.85) * (\mu - 1)/(\pi\mu + 10.5) + 0.07 \quad \textbf{Equation 4-19}$$

$$\xi = (-0.00082(D/t) + 0.079)\ln(\mu) + 0.05 \quad \textbf{Equation 4-20}$$

$$\xi = (-0.00072(D/t) + 0.78) * (\mu - 1)/(\pi\mu + 8.9) + 0.05 \quad \textbf{Equation 4-21}$$

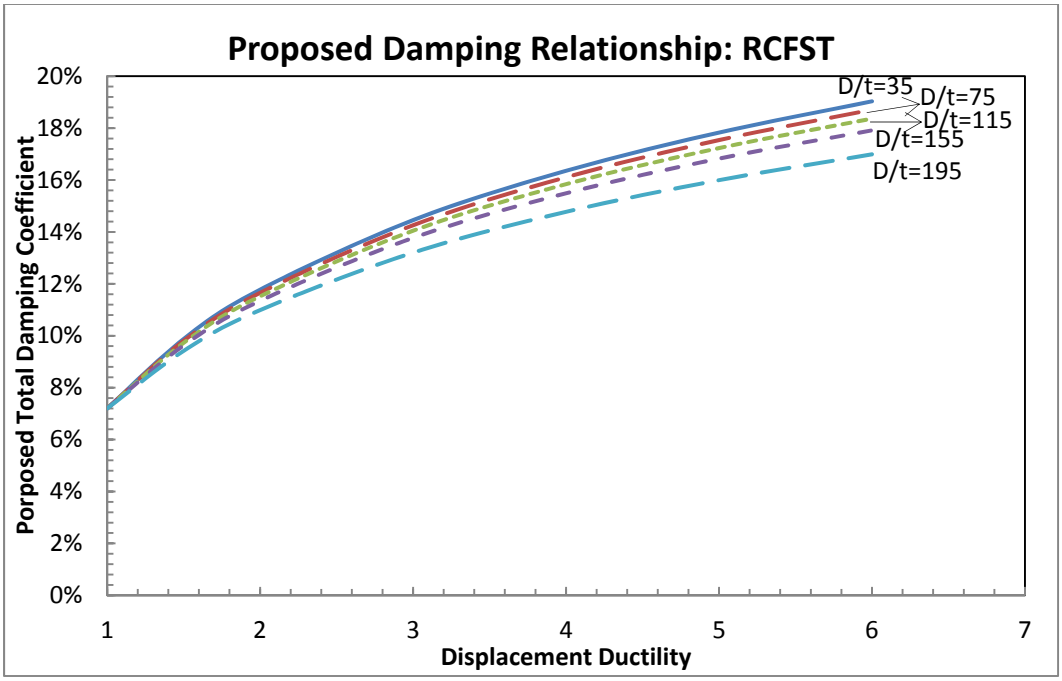

Figure 4-63 Proposed Total Damping Relationship

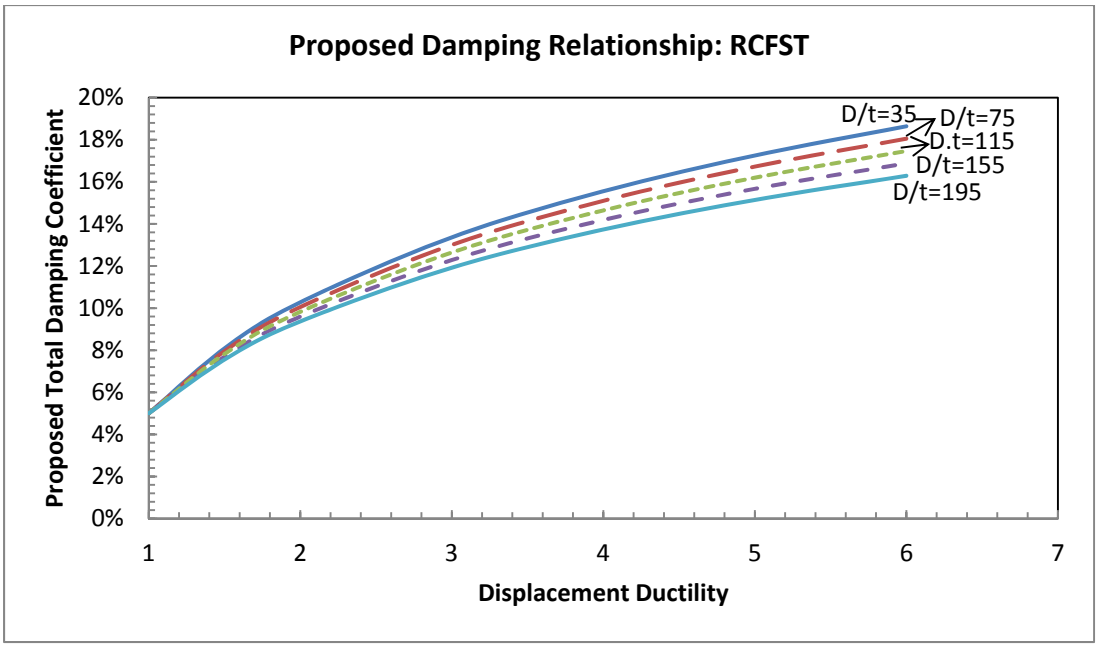

Figure 4-64 Proposed Total Damping (modified)

CHAPTER 5 PLASTIC HINGE LENGTH

5.1. Definition

Calculating displacements from strains and curvatures is an important step in displacement based design. Relating curvatures to displacements allows for the calculation of target displacements and for the generation of a force-displacement envelope. After yielding, the curvatures become nonlinear and calculating the displacements become more difficult. Integrating the curvature distribution about the top of the cantilever can be used to determine the displacement due to flexure in a cantilever (Equation 5-1). The plastic hinge length is an approximation of this method which separates the curvature distribution into two sections as seen in Figure 5-1.

$$\Delta = \int_0^L \Phi_{(l)} l \, dl \qquad \textbf{Equation 5-1}$$

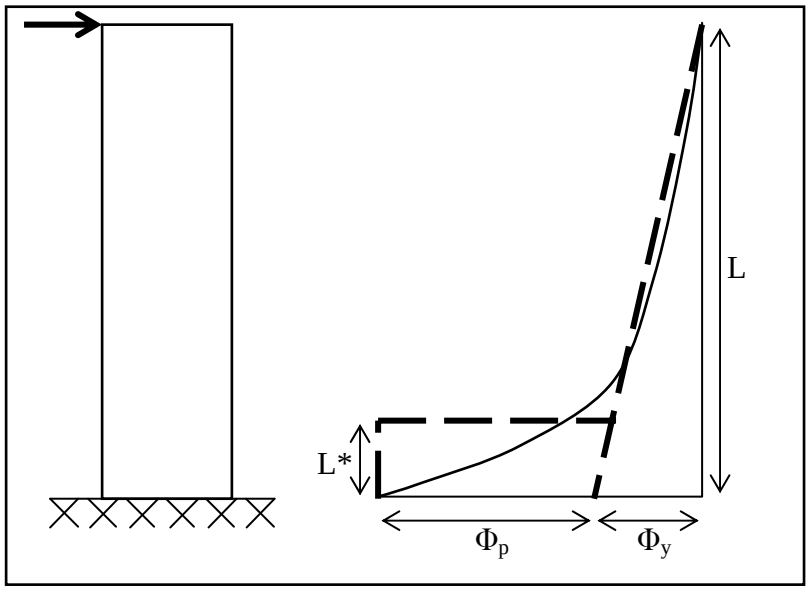

Figure 5-1 Plastic Hinge Length Diagram

Flexural displacement is not the only displacement observed in the displacement of typical reinforced concrete columns. The plastic hinge length includes two components: the first is the approximation of the length over which the curvature is at its maximum (L*) and the second is the strain penetration length. The expressions for each of the total plastic hinge length and the two components are shown in Equation 5-2, 5-3, and 5-4.

$$\mathbf{L_p = kL_c + L_{sp} \geq 2L_{sp}} \qquad \textbf{Equation 5-2}$$

$$L_{sp} = 0.022 f_{ye} d_{bl}[\text{MPa}] = 0.15 f_{ye} d_{bl}[\text{ksi}] \qquad \text{Equation 5-3}$$

$$k = 0.2(f_u/f_y - 1) \leq 0.08 \qquad \text{Equation 5-4}$$

The plastic hinge length expressions for concrete filled steel tubes are unknown. The experimental tests in this research project consisted of a constant moment region resulted in a region where the curvatures and strains were constant and the specimens were constant. This region essentially fixed the plastic hinge length.

5.2. Parametric Analyses

Analyses were performed to solve for the first part of the plastic hinge length expression (kLc) found in Equation 5-2. The total displacement was calculated by integrating the curvature diagram about the top of the cantilever, as demonstrated in Figure 5-2. The plastic hinge length due to the curvature distribution only (kL_c) was back calculated from the total displacement. The total displacement, which was integrated from the curvature distribution, can be broken down into yield and plastic displacement components (Equation 5-5). The yield and plastic displacements were calculated using Equation 5-6 and Equation 5-7. The combination of Equation 5-5 and 5-7 yields Equation 5-8 to solve for kLc.

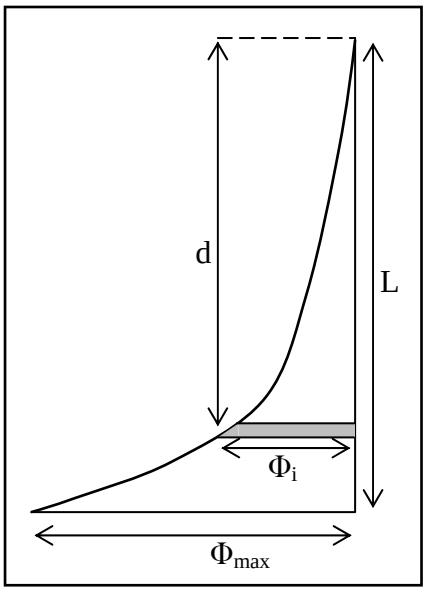

Figure 5-2 Integration of Curvature Diagram

$$\Delta = \Delta_y + \Delta_p \quad \text{Equation 5-5}$$

$$\Delta_y = \frac{\Phi_y L^2}{3} \quad \text{Equation 5-6}$$

$$\Delta_p = (\Phi - \Phi_y)(L)(kL) \quad \text{Equation 5-7}$$

$$kL = \left[\Delta - \frac{\Phi_y L^2}{3}\right] / [(\Phi - \Phi_{y)} L] \quad \text{Equation 5-8}$$

The plastic hinge length due to curvature distribution (kL) was calculated for multiple reinforcement ratios ranging from 0.75% to 3.75% and axial load ratios ranging from 0% to 15% for typical reinforced concrete cantilever columns and equivalent concrete filled steel tubes. The concrete filled steel tubes did not have any internal reinforcement, the tube thickness created a reinforcement ratio which was equal to that of the equivalent reinforced concrete section. The ratio of plastic hinge length due to curvature distribution to the total length of the column (k) for each axial load ratio is shown in Figure 5-3. The reinforced concrete columns are shown on the left of the figure for each combination of axial load and internal reinforcement ratios. The right side of the figure displays the comparison for the equivalent concrete filled steel tube columns. As seen in Equation 5-4, the maximum for the value 'k' is 0.08 for reinforced concrete columns. This is shown to be the average or maximum in the charts for the reinforced concrete columns in Figure 5-3.

The 'k' values for the concrete filled steel tubes do not have as much variation between the different reinforcement ratios. The average 'k' values for the CFSTs are approximately 0.4% greater than that of the reinforced concrete columns. This small difference will make an even smaller difference when inserted into the plastic hinge length equation. Without experimental tests to prove or disprove this data, it seems appropriate to use the convention reinforced concrete plastic length expressions for concrete filled steel tubes.

Concrete filled steel tubes are often used as piles, and serve as the column above ground and the foundation below ground. The below ground plastic hinge length will be dependent on the stiffness of the soil as well as the geometric properties. In-situ tests should be performed on concrete filled steel tubes to determine the effect of soil stiffness on the in-ground plastic hinge length.

Figure 5-3 Plastic Hinge Length Due to Curvature Distribution with respect to Curvature Ductility for RC and CFT cantilever columns

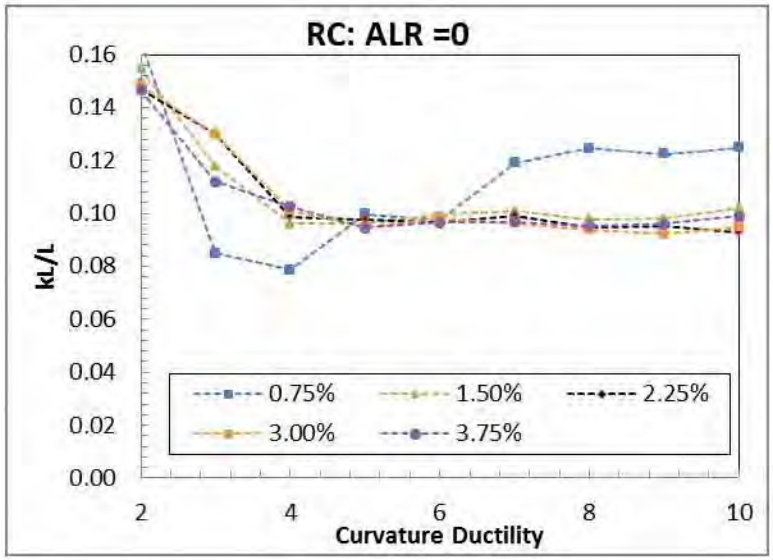
RC: ALR =0
kL/L
0.16
0.14
0.12
0.10
0.08
0.06
0.04
0.02
0.00
2
4
6
8
10
Curvature Ductility
0.75%
1.50%
2.25%
3.00%
3.75%

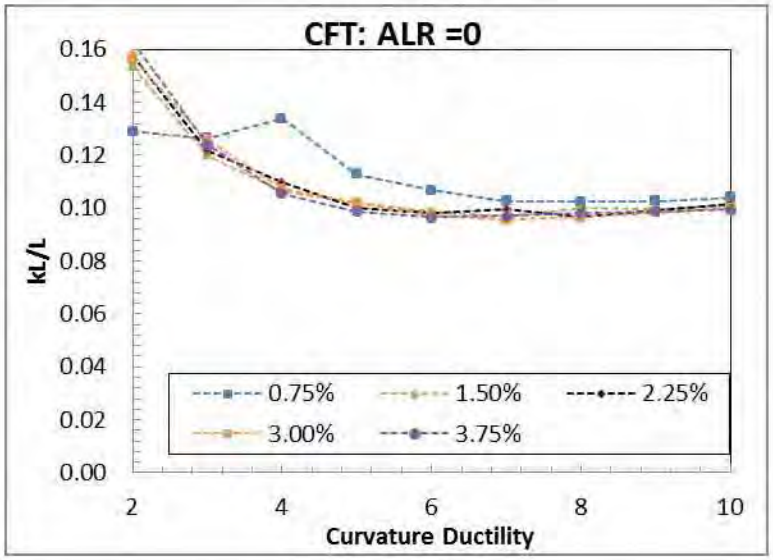
CFT: ALR =0
kL/L
0.16
0.14
0.12
0.10
0.08
0.06
0.04
0.02
0.00
2
4
6
8
10
Curvature Ductility
0.75%
1.50%
2.25%
3.00%
3.75%

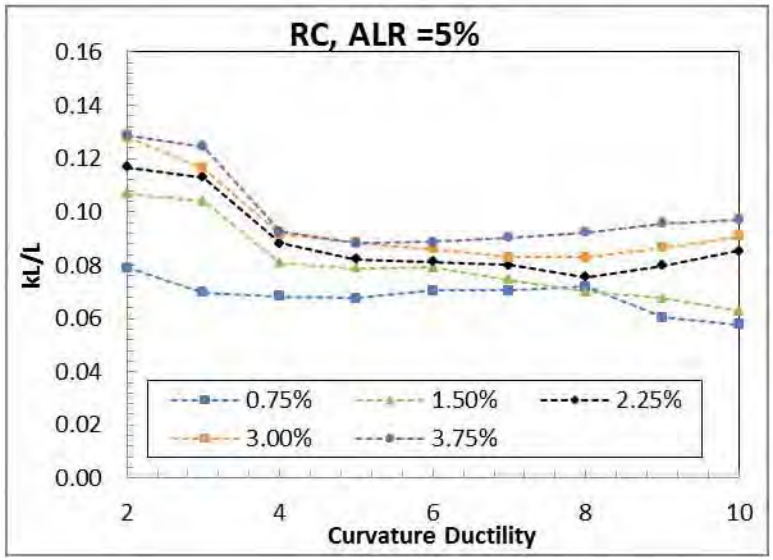
RC, ALR =5%
kL/L
0.16
0.14
0.12
0.10
0.08
0.06
0.04
0.02
0.00
2
4
6
8
10
Curvature Ductility
0.75%
1.50%
2.25%
3.00%
3.75%

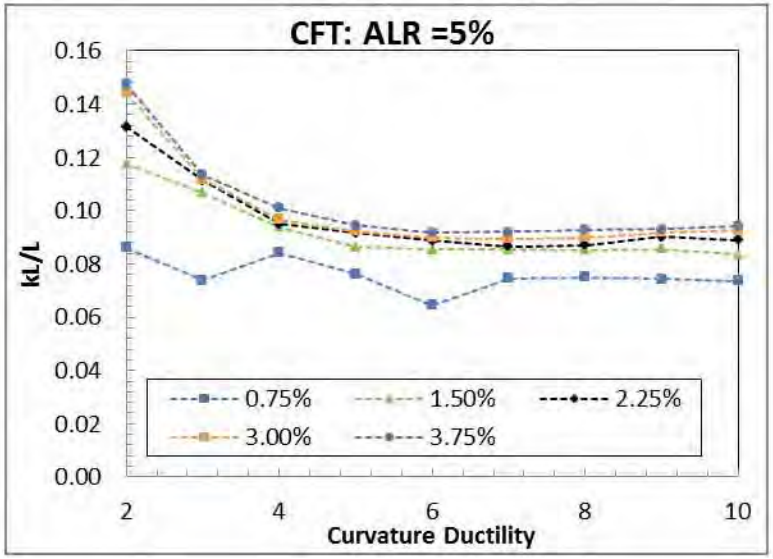
CFT: ALR =5%
kL/L
0.16
0.14
0.12
0.10
0.08
0.06
0.04
0.02
0.00
2
4
6
8
10
Curvature Ductility
0.75%
1.50%
2.25%
3.00%
3.75%

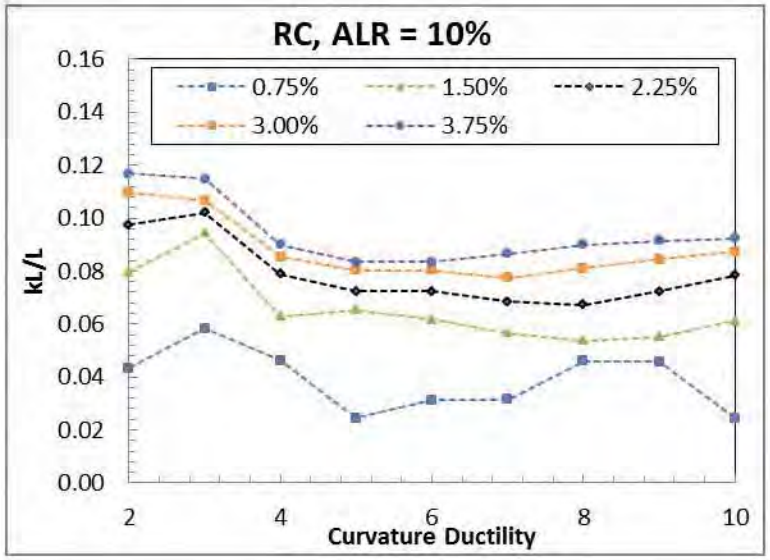
RC, ALR = 10%
0.75%
1.50%
2.25%
3.00%
3.75%
kL/L
0.16
0.14
0.12
0.10
0.08
0.06
0.04
0.02
0.00
2
4
6
8
10
Curvature Ductility

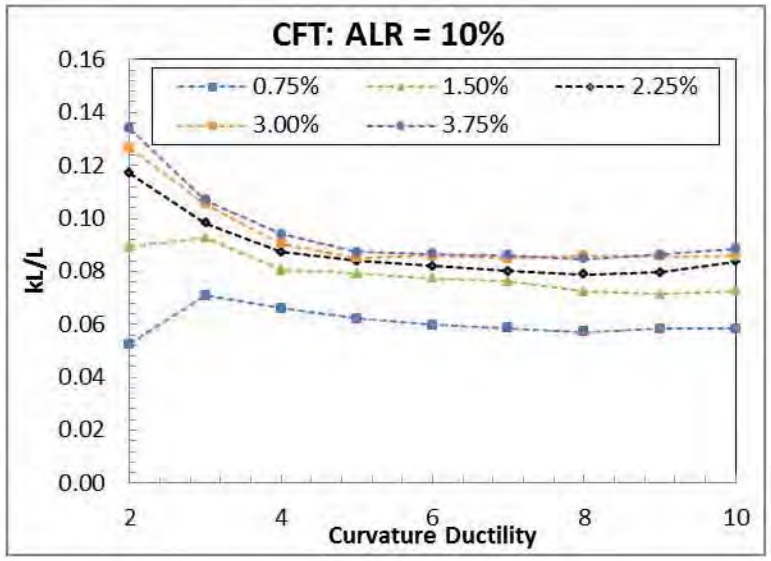
CFT: ALR = 10%
0.75%
1.50%
2.25%
3.00%
3.75%
kL/L
0.16
0.14
0.12
0.10
0.08
0.06
0.04
0.02
0.00
2
4
6
8
10
Curvature Ductility

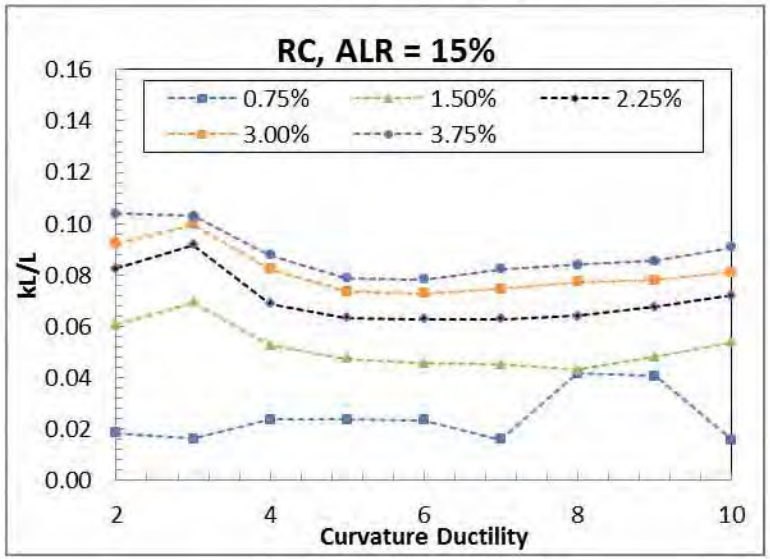
RC, ALR = 15%
0.75%
1.50%
2.25%
3.00%
3.75%
kL/L
0.16
0.14
0.12
0.10
0.08
0.06
0.04
0.02
0.00
2
4
6
8
10
Curvature Ductility

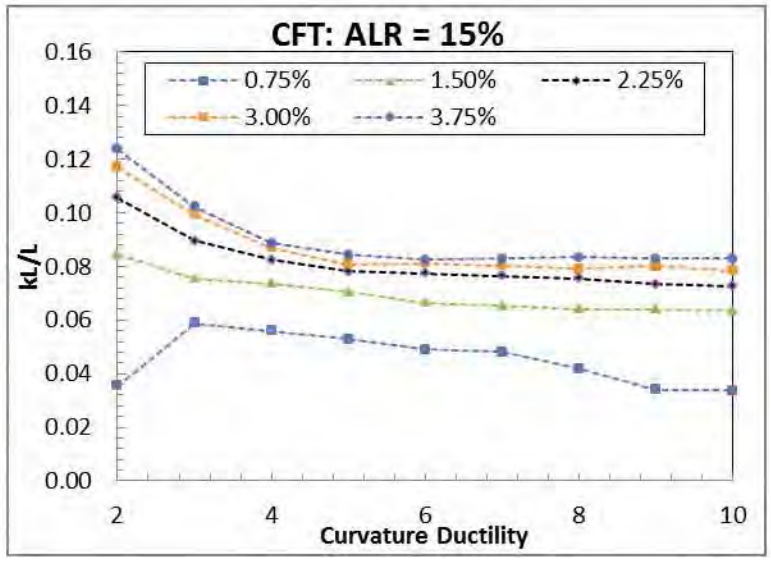
CFT: ALR = 15%
0.75%
1.50%
2.25%
3.00%
3.75%
kL/L
0.16
0.14
0.12
0.10
0.08
0.06
0.04
0.02
0.00
2
4
6
8
10
Curvature Ductility

CHAPTER 6 FINITE ELEMENT ANALYSIS

6.1. Model Description

ABAQUS Finite Element software was used to model the specimens tested in the experimental portion of the program under the same loading configuration. The specimens consisted of three materials: (1) the steel tube, (2) the concrete core, and (3) the internal reinforcing bars.

To decrease the computation time, the symmetry in the setup was used to simplify the model. The overall loading condition of the system before simplification is shown in Figure 6-1. The model was cut in half longitudinally, and the displacement in the 'z-direction' of the cut plane was restricted to zero, as seen in Figure 6-2. The model was then cut at mid-span; forcing the x-direction displacements to be zero. A roller allowing x-displacement was placed at the end of the model to allow the specimen to elongate and contract. The final simplified model is shown Figure 6-3.

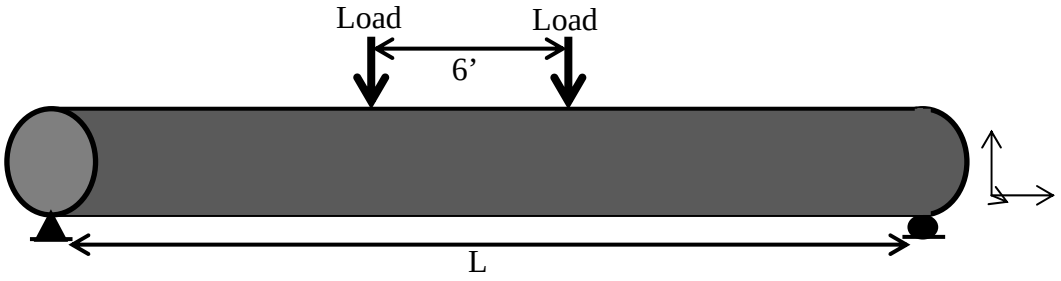

Figure 6-1 Full FEA Model before Simplification

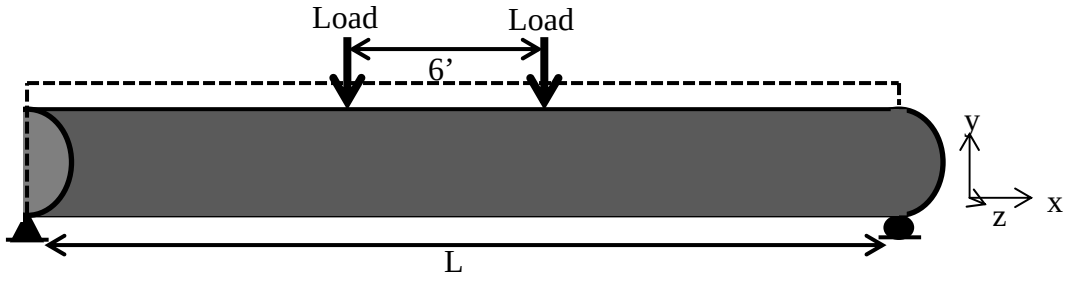

Figure 6-2 FEA model after first use of symmetry

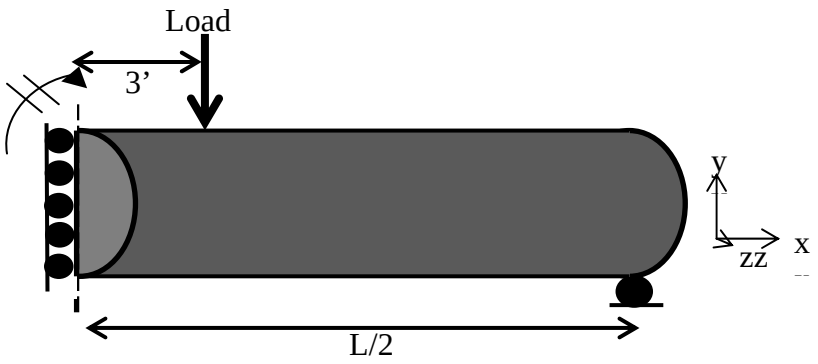

Figure 6-3 FEA model after second use of symmetry

6.2. **Material Models**

6.2.1. Steel Tube

The steel tube was modeled with 4-noded shell elements with 5 integration points through the thickness of the tube. The tensile tests from the experimental portion of the research program yielded a stress-strain curve which was directly used in ABAQUS. The elastic portion of the model was isotropic with Young's Modulus depending on the outcome of the tensile test and a Poisson's Ratio of 0.3. The plastic portion of the material model used a combined hardening method and the yield stresses and plastic strains were input from the results of the tensile test.

6.2.2. Concrete Core

The concrete core consisted of 8-node linear hexahedral elements. The elastic portion of the concrete model was defined with of a Young's modulus of 4300 ksi and a Poisson's ratio of 0. The concrete damaged plasticity model, found in ABAQUS, was utilized to model the plastic portion of the concrete response. The compressive behavior was defined using a yield stress one-half of the experimental concrete strength. The tensile behavior was defined using a yield stress one-tenth of the concrete strength and a cracking strain of 0. After the initial cracking, the tensile stress was set to zero. The following parameters defined the concrete damaged plasticity model: dilation angle of 30 degrees, eccentricity of 0.1, fb0/fc0 of 1.16, K of 0.67, and a viscosity parameter of zero.

6.2.3. Internal Reinforcing Bars

The internal reinforcing bars were modeled as 2-node beam elements. Tensile tests were also performed on the reinforcing bars during the experimental portion of this research program and the results from these tests were input to define Young's modulus and the stress-strain response after yielding.

6.3. Mesh

The meshes created on each of the individual parts correlated with one another in order to ensure compatibility between the materials. Outside of the plastic hinge region, the mesh spacing was set at six inches in length, and inside the constant moment region this mesh length was decreased to three inches to model the damage of the specimen. A figure of the mesh is shown in Figure 6-4.

Figure 6-4 Finite Element Mesh

6.4. Interactions

The major unknown in a concrete filled steel tube is the interaction between the steel tube and the concrete. The steel tube and the concrete core cannot be tied together because the tube would not be allowed to buckle and this type of interaction would force the strains to be compatible through the cross section which the experimental results proved to be a false assumption. Surface-to-surface contact with finite sliding was used to model the interaction between the steel and concrete. The tangential behavior was defined as a friction surface, using a coefficient of 0.5. Various friction coefficients were modeled but they had little impact on the behavior of the pile since the bearing pressure between the tube and core limits the amount of sliding. To model this bearing pressure, “hard” contact pressure was defined allowing separation after contact.

6.5. Monotonic Response

To create the response envelope for the cyclic tests, monotonic tests were performed in ABAQUS. The force, displacement, and strain results were compared for each specimen. Overall, the finite element results were in good agreement with the experimental tests. The force-displacement envelopes from ABAQUS are compared with the experimental data, for specimens with varying D/t ratios, during the first cycle of each displacement level in Figure 6-5. The tensile - strain displacement results from ABAQUS and the experimental tensile strains at the peak displacements for the first cycle of loading are shown in Figure 6-6. As

seen in the figures, the monotonic finite element model accurately predicts the force and strain response of the reinforced concrete filled steel tubes.

Figure 6-5 Comparison of Monotonic Force-displacement Envelopes from ABAQUS with experimental results

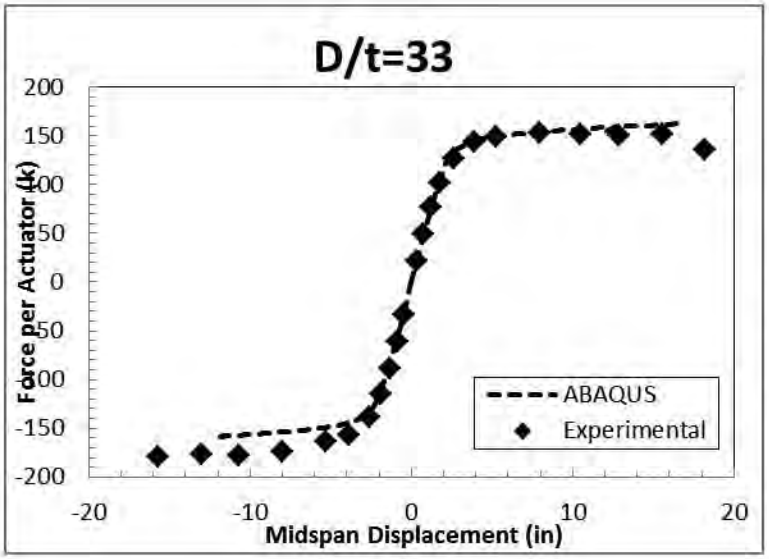
D/t=33
Force per Actuator (k)
Midspan Displacement (in)
ABAQUS
Experimental

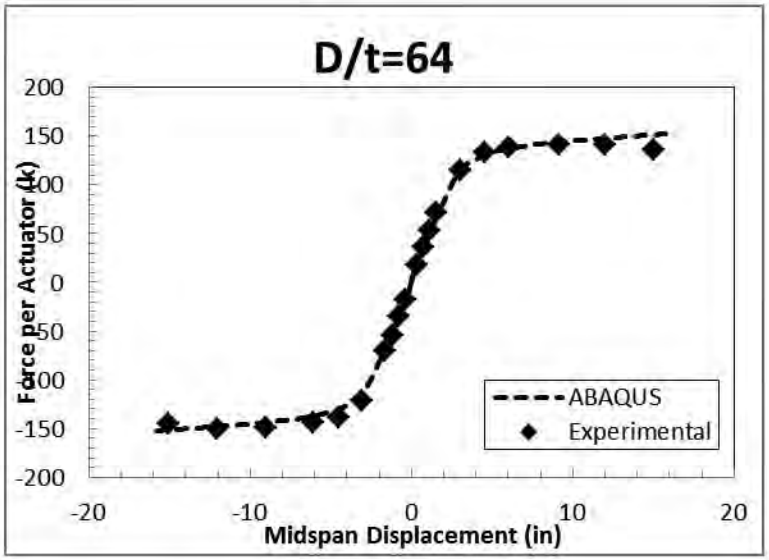
D/t=64
Force per Actuator (k)
Midspan Displacement (in)
ABAQUS
Experimental

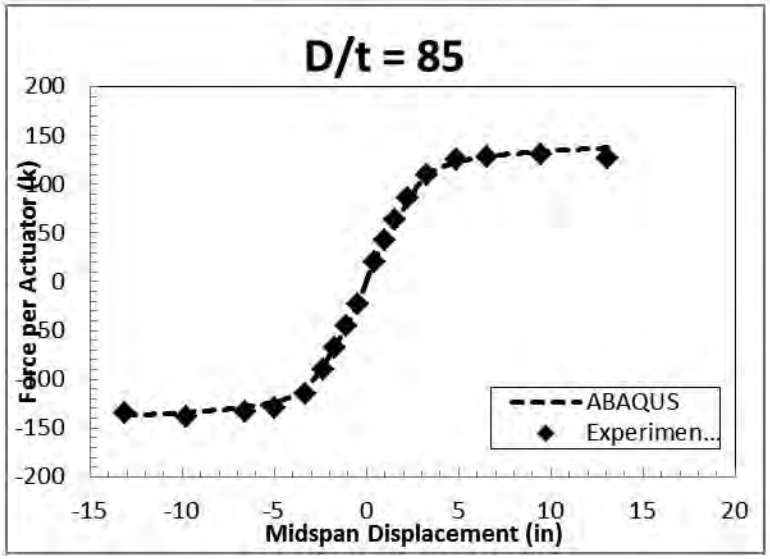
D/t = 85
Force per Actuator (k)
Midspan Displacement (in)
ABAQUS
Experimen...

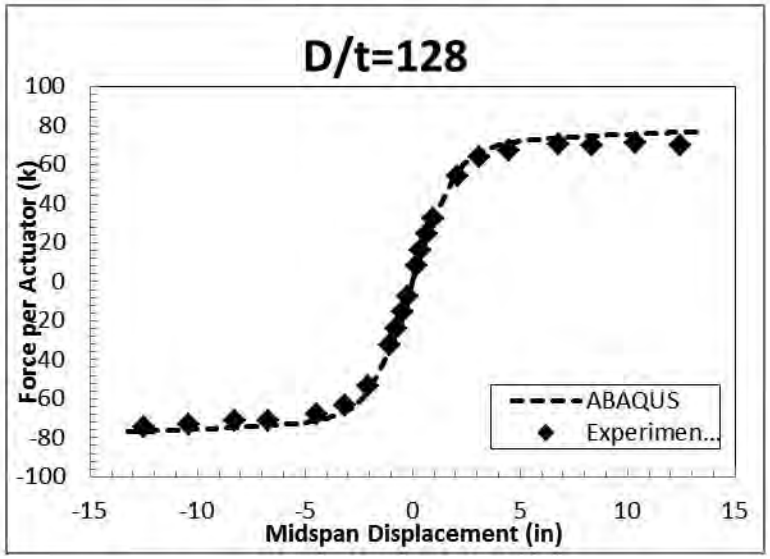
D/t=128
Force per Actuator (k)
Midspan Displacement (in)
ABAQUS
Experimen...

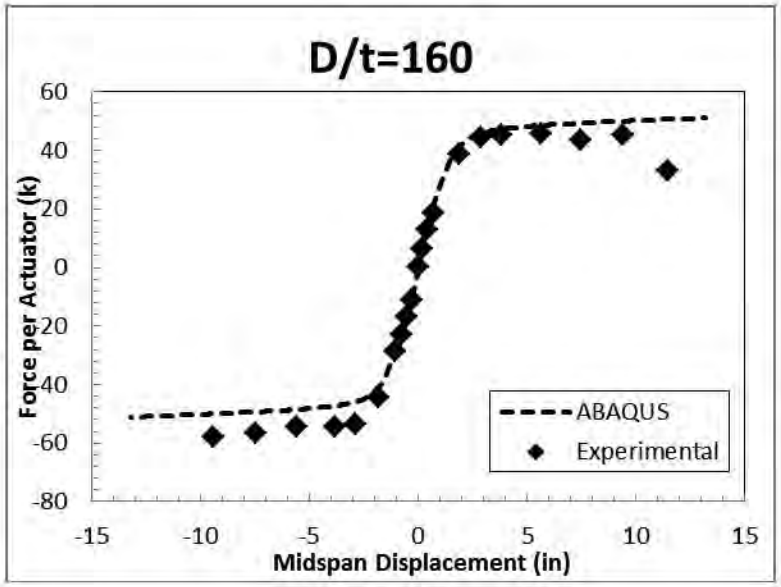
D/t=160
Force per Actuator (k)
Midspan Displacement (in)
ABAQUS
Experimental

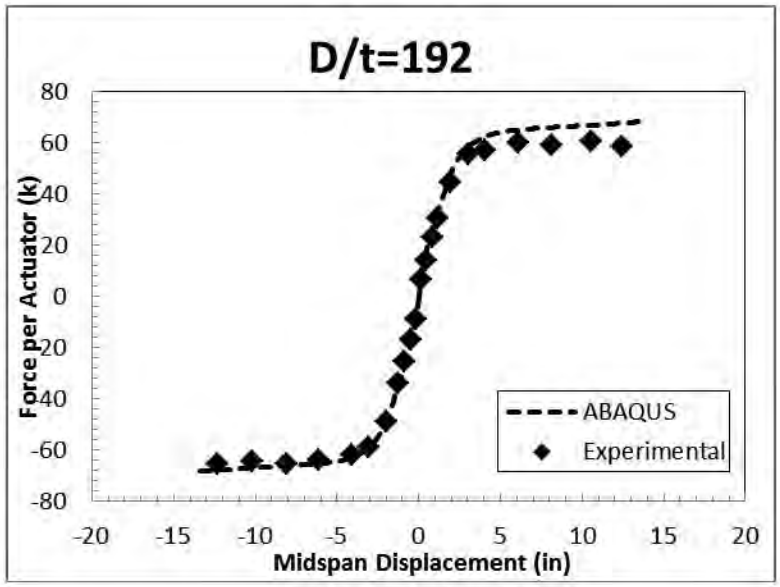
D/t=192
Force per Actuator (k)
Midspan Displacement (in)
ABAQUS
Experimental

Figure 6-6 Comparison of Monotonic Strain-Displacement Envelopes from ABAQUS with experimental results

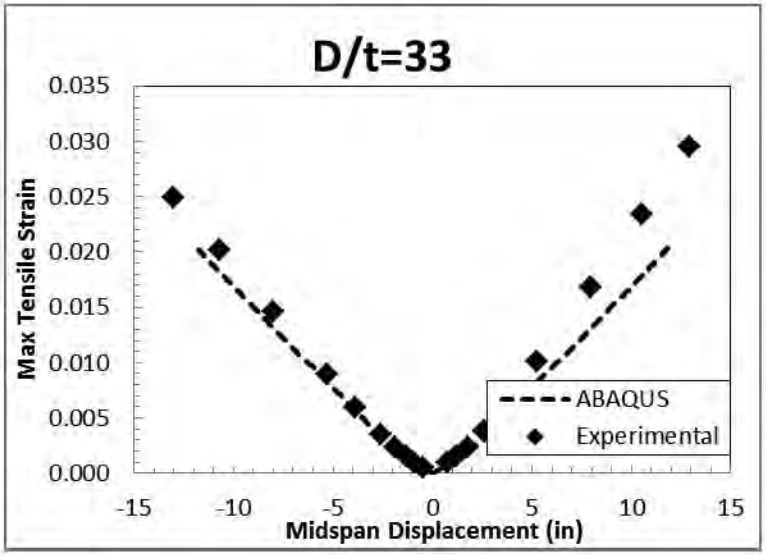
D/t=33
Max Tensile Strain
0.035
0.030
0.025
0.020
0.015
0.010
0.005
0.000
-15
-10
-5
0
5
10
15
Midspan Displacement (in)
ABAQUS
Experimental

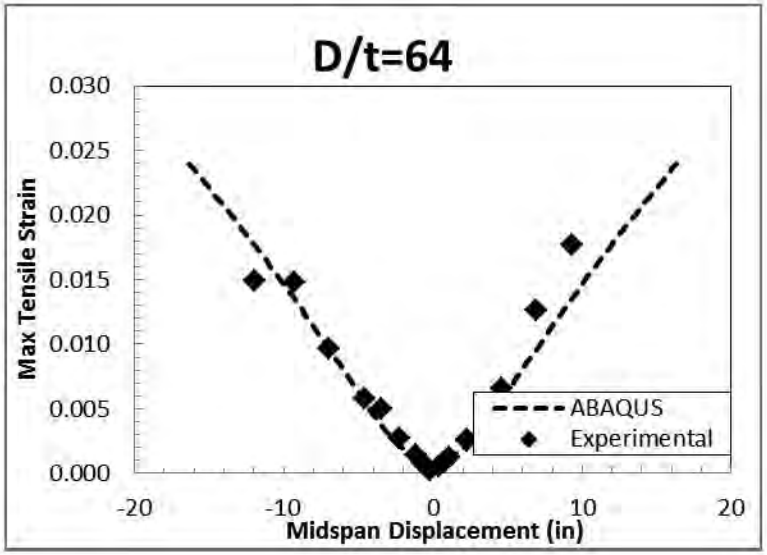
D/t=64
Max Tensile Strain
0.030
0.025
0.020
0.015
0.010
0.005
0.000
-20
-10
0
10
20
Midspan Displacement (in)
ABAQUS
Experimental

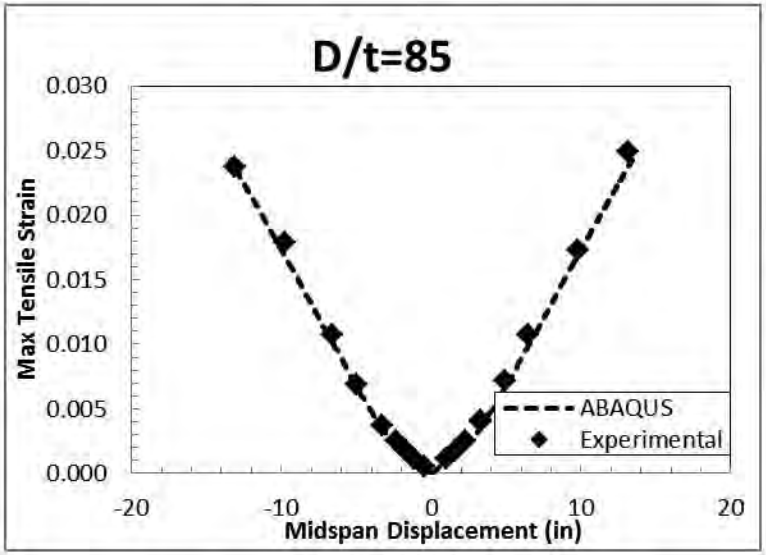
D/t=85
Max Tensile Strain
0.030
0.025
0.020
0.015
0.010
0.005
0.000
-20
-10
0
10
20
Midspan Displacement (in)
ABAQUS
Experimental

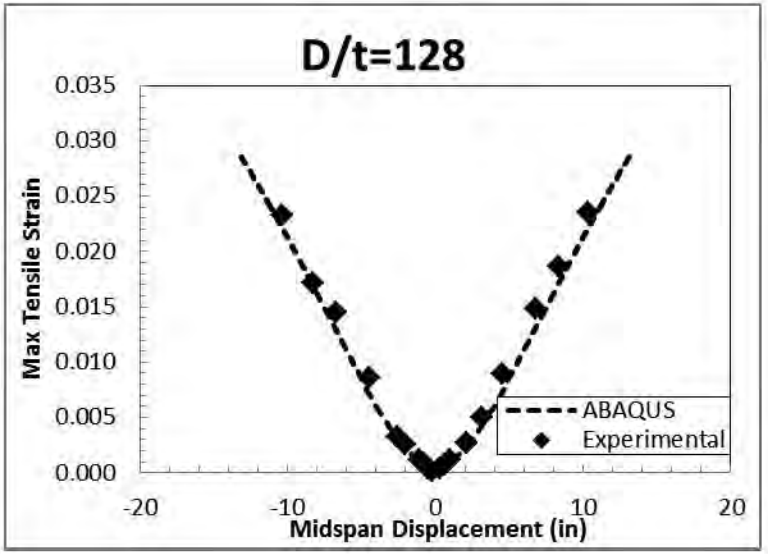
D/t=128
Max Tensile Strain
0.035
0.030
0.025
0.020
0.015
0.010
0.005
0.000
-20
-10
0
10
20
Midspan Displacement (in)
ABAQUS
Experimental

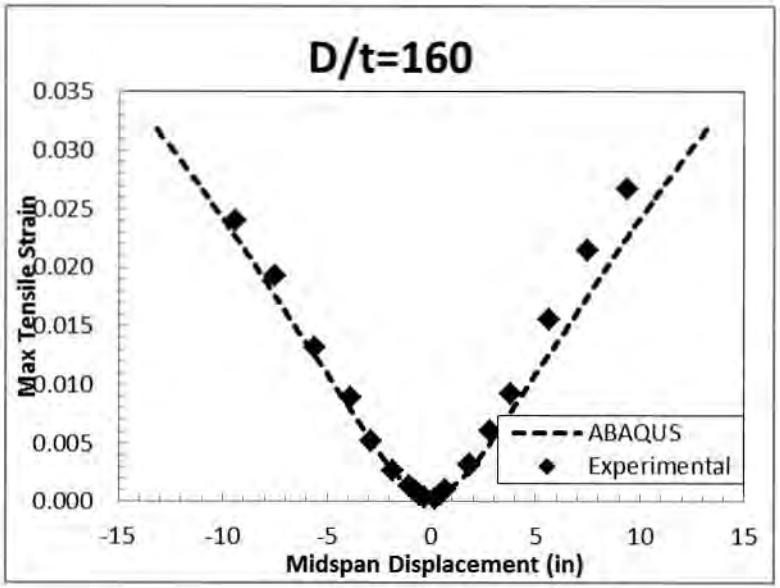
D/t=160
Max Tensile Strain
0.035
0.030
0.025
0.020
0.015
0.010
0.005
0.000
-15
-10
-5
0
5
10
15
Midspan Displacement (in)
ABAQUS
Experimental

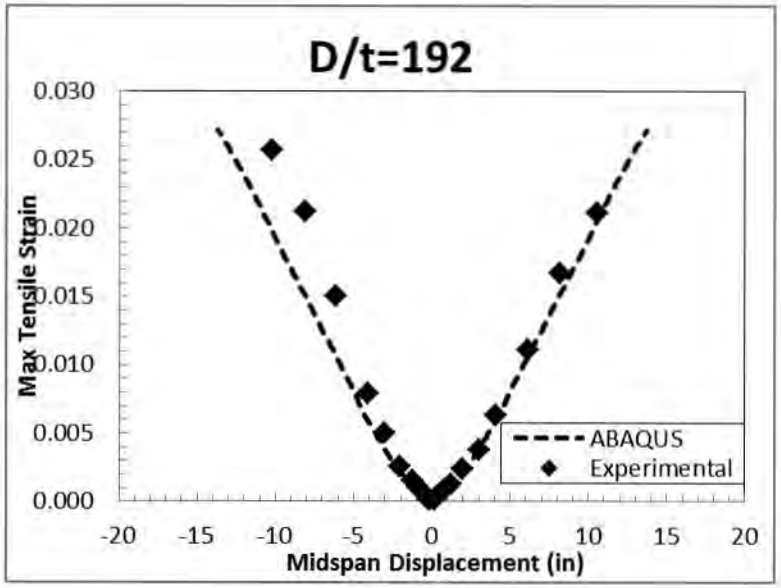
D/t=192
Max Tensile Strain
0.030
0.025
0.020
0.015
0.010
0.005
0.000
-20
-15
-10
-5
0
5
10
15
20
Midspan Displacement (in)
ABAQUS
Experimental

6.6. Cyclic Response

The main purposes of the finite element model were to predict damage in a system and investigate responses that were not measured during the experimental tests. The damage in reinforced concrete filled steel tubes consists of concrete cracking, outward buckling of the steel tube and rupture of the steel tube. To be able to predict the damage and look at material responses that were not measured during the test, such as the confined stress-strain response of the concrete, a cyclic loading must be applied to the system. A monotonic loading will not be able to predict the damage that occurs in cyclically loaded specimen.

The finite element models performed under monotonic loading were also modeled under cyclic loading. The displacements achieved in the loading history of the experimental tests were used as the displacements in the finite element model. The force-displacement hysteresis for a D/t ratio of 192 is shown in Figure 6-7. As seen in the figure, the force at the peak displacements for each loading cycle were predicted correctly by the finite element analysis, however the loading and unloading path is not correct. There was no pinching in the finite element analysis, whereas it did occur in the physical tests. This was due to the finite element model not modeling the cracks in the concrete opening and closing as the loads change direction. The concrete model needs to be altered to predict cracking under a cyclic loading.

Although, the loading response is not correct, the model did predict the buckling damage at the ends of the plastic hinge, where the moment gradient changes. A figure of this buckling is shown in Figure 6-8. The buckle appeared in ductility one, which agrees with the experimental results from this test.

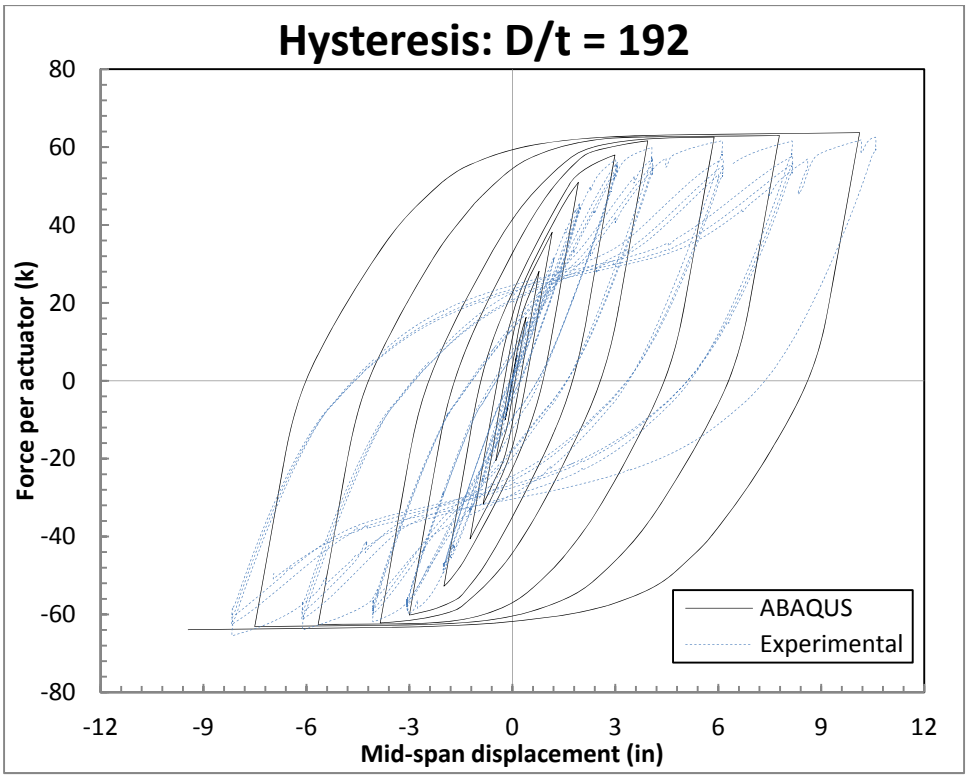

Figure 6-7 Force-displacement hysteresis

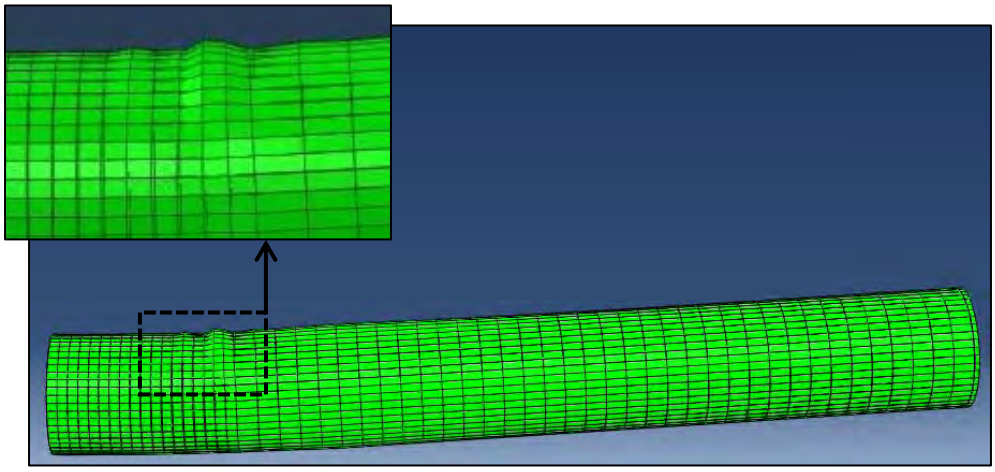

Figure 6-8 Buckling of the steel tube

6.7. **Summary**

The finite element model accurately predicted the forces, displacements, and strains of the reinforced concrete filled steel tubes under monotonic loading. Although buckling of the steel tube does occur in the cyclic model of the specimens, the cyclic hysteresis is not correct and the concrete model needs to be modified to include cracks closing and opening to accurately predict the full displacement response of concrete filled steel tubes under cyclic loading.

CHAPTER 7 CONCLUSIONS

7.1. Summary

This thesis summarized the results of a research program undertaken to study the effect of diameter-to-thickness ratio and amount of internal reinforcement on the behavior of pipe pile in an underground plastic hinge. Specifically, the effects of the selected parameters on the initiation of buckling and rupture of the steel pipe were studied. The experimental program consisted of large-scale testing of 12 reinforced concrete filled steel tubes.

The specimens were tested under reversed cyclic three-cycle set loading. Two point loads were placed in the center of the span, spaced six feet apart, to model the constant moment region created by soil. The typical behavior of the pile consisted of outward buckling of the pile throughout the constant moment region. The buckling of the pile continued to increase until the pipe ruptured along one of the buckled regions.

The thickness of the pipe was found to have a dramatic impact on the initiation of buckling of the steel pipe. The diameter-to-thickness ratio had a linear relationship to the strains and curvatures prior to buckling. The thinnest piles buckled earlier than the thicker piles. The thickness of the pipe had no effect on the rupture of the steel pipe. The piles ruptured at approximately 2.6% tensile strain and 0.015 1/in curvature prior to rupture; this was independent of the D/t ratio.

The thickness of the pipe did affect the energy dissipation and equivalent damping of the system. The thicker pipes dissipated more energy than the thinner pipes which resulted in higher damping ratios. The damping ratios ranged from 13.8% for a D/t of 192 to 17% for a D/t of 33 both at a displacement ductility of six. Expressions were created to determine the hysteretic and equivalent damping of reinforced concrete filled tubes as functions of the D/t ratio and displacement ductility.

The internal reinforcement ratio affected the flexural strength of the pile but did not affect the damage incurred in the specimen or the energy dissipation of the system.

Prior to buckling of the steel tube, strains were compatible throughout the section. After buckling of the steel tube initiated, strains were no longer compatible on the compressive side of the section due to extensive outward buckling of the tube. Although the strains were no longer compatible, conventional moment curvature analysis assuming the strains are compatible accurately predicts the flexural strength of the section because the compressive side of the pile develops the full compressive stress in the steel.

7.2. Design Recommendations

The following recommendations are made with respect to reinforced concrete filled steel tubes in flexure:

The displacement ductility for each pile was calculated by multiplying the experimental first yield displacement by the ratio of the nominal moment to the first yield moment. The nominal moment was defined when the concrete strain reached 0.004 and the first yield moment was calculated when the steel reached the yield strain determined from the tensile tests.

$\Delta_y = \Delta_y'(M_n/M_y)$

The D/t ratio affected the displacements, strains, and curvatures prior to buckling, as shown in the equations below.

Maximum tensile strain: $\varepsilon_{buckling} = -0.00011(D/t) + 0.021$

Section curvature: $\Phi_{buckling} = -0.0000064(D/t) + 0.00125$

Displacement ductility: $\mu_\Delta = -0.02(D/t) + 4.28$

Curvature ductility: $\mu_\Phi = -0.03(D/t) + 5.98$

The rupture of the pile was independent of D/t ratio and occurred at a maximum tensile strain of 2.6% and a section curvature of 0.015 (1/in).

The average displacement ductility prior to rupture was 5.3 and the average curvature ductility prior to rupture was 7.6. These ductilities were based off the equivalent yield displacement and curvature.

Assumptions of (1) plane sections remain plane and (2) strain compatibility can be used to generate accurate predictions of flexural strength of the section at a given level of strain and curvature.

The D/t ratio did affect the energy dissipation of the RCFSTs. The expressions for hysteretic damping and total damping with respect to displacement ductility and D/t ratio are shown below. The expressions are shown in two forms and each form will produce the same results. The displacement ductility should be calculated based off the equivalent yield displacement of the section, which is approximately twice that of the first yield displacement for RCFSTs. Also included are equations for total damping that originate at 5% damping at ducility 1 to retain consistency with equations for other systems, although they will slightly underestimate the damping in the low ductility range.

Hysteretic damping:

$\xi = 0.02 + (-0.0001(D/t)+0.08)\ \ln(\mu)$

$\xi = 0.02 + (-0.001(D/t)+0.8)*(\mu-1)/(\pi\mu+9.1)$

Total damping:

$\xi = 0.07 + (-0.00012(D/t)+0.072)\ \ln(\mu)$

$\xi = 0.07 + (-0.001(D/t)+0.85)*(\mu-1)/(\pi\mu+10.5)$

Total damping originating at 5% at ductility 1

$\xi = 0.05 + (-0.00082(D/t)+0.079)\ \ln(\mu)$

$\xi = 0.05 + (-0.00072(D/t)+0.78)*(\mu-1)/(\pi\mu+8.9)$

The plastic hinge length can be assumed to be the same as conventional reinforced concrete columns; however research needs to be performed to determine the effect of soil stiffness on the in-ground plastic hinge length.

The internal reinforcement ratio, at a given D/t ratio, did not affect the initiation of buckling, rupture, or damping.

7.3. Future Research

A constant moment region was created in the testing of the pipe piles in this research program to mimic the moment pattern created by the stiffness of the soil below ground. In order to validate the limit states and to determine the effect of soil stiffness on the plastic hinge length, pipe pile specimens should be tested in soil.

A reversed three-cycle load history was applied to each specimen to create the cyclic effects incurred during an earthquake. This research program did not take into account load histories, and different load histories should also be applied to determine the effect of variable loading histories on the behavior of the reinforced concrete filled steel tubes.

CHAPTER 8 REFERENCES

Boyd, F., Cofer, W., & McLean, D. (1995). Seismic performance of steel-encased concrete column under flexural loading. *ACI Structural Journal*, 355-365.

Caprani, C. (2007). The Moment Area Method - Mohr's Theorems, Structural Analysis III. Dublin: Dublin Institute of Technology.

Chang, X., Wei, Y.-Y., & Yun, Y.-C. (2012). Analysis of steel-reinforced concrete-filled steel tubular (SRCFST) columns under cyclic loading. *Construction and Building Materials*, 88-95.

Chang, X., Wei, Y.-Y., & Yun, Y.-C. (2012). Analysis of steel-reinforced concrete-filled steel tubular (SRCFST) columns under cyclic loading. *Construction and Building Materials*, 88-95.

Chen, B., & Wang, T. (2009). Overview of Concrete Filled Steel Tube Arch Bridges in China. *Practice Periodical on Structural Design and Construction*, 70-80.

Chitawadagi, M. V., & Narasimhan, M. C. (2009). Strength deformation behaviour of circular concrete filled steel tubes subjected to pure bending. *Journal of Constructional Steel Research*, 1836-1845.

Elchalakani, M., & Zhao, X.-L. (2008). Concrete-filled cold-formed circular steel tubes subjected to variable amplitude cyclic pure bending. *Engineering Structures, 30*, 287-299.

Elchalakani, M., Zhao, X., & Grzebieta, R. (2001). Concrete-filled circular steel tubes subjected to pure bending. *Journal of Constructional Steel Research*, 1141-1168.

Elchalakani, M., Zhao, X.-L., & Grzebieta, R. (2004). Concrete-filled steel circular tubes subjected to constant amplitude cyclic pure bending. *Engineering Structures*, 2125-2135.

Elremaily, A., & Azizinamini, A. (2002). Behavior and strength of circular concrete-filled tube columns. *Journal of Constructional Steel Research*, 1567-1591.

Fam, A., Quie, F., & Rizkalla, S. (2004). Concrete-Filled Steel Tubes Subjected to Axial Compression and Lateral Cyclic Loads. *Journal of Structural Engineering*, 631-640.

Furlong, R. (1968). Design of Steel-Encased Concrete Beam-Columns. *ASCE Journal of Structural Division*, 267-281.

Gajalakshmi, P., & Helena, H. J. (2012). Behaviour of concrete-filled steel columns subjected to lateral cyclic loading. *Journal of Constructional Steel Research*, 55-63.

Giakoumelis, G., & Lam, D. (2004). Axial capacity of circular concrete-filled tube columns. *Journal of Constructional Steel Research*, 1049-1068.

Gonzalez Roman, L. A., Kowalsky, M. J., Nau, J., & Hassan, T. (2008). *Reversal Cyclic Testing of Full Scale Pipe Piles.* Raleigh: North Carolina State University.

Gupta, P., Sarda, S., & Kumar, M. (2007). Experimental and computational study of concrete filled steel tubular columns under axial loads. *Journal of Constructional Steel Research*, 182-193.

Han, L.-H. (2004). Flexural behaviour of concrete-filled steel tubes. *Journal of Constructional Steel Research*, 313-337.

Han, L.-H., Liao, F.-Y., Tao, Z., & Hong, Z. (2009). Performance of concrete filled steel tube reinforced concrete columns subjected to cyclic bending. *Journal of Constructional Steel Research*, 1607-1616.

Han, L.-H., Lu, H., Yao, G.-H., & Liao, F.-Y. (2006). Further study on the flexural behaviour of concrete-filled steel tubes. *Journal of Constructional Steel Research*, 554-565.

Kilpatrick, A., & Rangan, B. (1997). *Deformation-Control Analysis of Composite Concrete Columns.* Perth: Curtin University of Technology.

Lu, Y., & Kennedy, D. (1992). *The flexural behavior of concrete-filled hollow structural sections.* Edmonton: Department of Civil Engineering University of Alberta.

Marson, J., & Bruneau, M. (2004). Cyclic Testing of Concrete-Filled Circular Steel Bridge Piers having Encased Fixed-Based Detail. *Journal of Bridge Engineering*, 14-23.

Nezamian, A., R., A.-M., & P., G. (2006). Bond strength of concrete plugs embedded in tubular steel piles under cyclic loading. *Canadian Journal of Civil Engineering*, 111-125.

Park, R. (1983). Seismic Performance of Steel-Encased Concrete Piles.

Priestley, M., Calvi, G., & Kowalsky, M. (2007). *Displacement Based Seismic Design of Structures.* Pavia: IUSS PRess.

Roeder, C. W., Cameron, B., & Brown, C. B. (1999). Composite Action in Concrete Filled Tubes. *Journal of Structural Engineering*, 631-640.

Rupp, J. F. (2012). Modeling of Steel-Jacketed Reinforced Concrete under Axial Compressive Loads. Ohio State University.

Thayalan, P., Aly, T., & Patnaikuni, I. (2009). Behaviour of concrete-filled steel tubes under static and variable repeated loading. *Journal of Constructional Steel Research*, 900-908.

Virdi, K., & Dowling, P. (1975). *Bond strength in concrete-filled circular steel tubes.* London: Imperial College.

CHAPTER 9 APPENDICES

Appendix A: Force – Displacement Hystereses

This appendix shows the force-displacement hysteresis for the experimental tests. Figure 9-1 shows the force – displacement hysteresis for the first set of experimental tests. The D/t ratios vary and all the specimens had an internal reinforcement ratio of 1.7%. Figure 9-2 shows the force – displacement hysteresis for the second set of experimental tests, with varying internal reinforcement ratios.

Figure 9-1 Force – displacement hysteresis for varying D/t ratios

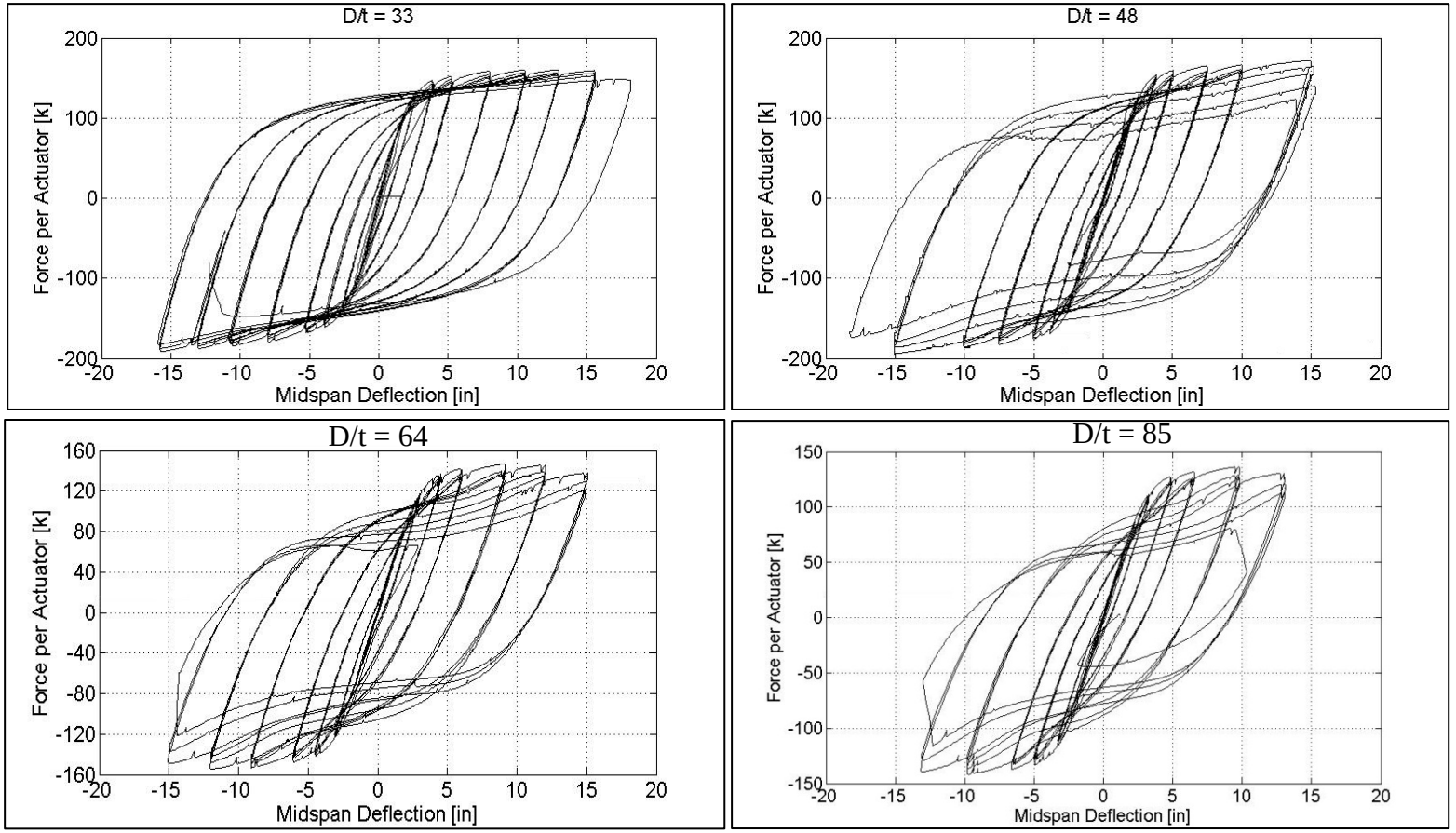
D/t = 33
Force per Actuator [k]
Midspan Deflection [in]
D/t = 48
Force per Actuator [k]
Midspan Deflection [in]
D/t = 64
Force per Actuator [k]
Midspan Deflection [in]
D/t = 85
Force per Actuator [k]
Midspan Deflection [in]

Figure 9-2 Force – displacement hysteresis for varying internal reinforcement ratios

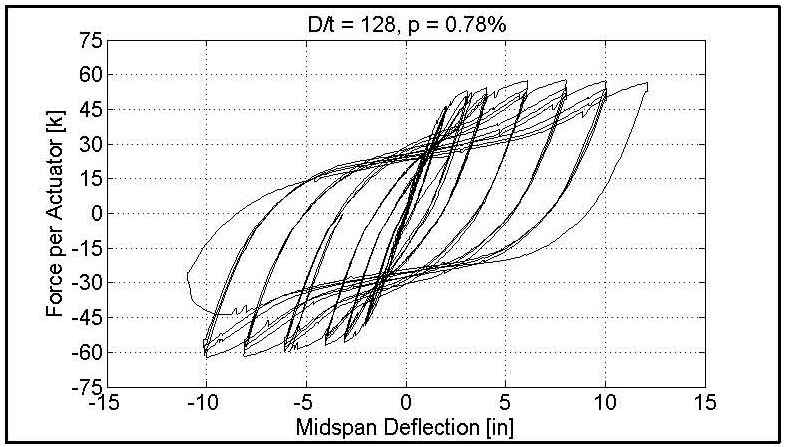
D/t = 128, p = 0.78%
Force per Actuator [k]
Midspan Deflection [in]
75
60
45
30
15
0
-15
-30
-45
-60
-75
-15
-10
-5
0
5
10
15

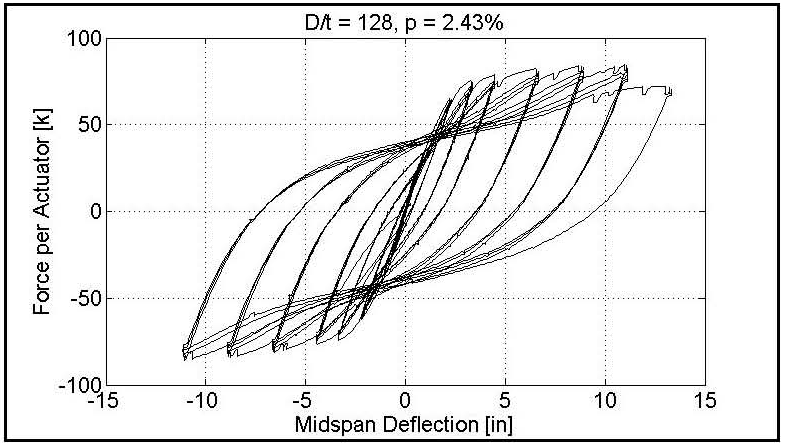
D/t = 128, p = 2.43%
Force per Actuator [k]
Midspan Deflection [in]
100
50
0
-50
-100
-15
-10
-5
0
5
10
15

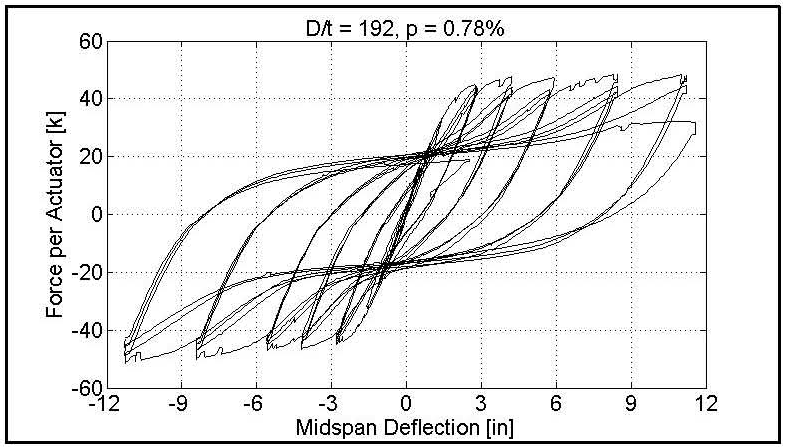
D/t = 192, p = 0.78%
Force per Actuator [k]
Midspan Deflection [in]
60
40
20
0
-20
-40
-60
-12
-9
-6
-3
0
3
6
9
12

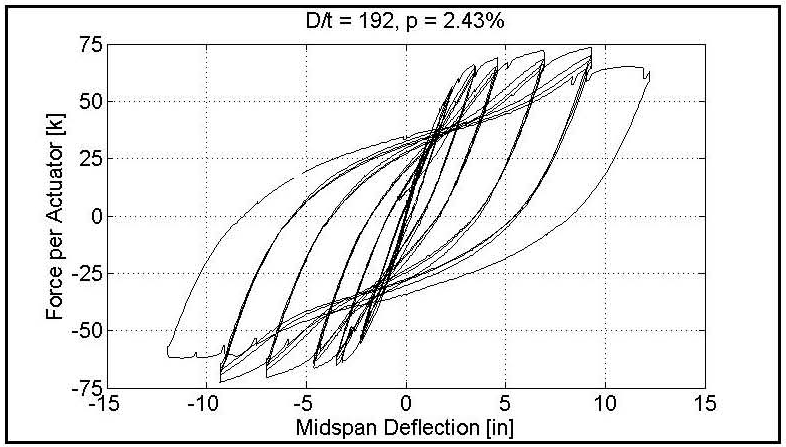
D/t = 192, p = 2.43%
Force per Actuator [k]
Midspan Deflection [in]
75
50
25
0
-25
-50
-75
-15
-10
-5
0
5
10
15

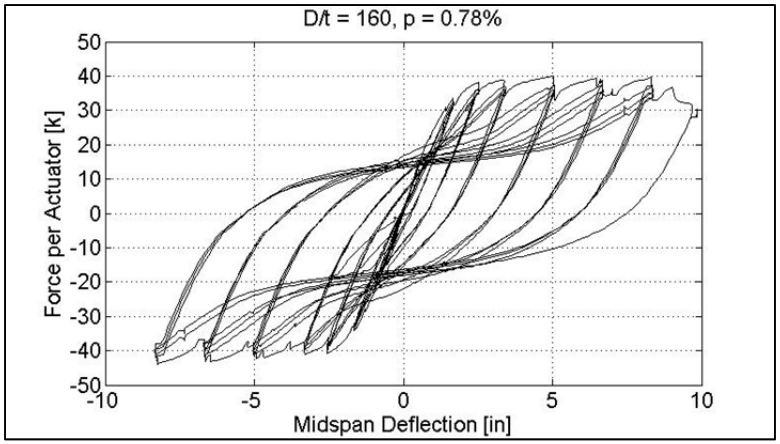
D/t = 160, p = 0.78%
Force per Actuator [k]
Midspan Deflection [in]
50
40
30
20
10
0
-10
-20
-30
-40
-50
-10
-5
0
5
10

Appendix B: Force – Displacement Hysteretic Loops

The force-displacement hysteretic loops used to calculate the damping are shown for all of the experimental tests below. Not all of the tests reach the same ductility level and therefore there not all the tests have the same number of loops. The hysteretic loops for D/t ratios of 33 and 192 are shown previously.

Figure 9-3 Force-displacement hysteretic loops for D/t ratio of 48

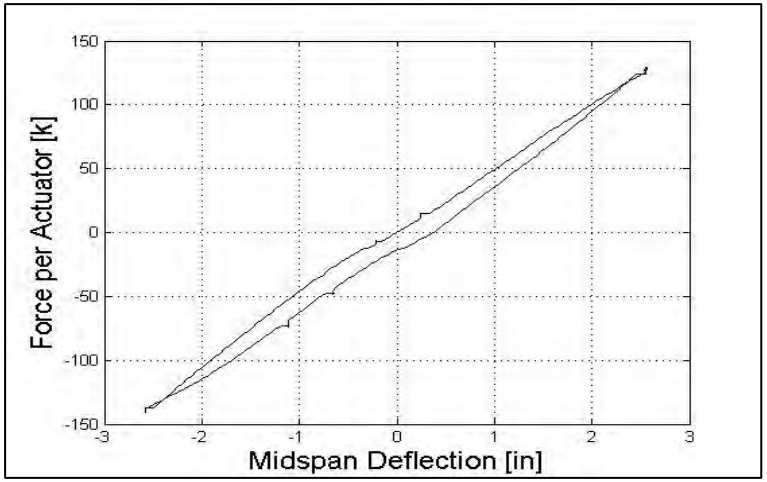

Ductility 1

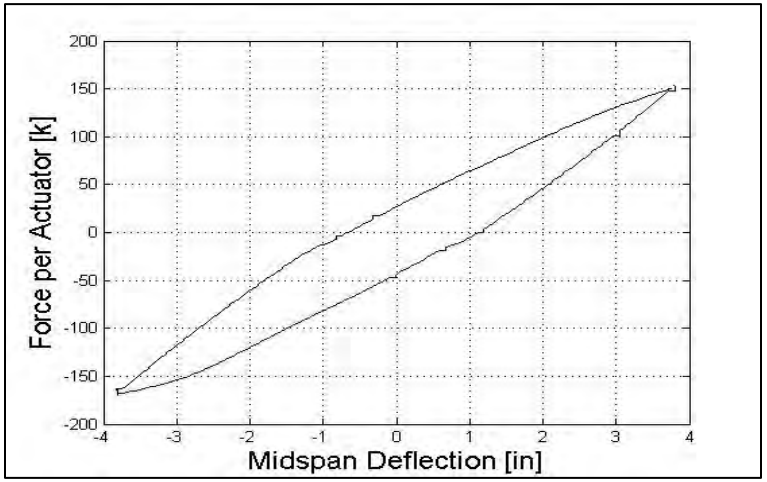

Ductility 1.5

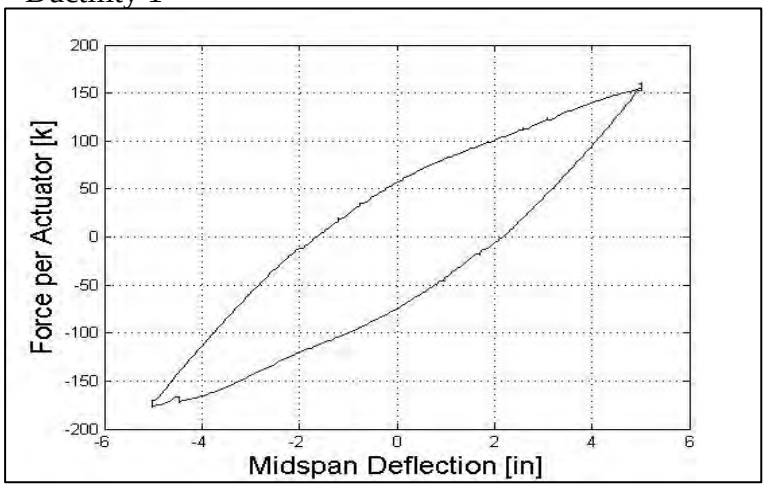

Ductility 2

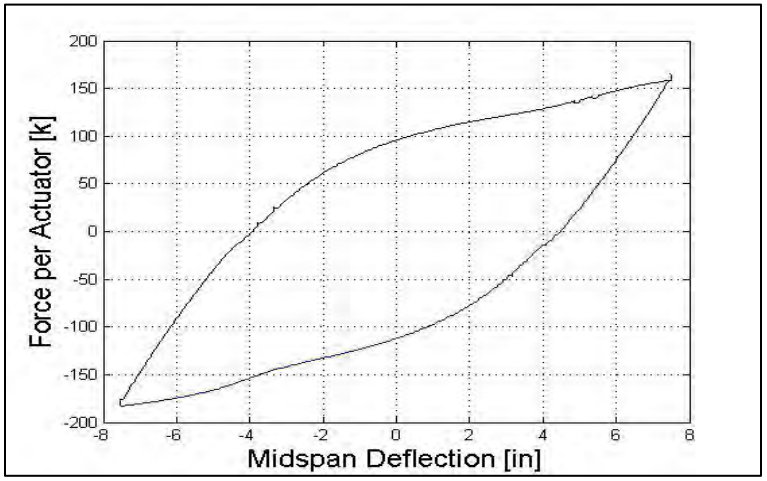

Ductility 3

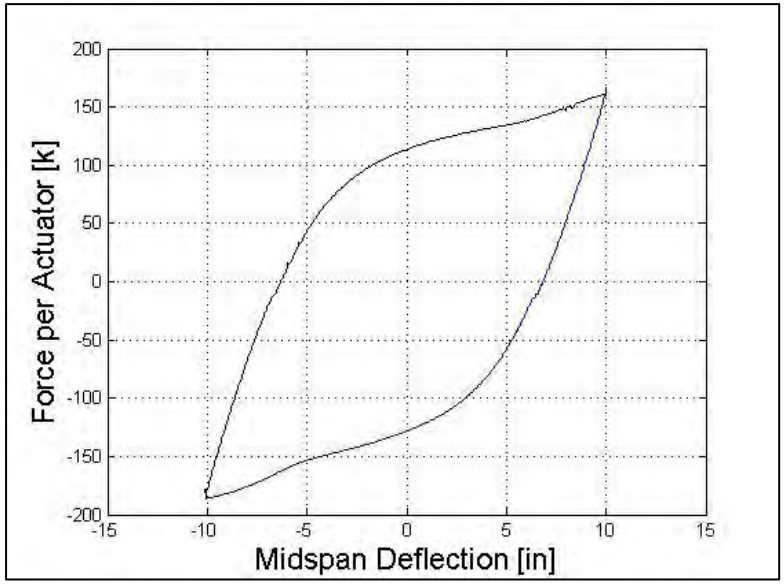

Ductility 4

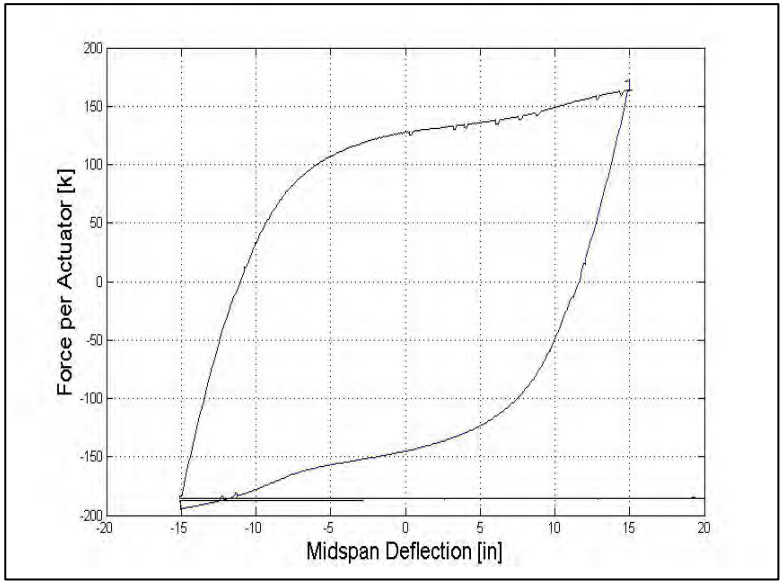

Ductility 6

Figure 9-4 Force-displacement hysteretic loops for D/t ratio of 64

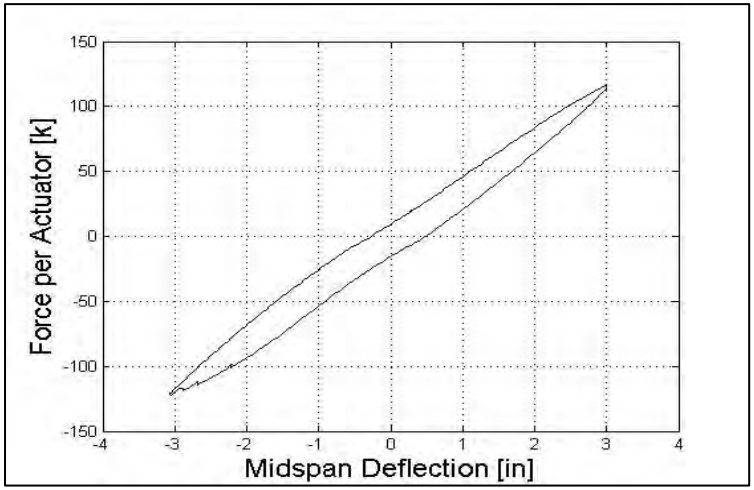

Ductility 1

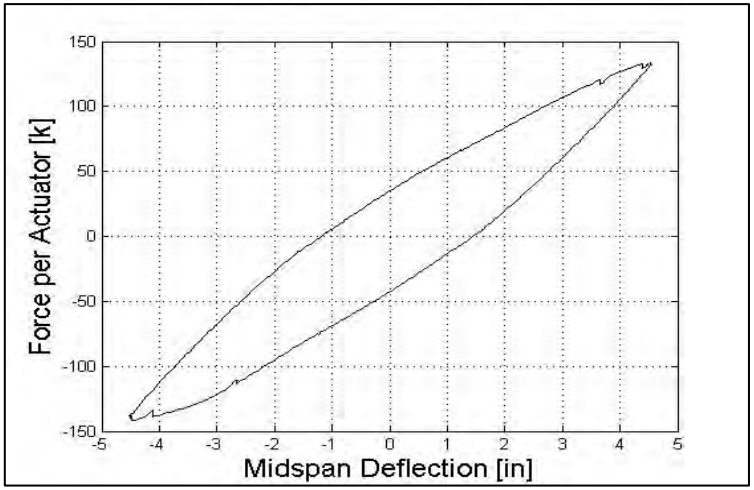

Ductility 1.5

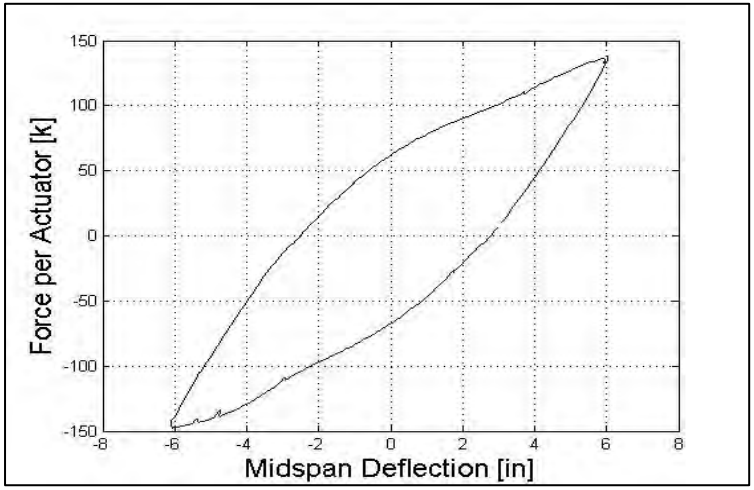

Ductility 2

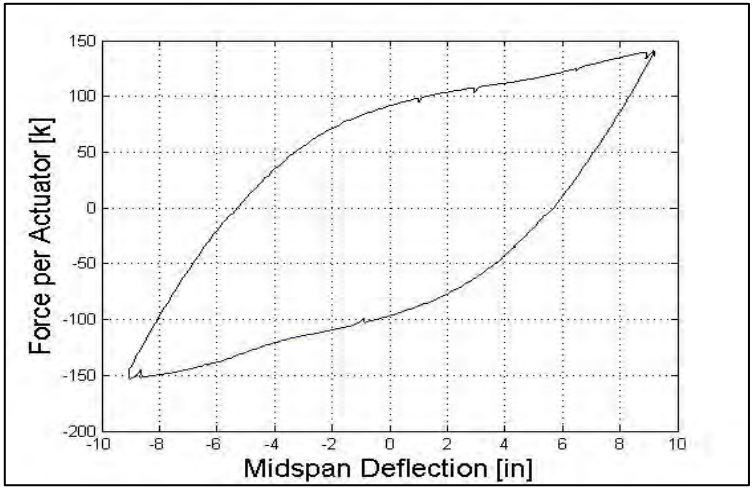

Ductility 3

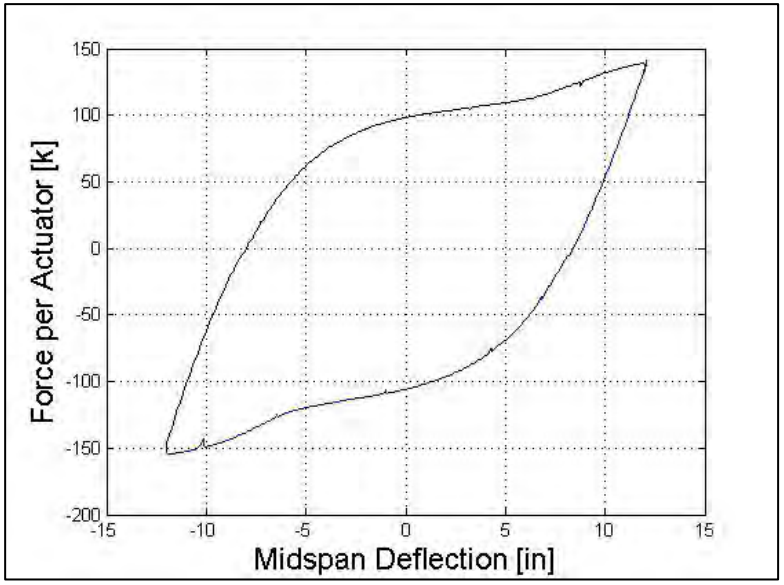

Ductility 4

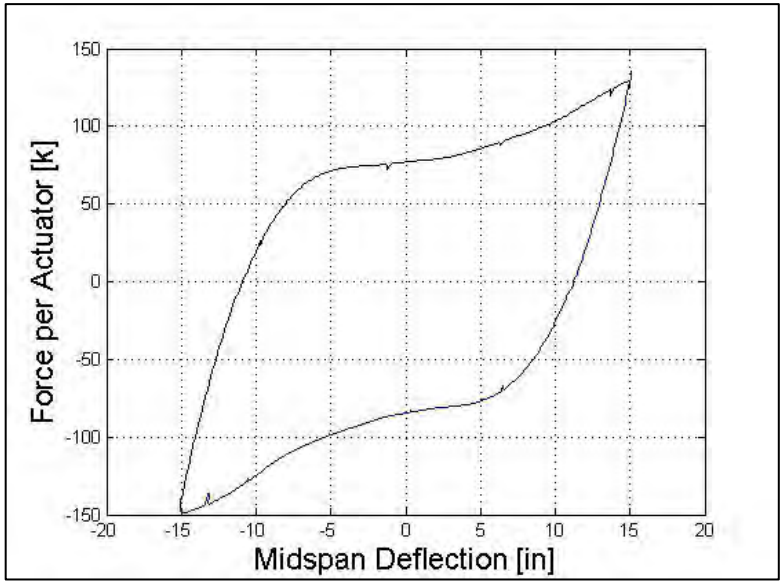

Ductility 5

Figure 9-5 Force-displacement hysteretic loops for D/t ratio of 85

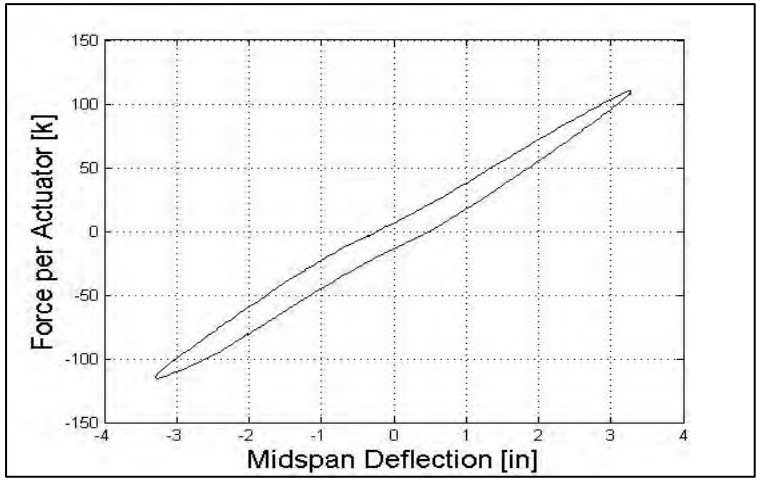

Ductility 1

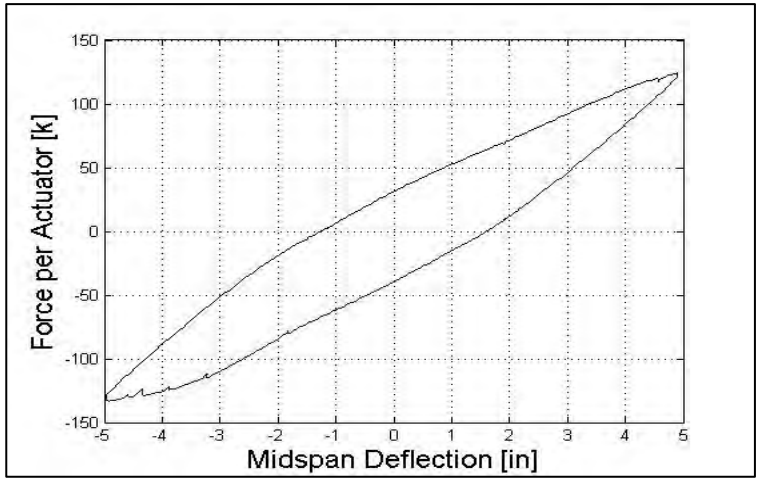

Ductility 1.5

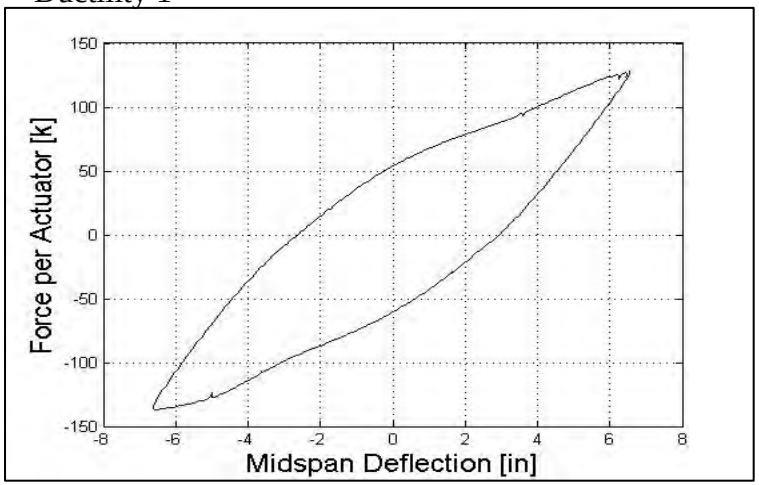

Ductility 2

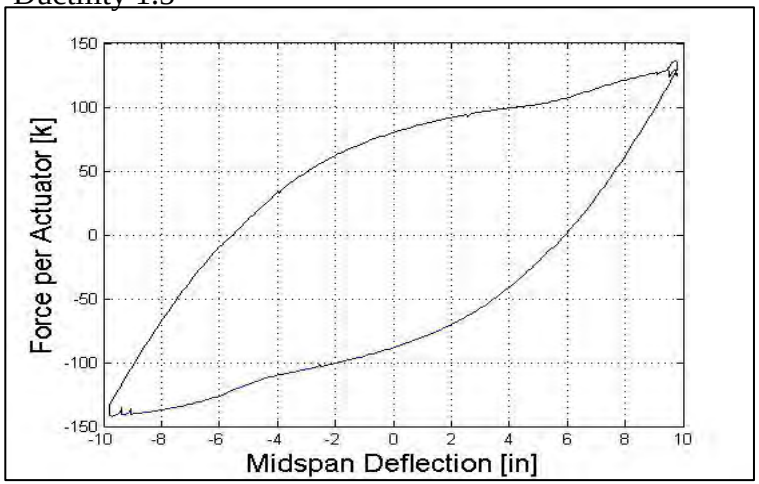

Ductility 3

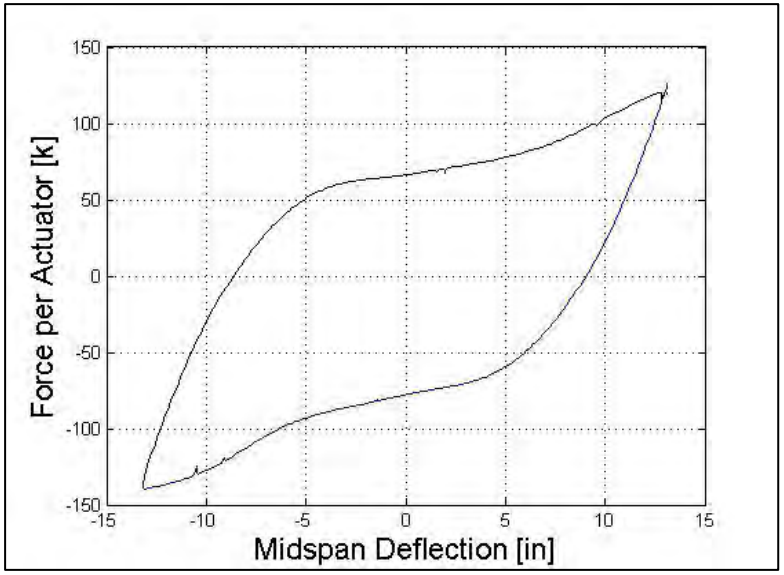
Force per Actuator [k]
Midspan Deflection [in]
150
100
50
0
-50
-100
-150
-15
-10
-5
0
5
10
15
Ductility 4

Figure 9-6 Force-displacement hysteretic loops for D/t ratio of 128

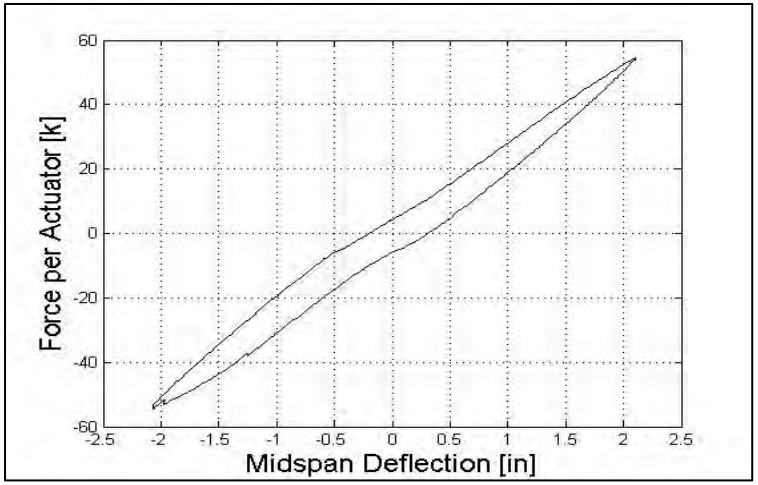

Ductility 1

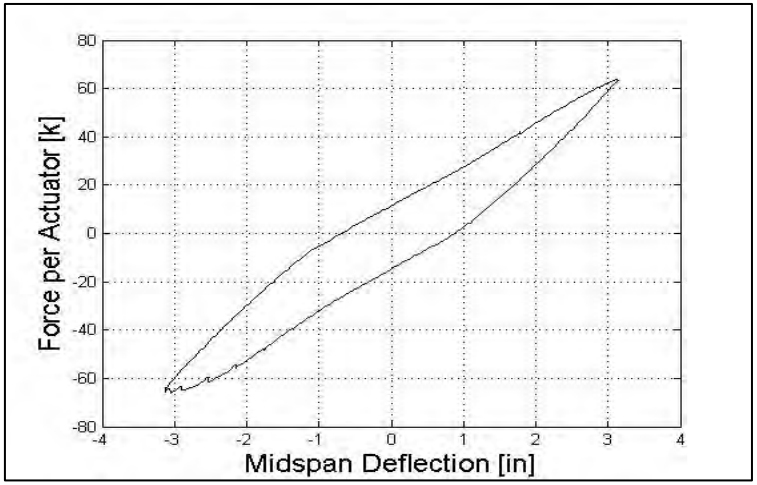

Ductility 1.5

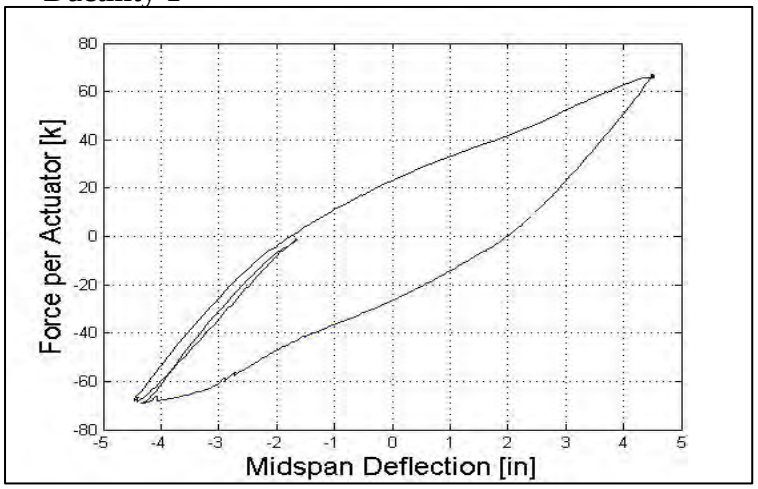

Ductility 2

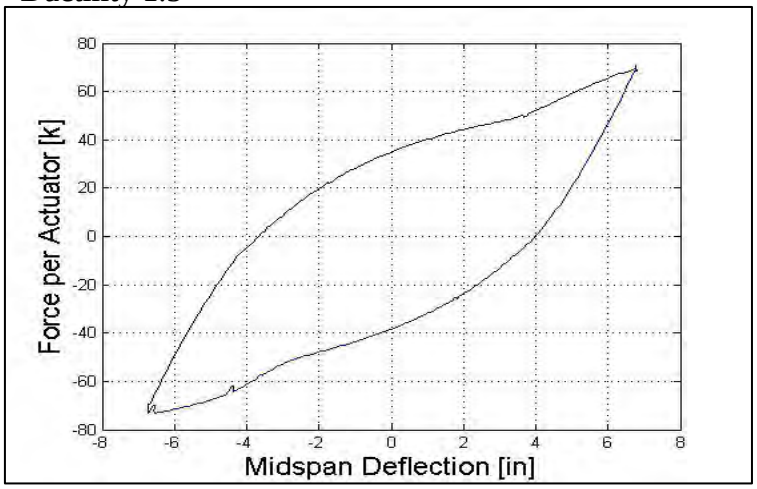

Ductility 3

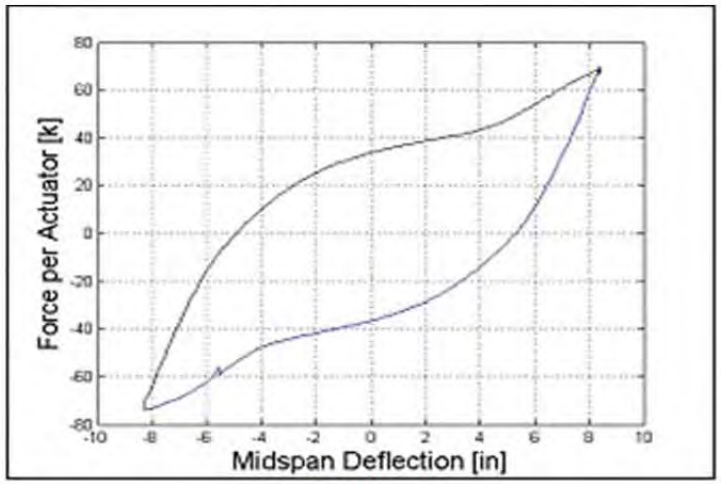

Ductility 4

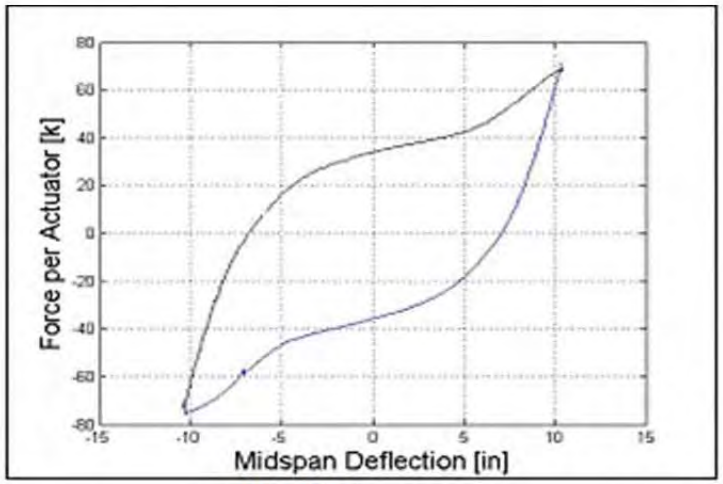

Ductility 5

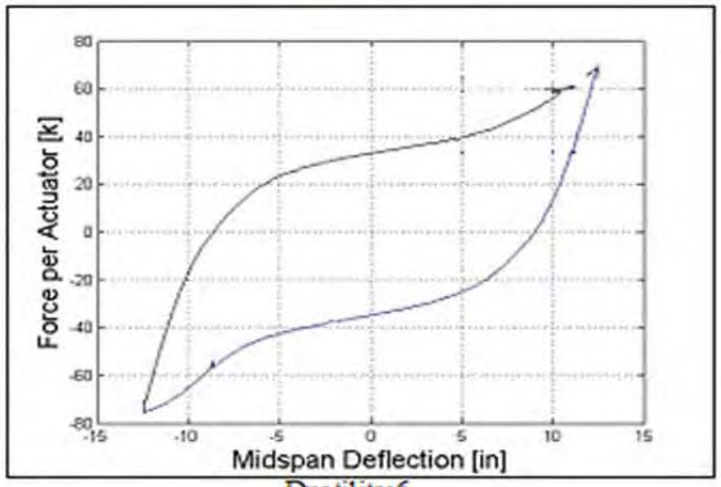

Ductility 6

Figure 9-7 Force-displacement hysteretic loops for D/t ratio of 160

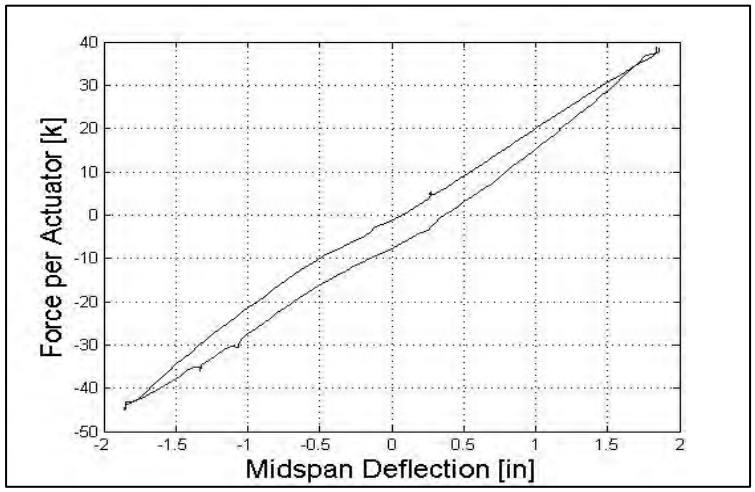

Ductility 1

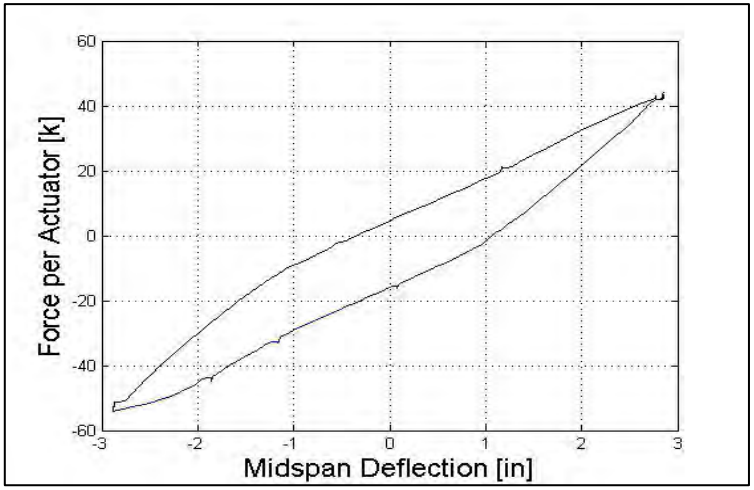

Ductility 1.5

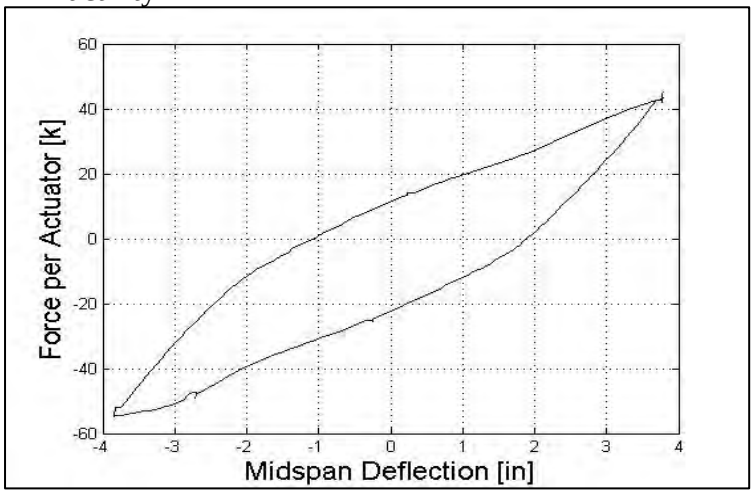

Ductility 2

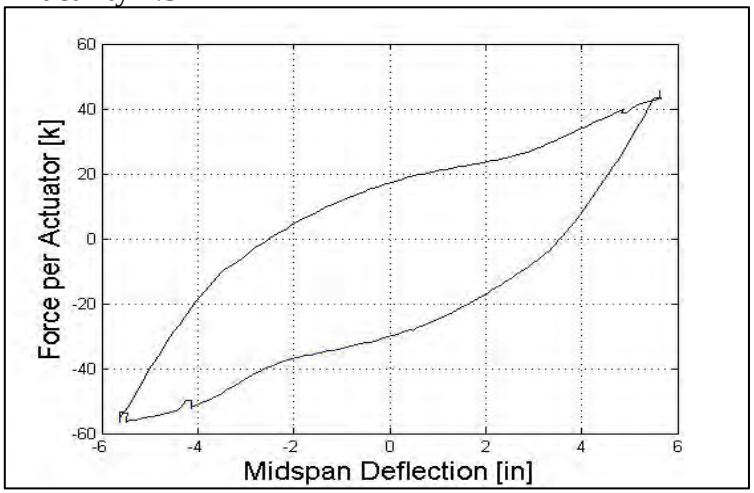

Ductility 3

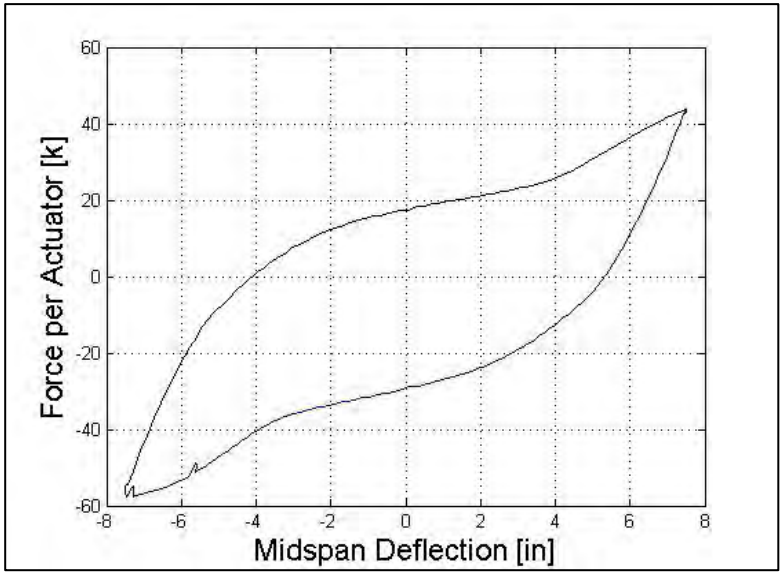

Ductility 4

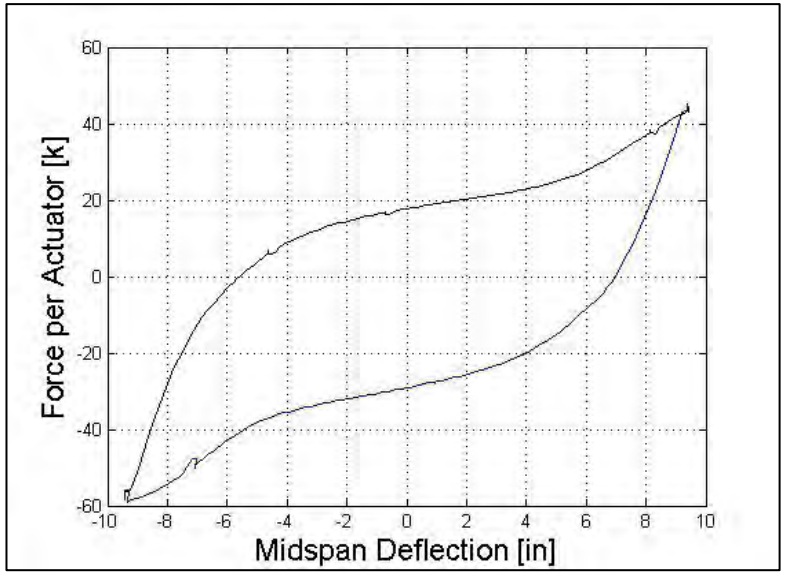

Ductility 5

Appendix C: Moment-Curvature Hysteretic Loops

The moment-curvature hysteretic loops are shown for varying D/t ratios below. Not all of the tests reach the same ductility level and therefore there not all the tests have the same number of loops.

Figure 9-8 Moment Curvature Hysteretic Loops for a D/t ratio of 33

Ductility 1

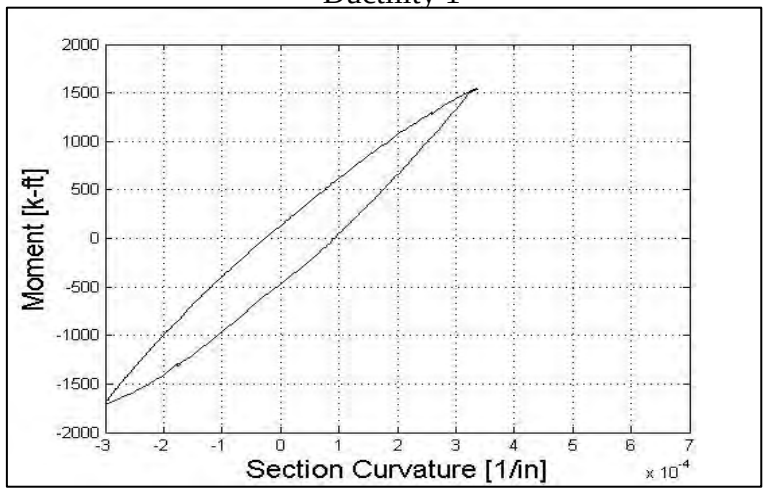

Ductility 1.5

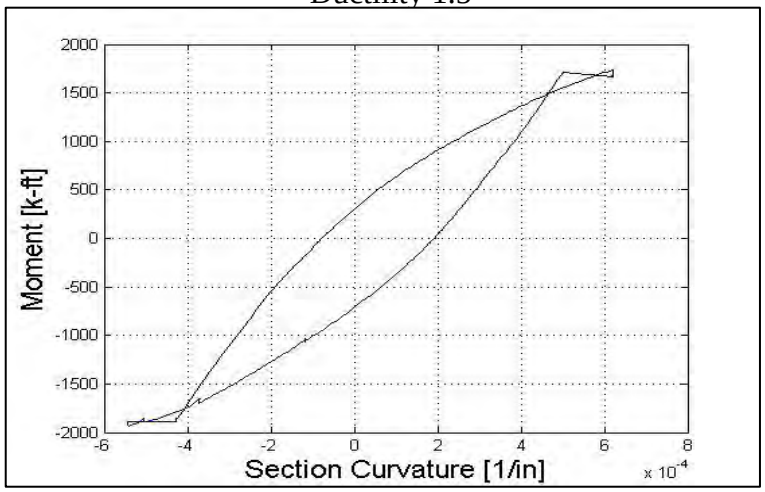

Ductility 2

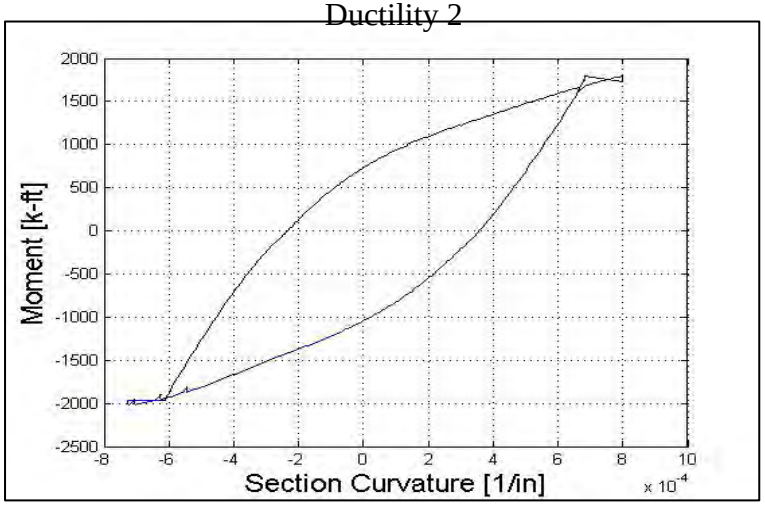

Ductility 3

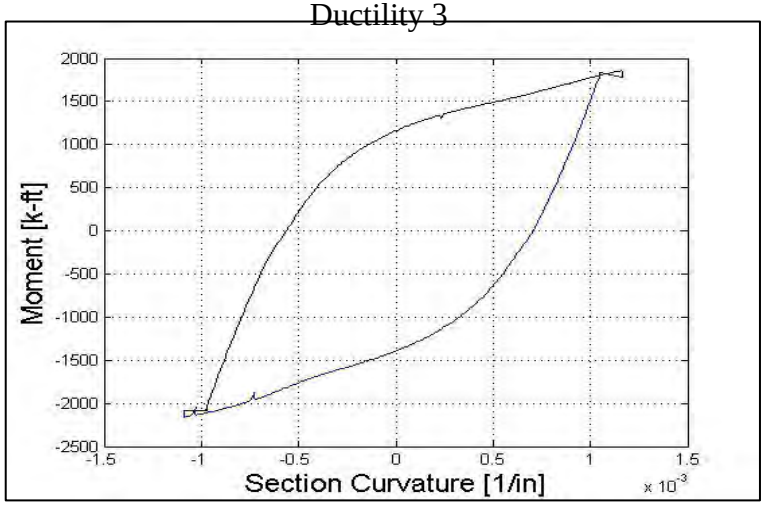

Ductility 4

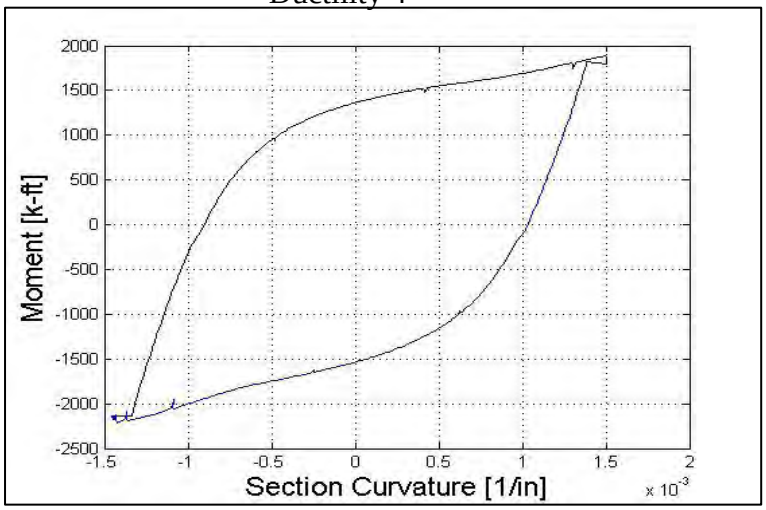

Ductility 5

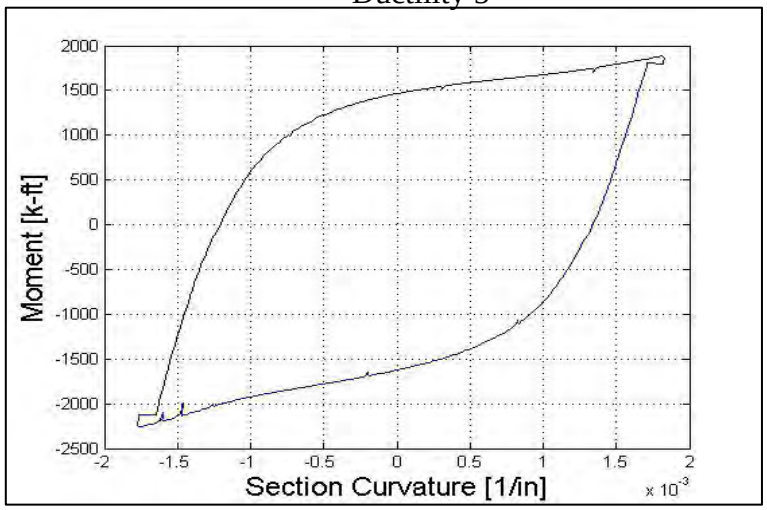

Ductility 6

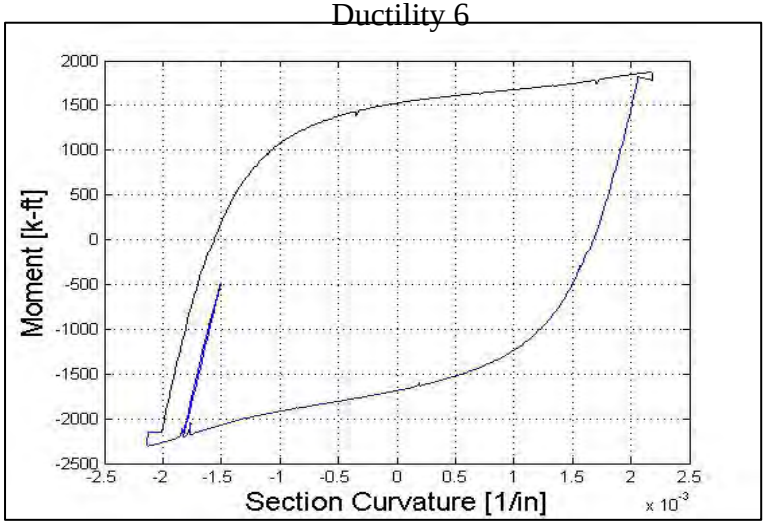

Figure 9-9 Moment Curvature Hysteretic Loops for a D/t ratio of 6

Ductility 1

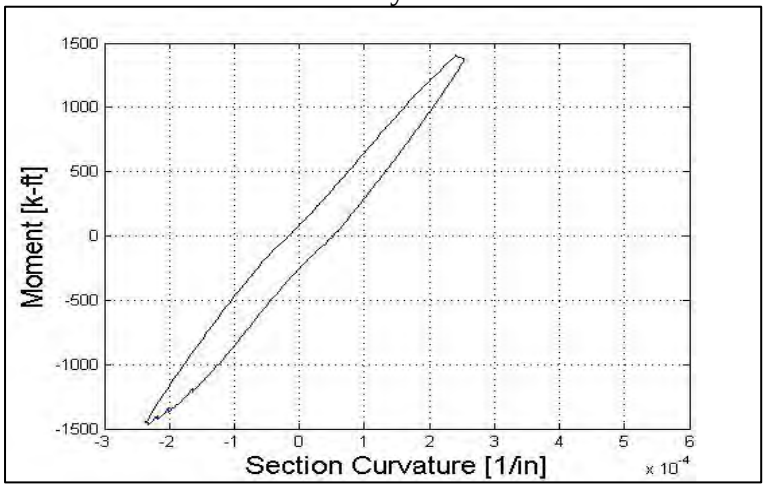

Ductility 1.5

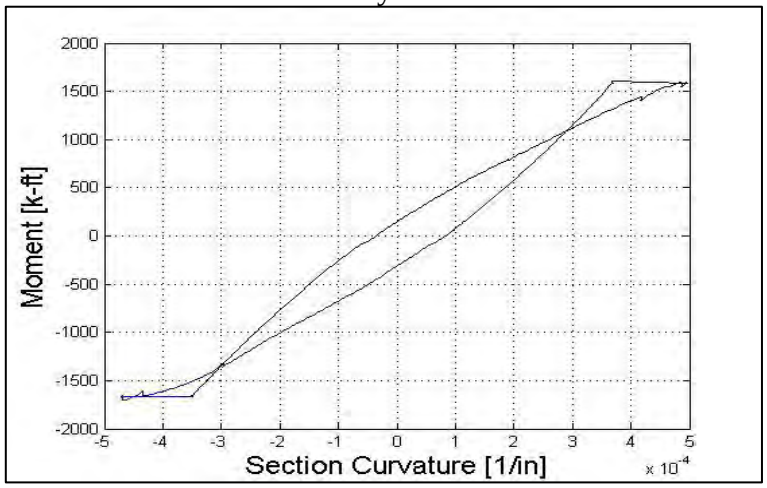

Ductility 2

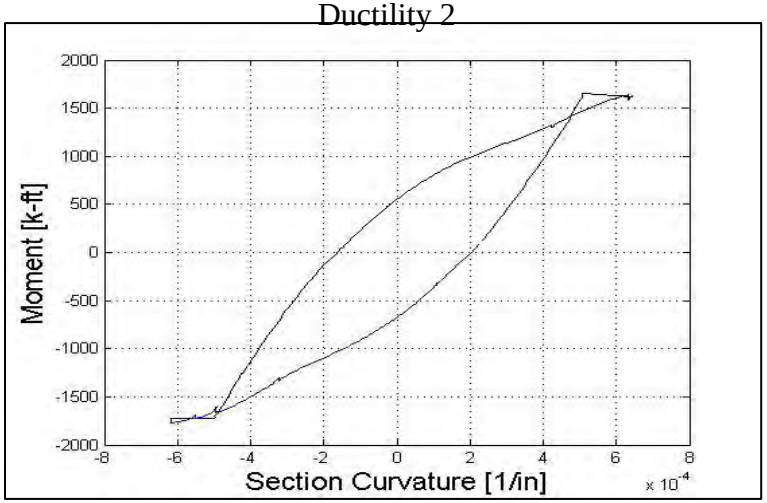

Ductility 3

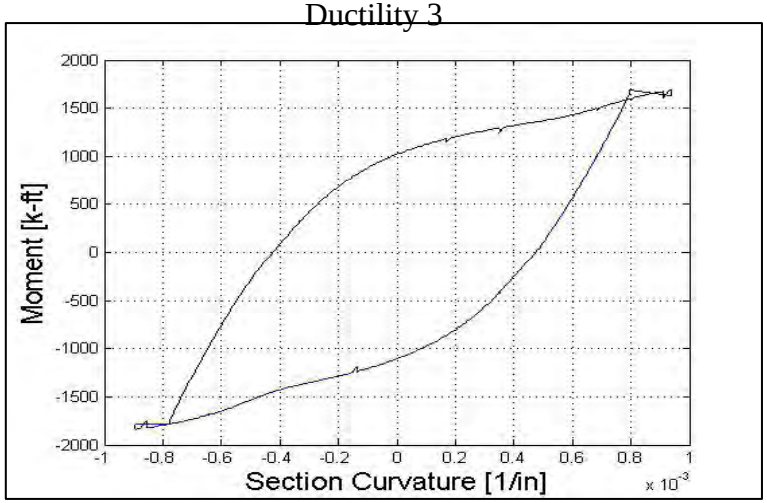

Ductility 4

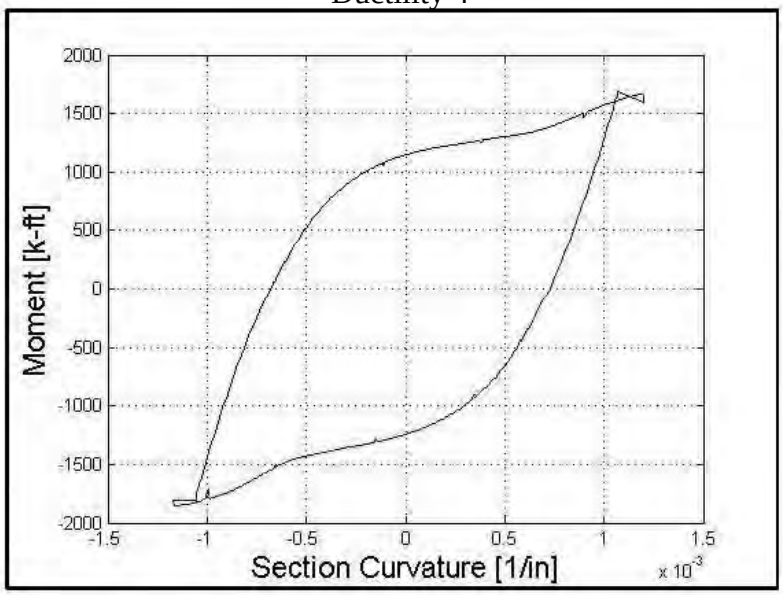

Ductility 5

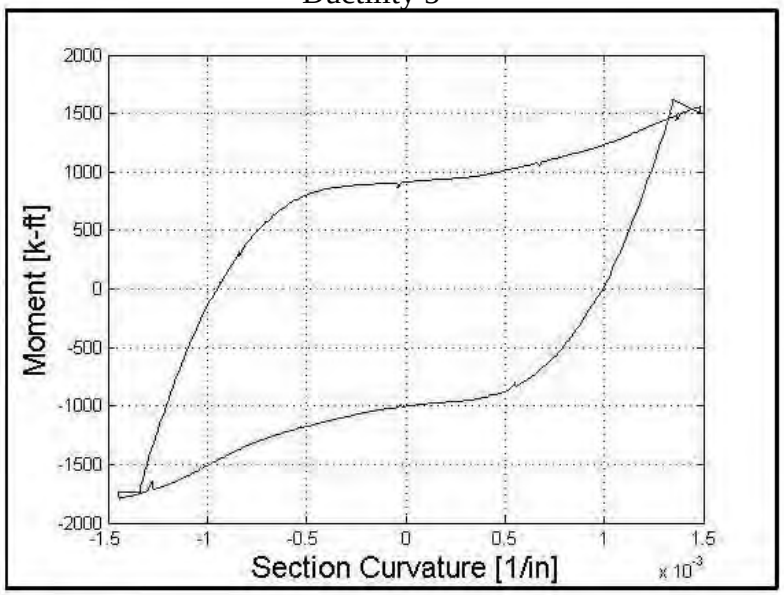

Figure 9-10 Moment Curvature Hysteretic Loops for a D/t ratio of 85

Ductility 1

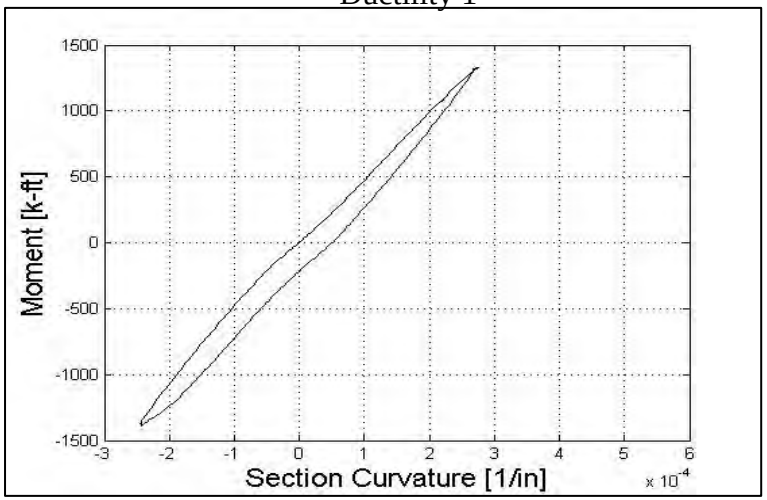

Ductility 1.5

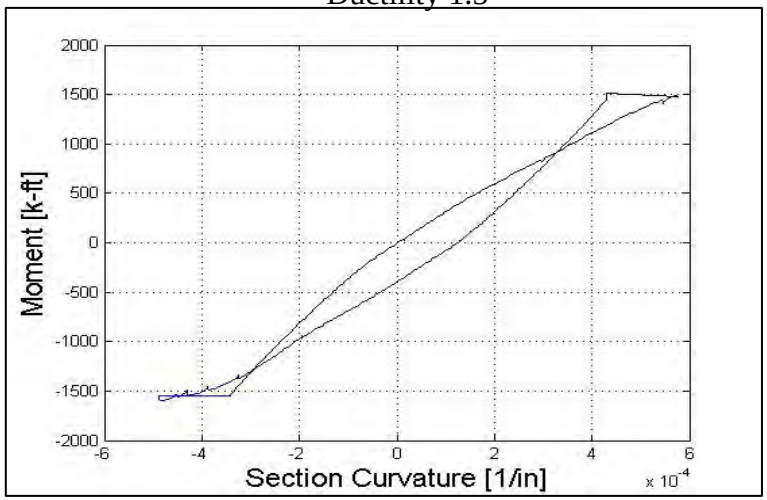

Ductility 2

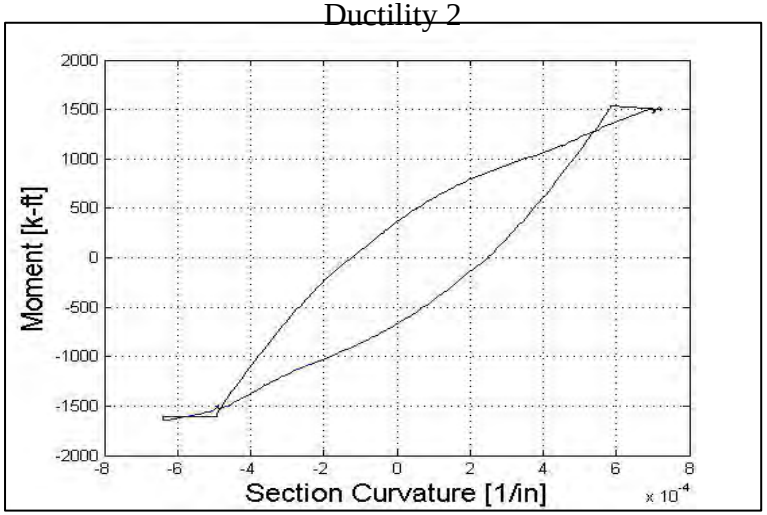

Ductility 3

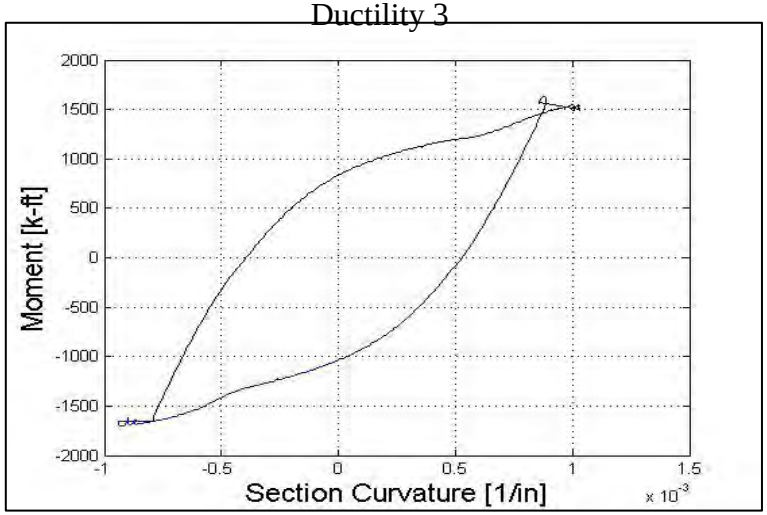

Ductility 4

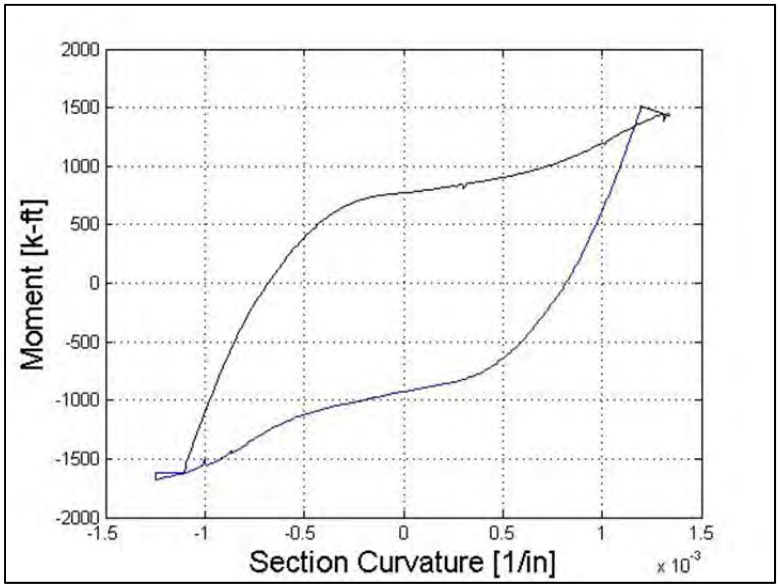
Moment [k-ft]
2000
1500
1000
500
0
-500
-1000
-1500
-2000
-1.5
-1
-0.5
0
0.5
1
1.5
Section Curvature [1/in]
x 10^-3

Figure 9-11 Moment Curvature Hysteretic Loops for a D/t ratio of 128

Ductility 1

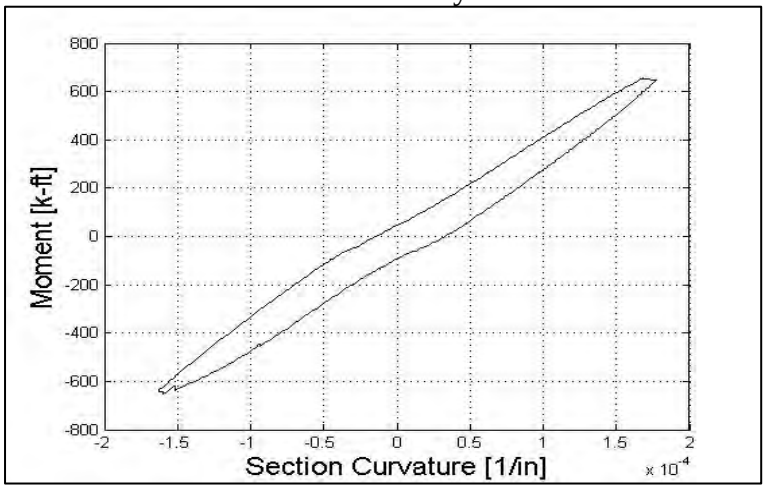

Ductility 1.5

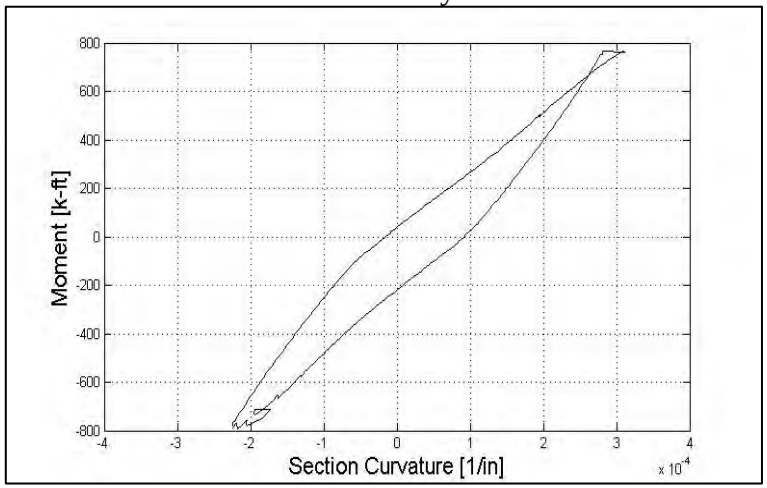

Ductility 2

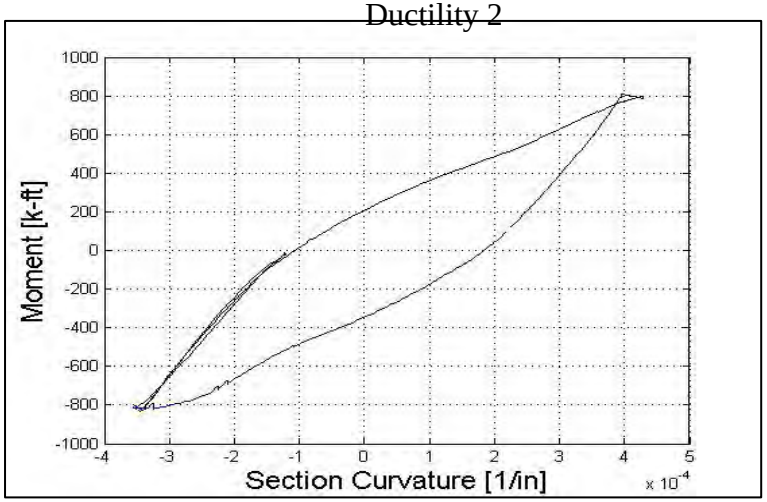

Ductility 3

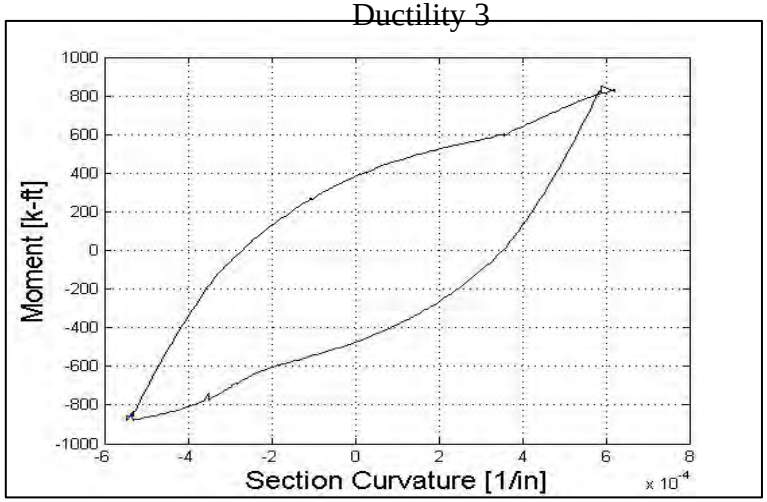

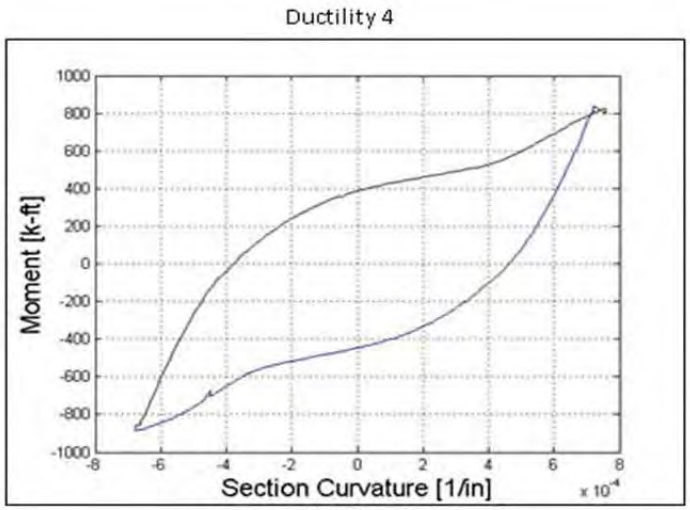
Ductility 4
Moment [k-ft]
Section Curvature [1/in]
x 10^-4

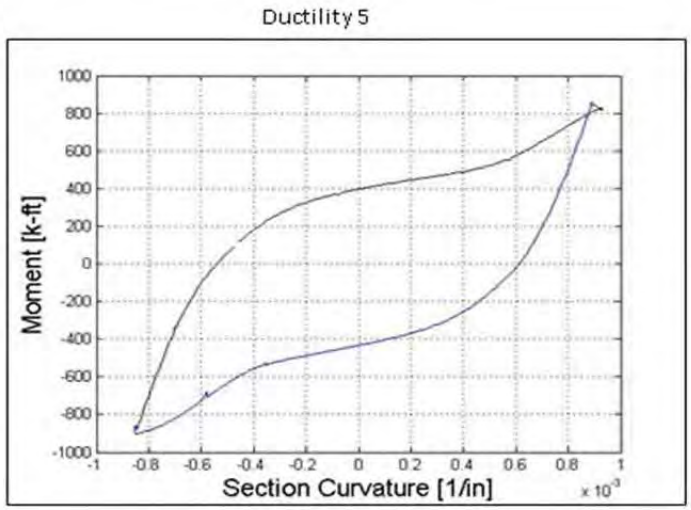
Ductility 5
Moment [k-ft]
Section Curvature [1/in]
x 10^-3

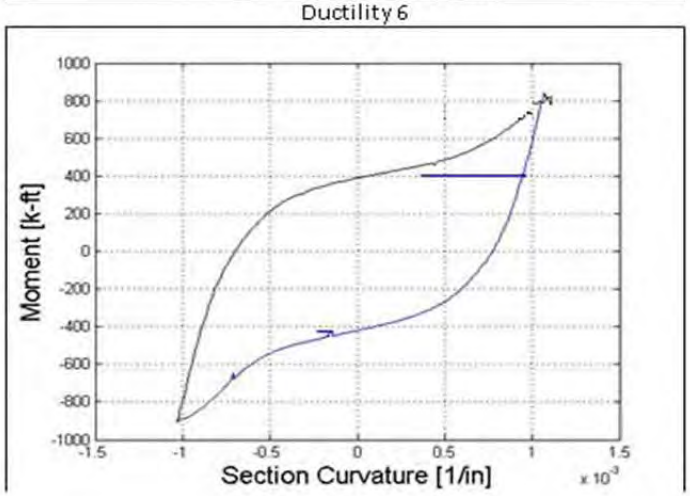
Ductility 6
Moment [k-ft]
Section Curvature [1/in]
x 10^-3

Figure 9-12 Moment Curvature Hysteretic Loops for a D/t ratio of 160

Ductility 1

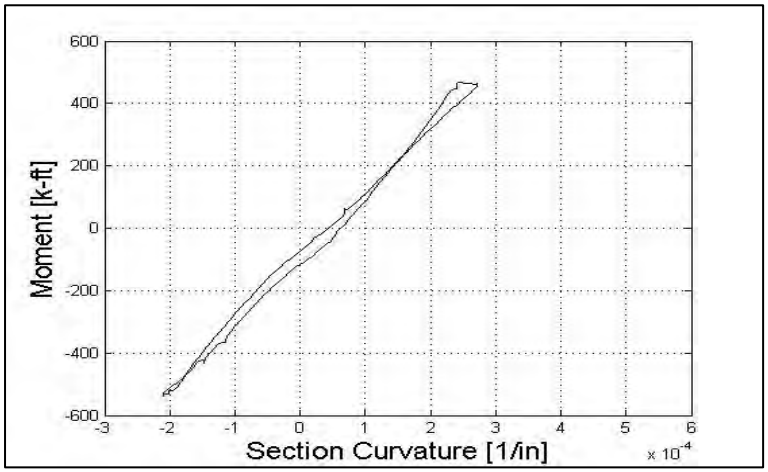

Ductility 1.5

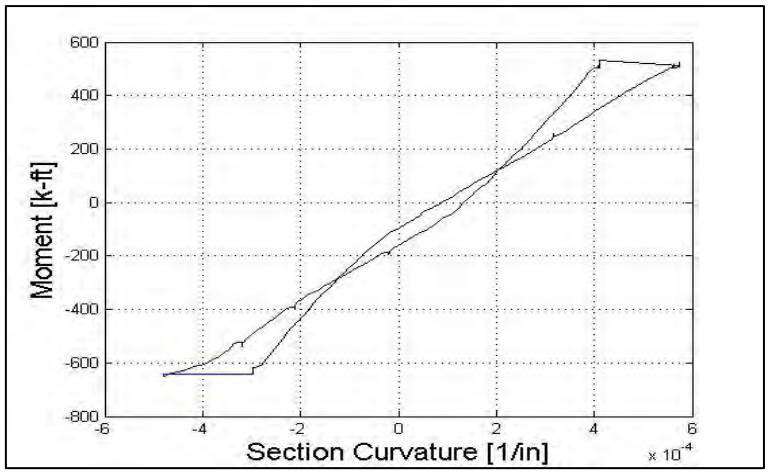

Ductility 2

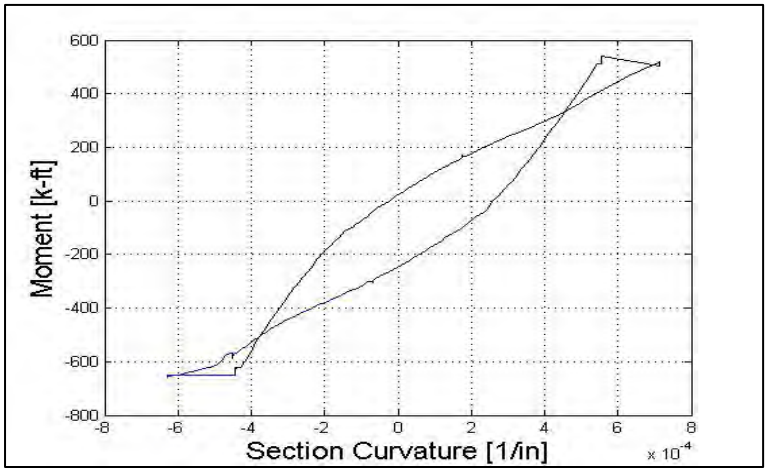

Ductility 3

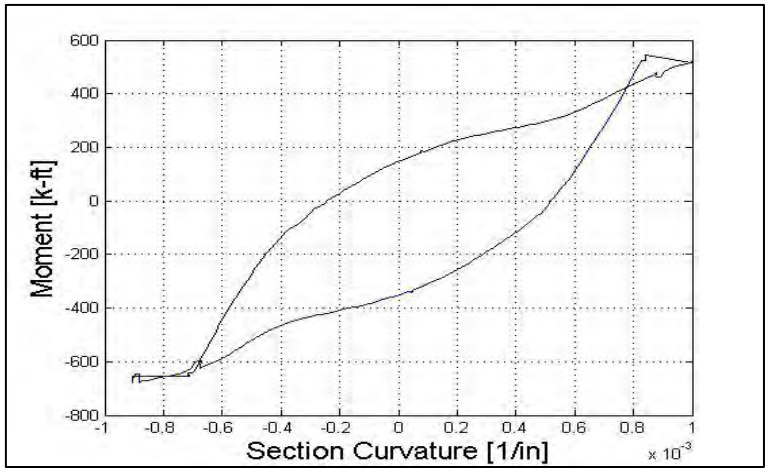

Ductility 4

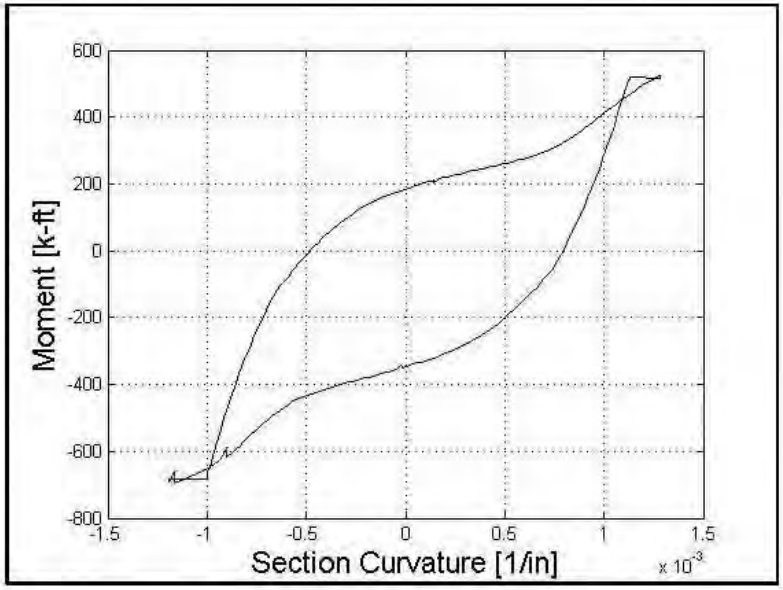

Ductility 5

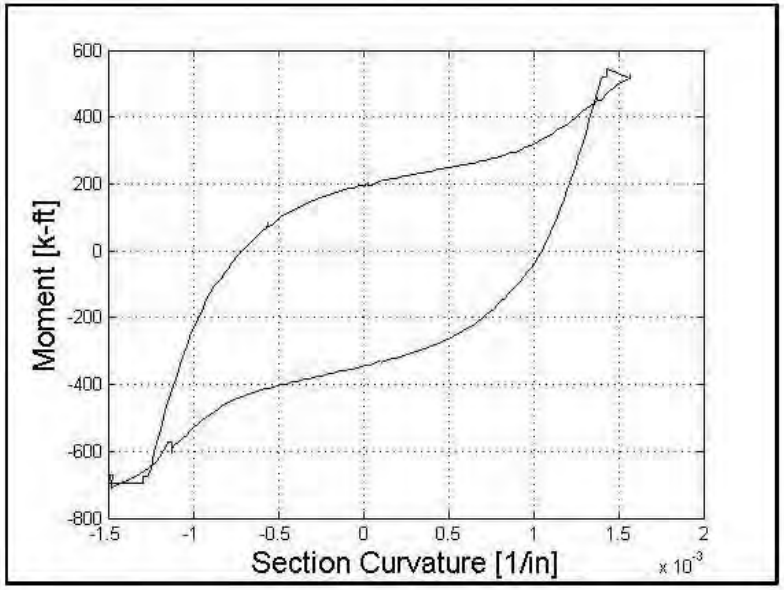

Figure 9-13 Moment Curvature Hysteretic Loops for a D/t ratio of 192

Ductility 1

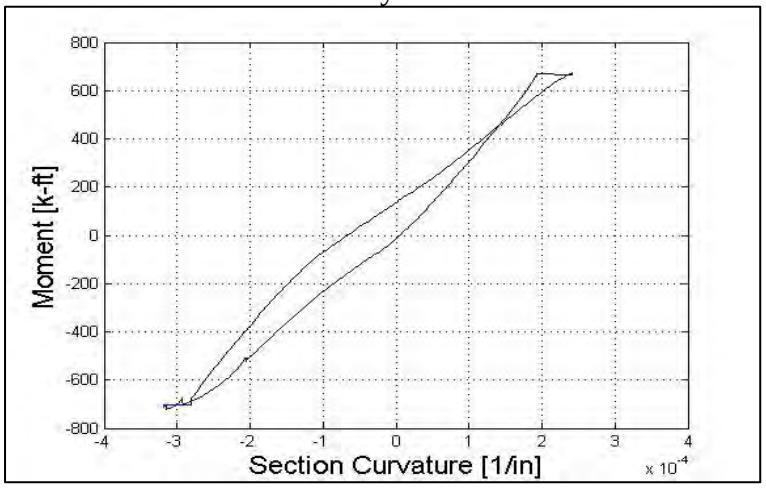

Ductility 1.5

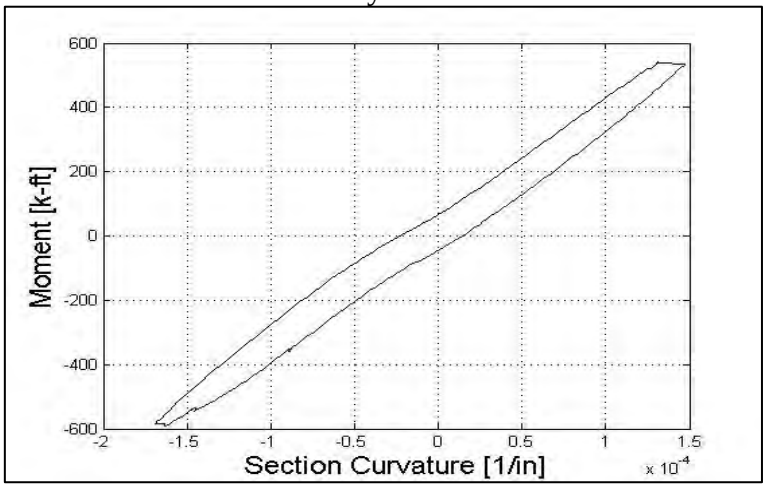

Ductility 2

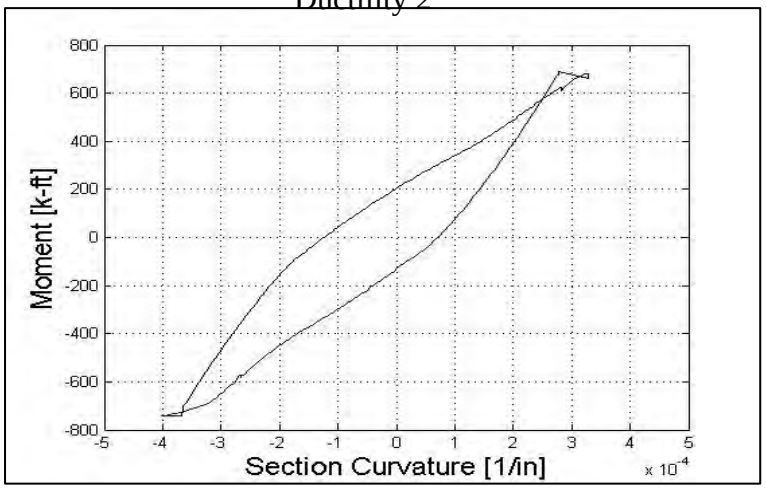

Ductility 3

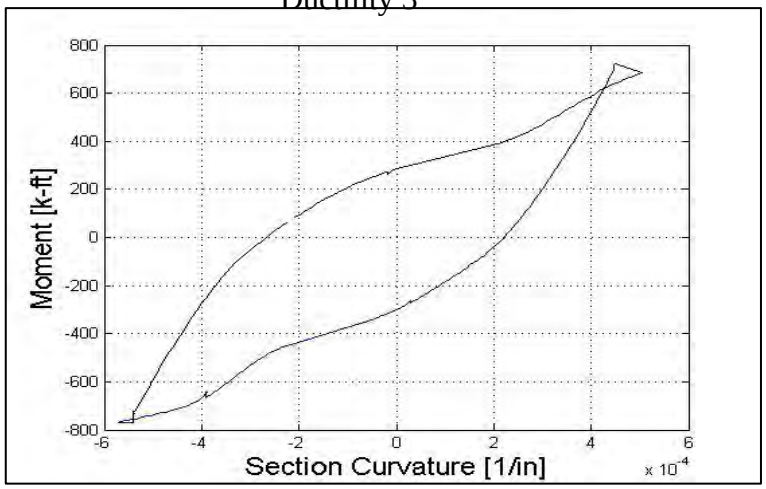

Ductility 4

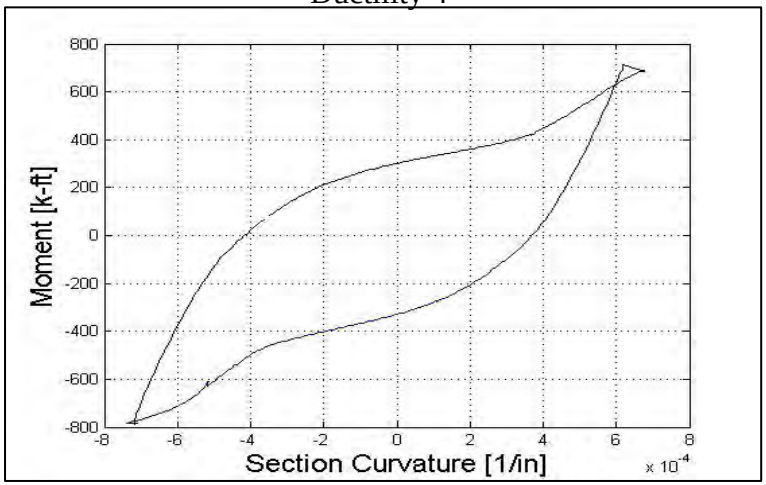

Ductility 5

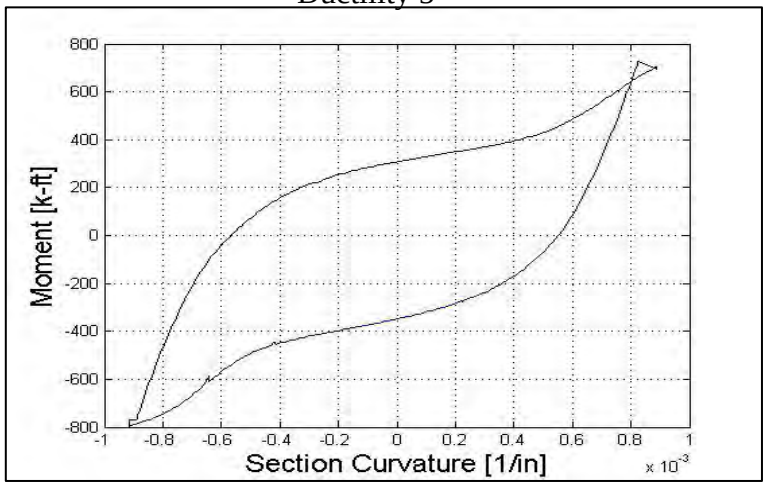

Ductility 6

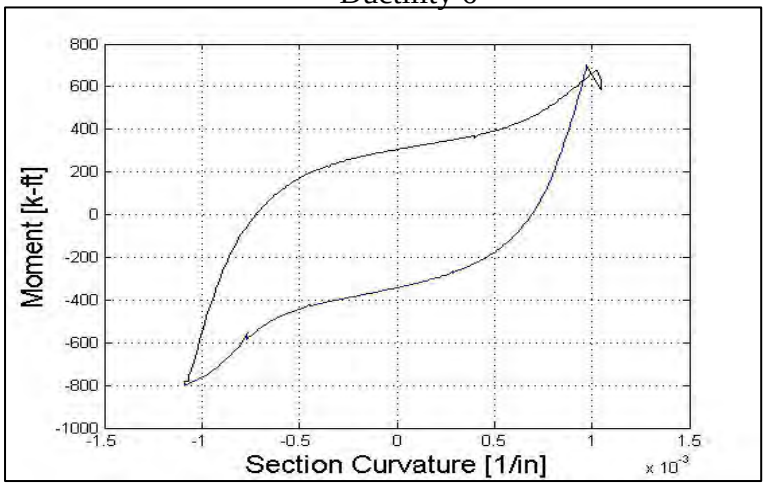

Appendix D: Moments, forces, strains, curvatures and displacements for each cycle

The mid-span displacements, force in each actuator, moment in the constant moment region, maximum tensile strains, extrapolated curvatures and extrapolated compressive strains for each test at the end of every loading cycle are tabulated in this appendix.

Table 9-1 Peak Cycle data (D/t = 33)

Cycle		Displ (in)	Force (k)	Moment (k ft)	Option Two			
					Curv (1/in)	NA Depth (in)	Tensile Strain	Comp Strain
1/4 Fy	push	0.32	21.5	193.7	-0.00004	0.34	0.0005	-0.0004
	pull	-0.46	-33.3	-299.3	0.00005	-1.27	0.0005	-0.0004
1/2 Fy	push	0.73	49.1	441.6	-0.00008	1.12	0.0009	-0.0008
	pull	-0.89	-61.6	-554.8	0.00009	-0.62	0.0010	-0.0008
3/4 Fy	push	1.21	76.4	687.8	-0.00014	1.11	0.0016	-0.0012
	pull	-1.33	-89.3	-803.3	0.00014	-0.96	0.0015	-0.0013
Fy	push	1.80	101.8	916.0	-0.00021	1.12	0.0023	-0.0019
	pull	-1.87	-115.3	-1037.4	0.00021	-1.44	0.0024	-0.0018
Ductility 1	push 1	2.62	126.3	1136.7	-0.00032	1.41	0.0037	-0.0028
	pull 1	-2.61	-138.8	-1249.0	0.00030	-1.74	0.0035	-0.0025
	push 2	2.63	127.6	1148.8	-0.00033	1.51	0.0038	-0.0028
	pull 2	-2.62	-138.2	-1243.4	0.00029	-1.96	0.0035	-0.0024
	push 3	2.63	126.3	1136.6	-0.00034	1.70	0.0040	-0.0028
	pull 3	-2.62	-138.2	-1244.0	0.00029	-2.07	0.0035	-0.0023
Ductility 1.5	push 1	3.91	143.0	1287.4	-0.00056	1.68	0.0065	-0.0047
	pull 1	-3.90	-157.1	-1413.8	0.00049	-2.14	0.0059	-0.0038
	push 2	3.92	139.2	1252.4	-0.00056	1.82	0.0066	-0.0046
	pull 2	-3.90	-153.9	-1384.7	0.00050	-2.14	0.0061	-0.0039
	push 3	3.94	139.7	1257.6	-0.00055	1.96	0.0066	-0.0044
	pull 3	-3.99	-155.0	-1395.2	0.00052	-2.11	0.0063	-0.0041
Ductility 2	push 1	5.26	149.3	1343.8	-0.00081	2.01	0.0097	-0.0064
	pull 1	-5.27	-164.1	-1476.6	0.00071	-2.52	0.0089	-0.0053
	push 2	5.27	143.9	1294.7	-0.00084	2.04	0.0101	-0.0067
	pull 2	-5.27	-160.1	-1441.3	0.00071	-2.54	0.0089	-0.0053
	push 3	5.27	141.2	1271.1	-0.00082	2.19	0.0101	-0.0064
	pull 3	-5.28	-157.1	-1413.9	0.00072	-2.54	0.0090	-0.0054
Ductility 3	push 1	7.97	152.5	1372.5	-0.00128	2.38	0.0159	-0.0098
	pull 1	-7.98	-173.8	-1564.5	0.00112	-3.03	0.0146	-0.0078
	push 2	7.98	148.5	1336.6	-0.00135	2.50	0.0169	-0.0101
	pull 2	-7.98	-168.7	-1518.3	0.00112	-3.16	0.0147	-0.0076
	push 3	7.98	146.1	1314.9	-0.00136	2.56	0.0171	-0.0101
	pull 3	-7.99	-165.4	-1488.2	0.00112	-3.18	0.0148	-0.0076

Table 9-1 continued

Ductility 4	push 1	10.50	151.6	1364.6	-0.00179	2.62	0.0226	-0.0132
	pull 1	-10.68	-177.8	-1600.6	0.00152	-3.31	0.0202	-0.0102
	push 2	10.52	149.8	1347.8	-0.00183	2.78	0.0234	-0.0132
	pull 2	-10.70	-171.9	-1546.8	0.00151	-3.49	0.0203	-0.0098
	push 3	10.53	149.1	1341.6	-0.00185	2.84	0.0237	-0.0132
	pull 3	-10.71	-168.9	-1520.3	0.00151	-3.49	0.0204	-0.0099
Ductility 5	push 1	12.91	150.6	1355.5	-0.00224	2.83	0.0288	-0.0161
	pull 1	-13.01	-177.2	-1595.0	0.00184	-3.55	0.0249	-0.0119
	push 2	12.90	149.8	1347.8	-0.00228	2.96	0.0295	-0.0160
	pull 2	-13.00	-173.0	-1556.8	0.00184	-3.69	0.0252	-0.0116
	push 3	12.90	146.9	1322.1	-0.00230	3.06	0.0301	-0.0160
	pull 3	-13.00	-171.7	-1545.2	0.00182	-3.83	0.0251	-0.0112
Ductility 6	push 1	15.55	151.6	1364.0	-0.00267	3.16	0.0352	-0.0183
	pull 1	-15.72	-179.6	-1616.7	0.00212	-3.91	0.0295	-0.0129
	push 2	15.56	148.5	1336.9	-0.00267	3.37	0.0357	-0.0177
	pull 2	-15.78	-182.4	-1641.8	0.00203	-4.07	0.0286	-0.0121
	push 3	15.61	146.9	1322.3	-0.00252	3.61	0.0342	-0.0161
	pull 3	-15.85	-171.0	-1539.4	0.00173	-4.89	0.0257	-0.0088

Table 9-2 Peak Cycle data (D/t = 48, ρ=1.6%)

Cycle		Displ (in)	Force (k)	Moment (k ft)	Curv (1/in)	NA Depth (in)	Tensile Strain	Comp Strain
1/4 Fy	push	0.38	24.44	293.29	-0.00003	2.62	0.0004	-0.0003
	pull	-0.41	-24.32	-291.85	0.00001	-5.08	0.0001	0.0000
1/2 Fy	push	0.78	46.50	557.97	-0.00006	2.17	0.0009	-0.0006
	pull	-0.81	-47.11	-565.31	0.00004	-2.68	0.0006	-0.0004
3/4 Fy	push	1.19	68.20	818.44	-0.00009	2.54	0.0013	-0.0009
	pull	-1.19	-67.61	-811.35	0.00006	-4.04	0.0010	-0.0005
Fy	push	1.60	89.13	1069.54	-0.00012	2.84	0.0017	-0.0011
	pull	-1.60	-91.26	-1095.10	0.00009	-3.34	0.0013	-0.0008
Ductility 1	push 1	2.55	127.57	1530.82	-0.00020	2.85	0.0030	-0.0019
	pull 1	-2.58	-139.97	-1679.65	0.00019	-2.62	0.0028	-0.0018
	push 2	2.57	129.43	1553.18	-0.00021	3.09	0.0031	-0.0018
	pull 2	-2.53	-135.48	-1625.74	0.00018	-2.83	0.0027	-0.0017
	push 3	2.53	125.55	1506.60	-0.00020	2.80	0.0030	-0.0019
	pull 3	-2.48	-133.12	-1597.47	0.00018	-3.09	0.0026	-0.0016
Ductility 1.5	push 1	3.80	153.18	1838.19	-0.00032	3.66	0.0050	-0.0027
	pull 1	-3.81	-168.76	-2025.08	0.00032	-3.51	0.0050	-0.0027
	push 2	3.76	150.41	1804.95	-0.00032	3.97	0.0052	-0.0026
	pull 2	-3.75	-164.31	-1971.68	0.00033	-3.20	0.0050	-0.0029
	push 3	3.77	147.97	1775.59	-0.00033	3.97	0.0052	-0.0026
	pull 3	-3.75	-162.96	-1955.48	0.00033	-3.43	0.0050	-0.0028
Ductility 2	push 1	4.96	159.38	1912.61	-0.00045	4.22	0.0073	-0.0035
	pull 1	-5.02	-176.21	-2114.52	0.00050	-3.50	0.0078	-0.0043
	push 2	5.00	154.41	1852.96	-0.00048	4.29	0.0078	-0.0037
	pull 2	-5.02	-172.17	-2066.01	0.00052	-3.30	0.0080	-0.0045
	push 3	5.03	152.16	1825.88	-0.00048	4.33	0.0079	-0.0037
	pull 3	-5.02	-169.12	-2029.47	0.00053	-3.27	0.0082	-0.0047
Ductility 3	push 1	7.46	165.37	1984.42	-0.00076	4.56	0.0126	-0.0057
	pull 1	-7.43	-182.45	-2189.36	0.00086	-3.89	0.0137	-0.0070
	push 2	7.44	158.48	1901.81	-0.00081	4.75	0.0135	-0.0059
	pull 2	-7.53	-178.26	-2139.08	0.00091	-3.67	0.0143	-0.0076
	push 3	7.39	155.43	1865.19	-0.00080	5.03	0.0137	-0.0056
	pull 3	-7.52	-175.33	-2103.98	0.00090	-3.99	0.0144	-0.0072

Table 9-2 continued

Ductility 4	push 1	9.99	166.47	1997.66	-0.00109	5.03	0.0186	-0.0076
	pull 1	-10.09	-186.31	-2235.77	0.00124	-4.21	0.0201	-0.0097
	push 2	9.97	161.34	1936.07	-0.00116	4.94	0.0196	-0.0082
	pull 2	-10.08	-182.19	-2186.33	0.00125	-4.36	0.0205	-0.0096
	push 3	9.82	158.32	1899.79	-0.00114	5.03	0.0195	-0.0080
	pull 3	-10.05	-180.13	-2161.52	0.00128	-4.08	0.0206	-0.0102
Ductility 6	push 1	14.66	171.49	2057.82	-0.00162	5.22	0.0278	-0.0110
	pull 1	-15.07	-194.17	-2330.02	0.00195	-4.05	0.0312	-0.0155
	push 2	15.15	164.22	1970.66	-0.00142	6.65	0.0264	-0.0076
	pull 2	-15.00	-187.05	-2244.63	0.00139	-6.17	0.0253	-0.0081
	push 3	14.91	155.48	1865.70	-0.00075	13.35	0.0189	0.0010
	pull 3	-14.67	-178.21	-2138.48	0.00110	-7.93	0.0220	-0.0045
Ductility 8	push 1	15.34	140.50	1685.98	-0.00046	21.68	0.0154	0.0044
	pull 1	-18.02	-173.48	-2081.78	0.00061	-15.29	0.0166	0.0020
	push 2	13.76	123.02	1476.23	-0.00070	13.67	0.0181	0.0012

Table 9-3 Peak Cycle data (D/t = 64, ρ=1.6%)

Cycle		Displ (in)	Force (k)	Moment (k ft)	Curv (1/in)	NA Depth (in)	Tensile Strain	Comp Strain
1/4 Fy	push	0.31	17.4	208.8	-0.00002	1.01	0.0003	-0.0003
	pull	-0.37	-17.8	-213.5	0.00003	-1.47	0.0003	-0.0003
1/2 Fy	push	0.70	35.6	427.3	-0.00005	3.33	0.0007	-0.0004
	pull	-0.78	-35.4	-424.3	0.00005	-1.94	0.0007	-0.0005
3/4 Fy	push	1.12	53.3	639.3	-0.00010	0.94	0.0013	-0.0011
	pull	-1.21	-54.1	-649.7	0.00008	-2.29	0.0011	-0.0008
Fy	push	1.55	71.7	860.0	-0.00013	1.82	0.0017	-0.0013
	pull	-1.61	-70.9	-850.5	0.00011	-1.91	0.0016	-0.0011
Ductility 1	push 1	3.00	115.0	1379.9	-0.00025	2.56	0.0037	-0.0024
	pull 1	-3.07	-121.2	-1454.7	0.00023	-2.74	0.0034	-0.0022
	push 2	3.00	116.3	1395.3	-0.00024	3.09	0.0037	-0.0022
	pull 2	-3.09	-121.3	-1455.6	0.00024	-2.71	0.0035	-0.0022
	push 3	3.00	115.9	1391.3	-0.00024	3.19	0.0037	-0.0022
	pull 3	-3.08	-119.5	-1433.7	0.00025	-2.70	0.0036	-0.0023
Ductility 1.5	push 1	4.54	133.8	1605.2	-0.00043	3.51	0.0066	-0.0036
	pull 1	-4.52	-139.2	-1670.1	0.00041	-3.45	0.0064	-0.0035
	push 2	4.49	131.5	1578.6	-0.00043	3.66	0.0068	-0.0036
	pull 2	-4.54	-137.4	-1649.0	0.00042	-3.53	0.0066	-0.0036
	push 3	4.50	130.2	1562.2	-0.00045	3.52	0.0070	-0.0038
	pull 3	-3.86	-125.8	-1509.3	0.00035	-3.76	0.0055	-0.0029
Ductility 2	push 1	6.03	137.9	1655.3	-0.00065	3.87	0.0103	-0.0053
	pull 1	-6.09	-143.4	-1721.3	0.00065	-3.99	0.0104	-0.0052
	push 2	6.04	134.7	1616.7	-0.00066	4.46	0.0109	-0.0050
	pull 2	-6.05	-141.5	-1697.7	0.00067	-3.95	0.0106	-0.0054
	push 3	6.03	131.9	1582.8	-0.00069	4.21	0.0111	-0.0053
	pull 3	-6.04	-138.8	-1665.1	0.00067	-3.95	0.0108	-0.0054
Ductility 3	push 1	9.15	141.0	1691.7	-0.00108	4.49	0.0178	-0.0081
	pull 1	-9.06	-148.7	-1785.0	0.00108	-4.69	0.0181	-0.0079
	push 2	9.20	136.0	1631.7	-0.00114	4.84	0.0191	-0.0081
	pull 2	-9.06	-148.4	-1780.6	0.00111	-4.71	0.0185	-0.0081
	push 3	9.10	136.4	1636.6	-0.00111	5.02	0.0189	-0.0077
	pull 3	-9.07	-145.9	-1751.4	0.00111	-4.60	0.0184	-0.0082

Table 9-3 continued

Ductility 4	push 1	12.04	140.9	1691.2	-0.00143	4.86	0.0241	-0.0102
	pull 1	-12.02	-150.2	-1802.3	0.00145	-4.35	0.0237	-0.0111
	push 2	11.98	133.4	1601.1	-0.00113	5.98	0.0203	-0.0068
	pull 2	-11.97	-146.1	-1753.0	0.00134	-4.88	0.0226	-0.0095
	push 3	11.91	133.5	1601.6	-0.00102	6.56	0.0189	-0.0055
	pull 3	-11.84	-141.8	-1701.3	0.00143	-4.52	0.0236	-0.0107
Ductility 5	push 1	15.06	135.4	1624.4	-0.00134	5.60	0.0236	-0.0086
	pull 1	-15.06	-145.1	-1741.3	0.00212	-3.22	0.0322	-0.0186
	push 2	14.97	125.1	1501.2	-0.00137	5.29	0.0237	-0.0092
	pull 2	-14.95	-133.5	-1601.8	0.00133	-6.41	0.0245	-0.0074
	push 3	14.91	118.7	1424.2	-0.00136	4.85	0.0229	-0.0097
	pull 3	-14.28	-60.5	-725.8	0.00096	-9.37	0.0204	-0.0025

Table 9-4 Peak Cycle data (D/t = 85, ρ=1.6%)

Cycle		Displ (in)	Force (k)	Moment (k ft)	Curv (1/in)	NA Depth (in)	Tensile Strain	Comp Strain
1/4 Fy	push	0.40	20.2	242.2	-0.00003	2.13	0.0004	-0.0003
	pull	-0.50	-23.6	-282.7	0.00003	-2.84	0.0005	-0.0003
1/2 Fy	push	1.00	42.6	510.8	-0.00007	2.97	0.0011	-0.0007
	pull	-1.12	-45.6	-547.0	0.00008	-1.87	0.0011	-0.0008
3/4 Fy	push	1.57	64.0	767.7	-0.00012	2.76	0.0018	-0.0011
	pull	-1.72	-67.6	-811.8	0.00013	-1.65	0.0018	-0.0013
Fy	push	2.23	86.4	1036.6	-0.00018	2.23	0.0025	-0.0017
	pull	-2.35	-89.5	-1073.4	0.00018	-2.15	0.0025	-0.0017
Ductility 1	push 1	3.27	110.0	1319.8	-0.00027	3.02	0.0040	-0.0024
	pull 1	-3.29	-114.3	-1371.9	0.00025	-3.07	0.0037	-0.0022
	push 2	3.27	110.4	1325.3	-0.00027	3.11	0.0041	-0.0024
	pull 2	-3.29	-113.0	-1355.7	0.00024	-3.23	0.0037	-0.0021
	push 3	3.27	107.9	1294.5	-0.00027	3.28	0.0041	-0.0023
	pull 3	-3.28	-110.6	-1326.7	0.00025	-3.17	0.0037	-0.0022
Ductility 1.5	push 1	4.88	125.7	1507.9	-0.00050	1.83	0.0069	-0.0051
	pull 1	-4.97	-129.5	-1553.5	0.00041	-4.55	0.0068	-0.0031
	push 2	4.90	122.9	1474.5	-0.00050	2.20	0.0071	-0.0049
	pull 2	-4.88	-128.8	-1545.4	0.00041	-4.81	0.0068	-0.0029
	push 3	4.92	121.7	1460.0	-0.00052	2.22	0.0075	-0.0051
	pull 3	-4.76	-123.4	-1480.9	0.00040	-4.78	0.0067	-0.0029
Ductility 2	push 1	6.55	127.9	1534.9	-0.00057	5.48	0.0100	-0.0037
	pull 1	-6.61	-133.8	-1605.9	0.00062	-5.15	0.0107	-0.0043
	push 2	6.49	125.3	1504.1	-0.00062	5.33	0.0108	-0.0041
	pull 2	-6.50	-131.3	-1575.1	0.00063	-5.04	0.0108	-0.0044
	push 3	6.51	123.4	1480.3	-0.00059	5.88	0.0105	-0.0036
	pull 3	-6.50	-131.2	-1574.2	0.00059	-5.54	0.0103	-0.0038
Ductility 3	push 1	9.48	130.6	1567.4	-0.00098	5.39	0.0170	-0.0065
	pull 1	-9.80	-138.2	-1658.3	0.00105	-5.05	0.0179	-0.0073
	push 2	9.80	125.2	1503.0	-0.00094	6.39	0.0173	-0.0053
	pull 2	-9.82	-133.3	-1599.6	0.00090	-6.01	0.0163	-0.0054
	push 3	9.80	121.7	1460.8	-0.00091	6.23	0.0166	-0.0053
	pull 3	-9.37	-124.8	-1498.1	0.00101	-4.51	0.0167	-0.0076

Table 9-4 continued

Ductility 4	push 1	13.08	126.5	1517.5	-0.00138	4.37	0.0226	-0.0105
	pull 1	-13.14	-134.8	-1617.7	0.00147	-4.17	0.0237	-0.0115
	push 2	13.09	118.8	1425.6	-0.00162	3.43	0.0249	-0.0139
	pull 2	-13.10	-125.8	-1509.1	0.00131	-4.95	0.0222	-0.0092
	push 3	13.08	111.7	1340.9	-0.00184	2.00	0.0258	-0.0184
	pull 3	-13.00	-57.5	-689.6	0.00101	-6.07	0.0183	-0.0060

Table 9-5 Peak Cycle data (D/t = 128, ρ=1.6%)

Cycle		Displ (in)	Force (k)	Moment (k ft)	Curv (1/in)	NA Depth (in)	Tensile Strain	Comp Strain
1/4 Fy	push	0.17	8.3	99.3	-0.00001	0.45	0.0002	-0.0002
	pull	-0.20	-7.5	-90.5	0.00001	0.90	0.0001	-0.0001
1/2 Fy	push	0.35	16.2	194.6	-0.00003	0.32	0.0004	-0.0004
	pull	-0.46	-15.7	-188.5	0.00003	-2.02	0.0004	-0.0003
3/4 Fy	push	0.66	24.3	291.6	-0.00005	2.20	0.0007	-0.0005
	pull	-0.76	-24.0	-288.0	0.00006	-1.88	0.0008	-0.0006
Fy	push	0.98	32.5	390.1	-0.00008	2.36	0.0012	-0.0008
	pull	-1.06	-32.2	-386.9	0.00008	-2.73	0.0012	-0.0008
Ductility 1	push 1	2.10	54.0	648.2	-0.00017	3.19	0.0025	-0.0015
	pull 1	-2.07	-53.7	-645.0	0.00017	-3.64	0.0026	-0.0014
	push 2	2.10	54.5	653.5	-0.00016	4.26	0.0025	-0.0012
	pull 2	-2.08	-53.7	-643.9	0.00017	-3.65	0.0027	-0.0015
	push 3	2.10	53.6	643.4	-0.00017	4.08	0.0027	-0.0013
	pull 3	-2.08	-52.7	-632.7	0.00017	-3.85	0.0026	-0.0014
Ductility 1.5	push 1	3.12	63.7	764.3	-0.00028	4.89	0.0047	-0.0020
	pull 1	-2.53	-59.4	-712.7	0.00019	-5.55	0.0033	-0.0012
	push 2	3.14	63.4	761.0	-0.00030	5.00	0.0050	-0.0021
	pull 2	-3.13	-63.6	-763.1	0.00027	-5.41	0.0048	-0.0018
	push 3	3.14	62.3	748.1	-0.00030	5.15	0.0051	-0.0020
	pull 3	-3.14	-62.6	-751.3	0.00030	-5.06	0.0051	-0.0021
Ductility 2	push 1	4.49	67.4	809.4	-0.00045	6.02	0.0081	-0.0027
	pull 1	-4.45	-67.8	-814.2	0.00048	-6.45	0.0089	-0.0027
	push 2	4.51	65.5	785.8	-0.00047	6.49	0.0088	-0.0026
	pull 2	-4.46	-66.7	-800.9	0.00046	-7.32	0.0089	-0.0022
	push 3	4.51	64.1	769.3	-0.00052	5.91	0.0093	-0.0032
	pull 3	-4.47	-66.7	-800.3	0.00043	-8.16	0.0086	-0.0016
Ductility 3	push 1	6.78	70.7	848.1	-0.00079	6.24	0.0143	-0.0045
	pull 1	-6.71	-71.6	-858.7	0.00080	-6.50	0.0149	-0.0044
	push 2	6.79	68.5	822.0	-0.00074	6.92	0.0141	-0.0038
	pull 2	-6.72	-69.5	-834.1	0.00080	-6.20	0.0146	-0.0046
	push 3	6.79	66.2	794.4	-0.00083	5.86	0.0147	-0.0051
	pull 3	-6.71	-67.4	-808.3	0.00076	-6.49	0.0140	-0.0042

Table 9-5 continued

Ductility 4	push 1	8.37	70.0	839.9	-0.00108	5.38	0.0187	-0.0071
	pull 1	-8.27	-71.2	-854.3	0.00092	-6.67	0.0172	-0.0049
	push 2	8.37	66.5	797.9	-0.00101	6.47	0.0186	-0.0056
	pull 2	-8.29	-71.1	-853.4	0.00096	-6.51	0.0177	-0.0053
	push 3	8.38	64.7	775.8	-0.00109	5.62	0.0192	-0.0070
	pull 3	-8.27	-66.1	-793.3	0.00116	-5.19	0.0199	-0.0079
Ductility 5	push 1	10.35	71.5	857.6	-0.00133	5.82	0.0237	-0.0082
	pull 1	-10.38	-72.9	-875.2	0.00141	-4.98	0.0240	-0.0099
	push 2	10.38	67.9	815.3	-0.00125	6.30	0.0229	-0.0071
	pull 2	-10.41	-70.3	-843.5	0.00149	-4.74	0.0250	-0.0108
	push 3	10.36	66.5	798.0	-0.00127	6.22	0.0232	-0.0074
	pull 3	-10.43	-68.1	-816.7	0.00153	-4.58	0.0254	-0.0114
Ductility 6	push 1	12.47	69.9	838.9	-0.00155	6.18	0.0282	-0.0090
	pull 1	-12.48	-74.5	-893.7	0.00164	-5.14	0.0282	-0.0113
	push 2	12.49	64.9	778.5	-0.00152	6.70	0.0284	-0.0080
	pull 2	-12.50	-71.7	-860.3	0.00163	-5.37	0.0283	-0.0108
	push 3	12.68	55.9	671.2	-0.00141	6.81	0.0265	-0.0073

Table 9-6 Peak Cycle data (D/t = 160, ρ=1.6%)

Cycle		Displ (in)	Force (k)	Moment (k ft)	Curv (1/in)	NA Depth (in)	Tensile Strain	Comp Strain
1/4 Fy	push	0.01	0.3	3.0	0.00007	-3.68	-0.0004	0.0010
	pull	-0.32	-11.1	-99.7	0.00004	1.54	0.0004	-0.0005
1/2 Fy	push	0.18	6.5	58.1	-0.00003	-0.13	0.0003	-0.0003
	pull	-0.54	-16.7	-150.5	0.00005	-1.34	0.0006	-0.0005
3/4 Fy	push	0.43	12.7	114.4	-0.00005	2.63	0.0006	-0.0004
	pull	-0.80	-22.7	-204.7	0.00009	-1.70	0.0010	-0.0007
Fy	push	0.67	18.5	166.1	-0.00008	2.07	0.0010	-0.0007
	pull	-1.07	-28.5	-256.7	0.00012	-1.32	0.0014	-0.0011
Ductility 1	push 1	1.85	38.9	350.4	-0.00025	2.62	0.0031	-0.0018
	pull 1	-1.85	-44.3	-399.0	0.00021	-2.46	0.0026	-0.0016
	push 2	1.86	38.4	345.6	-0.00025	2.60	0.0032	-0.0019
	pull 2	-1.85	-43.9	-395.2	0.00022	-2.31	0.0027	-0.0017
	push 3	1.86	37.7	339.5	-0.00025	2.70	0.0032	-0.0018
	pull 3	-1.85	-43.5	-391.9	0.00021	-2.48	0.0027	-0.0016
Ductility 1.5	push 1	2.85	44.3	398.4	-0.00049	2.57	0.0061	-0.0036
	pull 1	-2.88	-53.6	-482.7	0.00039	-3.29	0.0052	-0.0026
	push 2	2.85	42.5	382.4	-0.00046	3.27	0.0061	-0.0031
	pull 2	-2.88	-52.3	-470.4	0.00039	-3.49	0.0052	-0.0025
	push 3	2.85	41.9	377.5	-0.00046	3.35	0.0061	-0.0030
	pull 3	-2.89	-51.9	-467.1	0.00039	-3.38	0.0053	-0.0026
Ductility 2	push 1	3.78	45.1	405.7	-0.00067	3.32	0.0089	-0.0045
	pull 1	-3.84	-54.3	-488.7	0.00066	-3.46	0.0089	-0.0043
	push 2	3.77	42.0	378.4	-0.00066	4.05	0.0092	-0.0039
	pull 2	-3.80	-52.5	-472.3	0.00061	-3.97	0.0085	-0.0037
	push 3	3.78	41.7	375.4	-0.00073	3.25	0.0096	-0.0049
	pull 3	-3.80	-51.8	-466.3	0.00064	-3.44	0.0086	-0.0042
Ductility 3	push 1	5.62	45.5	409.5	-0.00108	3.96	0.0151	-0.0065
	pull 1	-5.61	-54.5	-490.6	0.00095	-3.80	0.0132	-0.0059
	push 2	5.64	43.0	386.7	-0.00110	4.13	0.0156	-0.0065
	pull 2	-5.64	-51.9	-467.5	0.00103	-3.70	0.0141	-0.0065
	push 3	5.65	41.2	370.7	-0.00120	3.46	0.0162	-0.0079
	pull 3	-5.67	-52.3	-471.1	0.00110	-3.30	0.0146	-0.0074

Table 9-6 continued

Ductility 4	push 1	7.46	43.3	389.8	-0.00158	3.35	0.0211	-0.0105
	pull 1	-7.49	-56.8	-511.0	0.00141	-3.62	0.0193	-0.0090
	push 2	7.51	43.1	388.0	-0.00159	3.45	0.0214	-0.0104
	pull 2	-7.53	-55.2	-496.5	0.00148	-3.51	0.0200	-0.0096
	push 3	7.50	41.7	375.3	-0.00155	4.02	0.0218	-0.0093
	pull 3	-7.54	-53.5	-481.2	0.00137	-3.99	0.0192	-0.0083
Ductility 5	push 1	9.40	45.3	407.3	-0.00223	2.86	0.0287	-0.0160
	pull 1	-9.41	-57.8	-520.4	0.00171	-4.05	0.0240	-0.0102
	push 2	9.41	43.1	388.0	-0.00188	4.27	0.0268	-0.0108
	pull 2	-9.46	-56.3	-506.9	0.00173	-4.25	0.0247	-0.0100
	push 3	9.42	41.6	374.5	-0.00194	4.02	0.0272	-0.0116
	pull 3	-9.47	-54.6	-491.8	0.00167	-4.63	0.0244	-0.0089
Ductility 6	push 1	11.42	33.1	298.3	-0.00189	4.46	0.0273	-0.0105

Table 9-7 Peak Cycle data (D/t = 192, ρ=1.6%)

Cycle		Displ (in)	Force (k)	Moment (k ft)	Curv (1/in)	NA Depth (in)	Tensile Strain	Comp Strain
1/4 Fy	push	0.14	6.5	77.9	-0.00001	0.45	0.0002	-0.0002
	pull	-0.21	-8.9	-106.3	0.00001	0.48	0.0002	-0.0002
1/2 Fy	push	0.42	14.3	171.3	-0.00003	2.07	0.0005	-0.0003
	pull	-0.50	-16.9	-202.8	0.00005	-1.68	0.0006	-0.0005
3/4 Fy	push	0.82	23.0	276.2	-0.00006	3.44	0.0009	-0.0005
	pull	-0.86	-25.4	-304.4	0.00008	-2.11	0.0011	-0.0008
Fy	push	1.20	30.8	369.3	-0.00008	3.91	0.0013	-0.0007
	pull	-1.24	-33.8	-405.4	0.00010	-3.71	0.0015	-0.0008
Ductility 1	push 1	1.95	44.5	534.1	-0.00015	4.16	0.0024	-0.0012
	pull 1	-2.01	-48.7	-584.1	0.00016	-3.83	0.0026	-0.0013
	push 2	1.96	44.8	538.1	-0.00014	5.09	0.0023	-0.0009
	pull 2	-2.02	-48.5	-582.6	0.00016	-3.89	0.0026	-0.0013
	push 3	1.98	44.4	533.2	-0.00015	4.37	0.0024	-0.0011
	pull 3	-1.99	-47.5	-570.1	0.00015	-4.27	0.0025	-0.0012
Ductility 1.5	push 1	3.06	55.7	668.1	-0.00021	6.12	0.0038	-0.0012
	pull 1	-3.07	-58.7	-704.7	0.00030	-4.47	0.0050	-0.0023
	push 2	3.06	55.4	664.4	-0.00022	6.53	0.0041	-0.0012
	pull 2	-3.05	-57.9	-694.6	0.00023	-6.74	0.0042	-0.0012
	push 3	2.98	53.9	646.4	-0.00024	5.87	0.0043	-0.0015
	pull 3	-3.06	-57.6	-691.3	0.00022	-7.28	0.0042	-0.0010
Ductility 2	push 1	4.06	57.4	688.3	-0.00036	5.90	0.0064	-0.0022
	pull 1	-4.07	-61.8	-741.8	0.00048	-4.66	0.0079	-0.0035
	push 2	4.08	54.9	659.3	-0.00041	4.79	0.0069	-0.0030
	pull 2	-4.07	-60.0	-720.4	0.00048	-4.77	0.0080	-0.0035
	push 3	4.09	55.1	660.9	-0.00041	5.06	0.0070	-0.0028
	pull 3	-4.07	-59.1	-708.9	0.00047	-4.88	0.0079	-0.0033
Ductility 3	push 1	6.12	60.3	723.2	-0.00063	5.55	0.0111	-0.0041
	pull 1	-6.10	-64.0	-767.7	0.00094	-3.94	0.0150	-0.0076
	push 2	6.14	57.0	683.9	-0.00070	5.19	0.0121	-0.0048
	pull 2	-6.14	-60.9	-731.1	0.00095	-3.80	0.0151	-0.0078
	push 3	6.15	55.3	663.5	-0.00071	4.52	0.0117	-0.0053
	pull 3	-6.13	-59.1	-709.7	0.00097	-3.62	0.0151	-0.0081

Table 9-7 continued

Ductility 4	push 1	8.14	59.3	712.1	-0.00093	5.87	0.0167	-0.0057
	pull 1	-8.09	-65.3	-783.3	0.00131	-4.25	0.0213	-0.0102
	push 2	8.17	57.0	683.5	-0.00102	4.68	0.0170	-0.0074
	pull 2	-8.17	-62.6	-751.6	0.00110	-6.48	0.0204	-0.0061
	push 3	8.17	54.9	658.6	-0.00100	4.82	0.0167	-0.0071
	pull 3	-8.18	-60.6	-726.7	0.00116	-5.47	0.0202	-0.0076
Ductility 5	push 1	10.59	60.7	728.6	-0.00113	6.65	0.0211	-0.0061
	pull 1	-10.21	-64.3	-771.8	0.00151	-5.03	0.0257	-0.0105
	push 2	10.62	58.0	696.3	-0.00100	8.60	0.0205	-0.0034
	pull 2	-10.17	-62.7	-752.0	0.00135	-5.83	0.0241	-0.0083
	push 3	10.41	54.3	651.3	-0.00126	5.36	0.0219	-0.0084
	pull 3	-10.25	-60.3	-723.4	0.00131	-6.22	0.0240	-0.0076
Ductility 6	push 1	12.42	58.5	701.6	-0.00133	6.45	0.0245	-0.0074
	pull 1	-12.29	-65.3	-783.1	0.00151	-6.78	0.0283	-0.0079
	push 2	12.51	48.7	584.0	-0.00112	9.86	0.0246	-0.0024
	pull 2	-12.50	-53.2	-638.9	0.00121	-9.91	0.0265	-0.0025
	push 3	12.34	36.8	441.0	-0.00059	19.82	0.0186	

Table 9-8 Peak Cycle data (D/t = 128, ρ=0.78%)

Cycle		Displ (in)	Force (k)	Moment (k ft)	Curv (1/in)	NA Depth (in)	Tensile Strain	Comp Strain
1/4 Fy	push	0.17	8.0	96.1	-0.00001	1.74	0.0002	-0.0001
	pull	-0.25	-8.1	-97.6	0.00003	1.50	0.0003	-0.0003
1/2 Fy	push	0.47	16.4	196.5	-0.00004	1.30	0.0005	-0.0004
	pull	-0.54	-16.4	-196.2	0.00005	-0.70	0.0006	-0.0005
3/4 Fy	push	0.82	24.6	295.4	-0.00006	2.80	0.0009	-0.0006
	pull	-0.89	-24.7	-296.3	0.00006	-2.74	0.0009	-0.0006
Fy	push	1.19	32.9	395.1	-0.00009	2.84	0.0014	-0.0009
	pull	-1.24	-33.0	-396.4	0.00010	-2.23	0.0014	-0.0010
Ductility 1	push 1	2.02	46.2	554.1	-0.00016	3.90	0.0026	-0.0013
	pull 1	-2.02	-47.7	-572.6	0.00016	-3.26	0.0024	-0.0014
	push 2	2.02	45.9	550.4	-0.00016	4.33	0.0027	-0.0013
	pull 2	-2.04	-47.5	-570.2	0.00015	-3.77	0.0024	-0.0013
	push 3	2.02	44.8	537.7	-0.00018	3.31	0.0027	-0.0015
	pull 3	-2.04	-47.0	-563.6	0.00015	-4.08	0.0024	-0.0012
Ductility 1.5	push 1	3.09	52.3	627.9	-0.00033	4.00	0.0053	-0.0026
	pull 1	-3.07	-53.4	-640.9	0.00025	-5.65	0.0044	-0.0016
	push 2	3.03	50.3	603.4	-0.00036	3.81	0.0057	-0.0029
	pull 2	-3.07	-53.5	-642.3	0.00025	-5.65	0.0044	-0.0016
	push 3	3.04	48.0	576.0	-0.00037	3.76	0.0059	-0.0031
	pull 3	-3.07	-52.9	-634.5	0.00029	-3.85	0.0045	-0.0023
Ductility 2	push 1	4.04	52.7	632.5	-0.00046	5.36	0.0080	-0.0030
	pull 1	-4.04	-55.4	-664.5	0.00040	-5.11	0.0069	-0.0028
	push 2	4.06	50.6	607.2	-0.00045	6.12	0.0082	-0.0027
	pull 2	-4.05	-55.0	-659.6	0.00036	-7.54	0.0070	-0.0016
	push 3	4.06	50.9	610.3	-0.00046	6.63	0.0085	-0.0025
	pull 3	-4.05	-53.6	-642.8	0.00036	-7.88	0.0071	-0.0015
Ductility 3	push 1	6.07	54.2	650.5	-0.00066	7.35	0.0128	-0.0031
	pull 1	-6.11	-58.8	-705.5	0.00064	-6.78	0.0120	-0.0033
	push 2	6.05	52.8	633.6	-0.00060	9.16	0.0127	-0.0017
	pull 2	-6.10	-56.9	-683.2	0.00057	-8.47	0.0116	-0.0020
	push 3	6.04	51.4	617.3	-0.00069	7.41	0.0134	-0.0032
	pull 3	-6.10	-55.4	-665.3	0.00055	-8.64	0.0113	-0.0018

Table 9-8 continued

Ductility 4	push 1	8.03	55.8	669.5	-0.00089	7.74	0.0177	-0.0038
	pull 1	-8.10	-58.5	-701.5	0.00081	-7.58	0.0158	-0.0036
	push 2	8.03	52.3	627.8	-0.00093	7.82	0.0185	-0.0039
	pull 2	-8.09	-58.0	-695.9	0.00083	-7.46	0.0162	-0.0038
	push 3	8.04	50.6	607.2	-0.00097	7.38	0.0187	-0.0045
	pull 3	-8.11	-55.9	-670.7	0.00091	-6.01	0.0164	-0.0055
Ductility 5	push 1	10.02	55.2	662.6	-0.00144	4.56	0.0239	-0.0107
	pull 1	-10.09	-61.2	-733.9	0.00107	-7.47	0.0208	-0.0048
	push 2	10.04	52.5	630.1	-0.00140	5.48	0.0244	-0.0091
	pull 2	-10.13	-58.9	-706.7	0.00108	-7.20	0.0206	-0.0052
	push 3	10.05	50.4	604.8	-0.00134	6.11	0.0242	-0.0079
	pull 3	-10.14	-55.5	-665.9	0.00096	-9.08	0.0203	-0.0028
Ductility 6	push 1	12.10	54.3	652.2	-0.00163	5.31	0.0282	-0.0109

Table 9-9 Peak Cycle data (D/t = 128, ρ=2.43%)

Cycle		Displ (in)	Force (k)	Moment (k ft)	Curv (1/in)	NA Depth (in)	Tensile Strain	Comp Strain
1/4 Fy	push	0.16	8.8	105.8	-0.00001	-0.94	0.0002	-0.0002
	pull	-0.17	-8.4	-100.7	0.00001	0.59	0.0002	-0.0002
1/2 Fy	push	0.37	17.8	214.1	-0.00003	0.58	0.0004	-0.0004
	pull	-0.41	-17.3	-207.9	0.00003	-2.85	0.0004	-0.0003
3/4 Fy	push	0.67	26.6	319.1	-0.00005	2.05	0.0007	-0.0005
	pull	-0.72	-26.2	-313.9	0.00006	-2.06	0.0008	-0.0006
Fy	push	0.99	36.0	432.2	-0.00007	3.20	0.0011	-0.0006
	pull	-1.04	-34.8	-418.1	0.00008	-2.68	0.0011	-0.0007
Ductility 1	push 1	2.23	64.1	769.0	-0.00018	2.77	0.0026	-0.0016
	pull 1	-2.21	-61.7	-740.4	0.00018	-3.14	0.0027	-0.0016
	push 2	2.24	63.9	767.0	-0.00018	3.21	0.0027	-0.0016
	pull 2	-2.21	-60.6	-727.1	0.00018	-3.37	0.0027	-0.0015
	push 3	2.24	63.1	757.0	-0.00018	3.43	0.0027	-0.0015
	pull 3	-2.21	-60.1	-721.2	0.00018	-3.55	0.0027	-0.0015
Ductility 1.5	push 1	3.34	73.9	886.6	-0.00029	3.80	0.0046	-0.0024
	pull 1	-3.35	-72.4	-868.7	0.00032	-3.74	0.0050	-0.0026
	push 2	3.36	72.9	874.4	-0.00030	4.25	0.0049	-0.0023
	pull 2	-3.35	-71.6	-859.5	0.00032	-3.76	0.0050	-0.0026
	push 3	3.36	72.0	864.3	-0.00031	3.86	0.0049	-0.0025
	pull 3	-3.35	-71.1	-852.9	0.00033	-3.71	0.0052	-0.0028
Ductility 2	push 1	4.47	75.6	907.5	-0.00044	3.55	0.0068	-0.0037
	pull 1	-4.43	-74.9	-898.5	0.00044	-4.97	0.0074	-0.0031
	push 2	4.47	73.9	887.1	-0.00044	4.11	0.0071	-0.0035
	pull 2	-4.45	-73.8	-886.0	0.00047	-4.77	0.0078	-0.0034
	push 3	4.47	73.7	884.1	-0.00045	3.90	0.0072	-0.0037
	pull 3	-4.46	-73.2	-878.1	0.00047	-4.74	0.0079	-0.0034
Ductility 3	push 1	6.64	80.3	963.4	-0.00067	4.76	0.0113	-0.0049
	pull 1	-6.64	-80.2	-962.3	0.00065	-6.10	0.0117	-0.0038
	push 2	6.65	77.6	931.5	-0.00054	7.60	0.0107	-0.0024
	pull 2	-6.65	-78.8	-945.3	0.00072	-4.71	0.0120	-0.0052
	push 3	6.65	76.7	920.6	-0.00062	6.76	0.0115	-0.0032
	pull 3	-6.67	-77.8	-933.4	0.00072	-5.28	0.0125	-0.0049

Table 9-9 continued

Ductility 4	push 1	8.89	82.3	987.1	-0.00081	7.25	0.0156	-0.0039
	pull 1	-8.87	-82.9	-994.3	0.00105	-4.35	0.0172	-0.0080
	push 2	8.89	77.7	932.9	-0.00085	8.19	0.0172	-0.0032
	pull 2	-8.90	-79.7	-956.3	0.00099	-5.86	0.0176	-0.0061
	push 3	8.90	77.7	932.4	-0.00086	8.89	0.0180	-0.0027
	pull 3	-8.91	-78.2	-938.1	0.00100	-6.04	0.0180	-0.0060
Ductility 5	push 1	11.12	82.2	986.9	-0.00102	8.95	0.0213	-0.0031
	pull 1	-11.09	-84.0	-1007.9	0.00117	-7.18	0.0224	-0.0056
	push 2	11.13	80.5	965.5	-0.00109	9.19	0.0232	-0.0031
	pull 2	-11.12	-80.9	-971.2	0.00124	-6.77	0.0232	-0.0065
	push 3	11.12	77.3	927.7	-0.00094	12.36	0.0229	0.0003
	pull 3	-11.15	-79.8	-957.5	0.00125	-6.80	0.0236	-0.0065
Ductility 6	push 1	13.32	69.2	830.9	-0.00082	15.39	0.0226	0.0028

Table 9-10 Peak Cycle data (D/t = 160, ρ=0.78%)

Cycle		Displ (in)	Force (k)	Moment (k ft)	Curv (1/in)	NA Depth (in)	Tensile Strain	Comp Strain
1/4 Fy	push	0.06	2.3	20.3	-0.00001	-0.91	0.0001	-0.0002
	pull	-0.12	-3.0	-26.9	0.00001	-3.69	0.0001	-0.0001
1/2 Fy	push	0.22	6.6	59.3	-0.00002	3.27	0.0003	-0.0001
	pull	-0.40	-10.6	-95.5	0.00004	-2.39	0.0005	-0.0003
3/4 Fy	push	0.45	13.1	118.2	-0.00006	1.73	0.0007	-0.0005
	pull	-0.66	-15.8	-142.3	0.00007	-2.05	0.0009	-0.0006
Fy	push	0.63	17.1	154.0	-0.00008	3.29	0.0010	-0.0005
	pull	-0.93	-20.7	-186.1	0.00010	-2.33	0.0012	-0.0008
Ductility 1	push 1	1.66	33.2	298.6	-0.00020	3.16	0.0027	-0.0014
	pull 1	-1.66	-33.8	-303.9	0.00018	-3.18	0.0024	-0.0013
	push 2	1.67	32.8	295.5	-0.00020	2.96	0.0026	-0.0014
	pull 2	-1.64	-33.2	-298.8	0.00019	-2.85	0.0024	-0.0014
	push 3	1.65	31.9	287.5	-0.00019	3.89	0.0026	-0.0011
	pull 3	-1.66	-33.0	-297.2	0.00018	-3.37	0.0024	-0.0012
Ductility 1.5	push 1	2.52	37.2	335.0	-0.00040	2.64	0.0050	-0.0029
	pull 1	-2.54	-39.5	-355.7	0.00030	-4.42	0.0043	-0.0017
	push 2	2.53	36.5	328.9	-0.00037	3.90	0.0051	-0.0022
	pull 2	-2.55	-39.5	-355.7	0.00033	-4.20	0.0047	-0.0019
	push 3	2.53	35.9	322.8	-0.00039	3.41	0.0052	-0.0025
	pull 3	-2.55	-39.0	-350.7	0.00037	-3.53	0.0050	-0.0024
Ductility 2	push 1	3.38	38.5	346.3	-0.00056	4.07	0.0078	-0.0033
	pull 1	-3.32	-40.4	-363.8	0.00056	-3.84	0.0077	-0.0034
	push 2	3.42	37.2	334.4	-0.00057	4.74	0.0084	-0.0030
	pull 2	-3.32	-39.1	-351.6	0.00063	-3.38	0.0084	-0.0042
	push 3	3.43	36.0	324.1	-0.00054	5.38	0.0084	-0.0025
	pull 3	-3.33	-38.7	-348.7	0.00058	-4.00	0.0082	-0.0035
Ductility 3	push 1	5.04	38.5	346.9	-0.00085	5.36	0.0131	-0.0040
	pull 1	-5.00	-41.5	-373.8	0.00090	-4.33	0.0129	-0.0051
	push 2	5.07	36.8	331.6	-0.00094	5.04	0.0141	-0.0047
	pull 2	-5.02	-40.7	-366.0	0.00089	-4.22	0.0126	-0.0051
	push 3	5.06	35.2	316.4	-0.00090	5.55	0.0140	-0.0040
	pull 3	-5.04	-39.9	-358.8	0.00089	-4.45	0.0129	-0.0050

Table 9-10 continued

Ductility 4	push 1	6.66	38.7	348.1	-0.00125	4.80	0.0185	-0.0065
	pull 1	-6.63	-42.4	-381.6	0.00127	-3.98	0.0177	-0.0076
	push 2	6.68	36.7	330.7	-0.00123	4.99	0.0184	-0.0061
	pull 2	-6.67	-41.0	-369.0	0.00125	-4.27	0.0179	-0.0072
	push 3	6.68	34.9	314.1	-0.00133	4.49	0.0193	-0.0073
	pull 3	-6.69	-40.3	-362.6	0.00134	-3.70	0.0184	-0.0085
Ductility 5	push 1	8.32	38.1	342.8	-0.00148	5.24	0.0226	-0.0070
	pull 1	-8.28	-42.7	-384.3	0.00148	-4.61	0.0216	-0.0080
	push 2	8.35	36.3	326.9	-0.00144	5.73	0.0227	-0.0062
	pull 2	-8.31	-40.6	-365.5	0.00142	-5.21	0.0216	-0.0068
	push 3	8.34	34.4	309.4	-0.00131	6.50	0.0216	-0.0046
	pull 3	-8.33	-39.9	-359.4	0.00128	-6.52	0.0212	-0.0045

Table 9-11 Peak Cycle data (D/t = 192, ρ=0.78%)

Cycle		Displ (in)	Force (k)	Moment (k ft)	Curv (1/in)	NA Depth (in)	Tensile Strain	Comp Strain
1/4 Fy	push	0.24	8.6	103.3	-0.00002	1.29	0.0002	-0.0002
	pull	-0.29	-8.4	-100.2	0.00002	-2.00	0.0003	-0.0002
1/2 Fy	push	0.52	16.7	200.6	-0.00004	2.91	0.0006	-0.0004
	pull	-0.69	-16.2	-195.0	0.00005	-3.45	0.0008	-0.0004
3/4 Fy	push	0.94	24.5	294.5	-0.00007	3.86	0.0011	-0.0006
	pull	-1.13	-24.5	-293.7	0.00008	-4.13	0.0013	-0.0007
Fy	push	1.39	32.9	394.3	-0.00010	4.84	0.0016	-0.0007
	pull	-1.59	-32.9	-395.1	0.00012	-3.90	0.0019	-0.0010
Ductility 1	push 1	2.80	43.9	527.3	-0.00021	5.59	0.0037	-0.0013
	pull 1	-2.79	-44.4	-532.4	0.00031	-3.55	0.0048	-0.0026
	push 2	2.82	43.3	519.4	-0.00019	7.15	0.0037	-0.0009
	pull 2	-2.80	-42.8	-514.1	0.00031	-3.72	0.0049	-0.0026
	push 3	2.83	43.2	518.0	-0.00024	5.51	0.0042	-0.0016
	pull 3	-2.81	-42.6	-511.2	0.00031	-3.65	0.0049	-0.0026
Ductility 1.5	push 1	4.19	45.6	547.0	-0.00050	4.17	0.0080	-0.0039
	pull 1	-4.18	-44.2	-530.4	0.00048	-5.59	0.0085	-0.0031
	push 2	4.22	43.1	516.8	-0.00049	5.32	0.0085	-0.0033
	pull 2	-4.18	-43.8	-526.2	0.00042	-7.34	0.0082	-0.0020
	push 3	4.22	41.8	501.3	-0.00047	5.71	0.0084	-0.0030
	pull 3	-4.18	-43.4	-521.1	0.00044	-7.16	0.0084	-0.0021
Ductility 2	push 1	5.90	45.1	540.7	-0.00069	6.54	0.0127	-0.0038
	pull 1	-5.58	-45.9	-551.0	0.00058	-8.30	0.0117	-0.0021
	push 2	5.73	42.6	510.9	-0.00073	6.26	0.0134	-0.0042
	pull 2	-5.59	-44.5	-533.9	0.00063	-7.41	0.0122	-0.0029
	push 3	5.73	40.3	483.9	-0.00067	6.91	0.0126	-0.0034
	pull 3	-5.60	-43.9	-526.7	0.00065	-6.84	0.0123	-0.0034
Ductility 3	push 1	8.45	47.8	573.9	-0.00105	6.35	0.0192	-0.0059
	pull 1	-8.41	-48.5	-582.4	0.00098	-7.43	0.0191	-0.0045
	push 2	8.46	44.2	530.0	-0.00116	6.12	0.0210	-0.0068
	pull 2	-8.42	-46.7	-560.0	0.00115	-5.68	0.0203	-0.0072
	push 3	8.46	42.2	505.9	-0.00115	6.38	0.0211	-0.0065
	pull 3	-8.42	-44.9	-539.1	0.00111	-5.97	0.0199	-0.0067

Table 9-11 continued

Ductility 4	push 1	11.22	47.6	571.7	-0.00143	6.81	0.0270	-0.0074
	pull 1	-11.25	-50.2	-602.1	0.00138	-6.35	0.0254	-0.0078
	push 2	11.24	44.8	537.2	-0.00126	8.73	0.0261	-0.0041
	pull 2	-11.28	-47.4	-568.3	0.00144	-5.97	0.0259	-0.0087
	push 3	11.58	28.1	337.7	-0.00114	8.68	0.0235	-0.0038
	pull 3	-11.29	-44.5	-534.1	0.00144	-6.00	0.0260	-0.0087

Table 9-12 Peak Cycle data (D/t = 192, ρ=2.43%)

Cycle		Displ (in)	Force (k)	Moment (k ft)	Curv (1/in)	NA Depth (in)	Tensile Strain	Comp Strain
1/4 Fy	push	0.19	9.2	110.2	-0.00001	3.86	0.0002	-0.0001
	pull	-0.18	-7.5	-90.3	0.00002	-0.18	0.0002	-0.0002
1/2 Fy	push	0.43	16.7	200.9	-0.00003	4.79	0.0005	-0.0002
	pull	-0.43	-15.4	-184.7	0.00003	-2.72	0.0005	-0.0003
3/4 Fy	push	0.73	24.9	299.2	-0.00006	2.60	0.0009	-0.0006
	pull	-0.75	-24.1	-289.0	0.00005	-4.27	0.0008	-0.0004
Fy	push	1.07	33.1	397.0	-0.00008	3.61	0.0012	-0.0007
	pull	-1.10	-32.7	-392.5	0.00009	-2.60	0.0014	-0.0009
Ductility 1	push 1	2.31	56.2	674.8	-0.00014	5.83	0.0025	-0.0009
	pull 1	-2.27	-54.3	-651.2	0.00019	-2.16	0.0027	-0.0019
	push 2	2.31	55.4	664.9	-0.00016	4.93	0.0026	-0.0011
	pull 2	-2.27	-54.2	-649.8	0.00014	-4.61	0.0024	-0.0011
	push 3	2.30	54.4	652.2	-0.00014	5.75	0.0026	-0.0009
	pull 3	-2.27	-53.5	-641.8	0.00020	-2.26	0.0028	-0.0019
Ductility 1.5	push 1	3.47	64.9	779.3	-0.00027	4.83	0.0046	-0.0020
	pull 1	-3.46	-63.0	-756.0	0.00035	-2.06	0.0050	-0.0035
	push 2	3.47	64.3	771.0	-0.00027	5.37	0.0048	-0.0018
	pull 2	-3.47	-63.0	-755.5	0.00038	-1.62	0.0051	-0.0039
	push 3	3.47	63.1	757.6	-0.00029	5.00	0.0049	-0.0020
	pull 3	-3.47	-61.1	-733.5	0.00039	-0.89	0.0050	-0.0043
Ductility 2	push 1	4.60	67.1	805.2	-0.00039	4.77	0.0065	-0.0028
	pull 1	-4.61	-65.0	-780.1	0.00037	-3.80	0.0058	-0.0030
	push 2	4.60	65.2	782.0	-0.00039	5.04	0.0066	-0.0027
	pull 2	-4.60	-61.8	-741.6	0.00042	-2.70	0.0062	-0.0039
	push 3	4.60	63.4	761.2	-0.00034	6.28	0.0063	-0.0020
	pull 3	-4.62	-62.5	-750.2	0.00042	-3.21	0.0063	-0.0036
Ductility 3	push 1	6.94	70.6	847.4	-0.00073	3.82	0.0115	-0.0060
	pull 1	-7.01	-68.2	-818.8	0.00056	-5.17	0.0096	-0.0038
	push 2	6.94	67.2	806.7	-0.00080	3.66	0.0126	-0.0067
	pull 2	-7.01	-66.3	-795.6	0.00062	-4.38	0.0102	-0.0048
	push 3	6.93	65.8	789.1	-0.00082	3.83	0.0129	-0.0067
	pull 3	-7.00	-64.7	-776.6	0.00065	-4.41	0.0106	-0.0049

Table 9-12 continued

Ductility 4	push 1	9.29	72.3	868.0	-0.00108	4.12	0.0175	-0.0085
	pull 1	-9.31	-68.8	-825.8	0.00095	-3.58	0.0148	-0.0080
	push 2	9.30	69.4	833.1	-0.00104	5.04	0.0176	-0.0072
	pull 2	-9.32	-68.3	-819.2	0.00103	-3.63	0.0161	-0.0086
	push 3	9.30	67.2	806.5	-0.00100	5.31	0.0174	-0.0067
	pull 3	-9.31	-65.7	-787.8	0.00100	-4.22	0.0162	-0.0078
Ductility 5	push 1	12.23	59.6	715.2	-0.00085	7.40	0.0164	-0.0039
	pull 1	-11.96	-57.2	-686.9	0.00082	-6.05	0.0149	-0.0049

Appendix E: Calculated stress on surface of steel pipe using bilinear steel model

The stresses in the steel tube were calculated using the measured strains and the cyclic steel model. The stress values for the extreme tensile and compression fibers are shown below.

Table 9-13 Calculated Stresses from Bilinear Stress Model

		D/t =	33	D/t =	64	D/t =	85	D/t =	128
		p =	1.60%	p =	1.60%	p =	1.60%	p =	1.60%
Cycle		Stress (ksi)		Stress (ksi)		Stress (ksi)		Stress (ksi)	
		Top of Pile	Bottom of Pile	Top of Pile	Bottom of Pile	Top of Pile	Bottom of Pile	Top of Pile	Bottom of Pile
1/4 Fy	push	-4.98	13.41	-10.85	17.35	-10.20	18.70	-3.73	-2.76
1/4 Fy	pull	18.57	-18.12	12.75	-3.65	17.47	-25.61	3.00	3.53
1/2 Fy	push	-20.23	26.38	-18.73	26.47	-19.64	32.31	-4.95	7.04
1/2 Fy	pull	-34.86	-32.24	27.55	-18.43	32.99	79.23	15.20	-17.49
3/4 Fy	push	-44.67	56.82	-34.88	42.81	-35.42	83.54	-12.85	20.52
3/4 Fy	pull	57.96	-39.08	43.48	-30.71	49.14	-78.29	66.20	-24.36
Fy	push	-58.97	58.57	-44.61	62.41	-48.05	83.76	-13.81	18.32
Fy	pull	58.56	-58.47	58.37	-39.61	71.88	-79.13	38.90	-29.84
μ 1	push	-58.59	58.78	-87.02	65.40	-68.10	84.25	-36.73	47.52
μ 1	pull	58.72	-58.55	44.33	-65.21	79.14	-79.28	-47.52	-47.54
μ 1.5	push	-58.82	59.13	-84.99	65.66	-78.99	80.28	47.53	47.66
μ 1.5	pull	59.03	-58.70	46.73	-65.29	79.54	-79.42	47.64	-47.61
μ 2	push	-59.06	59.60	-82.94	65.96	-79.17	79.94	47.58	48.05
μ 2	pull	59.45	-58.86	49.25	-65.38	80.00	-79.52	48.27	-47.93
μ 3	push	-59.55	60.52	-81.01	66.66	-79.26	80.76	47.52	48.63
μ 3	pull	60.16	-59.21	52.10	-65.37	80.80	-79.14	48.85	-48.55
μ 4	push	-59.98	61.39	-79.81	67.10	-77.25	81.63	46.23	48.78
μ 4	pull	60.89	-59.58	55.45	67.57	81.72	-77.02	49.41	-47.85
μ 5	push	-60.38	62.26	-74.08	-46.16			-45.72	49.00
μ 5	pull	61.53	-60.09	58.91	-124.57			49.74	-47.19
μ 6	push	-60.83	63.07					-36.92	49.34
μ 6	pull	62.15	-61.95					50.03	-46.47

Table 9-13 continued

		D/t =	160	D/t =	192	D/t =	160	D/t =	192
		p =	1.60%	p =	1.60%	p =	0.78%	p =	0.78%
Cycle		Stress (ksi)		Stress (ksi)		Stress (ksi)		Stress (ksi)	
		Top of Pile	Bottom of Pile	Top of Pile	Bottom of Pile	Top of Pile	Bottom of Pile	Top of Pile	Bottom of Pile
1/4 Fy	push	2.92	-3.36	-2.82	3.52	-0.98	0.96	-7.95	6.45
1/4 Fy	pull	7.94	-9.98	4.85	1.69	1.25	-3.68	1.09	-4.98
1/2 Fy	push	0.99	-2.16	-0.91	9.91	-4.53	9.03	-7.43	13.77
1/2 Fy	pull	21.25	-16.80	14.79	-9.40	5.16	-5.82	19.00	-11.97
3/4 Fy	push	-4.05	0.00	-8.23	28.21	-9.41	0.00	-10.41	26.61
3/4 Fy	pull	23.38	-20.49	39.03	-14.29	15.91	-11.96	33.27	-19.79
Fy	push	-15.19	16.63	-12.11	43.46	-10.61	0.00	-16.94	40.85
Fy	pull	34.82	-22.95	37.89	-19.90	19.61	-17.57	46.93	-26.35
μ 1	push	-26.18	47.63	-23.46	48.16	-22.93	47.54	-41.33	47.58
μ 1	pull	47.56	-47.37	48.10	-45.91	43.27	-37.44	47.88	-47.46
μ 1.5	push	-47.50	47.73	-54.03	48.30	-36.78	47.58	-47.45	47.91
μ 1.5	pull	47.63	-47.45	43.11	-47.81	47.77	-47.52	48.23	-47.28
μ 2	push	-47.52	47.93	-47.70	48.89	-47.45	47.77	-47.00	48.47
μ 2	pull	48.07	-47.17	48.72	17.05	48.07	-47.62	48.44	-46.65
μ 3	push	-47.09	48.60	-47.42	49.79	-47.39	48.73	-46.63	48.98
μ 3	pull	48.81	-46.68	49.27	-39.77	48.34	-47.19	49.21	-46.21
μ 4	push	-46.64	49.05	-46.93	50.77	-46.85	49.34	-45.90	49.51
μ 4	pull	48.87	-46.23	49.54	-45.38	48.53	-45.97	49.87	-45.70
μ 5	push	-46.44	49.36	-46.69	51.66	-46.52	49.75		
μ 5	pull	48.87	-46.00	49.80	-38.09	48.79	-45.53		
μ 6	push	-43.21	31.65	-46.48	52.61				
μ 6	pull			49.79	-43.60				

Table 9-13 continued

		D/t =	192	D/t =	128	D/t =	128
		p =	2.43%	p =	0.78%	p =	2.43%
Cycle		Stress (ksi)		Stress (ksi)		Stress (ksi)	
		Top of Pile	Bottom of Pile	Top of Pile	Bottom of Pile	Top of Pile	Bottom of Pile
1/4 Fy	push	-7.92	2.49	-5.98	9.03	-3.69	3.90
1/4 Fy	pull	-1.90	-4.42	3.93	-5.21	6.20	-4.16
1/2 Fy	push	-6.86	10.38	-31.01	-7.75	-3.35	14.61
1/2 Fy	pull	0.00	0.00	12.94	-5.88	19.04	-9.31
3/4 Fy	push	-14.16	24.53	-16.35	23.68	-8.89	22.87
3/4 Fy	pull	21.75	-14.87	18.96	-11.18	19.66	-15.56
Fy	push	-15.54	31.05	-5.68	34.72	-14.01	33.30
Fy	pull	37.29	-22.40	28.94	-11.43	31.89	-24.73
μ 1	push	-40.56	47.69	-31.89	47.59	-40.92	47.59
μ 1	pull	47.51	-47.45	47.51	-41.03	47.52	-47.50
μ 1.5	push	-49.79	48.02	-50.07	47.71	-47.57	47.80
μ 1.5	pull	46.33	-47.35	45.99	-47.45	47.72	-47.58
μ 2	push	-47.92	48.30	-47.67	47.80	-47.68	48.13
μ 2	pull	47.84	-46.98	47.94	-47.46	47.93	-47.72
μ 3	push	-47.76	48.69	-47.71	48.26	-47.79	48.59
μ 3	pull	48.44	-46.72	48.42	-47.30	48.27	-48.02
μ 4	push	-46.66	49.35	-47.58	48.92	-47.55	49.09
μ 4	pull	49.06	-46.06	48.84	-46.26	48.32	-47.17
μ 5	push	-46.00	29.06	-46.29	49.38	-46.85	49.72
μ 5	pull	49.06	-42.11	49.28	-45.72	48.85	-46.20
μ 6	push			-45.76	49.81	-46.20	49.70
μ 6	pull						

Appendix F: Steel Pipe Mill Certs

The mill certs for each pipe used in the experimental program are shown in the following order:

1) Test 2, OD = 24”, t =0.128”

2) Test 3, OD = 24”, t = 0.178”

3) Test 4, OD = 24”, t = 0.375”

4) Test 5, OD = 24”, t = 0.281”

5) Test 6, OD = 20”. t = 0.60”

6) Tests 7 – 10, OD = 20 or 24”, t = 0.128”

7) Tests 11-12, OD = 24”, t = 1.78”

Mill certs were not available for Test 1, it was excess material from a previous experimental program at N.C. State.

6/8/2011

CERTIFIED REPORT OF CHEMICAL ANALYSIS AND MECHANICAL TESTS

ACCREDITED
TESTING CERT # 2814.01

ArcelorMittal

SOLD TO	SHIPPED FROM
NAYLOR PIPE 1230 EAST 92ND STREET CHICAGO IL	ArcelorMittal Riverdale LLC. 13500 South Perry Avenue Riverdale, IL 60827
SHIP TO	**PURCHASE ORDER INFO**
NAYLOR PIPE C/O NATL PROC #2 C/O NATIONAL PROCESSING 4506 W. CLINE AVE PLANT 2 EAST CHICAGO IN	PO#: 55291 LoadID # 01594896 SO#: 516352 Carrier: Sowka Express Shipped: 6/7/2011

ORDER ITEM INFORMATION

Heat	Coil	Thickness (in)	Width (in)	Weight (tons)	Reduction Ratio
A27765	845790	0.128	56.750	25.6	94.09% (17:1)

PRODUCT INFORMATION

Grade	Part Number	Comments
SAE 1022 MOD4	HB1285675-09	

This material was melted and manufactured in the USA. All products are strand cast and free of mercury or radioactive elements. Elongation based on 2" gage length

MECHANICAL PROPERTIES

Heat	Coil	Yield (ksi)	Tensile (ksi)	El (%)	Lir	N-Value	N-Range	Hardness	Ft-lbs	°F	Size	Dir

* Material testing in accordance with ISO 17025 by an accredited lab.

CHEMICAL PROPERTIES

Heat	C	Mn	P	S	Si	Cu	Ni	Cr	Mo	Cb	V	Al
A27765	.20	.77	.008	.004	.03	.04	.02	.03	.00	.001	.000	.030
	N	Se	B	Ti	Ca	Sb						
	.0059	.002	.0000	.0020	.0010	.0010						

Chemical analysis was performed by ArcelorMittal Riverdale, Inc. in accordance with the Current Version of ASTM E415 and E1019.

We hereby certify the above is correct as contained in the records of the corporation. All tests peformed to the current standard to date unless otherwise noted. Uncertainties of measurements estimated and are available upon request. These results relate only to the items tested. Test results marked with an asterisk (*) were reported by an external accredited lab.

Peter Gaudreau
Metallurgist

KIEH

METALLURGICAL SERVICES
(708) 544-8811 544-8820 FAX

Laboratory:
837 MANNHEIM RD.
BELLWOOD, IL 60104

Date received 15-Jun-2011
15-Jun-2011
Report 111 24042 c of d pages

Naylor Pipe Company
1230 E. 92nd St.
Chicago, IL 60619-7997

Account 1302

P.O. 4222

Attn : James Martin

our 32th year est. 1979

Test report /

Sample identity	Y.S. lbs/in^2	T.S. lbs/in^2	%E 2"
E31783 10Gax20"&36" MITTAL A27765	49,200	74,500	27.5
ASTM A139 grB min. requirements	35,000	60,000	21.50

This samples reported properties conform to the requirements of an ASTM A139 grB material.

STATE OF ILLINOIS
REGISTRATION EXPIRES
PROFESSIONAL ENGINEER
IATROPULOS

Mechanical:ASTM E8/A370 Y.S.0.2%offset []trans. *broke out of g.1. ¦1"g.1.

2/4/2011

CERTIFIED REPORT OF CHEMICAL ANALYSIS AND MECHANICAL TESTS

ACCREDITED
TESTING CERT # 2914.01

ArcelorMittal

SOLD TO	VENDOR
NAYLOR PIPE 1230 EAST 92ND STREET CHICAGO IL	ArcelorMittal Riverdale, Inc. 13500 South Perry Avenue Riverdale, IL 60827
SHIP TO	**ORDER INFORMATION**
NAYLOR PIPE C/O NATL PROC #2 C/O NATIONAL PROCESSING 4506 W. CLINE AVE. PLANT 2 EAST CHICAGO IN	PO#: 55160 Invoice # 0500061958 SO#: 489829 Carrier Sowka Express Shipped: 12/14/2010

DIMENSIONAL INFORMATION

Heat	Coil	Thickness (in)	Width (in)	Weight (tons)	Reduction Ratio
B30005	830666	0.178	36.750	16	91.78% (12:1)
B30005	830667	0.178	36.750	15.8	91.78% (12:1)
B30005	830668	0.178	36.750	16.1	91.78% (12:1)
B30005	830669	0.178	36.750	16.9	91.78% (12:1)
B30005	830670	0.178	36.750	16.9	91.78% (12:1)

PRODUCT INFORMATION

Grade	Part Number	Comments
ASTM A139 GRD B MOD1	HB1783675-03	

We certify that this material meets the provisions of the 'Buy America' program. This material was melted and manufactured in the USA. All products are strand cast and free of mercury or radioactive elements. Elongation based on 2" gage length.

MECHANICAL / PHYSICAL TEST RESULTS *

Heat	Coil	Yield (ksi)	Tensile (ksi)	El (%)	Dir	N-Value	N-Range	Hardness	Ft-lbs	°F	Size	Dir

* Material tested in accordance with ISO 17025 by an accredited lab.

CHEMICAL TEST RESULTS (%wt)

Heat	C	Mn	P	S	Si	Cu	Ni	Cr	Mo	Cb	V	Al
B30005	.22	.75	.010	.005	.03	.03	.01	.03	.00	.000	.003	.033

N	Sn	B	Ti	Ca	Sb
.0058	.001	.0003	.0010	.0010	.0000

Chemical analysis was performed by ArcelorMittal Riverdale, Inc. in accordance with the Current revision of ASTM E415 and E1019.

We hereby certify the above is correct as contained in the records of the corporation. All tests peformed to the current standard to date unless otherwise noted. Uncertainties of measurements estimated and are available upon reques These results relate only to the items tested. Test results marked with an asteris (*) were reported by an external accredited lab.

Peter Gaudreau
Metallurgist

KIEH

METALLURGICAL SERVICES
(708) 544-8811 544-8820 FAX

Laboratory:
837 MANNHEIM RD
BELLWOOD, IL 60104

Date received 18-Mar-2011
18-Mar-2011
Report 111 11083 b of d pages

Naylor Pipe Company
1230 E. 92nd St.
Chicago, IL 60619-7997

Account 1302

P.O. 3151

Attn : James Martin

our 32th year est. 1979

Test report /

Sample identity	Y.S. lbs/in^2	T.S. lbs/in^2	%E 2"
E28512 3/16x36" MITTAL B3Q005	46,000	72,000	33.5
ASTM A139 grB min. requirements	35,000	60,000	24.00

This samples reported properties conform to the requirements of an ASTM A139 grB material.

ASTM A252 gr2 min. requirements	35,000	60,000	20.00

This samples reported properties conform to the requirements of an ASTM A252 gr2 material.

CHRISTOS IATRO
PROFESSIONAL E
REGISTRATIO

Mechanical:ASTM E8/A370 Y.S.0.2%offset []trans. *broke out of g.l. [] g.l.

ISO 9001:2000 CERTIFIED

AMERICAN STEEL PIPE
A division of American Cast Iron Pipe Co.,
P.O. Box 2727, Birmingham, AL 35202-2727
QUALIFICATION REPORT OF SHIPMENT

DATE: 07/JAN/2011

CUSTOMER ADDRESS: CONSOLIDATED PIPE & SUPPLY
P O BOX 2472
BIRMINGHAM AL 35201

Customer Order Number: S13-10501
MFG Order Number: S109568

SPECIAL NOTES

PIPE WERE NDT TESTED USING AN ULTRASONIC TEST METHOD CALIBRATED ON ID & OD N-10 NOTCHES
HYDROSTATIC TEST DURATION 10 SECONDS. MAX ALLOWABLE PCM .25.
MINIMUM WELD SEAM ANNEAL TEMPERATURE 1600 DEGREES F FOR ALL PIPE.
CHARPY ACCEPTANCE CRITERIA MIN. ENERGY 15/HEAT, MIN. SHEAR AREA N/A.

SHIPMENT DESCRIPTION

LINE	PIECES	FOOTAGE	SIZE	WALL	SHIP. NO 1-2	SPECIFICATIONS	GRADE
1	18	722.7	24.00	.375	ERW API LINE PIPE	API 5L, PSL2	BMX42M
						ASTM A53-01	B
						ASME SA53-04	B

All tests are from the body of the pipe in the transverse direction unless otherwise noted.
Standard tensile gage length 1-1/2" x 2".

HEAT	C	MN	P	S	CB	SI	TI	CU	NI	MO	CR	V	AL	B	N	C.E.	Coil / Pipe
A017936 * LINE 1							EDITION REFERENCE 4 & 5 YEAR 2010 Yield Strength by Strap										
H=	0.060	0.619	0.009	0.002	0.029	0.260	0.002	0.120	0.040	0.010	0.050	0.003	0.035	.0001	.0075	0.110	0005
P=	0.065	0.626	0.008	0.005	0.023	0.247	0.003	0.111	0.051	0.013	0.024	0.001	0.029	.0000	.0000	0.113	09/17

M=Weld Ten. 75.5 ksi Ten. 75.0 ksi Yield 59.3 ksi %EL 38.5 RB 87 Hydro: 1180 Psi RUN: 47-0
Y/T RATIO = 0.79

Attachments

PAGE 1
Continued

Issue No.: 6

Form Date: 10/18/2004

QD-AW3F055

ISO 9001:2000 CERTIFIED

Date: 07/JAN/2011

CUSTOMER NAME: CONSOLIDATED PIPE & SUPPLY
Charpy "V" Notch Tests

Customer Order Number: S13-10501
MFG Order Number: S109568

HEAT NO.	SIZE	TEMP	Energy (FT./LBS.)			AVG.	Fracture Appearance (% Shear Area)			AVG.	Line #
A017936-	.750	32	202.0	208.0	204.0	204.7	100	100	100	100.0	1
A017935-	.750	32	200.0	208.0	204.0	204.0	100	100	100	100.0	1
			ALL HEAT AVERAGE =			204.3				100.0	

Legend Analyses:

A-Z - Additional Testing
H - Heat Analysis
P - Product Analysis
M- Mechanical Properties
R - Retest
L - Longitudinal
T - Transitional
W - Weld Line

Hydrostatic Test: OK
Flattening Test: OK

EDITION REFERENCE 1: API 5L 41ST EDITION 4/1/1995
EDITION REFERENCE 2: API 5L 42ND EDITION 7/1/2000
EDITION REFERENCE 3: API 5L 43RD EDITION 10/4/2004
EDITION REFERENCE 4: API 5L 44TH EDITION 10/1/2008
EDITION REFERENCE 5: ASTM/ASME ANNUAL BOOK OF STANDARDS SECT.1, VOL 01.01

* Manufactured and Melted in the USA.

We hereby certify that the above figures are correct as contained in the records of this company, and that the pipe were manufactured, tested and inspected in compliance with the Latest edition of the applicable specification, in Birmingham, Alabama, U.S.A.

Noel A. Gordon
Manager of Quality Assurance - Steel Pipe

PAGE 3

ISO 9001:2000 CERTIFIED

AMERICAN STEEL PIPE
A division of American Cast Iron Pipe Co.,
P.O. Box 2727, Birmingham, AL 35202-2727
QUALIFICATION REPORT OF SHIPMENT

DATE: 07/JUN/2011

CUSTOMER ADDRESS: CONSOLIDATED PIPE & SUPPLY
P O BOX 2472
BIRMINGHAM AL 35201

Customer Order Number: S13-10966
MFG Order Number: S109855

SPECIAL NOTES

PIPE WERE NDT TESTED USING AN ULTRASONIC TEST METHOD CALIBRATED ON ID & OD N-10 NOTCHES
HYDROSTATIC TEST DURATION 10 SECONDS. MAX ALLOWABLE PCM .25.
MINIMUM WELD SEAM ANNEAL TEMPERATURE 1600 DEGREES F FOR ALL PIPE.
CHARPY ACCEPTANCE CRITERIA MIN. ENERGY 10/HEAT, MIN. SHEAR AREA N/A.

SHIPMENT DESCRIPTION

LINE	PIECES	FOOTAGE	SIZE	WALL	SHIP. NO 1	SPECIFICATIONS	GRADE
1	15	596.5	24.00	.281	ERW API LINE PIPE	API 5L, PSL2	X60M

All tests are from the body of the pipe in the transverse direction unless otherwise noted.
Standard tensile gage length 1-1/2" x 2".

HEAT	C	MN	P	S	CB	SI	TI	CU	NI	MO	CR	V	AL	B	N	C.E.	Coil Pipe
83204	* LINE 1						EDITION REFERENCE 4						Yield Strength by Strap				
H=	0.050	1.270	0.013	0.003	0.064	0.174	0.016	0.030	0.010	0.010	0.030	0.004	0.055	.0003	.0062	0.125	0022
P=	0.052	1.286	0.013	0.006	0.066	0.154	0.014	0.026	0.025	0.006	0.017	0.006	0.053	.0001	.0000	0.125	15/31

M=Weld Ten. 81.5 ksi Ten. 90.2 ksi Yield 71.8 ksi %EL 30.0 RB 93 Hydro: 1270 Psi RUN: 39-0
Y/T RATIO = 0.80

Attachments

PAGE 1
Continued

Issue No.: 6

Form Date: 10/18/2004

QD-AW3F055

ISO 9001:2000 CERTIFIED

Date: 07/JUN/2011

CUSTOMER NAME: CONSOLIDATED PIPE & SUPPLY

Customer Order Number S13-10966

MFG Order Number S109855

HEAT	C	MN	P	S	CB	SI	TI	CU	NI	MO	CR	V	AL	B	N	C.E.	Coil Pipe
83204	* LINE 1						EDITION REFERENCE 4						Yield Strength by Strap				
H=	0.050	1.270	0.013	0.003	0.064	0.174	0.016	0.030	0.010	0.010	0.030	0.004	0.055	.0003	.0062	0.125	0022
P=	0.049	1.277	0.012	0.006	0.062	0.153	0.014	0.025	0.024	0.006	0.017	0.005	0.052	.0000	.0000	0.121	20/20
Y/T RATIO = 0.79																	
83206	* LINE 1						EDITION REFERENCE 4						Yield Strength by Strap				
H=	0.060	1.230	0.010	0.003	0.059	0.185	0.017	0.020	0.010	0.010	0.030	0.004	0.039	.0003	.0073	0.133	0010
P=	0.057	1.233	0.009	0.006	0.062	0.161	0.015	0.025	0.026	0.007	0.015	0.005	0.038	.0000	.0000	0.127	15/31
M=Weld Ten. 79.7 ksi Ten. 87.8 ksi Yield 70.9 ksi %EL 27.0 RB 94 Hydro: 1270 Psi RUN: 39-0																	
Y/T RATIO = 0.81																	
83206	* LINE 1						EDITION REFERENCE 4						Yield Strength by Strap				
H=	0.060	1.230	0.010	0.003	0.059	0.185	0.017	0.020	0.010	0.010	0.030	0.004	0.039	.0003	.0073	0.133	0011
P=	0.056	1.239	0.010	0.006	0.062	0.164	0.014	0.014	0.024	0.007	0.009	0.005	0.039	.0000	.0000	0.126	/
M=Weld Ten. 00.0 ksi Ten. 00.0 ksi Yield 00.0 ksi %EL 00.0 RB 00 Hydro: 1270 Psi RUN: 39-0																	
Y/T RATIO = 0.00																	
83207	* LINE 1						EDITION REFERENCE 4						Yield Strength by Strap				
H=	0.050	1.240	0.009	0.004	0.070	0.184	0.018	0.040	0.010	0.010	0.030	0.004	0.045	.0003	.0066	0.124	0020
P=	0.063	1.258	0.009	0.007	0.071	0.164	0.015	0.043	0.029	0.007	0.014	0.006	0.046	.0000	.0000	0.136	15/29
M=Weld Ten. 81.2 ksi Ten. 91.8 ksi Yield 74.8 ksi %EL 33.0 RB 95 Hydro: 1270 Psi RUN: 39-0																	
Y/T RATIO = 0.81																	
83207	* LINE 1						EDITION REFERENCE 4						Yield Strength by Strap				
H=	0.050	1.240	0.009	0.004	0.070	0.184	0.018	0.040	0.010	0.010	0.030	0.004	0.045	.0003	.0066	0.124	0020
P=	0.062	1.250	0.009	0.007	0.071	0.162	0.015	0.043	0.029	0.007	0.013	0.006	0.046	.0000	.0000	0.134	06/12
Y/T RATIO = 0.82																	

Attachments

ISO 9001:2000 CERTIFIED

CUSTOMER NAME: CONSOLIDATED PIPE & SUPPLY

Customer Order Number S13-10966

MFG Order Number S109855

Date: 07/JUN/2011

HEAT	C	MN	P	S	CB	SI	TI	CU	NI	MO	CR	V	AL	B	N	C.E.	Coil / Pipe
84424	* LINE 1						EDITION REFERENCE 4						Yield Strength by Strap				
H=	0.060	1.250	0.010	0.002	0.062	0.187	0.017	0.020	0.010	0.010	0.030	0.004	0.039	.0003	.0052	0.134	0016
P=	0.055	1.278	0.010	0.006	0.064	0.174	0.015	0.020	0.029	0.006	0.017	0.006	0.036	.0001	.0000	0.129	15/30
M=Weld Ten. 81.0 ksi Ten. 90.6 ksi Yield 72.5 ksi %EL 33.5 RB 94 Hydro: 1270 Psi RUN: 39-0																	
Y/T RATIO = 0.80																	
84424	* LINE 1						EDITION REFERENCE 4						Yield Strength by Strap				
H=	0.060	1.250	0.010	0.002	0.062	0.187	0.017	0.020	0.010	0.010	0.030	0.004	0.039	.0003	.0052	0.134	0017
P=	0.052	1.274	0.009	0.006	0.059	0.170	0.014	0.019	0.027	0.006	0.015	0.005	0.033	.0000	.0000	0.124	/
M=Weld Ten. 00.0 ksi Ten. 00.0 ksi Yield 00.0 ksi %EL 00.0 RB 00 Hydro: 1270 Psi RUN: 39-0																	
Y/T RATIO = 0.00																	
84430	* LINE 1						EDITION REFERENCE 4						Yield Strength by Strap				
H=	0.050	1.220	0.010	0.003	0.063	0.193	0.017	0.020	0.010	0.010	0.040	0.003	0.044	.0003	.0046	0.123	0019
P=	0.054	1.258	0.011	0.006	0.068	0.180	0.015	0.025	0.029	0.008	0.018	0.005	0.046	.0001	.0000	0.127	15/29
M=Weld Ten. 80.6 ksi Ten. 92.4 ksi Yield 68.9 ksi %EL 30.5 RB 94 Hydro: 1270 Psi RUN: 39-0																	
Y/T RATIO = 0.75																	
84430	* LINE 1						EDITION REFERENCE 4						Yield Strength by Strap				
H=	0.050	1.220	0.010	0.003	0.063	0.193	0.017	0.020	0.010	0.010	0.040	0.003	0.044	.0003	.0046	0.123	0019
P=	0.050	1.248	0.010	0.006	0.065	0.178	0.015	0.024	0.028	0.007	0.019	0.005	0.045	.0000	.0000	0.122	07/15
Y/T RATIO = 0.82																	

Attachments

PAGE 3
Continued

Issue No.: 6

Form Date: 10/18/2004

QD-AW3F055

ISO 9001:2000 CERTIFIED

Date: 07/JUN/2011

Customer Order Number: S13-10966 | MFG Order Number: S109855

CUSTOMER NAME: CONSOLIDATED PIPE & SUPPLY

Charpy "V" Notch Tests

HEAT NO.	SIZE	TEMP	Energy (FT./LBS.)			AVG.	Fracture Appearance (% Shear Area)			AVG.	Line #
83204 -	.500	32	66.0	57.0	51.0	58.0	100	100	100	100.0	1
83206 -	.500	32	61.0	60.0	64.0	61.7	100	100	100	100.0	1
83207 -	.500	32	54.0	58.0	53.0	55.0	100	100	100	100.0	1
84424 -	.500	32	60.0	56.0	47.0	54.3	100	100	100	100.0	1
84430 -	.500	32	57.0	55.0	60.0	57.3	100	100	100	100.0	1
						ALL HEAT AVERAGE = 57.3				100.0	

Legend Analyses:

A-Z - Additional Testing
H - Heat Analysis
P - Product Analysis
M- Mechanical Properties
R - Retest
L - Longitudinal
T - Transitional
W - Weld Line

Hydrostatic Test: OK
Flattening Test: OK

EDITION REFERENCE 1: API 5L 41ST EDITION 4/1/1995
EDITION REFERENCE 2: API 5L 42ND EDITION 7/1/2000
EDITION REFERENCE 3: API 5L 43RD EDITION 10/4/2004
EDITION REFERENCE 4: API 5L 44TH EDITION 10/1/2008
EDITION REFERENCE 5: ASTM/ASME ANNUAL BOOK OF STANDARDS SECT.1, VOL 01.01

* Manufactured and Melted in the USA.

We hereby certify that the above figures are correct as contained in the records of this company, and that the pipe were manufactured, tested and inspected in compliance with the Latest edition of the applicable specification, in Birmingham, Alabama, U.S.A.

James B. Baird
James B. Baird
Manager of Quality Assurance - Steel Pipe

Atlas ABC Corp (Atlas Tube Chicago)
1855 East 122nd Street
Chicago, Illinois, USA
60633
Tel: 773-646-4500
Fax: 773-646-6128

Atlas Tube
JMC STEEL GROUP

Ref.B/L: 80474820
Date: 03.20.2012
Customer: 1281

MATERIAL TEST REPORT

Sold to

Consolidated Pipe & Supply Co
PO Box 2472
BIRMINGHAM AL 35204
USA

Shipped to

Consolidated Pipe #3 Yard
801 LaBarge Drive
BESSEMER AL 35022
USA

Material: 20.000x625x42'0"D(1x1).A2523 **Material No:** R20000625 **Made In:** USA
Melted in: USA

Sales order: 701043 **Purchase Order:** S13-20354

Heat No	C	Mn	P	S	Si	Al	Cu	Cb	Mo	Ni	Cr	V	Ti	B	N
D40620	0.190	0.770	0.013	0.005	0.016	0.050	0.020	0.004	0.002	0.010	0.030	0.001	0.001	0.000	0.007

Bundle No	PCs	Yield	Tensile	Eln.2in	Certification	CE: 0.33
M900493818	1	063298 Psi	081487 Psi	37 %	ASTM A252-10 GR 3	

Material Note:
Sales Or.Note: ALSO MEETS ASTM A500-10 GRADE B&C

Material: 20.000x625x42'0"D(1x1).A2523 **Material No:** R20000625 **Made In:** USA
Melted in: USA

Sales order: 701043 **Purchase Order:** S13-20354

Heat No	C	Mn	P	S	Si	Al	Cu	Cb	Mo	Ni	Cr	V	Ti	B	N
D40620	0.190	0.770	0.013	0.005	0.016	0.050	0.020	0.004	0.002	0.010	0.030	0.001	0.001	0.000	0.007

Bundle No	PCs	Yield	Tensile	Eln.2in	Certification	CE: 0.33
M900493817	1	063298 Psi	081487 Psi	37 %	ASTM A252-10 GR 3	

Material Note:
Sales Or.Note: ALSO MEETS ASTM A500-10 GRADE B&C

Material: 20.000x625x42'0"D(1x1).A2523 **Material No:** R20000625 **Made In:** USA
Melted in: USA

Sales order: 701043 **Purchase Order:** S13-20354

Heat No	C	Mn	P	S	Si	Al	Cu	Cb	Mo	Ni	Cr	V	Ti	B	N
D40620	0.190	0.770	0.013	0.005	0.016	0.050	0.020	0.004	0.002	0.010	0.030	0.001	0.001	0.000	0.007

Bundle No	PCs	Yield	Tensile	Eln.2in	Certification	CE: 0.33
M900493816	1	063298 Psi	081487 Psi	37 %	ASTM A252-10 GR 3	

Material Note:
Sales Or.Note: ALSO MEETS ASTM A500-10 GRADE B&C

Authorized by Quality Assurance:
The results reported on this report represent the actual attributes of the material furnished and indicate full compliance with all applicable specification and contract requirements.
D1.1 method.

Steel Tube Institute

Metals Service Center Institute

Atlas ABC Corp (Atlas Tube Chicago)
1855 East 122nd Street
Chicago, Illinois, USA
60633
Tel: 773-646-4500
Fax: 773-646-6128

Atlas Tube
JMC STEEL GROUP

Ref.B/L: 80474820
Date: 03.20.2012
Customer: 1281

MATERIAL TEST REPORT

Sold to

Consolidated Pipe & Supply Co
PO Box 2472
BIRMINGHAM AL 35204
USA

Shipped to

Consolidated Pipe #3 Yard
801 LaBarge Drive
BESSEMER AL 35022
USA

Material: 20.000x625x42'0"0(1x1).A2523 **Material No:** R20000625 **Made in:** USA **Melted in:** USA

Sales order: 701043 **Purchase Order:** S13-20354

Heat No	C	Mn	P	S	Si	Al	Cu	Cb	Mo	Ni	Cr	V	Ti	B	N
D40620	0.190	0.770	0.013	0.005	0.016	0.050	0.020	0.004	0.002	0.010	0.030	0.001	0.001	0.000	0.007

Bundle No	PCs	Yield	Tensile	Eln.2in	Certification	CE: 0.33
M900493815	1	063298 Psi	081487 Psi	37 %	ASTM A252-10 GR 3	

Material Note:
Sales Or.Note: ALSO MEETS ASTM A500-10 GRADE B&C

Material: 20.000x625x30'0"0(1x1).A2523 **Material No:** R200006253000-A252 **Made in:** USA **Melted in:** USA

Sales order: 701043 **Purchase Order:** S13-20354

Heat No	C	Mn	P	S	Si	Al	Cu	Cb	Mo	Ni	Cr	V	Ti	B	N
M28688	0.200	0.800	0.010	0.010	0.015	0.052	0.040	0.005	0.004	0.010	0.030	0.001	0.001	0.000	0.003

Bundle No	PCs	Yield	Tensile	Eln.2in	Certification	CE: 0.35
M900480354	1	059102 Psi	075245 Psi	40 %	ASTM A252-10 GR 3	

Material Note:
Sales Or.Note:

Authorized by Quality Assurance:
The results reported on this report represent the actual attributes of the material furnished and indicate full compliance with all applicable specification and contract requirements.
Steel Tube Institute D1.1 method.

Metals Service Center Institute

7/9/2011

CERTIFIED REPORT OF CHEMICAL ANALYSIS AND MECHANICAL TESTS

TESTING CERT # 2914.01

ArcelorMittal

SOLD TO	VENDOR
NAYLOR PIPE 1230 EAST 92ND STREET CHICAGO IL	ArcelorMittal Riverdale LLC. 13500 South Perry Avenue Riverdale, IL 60827

SHIP TO	ORDER INFORMATION
NAYLOR PIPE C/O NATL PROC #2 C/O NATIONAL PROCESSING 4506 W. CLINE AVE. PLANT 2 EAST CHICAGO IN	PO#: 55339 LoadID # 01608977 SO#: 520551 Carrier: Sowka Express Shipped: 7/8/2011 Invoice # 0500074832

CERTIFIED DIMENSIONAL INFORMATION

Heat	Coil	Thickness (in)	Width (in)	Weight (tons)	Reduction Ratio
B32265	848023	0.128	36.750	17.4	94.09% (17:1)

PRODUCT INFORMATION

Grade	Part Number	Comments
SAE 1022 MOD4	HB1283675-03	

This material was melted and manufactured in the USA. All products are strand cast and free of mercury or radioactive elements. Elongation based on 2" gage length.

MECHANICAL / PHYSICAL TEST RESULTS*

Heat	Coil	Yield (ksi)	Tensile (ksi)	El (%)	Dir	N-Value	N-Range	Hardness	Ft-lbs	°F	Size	Dir

* Material tested in accordance with ISO 17025 by an accredited lab.

CHEMICAL TEST RESULTS

Heat	C	Mn	P	S	Si	Cu	Ni	Cr	Mo	Cb	V	Al
B32265	.20	.78	.014	.003	.05	.06	.02	.04	.00	.001	.006	.033

N	Sn	B	Ti	Ca	Sb
.0056	.003	.0000	.0030	.0010	.0010

Chemical analysis was performed by ArcelorMittal Riverdale, Inc. in accordance with the Current Version of ASTM E415 and E1019

We hereby certify the above is correct as contained in the records of the corporation. All tests peformed to the current standard to date unless otherwise noted. Uncertainties of measurements estimated and are available upon request. These results relate only to the items tested. Test results marked with an asterisk (*) were reported by an external accredited lab.

Peter Gaudreau
Metallurgist

KIEH

METALLURGICAL SERVICES
(708) 544-8811 544-8820 FAX

Laboratory:
837 MANNHEIM RD.
BELLWOOD, IL 60104

Date received 14-Oct-2011
Report 13-Oct-2011
111 41060 a of b pages

Naylor Pipe Company
1230 E. 92nd St.
Chicago, IL 60619-7997

Account 1302

P.O. 4324

Attn : James Martin

our 32th year est. 1979

Test report /

Sample identity	Y.S. lbs/in^2	T.S. lbs/in^2	%E 2"
B32637 10Gax36" MITTAL B32265	51,000	72,500	30.5
ASTM A139 grB min. requirements	35,000	60,000	21.50

This samples reported properties conform to the requirements of an ASTM A139 grB material.

IATROPOL
PROFESSIONAL ENGINEER
REGISTRATION

Mechanical:ASTM E8/A370 Y.S.0.2%offset []trans. *broke out of g.l. ¦1"g.l.

2/4/2011

CERTIFIED REPORT OF CHEMICAL ANALYSIS AND MECHANICAL TESTS

ACCREDITED
TESTING CERT # 2914.01

ArcelorMittal

SOLD TO	VENDOR
NAYLOR PIPE 1230 EAST 92ND STREET CHICAGO IL	ArcelorMittal Riverdale, Inc. 13500 South Perry Avenue Riverdale, IL 60827

SHIP TO	ORDER INFORMATION
NAYLOR PIPE C/O NATL PROC #2 C/O NATIONAL PROCESSING 4506 W. CLINE AVE. PLANT 2 EAST CHICAGO IN	PO#: 55160 Invoice # 0500061896 SO#: 489829 Carrier Sowka Express Shipped: 12/13/2010

DIMENSIONAL INFORMATION

Heat	Coil	Thickness (in)	Width (in)	Weight (tons)	Reduction Ratio
B30004	830663	0.178	36.750	16	91.78% (12:1)
B30004	830661	0.178	36.750	15.9	91.78% (12:1)
B30004	830660	0.178	36.750	15.6	91.78% (12:1)

PRODUCT INFORMATION

Grade	Part Number	Comments
ASTM A139 GRD B MOD1	HB1783675-03	

We certify that this material meets the provisions of the 'Buy America' program. This material was melted and manufactured in the USA. All products are strand cast and free of mercury or radioactive elements. Elongation based on 2" gage length.

MECHANICAL / PHYSICAL TEST RESULTS *

Heat	Coil	Yield (ksi)	Tensile (ksi)	El (%)	Dir	N-Value	N-Range	Hardness	Ft-lbs	°F	Size	Dir

* Material tested in accordance with ISO 17025 by an accredited lab.

CHEMICAL TEST RESULTS (%wt)

Heat	C	Mn	P	S	Si	Cu	Ni	Cr	Mo	Cb	V	Al
B30004	.22	.72	.008	.006	.03	.03	.01	.02	.00	.000	.003	.036

N	Sn	B	Ti	Ca	Sb
.0065	.001	.0003	.0010	.0010	.0000

Chemical analysis was performed by ArcelorMittal Riverdale, Inc. in accordance with the Current revision of ASTM E415 and E1019.

We hereby certify the above is correct as contained in the records of the corporation. All tests peformed to the current standard to date unless otherwise noted. Uncertainties of measurements estimated and are available upon reques These results relate only to the items tested. Test results marked with an asteris (*) were reported by an external accredited lab.

Peter Gaudreau
Metallurgist

KIEH

METALLURGICAL SERVICES
(708) 544-8811 544-8820 FAX

Laboratory:
837 MANNHEIM RD.
BELLWOOD, IL 60104

Date 25-Nov-2011
received 23-Nov-2011
Report 111 47050 a of a pages

Naylor Pipe Company
1230 E. 92nd St.
Chicago, IL 60619-7997

Account 1302

P.O. 4343

Attn : James Martin

our 32th year est. 1979

Test report /

Sample identity	Y.S. lbs/in^2	T.S. lbs/in^2	%E 2"
E28511 3/16x36" MITTAL B30004	46,900	71,000	30.0
Minimum requirements of an ASTM:			
A139 grB	35,000	60,000	24.00
A252 gr2	35,000	60,000	20.00
A252 gr3	35,000	60,000	16.00

This samples reported properties conform to the requirements of an ASTM:
A139 grB / A252 gr2 / A252 gr3 material.

CHRISTOS IATROPULOS
PROFESSIONAL ENGINEER
REGISTRATION

Mechanical:ASTM E8/A370 Y.S.0.2%offset []trans. *broke out of g.1. ¦1"g.1.